



**IBER
SEN
SOR** **2024** **13° CONGRESO
IBEROAMERICANO
DE SENSORES**
Buenos Aires
21 al 24 octubre

ACTAS DEL 13° CONGRESO IBEROAMERICANO DE SENSORES

Proceedings of the XIII Ibero American Congress of Sensors

Anais do 13° Congresso Ibero Americano de Sensores

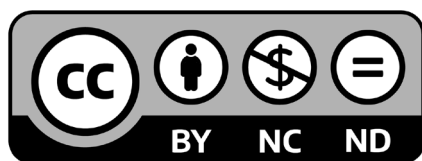


INTI Instituto Nacional
de Tecnología Industrial



Secretaría de
Industria y Comercio
Ministerio de Economía





Esta obra se distribuye bajo una licencia Creative Commons Atribución/Reconocimiento-NoComercial-SinDerivados 4.0 Internacional

<https://creativecommons.org/licenses/by-nc-nd/4.0/>

Actas del XIII Congreso Iberoamericano de Sensores - Ibersensor 2024 : proceedings of the XIII Ibero-American Congress of Sensors - Ibersensor 2024 - Anais do 13º Congresso Ibero-Americano de Sensores - Ibersensor 2024 / Editado por Laura Malatto ; Alex Lozano ; Mijal Mass. - 1a ed - San Martín : Instituto Nacional de Tecnología Industrial - INTI, 2024.

Libro digital, PDF

Archivo Digital: descarga y online

ISBN 978-950-532-547-4

1. Nanotecnología. I. Malatto, Laura, ed. II. Lozano, Alex, ed. III. Mass, Mijal, ed. IV. Título.

CDD 620.5



ACTAS DEL 13º CONGRESO IBEROAMERICANO DE SENSORES

Proceedings of the XIII Ibero American Congress of Sensors
Anais do 13º Congresso Ibero Americano de Sensores

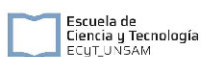
Con el apoyo de



Sponsors



Avales institucionales



Organizan



Chair: Mijal Mass

Co-chair: Laura Malatto

Co-chair: Alex Lozano

COMITÉ ORGANIZADOR | Organizing Committee | Comitê Organizador

- Mijal Mass [Chair], Instituto Nacional de Tecnología Industrial (INTI), AR
- Laura Malatto [Co-chair], Instituto Nacional de Tecnología Industrial (INTI), AR
- Alex Lozano [Co-chair], Instituto Nacional de Tecnología Industrial (INTI), AR
- Diego Brengi, Instituto Nacional de Tecnología Industrial (INTI), AR
- Paola Colombo, Instituto Nacional de Tecnología Industrial (INTI), AR
- Gabriel Ybarra, Instituto Nacional de Tecnología Industrial (INTI), AR
- María Julieta Comin, Instituto Nacional de Tecnología Industrial (INTI), AR
- María de los Angeles Cappa, Instituto Nacional de Tecnología Industrial (INTI), AR
- María Eugenia Suárez, Instituto Nacional de Tecnología Industrial (INTI), AR
- Karina Bertrand, Instituto Nacional de Tecnología Industrial (INTI), AR
- Gloria Longinotti, Instituto Nacional de Tecnología Industrial (INTI), AR
- Eliana Mangano, Instituto Nacional de Tecnología Industrial (INTI), AR

COMITÉ PERMANENTE | Permanent Committee | Comitê Permanente

- Alfredo Gonzalez Fernandez, Instituto Nacional de Astrofísica, Óptica y Electrónica (INAOE), MX
- Antônio Carlos Seabra, Universidade de São Paulo, BR
- Carlos Domínguez Horna, Instituto de Microelectrónica de Barcelona (IMB-CNM), CSIC, ES
- Cecilia Jiménez Jorquera, Instituto de Microelectrónica de Barcelona (IMB-CNM), CSIC, ES
- Elizabeth Sánchez, Universidad Técnica Federico Santa María, CL
- Enrique Ernesto Valdés Zaldivar, Universidad de Oviedo-DIEECS, ES
- Francisco Valdés Perezgasga, Instituto Tecnológico de la Laguna-DIEE, MX
- Fredy Segura-Quijano, Universidad de los Andes, CO
- Hector Gómez, Universidad de la República-IFFC, UY
- Idalia Ramos, Universidad de Puerto Rico en Humacao, PR
- Jahir Orozco Holguín, Universidad de Antioquia (UA), CO
- Juan Pablo Agusil Antonoff, Instituto de Microelectrónica de Barcelona (IMB-CNM), ES
- Jorge José Santiago-Avilés, University of Pennsylvania, ESE, US
- José Antonio Plaza, Instituto de Microelectrónica de Barcelona (IMB-CNM), CSIC, ES
- José Antonio Rodríguez, Universidad de la Habana-Facultad de Física, CU
- Julián Alonso Chamarro, Grup de Sensors i Biosensors, Universitat Autònoma de Barcelona, ES
- Julio Enrique Duarte, Universidad Pedagógica y Tecnológica de Colombia, CO
- Manel del Valle, Universitat Autònoma de Barcelona, ES

- Manuela Vieira, Instituto Superior de Engenharia de Lisboa-ISEL, PT
- María Gabriela Calle, Universidad del Norte, CO
- Maria Teresa Gomes, Universidade de Aveiro, PT
- Mariano Aceves, Instituto Nacional de Astrofísica, Óptica y Electrónica (INAOE), MX
- Mario Ricardo Góngora-Rubio, Instituto de Pesquisas Tecnológicas, BR
- Marta Veríssimo, Universidade de Aveiro, PT
- Olimpia Arias de Fuentes, Universidad de la Habana, IMRE, CU
- Paula Louro, ISEL/IPL y CTS-UNINOVA, PT

COMITÉ CIENTÍFICO | Scientific Committee | Comitê Científico

- Alfredo Gonzalez Fernandez, Instituto Nacional de Astrofísica, Óptica y Electrónica (INAOE), MX
- António Carlos Seabra, Universidade de São Paulo, BR
- Carlos Domínguez Horna, Instituto de Microelectrónica de Barcelona (IMB-CNM), CSIC, ES
- Cecilia Jiménez Jorquera, Instituto de Microelectrónica de Barcelona (IMB-CNM), CSIC, ES
- Elizabeth Sánchez, Universidad Técnica Federico Santa María, CL
- Enrique Ernesto Valdés Zaldivar, Universidad de Oviedo-DIEECS, ES
- Francisco Valdés Perezgasga, Instituto Tecnológico de la Laguna-DIEE, MX
- Fredy Segura-Quijano, Universidad de los Andes, CO
- Hector Gómez, Universidad de la República-IFFC, UY
- Idalia Ramos, Universidad de Puerto Rico en Humacao, PR
- Jahir Orozco Holguín, Universidad de Antioquia (UA), CO
- Jorge José Santiago-Avilés, University of Pennsylvania, ESE, US
- José Antonio Plaza, Instituto de Microelectrónica de Barcelona (IMB-CNM), CSIC, ES
- José Antonio Rodríguez, Universidad de la Habana-Facultad de Física, CU
- Juan Pablo Agusil Antonoff, Instituto de Microelectrónica de Barcelona (IMB-CNM), ES
- Julián Alonso Chamarro, Grup de Sensors i Biosensors, Universitat Autònoma de Barcelona, ES
- Julio Enrique Duarte, Universidad Pedagógica y Tecnológica de Colombia, CO
- Manel del Valle, Universitat Autònoma de Barcelona, ES
- Manuela Vieira, Instituto Superior de Engenharia de Lisboa-ISEL, PT
- María Gabriela Calle, Universidad del Norte, CO
- Maria Teresa Gomes, Universidade de Aveiro, PT
- Mariano Aceves, Instituto Nacional de Astrofísica, Óptica y Electrónica (INAOE), MX
- Mario Ricardo Góngora-Rubio, Instituto de Pesquisas Tecnológicas, BR
- Marta Veríssimo, Universidade de Aveiro, PT
- Olimpia Arias de Fuentes, Universidad de la Habana, IMRE, CU
- Paula Louro, ISEL/IPL y CTS-UNINOVA, PT

ÍNDICE | Index | Índice

Prefacio

Preface | Prefácio

PÁG.
13

Presentaciones Plenarias

Plenary Presentations | Apresentações Plenárias

PÁG.
16

Galo J. A. A. Soler-Illia

Escuela de Bio y Nanotecnologías, Instituto de Nanosistemas, Universidad Nacional de General San Martín. Argentina

“Mesoporous thin films: exploiting new nanospace features for electrochemical and optical sensing”

17

Eloi Ramon

Instituto de Microelectrónica de Barcelona (IMB-CNM, CSIC). España

“Organic Microelectronics for Transient Smart Devices: A New Opportunity for More Sustainable Electronics”

18

José Antonio Plaza

Instituto de Microelectrónica de Barcelona (IMB-CNM, CSIC). España

“Intracellular chips for cell mechanics”

19

Nicolás Calarco

Grupo de Microelectrónica, Departamento de Ingeniería, Universidad Católica del Uruguay (DIE-UCU). Uruguay

“Circuitos Integrados Fotodetectores, Aplicaciones Alternativas y Posibilidades de Fabricación”

20

Cecilia Jiménez

Instituto de Microelectrónica de Barcelona (IMB-CNM, CSIC). España

“SMART multi-sensor systems enabling real time water quality assessment and early prediction of pollutants”

21

Adão Villaverde

Escola Politécnica da Pontifícia Universidade Católica do RS - PUCRS

Assuntos Estratégicos de Semicondutores no Parque Tecnológico da PUCRS-TECNO PUC. Brasil

“Os semicondutores no mundo, a sua desconcentração e como a região LATAM pode ser incorporada na cadeia global”

23

Edelweis Ritt

CEITEC S.A – Semiconductors. Brasil

“CEITEC, the SiC wafer fab in South America”

25

Mariano Real	26
Departamento de Metrología Cuántica, Instituto Nacional de Tecnología Industrial (INTI). Argentina	
“Uso del efecto Hall cuántico como patrón de resistencia eléctrica”	
Alex Lozano	27
Centro de Micro y Nanoelectrónica del Bicentenario, Dirección Técnica de Micro y Nanotecnologías, INTI. Argentina	
“Micro y Nanotecnología en INTI - Desarrollos y aplicaciones en el área de Sensores”	
Manel Del Valle	28
Grup de Sensors i Biosensors, Universitat Autònoma de Barcelona. España	
“Lenguas electrónicas: sensores, materiales y aplicaciones”	
Marcela Rodríguez	29
Departamento de Físicoquímica, Facultad de Ciencias Químicas, Universidad Nacional de Córdoba (INFIQC). Argentina	
“Sistemas “Nano-Lego”: el juego de la inspiración en el diseño de biosensores”	

Presentaciones Orales y Pósters

PÁG.
30

Oral Presentations and Posters | Apresentações Oraís e Pôsteres



Sensores de ondas acústicas

Acoustic wave sensors
Sensores de ondas acústicas

Microsensores y microactuadores MEMS

MEMS, microsensors and microactuators
Microsensores e microatuadores MEMS

Sensores físicos

Physical sensors
Sensores físicos

- Optimización de forma y fabricación de transductores ultrasónicos de PVDF 32
- Microsensor for tear viscosity analysis: a novel approach for its clinical use 36
- Diseño de Sensores Ópticos mediante Método Inverso: Estructuras Fotónicas 1D Optimizadas por Redes Neuronales 39
- Love Surface Acoustic Wave-based-Sensor : Characterization of Microfluidic Biosensing System 43
- Liberation of Functionalized Chips and Cells from various Surfaces 46
- Correlation between structural quality and magnetotransport properties in planar Hall effect sensors 49
- Effect of underlayers and deposition under external magnetic field on the anisotropy of Ni₈₀Fe₂₀ and Co₉₀Fe₁₀ thin films for sensors 52



- Testigo de corte de cadena de frío para la visualización de la exposición a 55
temperaturas predeterminadas
- Dispositivo de evidencia de congelamiento 57
- Microtomografías basadas en sensores de imagen CMOS y algoritmos de 58
reconstrucción convencionales

2

Microsistemas analíticos integrados y lab-on-a-chip (LOC)

Analytical integrated microsystems and lab-on-a-chip (LOC)

Microsistemas analíticos integrados e lab-on-a-chip (LOC)

Sensores microfluídicos

Microfluidic sensors

Sensores microfluídicos

- Microanalizadores automáticos modulares para la monitorización y control 62
del proceso de purificación hidrometalúrgica de zinc
- A análise por injeção em fluxo e sensores 65
- Simulación numérica y caracterización de una plataforma microfluídica 69
generadora de gotas
- Automatic microanalyzer for cobalt monitoring in the hydrometallurgical 73
production of zinc
- Microanalizador para la monitorización del ion Cobre (II) en el proceso 75
hidrometalúrgico de obtención de Zinc
- Automatic microanalyzer for cadmium monitoring in the hydrometallurgical 79
production of zinc
- Point-of-care analyser for potentiometric determination of ammonium ion in 81
whole blood
- Analytical microsystem with pervaporation stage for ammonium monitoring 84
in industrial wastewater
- Controlled insertion of silver nanoparticles in LbL nanostructures: fine-tuning 86
the sensing units of an impedimetric e-tongue
- Development of microfluidic biosensors for studying epithelial cells 90
processes by impedance spectroscopy
- Optofluidic set up for production and measurement of Sodium-Alginate 93
microdroplets
- Proyectos de Microfluídica en el Departamento de Micro y Nanotecnología- 97
CNEA-CAC
- Oil spacer for droplet frequency control in 3D printed microfluidic devices 100
coupled to contactless conductivity detectors

3

Biosensores

Biosensors

Biosensores

- Gold nanostars-based plasmonic platform for photoelectrochemical 104
detection of C-reactive protein
- Portable biosensing device for in vitro diagnostic of pathogenic bacteria 106
- Traffic light-based point-of-care test for the rapid stratification of fever syndromes 110
- Laccase electrochemical biosensor based on carbon nanotubes modified 114
with diazonium salt
- Coacervates Improve Nucleotide Biosensors through Sequestration 118
- Development of an electrochemical immunosensor for SARS-CoV-2 122
detection and clinical validation
- Desarrollo de biosensores basados en ácidos nucleicos para la detección de genes 126
implicados en la degradación de xenobióticos en ambientes contaminados
- Avances y desafíos en el desarrollo de un aptasensor electroquímico para atrazina 130
- An Automated Low-Cost SPR Sensor for Glyphosate Detection in Potable Water 133
- Development of a real-time toxicity biosensor based on bacterial motility 137
- Rapid screening test for Streptococcus agalactiae neonatal infections 141
combining portable PCR and electrochemical genosensing

4

Sensores químicos

Chemical sensors

Sensores químicos

Sensores electroquímicos

Electrochemical sensors

Sensores eletroquímicos

Sensores optoquímicos

Optochemical sensors

Sensores optoquímicos

- Detección de drogas de abuso empleando matrices de sensores voltamétricos 146
y principios de lengua electrónica
- An IoT Electrochemical Sensor based on a Conductive Polymer-modified 150
Electrode for Levofloxacin Determination
- Electrochemical performance of a hybrid material of Ce(OH)CO₃ and 154
carbon nanotubes
- Sensor electroquímico compósito de grafito modificado con quitosano y 158
azure-A para el monitoreo in-situ de la frescura en pescado
- A laser biospeckle sensor applied to processes in the fishing industry: a highly 162
sensitive monitor solution

- A proof of concept for a porous silicon-polymer hybrid sensor 165
- Fluorescent Probe-Based Detection and Quantification of Polylactic Acid (PLA) Nanoparticles 169
- Optimización de un sensor no enzimático para la determinación impedimétrica de glucosa salival 172
- Electrodo de grafito modificado para la detección electroquímica de glifosato en agua 176
- Mejoras en la Producción Agrícola y Reducción del Impacto Ambiental en la Industria Agrícola en Suelos de Diferente Tipología Mediante el uso de Sondas de Nutrición 180
- Hacia un Sensor Electroquímico Basado en Carbohidratos de Leishmania 184
- Sensor electroquímico para la evaluación de la corrosión de estructuras de hormigón armado 188
- Biofuncionalización de electrodos de carbono serigrafados para la detección de arsénico (III) 191
- A Simplified Do-It-Yourself Protocol for Manufacturing Dual-Detection Paper-Based Analytical Devices for Saliva-Based Diagnostics 195
- Use of Peanut Shell Biochar in the Formulation of Inks for Screen-Printed Electrodes 199
- Enhanced performance of plastic electrodes doped with chemically activated biochar from peanut shells 202
- Towards new colorimetric detection strategies to detect loop-mediated isothermal amplification products in the Point-of-Care 205

5

Diseño y tecnología de sensores
 Design and technology of sensors
 Design e tecnologia de sensores

- Study of the maximum 2D-Silicon-based particle size that can be internalized by living cells 209
- Piezoelectric impact sensor and infrared array sensor: comparative study for precision seeders 213
- Challenges in bottom cladding planarization of a waveguide for electrophotonic sensors 217
- Low-cost microwave sensor for detecting the first generation of microplastic in aqueous media 221
- Elaboración de sensores finos de posición en Argentina 225
- Construcción de un dispositivo de medición de resistencia eléctrica transepitelial-endotelial (TEER) aplicable a la investigación de cultivos celulares 229
- Desarrollo de sensores solares para uso espacial 233

- Desarrollo de sensores solares para aplicaciones terrestres 237
- Diseño de un medidor de flujo “drop and play” para el monitoreo de canales de irrigación 241
- Desarrollo de un microdosímetro de estado sólido para uso en protonterapia 244
- Microfabricated heaters for thin films TCR characterization 248

6

Nuevos materiales y nanomateriales para sensores

New materials and nanomaterials for sensors

Novos materiais e nanomateriais para sensores

- Unveiling the link between morphology and humidity sensitivity in rare-earth-doped ceria nanostructures 253
- Exploration of wavelength-selective photodiodes for Si-based integrated electrophotonic sensors 257
- Síntesis no hidrolítica de ZnO como precursor para el dopaje con metales de transición en la fabricación de sensores 261
- Desarrollo de una película sensora de alta sensibilidad para gas H₂S usando SnO₂ nanoestructurado 264
- Análisis de epitaxias de Hg_{1-x}Cd_xTe obtenidas por VPE 267
- Enhancing bacterial detection with bactericidal nanostructured titania electrodes 271
- Metal nitride nanofilms applied in a microfluidic, impedimetric e-tongue for soil analyses 273
- High-entropy nitride coatings applied as sensing units in an impedimetric e-tongue 276
- Effect of mineralizing agent on the performance of ceria-based nanomaterials towards gas sensors 279
- Synthesis, structural and electrical characterization of ZnO:In₂O₃ heterostructures 283

7

Sensores en electrónica impresa

Printed electronic sensors

Sensores em eletrônica impressa

- Dispositivos electrónicos impresos mediante tecnología Inkjet basados en nanopartículas de plata 287
- Sensor resistivo flexible desarrollado con tecnologías de electrónica impresa 290
- Optimización de formulación de tintas y diseño de electrodos para impresión inkjet de sensores de pH 294
- Calefactor flexible para fluidos intravenosos obtenidos por procesos de electrónica impresa 298

8

Acondicionamiento de señales e instrumentación

Signal conditioning and instrumentation

Condicionamento de sinais e instrumentação

Sensores inteligentes y redes inalámbricas

Smart sensors and wireless networks

Sensores inteligentes e redes sem fio

- Utilización de sensor de humedad y temperatura digital para la estimación del contenido de humedad de equilibrio de la madera 303
- Mobility of AGVs supported with Visible Light Communication 307
- Non-Invasive Moisture Sensing and Classification Using Ultra-Wideband Signals 311
- Sistema de Enfriamiento para Hipotermia Cerebral Selectiva 315
- Detección de pozos en placas de ensayos mediante redes neuronales y transferencia de conocimiento 318
- Tecnología IoT para Sensores Inteligentes y Redes Inalámbricas: Un Enfoque en la Evolución hacia un Nodo de Monitoreo Ambiental 322
- Enhancing Urban Intersection Efficiency: Leveraging Visible Light Communication for Traffic Optimization 326
- Indoor Guidance in Multi-Terminal Airports through Visible Light Communication 330
- Quantification and Characterization of Microplastics Using an App and Smartphone 334

Estadísticas 2024

2024 Statistics | Estatísticas 2024

PÁG.
337

Índice de autores

Authors index | Índice de autores

PÁG.
341

PREFACIO

IBERSENSOR es un foro de la comunidad científica de habla hispana y portuguesa, que trabaja en áreas de desarrollo de sensores de todo tipo y sus aplicaciones.

Este evento bienal ha sido realizado con éxito en doce ocasiones consecutivas: la primera en 1998 en La Habana (Cuba), la segunda en 2000 en Buenos Aires (Argentina), y le siguieron 2002 Lima (Perú), 2004 Puebla (México), 2006 Montevideo (Uruguay), 2008 San Pablo (Brasil), 2010 Lisboa (Portugal), 2012 San Juan de Puerto Rico (Puerto Rico), 2014 Bogotá (Colombia), 2016 Valparaíso (Chile), 2018 Barcelona (España) y el evento de 2020 en Aveiro (Portugal) fue suspendido debido a la pandemia, realizándose luego en el año 2022.

Nos complace presentarles las Actas del 13er Congreso Iberoamericano de Sensores - Ibersensor 2024, organizado del 21 al 24 de octubre de 2024 en el Instituto Nacional de Tecnología Industrial - INTI, Buenos Aires, Argentina.

En esta edición, hemos contado con presentaciones plenarias de conferencistas reconocidos internacionalmente, presentaciones orales y pósters, visitas a laboratorios de INTI y de la Fundación Argentina de Nanotecnología - FAN, y un panel de debate en la temática de semiconductores.

Entre los temas que se profundizaron se destacan: sensores electroquímicos, químicos, físicos, optoquímicos, de ondas acústicas, en electrónica impresa, microfluídicos, inteligentes y redes inalámbricas; biosensores; diseño y tecnología de sensores; nuevos materiales y nanomateriales para sensores; microsistemas analíticos integrados y Lab-on-a-chip (LOC); acondicionamiento de señales e instrumentación; entre otros.

Agradecemos los avales institucionales y las contribuciones financieras de los sponsors y subsidios otorgados, a las autoridades del INTI, al Comité Organizador y especialmente a las múltiples áreas del Instituto que colaboraron para el desarrollo exitoso del evento.

Finalmente queremos agradecer al Comité Permanente por habernos dado la oportunidad de llevar adelante Ibersensor 2024, y a todos los conferencistas y participantes del mismo.

Deseamos poder reencontrarnos en Colombia en 2026.



Laura Malatto
Comité Organizador
Co-chair



Alex Lozano
Comité Organizador
Co-chair



Mijal Mass
Comité Organizador
Chair

PREFACE

IBERSENSOR is a forum for the Spanish and Portuguese speaking scientific community, working in the field of development and applications of sensors.

This biennial event has been successfully held on twelve consecutive occasions: the first in 1998 in Havana (Cuba), the second in 2000 in Buenos Aires (Argentina), and it was followed in 2002 Lima (Peru), 2004 Puebla (Mexico), 2006 Montevideo (Uruguay), 2008 Sao Paulo (Brazil), 2010 Lisbon (Portugal), 2012 San Juan de Puerto Rico (Puerto Rico), 2014 Bogotá (Colombia), 2016 Valparaíso (Chile), 2018 Barcelona (Spain) and the event 2020 in Aveiro (Portugal) that was suspended due to the pandemic, later taking place in 2022.

We are pleased to present to you the Proceedings of the 13th Ibero-American Congress on Sensors - Ibersensor 2024, organized from October 21 to 24, 2024 at Instituto Nacional de Tecnología Industrial - INTI, Buenos Aires, Argentina.

In this edition, we have had plenary presentations by internationally recognized speakers, oral and poster presentations, visits to laboratories of the INTI and the Fundación Argentina de Nanotecnología - FAN, and a debate panel on the topic of semiconductors.

Among the topics that were explored in depth were: electrochemical, chemical, physical, optochemical and acoustic wave sensors, printed electronics, microfluidics, smart sensors and wireless networks, biosensors, sensor design and technology, new materials and nanomaterials for sensors, microsensors and microactuators (MEMS), analytical integrated microsystems and Lab-on-a-chip (LOC), signal conditioning and instrumentation; among others.

We appreciate the institutional endorsements and the financial contributions of the sponsors and support granted, to the INTI authorities, to the Organizing Committee and especially to the multiple areas of the Institute that collaborated for the successful development of the event.

Finally, we want to thank the Permanent Committee for giving us the opportunity to carry out Ibersensor 2024, and all the speakers and participants.

We are looking forward to seeing you again in Colombia in 2026.



Laura Malatto
Comité Organizador
Co-chair



Alex Lozano
Comité Organizador
Co-chair



Mijal Mass
Comité Organizador
Chair

PREFÁCIO

IBERSENSOR é um fórum para a comunidade científica de língua espanhola e portuguesa, que atua nas áreas de desenvolvimento de sensores de todos os tipos e suas aplicações.

Este evento bienal foi realizado com sucesso em doze ocasiões consecutivas: a primeira em 1998 em La Habana (Cuba), a segunda em 2000 em Buenos Aires (Argentina), e foi seguida em 2002 Lima (Peru), 2004 Puebla (México), 2006 Montevideo (Uruguay), 2008 São Paulo (Brasil), 2010 Lisboa (Portugal), 2012 San Juan de Puerto Rico (Puerto Rico), 2014 Bogotá (Colômbia), 2016 Valparaíso (Chile), 2018 Barcelona (Espanha) e o evento 2020 em Aveiro (Portugal) foi suspenso devido à pandemia, tendo lugar posteriormente em 2022.

Temos o prazer de apresentar a vocês os Anais do 13º Congresso Ibero-Americano de Sensores - Ibersensor 2024, organizado de 21 a 24 de outubro de 2024 no Instituto Nacional de Tecnología Industrial - INTI, Buenos Aires, Argentina.

Nesta edição contamos com apresentações plenárias de palestrantes reconhecidos internacionalmente, apresentações orais e pôsteres, visitas aos laboratórios do INTI e da Fundación Argentina de Nanotecnología - FAN, e um painel de debate sobre o tema semicondutores.

Entre os temas explorados em profundidade estavam: sensores eletroquímicos, químicos, físicos, optoquímicos, de ondas acústicas, eletrônica impressa, microfluídica, sensores inteligentes e redes sem fio; biossensores; design e tecnologia de sensores; novos materiais e nanomateriais para sensores; microsistemas analíticos integrados e Lab-on-a-chip (LOC); condicionamento e instrumentação de sinais; entre outros.

Agradecemos os endossos institucionais e as contribuições financeiras dos patrocinadores e subsídios concedidos, às autoridades do INTI, ao Comitê Organizador e especialmente às múltiplas áreas do Instituto que colaboraram para o sucesso do desenvolvimento do evento.

Por último, queremos agradecer ao Comitê Permanente por nos ter dado a oportunidade de realizar o Ibersensor 2024, e a todos os oradores e participantes.

Esperamos poder nos encontrar novamente na Colômbia em 2026.



Laura Malatto
Comité Organizador
Co-chair



Alex Lozano
Comité Organizador
Co-chair



Mijal Mass
Comité Organizador
Chair



PRESENTACIONES PLENARIAS

Plenary presentations

Apresentações plenárias

MESOPOROUS THIN FILMS: EXPLOITING NEW NANOSPACE FEATURES FOR ELECTROCHEMICAL AND OPTICAL SENSING

Galo J. A. A. Soler-Illia

Instituto de Nanosistemas, Escuela de Bio y Nanotecnologías, Universidad Nacional de General San Martín
Av. 25 de Mayo 1169, 1650. San Martín.
Argentina

e-mail: gsoler-illia@unsam.edu.ar
www.unsam.edu.ar/institutos/ins

Mesoporous materials with high surface area and highly controlled mesopore diameter (2-50 nm) constitute highly tunable nanoarchitectures. The pore symmetry and surface can be finely tailored, and “decorated” with molecular, bioactive or nanoscale functions. The possibility of combining chemical synthesis, self-assembly and orthogonal surface reactions gives us a broad palette for creating exciting multiscale nanomaterials that mimic the complexity of those found in Nature.

Mesoporous thin films (MTF) provide an exciting avenue in the fields of advanced sensing and energy, by fully exploiting their architectures, functional positioning, surface processes and nanofluidics. Current synthetic and production strategies permit to easily and reproducibly prepare optical quality thin films, electrodes or photonic crystals on a variety of substrates, which makes them useful as optical or electrochemical sensors.

MTF offer a variety of sensing possibilities through molecular sieving, selective electrostatic or steric exclusion and preconcentration effects, which are a consequence of mesopore confinement and surface functionalization. Mesoporosity is an advantage for improved transport properties, tunable charge management and optical responsivity. Plus, the synthetic methods are fully compatible with processes taking place in electronics and optics industry, making MTF an interesting platform for future integrated optical and electrochemical nose devices.

We will present examples of MTF rational design and production aiming at applications in selective electrochemical and optical sensing. We will give examples on how the combination and feedback of synthesis, characterization and modeling leads to pre-designed functional electrodes or optical devices such as responsive photonic crystals, in which the final properties are programmed in their structure at several length scales and interfaces. We will demonstrate the possibilities of designing and building novel sensing devices based in nano-enabled processes such as perm-selectivity, selective condensation or confined bioaffinity. The only limit is magination.

ORGANIC MICROELECTRONICS FOR TRANSIENT SMART DEVICES: A NEW OPPORTUNITY FOR MORE SUSTAINABLE ELECTRONICS

Dr. Eloi Ramon

Researcher at the Institute of Microelectronics of Barcelona (IMB-CNM-CSIC) and leads the Integrated Circuits and Systems (ICAS) group.

España

e-mail: eloi.ramon@imb-cnm.csic.es

Over the past two decades, the rapid evolution of electronics has been driven by the development of novel materials and microfabrication technologies. These advancements have opened new avenues, particularly in the fields of additive manufacturing technologies applied to the fabrication of sustainable, flexible, and organic integrated circuits and systems.

Technological advances in additive manufacturing, printed, and organic electronics offer cost-effective, flexible, biocompatible, sustainable, and eco-friendly solutions for smart and sustainable systems. Printing technologies enable low-cost, large-area coverage with customizable designs.

Since the discovery of organic semiconducting materials 40 years ago, numerous efforts have been made to establish a new application field alongside conventional electronics. In contrast to microelectronics, which is primarily based on silicon, organic electronics has proven to be a viable technology for fabricating devices on plastic, paper, and flexible substrates. This is due to its capability for low-cost, high-volume, and high-throughput production of electronic devices. The introduction of eco-friendly and biodegradable materials to consumer flexible electronics is expected to significantly reduce environmental issues and eliminate the costs and risks associated with recycling operations.

The integration of the aforementioned technologies will pave the way for a wide range of low-cost electronic devices with acceptable lifespans for applications in healthcare, food monitoring, IoT, and many others.

INTRACELLULAR CHIPS FOR CELL MECHANICS

José Antonio Plaza

Instituto de Microelectrónica de Barcelona (IMB-CNM, CSIC)

España

e-mail: joseantonio.plaza@imb-cnm.csic.es

¿Sabes qué la parte física de tus células es tan importante como la parte bioquímica? En particular la mecánica celular es fundamental en la mayoría de procesos celulares, desde la división y migración hasta el desarrollo. Sin embargo, es un campo científico que todavía está en su infancia. Ello es debido a la falta de herramientas para su estudio. En la conferencia podremos ver si desde el campo de los chips podemos aportar este tipo de herramientas.

CIRCUITOS INTEGRADOS FOTODETECTORES, APLICACIONES ALTERNATIVAS Y POSIBILIDADES DE FABRICACIÓN

Dr. Nicolás Calarco

Grupo de Microelectrónica del Departamento de Ingeniería de la Universidad Católica del Uruguay (DIE-UCU)
Uruguay

e-mail: Nicolascalarco@gmail.com

En nuestra vida cotidiana utilizamos continuamente fotodetectores que se encuentran embebidos en prácticamente todos los dispositivos electrónicos que utilizamos. Por ejemplo, los dispositivos móviles y computadoras portátiles tienen cámaras integradas, las puertas automáticas tienen sensores de movimiento, el ratón de las computadoras tiene un sensor óptico para detectar el movimiento, entre cientos de otros ejemplos. Pero ¿cómo funcionan? ¿Para qué podemos utilizarlos? ¿Qué sucede cuando el objetivo no es específicamente capturar una imagen, sino hacer algún cálculo relacionado?

En esta charla se expondrán los principios básicos de funcionamiento de los fotodetectores integrados comerciales y sus limitaciones. Además, se explorarán otro tipo de aplicaciones donde no es del todo conveniente registrar las imágenes, particularmente aplicaciones de detección de movimiento de patrones a alta velocidad. Finalmente se mostrarán opciones de fabricación actuales para quienes estén interesados en explorar el mundo de los circuitos integrados fotodetectores.

SMART MULTI-SENSOR SYSTEMS ENABLING REAL TIME WATER QUALITY ASSESSMENT AND EARLY PREDICTION OF POLLUTANTS

Cecilia Jimenez Jorquera

Instituto de Microelectrónica de Barcelona (IMB-CNM, CSIC)

España


e-mail: Cecilia.jimenez@csic.es

We present in that talk a research line of the Institute of Microelectronics of Barcelona (IMB-CNM) devoted to the development of predictive multiparametric monitoring probes for precise control of industrial aquatic processes based on innovative smart microsensing technology. These probes are made up with different sensors developed at the IMB-CNM Clean room with microelectronic technology, which confers robustness, miniaturisation and scalability to its production. In addition, they incorporate neuromorphic intelligence that further allows to correct aging and interferences for the sensors during operation, thus minimising the need for calibration. This solution has been evaluated in several scenarios like the entrance of river water to a drinking-water plant (DWP) from the company AGBAR and a recirculating aquaculture system in close partnership with IRTA.

To build a healthy planet for all, the European Green Deal requires the EU to better monitor, report, prevent and remediate pollution of air, water, soil and consumer products. There are also new EU directives to control contamination of drinking water. These include the obligation of Member States to guarantee access to drinking water for all European citizens, and establish very high-quality standards for its supply. For all these reasons, water analysis is key to preventing environmental, health and industrial risks for sustainable development.

Sectors such as drinking water networks, aquaculture and hydroponics need to continually monitor water composition to avoid contamination, increase productivity and/or comply with increasingly strict regulations. However, commercial analytical devices are currently expensive, bulky, limited to a few parameters, and require frequent calibrations. None of them is capable of autonomously predicting and controlling variations in water quality and industrial processes, requiring instead intensive manual maintenance that increases operating costs.

In this context, we propose the development of smart multi-sensor systems fabricated with cost-effective microelectronic technology combined with powerful data fusion tools like neural networks, to achieve a predictive system for on-line water quality monitoring. This system contains multi-sensor electrochemical sensors manufactured with microelectronic technology, being therefore robust, miniaturizable and scalable in its production. They detect indicators like pH, conductivity, temperature, chlorine, and ions (nitrate, phosphate, ammonium). Sensors are combined with local neuromorphic intelligence that, in addition to its predictive capabilities, allows to correct sensor drift, aging and interferences produced during their operation: These



corrections minimize and even avoid need for calibration during long-term periods of continuous monitoring. This smart system has been evaluated in two industrial scenarios: A drinking water treatment plant and a pilot aquaculture production plant.

Results of these two applications and discussion of the technology feasibility will be presented.

Referencias:

- The European Green Deal COM (2019) 640.
- https://ec.europa.eu/commission/presscorner/detail/en/ip_20_2417
- Sensors and Actuators B: Chemical, Volume 353, 2022, 131123, ISSN 0925-4005/ Frontiers of Neuroscience, 2021, volume 15, 771480

OS SEMICONDUTORES NO MUNDO, A SUA DESCONCENTRAÇÃO E COMO A REGIÃO LATAM PODE SER INCORPORADA NA CADEIA GLOBAL

Adão Villaverde

Escola Politécnica da Pontifícia Universidade Católica do RS - PUCRS

Assuntos Estratégicos de Semicondutores no Parque Tecnológico da PUCRS - TECNOPUC

Brasil

e-mail: adaorrvillaverde@gmail.com

Estão em curso mudanças e transformações não apenas nos ativos tangíveis, mas sobretudo na forma como os indivíduos trabalham, vivem e se relacionam em sociedade. Neste contexto é que temos que compreender a importância da microeletrônica e a produção de semicondutores.


Este trabalho se propõe a refletir e propor sobre o desenvolvimento da história da humanidade, a partir de suas revoluções industriais, e sua chegada à sociedade do conhecimento, que se insere na Era do Silício.

Analisa os cenários dos semicondutores no mundo, os problemas de sua concentração nos países do Pacífico do leste, as demandas da crise pandêmica, seu potencial econômico e comercial, de soberania científico-técnica e seu caráter geopolítico.

Verifica também que tem mercado para a produção de chips chamados maduros, aqueles de escala manométrica intermediária, não no estado arte, sobretudo por sua enorme demanda.

Verifica também as políticas de Estado no Brasil sobre o tema, seus instrumentos de ação, chegando no planejamento, governança, gestão e resultados da fábrica de chips CEITEC, Centro de Excelência em Tecnologia Eletrônica Avançada, localizada em Porto Alegre, RS, Brasil, única de solução completa na América Latina. Que foi resultado de fundamentais políticas públicas, associados à academia e ao setor empresarial. E que conferiu ao sul do Brasil o domínio e a capacidade de pesquisar, desenvolver, prototipar, fabricar e comercializar chips. Aportando requisitos e elementos chaves para o Brasil e América Latina poderem manufaturar estes tão preciosos e valorizados dispositivos demandados pela época que vivemos. Porque possui uma fábrica de solução completa com sala limpa, água ultra pura, filtros de ar para controlar partículas, equipamentos para produção e recursos humanos qualificados que são demandados hoje pelo mundo inteiro. Mas que por um conjunto de razões, está desatualizada tecnologicamente, onde propõe-se sugestões e ajustes aos seus impasses, fundamentalmente um upgrade ou uma nova rota tecnológica, sobretudo pelas novas demandas, como descarbonização e transição energética, necessitando despende apenas entre 5% a 10% do que custaria fazer uma nova fábrica, com nodo tecnológico para produção dos chips maduros.

E além de tudo isto, vem o principal que seria o corte na dependência da importação destes



dispositivos, para superação do déficit tecnológico do país e da região no campo dos semicondutores. Pois o seu conhecimento, saber e expertise no tema, são os principais ativos intangíveis que região tem para transformar a inovação tecnológica em valor às organizações e à sociedade.

• Palavras-chave: Tecnologia. Semicondutores. Chips. Inovação. Expertise

CEITEC, THE SIC WAFER FAB IN SOUTH AMERICA

Edelweis Ritt

CEITEC S.A – Semiconductors

Brasil

e-mail: edelweis.ritt@ceitec-sa.com

The presentation will focus on CEITEC's strategy in power electronics and the alignment of this strategy with the New Brazilian Industry and Energy transition.

USO DEL EFECTO HALL CUÁNTICO COMO PATRÓN DE RESISTENCIA ELÉCTRICA

Mariano Real

Departamento de Metrología Cuántica, Instituto Nacional de Tecnología Industrial (INTI)
Argentina
e-mail: mreal@inti.gob.ar

Hace años que el INTI mantiene las unidades eléctricas por medio de la realización del ohm y el volt. Para ello se utilizan el efecto Hall cuántico y el efecto Josephson respectivamente.

En esta charla introduciremos el uso del efecto Hall cuántico como patrón de resistencia eléctrica, donde la realización de la unidad requiere dispositivos de sistemas bidimensionales de electrones, que resultan ser un sistema cuántico topológicamente protegido [1]. Sistemas como estos resultan ser extremadamente robustos ante cambios, ya sea de condiciones de contorno de medición como de propiedades del material. Por ello, el efecto Hall cuántico es de gran interés metrológico y también una plataforma de investigación a nivel mundial, con gran actividad desde hace años.

El instituto contaba con dispositivos realizados en otros institutos, basados en heteroestructuras de GaAs/AlGaAs y a lo largo de los años se han desarrollado localmente las técnicas que nos permitieron generarlos en Argentina. Permitiendo también desarrollar otro tipo de aplicaciones, como por ejemplo sistemas de medición de diferencias de temperatura a temperaturas criogénicas (300 mK) y de estudio del comportamiento del efecto Hall cuántico como sistema termoeléctrico [2 - 4].

En la charla describiré el efecto y sus propiedades, para luego comentar sobre el uso de los dispositivos y su fabricación. También comentaré la medición de sus propiedades termoeléctricas y de su uso como sensores de diferencias térmicas.

Referencias:

- [1] Tong, David. "Lectures on the quantum Hall effect." arXiv preprint arXiv:1606.06687 (2016).
- [2] Controlled generation and detection of a thermal bias in Corbino devices under the quantum Hall regime, MA Real, et. al. Applied Physics Letters 122 (10).
- [3] Thermoelectric cooling properties of a quantum Hall Corbino device
J Herrera Mateos, et. al. Physical Review B 103 (12), 125404.
- [4] Thermoelectricity in quantum hall corbino structures, M Real, et. al. Physical Review Applied 14 (3), 034019.

MICRO Y NANOTECNOLOGÍA EN INTI - DESARROLLOS Y APLICACIONES EN EL ÁREA DE SENSORES

Ing. Alex Lozano

Centro de Micro y Nanoelectrónica del Bicentenario (CMNB).

Dirección Técnica de Micro y Nanotecnologías. Instituto Nacional de Tecnología Industrial (INTI).

Argentina.

e-mail: alozano@inti.gob.ar

En el Centro de Micro y Nanoelectrónica de INTI tiene como objetivo promover el desarrollo sustentable de la industria promoviendo la inserción de las Micro y Nanotecnologías a nivel nacional, generando competencias estratégicas, tecnologías innovativas y propiedad intelectual con la participación de empresas productoras de bienes y servicios y del sector académico. Con tal objetivo desarrolla capacidades, infraestructura, plataformas tecnológicas y recursos humanos calificados para proveer servicios de asistencia técnica, desarrollo e innovación y transferencia de tecnología a la industria nacional, desarrollando la industria nacional mediante la generación de nuevos productos con agregado de valor y posibilitando el acceso a nuevos mercados.

En dicho contexto, y a partir de las diferentes líneas y grupos de investigación y desarrollo del Centro, se trabaja en la integración de una gran variedad de tecnologías, tales como Micro y Nanofabricación, Microfluídica, Electrónica Impresa Funcional, sensores y biosensores, Nanomateriales Funcionales, encapsulados, Tecnologías Cerámicas, LTCC, PCB, Prototipado Microelectrónico, IoT, Visión Artificial, IA, Industria 4.0, entre otras, para el desarrollo de nuevos productos y transferencia de tecnología.

El objetivo de esta presentación es mostrar el estado actual de las líneas de trabajo de los diferentes grupos del CMNB, sus capacidades y los principales desarrollos vinculados al área de sensores y sus aplicaciones.

LENGUAS ELECTRÓNICAS: SENSORES, MATERIALES Y APLICACIONES

Manel del Valle

Grup de Sensors i Biosensors, Universitat Autònoma de Barcelona Bellaterra.
Barcelona, Spain.

e-mail: manel.delvalle@uab.cat

Esta conferencia presentará una introducción a los sistemas de análisis tipo lengua electrónica, que son aquellos que emplean matrices de sensores electroquímicos como proveedores de información química, en particular en el caso de muestras líquidas. En esta charla se ofrece una visión general de las diferentes variantes propuestas hasta el momento, tanto en cuanto a la naturaleza de los sensores utilizados, como a los materiales que se pueden emplear. Mención especial se dará a las lenguas bioelectrónicas, es decir, cuando se incorporan uno o varios biosensores a la matriz. En particular, dada la mayor dimensionalidad que ocurre cuando se utilizan sensores voltamperométricos, se presentarán algunas estrategias que facilitan su uso. Finalmente, se ilustrarán algunos ejemplos relevantes de aplicación, en identificaciones cualitativas o en determinaciones cuantitativas, sobre todo en campos como el ambiental, el de alimentos o el de la seguridad.

SISTEMAS “NANO-LEGO”: EL JUEGO DE LA INSPIRACIÓN EN EL DISEÑO DE BIOSENSORES

Marcela Rodríguez

Dpto. de Físicoquímica, Facultad de Ciencias Químicas, Universidad Nacional de Córdoba (INFIQC)
Argentina

e-mail: manel.delvalle@uab.cat

El diseño de sistemas de vanguardia empleando nanomateriales funcionales modificados con moléculas de biocaptura constituye una alternativa interesante para el monitoreo de un amplio espectro de biomarcadores relevantes en el ámbito clínico, así como de indicadores de impacto toxicológico y ambiental. Los nanomateriales proporcionan una elevada densidad de sitios activos y un microambiente biocompatible, lo que permite la inmovilización de numerosas biomoléculas mientras se conserva su bioactividad. Además, desempeñan un papel crucial en la amplificación de la señal eléctrica generada durante el evento de biorreconocimiento, contribuyendo a desarrollar metodologías de transducción altamente eficientes.

En este sentido, los nanomateriales, en estrecha asociación con biomoléculas, pueden emplearse como sistemas “Nano-Lego” para la construcción de biosensores electroquímicos con transducción “label-free”, que sean de respuesta rápida, portables y de bajo costo, prescindiendo del uso de marcadores del evento de reconocimiento biomolecular.

En esta oportunidad se analizarán diversas estrategias de modificación de transductores electroquímicos basadas en el uso de nanomateriales, entre los que se incluyen nanotubos de carbono, grafeno y nanoestructuras metálicas y semiconductoras. La estrecha asociación de nanomateriales y biomoléculas de reconocimiento tales como aminoácidos, polipéptidos, enzimas redox y secuencias de ADN permiten la detección de biomarcadores relevantes tanto en las áreas del diagnóstico clínico y toxicológico, como en el monitoreo de indicadores de daño ambiental. Otro aspecto que se abordará es el diseño de biosensores que utilizan aptámeros como moléculas de biocaptura, en combinación con nanomateriales o estructuras supramoleculares, para lograr una amplificación eficiente de la respuesta generada durante el evento de reconocimiento. Desde esta perspectiva, se demostrarán las ventajas de los aptasensores aplicados a la determinación de biomarcadores de importancia clínica, así como nuevos enfoques en esta dirección.



**PRESENTACIONES
ORALES Y PÓSTERS**

Oral presentations and posters

Apresentações orais e pôsteres



1 |

Sensores de ondas acústicas

Acoustic wave sensors

Sensores de ondas acústicas

Microsensores y microactuadores MEMS

MEMS, microsensors and microactuators

Microssensores e microatuadores MEMS

Sensores físicos

Physical sensors

Sensores físicos

Optimización de forma y fabricación de transductores ultrasónicos de PVDF

Diego A. Cowes

Depto. ICES

CNEA

Villa Maipú, Argentina

diegocowes@cnea.gov.ar

J. Ignacio Mieza

Depto. daño por hidrógeno

CNEA

Villa Maipú, Argentina

mieza@cnea.gov.ar

Martín P. Gómez

Depto. ICES

CNEA

Villa Maipú, Argentina

mpgomez@cnea.gov.ar

Abstract—El desplazamiento lateral de campos ultrasónicos producto del fenómeno de onda guiada disipativa (leaky guided waves) constituye un desafío para la inversión de la información, ya que transductores de dimensiones acotadas rara vez pueden ser descritos por ondas planas correctamente. En este trabajo se muestra un modelo de Espectro Angular que sirve para simular el campo transmitido a través de placas anisotrópicas en inmersión para ensayos de goniometría ultrasónica y la señal recibida por un receptor sometido a dicho campo. El objetivo del trabajo es optimizar la forma del receptor para que las señales puedan ser descritas por ondas planas lo suficientemente bien como para evitar modelos más complejos, ahorrando tiempo de cálculo posterior. Se fabricó un receptor piezoeléctrico de fluoruro de polivinilideno (PVDF) de acuerdo a los hallazgos de la optimización, que mostró ser exitoso para el fin propuesto.

Keywords—Ultrasonido, Piezoeléctrico, PVDF, PZT, Onda Plana

I. INTRODUCCIÓN

Una dificultad de la goniometría ultrasónica reside en que las ondas en incidencia oblicua viajan dentro del material que actúa como guía de onda, generando el desplazamiento lateral de los ecos sucesivos, como se muestra en la Fig. 1. El modelo de onda plana contempla este fenómeno, pero rara vez se ajusta a los experimentos porque el transductor receptor de dimensiones finitas no alcanza a adquirir toda la energía dispersada. Un modelo de onda finita puede simular este fenómeno, pero requiere la integración doble de todos los vectores de onda existentes debido a la difracción del haz, lo cual incrementa rápidamente la complejidad y tiempo computacional. Dado que el ajuste del modelo a los datos experimentales se hace a partir de un proceso iterativo que requiere numerosas evaluaciones, contar con una configuración experimental que se aproxime suficientemente a propagación de onda plana evita el requisito de un modelo de haz finito, por ende reduciendo considerablemente la cantidad de operaciones. Una solución parcial fue propuesta por Hosten et al. [1] luego revistada en [2] denominada técnica de onda plana sintética, la cual consiste en la simulación de un receptor infinito mediante el escaneo lateral del campo y la suma de las señales recibidas. Investigaciones posteriores implementaron el uso de transductores grandes para lograr un mejor acuerdo

entre el coeficiente de transmisión medido y la teoría de onda plana sin la necesidad de escanear el campo. Castaings utilizó un receptor grande [3], por otro lado, Boudizi [4] diseñó un emisor grande de PZT, y Cawley et al [5] optó por tanto emisor como receptor grandes. Más tarde se incorporó el uso de transductores fabricados a partir de fluoruro de polivinilideno (PVDF) [6], [7] que demostró ser una elección adecuada para esta aplicación. El PVDF es un polímero piezoeléctrico que posee algunas ventajas sobre elementos cerámicos. En particular, sus pérdidas internas producen una respuesta oscilatoria amortiguada que resulta en pulsos cortos en el tiempo que poseen una excelente resolución temporal, útil en la determinación de tiempos de vuelo. A su vez, su amplio espectro es útil para la medición de coeficientes de reflexión y transmisión. Adicionalmente, su baja impedancia acústica es cercana a la del agua, por lo que no se requieren capas adaptadoras de impedancia. Además, el PVDF se comercializa en láminas delgadas, que puede ser utilizadas para fabricar transductores con formas arbitrarias [8].

Sin embargo, debido a su baja constante dieléctrica, altas pérdidas dieléctricas y bajo acoplamiento electromecánico, la impedancia capacitiva del PVDF domina eléctricamente por sobre la carga acústica [9]. La capacidad, al ser función del área, implica que la respuesta del transductor es altamente dependiente de la forma del transductor. Esto fue mostrado en [10], donde se minimizó las pérdidas por inserción de un transductor de PVDF optimizando su superficie. Debido a esto, mientras que incrementar la superficie del transductor mejora su aproximación a comportamiento de onda plana, también lo desvía de su capacidad óptima decreciendo su sensibilidad y ancho de banda. El objetivo de este trabajo es diseñar un transductor de PVDF de superficie acotada cuya respuesta se asemeje a propagación de onda plana mediante la optimización de su forma y posición. Para este fin se explora el método del espectro angular que sirve para simular campos ultrasónicos en el dominio del tiempo, las frecuencias y los vectores de onda, así como también es útil para simular señales adquiridas en estos campos por transductores de dimensiones finitas. El proceso de optimización y su implementación en GPU se describen en la sección III.

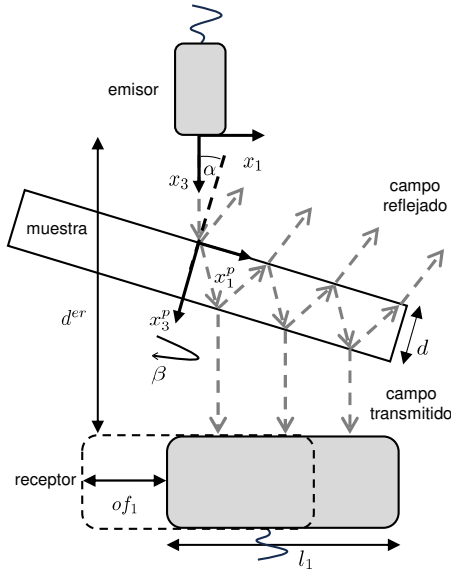


Fig. 1. Diagrama de un experimento de goniometría ultrasónica. Se utilizan las flechas para mostrar el desplazamiento del haz por refracción.

II. MARCO TEÓRICO

La velocidad particular de una onda puede ser expresada a través de la descomposición de Helmholtz como

$$v_i = [\nabla\phi]_i + [\nabla \times \psi_j]_i \quad (1)$$

donde ϕ es un potencial escalar asociado a una onda longitudinal y ψ_j un potencial vectorial asociado a una onda transversal. Para un medio no viscoso que no resiste deformación de corte, el potencial escalar puede ser descrito como una onda plana de la forma

$$\phi = \Phi \exp(i(k_i x_i - \omega t)). \quad (2)$$

El campo finito en la cara de un transductor emisor puede descomponerse como la suma de ondas planas, suprimiendo el término temporal $\exp(-i\omega t)$, como

$$\phi(x_1, x_2, 0) = \frac{1}{4\pi^2} \iint \Phi^e(k_1, k_2) \exp(i(k_1 x_1 + k_2 x_2)) dk_1 dk_2. \quad (3)$$

Por otro lado, si el transductor actúa como un pistón y el potencial de velocidad es conocido en su cara, la amplitud de potencial de velocidad, o directividad del transductor, se obtiene como

$$\Phi^e(k_1, k_2) = \iint \phi(x_1, x_2, 0) \exp(-i(k_1 x_1 + k_2 x_2)) dx_1 dx_2. \quad (4)$$

Esta descomposición permite el cálculo del campo en un plano paralelo a través del factor de propagación $H = \exp(ik_3 x_3)$ como

$$\phi(x_1, x_2, x_3) = \frac{1}{4\pi^2} \iint \Phi^e(k_1, k_2) \exp(i(k_1 x_1 + k_2 x_2)) \cdot \exp(ik_3 x_3) dk_1 dk_2, \quad (5)$$

donde, para un medio isotrópico, el componente k_3 del vector de onda se obtiene como

$$k_3 = \begin{cases} \sqrt{k^2 - k_1^2 - k_2^2} & \text{if } k^2 \geq k_1^2 + k_2^2 \\ i\sqrt{k_1^2 + k_2^2 - k^2} & \text{if } k^2 < k_1^2 + k_2^2, \end{cases} \quad (6)$$

donde $k = \frac{\omega}{c}$ es el número de onda y c es la velocidad del sonido en el fluido. Cuando es real describe ondas propagativas y cuando es imaginario describe ondas inhomogéneas que decaen exponencialmente con la distancia. Por esto, las ondas inhomogéneas solo están presentes en la cercanía del transductor y por consiguiente los componentes imaginarios pueden omitirse en los cálculos [11]. Este procedimiento se denomina Método de Espectro Angular (Angular Spectrum Method), y una gran ventaja del mismo consiste en que se puede implementar a través de la Transformada Rápida de Fourier (FFT), que al ser un algoritmo altamente optimizado es rápido. La ec. 4 puede reescribirse como

$$\Phi^e(k_1, k_2) = FFT\{\phi(x_1, x_2, 0)\}, \quad (7)$$

y la ec. 5 puede reescribirse como

$$\begin{aligned} \phi(x_1, x_2, x_3) &= iFFT\{FFT\{\phi(x_1, x_2, 0)\}H(k_1, k_2, x_3)\} \\ &= iFFT\{\Phi^e(k_1, k_2)H(k_1, k_2, x_3)\}. \end{aligned} \quad (8)$$

A. Proceso de recepción

A través de las relaciones de reciprocidad de Kino-Auld [12] [13] [14], la señal generada por un transductor insonificado por este campo puede expresarse como

$$S^{fb}(d^{er}, \omega) = \frac{\rho_f \omega}{8\pi^2 P(\omega)} \iint \iint k_3 \Phi^e(k_1, k_2) \exp(ik_3 d^{er}) \cdot \Phi^r(-k_1, -k_2) dk_1 dk_2, \quad (9)$$

donde d^{er} es la distancia emisor-receptor y $\Phi^r(-k_1, -k_2)$ es la directividad del receptor obtenida con la ecuación 4. Si una placa sólida anisotrópica se coloca entre los transductores, el coeficiente de transmisión relaciona el potencial incidente y el transmitido como $\Phi^I(k_1, k_2)T(k'_1, k'_2) = \Phi^T(k_1, k_2)$, donde la rotación de la placa está incluida en los vectores de onda como $(k'_1(kx, ky), k'_2(kx, ky))$, a partir de una rotación pasiva. Las ondas inhomogéneas que surgen en las interfaces sólido-líquido no son descartadas porque son críticas para el coeficiente T . El campo transmitido en el plano receptor se obtiene como

$$\phi(x_1, x_2, d^{er}) = \frac{1}{4\pi^2} \iint \iint \Phi^e(k_1, k_2) \exp(i(k_1 x_1 + k_2 x_2)) \cdot T(k'_1, k'_2) \exp(ik_3 d^{er}) dk_1 dk_2, \quad (10)$$

y la señal generada por el receptor por este campo es

$$S^{fb}(d^{er}, \omega) = \frac{\rho_f \omega}{8\pi^2 P(\omega)} \iint \iint k_3 \Phi^e(k_1, k_2) T(k'_1, k'_2) \cdot \exp(ik_3 d^{er}) \Phi^r(-k_1, -k_2) dk_1 dk_2. \quad (11)$$

Las ecs. 11 y 9 representan el Modelo de Haz Finito (FBM) con y sin la presencia de un sólido respectivamente. Por otro lado, si el transductor tiende a una superficie infinita,

su directividad tiende a una función delta, i.e. solo permanece el componente normal $k_x = k_y = 0$ y se obtiene propagación de onda plana. En este caso la integral doble se reduce a

$$S^{pw}(d^{er}, \omega) = \frac{\rho_f \omega}{8\pi^2 P(\omega)} k_3(0, 0) T'(0, 0) \exp(ik_3(0, 0)d^{er}) \quad (12)$$

donde $k_3(0, 0) = k$ y $T'(0, 0) = T(k'_1(0, 0), k'_2(0, 0))$. Considerando $\frac{\rho_f \omega k}{8\pi^2 P(\omega)} = \Gamma(\omega)$ como el módulo de la respuesta al impulso del sistema adquirida en ausencia de la placa, el Modelo de Onda Plana (PWM) resulta en

$$S^{pw}(d^{er}, \omega) = \Gamma(\omega) T(\omega) \exp(ikd^{er}). \quad (13)$$

Luego, la diferencia entre modelos se denomina error de haz finito (FBE) y se describe como

$$FBE = (S^{pw}(d^{er}, \omega) - S^{fb}(d^{er}, \omega))^2. \quad (14)$$

Para errores lo suficientemente pequeños, la ec. 13 puede utilizarse en lugar de la ec. 11 evitando la carga numérica de la integral doble, lo cual representa el principal objetivo de este capítulo.

B. Campos pulsados

Típicamente, los campos ultrasónicos son finitos tanto en espacio como en tiempo, por lo que el análisis monocromático se expande a comportamiento de banda ancha recuperando el término temporal $\exp(-i\omega t)$ con una transformada de Fourier adicional del dominio de frecuencias al dominio temporal para el potencial como

$$\phi(x_1, x_2, x_3, t) = \int_{-\infty}^{\infty} \phi(x_1, x_2, x_3, \omega) \exp(-i\omega t) d\omega, \quad (15)$$

y para la señal recibida como

$$s(d^{er}, t) = \int_{-\infty}^{\infty} S(d^{er}, \omega) \exp(-i\omega t) d\omega. \quad (16)$$

III. OPTIMIZACIÓN

El objetivo de esta sección consiste en optimizar su forma mientras se acota su superficie. Para esto, se implementó un procedimiento de optimización en el que la forma del receptor se varía hasta que se minimiza el error entre el modelo de haz finito y el modelo de onda plana. Esto se llevó a cabo con el algoritmo Evolución Diferencial, que es un proceso evolutivo, estocástico y paralelo de búsqueda directa introducido por Storn and Price [15]. Este algoritmo ha mostrado ser efectivo para optimizaciones globales y se lo eligió de forma empírica entre distintos algoritmos disponibles en la biblioteca de Python pymoo [16]. Una optimización típica consiste en 40 individuos que evolucionan durante 500 generaciones. El procedimiento de optimización puede resumirse en los pasos siguientes:

- 1) Se genera al azar una población de 40 individuos.
- 2) Cada individuo consiste en 10 vértices que definen un polígono cerrado. Este polígono se ajusta con una curva spline para suavizar los bordes del polígono. El área encerrada representa la superficie del receptor.

- 3) La superficie se transforma con la FFT de la Eq. 4. para obtener la función de directividad $\Phi^r(-k_1, -k_2)$.
- 4) El modelo de haz finito se evalúa para cada individuo para una grilla de 9 α por 13 β rotaciones, 256 k_1 por 256 k_2 autovectores y 64 frecuencias ω . Como la directividad del emisor y los coeficientes de transmisión son independientes de cada individuo, se calcula previamente y se los recupera de la memoria para cada cálculo de la Eq. 11, que consiste principalmente en multiplicación y suma de estos arreglos con la función de directividad de cada individuo.
- 5) El error entre modelos (FBE) se calcula de acuerdo a la Eq. 14.
- 6) El error es usado por el algoritmo de Evolución Diferencial para generar la población subsecuente. A la vez impone una cota a la superficie del polígono para que se mantenga por debajo de los 700 mm².
- 7) Al final el individuo con menor error se almacena.

Debido a la gran dimensionalidad del problema ($\alpha(9), \beta(13), k_1(256), k_2(256), \omega(64)$), acoplado al hecho que cada iteración es similar a la siguiente, la inversión fue implementada en arquitectura de unidades de procesamiento gráficas (GPU) logrando una importante reducción en los tiempos de cálculo. Para este propósito se utilizó la biblioteca CuPy [17].

A. Resultados

El procedimiento de optimización se llevó a cabo para dos materiales de interés: un acero austenítico SAE-304 y un CFRP unidireccional, cuyas matrices de rigidez se incluyen en el anexo. Se fijó el espesor de las placas en 1 mm. Debido a la simetría del material, el ángulo β se varió entre -90° y 90° , mientras que el ángulo α se varió entre 0° y 45° , debido a que por encima de este ángulo se transmite poca energía. El coeficiente de transmisión $T(k_1, k_2)$ fue pre-calculado como un arreglo de α por β por k_1 por k_2 por ω y recuperado para cada iteración. La directividad del emisor $\Phi^e(k_1, k_2)$ fue calculada para un pistón circular de 6 mm.

Las formas resultantes se muestran en la Fig. 2, donde el emisor se muestra como referencia. Los resultados para el acero austenítico son consistentes con la Fig. 2 ya que la forma es elongada en la dirección x_1 positiva y su centro desplazado también está desplazado en la dirección x_1 positiva. El hecho que la forma no sea simétrica con respecto a la dirección x_2 puede estar relacionado con el fenómeno de torcimiento de haz.

Dada la discrepancia entre las formas optimizadas, se eligió una forma rectangular con $l_1 = 50$ mm y $l_2 = 20$ mm para cubrir aproximadamente ambas, la cual se incluye en la Fig. 2. Aunque no es ideal, esta forma representa un compromiso viable y se utilizó para fabricar el receptor de PVDF. El receptor piezoeléctrico se construyó utilizando una lámina de PVDF de 28 μm de espesor con electrodos de pintura de plata. Este sensor se colocó en una carcasa de aluminio donde se vertió resina epoxy que sirve como material de soporte. El electrodo delantero se extendió hasta la carcasa con pintura

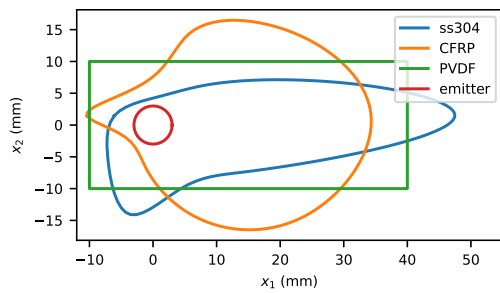


Fig. 2. Resultados del procedimiento de optimización. "ss304" es la forma optimizada para la placa de acero, "CFRP" es la forma optimizada para la placa de compuesto. La forma y posición del emisor se muestran como referencia y el transductor fabricado es la forma rectangular denominada "PVDF".

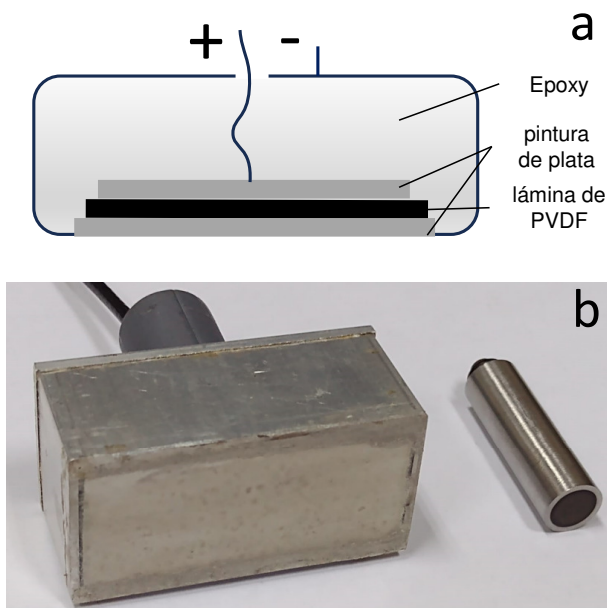


Fig. 3. (a) Detalle de fabricación de receptor piezoeléctrico de PVDF. (b) Fotografía del transductor fabricado (izquierda) junto a un transductor comercial (derecha).

de plata para proporcionar contacto eléctrico y apantallado a ondas de radio frecuencia. El electrodo trasero fue conectado con un cable y una pequeña gota de pintura de plata. Por último, una fina capa de resina epoxy se aplicó por sobre la cara delantera para proporcionar protección a la corrosión. Un esquema de la construcción se muestra en la Fig. 3.

Se observa excelente acuerdo entre la medición y el modelo de onda plana, indicando que el receptor de PVDF desarrollado permite asumir propagación de onda plana y así reducir considerablemente el número de operaciones. Por ejemplo, en este capítulo, los cálculos del modelo de haz finito requiere una grilla de 2^8 por 2^8 vectores de onda, que para propagación de onda plana se reducen uno solo.

IV. CONCLUSIÓN

El método del Espectro Angular demostró ser útil para la simulación de campos emitidos por transductores finitos para señales pulsadas. Este modelo, implementado para arquitectura de interfaces gráficas permitió encontrar formas de receptores ultrasónicos que aproximen su comportamiento a ondas planas, lo que permite una reducción significativa en la inversión de las señales para su utilización en caracterización y diagnóstico de materiales. Se construyó un receptor de PVDF de acuerdo a los resultados de la optimización, el cual demostró ser exitoso para los fines planteados.

REFERENCES

- [1] B. Hosten, M. Castaings, "Transfer matrix of multilayered absorbing and anisotropic media. measurements and simulations of ultrasonic wave propagation through composite materials", *The Journal of the Acoustical Society of America* 94 (3) (1993) 1488–1495.
- [2] J. Jocker, D. Smeulders, "Minimization of finite beam effects in the determination of reflection and transmission coefficients of an elastic layer", *Ultrasonics* 46 (1) (2007) 42–50.
- [3] M. Castaings, B. Hosten, T. Kundu, "Inversion of ultrasonic, planewave transmission data in composite plates to infer viscoelastic material properties", *NDT & E International* 33 (6) (2000) 377–392.
- [4] Y. Bouzidi, D. R. Schmitt, "A large ultrasonic bounded acoustic pulse transducer for acoustic transmission goniometry: Modeling and calibration", *The Journal of the Acoustical Society of America* 119 (1) (2006) 54–64.
- [5] P. Cawley, B. Hosten, "The use of large ultrasonic transducers to improve transmission coefficient measurements on viscoelastic anisotropic plates", *The Journal of the Acoustical Society of America* 101 (3) (1997) 1373–1379.
- [6] J. C. Adamowski, M. A. B. Andrade, N. Perez, F. Buiocchi, "A large aperture ultrasonic receiver for through-transmission determination of elastic constants of composite materials", in: 2008 IEEE Ultrasonics Symposium, IEEE, 2008.
- [7] P. Puthillath, C. Krishnamurthy, K. Balasubramaniam, "Hybrid inversion of elastic moduli of composite plates from ultrasonic transmission spectra using PVDF plane wave sensor", *Composites Part B: Engineering* 41 (1) (2010) 8–16.
- [8] L. Brown, "Design considerations for piezoelectric polymer ultrasound transducers", *IEEE Transactions on Ultrasonics, Ferroelectrics and Frequency Control* 47 (6) (2000) 1377–1396.
- [9] R. Swartz, J. Plummer, "On the generation of high-frequency acoustic energy with polyvinylidene fluoride", *IEEE Transactions on Sonics and Ultrasonics* 27 (6) (1980) 295–302.
- [10] M. Sherar, "The design and fabrication of high frequency poly(vinylidene fluoride) transducers", *Ultrasonic Imaging* 11 (2) (1989) 75–94.
- [11] L. W. Schmerr, S.-J. Song, "Ultrasonic Nondestructive Evaluation Systems", Springer US, 2007.
- [12] B. Auld, "General electromechanical reciprocity relations applied to the calculation of elastic wave scattering coefficients", *Wave Motion* 1 (1) (1979) 3–10.
- [13] G. S. Kino, "The application of reciprocity theory to scattering of acoustic waves by flaws", *Journal of Applied Physics* 49 (6) (1978) 3190–3199.
- [14] A. Atalar, "A fast method of calculating diffraction loss between two facing transducers", *IEEE Transactions on Ultrasonics, Ferroelectrics and Frequency Control* 35 (5) (1988) 612–618.
- [15] R. Storn, K. Price, "Differential evolution – a simple and efficient heuristic for global optimization over continuous spaces", *Journal of Global Optimization* 11 (4) (1997) 341–359.
- [16] J. Blank, K. Deb, "pymoo: Multi-objective optimization in python", *IEEE Access* 8 (2020) 89497–89509.
- [17] R. Okuta, Y. Unno, D. Nishino, S. Hido, C. Loomis, "Cupy: A numpy compatible library for nvidia gpu calculations", in: Proceedings of Workshop on Machine Learning Systems (LearningSys) in The Thirty first Annual Conference on Neural Information Processing Systems (NIPS), 2017.

Microsensor for tear viscosity analysis: a novel approach for its clinical use

Gabriel Muñoz¹, Martín Millicovsky², Juan Cerrudo¹, Albano Peñalva¹, Juan Reta¹ and Martín Zalazar^{1,2}

¹Facultad de Ingeniería, Universidad Nacional de Entre Ríos (FI-UNER)

²Instituto de Investigación y Desarrollo en Bioingeniería y Bioinformática (IBB), FI-UNER-CONICET
Oro Verde, Entre Ríos, Argentina
martin.zalazar@uner.edu.ar

Abstract—The essential role of tear viscosity in maintaining ocular health is highlighted by its direct influence on the speed and pattern of tear flow, which are foundational for protecting, hydrating, and lubricating the ocular surface. Effective ocular moistening and shielding against external irritants are ensured by proper viscosity, while significant deviations from this balance can lead to conditions like dry eye syndrome. Despite their significance, practical challenges are often presented by traditional devices for measuring tear viscosity due to their high procurement and maintenance costs, as well as their requirement for substantial sample volumes. A novel approach to evaluating tear viscosity is introduced in this study through Quartz Crystal Microbalance (QCM) technology, offering benefits such as reduced sample consumption and expedited results. Tear samples from eight individuals were analyzed using the device, and the resulting viscosity range was compared with literature values. These findings contribute to understanding tear viscosity variation among individuals and its implications for ocular health. Ultimately, the commercialization of the device as a tool for objectively assessing tear fluid in patients with ocular surface disease is sought through these advancements. This innovation holds promise for enhancing the diagnosis and management of various ocular pathologies.

Keywords— Dry Eye, Ocular pathologies, Quartz crystal microbalance, Tears

I. INTRODUCTION

The function of tear viscosity lies in its capacity to contribute to ocular health and the protection of the corneal surface. Additionally, it plays a role in ensuring the stability of the tear film and in facilitating its distribution over the ocular surface. This physical property is influenced by various factors, including the composition of tears and their interaction with the ocular environment [1]. A thorough understanding of tear viscosity is deemed crucial for the comprehension of tear film stability, comfort levels, and the prevalence of ocular disorders, including dry eye syndrome, a condition affecting millions of people worldwide [2]. Tears with elevated viscosity may demonstrate diminished spreading capabilities, thereby jeopardizing their effectiveness in providing adequate hydration and lubrication to the ocular surface, a phenomenon often associated with dry eye and its symptoms, including dryness and irritation [3].

Different principles of operation are employed by viscometers available in medical and laboratory applications [4]. Rotational viscometers, such as the Rheotest and Cannon-Fenske, utilize a rotating rotor to measure the resistance of a liquid to flow [5]. On the other hand, capillary viscometers, such as the Ubbelohde, obtain viscosity by forcing a liquid to flow in a capillary tube [6]. Finally, cone and plate viscometers involve the use of a cone and a plate to measure viscosity under different shear conditions [7]. The volumes handled by these viscometers vary by type and brand but are not less than 0.5 ml, which is a relatively large volume when

compared to the volume of tears. Moreover, these instruments can be costly, posing challenges for widespread use and accessibility [8].

The Quartz Crystal Microbalance (QCM) sensor is distinguished by its capacity to have its resonance frequency altered in response to variations in accumulated mass on the surface [9]. One distinct advantage is its requirement for a small sample volume for operation [10], making it ideal for the characterization of biological substances with limited volumes. The measurement of viscosity using a QCM has been explored, revealing a complex measurement process that demanded enhanced accuracy [11]. However, a newly introduced method incorporating simple equations has simplified the measurement process, improving precision in determining liquid viscosity. This innovative technique allows for the characterization of tear viscosity by monitoring frequency shifts on a sensor caused by changes in sample liquid volumes [12].

In this study, the last-mentioned method is implemented in a medical device prototype, which was specifically created to operate with small sample volumes with the purpose of evaluating human tear viscosity as an innovative approach for diagnosing ocular pathologies. An exploratory study is addressed with QCM technology, in an effort to overcome the limitations of traditional viscosity measurement methods. Advantages such as reduced sample consumption and faster results are offered for viscosity quantification in human tears. A graphical abstract is depicted in Fig. 1.

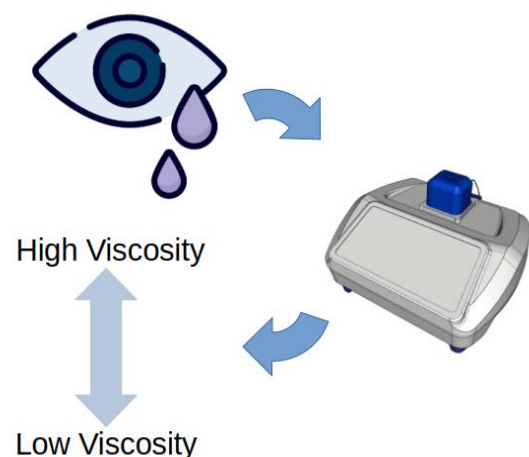


Fig. 1. Development of a specifically designed monitoring system for tear viscosity studies using QCM. Despite the popularity of customized QCM systems for specific experiments and the availability of commercial systems with high-quality components, a deficiency in specifically tailored systems for tear studies is observed. A prototype for tear study experimentation was previously constructed by the authors [13]; however, improvements have been introduced in this new device.

II. MATERIALS AND METHODS

A. Hardware

The detection module was designed in Autodesk Fusion 360 and manufactured using MSLA technology with a Creality LD-006 printer, employing photosensitive resin. It features dimensions of 44 mm in width, 40 mm in length, 15 mm in height, and weighs 21.5 grams. A PCB connecting the NanoVNA measuring instrument with the QCM was designed using the open-source software KiCad. Electrical connectivity was established through an SMA connector (Amphenol, low noise) and gold-plated pogo pins. The piezoelectric crystal, obtained from Novaetech SRL, is of AT cut, with a resonance frequency close to 10 MHz. The gold electrode comprises a single-sided titanium adhesion layer, with diameters of 11.5 mm for the front electrode and 6 mm for the rear electrode. Fig. 2 illustrates the QCM and the module; atop the module, there is a designated space for liquid introduction. Crystal placement is expedited and straightforward, facilitated by contact with a silicone O-ring that stabilizes pressure and prevents leakage.

Controlling temperature effects is significant when high accuracy measurements are desired [14]. Thus, a temperature control system was developed based on a Peltier cell (TEC1-12706), and powered by 12 V and 6 A. The thermal control has a nominal working range of 18°C to 28°C, allowing for bidirectional heating and cooling. A Raspberry Pi Pico was chosen as the control device for its flexibility, compact size, and low cost, and a thermistor (NTC 3950) was used for temperature acquisition. The PID control program, implemented in C, regulates the current through the Peltier cell.

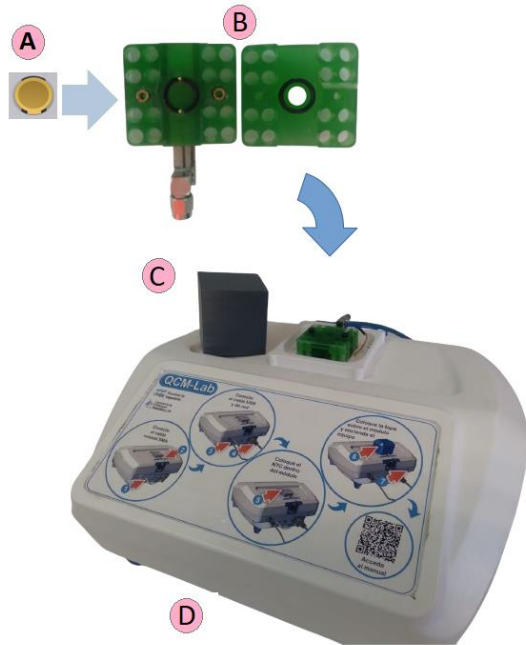


Fig. 2. For each measurement, the QCM is placed inside the detector module, which is then integrated into the system containing the temperature control and the NanoVNA. Using a micropipette, tears are deposited into the hole of the module, after which a protective cover is placed over the detector module, and temperature control is initiated before taking the corresponding measurements. QCM (A), Detection module (B), Protective cover (C), System containing the temperature control and the NanoVNA (D).

B. Viscosity measurement

In the method utilized in this study, the resonance frequency of a QCM is measured in air. Subsequently, a volume of sample liquid VL1 is deposited onto the surface of the sensor, resulting in a resonance frequency f_1 being the first frequency change $\Delta f_1 = f_1 - f_0$. If another sample of liquid is added on top of the already loaded sensor, the total volume becomes VL2, and the second frequency change is $\Delta f_2 = f_2 - f_0$. As the volume changes from VL1 to VL2, so does the resonance frequency $\Delta f_2 - \Delta f_1$. The viscosity of the tear was determined using the equation [12]:

$$\eta = \left(\frac{k_{pf} c_{pf}}{(\Delta f_2 - \Delta f_1) V_{L2} f_0} \right) \times \left(\frac{\Delta f_1 V_{L2} - V_{L1} (\Delta f_2 - \Delta f_1)}{k_{tf} c_{lf}} \right)^2 \quad (1)$$

where K_{pf} is the pressure sensitivity coefficient of the sensor, K_{tf} is the stress sensitivity coefficient, C_{pf} is a pressure-frequency coefficient, C_{lf} is a stress-frequency coefficient of the QCM in the liquid phase, and η denotes the viscosity of the liquid.

For all the frequency measurements, the third harmonic of the QCM was used because it provides greater sensitivity to variations of mass and viscosity compared to the fundamental frequency, thus allowing for the precise detection of more subtle changes in the adsorbed layers [15].

C. Sample analysis

50 μ L of tear samples from 8 volunteers were collected at the Prototyping Laboratory of the Faculty of Engineering, Oro Verde, Argentina, utilizing a capillary tube to minimize contamination and ensure accurate sample collection (Fig. 3). The capillary tube was carefully positioned without direct contact with the eye or conjunctiva to prevent any interference with tear composition. The present study adhered to ethical guidelines outlined by the Central Committee of Bioethics in Medical Practice and Research in the province of Entre Rios, Argentina. Prior to data collection, informed consent was obtained from each participant, emphasizing their autonomy and right to withdraw from the study at any time without facing any consequences. Participants were also provided with detailed information about the study objectives, procedures, and potential risks involved, ensuring their full comprehension and informed decision-making.



Fig 3. Volunteers were instructed to tilt their heads slightly towards the right for tear collection in the right eye, and vice versa for the left eye. They were then instructed to blink a couple of times and look up and in. The microcapillary tube was positioned towards the temporal canthus of the eye, ensuring that one edge of the tube rested in the tear lake at the temporal canthus while avoiding direct contact with the eyelids and conjunctiva.

III. RESULTS

The viscosity of tears from eight different volunteers is shown in Fig. 4, with measurements conducted using (1). An initial volume of 50 μL and a final volume of 40 μL were employed for each tear sample. Variations in tear viscosity among the different individuals were revealed within the expected range for individuals without dry eye [16].

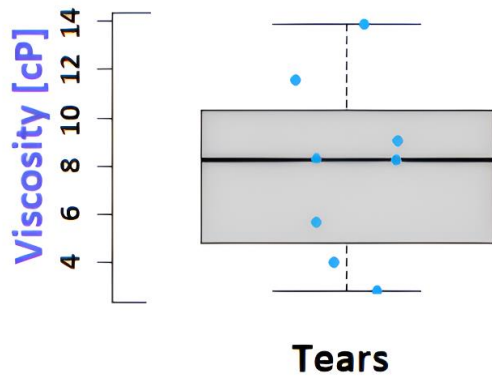


Fig. 4. The viscosity of tears from eight volunteers was measured, resulting in an average viscosity of 7.93 cP and a standard deviation of 3.22 cP. The measurement process was conducted under controlled temperature conditions, and multiple repetitions of each measurement were performed to ensure the accuracy and reproducibility of the results.

These findings suggest the existence of individual variability in tear viscosity, highlighting the importance of personalized assessment in the diagnosis and treatment of ocular conditions. Future studies with a larger sample size and longitudinal design could further elucidate the factors influencing tear viscosity and its implications for ocular health.

IV. DISCUSSION AND CONCLUSION

An average viscosity of 7.93 cP was observed in human tears for these individual samples, falling within the typical range of viscosity for human tears, which typically ranges from 1 to 10 cP [16]. Efforts are underway to establish normative viscosity values in healthy volunteers and pathological ranges in individuals with dry eye syndrome, essential for validating the efficacy of the device.

Nevertheless, the need for further research involving a larger number of individuals to explore viscosity variability in different demographic groups and medical conditions is emphasized. This approach would contribute to a more comprehensive understanding of these findings and their potential clinical applications.

ACKNOWLEDGMENT

This work was supported by Agencia Nacional de Promoción Científica y Tecnológica, PICT StartUp 4655: Biosensor para la evaluación cualitativa y cuantitativa de la lágrima. We want to thank to the Electronics Prototyping & 3D Lab of the National University of Entre Rios for giving us the facilities to develop and evaluate our prototype. We want

to thank to the ophthalmologists, Lucía Domínguez and Rodrigo Torres, for their willingness and advice.

REFERENCES

- [1] A. Recchioni, E. Mocchiardini, E. Ponzini and S. Tavazzi, "Viscoelastic properties of the human tear film", *Experimental Eye Research*, vol.219, April 2022. doi:10.1016/j.exer.2022.109083.
- [2] S. Arshinoff, I. Hofmann, and H. Nae, "Role of rheology in tears and artificial tears", *Journal of Cataract and Refractive Surgery*, vol. 47, pp. 655–661, May 2021. doi:10.1097/j.jcrs.0000000000000508.
- [3] J. Weng, M. K. Fink and A. Sharma, "A Critical Appraisal of the Physicochemical Properties and Biological Effects of Artificial Tear Ingredients and Formulations", *International Journal of Molecular Science*, vol. 24, February 2023. doi:10.3390/ijms24032758.
- [4] C. H. Shih, C. C. Chang, C. Y. Liu and Wu H. C., "The centrifugal viscometer", *Biomicrofluidics*, vol. 15, September 2021, doi:10.1063/5.0060908.
- [5] K. Valachova, K. Svik, C. Biro, M. N. Collins, R. Jurcik, L. Ondruska and Soltes L., "Impact of Ergothioneine, Hercynine, and Histidine on Oxidative Degradation of Hyaluronan and Wound Healing", *Polymers*, vol. 13, January 2021, doi: 10.3390/polym13010095.
- [6] H. Iwashita, K. Mabuchi, T. Itokawa, Y. Okajima, T. Suzuki and Y. Hori, "Evaluation of the Lubricating Effect of Hyaluronic Acid on Contact Lenses Using a Pendulum-Type Friction Tester Under Mimicking Physiological Conditions", *Eye & Contact Lens: Science & Clinical Practice*, vol. 48, pp. 83-87, February 2022, doi:10.1097/ICL.0000000000000853.
- [7] J. D. Greenlee, Z. Zhang, T. Subramanian, K. Liu and M.R. King, "TRAIL-conjugated liposomes that bind natural killer cells to induce colorectal cancer cell apoptosis", *Biomedical Materials Research*, vol. 12, pp. 110-120, September 2024. doi:10.1002/jbm.a.37621.
- [8] K. Sakamoto, K. Kobayashi, K. Tabira, Y. Hachiya and K. Ohno, "Evaluation of viscosity and surface tension of low-volume samples using glass capillary", *Japanese Journal of Applied Physics* vol. 59, 2020, doi: 107002. 10.35848/1347-4065/abb9c8.
- [9] S.Sauerbrey, "The Use of Quartz Oscillators for Weighing Thin Layers and for Microweigh-ing", *Journal of Physics*, vol.155, pp. 206-222, 1959. doi:10.1007/BF01337937.
- [10] D. Johannsmann, "The Quartz Crystal Microbalance in Soft Matter Research", Springer, 2015. doi :10.1007/978-3-319-07836-6
- [11] K. K. Kanazawa, and J. G. Gordon, "Frequency of a quartz microbalance in contact with liquid", *Analytical Chemistry*, vol.57, pp. 1770-1771, July 1984. doi: 10.1021/ac00285a062.
- [12] F. Tan, D. Y. Qiu, L. P. Guo, P. Ye, H. Zeng, J. Jiang, Y. Tang and Y.C. Zhang, "Separate density and viscosity measurements of unknown liquid using quartz crystal microbalance", *AIP Advances*, vol. 6, September 2016. doi: 10.1063/1.4963298.
- [13] G. G. Muñoz, M. J. Millicovsky, J.M. Reta, J. I. Cerrudo, A. Peñalva, M. Matchey, R. Torres and M. Zalazar, "Quartz crystal microbalance with dissipation monitoring for biomedical applications: Open source and low cost prototype with active temperature control", *Hardware X*, vol.14, March 2023. doi: 10.1016/j.ohx.2023.e00416.
- [14] Y. Tsuchiya, H. Kukita, T. Shiobara, K. Yukumatsu, and E. Miyazaki, "Temperature Controllable QCM Sensor with Accurate Temperature Measurement for Outgas and Contamination Assessment", *IEEE Sensors*, 2019. doi:10.1109/SENSOR43011.2019.8956952.
- [15] E. Corradi, M. Agostini, G. Greco, D. Massida, M. Santi, M. Calderini, G. Signore and M. Cecchini, "An objective, principal-component-analysis (PCA) based, method which improves the quartz-crystal-microbalance (QCM) sensing performance", *Sensors and Actuators: Physical*, vol. 315, November 2020. doi.org/10.1016/j.sna.2020.112323.
- [16] J. M. Tiffany, "The viscosity of human tears", *International Ophthalmology*, vol. 15, pp. 371–376, November 1991. doi.org/10.1007/BF00137947.

Diseño de sensores ópticos mediante método inverso: estructuras fotónicas 1D optimizadas por redes neuronales

Agustina Viaggio
Departamento de Inteligencia Artificial
INTI
Bs. As., Argentina
aviaggio@inti.gov.ar

María Luz Martínez Ricci
INQUIMAE
CONICET
CABA, Argentina
mricci@qi.fcen.uba.ar

Diego Ariel Onna
INQUIMAE
CONICET
CABA, Argentina
diego.onna@qi.fcen.uba.ar

Resumen—El sensado mediante Estructuras Fotónicas Unidimensionales (IDEFs) mesoporosas es altamente prometedor, gracias a que pueden realizar mediciones telemétricas y no invasivas. En este estudio, se llevó a cabo el diseño inverso de IDEFs para desarrollar un sensor óptico de bajo costo y fácil lectura para la detección de gases. En particular, se utilizó vapor de agua como molécula modelo. El diseño inverso se realizó empleando ResGLOnet, una herramienta basada en redes neuronales residuales generativas, obteniéndose IDEFs no periódicas con buen rendimiento. Se realizaron distintos casos de optimización, considerando materiales con diferentes grados de porosidad.

Index Terms—Estructura fotónica, materiales mesoporosos, redes neuronales, sensores, diseño inverso, nanofotónica

I. INTRODUCCIÓN

El desarrollo de sensores ópticos presenta un gran potencial en áreas como la biomedicina, el monitoreo ambiental y la ingeniería química, con buen desempeño en la sensibilidad, eficiencia, portabilidad, inmunidad a interferencias electromagnéticas y rapidez de respuesta [1] [2]. En el caso de sensores ópticos de gases comerciales, la espectroscopia de absorción es la técnica principal debido a su alta sensibilidad. En general, para muchas aplicaciones se busca la miniaturización del sensor pero esto implica una pérdida de la sensibilidad, ya que requieren de un camino de absorción largo. Una solución a este problema es utilizar sensores ópticos basados en nanomateriales estructurados cuya respuesta óptica es conocida, como los cristales fotónicos (CFs), que son estructuras periódicas de materiales dieléctricos [2]. Una característica notable de los CFs porosos es que su espectro se desplaza en función del índice de refracción del compuesto que llena los poros, n_{poro} , y este corrimiento se puede calcular y es detectable con un espectrofotómetro [3] [4]. Esta característica otorga flexibilidad para seleccionar el rango de longitudes de onda de trabajo, ya que el desplazamiento a detectar no está condicionado por la frecuencia de absorbancia del gas. En particular, es posible trabajar en el rango visible del espectro electromagnético, $\Delta\lambda = [400-750] \text{ nm}$, cuando los espesores de las capas del CF se encuentran en la nanoescala. Por otro lado, si se ilumina al CF con una fuente cuyo espectro

sea angosto, por ejemplo un LED, es posible reemplazar el espectrofotómetro por un LDR (*Light Dependent Resistor*), que mide la intensidad del campo electromagnético por unidad de área y de tiempo que incide sobre su superficie [5]. El LDR ofrece una lectura simplificada y costos reducidos, sin dar precisiones sobre la forma del espectro, a diferencia del espectrofotómetro.

Debido a la creciente necesidad de prestaciones altamente especializadas y personalizadas, un desafío diferente consiste en definir una respuesta específica deseada y buscar las nanoestructuras que la cumplen, considerando su capacidad de manipular el comportamiento del campo electromagnético en función de los materiales, formas y tamaños. En términos generales, el proceso que busca comprender la estructura o composición interna de un objeto a partir de su función, comportamiento, resultado observado, o incluso deseado es conocido como diseño inverso. En lugar de partir de un diseño preexistente y predecir su resultado, el diseño inverso busca un determinado resultado, analizándolo, para luego retroceder identificando la configuración que lo genera. En el campo de la fotónica, los métodos inversos como los métodos de optimización adjuntos (*adjoint-methods* en inglés) [6], optimización topológica [7] y algoritmos genéticos [8], presentaron un salto exitoso en el diseño de dispositivos fotónicos con nuevas funcionalidades [9] [10]. Sin embargo, estas técnicas son lentas y computacionalmente costosas debido a la alta dimensionalidad del espacio de posibles soluciones a muestrear en busca del óptimo global [11]. El uso de modelos basados en redes neuronales profundas ha surgido como una alternativa prometedora para el diseño inverso de sistemas ópticos nanoestructurados con muchos grados de libertad, debido a su capacidad de procesamiento.

En este trabajo se propone relajar la condición de periodicidad de los CFs sobre una base de diferentes materiales dieléctricos con variadas porosidades y empleando una red neuronal residual generativa, ResGLOnet (Residual Global Networks) [12], optimizar la estructura fotónica unidimensional (IDEF) -apilamiento de películas delgadas planas- en función de un espectro deseado, el cual se detallará en la

sección III-A. El diseño inverso de IDEFs consiste en buscar el conjunto óptimo de los parámetros índices de refracción n y espesores e para lograr una respuesta óptica deseada en un rango longitudes de onda de interés. Las distintas combinaciones de estos parámetros de diseño definen el espacio de soluciones, cuyos grados de libertad se incrementan con el número de capas, rango de espesores y número de materiales disponibles. Una ventaja de ResGLOnet es que los tiempos de entrenamiento son cortos en comparación con otros enfoques [12]. Sumado, a que el entrenamiento puede realizarse en una CPU convencional y sin requerir el uso de GPUs. Por otro lado, en vista a las aplicaciones tecnológicas de las IDEFs, es deseable contar con un enfoque que genere un catálogo de propuestas que ajusten las especificaciones en la respuesta óptica para poder compararlas según los requerimientos y condicionamientos de fabricación y seleccionar criteriosamente el mejor diseño. Como se describe en la sección III, ResGLOnet resulta adecuada para esta tarea al ser una red neuronal generativa que provee una población de IDEFs óptimas.

Considerando el dispositivo de bajo costo compuesto por un LED-IDEF porosa-LDR, figura 1, se aplica ResGLOnet al diseño inverso de las IDEFs que ajusten un espectro escalón unitario sintonizado en el espectro de emisión del LED. La sensibilidad de este dispositivo va a depender de cómo afecta a la intensidad transmitida medida por el LDR el desplazamiento del espectro de la IDEF como consecuencia de la entrada de un gas. En este sentido, se busca que la IDEF actúe como filtro respecto del campo electromagnético incidente cuando se cambia n_{poro} .

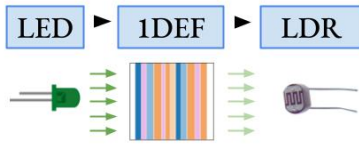


Figura 1. Esquema del sensor propuesto.

II. MÉTRICA DE SENSIBILIDAD DEL SENSOR

Al considerar IDEFs mesoporosas, con diámetros de poro entre 2 nm y 50 nm, interconectados y accesibles desde el exterior, cuando se las expone a un compuesto volátil, si existe afinidad química entre las moléculas del compuesto volátil y las paredes del poro, estas moléculas son atraídas hacia el interior de los poros. Una vez que las moléculas ingresan a los poros, el fenómeno de capilaridad juega un papel importante en permitir que estas moléculas se distribuyan dentro de los poros y se concentren. Bajo ciertas condiciones de temperatura y presión, las moléculas pueden condensarse en su fase líquida dentro de los poros, provocando un cambio brusco en n_{poro} y el consecuente desplazamiento del espectro. En este trabajo se emplea vapor de agua como gas modelo y se comparan dos condiciones, cuando se expone a la IDEF a aire, con $n_{poro} = 1$, y a vapor de agua, que implica agua en los poros, con

$n_{poro} = 1,33$. Matemáticamente, la señal medida por el LDR puede expresarse como el área bajo la curva del espectro de luz incidente, que está compuesto por el espectro de emisión del LED modulado por el espectro de transmisión de la IDEF y, a su vez, modulado por la respuesta espectral del LDR, $led(\lambda) \cdot T(\lambda) \cdot ldr(\lambda)$. Por lo tanto, el modelo matemático de medición del sensor puede describirse como:

$$\begin{aligned} señal_{aire} &= \int_{\lambda_{min}}^{\lambda_{max}} ldr(\lambda) \cdot led(\lambda) \cdot T(\lambda)_{aire} d\lambda \\ señal_{agua} &= \int_{\lambda_{min}}^{\lambda_{max}} ldr(\lambda) \cdot led(\lambda) \cdot T(\lambda)_{agua} d\lambda \\ diferencia &= señal_{aire} - señal_{agua} \end{aligned} \quad (1)$$

Se define dif_rel como el cociente entre $|diferencia|$ y el espectro del LED, que se estima como el área bajo la curva de su espectro de emisión:

$$dif_rel = \frac{|diferencia|}{\int_{\lambda_{min}}^{\lambda_{max}} led(\lambda) \cdot led(\lambda) d\lambda} \quad (2)$$

Se puede ver que $0 < dif_rel < 1$. Específicamente, $dif_rel = 0$ cuando $señal_{aire} = señal_{agua}$, y $dif_rel = 1$ cuando la IDEF transmite totalmente la luz incidente para una condición, mientras que la refleja completamente para la otra, en el rango de longitudes de onda de emisión del LED. Esto corresponde al caso en que la IDEF actúa como un filtro ideal. El desafío radica en encontrar las IDEFs que maximicen la sensibilidad del sensor.

III. DISEÑO INVERSO DE ESTRUCTURAS FOTÓNICAS UNIDIMENSIONALES CON RESGLONET

Lograr el diseño inverso de IDEFs con libre elección de materiales de las capas y espesores es un desafío ya que los materiales son descritos por su índice de refracción, que son valores discretos y dependientes de la longitud de onda, mientras que los espesores son parámetros de valores continuos. Es decir, se tiene un problema de diseño inverso categórico para índices de refracción, que habitualmente se resuelve como un problema de clasificación, y un problema de valores continuos para los espesores, que suele resolverse como un problema de regresión. Esta doble característica en los parámetros de diseño del problema lo vuelven un desafío en sí mismo. Jiang y Fan [12] aportaron un enfoque denominado ResGLOnet, basado en redes neuronales residuales generativas, que resuelve el conjunto de espesores y materiales que mejor ajusten un espectro de reflectividad deseado. ResGLOnet es un optimizador que combina una red neuronal residual generativa de IDEFs con un simulador electromagnético de espectros de reflectividad basado en el Método de la Matriz Transferencia (MTT), para realizar una optimización basada en poblaciones. La optimización basada en poblaciones es un método que se caracteriza por generar muestras de soluciones candidatas de forma aleatoria, las cuales son sometidas a un proceso de evolución iterativo con el objetivo de converger hacia soluciones de mayor calidad

minimizando el Error Cuadrático Medio, Err^2 , entre los espectros de reflectividad calculados mediante el MTT y el espectro deseado. Dado que en este trabajo se consideraron materiales sin pérdidas, se puede aplicar ResGLOnet para ajustar un espectro de transmisión deseado ya que vale que $T = 1 - R$.

III-A. Condiciones de optimización

En este estudio, se emplea una función escalón unitario como espectro deseado, que se muestra en línea negra sólida en la figura 2. Para la biblioteca de materiales, se utilizaron parámetros de índices de refracción correspondientes a materiales sintetizados mediante sol-gel cuyas especificaciones se encuentran en [17] [16] [18]. Se trabajó con dos series: la serie P incluye exclusivamente los materiales porosos SiO_2P , TiO_2P y ZrO_2P , con volúmenes porosos del 42%, 45% y 26%, respectivamente. Mientras que la serie PD combina materiales porosos con materiales densos, incorporando SiO_2 , TiO_2 y ZrO_2 . Mediante esta técnica de síntesis química es posible obtener IDEFs de espesor máximo $\approx 1 \mu m$, limitando el número de capas total N . Por un lado, cuanto mayor N , mejor será el ajuste del espectro. Por otro lado, cuanto menor N , se facilita la fabricación y disminuyen los costos. En este contexto, se buscaron IDEFs óptimas para tres condiciones de N : cuando N es grande, con $N = 24$, y para $N = 12$ y 8, valores cercanos al N máximo realizable en un laboratorio. Se definió el rango de espesores de cada una de las películas delgadas $e = [20, 200] nm$, se supuso que el índice de refracción del superestrato $n_{super} = 1$, que las IDEFs están depositadas sobre vidrio con $n_s = 1,46$. La incidencia del campo electromagnético se consideró normal a la superficie de las películas y el rango de longitud de onda incidente se fijó en $\Delta\lambda = [450, 575] nm$.

Todas las optimizaciones, tanto de la serie P como la PD, se realizaron suponiendo parámetros para los índices de refracción de los materiales tal que $n_{poro} = 1$. Posteriormente, una vez obtenidas las IDEFs óptimas, se calculó mediante el MMT, implementado por pymultilayer [15], el desplazamiento asociado a $n_{poro} = 1,33$, para considerar el corrimiento del espectro debido a la exposición al vapor de agua y calcular dif_rel .

IV. RESULTADOS Y DISCUSIÓN

En esta sección se presentan y discuten los resultados obtenidos con ResGLOnet al problema del diseño inverso de IDEFs con 24, 12 y 8 capas que mejor ajusten el espectro escalón unitario para las series P y PD. En la figura 2, se ilustran las IDEFs óptimas y sus espectros asociados en línea sólida, y los correspondientes a $n_{poro} = 1,33$ se muestran en línea punteada, los cuales se incorporan para observar el desplazamiento del espectro. En cada caso, el espectro escalón se representa en línea negra sólida. El desplazamiento (Dto.) se calcula a partir de la diferencia entre los espectros en $T = 0,6$. Además, se calcula la pendiente (Pte.) en ese punto para obtener información sobre la agudeza del flanco. También se calcula el contraste (Cte.), como la diferencia entre el máximo

y el mínimo de cada espectro. Por último, se calcula dif_rel para obtener la sensibilidad del sensor. Todos estos valores se sintetizan en la tabla I, junto al Err^2 del ajuste.

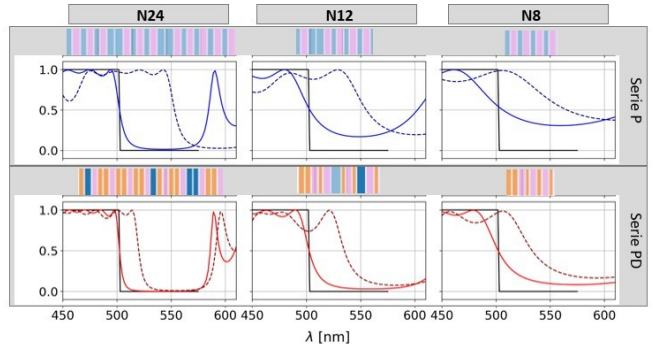


Figura 2. Espectros de transmisión óptimos. En azul, corresponden a la serie P, y en rojo, a la serie PD. Los espectros a $n_{poro} = 1$ se muestran en línea sólida, y a $n_{poro} = 1,33$ en línea punteada. En negro se representa el espectro escalón unitario. Se presentan las IDEFs obtenidas en cada caso, donde los materiales se representan según los colores violeta oscuro: SiO_2 , violeta claro: SiO_2P , naranja oscuro: TiO_2 , naranja claro: TiO_2P , azul oscuro: ZrO_2 , azul claro: ZrO_2P .

Tabla I
ESTUDIO DEL DESPLAZAMIENTO, PENDIENTE, CONTRASTE, dif_rel Y Err^2 DE LOS ESPECTROS DE TRANSMISIÓN ÓPTIMOS.

	Serie	Dto. [nm]	Pte. [1/nm]	Cte.	dif_rel	Err^2
N24	P	50.4	0.087	0.99	0.8	0.05
	PD	17.6	0.136	1.00	0.3	0.03
N12	P	51.4	0.027	0.83	0.61	0.24
	PD	32.0	0.056	0.97	0.55	0.08
N8	P	54.7	0.013	0.69	0.44	0.49
	PD	29.9	0.030	0.91	0.43	0.17

Analizando las soluciones de ResGLOnet para $N = 24$ que mejor ajustan el escalón empleando los materiales mesoporosos de la serie P de la figura 2 y la tabla I, se observa una buena correspondencia cualitativa con la forma del espectro deseado. Como es de esperar, para $N = 12$ y 8 aumenta el Err^2 , apartándose del espectro ideal. Esto se refleja en un ensanchamiento del flanco y una pérdida de contraste. En cuanto al desplazamiento del espectro en función de n_{poro} , es similar para los tres N analizados. Con la incorporación de materiales densos a la biblioteca de materiales, en la serie PD mejora el ajuste en comparación con el de la serie P, lo que se refleja en un aumento de la pendiente del flanco y del contraste para todos los N . Pero por otro lado, como era de esperar, al disminuir el volumen poroso disminuye el desplazamiento.

En las IDEFs óptimas de la figura 2, se destaca que al disminuir el número de capas N las soluciones convergen en una elección de los dos materiales cuyo contraste de índices de refracción es máximo tanto en la serie P, con SiO_2P y ZrO_2P , como en la serie PD, con SiO_2P y TiO_2 . En particular, en la serie PD es más evidente el efecto del aumento de la variabilidad en los materiales al aumentar N , como se observa en el gráfico de la figura 3 que representa la frecuencia

$\frac{N_i}{N}$ con i los materiales de la biblioteca. En todos los casos se obtuvieron soluciones no periódicas en los espesores.

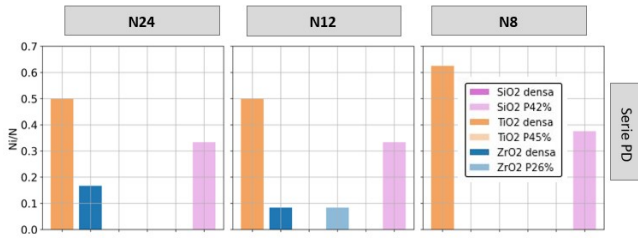


Figura 3. Histograma de los materiales de las capas de las IDEFs de la serie PD.

Al comparar los valores de $diff_rel$ de la tabla I, recordando que cuanto mayor su valor, mejor el rendimiento del sensor, se desprende que para $N = 24$ la serie P posee un mejor rendimiento que la serie PD. Lo mismo sucede para $N = 12$ y 8, aunque mantienen un rendimiento similar entre ambas bibliotecas de materiales. En cuanto al Err^2 , como es de esperar, crece con la disminución N . Es interesante notar que para todos los N , la serie P a pesar de tener el mayor Err^2 , tiene buen rendimiento como sensor.

Por último, un aspecto relevante a evaluar es si relajar los espesores y periodicidad del CF mejora el rendimiento del sensor. En el caso del CF de $SiO_2P - TiO_2P$ de 24 capas, se encontró un valor máximo de $diff_rel = 0,72$ dentro del barrido de espesores en el rango $e = [20, 200] nm$, correspondiente a $e_{SiO_2P} = 79 nm$ y $e_{TiO_2P} = 110 nm$. Es decir, la IDEFs mesoporosa óptima de 24 capas supera en un 11 % al rendimiento teórico del CF mesoporoso de igual número de capas.

V. CONCLUSIONES

Se aplicó la metodología basada en redes neuronales residuales generativas, ResGLOnet, al diseño inverso de IDEFs mesoporosas destinadas a la detección de vapor de agua, como gas modelo. Se obtuvieron IDEFs aperiódicas que ajustaron adecuadamente el espectro deseado escalón unitario. Esta metodología permitió generar diseños óptimos de IDEFs que se ajustaron a las especificaciones de respuesta óptica requeridas en la región espectral de interés del dispositivo de sensado propuesto, considerando limitaciones y condicionantes de fabricación que abarcan aspectos como el número de capas, los espesores máximos y mínimos y los materiales disponibles. La mejora en el desempeño teórico respecto al CF mesoporoso de 24 capas motiva continuar esta línea de trabajo a fin de llevar a cabo aplicaciones avanzadas en el ámbito de la óptica.

Como perspectiva, en el área experimental, la síntesis y caracterización de las IDEFs propuestas por ResGLOnet es

un paso fundamental para verificar su viabilidad y desempeño en condiciones reales. En relación al área electromagnética, la incorporación de parámetros adicionales, como el ángulo de incidencia y la polarización, abre nuevas posibilidades para lograr una personalización más completa y un control más preciso de las propiedades ópticas. Por último, en el área de aprendizaje automático, se puede superar el desempeño si se implementan modificaciones a la función de pérdida que guía el entrenamiento con el objetivo de que se adapte al problema específico de optimización.

REFERENCIAS

- [1] T. Li, G. Liu, H. Kong, G. Yang, G. Wei y X Zhou, "Recent advances in photonic crystal-based sensors," *Coordination Chemistry Reviews*, vol. 475, pp. 214909, 2023.
- [2] J.K. Goyal, H.S. Dutta y S. Pal, "Recent advances and progress in photonic crystal-based gas sensors," vol. 50, pp.203001, 2017.
- [3] Y. Zhang, Y. Zhao y Q. Wang, "Measurement of methane concentration with cryptophane E infiltrated photonic crystal microcavity," *sensors and Actuators B: Chemical*, vol. 209, pp. 431-437, 2015.
- [4] A. Ghosh, A. Pal y N. Ranjan Das, "An approach to design photonic crystal gas sensor using machine learning," *Optik*, vol. 208, pp. 163997, 2020.
- [5] R.M. Caraballo, D. Onna, N. López Abdala, G.J.A.A. Soler Illia y M. Hamer, "Metalloporphyrins into mesoporous photonic crystals: towards molecularly-tuned photonic sensing devices," vol. 309, pp.127712, 2020.
- [6] C. Lalau-Keraly, S. Bhargava, O. Miller y E. Yablonovitch, "Adjoint shape optimization applied to electromagnetic design," *Optics express*, vol. 21, pp. 21693-21701, 2013.
- [7] S.D. Campbell, D. Sell, R.P. Jenkins, E.B. Whiting, J.A. Fan and D.H. Werner, "Review of numerical optimization techniques for meta-device design," *Optical Materials Express*, vol. 9, pp. 1842-1863, 2019.
- [8] C.A.C. Coello, G.B. Lamont and D.A. Van Veldhuizen, "Evolutionary Algorithms for Solving Multi-Objective Problems," Springer, vol. 5, Berlin, 2007.
- [9] J.C.C. Mak, C. Sideris, J. Jeong, A. Hajimiri and J.K.S. Poon, "Binary particle swarm optimized 2x2 power splitters in a standard foundry silicon photonic platform," *Optics Letters*, vol. 41, pp. 3868-3871, 2016.
- [10] V. Ganapati, O.D. Miller and E. Yablonovitch, "Light Trapping Textures Designed by Electromagnetic Optimization for Subwavelength Thick Solar Cells," *IEEE Journal of Photovoltaics*, vol. 4, pp. 175-182, 2014.
- [11] P.R. Wiecha, A. Arbouet, C. Girard and O.L. Muskens, "Deep learning in nano-photonics: inverse design and beyond," *Photonics Research*, vol. 9, pp. B182-B200, 2021.
- [12] J. Jiang y J. Fan, "Multiobjective and categorical global optimization of photonic structures based on ResNet generative neural networks," *Nanophotonics*, vol. 10, no. 1, pp. 361-369, 2021.
- [13] <https://look.ams-osram.com/m/3dc70b328943ff0a/original/LT-T64G.pdf>.
- [14] <https://www.sunrom.com/download/628.pdf>.
- [15] L. Missoni, "pymultilayer: Implementación del MMT para el cálculo de los espectros de reflectividad y transmisión de EFs y el cálculo de los campos en cada región de interés," unpublished.
- [16] A. Zelcer y G.J.A.A. Soler-Illia, "Sorption and optical properties of sol-gel thin films measured by X-Ray Reflectometry and Ellipsometric Porosimetry," *Thin Solid Films*, vol. 520, pp. 853-4862, 2012.
- [17] M.C. Fuertes, M.P. Barrera y J. Plá, "One-step preparation of UV transparent highly ordered mesoporous zirconia thin films," *Journal of Materials Chemistry C*, vol. 1, pp. 1359-1367, 2013.
- [18] D. Onna, M.C. Marchi y M.L. Martínez Ricci, "Loading insoluble sulfides in mesoporous oxide films from precursors in solution," *Journal of Sol-Gel Science and Technology*, vol. 102, pp. 264-278, 2022.

Love Surface Acoustic Wave-based-Sensor : Characterization of Microfluidic Biosensing System

Martin Millicovsky¹, Gabriel Muñoz², Juan Cerrudo², Albano Peñalva², Juan Reta² and Martin Zalazar^{1,2}

¹Instituto de Investigación y Desarrollo en Bioingeniería y Bioinformática - Conicet, Oro Verde, Entre Ríos, Argentina

²Facultad de Ingeniería, Universidad Nacional de Entre Ríos, Oro Verde, Entre Ríos, Argentina

martin.zalazar@uner.edu.ar

Abstract— Biosensing plays a critical role in biomedical research, environmental monitoring, and clinical diagnostics, providing real-time detection and analysis of biomolecules. Powered by Surface Acoustic Wave (SAW) sensors, it offers unparalleled sensitivity and real-time detection in biomolecule analysis. The Love type Surface Acoustic Wave (LSAW) sensor stands out in fluid biosensing, demonstrating compatibility with microfluidic systems and sensitivity to physical properties due to the influence on surface acoustic wave propagation. Introducing a LSAW-based biosensing platform addresses the demand for sensitive, real-time detection in complex fluidic environments and enhance accuracy in biosensing applications. This paper presents a prototype biosensing system that integrates microfluidic techniques with polydimethylsiloxane (PDMS) for fluid circulation. The characterization involved analyzing the sensitivity and stability of the sensor over time using fluids with varying physical properties: distilled water, polyethylene glycol, and sodium chloride solutions. The results demonstrate that the development is on track, and the next step before biosensing would be to accurately differentiate fluid solutions at different concentrations and implement a temperature control to verify if the system performance can be further optimized.

Keywords—Biosensing, Surface Acoustic Wave, Love, Microfluidic, System.

I. INTRODUCTION

Biosensing entails the detection of biological molecules using biosensors like those based on Surface Acoustic Wave technology, which have revolutionized the field with unparalleled sensitivity and real-time detection capabilities [1]. The Love Surface Acoustic Wave sensor excels in fluid detection due to its heightened sensitivity and compatibility with microfluidics systems [2]. The device comprises a crystal resonator composed of interdigitated transducer (IDTs) on a piezoelectric substrate and its frequency response changes due to variations in the physical properties of the fluid affecting wave propagation speed [3]. Environmental factors as temperature, humidity and pressure also affect the frequency response and must be controlled [4].

The LSAW is considered a transmission line because the SAW propagates along a defined path on the piezoelectric substrate and a Vector Network Analyzer (VNA) is commonly used to measure the S21 insertion loss (IL) and phase [5]. An open-loop strategy is can be employed and explains that changes in SAW phase velocity cause a frequency shift (Δf) that corresponds to the measured phase shift ($\Delta\Phi$) at the working point [6] and depending on the properties of the sample analyzed by the LSAW, there will also be variations in its sensitivity [7].

For microfluidic applications involving LSAW, PDMS is frequently selected due to its biocompatibility, flexibility, and ease of fabrication, facilitating accurate fluid handling and seamless integration with LSAW sensors [8].

The potential applications of LSAW technology are vast, offering a wide range of system possibilities. This article introduces a LSAW-based microfluidic prototype designed for biomedical applications. The development involves a sensor module that integrates a PDMS chip and connects the sensor to both a VNA and an infusion pump.

II. MATERIALS AND METHODS

A. Microfluidic biosensing system

The sensing module comprises a 3D-printed base and cover (Crealty LD006 3D - Hellbot resin) designed based on a LSAW (AWsensors). The sensor has a resonance frequency of approximately 120 MHz, measuring 17 millimeters long, 8.5 millimeters wide, and 365 microns thick.

The base facilitates the precise positioning of both the crystal and the PDMS chip. The cover connects the sensor to a NanoVNA type H through gold-plated pogo pins and SMA connectors integrated onto a printed circuit board. The base is also equipped with inserts and guides to enable precise alignment with the cover and a final adjustment using four screws. On the other hand, the lid includes three inserts for a manual adjustment of the PDMS chip with screws. An exploded view of the sensing module set-up and the sensor utilized are depicted in Figure 1.

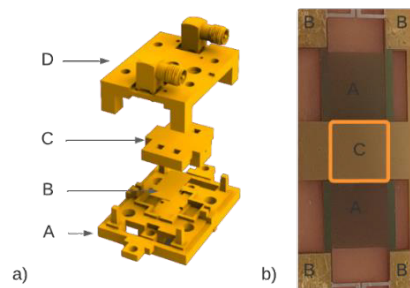


Fig. 1. a. Module Set-Up: Base (A)/Sensor (B), PDMS chip (C), Cover (D). b. Sensor. The LSAW is composed of an AT-quartz 36° Y-cut Z' substrate, aluminum IDTs (A) with wavelength $\lambda = 40 \mu\text{m}$ and a SiO₂ guiding layer through which the acoustic wave that entered as an electrical signal circulates. The crystal is finished with a 10nm chrome and 50nm thick gold sensing layer, where the electric contacts (B) for signal input-output are located. The sensing area originally measured 18.6 mm² and was delimited to 9.88 mm² (C) for this development.

The PDMS chip was created with a 3D-printed mold (Hellbot Magna 2 300 Printer) employing fused deposition modeling (FDM) and a precision nozzle of 200 microns. Within this mold, a 10:1 mixture of Sylgard184TM base elastomer and Sylgard184TM curing agent was introduced. Then, the mixture underwent vacuum-pumping process for one hour to eliminate entrapped bubbles. Subsequently, the mold was filled with the PDMS mixture and cured in an oven set at 50 degrees Celsius for a duration of 1 hour, facilitating the solidification of the PDMS material prior to demolding.

The design of the PDMS chip itself plays a pivotal role in its functionality, enabling both effective sealing and fluid circulation across the sensing area. This achievement was accomplished by integrating a 3.8 mm long and 2.6 mm wide O-ring positioned at a distance of 300 microns from the sensor and 450 microns from the IDTs, ensuring robust sealing properties. For fluid contact on the sensing area, the O-ring has an extrusion of 2.3 mm length and 1.1 mm width, allowing communication with the inlet and outlet horizontal channels. Both were made by inserting metal rods with a diameter of 500 microns into the mold, creating a U-shaped channel alongside the O-ring extrusion. On the other hand, to protect the sensor of environmental factors, the chip covers the IDTs with a distance of 900 microns leaving four strategically positioned holes for the gold-plated pogo pins.

For fluid circulation, the Razel A-99 infusion pump and microfluidic hoses were employed. fused deposition A 3d printed FDM base (Prusa i3 MK3 3D Printer) was made to elevate and align both the sensor module and the NanoVNA with the infusion pump, thus effectively shortening the length of the hoses and optimizing fluid flow. Furthermore, leveraging the same printing method, two protective covers were printed to guard the system from potential environmental factors. The first cover the walls of the sensor module lid, providing comprehensive protection. The second protector complete the safeguarding of the entire system, ensuring its integrity and reliability throughout the duration of experimental procedures. Figure 2 depicts the assembled biosensing system.

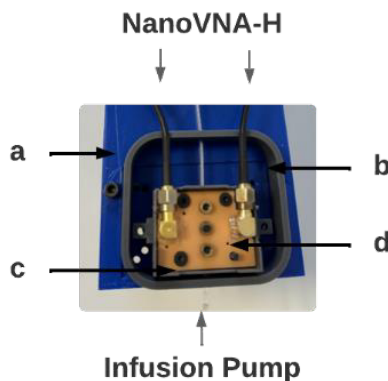


Fig. 2. Assembled biosensing system. The figure depicts the FDM base (a) and the first (b) and second (c) protector without their covers, allowing for an unobstructed view of the sensing module (d) connected to both the infusion pump and the NanoVNA-H from a top perspective.

B. Adaptation of NanoVNA-H software

The NanoVNA software can be downloaded from GitHub and is written in Python. Given its intended use, the decision was to modify the program code, as it is originally designed for various functions in the field of telecommunications. The primary tool of the instrument is the single frequency sweep, while for biosensing purposes, a variant called continuous sweep was developed. To utilize this function, important parameters such as sweep duration were added to the graphical interface. In addition, an algorithm was developed to study the amplitude and phase curve in real-time.

During a single sweep, bandwidth, resolution, and the 'Search' mode are set to determine the operating point. Subsequently, based on the total experiment time and the duration of the sweep, the number of sweeps to be performed in continuous mode is calculated, and 'Analyze' mode is selected to obtain phase and amplitude data for each sweep. The Continuous sweep data is automatically exported in Touchstone format (one file per sweep) and can also be exported in xlsx format, while single sweep data is exported as a Touchstone file.

C. System characterization

The characterization was divided in two experiments performed at room temperature without controlling the temperature of the volume covered by the two system protectors. The focus was placed on studying the stability and sensitivity of the sensor phase over time, as well as its ability to differentiate fluids with different physical characteristics. This was achieved using the descriptive statistical variables mean and standard deviation (std). According to the literature reviewed, the standard deviation, a measure that reflects the sensitivity of the sensor, changes depending on the properties of the sample under examination and this may exceed one degree on phase.

Prior to setting up the system, the sensor undergoes a cleaning process which involves submerging the sensor in 2% SDS detergent for five minutes, rinsing with distilled water, and drying with pure nitrogen gas. The first experiment aims to observe the stability and sensitivity of the frequency response of the sensor over forty minutes, without fluid circulation and with the PDMS chip in place. The objective was to determine how long it takes for the sensor to stabilize its response and how it varies over time.

The second and last test involves five stages of consecutively circulation of 20% Polyethylene glycol (Peg) 3350 solution, distilled water, a 5% sodium chloride (NaCl) solution, distilled water, and finally the same 20% PEG 3350 solution. The infusion pump was configured with a 10 m3 syringe and an approximate flow rate of 1.5 ul/sec. The fluids were changed based on the criterion that the response of the LSAW remained stable for at least 7 minutes. The objective of this experiment was to verify that the sensor could differentiate the fluids and return to a previous response by recirculating the PEG solution and cleaning both the Peg and sodium chloride solution with distilled water.

III. RESULTS

The sensor phase response for the first experiment can be observed in Figure 3. From minute 3.22 onwards, the phase entered a stable regime, registering a mean of 3.19° and a standard deviation of 0.16°.

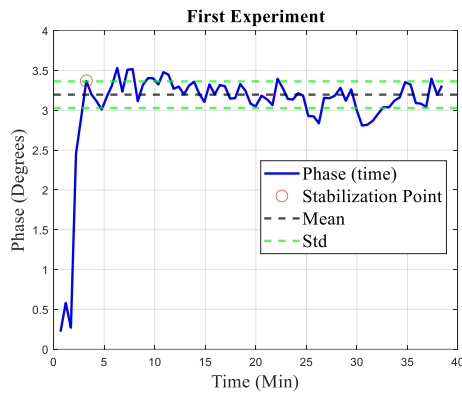


Fig. 3. Phase temporal response for first experiment. The stabilization point (red) indicates the moment in time when the response began to stabilize and entered into a regime of stability. During that time interval, the black dashed line indicates the mean, and the green lines represent the standard deviation.

The second experiment lasted nearly 130 minutes, and its phase temporal response is plotted on Figure 4. The moment when the phase entered a stability regime and when the fluid was changed were determined. Using both points in time, five vectors were constructed to represent the stability time of each fluid and its mean and std can be observed on Table 1. Additionally, for each fluid, the time it took for the sensor to reach the stability regime (stabilization point) was added.

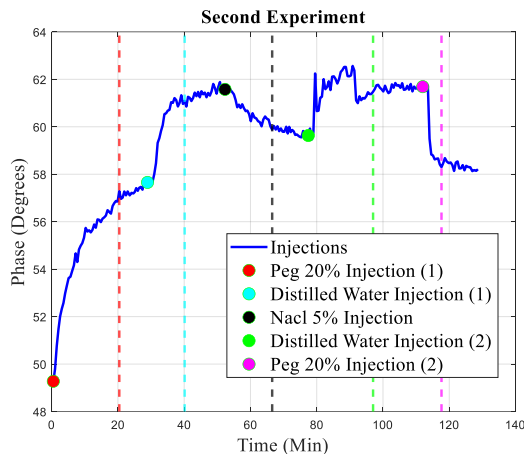


Fig. 4. Phase temporal response for second experiment. The points represent the fluid injection, while the dashed lines indicate the stabilization point.

TABLE I. SECOND EXPERIMENT PHASE AND STABILIZATION TIME

Injections	Stabilization Time (min)	Phase (Degrees)
Peg 20% (1)	20.41	57.31 +/- 0.21
Distilled Water (1)	11.21	61.39 +/- 0.23
Sodium Chloride 5%	14.24	59.79 +/- 0.14
Distilled Water (2)	19.55	61.64 +/- 0.12
Peg 20% (2)	5.66	58.34 +/- 0.16

Peg recirculation resulted in a phase returning to its initial value but increasing by nearly one degree. Distilled water cleaned Peg initially and NaCl subsequently, with phase returning to its original value without significant changes in mean and std. The time required for sensor stabilization varied across cases and Peg initial circulation took 20.41 min, while

its recirculation was 5.66 min. Distilled water circulation initially took 11.21 min, whereas NaCl cleaning required 19.55 min, indicating shorter cleaning time. Finally, NaCl circulation reached stability in 14.24 min.

IV. DISCUSSION AND CONCLUSION

The first experiment revealed that without circulating a fluid, it took 3.22 minutes to reach stabilization. This delay may be attributed to measurements starting immediately after system assembly, requiring some time before analysis. Despite this, the sensitivity, with 0.16° std, was acceptable considering that literature values can surpass one degree.

The second experiment confirmed an adequate LSAW sensitivity when circulating fluids as it successfully differentiated the three utilized and even reverted to a previous response. Each stability regime time was set to at least 7 minutes for mean and standard deviation calculations. Extending fluid circulation could reveal phase changes due to potential alterations in physical properties over time.

A prototype of a LSAW-based microfluidic biosensing system was developed. Characterization experiments were conducted focusing on the examination of sensor sensitivity and stability over time with and without using fluids. The results indicate potential applications before biosensing, such as analyzing solutions of varying concentrations and implementing a temperature control.

ACKNOWLEDGMENT

We are grateful to the Electronics Prototyping & 3D Lab of the National University of Entre Rios for giving us the facilities to develop and test our prototype.

REFERENCES

- [1] Go, D. B., Atashbar, M. Z., Ramshani, Z., & Chang, H. C. (2017). "Surface acoustic wave devices for chemical sensing and microfluidics: A review and perspective". In *Analytical Methods* (Vol. 9, Issue 28, pp. 4112–4134). Royal Society of Chemistry. <https://doi.org/10.1039/c7ay00690j/1>
- [2] J. Rauf, S., Qazi, H. I. A., Luo, J., Fu, C., Tao, R., Rauf, S., Yang, L., Li, H., & Fu, Y. (2021). "Ultrasensitive leaky surface acoustic wave immunosensor for real-time detection of alpha-fetoprotein in biological fluids". *Chemosensors*, 9(11). <https://doi.org/10.3390/chemosensors9110311>
- [3] Rocha-Gaso, M. I., March-Iborra, C., Montoya-Baides, Á., & Arnaú-Vives, A. (2009). "Surface Generated Acoustic Wave Biosensors for the Detection of Pathogens: A Review". In *Sensors* (Vol. 9, Issue 7, pp. 5740–5769). MDPI. <https://doi.org/10.3390/s90705740>
- [4] Caliendo, C., & Hamidullah, M. (2016). "A theoretical study of love wave sensors based on ZnO-glass layered structures for application to liquid environments". *Biosensors*, 6(4). <https://doi.org/10.3390/bios6040059>
- [5] Kim, G., Cho, B. K., Oh, S. H., & Kim, K. B. (2020). "Feasibility Study for the Evaluation of Chicken Meat Storage Time Using Surface Acoustic Wave Sensor". *Journal of Biosystems Engineering*, 45(4), 261–271. <https://doi.org/10.1007/s42853-020-00066-7>
- [6] Choudhari, A., Rube, M., Sadli, I., Sebeloue, M., Tamarin, O., & Dejous, C. (n.d.). "Love Wave acoustic sensors behavior in complex liquids". Multiparameter sensing using acoustic and electrical signals. In *IEEE SENSORS JOURNAL: Vol. XX*.
- [7] Rocha-Gaso, M. I., Renaudin, A., Sarry, F., & Beyssen, D. (2015). "Lab-on-a-chip based integrated hybrid technologies for biofluids manipulation and characterization". *Procedia Engineering*, 120, 687–690. <https://doi.org/10.1016/j.proeng.2015.08.750>
- [8] Tarbague, H., Lachaud, J.-L., Destor, S., Velutini, L., Pillot, J.-P., Bennetau, B., Moynet, D., Rebière, D., Pistre, J., & Dejous, C. (2009). "PDMS (Polydimethylsiloxane) Microfluidic Chip Molding for Love Wave Biosensor". *ECS Transactions*, 23(1), 319–325. <https://doi.org/10.1149/1.3183735>

Liberation of Functionalized Chips and Cells from various Surfaces

Juan Pablo Aguil
Micro- and NanoTools Group
 IMB-CNM (CSIC)
 Cerdanyola, Barcelona, Spain
 juanpablo.aguil@imb-cnm.csic.es

Adrian Rodríguez-Lau
Micro- and NanoTools Group
 IMB-CNM (CSIC)
 Cerdanyola, Barcelona, Spain
 adrian.rodriguez@imb-cnm.csic.es

Mònica Roldán
Unitat de Microscòpia Confocal
Servei de Medicina Genètica i
Molecular, IPER, SJD & Department
of Neurogenetics and Molecular
Medicine, IPER, IRSJD
 Esplugues de Llobregat, Spain
 monica.roldan@sjd.es

Marta Duch
Micro- and NanoTools Group
 IMB-CNM (CSIC)
 Cerdanyola, Barcelona, Spain
 marta.duch@imb-cnm.csic.es

María Isabel Arjona
Institut Jacques Monod (CNRS)
 Paris, France
 isabel.arjona@ijm.fr

José A. Plaza
Micro- and NanoTools Group
 IMB-CNM (CSIC)
 Cerdanyola, Barcelona, Spain
 joseantonio.plaza@imb-cnm.csic.es

Pau Mercier
Micro- and NanoTools Group
 IMB-CNM (CSIC)
 Cerdanyola, Barcelona, Spain
 pau.Mercier@imb-cnm.csic.es

Lara Cantarero
Laboratory of Neurogenetics and
Molecular Medicine, IPER, IRSJD &
CIBERER (ISCIII)
 Esplugues de Llobregat, Spain
 lara.cantarero@sjd.es

Abstract— Suspended miniaturized entities such as chips and cells play a crucial role in various fields including drug delivery, diagnostics, and biomedical science. However, the efficient liberation of these entities from their fabrication or culture surface without compromising their functionality remains a significant challenge. Here, we present a novel technology designed to address this challenge by employing a combination of controlled mechanical release and surface modification mechanisms.

Keywords— Anisotropy, microparticles, suspended chips, liberation, cells.

I. INTRODUCTION

Suspended chips and cells offer versatile platforms with diverse functionalities, making them indispensable in numerous fields such as healthcare, biotechnology, and materials science[1]. Nonetheless, effectively releasing these entities from their fabrication or culture surface without compromising their functionality remains a notable challenge[2]. Here we describe two main methods for the subsequent release of miniaturized entities as chips and cultured cells from their fabrication substrate or culture. The first approach uses the integration of mechanical fixtures which maintain the chips anchored during their fabrication and possible subsequent functionalization. These fixtures are later broken with a lateral load without altering the microparticle or its functionalization. These fixtures can consist in micromachined structures directly underneath the chips[2,3] or by the adhesion of the bulk material of the chip to the fabrication substrate[4,5]. Similarly, naturally attached cells can be later liberated following the same strategy. Alternatively, in our second approach, we strategically incorporate a release layer into the fabrication surface, facilitating the detachment of functionalized chips upon surface modification. Through a systematic experimental approach, we optimized the release processes to ensure minimal interference with the functionality of the chips. Furthermore, the versatility of the technology is demonstrated through its compatibility with various chip materials, including silicon, metal, and polymer. The scalability and ease

of integration into existing microfabrication workflows make the technology well-suited for both research and industrial applications.

II. MECHANICAL LIBERATION OF CHIPS

Silicon oxide, nickel and polymeric chips were fabricated onto silicon wafers following microfabrication techniques. The crucial step is creating a system where the chips could remain attached to the substrate during all the fabrication and subsequent functionalization (if required) steps, while allowing their on-demand release.

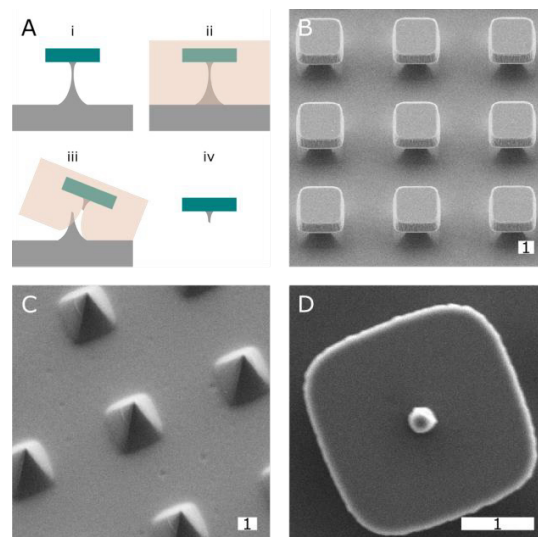


Fig. 1. Silicon oxide chips are liberated by mechanical loads to break the underlining anchor. **A:** **i)** The chips are fabricated with an anchor and remain in place during all fabrication processes. **ii)** Mounting media is poured over the chips and left to solidify. **iii)** The solidified mounting media is peeled-off from the substrate. **iv)** The mounting media is dissolved and the chips are recollected. SEM images, **B:** the fabricated chips on wafer, **C:** the remaining anchors after liberation of the chips, and **D:** the underside of a liberated chip. Scale bars represent the value in μm .

A. Releasing SiO₂ chips with micromachined anchor

We used silicon microtechnology to fabricate SiO₂ chips fixed to the silicon wafer substrate with a subjacent anchor[2,3]. As Fig. 1A shows, the design of the chips includes this anchor as the weakest part of the chip so that a lateral force selectively concentrates the mechanical stresses in that area, breaking this anchor and liberating the chips from the substrate. The fabricated chips are liberated by encasing them in liquid medium (Fluoromount) and letting it solidify. After solidification, the resulting membrane can be peeled-off along with the embedded chips. The chips can be then recollected by dissolving the membrane in an aqueous medium. SEM inspection of the fabricated chips shown in Fig. 1B show the orderly distribution of chips on the wafer. The remaining anchor portions of liberated chips are shown in Fig. 1C. A small portion of the anchor also remains on the underside of the chips, and it can be seen in Fig. 1D. This releasing method could provide the means to release silicon chips with different physical architectures together with chemical functionalization for several other bespoke applications.

B. Releasing Magnetic Nickel chips

Watts nickel electroplating was used to fabricate the magnetic barcodes shown in Fig. 2 [4]. Their subsequent release posed a great challenge, as traditional release methods using HF vapors damaged the chips. Therefore, a two-step liberation process was developed to obtain the suspended chips. Firstly, as shown in Fig. 2A ii), the chip/substrate set-up was heated to 200 °C and kept at that temperature for 20 min. Rapid cooling to 21 °C created a thermal shock weakening the adhesion at the metal/substrate interface. Secondly, the weakened chips were then covered with liquid mounting media and left to solidify. As with the SiO₂ chips, the resulting solid membrane was peeled-off, taking all the embedded chips with it. The chips were recollected after the membrane was dissolved in an aqueous solution.

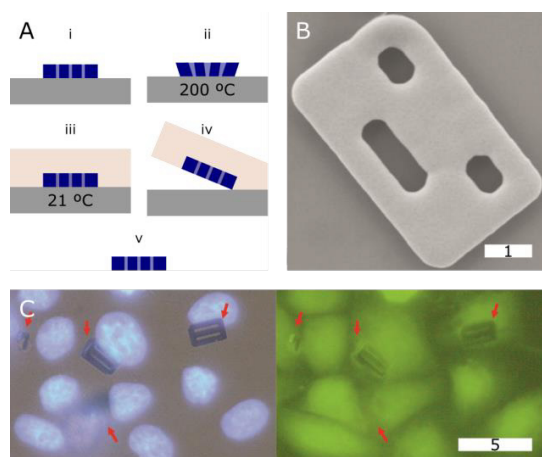


Fig. 2. Nickel barcode chips are liberated by thermal-shock and subsequent mechanical peel-off. **A: i)** The chips are fabricated on the wafer by electroplating. **ii)** The set-up is heated-up to 200 °C and rapidly cooled-down to 21°C. **iii)** Mounting media is poured over the chips and left to solidify. **iv)** The solidified mounting media is peeled-off from the substrate, liberating the chips. **v)** The mounting media is dissolved and the chips are recollected. **B:** SEM image of the fabricated chip. **C:** HeLa cells stained with DAPI (nuclei, blue) and the vital dye CellTracker (green). Red arrows point to the Ni barcodes. Scale bars represent the value in μm . Adapted from [4].

The resulting suspended magnetic barcodes were used for living cell tagging and manipulation[4]. HeLa cells were cultured with the barcodes, promoting cell-device contact. Confocal microscopy confirmed internalization of the barcodes, while viability assessment using fluorescent vital dye labeling revealed that barcode-bearing HeLa cells remained viable, comparable to neighboring cells (Fig. 2C).

C. Releasing Functionalized SU-8 chips

We fabricated a dense array of ordered SU-8 chips with standard polymeric photolithography (Fig. 3A i) [5]. The resulting array was subsequently derivatized with heterobifunctional crosslinkers to create reactive moieties on the surface of the chips. These reactive sites could be used to add chemical functionalities to the anchored chips, as shown in Fig. 3A ii). As presented previously, mounting medium was used to liberate the functionalized chips. The membrane is dissolved in an aqueous solution. Fluorescent dyes, labeled DNA, fluorescent proteins and quantum dots (QDs) were successfully immobilized onto SU-8 chips (Fig. 3 B-E).

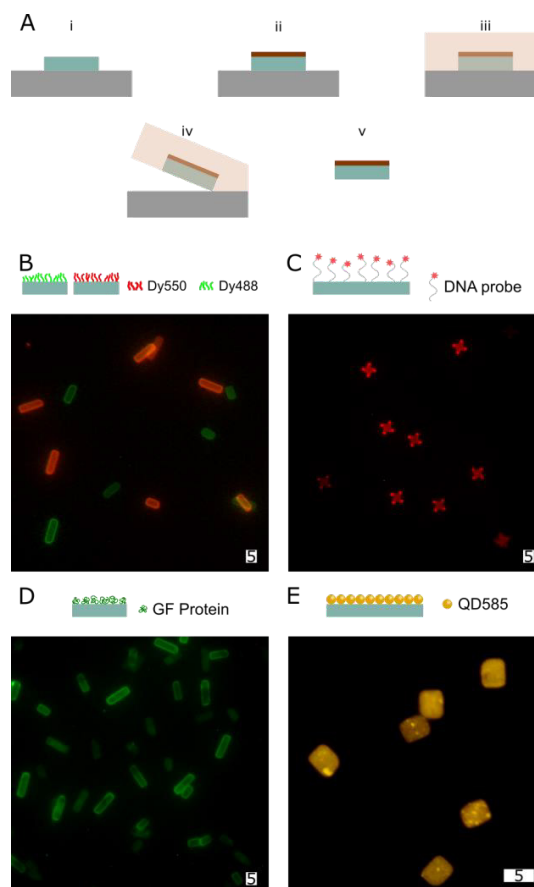


Fig. 3. Functionalized SU-8 chips are liberated by mechanical peel-off. **A: i)** The chips are fabricated on the wafer standard photolithography. **ii)** The upper surfaces of the chips are functionalized with (bio)chemical entities. **iii)** Mounting media is poured over the chips and left to solidify. **iv)** The solidified mounting media is peeled-off from the substrate, liberating the chips. **v)** The mounting media is dissolved and the chips are recollected. Fluorescence microscopy images of SU-8 chips functionalized with: **B:** fluorescent dye Dylight550 and Dylight488, **C:** Texas red-modified DNA. **D:** Green-fluorescent protein. **E:** Quantum dots with emission at 585 nm. Scale bars represent the value in μm . Adapted from [5].

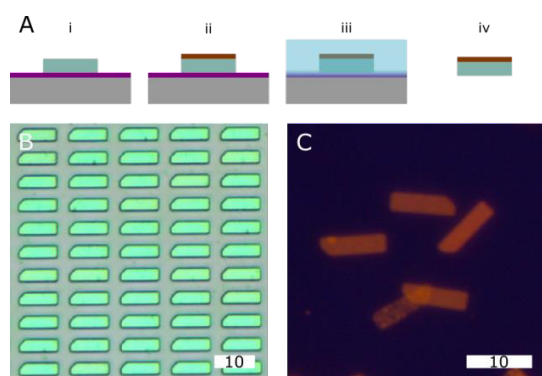


Fig. 4. Functionalized SU-8 chips are liberated by dissolving the underlying sacrificial layer. **A: i)** The chips are fabricated on the wafer standard photolithography over a soluble sacrificial layer. **ii)** The upper surfaces of the chips are functionalized with (bio)chemical entities. **iii)** The sacrificial layer is dissolved with an aqueous solution. **iv)** The chips are recollected. **B:** Microscopy images of SU-8 chips on the wafer. **C:** Liberated chips previously functionalized with Quantum dots with emission at 605 nm. Scale bars represent the value in μm .

III. LIBERATION OF CHIPS WITH SOLUBLE SACRIFICIAL LAYER

An alternative method to fabricate polymeric chips for a later on-demand release is to create a sacrificial layer between the main substrate and the chips. It is important to choose this sacrificial layer which can withstand the fabrication process, as photolithography, development, and if required, functionalization of the chips. Additionally, we required a sacrificial layer that could be eliminated without the risk of chemical or physical damage to the chips and/or their functionalities. Considering these constraints, we developed a water-soluble sacrificial layer consisting on a polymerized solution of polyvinyl alcohol coating the silicon wafer where the chips we subsequently fabricated. This layer can withstand the deposit of the uncured polymer, its patterning with photolithography, the developing of the unreacted polymer, and, when required, the addition of heterobifunctional crosslinkers for the addition of chemical functionalizations on the top surfaces of the chips. Fig. 4 presents the fabrication strategy followed to obtain liberated chips with the soluble sacrificial layer. As with previous results, we obtained a dense array of ordered chips on the wafer (Fig. 4B). As a proof of concept, amine-modified QDs with emission at 605 nm were selectively patterned onto the chips before release and the released chips can be seen in Fig. 4C.

IV. SUSPENSION OF FIXED CELLS

Releasing fixed cultured cells could offer several advantages in biological studies: flexibility in handling allowing for precise positioning and arrangement of cells on a desired substrate. It could enhance reproducibility, as fixed cells maintain their morphology properties, and could be transported into diverse characterization equipment. Lastly, this could help store fixed cells for longer periods compared to live cells. We used the liberation method to remove two different fixed and labeled cell lines from their culture substrate (Fig. 5A) and demonstrated that their morphology remains intact. The fluorescent confocal images in Fig. 5B show human fibroblasts on the coverslips while Fig. 5C shows the cells when liberated and resuspended in water. Fig. 5D-E show the same procedure for SH-SY5Y cells. It is worth noting that the cell's morphology and overall intracellular structure and distribution remain intact.

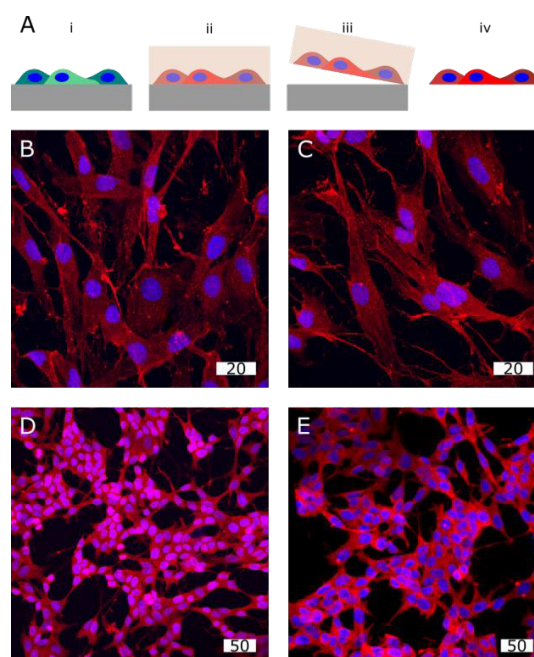


Fig. 5. Liberation of cultured cells. **A: i)** The cells are cultured over a coverslip. **ii)** After fixing and labeling the cells, mounting media is poured the culture and left to solidify. **iii)** The solidified mounting media is peeled-off from the substrate. **iv)** After dissolving the media, the cells are liberated. Fluorescence microscopy images with labeled actin (red) and nuclei (blue): **B:** Human fibroblasts over the coverslip and **C,** after liberation. **D:** SH-SY5Y cells over the coverslip and **E,** after liberation and recollection. Scale bars represent the value in μm .

The proposed technology offers a promising solution for the efficient liberation of chips and cultured cells from their fabrication/cultured surfaces by addressing key challenges associated with chip/cell detachment, including damage to their integrity and material compatibility.

ACKNOWLEDGMENTS

This project was financed by grants PID2020-115663GB-C31 funded by MICIU/AEI/10.13039/501100011033 and ERDF/EU, and Siner_2019-CRSII5 180351_14. The authors also thank the clean-room staff of IMB-CN^{M} (CSIC) for fabrication of the chips

REFERENCES

- [1] M. D. Neto, M. B. Oliveira, J. F. Mano, "Microparticles in Contact with Cells: From Carriers to Multifunctional Tissue Modulators," *Trends in Biotechnology*, 37, 9 (2019)
- [2] N. Torras, J. P. Aguil, P. Vázquez, M. Duch, A. M. Hernández-Pinto, J. Samitier, E. J. de la Rosa, J. Esteve, T. Suárez, L. Pérez-García, J. A. Plaza, "Suspended Planar Array Chip for Molecular Multiplexing at the Microscale," *Advanced Materials*, 28, 1449-1454 (2016)
- [3] J. P. Aguil, N. Torras, M. Duch, J. Esteve, L. Pérez-García, J. Samitier, J. A. Plaza, "Highly Anisotropic Suspended Planar Array Chips with Multidimensional Submicrometric Biomolecular Patterns," *Advanced Functional Materials*. Vol. 27, Issue 13, 1605912 (2017)
- [4] M. I. Arjona, C. González-Manchón, S. Durán, M. Duch, R. P. del Real, A. Kadambi, J. P. Aguil, M. Redondo-Horcajo, L. Pérez-García, E. Gómez, T. Suárez, J. A. Plaza, "Integrating magnetic capabilities to intracellular chips for cell trapping," *Scientific Reports* 11, 18495 (2021)
- [5] J. P. Aguil, M. I. Arjona, M. Duch, N. Fusté, J. A. Plaza, "Multidimensional Anisotropic Architectures on Polymeric Microparticles," *Small* 16, 20004691 (2020)

Correlation between structural quality and magnetotransport properties in planar Hall effect sensors

*Note: Sub-titles are not captured in Xplore and should not be used

Gerardo Ramírez
Laboratorio de Nanoestructuras
Magnéticas y Dispositivos
Instituto de Nanociencia y
Nanotecnología CNEA-CONICET
San Martin, Argentina
ORCID 0000-0003-4300-3706

Gabriel Bosch
Dept. Micro and Nanotecnología
Instituto de Nanociencia y
Nanotecnología CNEA-CONICET
San Martin, Argentina
gabrielbosch@cnea.gob.ar

Agostina Lo Giudice
Laboratorio de Nanoestructuras
Magnéticas y Dispositivos
Instituto de Nanociencia y
Nanotecnología CNEA-CONICET
San Martin, Argentina
agostina.logiudice@gmail.com

Andres Di Donato
Dept. Micro and Nanotecnología
Instituto de Nanociencia y
Nanotecnología CNEA-CONICET
San Martin, Argentina
didonatoandres@gmail.com

Lara Solis
Laboratorio de Nanoestructuras
Magnéticas y Dispositivos
Instituto de Nanociencia y
Nanotecnología CNEA-CONICET
San Martin, Argentina
ORCID 0000-0002-9915-0863

Laura B. Steren
Laboratorio de Nanoestructuras
Magnéticas y Dispositivos
Instituto de Nanociencia y
Nanotecnología CNEA-CONICET
San Martin, Argentina
ORCID 0000-0003-2224-9272

Resumen— Los sensores flexibles de campo magnético permiten el desarrollo de nuevas tecnologías como dispositivos para robótica blanda, dispositivos interactivos para realidad virtual y aumentada y diagnósticos en el punto de atención. Estas aplicaciones requieren dispositivos sensores con una alta sensibilidad a pequeños campos magnéticos. Para conseguir sensores con sensibilidad de detección adecuadas exploramos el efecto Hall planar en películas magnéticas delgadas de NiFe. En este trabajo investigamos las propiedades estructurales y magnéticas de sensores magnéticos flexibles por efecto Hall planar y las correlacionamos con su respuesta magnetoelectrónica.

Palabras Clave— Dispositivos flexibles, sensores magnéticos, efecto Hall planar

I. INTRODUCCIÓN

La electrónica flexible ha recibido un gran interés en la investigación debido a sus aplicaciones en dispositivos revolucionarios que incluyen desde pantallas flexibles,[1–3] paneles solares enrollables,[4,5] hasta sistemas e-skin como implantes dental para la detección de bacterias [6], dispositivos *wearable* para monitoreo de glucosa [7] o sistema de monitoreo neonatal con sensores ajustables a los movimientos de la piel [8]. Los sensores magnéticos flexibles son dispositivos electrónicos con capacidad de detección magnética que no solo son usados en navegación,[9] sistemas de diagnóstico médico [10–12] y almacenamiento de datos, si no que recientemente son potenciales candidatos para el desarrollo de dispositivos Lab-on-a-Chip [13].

Los sensores de campo magnético basados en el efecto Hall plano (PHE) son particularmente interesantes para detectar campos magnéticos débiles (inferiores al campo geomagnético), porque son intrínsecamente lineales alrededor del campo cero y muestran una gran sensibilidad [14]. Su funcionamiento se basa en la medición del cambio en la magnetorresistencia anisotrópica causada por un campo magnético externo en la geometría Hall [11–14]. Los sensores PHE presentan algunas ventajas intrínsecas respecto a otro

tipo de sensores, siendo una de las más atractivas su simplicidad de fabricación [12].

Se han reportado diferentes factores que impactan significativamente en la eficiencia y capacidad de detección de los sensores. Las capas metálicas pueden ser optimizadas definiendo la orientación preferencial de la capa activa [15–17]. El acoplamiento de intercambio puede usarse para definir un eje de anisotropía unidireccional que aunque limita la sensibilidad reduce su histéresis. La sensibilidad del sensor depende directamente de la corriente en la capa efectiva del sensor. En algunas publicaciones [18, 19] se propone una estructura de tricapa Ta(2)/IrMn(10)/Ta(3) [nm] en el que la sensibilidad aumenta significativamente si la capa intermedia es lo suficientemente gruesa como para debilitar el acoplamiento de intercambio, pero lo suficientemente delgada para que la derivación de corriente sea mínima.

Respecto de optimización de la geometría es posible obtener anisotropía uniaxial a partir de estructuras con una alta relación de aspecto utilizando solo la anisotropía de forma. De esta manera, se puede obtener un comportamiento mono-dominio en la película magnética [19, 20]. En particular, se ha reportado que para una geometría tipo elipse con una relación de aspecto superior a 10:1 (relación eje mayor a eje menor de la elipse), el comportamiento mono-dominio es mucho más estable que para una estructura rectangular. Finalmente, es posible inducir anisotropía uniaxial en una película ferromagnética crecida sobre un sustrato no plano [21]. Además, se ha reportado que el comportamiento de los sensores crecidos sobre sustratos rígidos y flexibles varían considerablemente. El estudio de sensores flexibles ha cobrado gran relevancia debido a que los dispositivos fabricados sobre sustratos ultradelgados mantienen su funcionalidad incluso con radios de curvatura del orden del milímetro [22]. Por otro lado, los sensores fabricados sobre soportes flexibles presentan comportamientos muy distintos dependiendo de la calidad y el espesor del sustrato.

En este trabajo presentamos un detallado estudio entre la calidad estructural y comportamiento magnético de sensores magnéticos rígidos y flexibles micro-fabricados, con sus propiedades de magneto-transporte.

II. MATERIALES Y MÉTODOS

Los sensores se realizaron microfabricando cruces Hall de Permalloy (Py) con un espesor de 40 nm en sustratos rígidos de Si(100) así como en láminas de polimida (Kapton) de 6 μm de espesor con una capa polimérica adicional de una fotorresina epoxy, y lámina Kapton con una cinta adhesiva de Kapton. La Fig. 1(a) muestra una imagen de microscopio del sensor microfabricado donde se evidencia la formación de la estructura y un deterioro del contacto derecho del dispositivo. El proceso de litografía definió adecuadamente los bordes de las estructuras como muestra la Fig. 1(b). Para mejorar el rendimiento del sensor, la cruz de Hall se conformó por una elipse con una relación de aspecto alta de 10:1 y un rectángulo perpendicular [Fig. 1(c)], con el objetivo de inducir un eje de magnetización preferido de la estructura Py mediante anisotropía de forma.

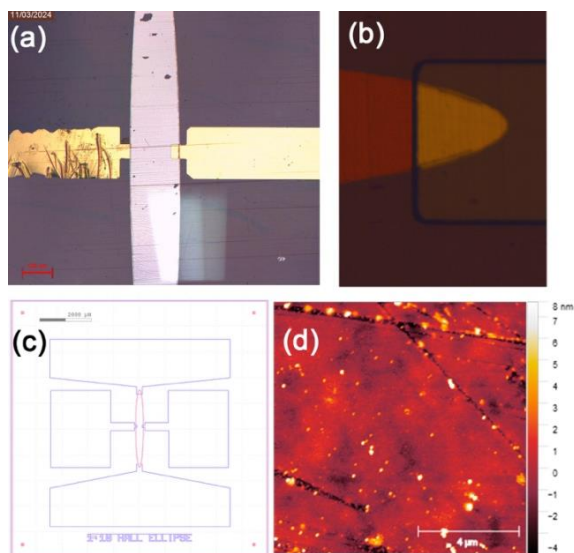


Figura 1: (a) Imagen de microscopía de la cruz Hall microfabricada para la muestra de NiFe crecida sobre resina/kapton, (b) Imagen de microscopio de la interface formada entre la elipse y el contacto. (c) Esquema de una cruz Hall compuesta por un rectángulo u una elipse con relación de forma 1:10. (d) Imagen de topografía de AFM para la muestra de NiFe crecida sobre Si(100).

Se utilizó un microscopio de fuerza magnética (AFM Veeco WYKO NT1100) para estudiar la estructura topográfica mediante el modo de *tapping*. El estudio magnetométrico se llevó a cabo utilizando un magnetómetro de muestra vibrante (VSM-Lakeshore 8600). Las mediciones se realizaron utilizando un campo magnético H aplicado a lo largo de varios ángulos en el plano (ϕ_H). La caracterización de propiedades de magnetotransporte se realizó a temperatura ambiente en un banco de medición equipado por un juego de bobinas de Helmholtz alimentada por una fuente de corriente, unidades tipo SMU (sourceter) y/o multímetros.

III. RESULTADOS Y DISCUSIÓN

La Fig. 1(d) muestra una imagen de topografía obtenida por AFM para la muestra de NiFe crecida sobre sustrato de Si(100). Las mediciones de evidencian una superficie poco rugosa (rms $\sim 1\text{nm}$) para la muestra crecida sobre el sustrato rígido, mientras que las crecidas sobre sustrato flexible parecen ser demasiado rugosas para ser medidas por AFM. Las mediciones de perfilometría sugieren una rugosidad de orden de 10 nm para las muestras crecidas sobre sustratos flexibles. En la Fig. 2 (a), (b) y (c), se muestran lazos de histéresis para las películas de NiFe crecidas sobre Si(100), cinta/kapton y resina/kapton respectivamente, donde H se aplicó en varias direcciones del sustrato en el plano, ϕ_H . La magnetización de saturación medida para todas las muestras fue cercana a $M_s = (800 \pm 100) \times 10^3 \text{ A/m}$, de acuerdo con M_s reportada para esta aleación. En la figura correspondiente a la muestra crecida sobre Si(100) [Fig. 2(a)], podemos observar que el campo coercitivo, $\mu_0 H_c$ [donde μ_0 es la permeabilidad al vacío, $\mu_0 = 4 \times 10^{-7} \text{ Tm/A}$], varía de 0.12 a 0.45 mT y la magnetización de remanencia normalizada M_r/M_s de 0.13 a 0.98, donde los máximos de $\mu_0 H_c$ y M_r/M_s que caracterizan el eje fácil de magnetización se encuentran en la dirección $[100]_{\text{Si}}$ mientras el eje difícil se encuentra a 90° a lo largo de la dirección $[010]_{\text{Si}}$. Esto indica la presencia de una pequeña anisotropía uniaxial que se puede observar en la variación angular de $\mu_0 H_c$ [Fig. 2(d)].

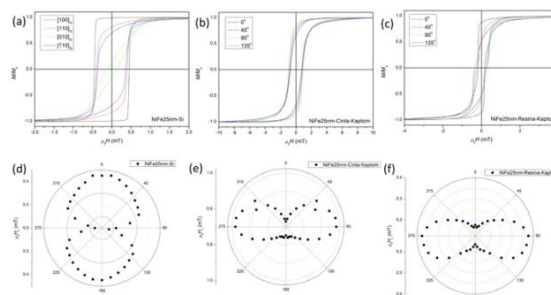


Figura 2: Lazos M vs. H para (a) NiFe sobre Si, (b) NiFe sobre cinta/kapton, (c) NiFe sobre resina/kapton. Variación angular de $\mu_0 H_c$ para (d) NiFe sobre Si, (e) NiFe sobre cinta/kapton, (f) NiFe sobre resina/kapton.

Los lazos de histéresis de la muestra crecida sobre cinta/kapton [Fig. 2(b)] muestran valores de $\mu_0 H_c$ que varían de 0.73 a 0.98 mT y M_r/M_s de 0.64 a 0.87. Aunque la variación angular de $\mu_0 H_c$ que muestra la Fig. 2(e) también presenta un eje uniaxial, esta muestra tiene un comportamiento más isotrópico que la muestra crecida sobre Si(100). Finalmente, la muestra crecida sobre resina/kapton [Fig. 2(c)] evidencia una curvatura en los lazos de histéresis que probablemente está relacionada a la formación de un eje biaxial superpuesto al eje uniaxial de la Fig. 2(f).

En la Fig. 3 se muestran las curvas de histéresis y respuesta lineal de la muestra NiFe crecida sobre resina/kapton al aplicar un campo magnético en una dirección fija en el espacio. Primero se aplicó un campo paralelo a la dirección de la corriente [Fig. 3(a)], realizando un ciclo completo entre $\pm 2.5\text{mT}$ y aplicando una corriente de prueba continua de 2 mA. Se realizó el mismo procedimiento aplicando un campo transversal a la dirección de la corriente [Fig. 3 (b)] mostrando la respuesta esperada para sensores Hall planares.

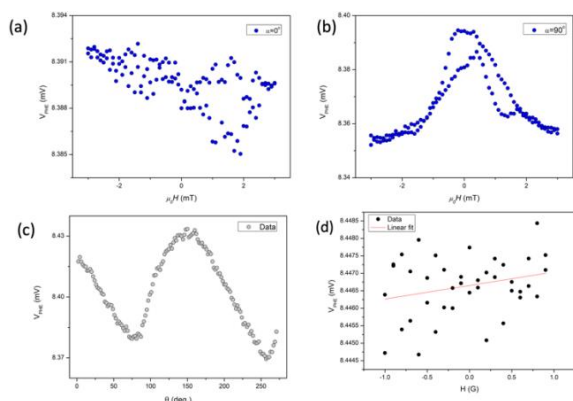


Figura 3: Propiedades de magneto-transporte de la muestra de NiFe sobre resina/kapton. Ciclos de histéresis para (a) $H // I$ y (c) $H \perp I$. (c) Respuesta angular correspondiente al efecto PHE. (d) Relación a bajos campos de $V(H)$ para determinación de la sensibilidad.

Es evidente el gran nivel de ruido en la respuesta magnetoeléctrica medida que atribuimos a la realización del proceso de *lift-off* de los contactos eléctricos. Debido a que no bastó solo con la inmersión en acetona para remover la fotorresina el proceso debió ser complementado con un baño ultrasónico, que en muchos casos provocó el quiebre de la película metálica de oro en la zona de contacto con la capa activa de NiFe. Las sensibilidades obtenidas a partir de la relación lineal de V_{PHE} a bajos campos son cercanas a $3 \times 10^{-3} \frac{V}{T}$, el cual en consistencia con el ruido presentado en las curvas de histéresis presenta bajos valores de sensibilidad.

Se caracterizó también la respuesta angular PHE del dispositivo al rotarlos dentro del juego de bobinas de Helmholtz. Como se observa, las mediciones se corresponden con respuestas del tipo $\sin(2\theta)$ de la cual se obtuvieron las magnitudes del efecto magnetorresistivo con valores cercanos a $0,19 \mu\Omega\text{cm}$.

IV. CONCLUSIÓN

En este trabajo hemos fabricado sensores flexibles de NiFe basados en el efecto Hall planar sobre sustratos rígidos de Si(100) y flexibles, resina/kapton y cinta/kapton. Los resultados de topografía mostraron una alta calidad para los sensores rígidos, con $rms \sim 1\text{nm}$, a diferencia de los sensores flexibles que presentan altas rugosidades inducidas por los sustratos flexibles. Los sensores muestran bajos campos coercitivos y un comportamiento más isotrópico para los sensores flexibles. Finalmente, la respuesta magnetotransporte presenta un ruido considerablemente alto y los dispositivos presentan una baja sensibilidad debido al deterioro en los contactos de Au luego del proceso de *lift-off* con acetona.

AGRADECIMIENTOS

Los autores agradecen el financiamiento de ANPCyT a través del PICT SERIEA-00415, PICT CAT-I-00156 y del programa de investigación e innovación Horizonte 2020 de la Unión Europea en el marco de MAGNAMED 734801.

REFERENCES

- [1] I. J. Chung, and I. Kang, "Flexible Display Technology – Opportunity and Challenges to New Business Application," *Mol. Cryst. Liquid Cryst*, vol. 507, A1, pp. 1-7, October 2009.
- [2] J. A. Rogers, Z. Bao, K. Baldwin, A. Dodabalapur, B. Crone, V. R. Raju, V. Kuck, H. Katz, K. Amundson, J. Ewing, P. Drzaic, "Paper-like electronic displays: large-area rubber-stamped plastic sheets of electronics and microencapsulated electrophoretic inks," *Proc. Natl. Acad. Sci. USA*, vol. 98, A9, pp. 4835, April 2001.
- [3] L. S. Zhou, A. Wanga, S. C. Wu, J. Sun, S. Park, T. N. Jackson, "All-organic active matrix flexible display," *Appl. Phys. Lett*, vol. 88, pp. 083502, February 2006.
- [4] F. C. Krebs, S. A. Gevorgyan, J. Alstrup, "A roll-to-roll process to flexible polymer solar cells: model studies, manufacture and operational stability studies," *J. Mater. Chem*, vol. 19, pp. 5442, 2009.
- [5] S. E. Shaheen, C. J. Brabec, N. S. Sariciftci, F. Padinger, T. Fromherz, J. C. Hummelen, "2.5% efficient organic plastic solar cells," *Appl. Phys. Lett*, vol. 78, pp. 841, 2001.
- [6] M.S. Mannoor, H. Tao, J.D. Clayton, A. Sengupta, D.L. Kaplan, R.R. Naik, N. Verma, F.G. Omenetto and M.C. McAlpine. "Graphene-based wireless bacteria detection on tooth enamel," *Nature communications*, vol. 3, A1, pp. 1-9, 2012.
- [7] Y. Chen, S. Lu, S. Zhang, Y. Li, Z. Qu, Y. Chen, B. Lu, X. Wang, X. Feng, "Skin-like biosensor system via electrochemical channels for noninvasive blood glucose monitoring," *Science advances*, vol. 3, A12, pp. e1701629, 2016.
- [8] Ha Uk Chung et. al. "Binodal, wireless epidermal electronic systems with in-sensor analytics for neonatal intensive care," *Science*, vol. 363, pp6430, 2019.
- [9] C. A. Di , F. Zhang , D. Zhu , "Organic transistor for bioelectronic applications," *Adv. Mater.* 2013 , 25 , 313.
- [10] Y. Zang , F. Zhang , C. A. Di , D. Zhu , "Advances of flexible pressure sensors toward artificial intelligence and health care applications," *Mater. Horiz.* 2015 , 2 , 140 .
- [11] J. Kim , M. Lee , H. J. Shim , R. Ghaffari , H. R. Cho , D. Son, Y. H. Jung , M. Soh , C. Choi , S. Jung , K. Chu , D. Jeon , S. T. Lee, J. H. Kim , S. H. Choi , T. Hyeon , D. H. Kim, "Stretchable silicon nanoribbon electronics for skin prosthesis" *Nat. Commun.* 2014, 5, 5747
- [12] G. Schwartz, B. C. Tee, J. Mei, A. L. Appleton, H. Kim do, H. Wang, Z. Bao, "Flexible Pressure Sensors with a Wide Detection Range Based on Self-Assembled Polystyrene Microspheres" *Nat. Commun.* 2013, 4, 1859 .
- [13] M. Volmer, and M. Avram, "Using permalloy based planar hall effect sensors to capture and detect superparamagnetic beads for lab on a chip applications," *Journal of Magnetism and Magnetic Materials*, vol. 381, 2015, pp. 481-487.
- [14] F.N. Van Dau, A. Schuhl, J.R Childress, M Sussiau, "Magnetic sensors for nanotesla detection using planar Hall effect," *Sensors and Actuators A: Physical*, vol. 53, 1996, pp. 256-260,
- [15] P.H. Wojciechowski et al. The multiple fracture of low-elongation thin films deposited on high-elongation substrates, *Journal of Vacuum Science & Technology A: Vacuum, Surfaces, and Films*, 7, 1282-1288 (1989).
- [16] A.F. Mayadas et al. Resistivity of Permalloy thin films, *Journal of Applied Physics*, 45 2780-2781 (1974).
- [17] D.W. Nix. Mechanical properties of thin films, *Metallurgical transactions A*, 20, 2217-2245 (1989).
- [18] T.Q. Hung et al. High field-sensitivity planar Hall sensor based on NiFe/Cu/IrMn trilayer structure, *Journal of Applied Physics* 107, 09E715 (2010).
- [19] V. Mor et al. Planar Hall effect sensors with shape induced effective single domain behavior, *Journal of Applied Physics*, 111, 07E519 (2012).
- [20] Y. Telepinsky et al. Towards a six-state magnetic memory element. *Applied Physics Letters*, 108, 182401 (2016).
- [21] F. Montaigne et al. Development of magnetoresistive sensors based on planar Hall effect for applications to microcompass, *Sensors and Actuators A: Physical*, 81, 324-327 (2000).
- [22] R.J. Phaneuf et al. Low-energy electron-microscopy investigations of orientational phase separation on vicinal Si (111) surfaces. *Physical review letters*, 67, 2986 (1991)

Effect of underlayers and deposition under external magnetic field on the anisotropy of Ni₈₀Fe₂₀ and Co₉₀Fe₁₀ thin films for sensors

Agostina Lo Giudice
Laboratorio de Nanoestructuras
Magneticas y Dispositivos
Instituto de Nanociencia y
Nanotecnologia CNEA-CONICET
San Martin, Argentina
agostina.logiudice@gmail.com

Andres Di Donato
Dept. Micro and Nanotecnologia
Instituto de Nanociencia y
Nanotecnologia CNEA-CONICET
San Martin, Argentina
andresdidonato@cnea.gov.ar

Augusto Roman
Laboratorio de Nanoestructuras
Magneticas y Dispositivos & Dept.
Micro & Nanotecnologia
Instituto de Nanociencia y
Nanotecnologia CNEA-CONICET
San Martin, Argentina
ORCID 0000-0002-7979-2076

Dante Mercado
Dept. Micro and Nanotecnologia
Instituto de Nanociencia y
Nanotecnologia CNEA-CONICET
San Martin, Argentina
dante.mercado2511@gmail.com

Lara Solis
Laboratorio de Nanoestructuras
Magneticas y Dispositivos
Instituto de Nanociencia y
Nanotecnologia CNEA-CONICET
San Martin, Argentina
ORCID 0000-0002-9915-0863

Laura B. Steren
Laboratorio de Nanoestructuras
Magneticas y Dispositivos
Instituto de Nanociencia y
Nanotecnologia CNEA-CONICET
San Martin, Argentina
ORCID 0000-0003-2224-9272

Abstract— Planar Hall Effect sensors are currently being revisited for their many advantages for biotechnology applications. However, achieving a minimal coercive field for small field sensing remains challenging with conventional ferromagnetic materials. In this work, we explore the magnetic properties of various Ni₈₀Fe₂₀ and Co₉₀Fe₁₀ -based multilayers using Ta, Cu, W and Ag underlayers and analyze the effect of external moderate magnetic fields during the deposition process on them. Our results indicate that both strategies could serve to tune the magnetic anisotropy and magnetization reversal of these structures, optimizing the magnetic sensors' performance.

Keywords—magnetic anisotropy, thin films, magnetic sensors

I. INTRODUCTION

Promising applications in the biotechnology field motivated the search for more sensitive and cheaper magnetoresistive sensors. Recently, sensors based on the Planar Hall Effect (PHE) started to attract more interest in sub-nT sensing due to their excellent sensibility at low magnetic fields, low-temperature drift, high signal-to-noise ratio, low cost, and ease of construction [1-2]. PHE sensors typically employ a single thin layer of permalloy (Ni₈₀Fe₂₀) a ferromagnetic material commonly used in magnetic-based sensors thanks to its low coercive field and high Anisotropic Magnetoresistance (AMR) ratio. Particularly for PHE sensors, as small as possible coercive field is required for small field sensing, which hinders the use of other typically used ferromagnetic materials such as Co₉₀Fe₁₀, which also has a high magnetization and AMR ratio [3]. Nonetheless, it is known that the use of metallic underlayers can drastically change the magnetic properties of a ferromagnetic thin film. According to Hoffman's ripple theory [4], this can be accomplished by grain size reduction and/or a change in preferred crystal orientation. Another way of affecting the magnetic anisotropy of thin films is to grow them under an external magnetic field. In Refs. [5] and [6] the authors showed that magnetic fields can affect film's roughness and change their grain orientation.

The goal of this work is to analyze the effect of metallic buffers and/or external magnetic fields applied during the deposition on the magnetic anisotropy of Ni₈₀Fe₂₀ and Co₉₀Fe₁₀ thin films in order to determine the optimal

materials for integration into PHE sensors. The metals selected as buffer layers were selected based on the crystalline structure of the ferromagnetic materials, [7-10].

II. EXPERIMENTAL DETAILS

For this study, two series of trilayers based on magnetic alloys were grown by DC magnetron sputtering on single-crystalline Si (100) substrates at room temperature. The samples were composed of 20nm-thick thin films of transition metal alloys FM with FM: Ni₈₀Fe₂₀ and Co₉₀Fe₁₀, 5nm-thick buffers and capping layers made of non-magnetic metals M (M: Ta, Ag, Cu, W)

Pressure values range from 2mTorr to 6mTorr, while power values vary between 25W and 100W.

The trilayers were deposited with and without an external magnetic field of Hex =300 Oe, applied parallel to the film's plane generated by an array of permanent Nb magnets installed in a custom substrate holder.

The crystalline structure of the samples was probed by X-ray diffraction and their morphology by Atomic Force Microscopy (AFM). The magnetic properties were measured in a Lake Shore Vibrating Sample Magnetometer at room temperature. The analysis of the magnetic anisotropy of the samples was performed by measuring the angular dependence of the magnetization curves at room temperature. The magnetization was measured with a magnetic field applied parallel to the film's surface and perpendicular to it. From the magnetization loops, the samples' coercive field H_c and remanence magnetization were derived.

III. RESULTS AND DISCUSSION

The X-ray diffraction patterns of the trilayers show that the magnetic layers structures are textured in the (111) direction. The width of the (111) FM diffraction peaks are rather slim indicating that the mean size of the crystallites that composed the films are of the order of a few nanometers, calculated using the Scherrer equation [11].

A typical image of the samples' surface topography is shown in Fig. 1. The roughness of the M/Ni₈₀Fe₂₀/M

trilayers is notably affected by the underlayers, varying from 0.32nm for Ta to 0.62nm for Ag. Instead, this parameter does not change notably with the different buffers for the M/Co₉₀Fe₁₀/M system.

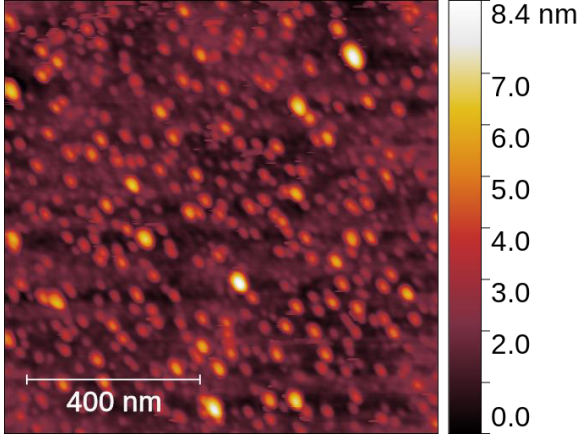


Fig. 1. 1 μ m \times 1 μ m Atomic Force Microscopy topography image for Ni₈₀Fe₂₀/Ta grown under an external magnetic field.

The magnetization loops, measured in-the-plane of the trilayers and perpendicular to them, indicate that the magnetization lays in-plane for the two series of samples. The in-plane angular dependence of the remanent magnetization of Ni₈₀Fe₂₀ films deposited onto Cu, Ag and Ta underlayers reveals that these systems have an in-plane uniaxial anisotropy that smoothly increases for samples grown under external magnetic field as is seen in Fig. 2. A much more accentuated effect is observed for W/Ni₈₀Fe₂₀/W (Fig. 2, right). The in-plane magnetization is isotropic for these trilayers for H_e = 0 Oe and becomes anisotropic when they are grown under a magnetic field.

The coercive field, H_c, increases consequently, for samples grown under a magnetic field. The smallest value, H_c = 1.34(2) Oe, is obtained for Ta/Ni₈₀Fe₂₀/Ta structures grown under no magnetic field, and increases to H_c = 2.50(4) Oe for the sample grown under external magnetic field. The coercivity is still higher, H_c=3.07(4), for W-buffered trilayers.

The effect of buffers on the magnetic anisotropy of the Co₉₀Fe₁₀ layers is different from the one observed in Ni₈₀Fe₂₀ films, as well as the response to the magnetic field during deposition. The polar plots of the normalized remanent magnetization of these trilayers are shown in Fig. 3. The Ag and Cu buffered- Co₉₀Fe₁₀ thin films grown with no external magnetic field show weak in-plane uniaxial anisotropies while the magnetization of those grown onto W is isotropic (Fig. 3 right). The behaviour of the last system does not change even for structures deposited under an external magnetic field. The anisotropy of the other trilayers (Fig. 3 left) changes notably for M/Co₉₀Fe₁₀/M samples (M: Ag and Cu) grown with H_e=300 Oe. The preexistent in-plane uniaxial anisotropy, K1 is notably increased and another uniaxial term, K2, with easy axis perpendicular to the previous one appears, being both mutually exclusive [12].

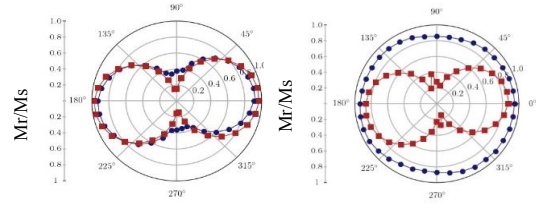


Fig. 2. Polar plots of normalized remanent magnetization (Mr/Ms) measured at 300K for (left) Ta/Ni₈₀Fe₂₀/Ta and (right) W/Ni₈₀Fe₂₀/W deposited under a 300 Oe external magnetic field (■) and without it (●), respectively.

The presence of both anisotropies, K1 and K2, is also noticeable at the angular dependence of the coercive field showing particular features that indicate the existence of different magnetization reversal mechanisms in these structures. It should be remarked that the coercive fields of Co₉₀Fe₁₀ thin films are of the order of several tenth of Oe, depending on the underlayer and are therefore systematically higher than those observed for Ni₈₀Fe₂₀ that do not exceed 4 Oe. These results are crucial for the design of the PHE sensors due to the possibility of tuning the coercivity according to sensors applications. A more detailed presentation of the magnetic characterization of these trilayers will be published elsewhere [13].

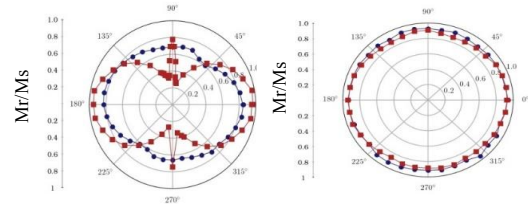


Fig.3. Polar plots of normalized remanent magnetization (Mr/Ms) measured at 300K for (left) Cu/Co₉₀Fe₁₀/Cu and (right) W/Co₉₀Fe₁₀/W deposited under a 300 Oe external magnetic field (■) and without it (●), respectively.

IV. CONCLUSIONS

In this work, we analyzed the impact of buffer layers and the application of a magnetic field during the fabrication process of Ni₈₀Fe₂₀ and Co₉₀Fe₁₀ films onto their magnetic anisotropy. Our results demonstrate the potential to reduce coercivity and alter the magnetic properties of magnetic films by employing various buffer layers. Additionally, our study shows that applying a magnetic field during the samples' growth can decrease the coercive field of CoFe-based structures which may result promising for future applications of this material in low magnetic field sensors. Complementary measurements of the textures, the form and size of the grain of the films are being made to gain depth in the understanding of the magnetic behavior of the structures reported in this short article.

REFERENCES

- [1] L. Ejsing, M. F. Hansen, A. K. Menon, H. A. Ferreira, D. L. Graham, and P. P. Freitas. *Appl. Phys. Lett.*, vol. 84, pp. 4729–4731, 2004.
- [2] N.T. Thanh, K.W. Kim, C.O. Kim, K.H. Shin and C.G. Kim, *J. Magn. Magn. Mater.*, vol 316, pp. 238-241, September 2007.
- [3] Amir Elzawwy *et al* 2021 *J. Phys. D: Appl. Phys.* **54** 353002
- [4] W. Brown, *IEEE Trans. Magn.*, vol. 6, pp. 121-129, 1970.
- [5] J. Chen, J. Ma, L. Wu, Y. Shen, and C.-W. Nan., *Sci. Bull.*, vol. 60, pp. 1214–1217, 2015.
- [6] C. Ma, H. He, F. Xia, Z. Xiao and Y. Liu, *Ceramics International*, vol. 46, pp. 695-701, 1997.
- [7] S. Cakmaktepe, M.I. Coskun and A. Yildiz, *J. Phys.*, vol. 53, pp. 112–118, 2013.
- [8] S. Cakmaktepe and S. Diken, *J. Optoelectronics and Advanced Mater.*, vol. 18, pp. 107-111, 2016.
- [9] H. Gong, M. Rao, D.E. Laughlin and D. N. Lambeth, *J. Appl. Phys.*, vol. 85, pp. 5750–5752, 1999.
- [10] S. S. Ahmad *et al*, *AIP Advances*, vol. 6, pp. 115101-115108, 2016.
- [11] P. Scherrer, *Göttinger Nachrichten Math. Phys.*, vol. 2, pp. 98–100, 1918.
- [12] B. Hazra, S.N. Kaul, S. Srinath, Z. Hussain, V. Raghavendra Reddy and J. Manivel Raja, *AIP Advances*, vol. 10, pp. 065017-065030, 2020.
- [13] A. Lo Giudice, PhD. thesis, Universidad Nacional de San Martin, 2024.

Testigo de corte de cadena de frío para la visualización de la exposición a temperaturas predeterminadas

Walter Sidlik
Diseño Bags S. A.
Buenos Aires, Argentina
Disenio.bags@gmail.com

Resumen— El testigo de corte de cadena de frío propuesto permite visualizar con claridad cuando un producto queda expuesto a una temperatura predeterminada durante un tiempo también predeterminado. Esto proporciona una forma rápida y efectiva de identificar si se ha producido una interrupción en la cadena de frío y si el producto puede haber sufrido deterioros.

Palabras clave—testigo, cadena de frío, sensor irreversible

I. INTRODUCCIÓN

En la distribución de productos que requieren condiciones de temperatura controlada, es crucial garantizar que no se rompa la cadena de frío durante el transporte y almacenamiento. La exposición a temperaturas no adecuadas puede causar deterioro en los productos y comprometer su calidad y seguridad.

La presente invención se encuentra en el campo de los dispositivos para el monitoreo y control de la cadena de frío, particularmente en la industria de la logística y distribución de productos sensibles a la temperatura.

II. FUNCIONAMIENTO

El testigo de corte de cadena de frío consiste en una cápsula termoformada plástica con un dorso cerrado por una película de aluminio. El aluminio de la tapa está recubierto con un adhesivo y cubierto por un papel siliconado, que al ser retirado permite pegarlo al producto (por ejemplo, una caja de cartón, envase de vidrio, bolsa, etc.). Esta cápsula se puede adherir fácilmente al embalaje del producto. El dispositivo cuenta con un canal circular que contiene una sustancia termo sensible coloreada adecuada para la temperatura objetivo de control, teñida por un colorante soluble en dicha sustancia, dicho canal rodea una cápsula con forma de botón separado por un anillo plano que separa ambos reservorios, este anillo está obturado por una termo soldadura débil manteniendo aislados los materiales contenidos en dichos reservorios.

El reservorio central contiene un material de color blanco finamente granulada con la propiedad de absorber fácilmente la sustancia termo sensible alojada en el canal, también contiene una esferita impregnada en la misma sustancia contenida en el canal pero de color negro.

La soldadura más fuerte es la perimetral de todo el dispositivo, la cual está efectuada por termo fusión del polietileno que conforma el interior de la tapa y del termo formado. Todo el perímetro está termo sellado fuertemente, asegurando la integridad del dispositivo (fig. 1).

El tipo de sustancia termo sensible utilizada varía según la temperatura objetivo de control, pudiendo abarcar un amplio

rango de temperaturas bajo cero y sobre cero mediante ajustes en la formulación.



Fig. 1. Render 3D del dispositivo sin activar.

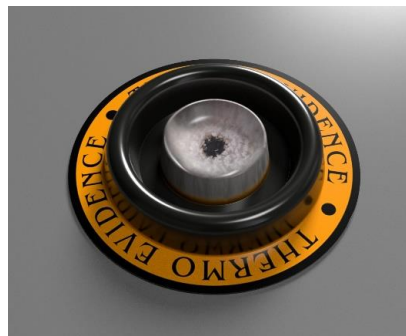


Fig. 2. Render 3D del dispositivo activado, listo para ser utilizado.

El funcionamiento del dispositivo es el siguiente: antes de su aplicación, se coloca el dispositivo en una temperatura notablemente inferior a la temperatura de fusión de la sustancia termo sensible, de modo que esta solidifique. Luego, se aplica el dispositivo al elemento que se desea controlar, y se introduce en un contenedor cuya temperatura esté dentro del rango deseado. Para activar el dispositivo, se ejerce presión sobre la semiesfera central hasta que colapse, esto genera una expansión del aire hacia los bordes, despegando la soldadura débil (fig. 2).

Si el dispositivo es expuesto a una temperatura mayor a la temperatura de fusión de la sustancia termo sensible, esta pasará de fase sólida a fase líquida, y por capilaridad se ubicará entre las dos láminas que están apoyadas entre sí. Esto hará que la sustancia termo sensible tome contacto con el material granulada, que tiene afinidad por la sustancia, y la absorberá, tiñéndose de su color característico (fig. 3 y 4). Este



Fig. 3 Render 3D del dispositivo con un revelado parcial.



Fig. 4 Render 3D del dispositivo con un revelado total.

proceso es irreversible, lo que indica de manera inequívoca que el producto en cuestión fue expuesto a una temperatura superior a la que puede soportar durante cierto período de tiempo, a partir de ese momento la esfera negra comenzará a

teñir el material circundante de forma gradual y de manera radial expansiva aportando una noción aproximada del tiempo que ha estado por encima de la temperatura de control, cabe mencionar que si la temperatura vuelve a estar por debajo de dicha temperatura el proceso de expansión se detendrá.

III. REIVINDICACIONES

Este dispositivo de evidencia es ideal para una amplia gama de aplicaciones donde es crucial determinar si un producto ha sido expuesto a condiciones de temperatura superiores a la de control. Desde el transporte de alimentos y productos farmacéuticos hasta la conservación de muestras biológicas, este dispositivo proporciona una solución efectiva y confiable para verificar la integridad de los productos sensibles a las temperaturas. Su diseño compacto y fácil de usar lo hace adecuado para su incorporación en diversos sistemas de almacenamiento y transporte, garantizando la calidad y seguridad de los productos en todo momento.

IV. CONCLUSIONES

El testigo de corte de cadena de frío proporciona una solución simple y efectiva para monitorear la exposición de productos sensibles a la temperatura durante el transporte y almacenamiento. Su cápsula termoformada plástica autoadhesiva y su capacidad para cambiar de color en respuesta a condiciones de temperatura específicas permiten una rápida detección de posibles interrupciones en la cadena de frío, ayudando así a prevenir el deterioro de los productos.

Dispositivo de evidencia de congelamiento

Walter Sidlik
 Diseño Bags S. A.
 Buenos Aires, Argentina
 Disenio.bags@gmail.com

Resumen— Este dispositivo proporciona una forma inequívoca e irreversible de determinar si un producto ha sido expuesto a temperaturas bajo cero. Está construido con una estructura laminada que incluye una película de PVC de 150 micrones, recubierta con polietileno de 50 micrones, y sellada con una película de aluminio de 12 micrones laminada con polietileno de 50 micrones. El dispositivo tiene una forma de media esfera con una depresión piramidal en la parte superior y un lado plano adhesivado con un liner siliconado para su fijación en cualquier superficie. En su interior, contiene una esfera de poliacrilato de sodio y agua destilada que permite su saturación. Cuando la esfera se congela, el agua que no puede ser absorbida por el poliacrilato se expande, causando grietas y colapsando la esfera. Esto proporciona una clara evidencia de exposición a temperaturas bajo cero.

Palabras clave— sensor irreversible, congelamiento

I. INTRODUCCIÓN

El dispositivo está diseñado para ser una herramienta confiable y fácil de usar para verificar la exposición de productos a temperaturas de congelación. Su construcción laminada garantiza su integridad y resistencia, mientras que su diseño compacto y autoadhesivo lo hace versátil para su aplicación en diversas superficies. La esfera de poliacrilato de sodio, saturada con agua destilada, ofrece una forma precisa de determinar si se ha producido congelamiento, ya que su colapso irreversible proporciona una evidencia visual clara.

II. FUNCIONAMIENTO

El dispositivo de evidencia de congelamiento funciona de manera ingeniosa y sencilla. Cuando se expone a temperaturas por debajo de 0°C, su diseño único permite que se produzca un cambio físico irreversible que indica claramente la exposición a condiciones de congelación (Fig. 1 y 2).

A. Absorción de agua y saturación

En condiciones normales, el dispositivo contiene una esfera de poliacrilato de sodio y agua destilada en su interior. El poliacrilato de sodio tiene una notable capacidad de absorción de agua, lo que permite que la esfera se sature con el líquido hasta alcanzar su capacidad máxima.



Fig.1. Fotografía de dispositivo que no fue expuesto a una temperatura menor a 0°C.

B. Congelamiento y expansión del agua

Cuando el dispositivo es expuesto a temperaturas bajo cero, el agua dentro de la esfera comienza a congelarse. Durante el proceso de congelación, el agua experimenta una expansión significativa, ya que su volumen aumenta al solidificarse en forma de hielo.

C. Presión y colapso de la esfera

La expansión del agua congelada dentro de la esfera ejerce una presión considerable sobre la estructura del dispositivo. Sin embargo, debido a la naturaleza no absorbente del poliacrilato de sodio, este material no puede acompañar la expansión del agua. Como resultado, la esfera experimenta un agrietamiento en su superficie y eventualmente colapsa bajo la presión generada por la expansión del hielo.

D. Evidencia visual de congelamiento

El colapso irreversible de la esfera proporciona una evidencia clara y definitiva de la exposición del dispositivo a temperaturas bajo cero. Este cambio físico es fácilmente identificable y no requiere de interpretaciones complejas, lo que lo convierte en un indicador confiable de la congelación del producto al que está adherido el dispositivo.

III. APLICACIONES

Este dispositivo de evidencia de congelamiento es ideal para una amplia gama de aplicaciones donde es crucial determinar si un producto ha sido expuesto a condiciones de congelación. Desde el transporte de alimentos y productos farmacéuticos hasta la conservación de muestras biológicas, este dispositivo proporciona una solución efectiva y confiable para verificar la integridad de los productos sensibles a las temperaturas. Su diseño compacto y fácil de usar lo hace adecuado para su incorporación en diversos sistemas de almacenamiento y transporte, garantizando la calidad y seguridad de los productos en todo momento.

IV. CONCLUSIONES

Se diseñó un dispositivo capaz de detectar congelamiento de forma irreversible.

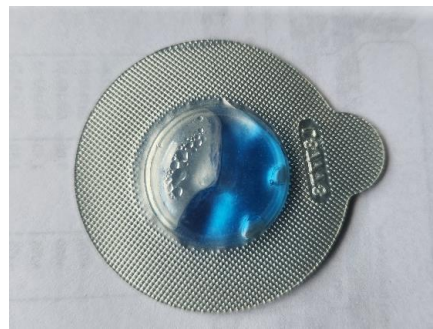


Fig.2. Fotografía de dispositivo luego de ser expuesto por debajo a 0°C y luego llevado nuevamente a una temperatura mayor a 0°C.

Microtomografías basadas en sensores de imagen CMOS y algoritmos de reconstrucción convencionales

Damián Leonel Corzi, José Lipovetzky, German Mato

Fabrizio Alcalde Bessia, Mariano Gomez Berisso

Instituto Balseiro, Universidad Nacional de Cuyo (UNCUYO)

Centro Atómico Bariloche, Comisión Nacional de Energía Atómica (CNEA)

Consejo Nacional de Investigaciones Científicas y Técnicas (CONICET)

Av. E. Bustillo 9500, R8402AGP, San Carlos de Bariloche, Río Negro, Argentina.

damian.corzi@ib.edu.ar

Abstract—El trabajo propone un arreglo experimental sencillo para obtener imágenes tomográficas de una alta resolución espacial utilizando sensores de imágenes CMOS comerciales, logrando aprovechar gracias al preprocesamiento del conjunto de imágenes obtenidas los efectos generados por el contraste de fase y la amplificación geométrica.

Index Terms—Sensores CMOS, Radiografías, Tomografías, Rayos X

I. INTRODUCTION

Los sensores de imágenes comerciales basados en la tecnología *complementary metal-oxide-semiconductor* (CMOS), originalmente diseñados para detectar luz visible, pueden ser utilizados como detectores de fotones de rayos X de baja energía [1]. Esta capacidad permite su utilización en diversas aplicaciones relacionadas con la captura de imágenes radiográficas de alta resolución o la espectroscopia para el estudio de fluorescencia [2], [3].

Cuando un fotón de rayos X interactúa con el sensor, situación que se conoce como evento, deposita su energía formando una nube de portadores de carga que puede distribuirse a lo largo de múltiples píxeles. En cada uno de estos píxeles, la carga se recolecta mediante estructuras conocidas como fotodiodos, dando origen a una señal eléctrica cuya intensidad es proporcional a la cantidad de portadores recolectados [4]. Si numerosos eventos ocurren en el mismo píxel (*pile-up*), existe la posibilidad de saturar la señal generada. Esta situación depende mayormente de la relación entre el flujo de fotones y el tiempo de exposición del sensor, por lo tanto su correcta configuración es esencial.

A partir del procesamiento de las imágenes obtenidas, se puede determinar la transmisión de los materiales presentes en una radiografía [5], permitiendo utilizar un conjunto de imágenes para obtener reconstrucciones tomográficas de los objetos tridimensionales. Debido a la elevada resolución del método y a algunos artefactos generados por la presencia de contraste de fase, las imágenes obtenidas requieren un preprocesamiento adicional la aplicación de algoritmos de reconstrucción clásicos.

De esta manera, el trabajo expone un arreglo experimental básico para obtener imágenes tomográficas de alta resolución espacial utilizando un sensor comercial del tipo CMOS y algoritmos de reconstrucción convencionales.

II. ARREGLO EXPERIMENTAL

La configuración básica para capturar imágenes tomográficas está formada por cuatro elementos, como se observa en la Fig. 1, y consiste en una fuente de rayos X, la muestra a ser irradiada, el sensor utilizado para detectar los fotones y el mecanismo de rotación.

La fuente de rayos X utilizada fue un tubo Microbox de blanco de tungsteno y kilovoltaje variable en un rango entre 20 *kV* y 100 *kV*. Las principales características de este tubo son su foco, el cual tiene un tamaño de 5 μm para potencias de trabajo menores a 7.5 *W*, y su generación continua, la cual garantiza un flujo constante y sin variaciones en el espectro de los fotones generados.

El sensor utilizado se trata de un MT9M001C12STM, el cual fue un sensor de imagen CMOS del tipo *rolling shutter* con una resolución SXGA y un tamaño de píxel de 5.2x5.2 μm^2 , lo que define un área activa con un ancho de 6.66 *mm* y un alto de 5.32 *mm*. La lectura del sensor se realiza mediante la plataforma Arducam UC-425, lo que permite una conexión de alta velocidad con cualquier ordenador y una adquisición sencilla de las imágenes capturadas.

La distancia entre el sensor y la fuente fue 72 *cm*, lo que garantiza que los rayos generados sean prácticamente paralelos al llegar a la superficie del sensor. Esto permite que la resolución del sistema sea principalmente definida por las características geométricas del sensor [5]. En el caso de las muestras, las mismas están ubicadas sobre el eje de un rotador a 48 *cm* de la fuente, el cual es controlado por un motor paso a paso permitiendo obtener imágenes en ángulos precisos. Este rotador está basado en un motor paso a paso y una caja de reducción, dotando al sistema de una resolución angular de 0.15 °, la cual es suficiente para obtener el

conjunto de imágenes necesario para aplicar los algoritmos de reconstrucción tomográfica.

Debido a que las imágenes radiográficas se tratan de proyecciones bidimensionales, las dimensiones máximas de las muestras irradiadas están limitadas por el tamaño del área activa del sensor. Por este motivo, a menos que se recurra a la captura de imágenes individuales y su posterior *stitching* [5], esta técnica estará limitada a muestras de pocos milímetros de largo.

Los parámetros de la cámara fueron configurados para garantizar en todas las capturas un histograma uniforme, definiendo valores de ganancias y offset analógicos para aprovechar la totalidad del rango dinámico de salida. En cuanto al tiempo de exposición, si bien el valor neto configurado es de 31 s, el mismo se obtiene a partir de la suma de numerosas imágenes capturadas con un menor tiempo de exposición. Esto permite incrementar la corriente del tubo sin saturar el sensor por *pile-up* y al mismo tiempo reducir el ruido asociado a la medición.

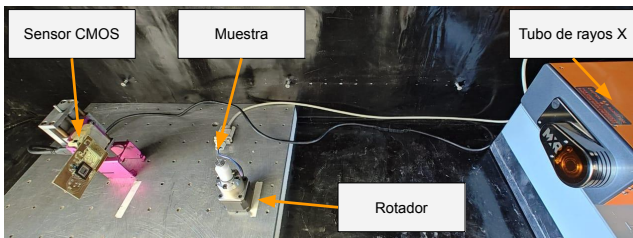


Fig. 1. Fotografía de los elementos básicos que componen un arreglo experimental utilizado para la captura de tomografías mediante un sensor de imágenes CMOS comercial.

III. IMAGENES RADIOGRAFICAS

La captura y el procesamiento de las imágenes obtenidas se realiza mediante *scripts* escritos en lenguaje Python, lo cual garantiza su portabilidad en diferentes sistemas operativos. El proceso de adquisición utiliza los módulos provistos por Arducam para el manejo de sus placas de adquisición y permite una fácil configuración del sensor.

Las imágenes capturadas son preprocesadas aplicando una corrección por *flat-field*, lo que permite mitigar no uniformidades en el flujo que llega a la superficie del sensor y el deterioro causado del sensor causado por efecto de la radiación, como es el caso de píxeles dañados o efecto de dosis total [6].

Esta corrección consiste en la captura de tres tipos de imágenes diferentes y su posterior procesamiento. La primera se conoce como *dark-field* (DI) y corresponde a una captura realizada con el tubo de rayos X apagado. La segunda se conoce como *flat-field* (FI) y es obtenida con el tubo encendido, pero sin la presencia de la muestra radiografiada (CI). Por último, la última imagen corresponde a la radiografía de la muestra de interés. La corrección implementada se basa en la ecuación Eq.1, donde el resultado es la transmisión de la muestra (TR).

Los resultados de aplicar esta corrección pueden observarse en la Fig. 2.

$$TR = \frac{CI - DI}{FI - DI} \quad (1)$$

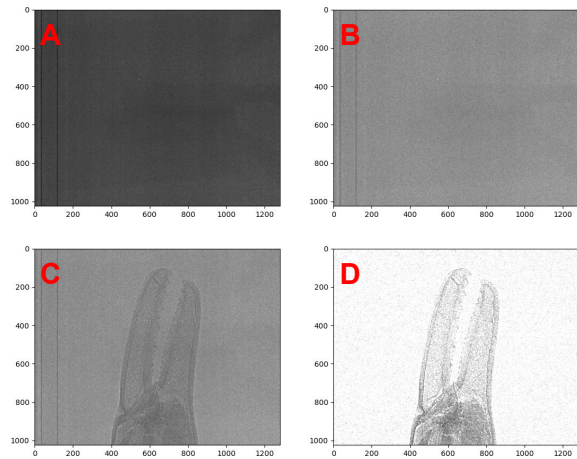


Fig. 2. Resultados de la aplicación de la corrección por *flat-field* a una imagen radiográfica capturada de una pinza de escorpión. En la figura se pueden observar las imágenes *dark-field* (A), *flat-field* (B) y la radiografía de la muestra (C). En la imagen de transmisión obtenida (D) se puede apreciar el nivel de detalle conseguido gracias al efecto del contraste de fase.

Al acercarse la muestra a la fuente se puede aprovechar el efecto de la amplificación geométrica para poder observar detalles que requieren una resolución mayor a la que puede ser obtenida considerando Nyquist. Adicionalmente, alejar la muestra del sensor permite visualizar un efecto conocido como contraste de fase, el se debe a las propiedades ondulatorias de los fotones de rayos X y las variaciones en su fase provocadas por los átomos del material, la cual se observa como un incremento del contraste en las interfaces de la muestra. El efecto combinado de la fase y la amplificación geométrica puede observarse en la Fig. 3.

Si bien el efecto de la fase es útil para amplificar el contraste entre las interfaces de distintos materiales, particularmente para materiales formados por átomos de bajo número atómico, esos incrementos en el contraste generan artefactos no deseados al utilizar algoritmos de reconstrucción convencionales.

IV. TOMOGRAFIAS

La obtención de las imágenes tomográficas inicia con la captura de imágenes radiográficas individuales, las cuales fueron tomadas cada 2 ° de rotación, obteniendo un conjunto de 180 imágenes. Adicionalmente, debido a la degradación del sensor provocada por efecto de dosis total, se deben capturar imágenes *flat-field* y *dark-field* al inicio y al final de la irradiación. Estas capturas finales permiten estimar mediante una interpolación lineal pequeñas variaciones utilizadas para mejorar la corrección por *flat-field*.

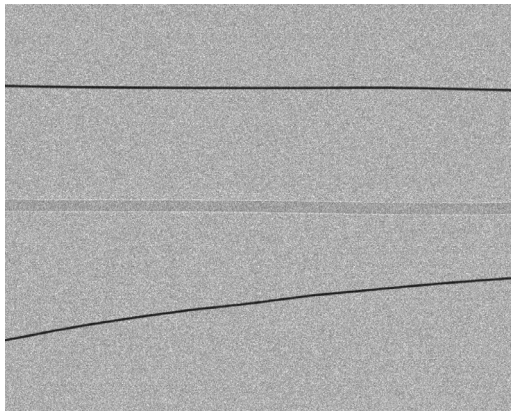


Fig. 3. Imagen radiográfica donde se observa el efecto que el contraste de fase genera en los bordes de un cabello humano (medio) de $78 \mu\text{m}$ de diámetro. Adicionalmente se puede observar un alambre de tungsteno (arriba) y un alambre de oro (abajo), ambos con un diámetro de $18 \mu\text{m}$, los cuales presentan una marcada atenuación de los fotones de rayos X.

Debido a la presencia del contraste de fase, se debe aplicar un preprocesamiento a cada una de las imágenes individuales. Este filtrado se realiza para obtener información del camino óptico total, formado por la componente de fase y transmisión de la muestra. Este procedimiento requiere conocer la geometría de irradiación y estimar los materiales que conforman el objeto [7].

Al conjunto de imágenes obtenidas se le aplica un procesamiento adicional para encontrar el centro de rotación mediante un análisis de los sinogramas y al mismo tiempo determinar si existen posibles desplazamientos transversales al eje de rotación que requieran ser corregidos.

Para obtener la reconstrucción tomográfica se utilizan *scripts* desarrollados en Python y el módulo Tomopy, el cual presenta un gran número de herramientas y algoritmos de reconstrucción. De todos estos algoritmos, el conocido como *algebraic reconstruction technique* fue el que presentó un mejor resultado en los análisis preliminares. En la Fig. 4 se puede observar algunas vistas en cortes de una reconstrucción.

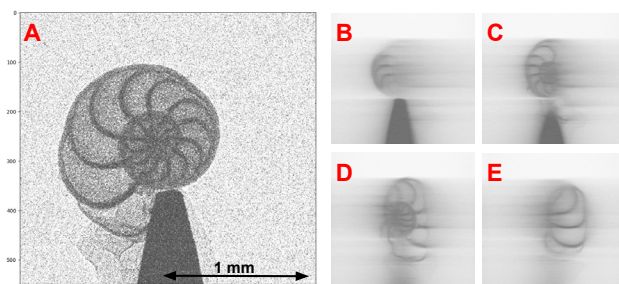


Fig. 4. Reconstrucción tomográfica del caparazón de un foraminífero del holoceno obtenido de la plataforma continental argentina. (A) Imagen radiográfica original tomada para un ángulo particular. (B) Vistas en corte de la reconstrucción obtenida utilizando algoritmos convencionales.

Finalmente, a partir de la reconstrucción se puede generar

un modelo tridimensional de la muestra tomografiada, lo cual puede visualizarse en la Fig. 5.

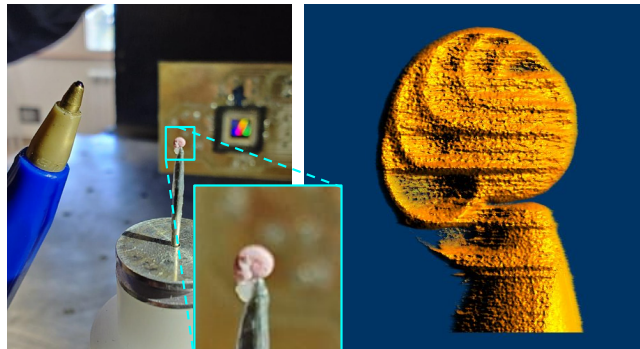


Fig. 5. Modelo tridimensional generado a partir de la reconstrucción tomográfica del caparazón. En la imagen se pueden observar la escala de la muestra (izquierda) y el modelo obtenido (derecha).

V. CONCLUSIÓN

La captura de imágenes tomográficas de alta resolución espacial puede realizarse utilizando sensores de imagen comerciales y un arreglo experimental sencillo. Adicionalmente, la degradación del sensor provocada por los efectos de la radiación puede ser mitigada correctamente al preprocesar las imágenes utilizando corrección por *flat-field*. Por último, los efectos generados por el contraste de fase pueden ser aprovechados para mejorar las imágenes obtenidas, lo cual permite utilizar algoritmos de reconstrucción convencionales y aprovechar la amplificación geométrica para obtener una mayor resolución.

REFERENCES

- [1] J. Lipovetzky, A. Cicuttin, M. L. Crespo, M. S. Haro, F. A. Bessia, M. Pérez, and M. G. Berisso, "Multi-spectral x-ray transmission imaging using a BSI CMOS image sensor," *Radiation Physics and Chemistry*, vol. 167, p. 108244, 2020.
- [2] F. Alcalde Bessia, M. Pérez, J. Lipovetzky, N. A. Piunno, H. Mateos, I. Sidelnik, J. J. Blostein, M. Sofó Haro, and M. Gómez Berisso, "X-ray micrographic imaging system based on COTS CMOS sensors," *International Journal of Circuit Theory and Applications*, vol. 46, no. 10, pp. 1848–1857, 2018.
- [3] M. Pérez, M. S. Haro, J. J. Blostein, A. Cicuttin, M. L. Crespo, F. A. Bessia, I. Sidelnik, M. G. Berisso, and J. Lipovetzky, "X-ray spectroscopy up to 17.6 keV using a commercial off the shelf CMOS image sensor," in *2020 Argentine Conference on Electronics (CAE)*. IEEE, 2020, pp. 69–72.
- [4] D. L. Corzi, J. Lipovetzky, M. Pérez, S. G. Gutierrez, M. S. Haro, F. A. Bessia, and M. G. Berisso, "Simulating charge collection efficiency in a CMOS pixel array for x-ray detection," in *2022 Argentine Conference on Electronics (CAE)*. IEEE, 2022, pp. 26–30.
- [5] D. L. Corzi, J. Lipovetzky, F. P. A. Bessia, L. Baqué, A.-S. Sergent, M. Pérez, M. S. Haro, I. C. A. Vinciguerra, A. Martínez-Meier, G. Dalla-Salda *et al.*, "Enhanced high-spatial resolution radiographic images based on COTS CMOS image sensors applied to wood dendrochronology and densitometry," *Radiation Measurements*, p. 107085, 2024.
- [6] N. Mail, P. O'Brien, and G. Pang, "Lag correction model and ghosting analysis for an indirect-conversion flat-panel imager," *J. Appl. Clin. Med. Phys.*, vol. 8, no. 3, pp. 137–146, 2007.
- [7] T. Weitkamp, D. Haas, D. Węgrzynek, and A. Rack, "Ankaphase: software for single-distance phase retrieval from inline x-ray phase-contrast radiographs," *Journal of synchrotron radiation*, vol. 18, no. 4, pp. 617–629, 2011.



2 |

Microsistemas analíticos integrados y lab-on-a-chip (LOC)

Analytical integrated microsystems and lab-on-a-chip (LOC)

Microssistemas analíticos integrados e lab-on-a-chip (LOC)

Sensores microfluídicos

Microfluidic sensors

Sensores microfluídicos

Microanalizadores automáticos modulares para la monitorización y control del proceso de purificación hidrometalúrgica de zinc

Karla Victoria Guevara Amatón
División de Posgrado e Investigación
TecNM/ IT La Laguna
Torreón, Coah. México
kvguevara@lalaguna.edu.mx

Hesner Coto Fuentes
División de Posgrado e Investigación
TecNM/ IT La Laguna
Torreón, Coah. México
hesnercf@lalaguna.edu.mx

David Izquierdo
Grupo de Tecnologías Fóticas,
Universidad de Zaragoza, Zaragoza,
Spain
d.izquierdo@unizar.es

Pedro Couceiro
Group of Sensors and Biosensors,
Universitat Autònoma de Barcelona,
Bellaterra, Spain
pedro.couceiro@autonoma.cat

V. E. Manqueros Aviles
División de Posgrado e Investigación
TecNM/ IT La Laguna
Torreón, Coah. México
edi.ma@lalaguna.edu.mx

Julian Alonso-Chamarro
Group of Sensors and Biosensors,
Universitat Autònoma de Barcelona,
Bellaterra, Spain
julian.alonso@uab.es

Antonio Calvo-López
Group of Sensors and Biosensors,
Universitat Autònoma de Barcelona,
Bellaterra, Spain
antonio.calvo@uab.cat

Francisco Valdés
División de Posgrado e Investigación
TecNM/ IT La Laguna
Torreón, Coah. México
fvaldesp@lalaguna.edu.mx

Abstract— En este trabajo se propone la monitorización de diferentes parámetros críticos para el control del proceso hidrometalúrgico de obtención de Zinc, en concreto de las etapas de purificación del líquido de lixiviado antes de la etapa de electrodeposición. Para ello se propone la utilización de diferentes microanalizadores automatizados desarrollados por el equipo de investigación para los elementos seleccionados y se presentarán los primeros resultados obtenidos en el análisis de muestras reales de las diferentes etapas de la purificación.

Keywords— microanalizadores, proceso hidrometalúrgico del zinc, Flow Injection Analysis, sistemas ópticos

I. INTRODUCCIÓN

El control de los procesos de producción industrial, y en concreto los relacionados con la hidrometalurgia, requiere de sistemas analíticos capaces de suministrar información que permitan seguir su evolución en función del tiempo. Dicha información ayuda a optimizar los procesos e implementar medidas correctoras en tiempo real si así fuera necesario. Para simplificar la obtención de dicha información y minimizar su coste, el presente trabajo tiene como objetivo el desarrollo de microanalizadores químicos de bajo coste de fabricación, operación y mantenimiento capaces de monitorizar, de forma automática, autónoma y continua, diferentes procesos industriales relacionados con la minería y la metalurgia.

La utilización de una estrategia de integración modular de elementos da versatilidad al proceso de construcción del microanalizador y permite modificar con sencillez su configuración para adaptarla a las singularidades de los diferentes procesos industriales que se deseen monitorizar.

Las tecnologías de microfabricación multicapa elegidas abren la posibilidad de obtener prototipos de forma simple y rápida, a bajo coste [1,2]. Permite además introducir con facilidad modificaciones en el diseño de las plataformas de microfluídica, estructura base de los microanalizadores, para adaptarlas a cada proceso y aplicación concreta. Adicionalmente, el diseño de los microanalizadores y sus actuadores asociados (válvulas, bombas, etc.) hacen posible, vía la electrónica de control y el software desarrollado,

reconfigurar automáticamente los parámetros operacionales del microanalizador. De este modo dichos parámetros pueden adaptarse, sin modificación de hardware, a las necesidades de la metodología analítica que se pretende implementar en cada situación.

En el presente trabajo se describe la construcción de microanalizadores para monitorización y control del proceso de obtención de Zinc y en particular de las diferentes etapas que integran del proceso de purificación hidrometalúrgica de la disolución neutra de lixiviación de zinc previo a su electrodeposición.

II. EXPERIMENTAL

A. El proceso global de obtención de Zinc

Las operaciones de purificación de la solución de lixiviación neutra inicial del proceso de obtención de Zinc tienen como objetivo eliminar elementos que se depositan conjuntamente con dicho metal durante la electrólisis final y que, por lo tanto, contaminan el producto obtenido. También se pretende eliminar elementos que reducen la eficiencia de la electrodeposición al reducir el sobrepotencial de hidrógeno.

En la figura 1 se muestran las diferentes etapas del proceso hidrometalúrgico global y del proceso de purificación.

La monitorización de la solución de purificación al final de cada una de las etapas de proceso que la componen debe garantizar la calidad de la solución entregada a la electrólisis y permitir, a la vez, controlar la dosificación de los reactivos utilizados. Cabe recordar que en base a la información obtenida se controla la capacidad de desviar y reciclar la solución que no cumple con las especificaciones de calidad requeridas. Hasta hace relativamente poco el control analítico se realizaba mediante la toma de muestras de cada etapa que posteriormente eran analizadas en el laboratorio de la planta. Recientemente se han introducido analizadores on-line para algunos elementos como el cobre o el cobalto.

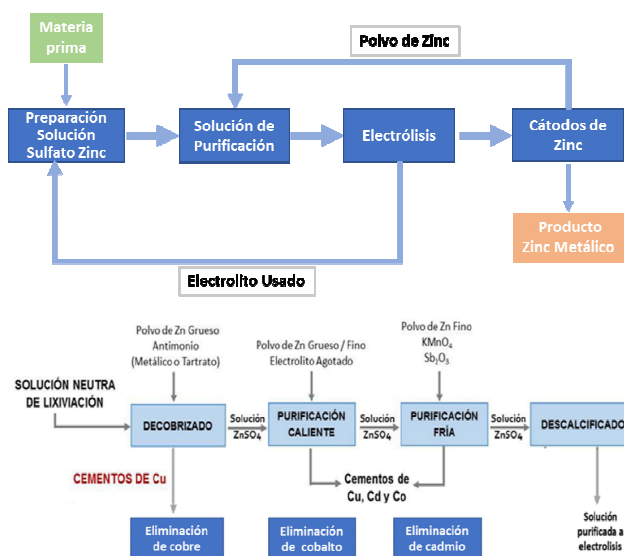


Fig. 1. A) Diagrama del flujo básico proceso global de obtención de Zinc. B) Proceso de purificación de la disolución de lixiviación.

En la tabla 1 se encuentran los rangos de concentración de los diferentes metales en la disolución neutra de lixiviado inicial y en la disolución purificada.

TABLA 1. COMPOSICIÓN DE LAS DISOLUCIONES EN CADA UNA DE LAS ETAPAS DEL PROCESO

Entrada Disolución Neutra		
[Zn]	150-155	g/L
[Co]	20 - 60	mg/L
[Cu]	500 - 2000	mg/L
[Cd]	400 - 1500	mg/L
Salida etapa decobrizado		
[Zn]	150-155	g/L
[Cu]	200 - 300	mg/L
[Co]	3 - 4	mg/L
[Cd]	20	mg/L
Salida etapa Purificación Caliente		
[Zn]	150-155	g/L
[Cu]	0,6	mg/L
[Co]	0,15	mg/L
[Cd]	10	mg/L
Salida Etapa Purificación Fría.		
[Zn]	155-168	g/L
[Cu]	0,6	mg/L
[Co]	0,15	mg/L
[Cd]	1	mg/L

La composición ideal de la solución purificada correspondería a la de la salida de la etapa de la purificación fría recogida en la tabla 1.

Para cada una de las etapas del proceso de purificación se ha identificado un parámetro crítico de control y se ha diseñado, fabricado y evaluado un microanalizador automatizado que permite la monitorización en tiempo real de dicho parámetro de forma automática y autónoma.

B. Fabricación de los microanalizadores

Las diferentes plataformas microfluídicas o microanalizadores desarrollados para analizar cada analito seleccionado integran microestructuras de mezcla (para poder realizar las reacciones colorimétricas necesarias) y una celda de detección (para la determinación colorimétrica de los compuestos obtenidos). Cada microanalizador se fabricó utilizando copolímero de olefina cíclica (COC) como

sustrato, con el proceso de fabricación que se describe en la literatura [2].

Por su parte, la microcolumna de intercambio aniónico utilizada se fabricó con material cerámico utilizando la tecnología LTCC [3].

C. Montaje experimental

La fig. 2 muestra un esquema del montaje experimental genérico utilizado para cada microsistema analítico desarrollado. El sistema microfluídico se ensambló utilizando microválvulas solenoides de tres vías (161T031, NResearch), una bomba peristáltica (Minipuls 3, Gilson) y tubos Tygon (diámetro interno de 1,2 mm) y de teflón (diámetro interno de 0,8 mm, Tecnyfluor). Las secuencias automáticas de actuación tanto para la calibración como para el análisis de la muestra se gestionaron mediante una unidad controladora de elementos fluídicos (Flow Test, Biotray) o un módulo de control electrónico PSoC 5 CY8C5868AXILP035(Cypress Semiconductor) y su software asociado. Esta permite disponer de un equipo a pie de proceso capaz de funcionar en condiciones autónomas.

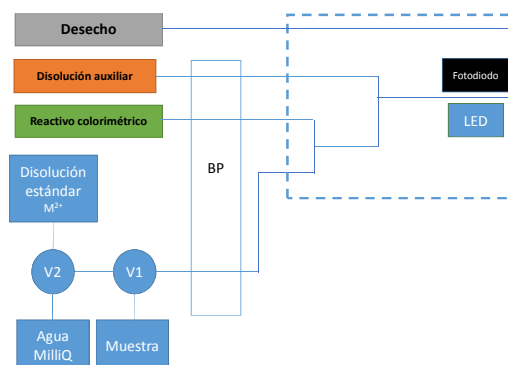


Fig. 2. Diagrama esquemático general del montaje experimental de cada microanalizador desarrollado, donde: Vx: microválvulas de 3 vías; BP: Bomba peristáltica. Área delimitada con líneas punteadas en azul correspondiente a la plataforma microfluídica.

El módulo de detección óptica integrado, con lock-in, miniaturizado y personalizado realizado en colaboración con el Grupo de Tecnologías Fotónicas de la Universidad de Zaragoza, está basado en el concepto de "llave-cerradura", donde la llave es la plataforma microfluídica y la cerradura el soporte [2]. Está compuesto por un LED de la longitud de onda adecuada para cada uno de los reactivos colorimétricos utilizados y un fotodiodo (Hamamatsu S1337-66BR). El funcionamiento y procesamiento de señales de sistema de detección se describe en detalle en [2]. Los datos obtenidos se envían inalámbricamente a una unidad de control central.

III. RESULTADOS Y DISCUSIÓN

A continuación, se describen las condiciones operacionales de cada etapa del proceso global de obtención de Zinc que van a prefigurar el diseño de los microanalizadores y los resultados obtenidos con cada uno de ellos [4].

A. Etapa de Decobrizado

El objetivo principal en esta etapa es precipitar gran parte del cobre presente en la solución neutra de lixiviación (>1000 mg/L) hasta niveles operativos adecuados de 200 - 300 mg/L de Cu y solubilizar el Sb hasta obtener concentraciones del orden 6 - 8 mg/L. La concentración de ambos elementos es crítica ya que junto con el polvo de zinc forman la pila galvánica requerida para la eliminación del Co

en la etapa de la Purificación Caliente. La monitorización en tiempo real del cobre es muy importante para realizar un adecuado control de la dosificación de polvo de Zinc hacia el tanque. Con este fin se ha desarrollado un microanalizador de ion cobre utilizando Batocuproina disulfonato como reactivo colorimétrico que cubre el rango de concentraciones requerido (100 - 1000 mg/l) para lo que ha sido necesario incorporar una etapa de dilución 1:100 de la muestra y los agentes complejantes necesarios para eliminar la interferencia de otros iones presentes.

B. Etapa de Purificación Caliente

El objetivo de esta etapa es precipitar el cobalto y parcialmente el cadmio hasta valores de concentración inferiores a 0.2 mg/L y 10 mg/L, respectivamente mediante la adición de polvo de zinc y utilizando el plomo (presente en el polvo de zinc), cobre y antimonio como catalizadores a una temperatura de 85 °C. La monitorización en tiempo real del Cobalto es muy importante para realizar un adecuado control de la dosificación del polvo de Zinc necesario para precipitarlo. Con este fin se ha desarrollado un microanalizador de ion cobalto utilizando la sal disódica del ácido 3-Hidroxi-4-nitroso-2,7-naftaleno disulfónico (NRS) como reactivo colorimétrico que cubre el rango de concentraciones requerido (0 a 3 mg/l). Se han incorporado diferentes agentes enmascarantes para eliminar la interferencia de otros iones como el cadmio, el cobre o el zinc.

C. Etapa de Purificación Fría

El objetivo de esta etapa es eliminar impurezas remanentes que llegaron en la solución de la etapa de Purificación Caliente, principalmente el Cadmio que no se logró precipitar en dicha etapa. La concentración de este elemento debe reducirse al final de la etapa hasta niveles inferiores a 1 mg/L. La monitorización en tiempo real del Cadmio es muy importante para realizar un adecuado control de la dosificación del polvo de Zinc necesario para precipitarlo. Con este fin se ha desarrollado un microanalizador colorimétrico de ion cadmio que cubre el

rango de concentraciones requerido (0 a 3 mg/l) para lo que ha sido necesario incorporar una microcolumna rellena de una resina de intercambio aniónico (AG 1-X8, Bio-Rad). Dicha columna permite retener el cadmio y el cobre en forma de complejo aniónico y eliminar la interferencia de zinc. Posteriormente utilizando Cadion como reactivo colorimétrico se mide el cadmio colorimétricamente.

IV. CONCLUSIONES

En este trabajo se presentaron los resultados obtenidos en la evaluación de los diferentes analizadores desarrollados y los primeros resultados obtenidos con muestras reales de la planta de Zinc de la empresa Peñoles ubicada en la ciudad de Torreón (México) que produce más de 200.000 toneladas/año de Zinc.

AGRADECIMIENTOS

Los autores agradecen el apoyo financiero del Ministerio de Ciencia e Innovación de España a través del proyecto PID2020-117216RB-I00 y de la Generalitat de Cataluña a través del proyecto 2021SGR00124. Los autores también agradecen el apoyo financiero de Met-Mex Peñoles S.A. de C.V. y el Tecnológico Nacional de México.

REFERENCIAS

- [1] K.V. Guevara, P. Couceiro, H.C. Fuentes, A. Calvo-López, N. Sánchez, H.A. Moreno Casillas, F. Valdés Perezgasga, J. Alonso-chamarro, "Microanalyser Prototype for On-Line Monitoring of Copper(II) Ion in Mining Industrial Processes", *Sensors*. 19 (2019) 3382.
- [2] O. Ymbern, N. Sánchez, A. Calvo-López, M. Puyol, J. Alonso-Chamarro, "Gas diffusion as a new fluidic unit operation for centrifugal microfluidic platforms", *Lab Chip*. 14 (2014).
- [3] N. Ibáñez-García, J. Alonso, C.S. Martínez-Cisneros, F. Valdés, "Green-tape ceramics. New technological approach for integrating electronics and fluidics in microsystems", *TrAC Trends Anal. Chem.* 27 (2008) 24–33.
- [4] C. Yang, B. Sun, "Chapter 1 - Introduction in Modelling Optimization and Control of Zinc Hydrometallurgical Purification Process", in: *Academic Press*, 2021: pp. 3–14.

A análise por injeção em fluxo e sensores

Maria Teresa S. R. Gomes*
 CESAM, Departamento de Química,
 Universidade de Aveiro
 Aveiro, Portugal
mtgomes@ua.pt

Marta I. S. Veríssimo
 CESAM, Departamento de Química,
 Universidade de Aveiro
 Aveiro, Portugal
mverissimo@ua.pt

Sumário—A Análise por Injeção em Fluxo (FIA) é simples de implementar em laboratórios sem muitos recursos. Traz algum nível de automação aos métodos de análise, usa tubos de reduzidas dimensões e adequa-se a sistemas analíticos com sensores químicos. Exige o controlo rigoroso dos caudais, mas a análise não necessita que se espere até que o equilíbrio seja atingido. A versatilidade da FIA é mostrada através de exemplos práticos, discutindo-se as vantagens e a inadequação de alguns tipos de transdutores a algumas opções.

Palavras Chave— análise por injeção em fluxo, FIA, sensor

INTRODUÇÃO

A análise de amostras é muitas vezes realizada de forma individualizada, evitando-se a contaminação cruzada, ainda que a introdução dos lotes de amostras no instrumento analítico possa ser feita recorrendo a um amostrador automático. Os sensores químicos, ao responderem de forma contínua ao analito, vieram tornar essas análises menos dispendiosas, possibilitar a miniaturização e, não raras vezes, a monitorização remota. A análise individualizada de padrões e amostras necessita que o sinal seja registado após se ter atingido o equilíbrio na interação do analito com a camada sensível do sensor. O estado de equilíbrio químico nem sempre é fácil de garantir, principalmente aquando da existência de uma variação, ainda que muitíssimo lenta, na linha de base. Alguma deriva na linha de base, por fatores difíceis de controlar, é vulgar, o que complica a decisão de quando registar o sinal da amostra, porque o analista espera a estabilização do mesmo. Muitas vezes resolve-se esta questão fazendo as leituras a tempos predeterminados.

A análise por injeção em fluxo (FIA), dada a sua simplicidade, veio introduzir alguma automação em situações onde o número de amostras é tão baixo que esta não pareceria ser uma necessidade. Amostras e padrões são sucessivamente injetados no sistema, e a contaminação é evitada assegurando que não chega ao detetor nenhuma amostra antes do sinal da linha de base ter sido reestabelecido. O sinal analítico é, na maioria das situações, a altura máxima do pico, deixando de haver hesitações quanto ao tempo ao qual se deve fazer a leitura. Sendo a resposta dos sensores rápida, uma pequena deriva na linha de base não irá afetar a resposta, desde que essa deriva seja mais lenta do que a resposta.

A simplicidade da injeção em fluxo, a rapidez na resposta e recuperação da linha de base, garantindo que a interação do analito com a camada sensível é reversível, e a elevadíssima reprodutibilidade da técnica são alguns dos fatores que fazem com a mesma reúna a preferência de muitos dos químicos analíticos que usam sensores químicos.

PRINCÍPIO DA ANÁLISE POR INJEÇÃO EM FLUXO COM DETECÇÃO POR SENSORES

O Princípio da injeção em fluxo

A análise por injeção em fluxo (FIA) foi proposta por Rusicka e Hansen em 1975 e consiste na injeção da amostra num fluido de transporte [1]. Em oposição à análise por fluxo segmentado, não há bolhas de ar introduzidas no caudal, que tinham a vantagem de separar amostras sucessivas, mas obrigavam geralmente à desgaseificação antes do detetor. A ideia de FIA, que hoje nos parece simples, foi inicialmente olhada com desconfiança, porque se pensava que as bolhas de ar seriam imprescindíveis, e até mal interpretada, porque confundida com a cromatografia, apenas porque algumas partes desse equipamento foram aproveitadas para a construção dos primeiros sistemas.

A possibilidade de fazer reagir o analito com um reagente apropriado para obtenção de um produto detetável é fácil de conseguir, fazendo confluir um caudal desse reagente com o de transporte, antes da porta de injeção da amostra. O contacto entre o reagente e a amostra tem que ser assegurado, e normalmente permite-se que, após o ponto de confluência, os mesmos permaneçam em contacto ao percorrerem uma serpentina com um comprimento adequado. A deteção reprodutível não exige que o equilíbrio seja atingido, apenas que o tempo de contacto e percurso até ao detetor não variem, o que é conseguido mantendo o comprimento dos tubos e os caudais. Em princípio, qualquer sensor que responda com um sinal mensurável à concentração do analito, ou do produto da reação com o mesmo poderá ser usado.

Como exemplo, mostra-se na Fig. 1 uma montagem para determinar nitrito por meio de um sensor ótico extrínseco.

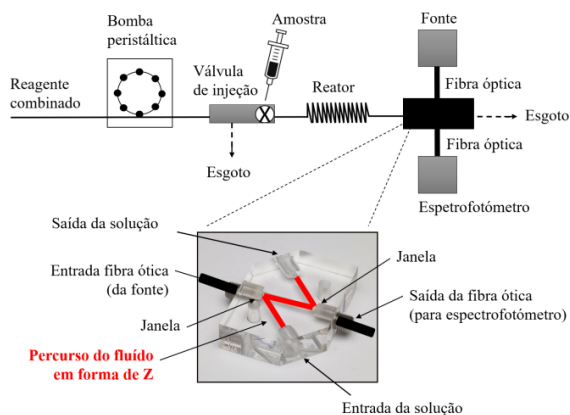


Fig.1. Esquema para análise de nitrito em água com um sensor ótico extrínseco.

Um caudal constante de 0.8 mL min^{-1} de um reagente de cor é conseguido por meio de uma bomba peristáltica. A amostra é injetada e forma-se um composto vermelho-violeta na reação do nitrito com a sulfanilamida e o cloreto de N-(1-naftil)etilenodiamina em meio ácido. O caudal passa por uma célula de absorção com um percurso ótico de 1 cm. Uma fonte de luz está ligada a uma fibra ótica que transporta a radiação até uma a janela de safira da célula. Uma outra fibra ótica coleta a luz à saída da célula e dirige-a para um espectrofotómetro, sendo registada a absorvência a 544 nm [2].

A. Como mover o fluido

O fluido pode ser forçado a mover-se por meio de uma bomba peristáltica. Grande parte das publicações com FIA utiliza uma bomba com diversos canais, o que permite ter diversas linhas de fluxo com diferentes fluidos. As bombas peristálticas são adequadas para a maioria dos detetores, embora produzam um movimento pouco uniforme, sendo o mesmo pulsado, o que causa problemas de instabilidade na linha de base dos sensores piezoelétricos, sensíveis a variações de pressão. Para estes, é preferível colocar os fluidos em frascos fechados, com uma entrada para um gás inerte (por exemplo nitrogénio) e um manómetro que permita controlar a pressão do gás no espaço de cabeça, por forma a forçar o líquido a sair de forma controlável. Consegue-se deste modo um caudal não pulsado, razoavelmente constante e suave.

Com caudais muito pequenos, que permitem poupar reagentes, mas ter um tempo de residência suficiente com amostras diminutas (poucos microlitros), é suficiente usar uma seringa com controlo automático da velocidade do êmbolo, para conseguir caudais do fluido de arraste de poucos microlitros por minuto. A Fig. 2 mostra fotografias da bomba peristáltica, do manómetro e frasco pressurizável com o fluido de arraste e da bomba de seringa.



Fig. 2. (a) bomba peristáltica, (b) manómetro e frasco pressurizável com o fluido de arraste e (c) bomba de seringa.

Controlo da dispersão e fluxo cortado

A dispersão do analito é uma varável a controlar. No caso da injeção em fluxo ser apenas um método para levar, de uma forma controlada, a amostra até ao sensor, o percurso deve ser o mais curto possível, para evitar a diluição da amostra e o consequente alargamento e diminuição da altura do sinal. É verdade que nas análises por cristais piezoelétricos se nota por vezes uma pequena subida da frequência aquando da injeção da amostra (ver Fig. 3), sendo aconselhável ter algum comprimento de tubo no percurso até ao sensor, para dar tempo a que esse pico de pressão desapareça e só depois surja o sinal analítico. A perturbação é temporalmente separada do sinal analítico.

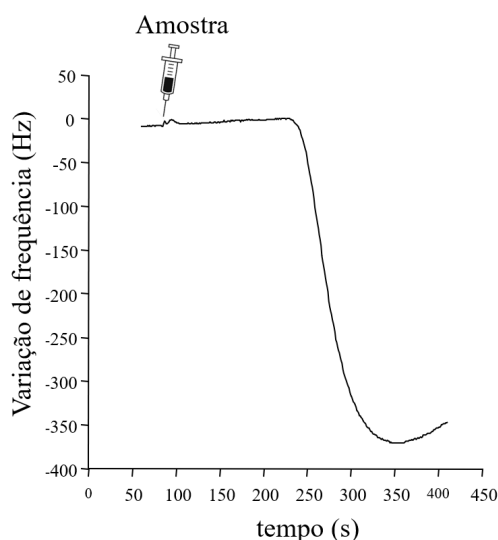


Fig.3. Frequência do cristal piezoelétrico revestido, com perturbação provocada pela injeção e pico da resposta produzida pelo analito (neste caso o pico é invertido e procura-se o mínimo da frequência)

Um comprimento de tubo maior deverá ser empregue no caso de se desejar que ocorra uma reação química, caso em que a espécie a detetar é o produto. Ainda assim, dever-se-á manter uma dispersão limitada para não degradar o sinal. Um modo de favorecer a formação do produto, sem aumentar a dispersão, consiste na paragem da bomba, ou outro sistema propulsor, por um tempo rigorosamente controlado. O método do fluxo cortado será vantajoso com deteção potenciométrica, mas traria muitos problemas na deteção piezoelétrica.

Detecção em fase gasosa

A injeção de gases em correntes gasosas raramente se vê, mas é muito útil. Nem todos os transdutores são adequados para a deteção na fase gasosa, sendo uma boa escolha sensores piezoelétricos e semicondutores de óxidos metálicos, em alternativa aos sensores potenciométricos, muito usados em solução. A análise de mercúrio será uma das que, à partida, faz sentido que a deteção seja feita na fase gasosa, uma vez que bastará reduzir o mercúrio a Hg^0 . O esquema na Fig. 4 mostra a análise do mercúrio em amostra aquosas, após redução do mesmo, separação do gás, secagem do mesmo e sua amálgama nos elétrodos de ouro de um cristal piezoelétrico [3].

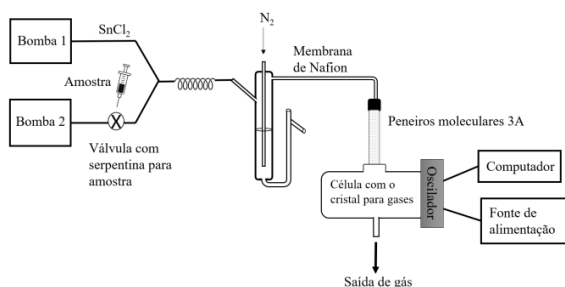


Fig. 4. Esquema usado na determinação de mercúrio em amostras aquosas com detecção com um cristal piezoelétrico.

Em muitas outras situações, o deslocamento de um analito para a fase gasosa e posterior detecção permite evitar que cheguem ao sensor interferentes não voláteis. Um bom exemplo é a detecção de dióxido de carbono e dióxido de enxofre em vinho [4,5]. O esquema pode ver-se na Figura 5.

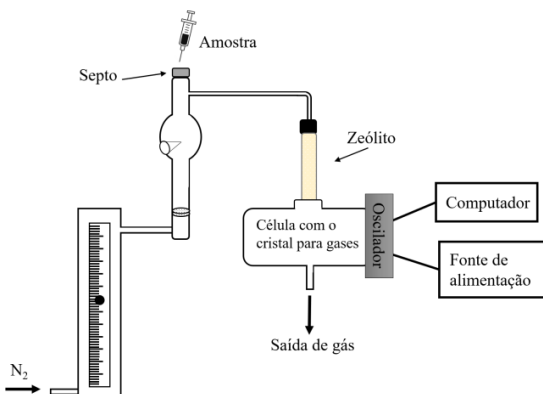


Fig. 5. Esquema da montagem para a determinação de CO_2 ou SO_2 no vinho, por deslocamento dos mesmos por uma corrente de nitrogénio que arrastará o gás até ao cristal piezoelétrico revestido com um composto adequado à detecção de um dos gases.

Microextração em fase sólida (SPME)

Pré-concentrar a amostra numa fibra durante um período de tempo controlado e posterior dessorção do analito num pequeno forno permite introduzir o analito na corrente gasosa, e quantificá-lo em amostras com concentrações inferiores ao limite de detecção do método. Na Fig. 6 pode ver-se um esquema com a fibra exposta, após a inserção da agulha do suporte da mesma no septo de uma célula tubular, com uma entrada lateral para o gás de arraste (N_2) [6].

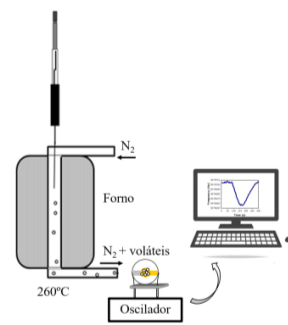


Fig. 6. Fibra de SPME inserida num forno aquecido a 260°C . Um caudal contante de nitrogénio transporta os compostos dessorvidos até ao sensor piezoelétrico.

Optimização do sistema FIA

A dispersão da amostra deve ser controlada. Não só o comprimento e diâmetro dos tubos é importante, mas o desenho das células de detecção e ainda aquelas que se usam para secar os gases. As células deverão ter um volume o mais reduzido possível, mas terão que acomodar um volume de amostra suficiente para se conseguir detetar o analito.

As figuras anteriores mostram variações no diâmetro dos tubos desde a injeção até à célula de detecção, ditadas por circunstâncias práticas de células executadas na oficina de sopragem de vidro da Universidade, com dimensões limitadas pelos diâmetros dos tubos roscados existentes, tubos que se destinavam a secar os gases antes da detecção e que terão que acomodar o agente secante sólido (ver Fig. 5), e dimensões do cristal piezoelétrico. A utilização de uma membrana de Nafion na secagem (Fig. 4 e Fig. 7) pode ser suficiente, evitando os tubos com secantes como sílica gel ou peneiros moleculares, mais largos.

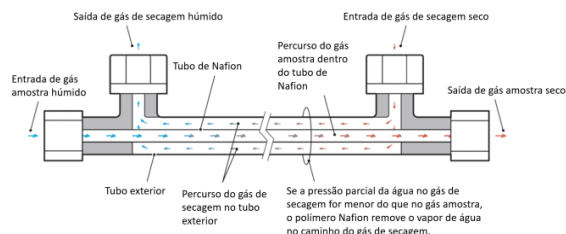


Fig. 7. Membrana de Nafion para secagem em contracorrente.

No nosso laboratório, as próprias células para o cristal sofreram grandes transformações ao longo do tempo, tendo presentemente dimensões mais reduzidas, quer se destinem a gases quer a líquidos (ver fotografias das mesmas na Fig. 8).

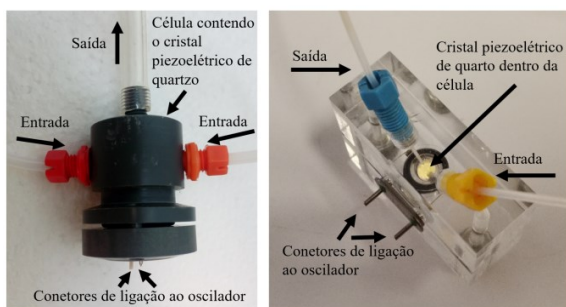


Fig.8. Fotografia de uma célula atual para um cristal piezoelétrico a) para detecção em fase gasosa b) para detecção em líquidos.

Na maioria dos trabalhos, as concentrações dos reagentes, os caudais dos mesmos e do fluido de transporte e o volume da amostra a injetar são selecionados tendo apenas em linha de conta a experiência anterior do analista e a observação da forma do sinal, que variará desde um pulso retangular, no ponto da injeção, passando por uma Lorentziana e atingindo eventualmente uma forma gaussiana, após um tempo de permanência mais longo, permitido quando se pretende que ocorra uma reação química. A forma e altura do pico dependem ainda do volume injetado. As variáveis de que depende o sinal poderão ser otimizadas recorrendo a métodos de otimização como o Simplex, ou Simplex modificado, usado na otimização de algumas variáveis experimentais para o método de análise de mercúrio com o desenho da Fig. 4. Otimizaram-se seis parâmetros: a concentração do ácido na corrente de transporte, o comprimento da serpentina da porta de injeção e da serpentina de mistura, os caudais do transportador da amostra, do redutor (SnCl_2), e da corrente de N_2 , que transporta o vapor de mercúrio até ao sensor [3].

AGRADECIMENTO

Os autores agradecem à FCT/MCTES o suporte financeiro ao CESAM (UIDP/50017/2020 + UIDB/50017/2020 + LA/P/0094/2020), por fundos nacionais.

REFERÊNCIAS

- [1] Ruzicka, J.; Hansen, E. H., Flow Injection Analysis; John Wiley & Sons.: Nova York, 1981.
- [2] Gomes, M.T.S.R. "Experiments for Instrumental Analysis Techniques," Chemistry Master Course, UA 2024.
- [3] Gomes, M. T. S. R.; Morgado E. V.; Oliveira, J. A. B. P. "Optimisation of a Flow Injection System with a Piezoelectric Quartz Crystal Detector for the Determination of Inorganic Mercury," Anal. Lett. 1999, 32, 2715-2723..
- [4] Gomes, M. T.; Rocha, T. A.; Duarte, A. C.; Oliveira, J. P. "Determination of Sulfur Dioxide in Wine Using a Quartz Crystal Microbalance," Anal. Chem. 1996, 68, 1561-1564.
- [5] Gomes, M. T. S. R.; Rocha, T. A. P.; Duarte, A. C.; Oliveira, J. A. B. P. "Quantification of CO_2 in Wines with Piezoelectric Crystals Coated with Tetramethylammonium Fluoride and Comparison with Other Methods," Anal. Chem. 1998, 70, 179-182.
- [6] Verissimo M. I. S.; Gamelas J.A.F.; Evtuguin D.V.; Gomes, M.T.S.R. "Determination of 5-hydroxymethylfurfural in honey using headspace-solid-phase microextraction coupled with a polyoxometalate coated piezoelectric quartz crystal," Food Chemistry 2017, 220, 420-426.

Simulación numérica y caracterización de una plataforma microfluídica generadora de gotas

Ana Canosa¹, Lara Eleonora Prado¹, Tomás Molina¹, Eliana Gabriela Mangano*¹, Laura Malatto*¹, Alex Lozano^{1,2}

¹Departamento de Micro y Nano Fabricación, Instituto Nacional de Tecnología Industrial (INTI)
Buenos Aires, Argentina *emangano@inti.gov.ar, lmalatto@inti.gov.a

²Dirección Técnica de Micro y Nano Tecnologías, Instituto Nacional de Tecnología Industrial (INTI)
Buenos Aires, Argentina

Resumen— El objetivo de este trabajo es evaluar el comportamiento de una plataforma microfluídica generadora de gotas. Para ello, se modela mediante simulación numérica el proceso de formación y se realizan caracterizaciones aplicando un rango de caudales con bombas de jeringa. Se presenta una metodología para determinar los parámetros de frecuencia y tamaño de las gotas. Los resultados se presentan para las gotas generadas en los rangos de 5 Hz a 100 Hz y 50 μm a 210 μm .

Keywords—microfluídica, microgotas, flow-focusing, microencapsulado.

I. INTRODUCCIÓN

Durante las últimas dos décadas han surgido diversas alternativas para la generación de gotas debido a la versatilidad de aplicaciones que poseen. En particular, los dispositivos o *chips* generadores de gotas tienen múltiples aplicaciones en salud, como la encapsulación de células, la creación de modelos de tejidos, la producción de nanopartículas y la síntesis de nuevos materiales. La encapsulación en gotas permite estudiar la biología celular y la farmacología, además de identificar nuevos fármacos y crear modelos de enfermedades [1]. También se utilizan en diagnósticos y terapias, así como para sintetizar nuevos materiales y modelos de tejidos para medicina regenerativa.

Los métodos para la generación de gotas se pueden dividir en técnicas activas y pasivas. Las técnicas activas requieren el uso de fuerzas externas para generar gotas. Sin embargo, debido a los altos costos asociados con las técnicas activas, surge el uso de técnicas pasivas. Estas aprovechan especialmente la geometría de los microcanales en el dispositivo y las propiedades físicas de los fluidos para generar gotas. Los métodos pasivos se pueden dividir según sus geometrías: coflujo, flujo cruzado y enfoque de flujo [2].

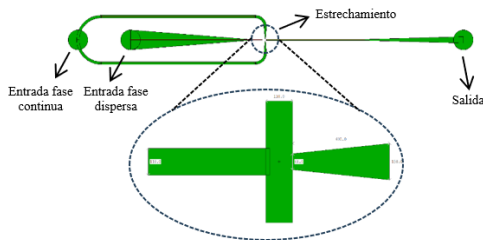


Fig. 1. Dispositivo 4 con sus partes principales referenciadas.

En [3] se diseñaron y microfabricaron dispositivos con geometría tipo enfoque de flujo (en inglés *flow-focusing*). En esta publicación, como continuación del trabajo mencionado, se presenta una metodología para caracterizar y simular numéricamente dichos *chips*. Este generador requiere dos

fases de líquidos inmiscibles. En esta investigación se utilizó como fase dispersa agua y como fase continua aceite (Fig. 1). Se busca definir frecuencia y ancho de las microgotas, representativo de su tamaño, a partir de distintos caudales de la fase dispersa fijando el caudal de la fase continua.

TABLA 1. MEDIDAS DE LOS CANALES

Chip	Fase dispersa [μm]	Fase continua [μm]	Estrechamiento [μm]	Salida [μm]
2	110	80	66	110
3	110	110	110	220
4	110	110	66	150

En la Tabla 1 se detallan las medidas de los canales de los dispositivos diseñados y simulados numéricamente.

II. SIMULACIÓN NUMÉRICA

Para las simulaciones se utilizó el programa ANSYS FluentTM, que cuenta con el modelo *Volume of Fluid* (VOF) para la resolución numérica de flujos inmiscibles. El sistema de ecuaciones de continuidad, Navier-Stokes y transporte de fases para este modelo es:

$$\frac{\partial \rho}{\partial t} + \nabla \cdot (\rho \vec{u}) = 0$$

$$\frac{\partial}{\partial t} (\rho \vec{u}) + \nabla \cdot (\rho \vec{u} \times \vec{u}) = -\nabla p + \nabla \cdot [\mu(\nabla \vec{u} + \nabla \vec{u}^T)] + \vec{F}_\sigma$$

$$\frac{\partial \alpha_q}{\partial t} + \vec{u} \cdot \nabla \alpha_q = 0$$

Donde ρ y μ son la densidad y viscosidad, \vec{u} es el campo de velocidad, p la presión, \vec{F}_σ la fuerza por tensión interfacial y α_q la fracción volumétrica de fase dispersa.

Se decidió modelar los dispositivos con un dominio bidimensional, tomando como referencia los trabajos de Ngo y Mehraji [4, 5]. El dominio se malló con un tamaño de celda de 5 μm con capas de inflación en las paredes.

La simulación se realizó con agua ($\rho_{\text{agua}} = 998 \text{ kg m}^{-3}$, $\mu_{\text{agua}} = 0,001 \text{ Pa.s}$) y aceite ($\rho_{\text{aceite}} = 1000 \text{ kg m}^{-3}$, $\mu_{\text{aceite}} = 0,049 \text{ Pa.s}$) como fases dispersa y continua respectivamente. La interacción principal entre fases está dada por la tensión interfacial $\sigma = 0,0244 \text{ N m}^{-1}$ [6]. Se consideró también la interacción de las fases con las paredes con un ángulo de contacto $\theta_w = 110^\circ$. Como condición de borde, se colocó una velocidad uniforme para cada entrada de $U = Q_{\text{fase}} / A_{\text{entrada}}$, acorde a los caudales experimentales.

Para el modelado numérico, se consideró flujo laminar y una resolución transitoria. En el modelo VOF se aplicó un esquema implícito con las opciones *Implicit Body Force*, *anti-diffusion* y *Continuum Surface Force*. Se resolvió con el algoritmo *Coupled* con los esquemas *Least Square Cell Based*, *PRESTO!*, *Second Order Upwind* y *Compressive* para el gradiente, la presión, el momento y la fracción de fase respectivamente. Para el paso temporal se aplicó el esquema *Second Order Bounded*. En la Fig. 2 se muestra una instancia del video de resultados de la simulación.

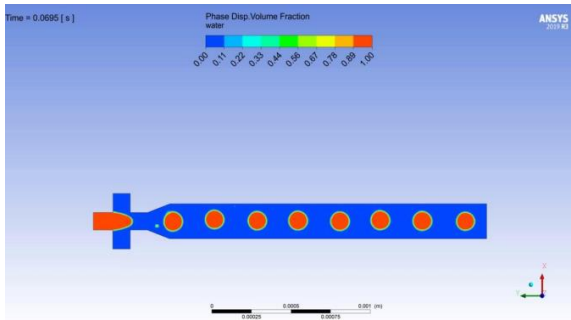


Fig. 2. Imagen de una instancia de la simulación del chip 3. Los colores representan la proporción de fases.

III. CARACTERIZACIÓN

Los dispositivos fueron fabricados con la técnica de soft lithography en la sala limpia de INTI. Para ello se preparó un micromolde utilizando una oblea de silicio standard de 100 mm de diámetro y fotoresina epoxy SU8-100 (MicroChem). El diseño se transfirió mediante litografía óptica utilizando una máscara flexible con una dosis de 650 mJ/cm² y $\lambda=365$ nm (EVG 620). Las réplicas se realizaron en polydimethylsiloxano (PDMS, Dow Corning Sylgard® 184) en una proporción 10:1 base-reticulante. Luego se degasaron y curaron a 80°C por 40 min. para su polimerización, se desmoldaron, cortaron los chips y perforaron las entradas y salidas. Finalmente los dispositivos se cerraron con portaobjetos de vidrio, previamente activados en un plasma de oxígeno (Diener Electronic, Femto) y un curado por 4 horas a 40°C.

TABLA 2. RANGO DE CAUDALES CONFIGURADOS

Chip	Análisis	Caudal aceite [ml/h]	Caudal agua [ml/h]	
			Máximo	Mínimo
2	Simulación	0,4	0,55	0,01
	Caracterización	0,4	0,55	0,01
3	Simulación	0,6	0,55	0,04
	Caracterización	0,6	0,55	0,04
4	Simulación	0,6	1,80	0,01
	Caracterización	0,6	0,55	0,01

Para estudiar el comportamiento de los generadores de gotas desarrollados se implementó un sistema integrado por bombas de jeringa, mangueras, conectores y tips. Este sistema permite inyectar de forma controlada distintos caudales de agua y aceite en cada entrada respectivamente.

Se utilizaron dos bombas de jeringa comerciales, una para la fase dispersa (APEMA, PC11UBT) y otra para la fase continua (LEEX, EN-S7). Para la observación en tiempo real se utilizó un microscopio óptico (Zeiss, PrimoStar) con una cámara de 240 fps (Fig. 3). Este sistema de adquisición permite obtener distintos videos para los caudales inyectados, los cuales se procesan para extraer los parámetros de interés.



Fig. 3. Banco de caracterización para la aplicación de microflujos.

En la Tabla 2 se presenta el rango de caudales utilizados tanto en simulación como en las caracterizaciones para los dispositivos 2, 3 y 4. Se decidió mantener constante el caudal de la fase continua, variando el de la fase dispersa, acorde con las prestaciones de las bombas utilizadas. La fase dispersa se evaluó con 15 pasos intermedios en el rango especificado.

IV. PROCESAMIENTO DE DATOS

Tanto en las simulaciones como en las caracterizaciones, los resultados obtenidos se procesaron con python para estudiar la frecuencia y el ancho de gota correspondientes a cada caudal.

Todas las imágenes que componen cada uno de los videos se procesaron para aumentar el contraste entre las gotas y el fondo. En cada una de estas imágenes se extrajeron dos líneas de píxeles (Línea 1 y Línea 2), transversales al canal y con una posición fija como se muestra en la Fig. 4. Luego, se promediaron los tonos de cada línea. Con estos valores se construyó la señal de proporción de fase dispersa, indicadora de la presencia de gotas.

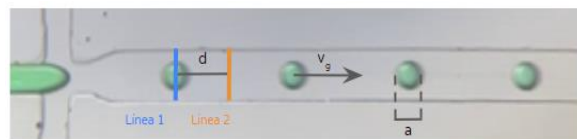


Fig. 4: Imagen del canal de salida con las líneas 1 y 2 dibujadas, donde d es la distancia entre líneas, v_g la velocidad de la gota y a su ancho.

Para el caso de las simulaciones numéricas esta señal se extrajo de forma directa del software de post-procesamiento. En la Fig. 5 se puede observar un ejemplo de estas señales, siendo cada pico representativo del pasar de una gota por la línea correspondiente. La información en las señales de ambas líneas es análoga pero defasada por un tiempo t_d . A partir de la obtención de las señales de proporción de fase, el cálculo de la frecuencia y el ancho fue análogo para simulación y caracterización.

Respecto al cálculo de la frecuencia (f), se contó la cantidad de picos (n) determinando las instancias de

comienzo (t_a) y finalización (t_b) de las gotas, para luego aplicar (1):

$$f = \frac{(n-1)}{t_b - t_a} \quad (1)$$

Para obtener el ancho (a) de las gotas se utilizó el tiempo t_d entre las señales de cada línea y el tiempo de duración del pico t_g , siendo v_g la velocidad de avance de esta, y aplicando (2):

$$v_g = \frac{d}{t_d} = \frac{a}{t_g} \Rightarrow a = \frac{d \cdot t_g}{t_d} \quad (2)$$

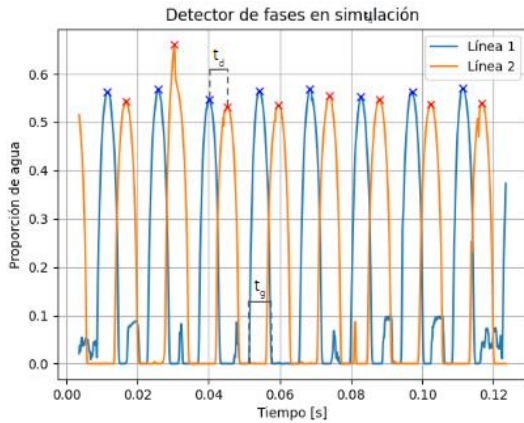


Fig. 5. Gráfico de señales de fase de una simulación numérica, donde t_d es el tiempo de desfase entre señales y t_g el tiempo que tarda una gota en pasar por la línea.

V. RESULTADOS Y DISCUSIÓN

En este apartado se analizan los resultados experimentales (Fig. 6 y 7, izquierda) y simulados (Fig. 6 y 7, derecha), comparando los parámetros en función del caudal de la fase dispersa.

A. Frecuencia de goteo

En la Fig. 6 se observa un aumento de la frecuencia de goteo al aumentar el caudal de la fase dispersa, siendo más

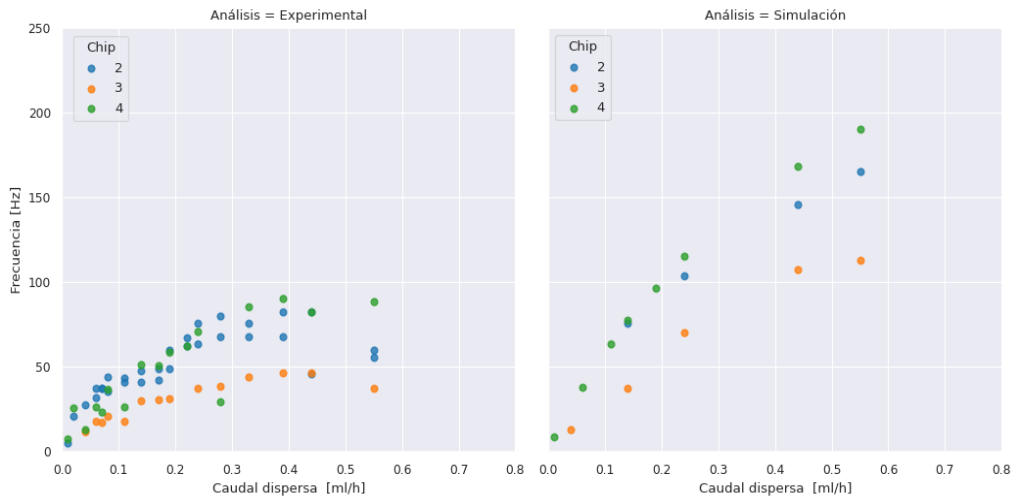


Fig. 6. Gráfico de comparación de frecuencias entre geometrías

pronunciado en las simulaciones. Confirmando lo esperado, el *chip* 3 con dimensiones mayores del estrechamiento y el canal de salida, muestra frecuencias menores de generación de gotas.

Las discrepancias entre las caracterizaciones y las simulaciones pueden justificarse por distintos fenómenos. En primer lugar, las bombas de jeringa utilizadas en lo experimental no inyectan caudal de forma constante, sino que tienen un período de fluctuación, lo cual afecta directamente al proceso de formación de gotas [7]. En segundo lugar, la forma y el tamaño de los canales microfluidicos no replican exactamente las dimensiones del diseño simulado. Adicionalmente, el material de los *chips*, PDMS, puede sufrir un hinchamiento por contacto con el aceite, modificando no solo la geometría sino también la hidrofobicidad.

B. Ancho de gota

En la Fig. 7 se presentan los resultados de ancho de gota obtenidos al variar el caudal de la fase dispersa. Las caracterizaciones no arrojaron una tendencia general como en el caso de la frecuencia. Sin embargo, en las simulaciones numéricas hay un claro incremento del ancho con el caudal. Esta diferencia podría deberse al período de fluctuación de las bombas de jeringa, como se mencionó anteriormente. Mientras que en la simulación el caudal inyectado es constante, en lo experimental los caudales fluctúan en cada caso.

Cabe mencionar que durante las caracterizaciones de los dispositivos las bombas de jeringa utilizadas presentaron una limitación por presión, permitiendo evaluar de forma acotada los *chips*.

VI. CONCLUSIONES

Se logró comprender el comportamiento de los dispositivos diseñados y microfabricados anteriormente. Se determinaron los rangos de caudal en los que se forman gotas en los *chips*

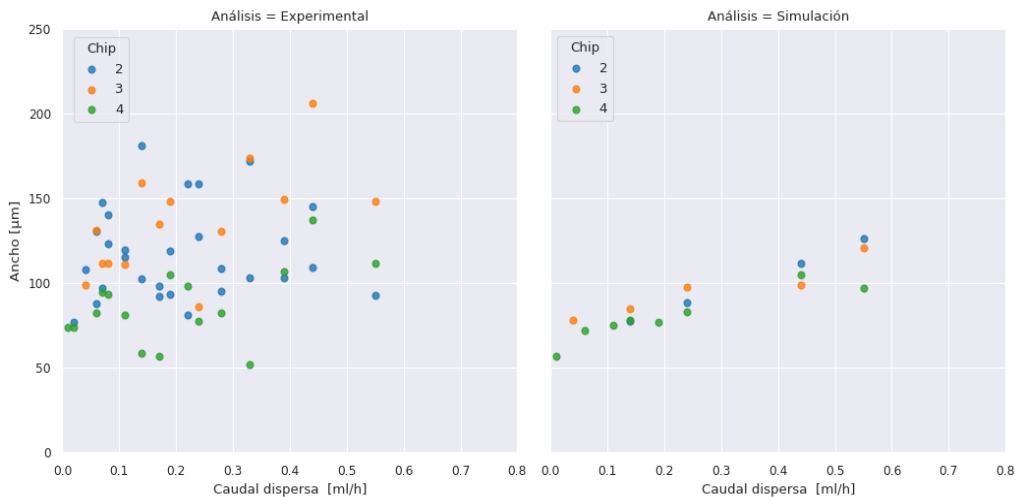


Fig. 7. Gráfico de comparación de anchos de gota entre geometrías

con el equipamiento disponible. Estos fueron luego simulados recreando las condiciones de entrada implementadas experimentalmente. De estos análisis se pudieron obtener los parámetros de interés del sistema, logrando analizar el proceso de formación de gotas de los *chips* presentes en la plataforma.

Se observó que la frecuencia de goteo y el tamaño de la gota aumenta con el caudal tanto en la caracterización y como en la simulación. Como se mencionó anteriormente, esta tendencia es menor en las caracterizaciones, lo que podría deberse a las condiciones experimentales (propiedades de los materiales y estructuras de los *chips*, caudal) con respecto a lo simulado. A su vez, se observó una relación entre los rangos de frecuencia y tamaño de cada dispositivo.

Se plantea como trabajo a futuro optimizar el proceso de microfabricación para replicar con mayor precisión el diseño planteado. En cuanto a la caracterización, se propone utilizar bombas de jeringa a presión constante y evaluar los dispositivos variando también el caudal de fase continua. Por último, se espera realizar una mayor cantidad de simulaciones para obtener más puntos de comparación.

AGRADECIMIENTOS

Los autores de este trabajo agradecemos a los siguientes departamentos del Instituto Nacional de Tecnología Industrial (INTI): por el préstamo de equipamiento, a Nanomateriales Funcionales y a Integración de Sistemas Micro y Nano

Electrónicos; por las mediciones de las propiedades de los fluidos, a Productos Químicos e Industriales; y por las mediciones de espesor del molde maestro, a Desempeño Mecánico de Productos.

REFERENCIAS

- [1] T. N. D. Trinh, H. D. K. Do, N. N. Nam, T. T. Dan, K. T. L. Trinh, and N. Y. Lee, "Droplet-Based Microfluidics: Applications in Pharmaceuticals," *Pharmaceuticals*, vol. 16, no. 7, p. 937, Jun. 2023, doi: 10.3390/ph16070937.
- [2] P. Zhu and L. Wang, "Passive and active droplet generation with microfluidics: a review," *Lab on a Chip*, vol. 17, no. 1, pp. 34–75, Nov. 2016, doi: 10.1039/C6LC01018K.
- [3] E. Mangano, M. Fiora, L. Malatto, A. Lozano, "Focused flow droplet generator", III Brazil-Argentine Microfluidics Congress/ VI Congreso de Microfluidica Argentina, libro de resúmenes, p. 62, Nov. 2022.
- [4] I. Ngo, T. Dang, C. Byon, S. Joo, "A numerical study on the dynamics of droplet formation in a microfluidic double T-junction". *Biomicrofluidics*, vol. 9, no. 2: 024107, Mar. 2015, doi: 10.1063/1.4916228.
- [5] S. Mehrabi and M. Saadatmand, "Flow regime mapping for a two-phase system of aqueous alginate and water droplets in T-junction geometry". *Physics of Fluids*, vol. 33 no. 7, 072009, Jul. 2021, doi: 10.1063/5.0051789.
- [6] A. De Vries, Y. L. Gomez, E. Van der Linden, and E. Scholten, "The effect of oil type on network formation by protein aggregates into oleogels," *RSC Adv.*, vol. 7, no. 19, pp. 11803–11812, Feb. 2017, doi: 10.1039/c7ra00396j.
- [7] W. Zeng, I. Jacobi, S. Li, and H. A. Stone, "Variation in polydispersity in pump- and pressure-driven micro-droplet generators," *Journal of Micromechanics and Microengineering*, vol. 25, no. 11, Oct. 2015, doi: 10.1088/0960-1317/25/11/115015.

Automatic microanalyzer for cobalt monitoring in the hydrometallurgical production of zinc

Antonio Calvo-López
Group of Sensors and Biosensors,
Universitat Autònoma de Barcelona,
Bellaterra, Spain
antonio.calvo@uab.cat

Francisco Valdés
División de Posgrado e Investigación
TecNM/ IT La Laguna
Torreón, Coah. México
fvaldesp@lalaguna.edu.mx

Natalia Fernández Vicente
Group of Sensors and Biosensors,
Universitat Autònoma de Barcelona,
Bellaterra, Spain
natalia.fernandezvi@autonoma.cat

Julian Alonso-Chamarro
Group of Sensors and Biosensors,
Universitat Autònoma de Barcelona,
Bellaterra, Spain
julian.alonso@uab.es

Mar Puyol Bosch
Group of Sensors and Biosensors,
Universitat Autònoma de Barcelona,
Bellaterra, Spain
mariadelmar.puyol@uab.cat

Abstract— This work focuses on the design, optimization, and application of an automated continuous flow microanalyzer for the colorimetric monitoring of cobalt in hydrometallurgical processes to obtain zinc.

Keywords— cobalt, microsystem, hydrometallurgical Zn production, Flow Injection Analysis

I. INTRODUCTION

Zinc is a nonferrous metal with interesting properties like excellent malleability, and abrasive and anti-corrosion resistance. For all this reasons, zinc has been widely employed in automotive, construction and shipping industries. However, zinc seldom exists in its elemental form in nature. It normally appears in combination with other metals such as copper, cadmium and lead in zinc ores. The production of zinc thus involves extraction of high-grade (99.995% purity) metallic zinc from these raw minerals using the zinc hydrometallurgical process. It is composed by different stages in which the monitoring at real time of the concentration of different metallic ions, usually present as impurities in the process solutions, is required. This analytical control allows optimizing the yield of the Zn hydrometallurgical process and the purity of the final product.

In this work, an automatic continuous-flow colorimetric analytical microsystem has been designed and optimized to monitor the concentration of cobalt present in zinc hydrometallurgical plants during the process of purification.

II. EXPERIMENTAL

A. Colorimetric reaction

3-Hydroxy-4-nitroso-2,7-naphthalenedisulfonic acid disodium salt (NRS) is a colorimetric reagent used to detect the presence of cobalt in solution [1]. Cobalt ions react with NRS to form an orange complex. The commonly used protocol consists of mixing the sample containing the metal in solution with NRS and sodium acetate solutions. Subsequently, the mixture is brought to boil and, upon cooling, nitric acid is added to reduce the pH of the solution to pH 3. These conditions favor the preferential formation of the Co-NRS complex and its stability over time, thus avoiding interferences from other metals present in the sample such as cadmium, copper or zinc [2] to complex. The maximum absorbance of the complex is at 540 nm.

B. Developed microanalyzer and experimental setup.

Fig 1. shows the experimental setup used. The system includes a multicommutation equipment with 2 solenoid microvalves to automate the calibration and sample analysis, and a microfluidic platform integrating mixing microstructures, and the detection cell for the colorimetric determination. NRS dissolved in sodium acetate buffer was used as selective colorimetric reagent. The interfering effect of other metals such as cadmium, copper and zinc were eliminated modulating the reaction conditions (order of addition of reagents, reaction time, and medium acidification).

The microanalyzer was fabricated using Cyclic Olefin Copolymer (COC) as substrate as described elsewhere [3].

The microfluidic system was assembled using three-way solenoid microvalves (161T031, NResearch), a peristaltic pump (Minipuls 3, Gilson), and Tygon (i.d. 1.2 mm) and Teflon (i.d. 0.8 mm, Tecnyfluor) tubing. The automatic sequences of actuation were managed using a flow controller unit (Flow Test, Biotray).

The miniaturized and customized optical detection module was composed of a 540 nm LED (Kingbright) and a photodiode (Hamamatsu S1337-66BR).

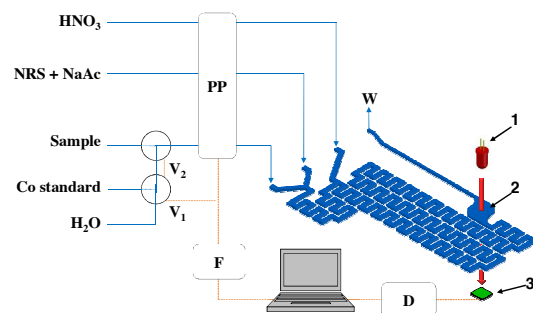


Fig. 1. Schematic diagram of the experimental setup where: V_1 , V_2 : 3-way microvalves; **PP**: Peristaltic pump; **F**: Flow controller unit (Flowtest); **D**: Detector; **W**: waste outlet; **1**: LED at 540 nm; **2**: Flow cell; **3**: Photodiode.

III. RESULTS AND DISCUSSION

A. Microsystem optimization

The configuration of the microanalyzer and the colorimetric reaction were optimized taking into account

different instrumental, hydrodynamic and chemical variables. Table I summarizes all the optimal options selected.

TABLE I. DIFFERENT OPTIMIZED VARIABLES

Optimized parameter	Range evaluated	Optimum
Reagents mixing order	Different combinations	1 st Sample 2 nd NRS + NaAc 3 rd HNO ₃
Reaction temperature (°C)	20 – 60	20
Analysis time (min)	1 – 60	3
Wavelength (nm)	400 – 700	540
[NRS] (%w/v)	0.5 – 1.5	0.5
Injection volume (μL)	86 – 1300	867
Flow rate (μL min ⁻¹)	350 – 850	600
Microvalve minimum multicommutation time (ms)	250 – 2000	500

The characterization and optimization of the colorimetric reaction was performed by conventional UV-Vis spectrophotometer. We evaluated how the order of addition of the reagents influences the absorbance spectrum and what is the effect of the main interferences. From these studies, we obtained the optimal values of reagent mixing order, temperature and measurement wavelength. The rest of the variables were optimized with the miniaturized continuous-flow system.

B. Analytical features

One calibration curve is shown in Fig. 2 with $\text{Absorbance} = (7 \cdot 10^{-5} \pm 3 \cdot 10^{-5}) + (1.30 \cdot 10^{-3} \pm 2 \cdot 10^{-5}) \cdot [\text{Co(II)}]$. The working range was set from 0.2 to 3 mg L⁻¹ Co²⁺ for this application. The LoD was 0.07 mg L⁻¹ Co²⁺ and the analysis time was less than 3 min.

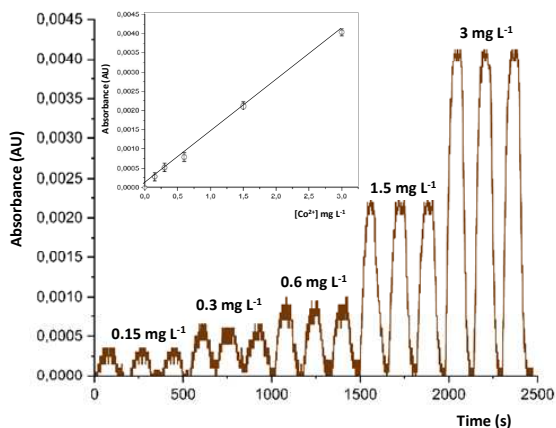


Fig. 2. Signal recording and calibration curve of cobalt standard solutions per triplicate.

C. Samples analysis

Different synthetic samples were prepared considering the expected concentrations of both the analyte and the interfering metals present in the real samples. Each of them was analyzed only once. Recovery percentages were around 100% in all cases except in samples with very high zinc concentrations and cobalt concentrations above 1.5 mg L⁻¹ (samples 24 and 28). As the expected range of concentrations

of zinc in real samples is very high, the working range of the analyzer would be 0.2 – 1.5 instead of 0.2 – 3 mg L⁻¹ Co²⁺.

TABLE II. REAL SAMPLES ANALYSIS

Sample	[Co ²⁺] _{Ladded} (mg L ⁻¹)	[Cd ²⁺] _{Ladded} (mg L ⁻¹)	[Cu ²⁺] _{Ladded} (mg L ⁻¹)	[Zn ²⁺] _{Ladded} (mg L ⁻¹)	[Co ²⁺] _{found} (mg L ⁻¹)	% rec.
1	0.3	3	3	3	0.3	99
2	0.6	3	3	3	0.6	95
3	1.5	3	3	3	1.5	99
4	3.0	3	3	3	3.0	98
5	0.3	1	0.6	300	0.3	99
6	0.6	1	0.6	300	0.6	96
7	1.5	1	0.6	300	1.5	98
8	3.0	1	0.6	300	2.9	98
9	0.3	1	0.6	600	0.3	96
10	0.6	1	0.6	600	0.6	96
11	1.5	1	0.6	600	1.5	100
12	3.0	1	0.6	600	3.0	98
13	0.3	1	0.6	1500	0.3	99
14	0.6	1	0.6	1500	0.6	95
15	1.5	1	0.6	1500	1.5	99
16	3.0	1	0.6	1500	2.9	97
17	0.3	1	0.6	3000	0.3	99
18	0.6	1	0.6	3000	0.6	94
19	1.5	1	0.6	3000	1.5	99
20	3.0	1	0.6	3000	2.5	84
21	0.3	1	0.6	6000	0.3	104
22	0.6	1	0.6	6000	0.6	93
23	1.5	1	0.6	6000	1.5	103
24	3.0	1	0.6	6000	2.4	80
25	0.3	1	0.6	150000	0.3	111
26	0.6	1	0.6	150000	0.5	89
27	1.5	1	0.6	150000	1.7	111
28	3.0	1	0.6	150000	2.3	76

IV. CONCLUSIONS

An automated analytical microsystem has been developed, using the FIA technique, to colorimetrically monitor the concentration of cobalt at different stages of the hydrometallurgical zinc refining process. The miniaturization of the analyzer simplifies its automation, allowing autonomous operation for the calibration and in situ analysis of samples, with low reagent consumption and the wastes generation. The analytical features are good to determine cobalt within the working range required.

ACKNOWLEDGMENT

The authors would like to thank the financial support from Spanish Ministry of Science and Innovation through the project PID2020-117216RB-I00 and Catalan government through the project 2021SGR00124. The authors also acknowledge financial support from Met-Mex Peñoles S.A. de C.V. and the Tecnológico Nacional de México.

REFERENCES

- [1] H. Yutaka, Y. Sayama, O. Koichi, "Sensitive and precise analytical methods for the determination of impurities in hydrometallurgical zinc refining by utilizing flow-injection technique", *Bunseki Kagaku*. 45 (1996) 1–18.
- [2] B. Purachat, S. Liawruangrath, P. Sooksamiti, S. Rattanaphani, D. Buddhasukh, "Univariate and Simplex Optimization for the Flow-Injection Spectrophotometric Determination of Copper Using Nitroso-R Salt as a Complexing Agent", *Anal. Sci.* 17 (2001) 443–448.
- [3] O. Ymber, N. Sánchez, A. Calvo-López, M. Puyol, J. Alonso-Chamarro, "Gas diffusion as a new fluidic unit operation for centrifugal microfluidic platforms", *Lab Chip*. 14 (2014).

Microanalizador para la monitorización de ion Cu(II) en el proceso hidrometalúrgico de obtención de Zinc

Karla Guevara
Departamento de Química-Bioquímica
TecNM/IT la Laguna
Torreón, Coah.México
kvguevara@lalaguna.tecnm.mx

Pedro Couceiro
Grupo Sensores y Biosensores
Universitat Autònoma de Barcelona
Barcelona, España
pedro.tavares.couceiro@gmail.com

Victor Manqueros
TecNM/ITSL
Lerdo, Durango, México
vema6791@gmail.com

Hesner Coto
División de Posgrado e Investigación
TecNM/IT la Laguna
Torreón, Coah. México
hesnercf@lalaguna.tecnm.mx

Julian Alonso-Chamarro
Grupo Sensores y Biosensores
Universitat Autònoma de Barcelona
Barcelona, España
Julian.Alonso@uab.es

Francisco Valdés
División de Posgrado e Investigación
TecNM/IT La Laguna
Torreón, Coah. México
fvaldesp@lalaguna.tecnm.mx

Resumen— Se presenta el desarrollo de un microanalizador modular para el monitoreo de ion de cobre (II) en procesos industriales hidrometalúrgicos. El microanalizador está integrado por un conjunto de diferentes módulos, siendo cada módulo responsable de la realización de una etapa del procedimiento analítico. Para el control y optimización en tiempo real de los procesos industriales implicados, el microanalizador automatiza todo el acondicionamiento de las muestras, la medida analítica y la adquisición y procesamiento de las señales y su transformación en información química. La determinación del ion cobre (II) se realiza mediante un reactivo específico de cobre que en presencia de este da lugar a un producto que medimos colorimétricamente. Así mismo, el microanalizador realiza una calibración automática mediante la medida sucesiva de patrones preparados por medio de la dilución por multiconmutación de una disolución stock del analito. El rango de trabajo del microanalizador abarca de 0.1-7 ppm de cobre. Dado que la concentración de cobre en la etapa del proceso hidrometalúrgico estudiada (Decobrizado del lixiviado) parte de concentraciones al rededor a 500 mg/L y debe salir con concentraciones en torno a 200 mg/L se ha implementado una etapa adicional en el microsistema para realizar una dilución 1:100 de la muestra. El microsistema, completamente automatizado, permite analizar cobre en el rango de trabajo requerido.

Palabras clave—microanalizador modular, cobre (II), acondicionamiento, adaptaciones y decobrizado.

I. INTRODUCCIÓN

El control y optimización de los procesos metalúrgicos industriales requiere de un monitoreo continuo de los parámetros químicos considerados clave. El monitoreo del ion cobre (II) en diferentes etapas del proceso hidrometalúrgico del Zinc es de gran importancia para optimizar el proceso, maximizando la cantidad y pureza del zinc obtenido, minimizando los tiempos de operación y evitando contingencias medioambientales [1]. Para conseguir este objetivo se requiere que cada una de las etapas del proceso estén equipadas con sistemas de control capaces de suministrar la información necesaria. En este sentido, es necesario contar con una instrumentación analítica sencilla, autónoma, automática, miniaturizada, de bajo costo de fabricación y mantenimiento con un bajo consumo de reactivos y poca generación de residuos.

Las etapas iniciales del proceso hidrometalúrgico de obtención de Zinc exigen la reducción de la concentración del contenido de diferentes especies interferentes en el electrolito de proceso. Para su eliminación se requiere la medición continua y constante de la concentración del ion Cu (II) en el electrolito del proceso ya que esa información permite optimizar la adición de los reactivos secuestrantes, determinar los tiempos de residencia en los reactores y el funcionamiento de estos. Las técnicas por excelencia para la determinación rutinaria pero discreta de las concentraciones de ion Cu (II) están basadas en Espectroscopia Absorción Atómica (AAS) o Espectrometría de Masa Inducido con Plasma (ICP) [2] y Fluorescencia de Rayos X [1]. El presente trabajo tiene como objetivo el desarrollo de un prototipo de microanalizador químico de bajo costo de fabricación, operación y mantenimiento capaz de monitorizar, de forma automática, autónoma y continua, que proporcione la concentración del ion cobre (II) en un tiempo menor al requerido por el laboratorio analítico del área de decobrizado del proceso de purificación de Zinc que utiliza las técnicas convencionales.

La integración modular de los diferentes elementos del microanalizador hacen que el proceso de fabricación sea más sencillo y su funcionamiento más versátil. El modularidad permite adaptar con rapidez tanto las condiciones operacionales como las características analíticas del instrumento en función de la composición de la muestra durante el monitoreo en diferentes puntos de la planta.

Para las medidas de absorción molecular, la optoelectrónica actual permite el uso de componentes ópticos robustos y miniaturizados como un LED y un fotodetector. Para la construcción del microanalizador, el uso de tecnología de fabricación multicapa sobre sustrato polimérico, permite diseñar estructuras microfluídicas tridimensionales donde se integran las operaciones unitarias del procedimiento analítico (Modulo plataforma microfluídica). El módulo de multiconmutación del microanalizador, es el encargado de la preparación de las disoluciones estándar para la calibración, de introducir las muestras y su adaptación en función de las condiciones operacionales requeridas. Utiliza para ello actuadores de gestión de fluidos (microválvulas solenoides, bombas, etc.). El módulo de control electrónico desarrollado y su software asociado, basado en un Sistema Programable en Chip

(Programable System on Chip, PSoC), hace posible el control de los elementos actuadores, la adquisición y procesamiento de los datos generados; y la reconfiguración automática de los parámetros operacionales del microanalizador.

Como primer prototipo se diseñó y desarrolló un microanalizador automático para Cu (II) cuyas características operacionales estaban enfocadas en monitorizar el impacto ambiental del proceso de extracción de aguas ácidas en minas subterráneas de cobre [3] (MFIACu V1). Posteriormente, el microanalizador se reconfiguró para adaptarlo a la monitorización de cobre y otros metales (trabajo en la UAB) en la etapa de purificación del lixiviado en el proceso de hidrometalúrgico de obtención de Zinc.

II. METODOLOGÍA

La determinación del ion cobre (II) se realiza mediante detección colorimétrica. Todos los reactivos empleados para la adaptación del módulo químico en este trabajo fueron de grado analítico. El acetato de sodio ($C_2H_3NaO_2$), hidrócloruro de hidroxilamina ($NH_2OH \cdot HCl$), Sal disódica del ácido batocuproindisulfónico (Batocuproina disulfónico ácido (BCDS)), 2-Cloroacetamida ($ClCH_2CONH_2$), ácido nítrico (HNO_3) y la disolución stock de cobre para ICP se adquirieron de Sigma Aldrich. La solución stock de Cu (II) (7 mg/l); la disolución de reactivo que contiene búfer de acetato 0.1M, hidroxilamina, BCDS, y 2-Cloroacetamida (ajustado a pH 4); y la disolución de HNO_3 (0.1 M) se prepararon en agua MilliQ.

El módulo de microfluídica se construyó utilizando copolímero de olefina cíclica (COC)(TOPAS). El módulo de detección óptica miniaturizado está compuesto por un lector óptico compacto fabricado en polimetilmetacrilato (PMMA) (Ferplast), con alojamiento integrado para un LED de 470 nm (Roithner Lasertechnik B5B-433- B505), y un fotodiodo (Hamamatsu S1337-66BR). El módulo fluido se ensambló utilizando microválvulas solenoides de tres vías (NResearch 161T031), una bomba peristáltica (Ismatec), tubos de tygon (d.i 1.14 mm) y PTFE (d.i. 0.8 mm, Tecnyfluor). El módulo de dilución está constituido por una bomba jeringa NE500 (New Era Pump Systems), jeringa de plástico de 20ml (Plastipak BD), agitador magnético Microstirrer (VELP), bomba peristáltica NKP-DC-S10B (Kamoer) y un contenedor de polipropileno estéril inerte 50 ml (Protect).

El módulo de control electrónico se construyó sobre una placa de circuito impreso diseñada internamente y construida por Shenzhen JLC Electronics Ltd. El módulo de control electrónico es un chip PSoC 5 CY8C5868AXI-LP035 (Cypress Semiconductor). El módulo del software fue desarrollado utilizando el lenguaje de programación C+.

III. RESULTADOS

Los microanalizadores tienen una estructura base modular que estaría compuesta en todos los casos por los módulos de: electrónica, software, detección, microfluídica, pretratamiento de muestra y química. En la Tabla 1 podemos observar la lista de los módulos integrados en los prototipos de microanalizador para cobre instalado en la mina de Milpillas (MFIACu V1) así como el diseñado para la monitorización del proceso de decobrizado en la Planta de Zinc de Torreón (MFIACu V2).

El primero fue optimizado para la monitorización de cobre en efluentes de mina en el rango entre 0.5-10 ppm. El camino óptico de la celda de detección fue de 1 mm. El segundo de los microanalizadores toma como base el MFIACu V1 introduciendo las modificaciones necesarias para que se cubran las condiciones operativas requeridas en relación al rango de concentración de cobre y matriz de las muestras del proceso de purificación. Entre las adaptaciones introducidas destaca la integración de un nuevo módulo de dilución.

TABLA 1.- Descripción esquemática de los módulos que componen los microanalizadores para la determinación de Cobre

Módulos	MFIACu V1 (Efluentes Mina Milpillas)	MFIACu V2 (Obtención de Zinc, Decobrizado)
Electrónica	ES-MFIACu	ES-MFIACu
Software	SW-MFIACu	SW-MFIACu
Detección: Óptica	ODS-MFIACu ($\lambda = 500$ nm)	ODS-MFIACu ($\lambda = 470$ nm)
Microfluídica	MFLS-MFIACu	MFLS-MFIACu
Química	CHS-MFIACu	CHS-MFIACu
Pretratamiento muestra: Dilución*	No Aplica	DS-MFIACu
Rango Cu (mg/L)	0.5-10	200-500

*Nuevo módulo. Módulos con adaptación en color café y módulos con rediseño en color azul.

La aplicación del microanalizador MFIACu V1 en las nuevas condiciones operacionales y tipo de muestra implicó su adaptación al nuevo rango de concentraciones de cobre a analizar (200-500 mg/L). Para ello se modificó el procedimiento de calibración a partir de un único patrón y el procesamiento de la recta de calibración generada para la obtención, por interpolación, de la concentración de cobre en las muestras. Se incorpora también un módulo adicional conectado en línea con el microanalizador donde la muestra se diluye automáticamente (figura 1). El módulo de dilución incorpora diferentes válvulas solenoides, una bomba de jeringa y una cámara de mezcla. El control de todos los elementos de gestión fluidica del nuevo módulo de dilución, así como la adecuación del proceso de calibración hace necesaria la implementación de un nuevo módulo de software de control que incorpore las tareas adicionales introducidas.

Considerando la composición de la muestra de proceso a analizar se optó también por el rediseño del módulo químico. Se preparó una solución buffer 0.1M de Ácido Acético/Acetato (pH 4) que incorpora BCDS (1 mM) como reactivo colorimétrico, hidroxilamina (60 mM) y cloroacetamida (26 mM) para minimizar interferencias de otros metales y limitar el crecimiento microbiano en la disolución. Utilizando esta disolución de reactivo, la longitud de onda óptima de 470 nm, por lo que en el módulo de detección óptica sólo se sustituyó el LED de 500 nm utilizado en el MFIACu V1 por otro de 470 nm.

En lo relativo al módulo microfluídico, se cambió el diseño geométrico de los canales de entrada a la plataforma fluidica, se diseñó un mezclador con líneas rectas para evitar acumulación de la muestra y en la celda de detección se conserva el camino óptico de 1mm.

El módulo de dilución incorpora diferentes elementos (actuadores) importantes como la bomba jeringa y el sistema de mezclado. La bomba jeringa realiza la limpieza del sistema de mezclado, así como la dilución 1:100 de la muestra real para su posterior análisis. La limpieza del módulo entre muestras se realiza por triplicado con agua MilliQ que es introducida en el módulo por la bomba de jeringa mediante aspiración/dosificación utilizando válvulas solenoides. Para evacuar la muestra diluida y la disolución de lavado de la cámara de dilución se utiliza una bomba peristáltica. Este módulo es imprescindible para adecuar la concentración de la muestra al rango de trabajo del microanalizador.

La introducción del nuevo módulo de dilución conectado al módulo microfluídico obliga a una ligera modificación de las condiciones operacionales de este último. Se deben reducir tanto el tiempo del calibrado por multiconmutación y como el de muestreo por lo que el caudal del microsistema se fijó en 1400 μ L/min.

La figura 1a muestra el diagrama del sistema utilizado anteriormente; y las modificaciones operacionales introducidas y el resultado del rediseño de los módulos se presentan de manera gráfica en el diagrama de la figura 1b.

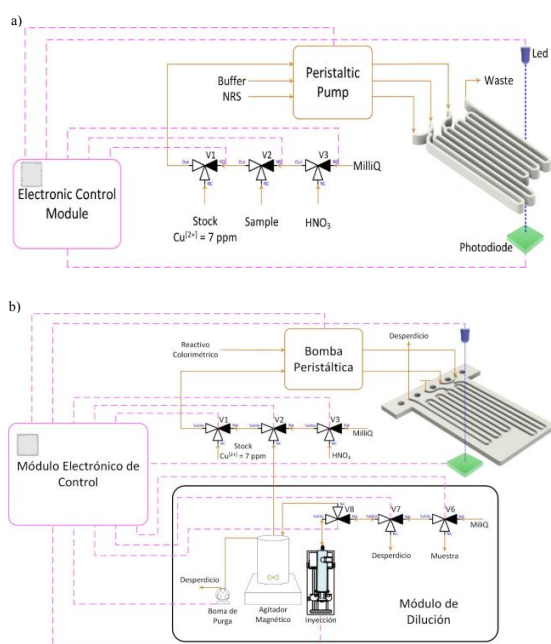


Fig. 1a Diagrama de sistema de microanalizador de cobre utilizado en Prototipo para efluente de agua de mina Milpillas.

Fig 1b. Diagrama de prototipo de microanalizador para área de decobrizado en planta de refinación de Zinc

Los datos experimentales obtenidos en las pruebas preliminares realizadas con el MFIACu2, optimizado para la monitorización de Cu (II) de la etapa de decobrizado del proceso de refinación hidrometalúrgica de Zn, se muestran en las figuras 2a y 2b.

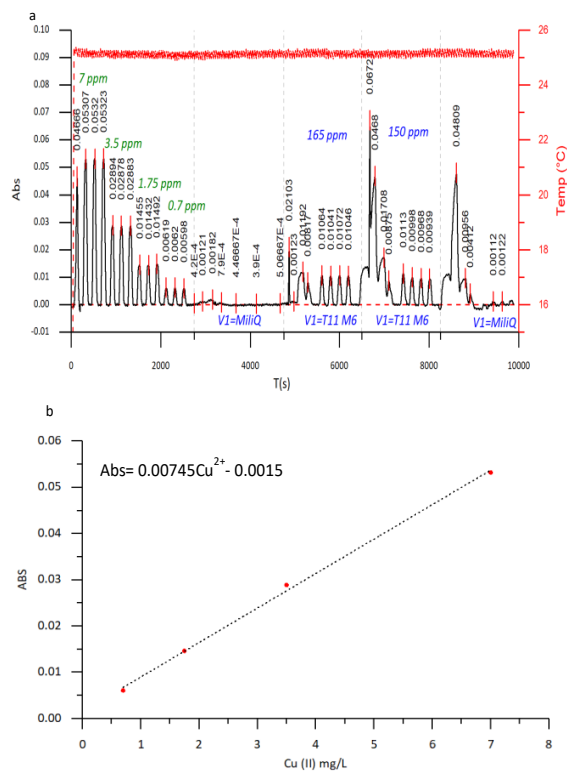



Fig 2a. Calibrado con solución estándar de Cu (II) a una concentración de 7 mg/L y muestreo en el laboratorio.

Fig 2b. Recta de la curva de calibración del microanalizador de cobre obteniendo la ecuación de la recta: $y = 0.00745x - 0.0015$ y una linealidad de $R^2 = 0.9983$

En la Figura 2a, se puede observar el calibrado por cuatro puntos realizado por multiconmutación, partiendo de una solución estándar de cobre (II) de 7mg/L. Así mismo cuatro inyecciones de dos muestras diferentes, provenientes del módulo de dilución. En la figura 2b muestra la recta de la curva de calibración realizada obtiene la ecuación de la recata como $Abs = 0.00745Cu^{2+} - 0.0015$

IV. CONCLUSIONES

El microsistema sistema analítico propuesto para la determinación de Cu (II) permite la monitorización continua de este parámetro de forma automática y autónoma a pie de proceso. Las modificaciones introducidas tanto en la configuración fluidica como en la detección o en la química con respecto al microanalizador MFIACu V1 permiten el muestreo, acondicionamiento y determinación automática del in Cu (II) en la etapa de decobrizado del proceso de obtención de zinc. De esta manera, el departamento de control y supervisión podrá obtener información del proceso con una mayor frecuencia que la conseguida con los análisis actuales de laboratorio. Esta información permitirá controlar tanto la dosificación de reactivos como los tiempos de residencia de la solución de lixiviación en los reactores durante el proceso de decobrizado.



El diseño y fabricación de microanalizadores utilizando una estrategia de integración modular de elementos permiten una fácil adecuación operacional de los dispositivos a las condiciones de cada proceso y/o aplicación en estudio. Dada la singularidad, tanto de los procesos a monitorizar como de la composición de las muestras implicadas, las tecnologías de fabricación elegidas permiten un prototipado rápido a bajo coste de pequeñas series de instrumentos versátiles, automáticos, autónomos y de reducido tamaño y consumo de reactivos y energía. Cabe mencionar que el prototipo de microanalizador aún se encuentra en la etapa de validación con muestras reales de proceso en condiciones de laboratorio. El paso siguiente será su instalación en la planta Zinc en Torreón de la empresa Peñoles

AGRADECIMIENTOS

Los autores agradecen el soporte financiero de Industrias Met-Mex Peñoles S.A. de C.V. y al Tecnológico Nacional de México.

REFERENCIAS

- [1] W.G. Davenport, M. King, M. Schlesinger, A.K. Biswas, "Extractive Metallurgy of Cooper", 4th ed.; Pergamon Press: Oxford, UK, 2002; ISBN 0444502068.
- [2] A. Manz, N. Graber, and H. M. Widmer, "Miniaturized total chemical analysis systems: A novel concept for chemical sensing," *Sensors Actuators B Chem.*, vol. 1, no. 1–6, pp. 244–248, Jan. 1990
- [3] K.V. Guevara, P. Couceiro, H. Coto, A. Calvo, N. Sández, H. Moreno, F. Valdés, J. Alonso, "Microanalyser Prototype for on-line Monitoring of copper (II) ion in mining industrial processes," *Sensors* 2019, 19, 3382; doi:10.3390/s191533.

Automatic microanalyzer for cadmium monitoring in the hydrometallurgical production of zinc

Antonio Calvo-López
Group of Sensors and Biosensors,
Universitat Autònoma de Barcelona,
Bellaterra, Spain
antonio.calvo@uab.cat

Mar Puyol Bosch
Group of Sensors and Biosensors,
Universitat Autònoma de Barcelona,
Bellaterra, Spain
mariadelmar.puyol@uab.cat

Rachid Haddouchi Serrano
Group of Sensors and Biosensors,
Universitat Autònoma de Barcelona,
Bellaterra, Spain
rachid.haddouchi@autonoma.cat

Francisco Valdés
División de Posgrado e Investigación
TecNM/ IT La Laguna
Torreón, Coah. México
fvaldesp@lalaguna.edu.mx

Mireia Serra Padullers
Group of Sensors and Biosensors,
Universitat Autònoma de Barcelona,
Bellaterra, Spain
mireia.serrapa@autonoma.cat

Julian Alonso-Chamarro
Group of Sensors and Biosensors,
Universitat Autònoma de Barcelona,
Bellaterra, Spain
julian.alonso@uab.es

Abstract— This work focuses on the design, optimization, and application of an automated continuous flow microanalyzer, integrating an ion exchange microcolumn, for the colorimetric monitoring of cadmium in hydrometallurgical processes to obtain zinc.

Keywords— cadmium, microsystem, hydrometallurgical Zn production, Flow Injection Analysis, ion exchange microcolumn

I. INTRODUCTION

Zinc is a nonferrous metal with interesting properties like excellent malleability, and abrasive and anti-corrosion resistance. For all these reasons, zinc has been widely employed in automotive, construction and shipping industries. However, zinc seldom exists in its elemental form in nature. It normally appears in combination with other metals such as copper, cadmium and lead in zinc ores. The production of zinc thus involves extraction of high-grade (99.995% purity) metallic zinc from these raw minerals using the zinc hydrometallurgical process. It is composed by different stages in which the monitoring at real time of the concentration of different metallic ions, usually present as impurities in the process solutions, is required. This analytical control allows optimizing the yield of the Zn hydrometallurgical process and the purity of the final product [1].

In this work, an automatic continuous-flow colorimetric analytical microsystem, integrating a separation step to maximize selectivity, has been designed and optimized to monitor the concentration of cadmium present in zinc hydrometallurgical plants during the process of purification.

II. EXPERIMENTAL

A. Colorimetric reaction

Cadion is one of the most common colorimetric reagents to determine cadmium. Cadmium ions react with the reagent to form a violet complex, which is dissolved in a micellar solution of nonionic surfactant Triton X-100. Triton X-100 helps to solubilize it, since otherwise Cadion and Cd^{2+} would not form any complex. The maximum absorbance of the complex formed occurs at 477nm. So that Cu^{2+} does not interfere with the analysis, potassium sodium tartrate is used as a masking agent.

B. Developed microanalyzer and experimental setup

Fig 1. shows the experimental setup used. The system includes a multicommutation equipment with 2 solenoid microvalves to automate the calibration and sample analysis,

an ion exchange microcolumn and a microfluidic platform which integrates mixing microstructures, and the detection cell for the colorimetric determination. Cadion was used as selective colorimetric reagent. The microcolumn fabricated with ceramic material using LTCC technology [2], was packed with an anion exchange resin (AG 1-X8, Bio-Rad), which is able to selectively retain Cd^{2+} and Cu^{2+} in the presence of iodide as $[\text{CdI}_4]^{2-}$ and $[\text{CuI}_4]^{2-}$. Thus, the other potentially interfering metals present at a very high concentration in sample solution like Zn^{2+} , are discarded. The interfering effect of copper was eliminated adding potassium sodium tartrate as masking agent in the citrate buffer.

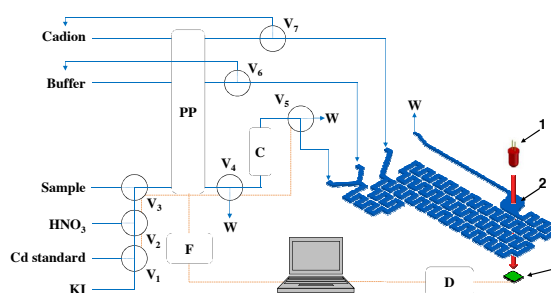


Fig. 1. Schematic diagram of the experimental setup where: V_n : 3-way microvalves; **PP**: Peristaltic pump; **C**: Ion exchange microcolumn; **F**: Flow controller unit (Flow test); **D**: Detector; **W**: Waste outlet; **1**: LED at 467 nm; **2**: Flow cell; **3**: Photodiode.

The microanalyzer was fabricated using Cyclic Olefin Copolymer (COC) as substrate as described elsewhere [3].

The microfluidic system was assembled using three-way solenoid microvalves (161T031, NResearch), a peristaltic pump (Minipuls 3, Gilson), and Tygon (i.d. 1.2 mm) and Teflon (i.d. 0.8 mm, Tecnyfluor) tubing. The automatic sequences of actuation were managed using a flow controller unit (Flow Test, Biotray).

The miniaturized and customized optical detection module was composed of a 467 nm LED (MP000438LED Multicomp Pro) and a photodiode (S1337-66BR Hamamatsu).

III. RESULTS AND DISCUSSION

A. Microanalyzer optimization

Table I shows the optimal values selected for each instrumental, hydrodynamic, and chemical variables evaluated.

TABLE I. DIFFERENT OPTIMIZED VARIABLES

Optimized parameter	Range evaluated	Optimum
Minimum multicommutation time (ms)	100 – 1000	500
Cation concentration (% volume)	0.001 – 0.02	0.012
Masking agent concentration (mM)	0 – 880	8.8
Injection volume (mL)	1.4 – 5.0	5.0
Flow rate ($\mu\text{L min}^{-1}$)	500 – 1500	550
Cleaning time between samples (s)	100 – 1200	200

B. Analytical features

One calibration curve is shown in Fig. 2 with $A = 4.96 \cdot 10^{-2} \pm 6 \cdot 10^{-4} [\text{Cd}^{2+}] + 4 \cdot 10^{-4} \pm 6 \cdot 10^{-4}$ with a r^2 of 0.9999. The working range was set from 0.09 to 2 mg L⁻¹ Cd²⁺ for this application. The LoD was 0.02 mg L⁻¹ Cd²⁺. The analysis time was less than 20 min including the retention and elution time inside the microcolumn, the colorimetric detection step and the cleaning time between samples. Nevertheless, by further optimization of the all the required steps, the analysis time per sample can be reduced to less than 10 minutes.

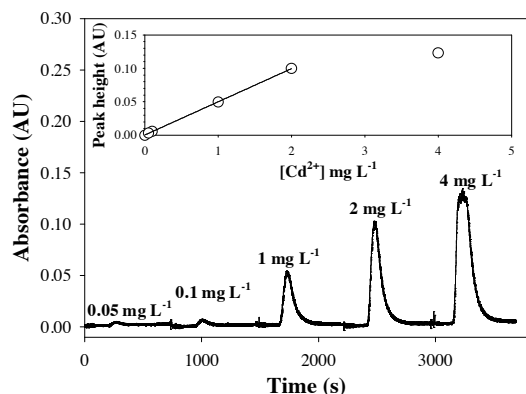


Fig. 2. Signal recording and calibration curve of cadmium.

C. Samples analysis

In this first evaluation stage, synthetic samples of Cd²⁺ with different concentrations of Cu²⁺ and Zn²⁺, which can be the main interfering metals due to reagent selectivity and high concentration issues respectively, were analyzed. The objective was to verify the proper function of the ion exchange microcolumn for cadmium separation and explore the limits of the masking agent for copper elimination. The expected concentrations of each metal in real samples depends on the stage of the process but, generally in the

cadmium removal stage they range between 0 - 2 mg L⁻¹ for Cd²⁺, 0 - 0.6 mg L⁻¹ for Cu²⁺ and up to 150 g L⁻¹ for Zn²⁺. Thus, all samples were prepared with 2 mg L⁻¹ Cd²⁺ and a combination of different concentrations of Cu²⁺ and Zn²⁺. Table II shows the results obtained. % recovery results for Cd²⁺ allow to state that it can be measured in the presence of copper as long as the sum of both metals is less than 5 mg L⁻¹. This is mainly due to the finite absorption capacity of the ion exchange column since the masking agent allow the selectively determination of Cd²⁺ in [Cu²⁺]/[Cd²⁺] ratios up to 100. However, since the expected concentration of Cd²⁺ and Cu²⁺ in samples at this stage of the Zn hydrometallurgical process is at most 2 and 0.6 mg L⁻¹ respectively, the microcolumn absorption capacity limitation will not be a problem. Regarding Zn²⁺ ion, it is not an interfering ion, even at high concentrations, because it is separated before the colorimetric determination. As many other metal ions different from cadmium and copper, zinc ion is not retained by the ion exchange resin.

TABLE II. Synthetic samples analysis

Sample	[Cd ²⁺] _{added} (mg L ⁻¹)	[Cu ²⁺] _{added} (mg L ⁻¹)	[Zn ²⁺] _{added} (mg L ⁻¹)	[Cd ²⁺] _{found} (mg L ⁻¹)	Cd ²⁺ % rec.
1	2	0	0	2.0	100
2	2	0.6	0	2.0	101
3	2	2.5	0	1.9	97
4	2	25	0	1.8	89
5	2	50	0	1.7	83
6	2	0	500	2.1	104
7	2	0.6	500	2.0	102

IV. CONCLUSIONS

A fully automated analytical microsystem, integrating an ion exchange microcolumn, has been developed to colorimetrically monitor the concentration of cadmium at different stages of the hydrometallurgical zinc refining process. The miniaturization of the analyzer simplifies its automation, allowing autonomous operation for the calibration and in situ analysis of samples. The analytical features demonstrate the potential to determine cadmium within the working range required in the presence of interfering ions such as copper and zinc, which can be present in the sample matrix. Further optimization will be carried out to reduce analysis time.

ACKNOWLEDGMENT

The authors would like to thank the financial support from Spanish Ministry of Science and Innovation through the project PID2020-117216RB-I00 and Catalan government through the project 2021SGR00124. The authors also acknowledge financial support from Met-Mex Peñoles S.A. de C.V. and the Tecnológico Nacional de México.

REFERENCES

- [1] C. Yang, B. Sun, Chapter 1 - "Introduction in Modelling Optimization and Control of Zinc Hydrometallurgical Purification Process", in: Academic Press, 2021: pp. 3–14.
- [2] N. Ibáñez-García, J. Alonso, C.S. Martínez-Cisneros, F. Valdés, "Green-tape ceramics. New technological approach for integrating electronics and fluidics in microsystems", *TrAC Trends Anal. Chem.* 27 (2008) 24–33.
- [3] O. Ymbert, N. Sáenz, A. Calvo-López, M. Puyol, J. Alonso-Chamarro, "Gas diffusion as a new fluidic unit operation for centrifugal microfluidic platforms", *Lab Chip.* 14 (2014).

Point-of-care analyser for potentiometric determination of ammonium ion in whole blood

Beatriz Rebollo-Calderón
Group of Sensors and Biosensors
(GSB), Universitat Autònoma de
Barcelona, Bellaterra, Spain
beatriz.rebollo@uab.cat

Rafael Artuch
Clinical Biochemistry Department,
Institut de Recerca de Sant Joan de
Déu (IRSJD), Barcelona, Spain
rafael.artuch@sjd.es

Antonio Calvo-López
Group of Sensors and Biosensors
(GSB), Universitat Autònoma de
Barcelona, Bellaterra, Spain
antonio.calvo@uab.cat

Javier Rosell-Ferrer
Research Centre for Biomedical
Engineering, Universitat Politècnica de
Catalunya, Barcelona, Spain
javier.rosell@upc.edu

Julian Alonso-Chamarro
Group of Sensors and Biosensors
(GSB), Universitat Autònoma de
Barcelona, Bellaterra, Spain
julian.alonso@uab.es

Aida Ormazábal
Clinical Biochemistry Department,
Institut de Recerca de Sant Joan de
Déu (IRSJD), Barcelona, Spain
aida.ormazabal@sjd.es

Mar Puyol Bosch
Group of Sensors and Biosensors
(GSB), Universitat Autònoma de
Barcelona, Bellaterra, Spain
mariadelmar.puyol@uab.cat

Abstract— In this work we present a novel automated point-of-care (POC) analyser for the potentiometric determination of ammonium ion in whole blood, composed by a detection, a fluid management, and a data acquisition and communication modules.

Keywords—ammonium, POC microsystem, whole blood, potentiometry

I. INTRODUCTION

High levels of NH_4^+ in blood constitute a condition known as hyperammonemia, which is the main pathological trait of some inborn errors of metabolism (IEM). They are characterized by the impairment of the ammonium elimination due to the mutation of some enzymes [1]. Consequently, NH_4^+ increases over the healthy levels, which reach up to $50 \mu\text{mol L}^{-1}$ in adults and children and up to $100 \mu\text{mol L}^{-1}$ in newborns. Concentrations higher than $200 \mu\text{mol L}^{-1}$ constitute severe hyperammonemic states which may lead to poor neurological outcomes and permanent brain damage [2]. Even higher concentrations are related to hyperammonemic coma and death. Besides IEM, there are other non-congenital conditions that may cause hyperammonemia, either due to a decreased detoxification as in cirrhosis and hepatic failure, or due to an increased production of the molecule as in the use of some drugs or in bacterial overgrowth [3,4]. In order to avoid severe affectations to the neurological system it is imperative to detect and treat hyperammonemic episodes in a reliable and fast manner.

Nowadays, sophisticated, expensive and large equipment is used for the analysis of blood NH_4^+ in reference hospitals, based on enzymatic spectrophotometric analytical methods [5]. They require expert personal to obtain plasma, as whole blood is not a suitable sample, and this procedure takes at least 15 minutes. In addition, NH_4^+ quickly increases in blood samples. For all these reasons, more portable equipment that allows the analysis of whole blood is required to permit its implementation at the bedside of the patients for point-of-care (POC) analysis.

This work focuses on the design, optimization, and validation of a fully automated continuous flow analyser, composed by a detection module, a fluid management

module and a data acquisition and communication module. The POC system was installed in the laboratory of the Hospital Sant Joan de Déu (HSJD, Esplugues de Llobregat) for its validation under continuous use for a period of two months, analyzing 283 blood samples in parallel with the reference method.

II. EXPERIMENTAL

A. POC design

The analytical system is composed by three different modules (Fig. 1): fluid management, detection, and data acquisition and communication.

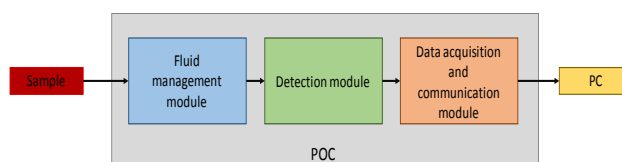


Fig. 1. Schematic representation of the three modules that constitute the POC analytical system.

The detection module consists of three different microfluidic modular units: 1) a micromixer where the samples mixes with NaOH solution to transform NH_4^+ into volatile NH_3 , 2) a gas-diffusion unit that contains a PVDF and protective membranes and 3) the sensing unit that contains the NH_4^+ ISE and a screen-printed Ag/AgCl electrode. All of them were fabricated using Cyclic Olefin Copolymer (COC) as substrate as described elsewhere [6].

The fluid management module contains all the elements that are responsible for fluid handling, such as pump, microvalves and software that controls these elements.

The data acquisition and communication module is composed by the potentiometer and the software that transfers the data via Bluetooth and that processes this data and displays the result on the display.

Experimental setup is shown in Fig. 2.

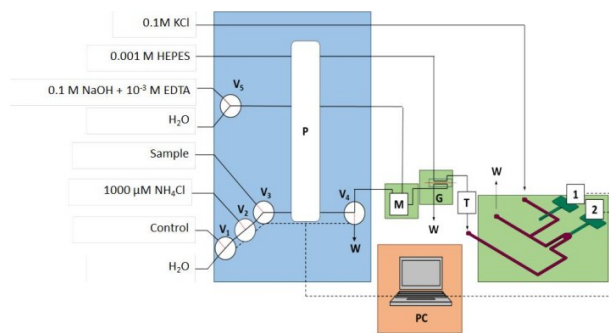


Fig. 2 Schematic representation of the automated experimental setup, with the fluid management module (blue), detection module (green) and the data acquisition and communication module (orange). 1) reference electrode, 2) indicator electrode, T) bubble trap, V) 3-way injection valve, P) peristaltic pump, M) micromixer, G) gas-diffusion unit, PC) computer, W) waste.

III. RESULTS AND DISCUSSION

A. System optimization

The hydrodynamic parameters used for this POC system was a flow rate of $650 \mu\text{L min}^{-1}$ and a time of injection of 20 s, which corresponds to an injection volume of $215 \mu\text{L}$.

The configuration of the gas-diffusion unit was optimized in order to extend the lifetime of the hydrophobic gas-diffusion membrane. With this same objective, a protective hydrophilic membrane of polycarbonate was introduced to prevent the damage of the gas-diffusion membrane due to red and white blood cells, platelets and lipophilic compounds present in blood.

The analytical system was designed in order to be able to carry out all the necessary steps for a complete analytical process in an automated manner; the personal is only needed in order to place and retire the sample tube and the cleaning solution. For this reason the required electronics and software were design and fabricated and different fluidic sequences were programmed.

B. Analytical features of the POC system

One calibration curve obtained with the proposed analyser is shown (Fig. 3) with $E = 57.8 \cdot \log [\text{NH}_4^+] + 273$, obtained by a single analysis of two concentrations, $50 \mu\text{M}$ and $100 \mu\text{M}$. This calibration curve is later corrected using the analysis of the same control solution of the reference method, generating a new calibration curve of the same slope but different Y-intercept: $E = 57.8 \cdot \log [\text{NH}_4^+] + 267$.

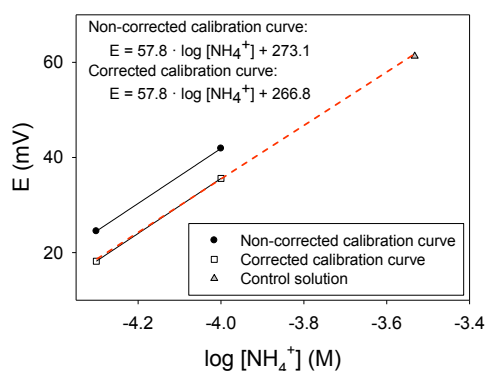


Fig. 3. Non-corrected (black) and corrected (white) calibration curve obtained with the POC system using NH_4^+ standard solutions of $50 \mu\text{M}$ and $100 \mu\text{M}$ obtained by multicommutation dilution. The analysis of the control solution appears as grey triangle.

The corresponding limit of detection (LD) for this corrected calibration curve was $24 \mu\text{M}$.

The repeatability was evaluated by 8 consecutive analysis of a blood sample and 10 consecutive analysis of the control solution, obtaining RSD values of 5 % and 3 %, respectively.

C. Validation with blood samples

The developed POC system was installed in the laboratory of the HSJD for a two-month evaluation under continuous use. During this period 238 blood samples were analysed in parallel with the developed potentiometric system and the reference method consisted of an automated spectrophotometric procedure carried out by an Architect ci8200 automated analyser (ABBOT, Park, Illinois, EEUU). The POC system provided very good results without significant differences with the reference method as it can be seen in Fig. 4 were the passing-bablok regression obtained was $E = 1 \cdot \log(\text{NH}_4^+) + 2$ and the interval of confidence (95% confidence) was -0.9 to $+1.0$ for the slope and -5 to $+6$ for the Y-intercept. Additionally, the agreement of both analytical methods is also supported by the paired t-test ($t_{\text{calc}} = 1.87$; $t_{\text{tab}} = 1.98$; $t_{\text{calc}} < t_{\text{tab}}$).

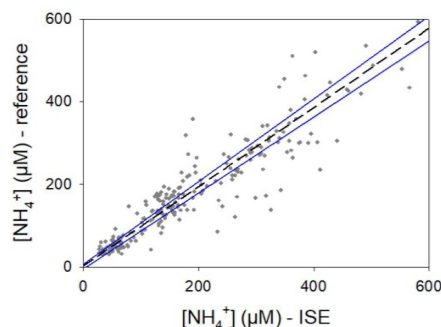


Fig. 4. Passing-Bablok regression (dashed line) with the IC (95%) indicated in blue. $N = 238$.

IV. CONCLUSIONS


A novel automated point-of-care (POC) analyser for the potentiometric determination of ammonium ion in whole blood has been designed, manufactured, optimized and validated using real blood samples. Results show a good correlation between the developed potentiometric analytical system and the reference method currently used by the HSJD. Therefore, this POC system constitutes a promising candidate for the determination of healthy and pathological levels of NH_4^+ in blood samples aimed at the monitoring of diseases characterized by hyperammonemia episodes.

ACKNOWLEDGMENT

This work was supported by the Institute of Health Carlos III (DTS18/00104 and DTS18/00075), the Spanish Ministry of Science and Innovation (MINECO-FEDER CTQ2017-85011-R, PID2020-117216RB and PDC2021-121558-100), and the Catalan government (2021SGR00124).

REFERENCES

- [1] E. Maines, G. Piccoli, A. Pascarella, F. Colucci, A.B. Burlina, "Inherited hyperammonemias: a Contemporary view on pathogenesis and diagnosis", *Expert Opin. Orphan Drugs*. 6 (2018) 105–116.
- [2] R. Raina, J.K. Bedoyan, U. Lichter-Konecki, P. Jouvett, S. Picca, N.A. Mew, M.C. Machado, R. Chakraborty, M. Vemuganti, M.K. Grewal, T. Bunchman, S.K. Sethi, V. Krishnappa, M. McCulloch, K. Alhasan, A. Bagga, R.K. Basu, F. Schaefer, G.

- 
- Filler, B.A. Warady, "Consensus guidelines for management of hyperammonaemia in paediatric patients receiving continuous kidney replacement therapy", *Nat. Rev. Nephrol.* 16 (2020) 471–482.
- [3] J. Häberle, "Clinical and biochemical aspects of primary and secondary hyperammonemic disorders", *Arch. Biochem. Biophys.* 536 (2013).
- [4] M. Tchan, "Hyperammonemia and lactic acidosis in adults: Differential diagnoses with a focus on inborn errors of metabolism", *Rev. Endocr. Metab. Disord.* 19 (2018) 69–79.
- [5] R. Goggs, S. Serrano, B. Szladovits, I. Keir, R. Ong, D. Hughes, "Clinical investigation of a point-of-care blood ammonia analyzer", *Vet. Clin. Pathol.* 37 (2008) 198–206.
- [6] O. Ymbern, N. Sández, A. Calvo-López, M. Puyol, J. Alonso-Chamarro, "Gas diffusion as a new fluidic unit operation for centrifugal microfluidic platforms", *Lab Chip.* 14 (2014).

Analytical microsystem with pervaporation stage for ammonium monitoring in industrial wastewater

Antonio Calvo-López
Group of Sensors and Biosensors,
Universitat Autònoma de Barcelona,
Bellaterra, Spain
antonio.calvo@uab.cat

Anna Martín Alcario
Group of Sensors and Biosensors,
Universitat Autònoma de Barcelona,
Bellaterra, Spain
anna.martinal@autonoma.cat

Mar Puyol Bosch
Group of Sensors and Biosensors,
Universitat Autònoma de Barcelona,
Bellaterra, Spain
mariadelmar.puyol@uab.cat

Julian Alonso-Chamarro
Group of Sensors and Biosensors,
Universitat Autònoma de Barcelona,
Bellaterra, Spain
julian.alonso@uab.es

Abstract— This work focuses on the design, optimization, and application of a continuous flow miniaturized analytical device with potentiometric detection integrating a pervaporation stage for the analysis of ammonium in real industrial wastewater samples.

Keywords—pervaporation, ammonium, microsystem, Flow Injection Analysis

I. INTRODUCTION

It is important to protect surface water quality as it affects natural aquatic ecosystems as well as the potential use of water for human consumption and in industrial applications. To follow government regulations, different water quality indicators must be determined and monitored. One of these is ammonium ion. Its presence at higher concentrations than the natural level is an important indicator of faecal pollution. Ammonia can enter the aquatic environment through direct means such as municipal and industrial wastewater, and indirect means such as nitrogen fixation, air deposition, and runoff from agricultural lands. A minimum concentration of $0.5 \text{ mg L}^{-1} \text{ NH}_4^+$ is established for drinking water because taste and odor problems as well as a decrease in the disinfection efficiency during the potabilization process will be expected if treated water contains concentrations higher than this level. In industrial wastewaters, concentration levels between 10 and $6000 \text{ mg L}^{-1} \text{ NH}_4^+$ can be found [1].

There are commercial analytical systems based on potentiometric ammonia sensors that can monitor ammonium with high selectivity thanks to the use of gas-diffusion membranes and the strategy of converting ammonium into ammonia gas through basification. This allows only ammonia to pass through this gas-diffusion membrane, thus preventing the rest of the sample matrix from reaching the potentiometric sensor. However, the complex matrix of wastewater can block the pores of the diffusion membrane, shortening the lifetime of analytical systems that use this strategy.

This work focuses on the design, optimization, and application of a modular analytical potentiometric device that integrates a pervaporation module to the analysis of ammonium in real wastewater samples. In this way, contact of the sample matrix with the diffusion membrane is avoided, improving analytical microsystem lifetime.

II. EXPERIMENTAL

A. Pervaporation as sample pretreatment strategy

Pervaporation is a separation method that involves the liquid-vapor phase change of the analyte. This technique is based on using a module that contains a donor channel, an air gap chamber and an acceptor channel (Fig.1). A gaseous diffusion membrane will be placed between the air gap chamber and the acceptor channel that will only allow gas to pass through. The pervaporation procedure consists of 4 main steps which are: 1) the ammonium conversion to ammonia gas inside the donor channel, 2) its (transfer) diffusion to the air gap chamber, 3) its diffusion through the gas-diffusion membrane and finally its conversion again to ammonium ion inside the acceptor channel.

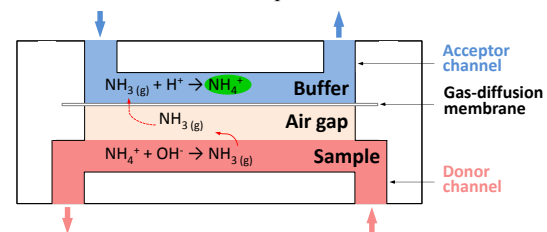


Fig. 1. Schematic representation of a pervaporation module.

B. Developed microanalyzer and experimental setup

Fig 2. show the experimental setup used. The analytical microsystem developed is formed by three modules: micromixing, pervaporation and detection. All of them were fabricated using Cyclic Olefin Copolymer (COC) as substrate as described elsewhere [2].

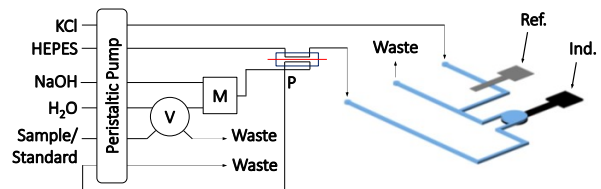


Fig. 2 Schematic diagram of the experimental setup where: V) six-way injection valve; M) micromixer; P) pervaporation module; Ref) reference electrode; Ind) indicator electrode.

The indicator and reference electrodes, an ammonium all-solid-state selective electrode based on nonactin ionophore and a screen-printed Ag/AgCl electrode, respectively, were integrated in the detection module.

III. RESULTS AND DISCUSSION

A. Microanalyzer optimization

The configuration of the pervaporation module was optimized considering different structural parameters. Subsequently, the flow rate and injection volume were also optimized. Table I summarize all the optimum options selected.

TABLE I. DIFFERENT OPTIMIZED VARIABLES

Optimized parameter	Range evaluated	Optimum
Channels shape	Linear, meander, spiral	Linear
Wettability modification of the donor channel	Surfactant use in solutions or cellulose as channel bed	Cellulose
Air chamber height (mm)	0.4 – 1.2	0.8
Injection volume (μL)	225 – 1000	750
Flow rate ($\mu\text{L min}^{-1}$)	200 – 600	400

To verify that each variable studied allow maintaining a balance between the donor channel and the air chamber without the channel liquid flooding it, a fluorescein solution was used to inspect the process. Fig 3 show the appearance of the optimized pervaporation module working correctly, visualizing how each solution flows through each channel without overflowing, keeping the air gap chamber empty.

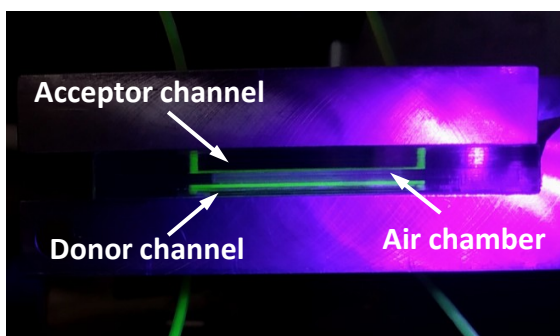


Fig. 3. Image of the pervaporation module working properly using fluorescein and UV light to visualize the liquids inside the microchannels.

B. Analytical features

One calibration curve obtained with the proposed microanalyzer is shown (Fig. 4) with $E(\text{mV}) = 59 \pm 1 \log[\text{NH}_4^+] + 300 \pm 3$; $r^2 = 0.9996$. The working range was set from 0.5 to 100 mg L^{-1} NH_4^+ for this application, although the sensor can measure up to 1000 mg L^{-1} NH_4^+ . The LoD was 0.1 mg L^{-1} NH_4^+ and the analysis time was 8 min

Repeatability studies were carried out through 10 consecutive injections of 3 standard solutions of 0.5, 10 and 100 mg L^{-1} NH_4^+ . RSD lower than 4 % were found.

Reproducibility was also evaluated throughout more than 2 months with different calibrations obtaining RSD values lower than 5% for the slope and the y-intercept.

C. Samples analysis

Spiked real wastewater samples with biomass provided by Evonik Industries company (Granollers, Spain) were

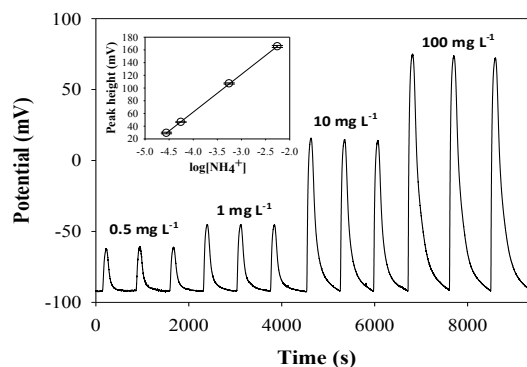


Fig. 4. Signal recording and calibration curve of ammonium per triplicate.

analyzed in triplicate. Table II show the results obtained. The recovery percentages were between 71 and 106 %.

TABLE II. REAL SAMPLES ANALYSIS

Sample	$[\text{NH}_4^+]_{\text{theoretical}}$ (mg L^{-1})	$[\text{NH}_4^+]_{\text{obtained}}$ (mg L^{-1})	% rec.
1	0.5	0.53 ± 0.04	105
2	1	1.0 ± 0.2	101
3	10	10 ± 2	102
4	6	4.3 ± 0.7	71
5	10	9.4 ± 0.8	94
6	15	15 ± 1	103
7	1	0.94 ± 0.07	94
8	2	2.1 ± 0.1	106
9	5	5 ± 2	98

IV. CONCLUSIONS

A pervaporation module has been designed, manufactured, optimized and characterized for its use in an analytical microsystem to monitor ammonium in wastewaters with a highly complex matrix. Once the pervaporation module is integrated with the mixing and detection modules, the analytical response features obtained are excellent for the proposed application. This statement is confirmed by the good results obtained from the analysis of spiked real samples.

ACKNOWLEDGMENT

The authors would like to thank the financial support from Spanish Ministry of Science and Innovation through the project PID2020-117216RB-I00 and Catalan government through the project 2021SGR00124.

REFERENCES

- [1] International Organization for Standardization. Water quality—Determination of ammonium. Geneva, 1986 (ISO5664:1984; ISO6778:1984; ISO7150-1:1984; ISO7150-2:1986).
- [2] O. Ymbern, N. Sández, A. Calvo-López, M. Puyol, J. Alonso-Chamarro, "Gas diffusion as a new fluidic unit operation for centrifugal microfluidic platforms", Lab Chip. 14 (2014).

“Controlled insertion of silver nanoparticles in LbL nanostructures: fine-tuning the sensing units of an impedimetric e-tongue”

Maria Helena Gonçalves
Gleb Wataghin Institute of Physics
State University of Campinas
Campinas, São Paulo 13083-970, Brazil
maria.hg@ifi.unicamp.br

Italo O. Mazali
Institute of Chemistry
University of Campinas
Campinas 13083-970, Brazil
mazali@unicamp.br

Maria Luisa Braunger
Centre for Education
Research and Innovation in Energy
Environment (CERI EE)
Douai 59508, France
malubraunger@yahoo.com.br

A. Riul Jr
Gleb Wataghin Institute of Physics
State University of Campinas
Campinas, São Paulo 13083-970, Brazil
riul@unicamp.br

Anerise de Barros
Institute of Chemistry
University of Campinas
Campinas 13083-970, Brazil
anerisedebarros@gmail.com

V. Rodrigues
Gleb Wataghin Institute of Physics
State University of Campinas
Campinas, São Paulo 13083-970,
Brazil varlei@ifi.unicamp.br

Abstract— Silver nanoparticles (AgNPs) are utilized to enhance device sensitivity by integrating them into polymers or carbon-based materials, creating nanocomposites with synergistic properties for detecting environmental changes. This study investigates the adsorption kinetics of AgNPs in multilayered layer-by-layer (LbL) structures, focusing on the impact of AgNPs concentration on film formation and their use as sensing units in an impedimetric microfluidic e-tongue. Adsorption kinetic studies are crucial for optimizing AgNPs adsorption and distribution within LbL structures, influencing future applications. By systematically varying the AgNP concentration in identical LbL architectures, we demonstrate their effectiveness in distinguishing food enhancers having umami taste profiles. Our microfluidic approach consistently achieves robust sample separation, highlighting the importance of precise parameter control for enhanced sensor performance across diverse analytical applications.

Keywords— e-tongue; metal nanoparticles; layer-by-layer films; impedance measurements; microfluidics; multisensor array

I. INTRODUCTION

Nanoparticles (NPs) hold significant promise in addressing diverse societal needs, particularly in the realm of developments analyzing complex liquids, environmental monitoring [1,2], precision agriculture [3–5], and disease detection [6]. Their usage stems from effects exhibited by localized surface plasmon resonance (LSPR) [7], surface-enhanced Raman spectroscopy (SERS) [8], electron transduction [9], and catalytic activity [10,11], which find application in diverse fields such as early cancer detection [12–14] and electronic tongues (e-tongues) [15–19]. E-tongues comprise an array of non-selective sensing units that collectively respond to various components, effectively generating a fingerprint of the analyzed sample [20]. They have proven successful in identifying and discriminating basic tastes [21–23], assessing beverages [24,25], wines [26,27], milk [28,29], coffees [30,31], beers, among others. These devices are particularly interesting in scenarios where human assessment is impractical, such as continuous monitoring of industrial processes and analysis of hazardous or unpleasant samples, including drugs, viruses, bacteria, toxins, and pollutants.

The layer-by-layer (LbL) assembly is particularly interesting for nanoscience as they share the same interacting forces and length scales, enabling a controlled formation of molecular

assemblies in distinct molecular architectures, with molecular level thickness control. It has already been exploited in impedimetric e-tongues with the LbL deposition of films having distinct electrical characteristics onto interdigitated electrodes (IDE). In summary, the electric response of the sensing units is influenced by the analytes where they are immersed, which can be easily detected in impedance measurements. Hensel et al. [58] employed a distinct approach by integrating physically synthesized AgNPs as sensing units in another impedimetric e-tongue setup, successfully distinguishing basic tastes and food enhancers having an umami taste profile. Our methodology shares similarities with the approach proposed by Hensel et al., for comparison purposes as their AgNPs are synthesized in the gas phase, with precise control over size and deposition onto a polymeric matrix. Here, we investigated the adsorption kinetics of chemically synthesized AgNPs, and their insertion in a polymeric matrix via the LbL assembly by controlling the NPs concentration and spatial distribution in the nanocomposites formed. We systematically studied the time required to optimize the adsorption of AgNPs in LbL assemblies, enabling the fabrication of distinct sensing units using the same polymer matrix. The LbL films are deposited onto electrodes linearly displayed in a microfluidic channel, with dynamic data acquisition as the liquids pass through the sensing units. We easily distinguished basic tastes and samples having an umami taste. With that, we emphasize the critical importance of fine-tuning the fabrication parameters of nanostructures applied as sensing units in sensor applications.

II. MATERIALS AND METHODS

A. Chemical synthesis of silver nanoparticles

AgNPs are chemically synthesized following the method outlined by Lee and Meisel [60]. In brief, 9 mg of silver nitrate (AgNO_3) is dissolved in 50 mL of ultrapure water with stirring and simultaneously heated to boiling on a hot plate. Upon reaching boiling point, 5 mL of 1% sodium citrate ($\text{Na}_3\text{C}_6\text{H}_5\text{O}_7$) is introduced into the solution. It is noteworthy that sodium citrate serves as both a reduction and stabilizing agent [60]. Following the addition of sodium citrate (initially colorless), the solution gradually transitions from yellow to green-ochre, indicating the formation of silver nanoparticles. Subsequently, the solution is stirred for 20 minutes before being allowed to cool to room temperature.

B. Layer-by-layer technique and deposition parameters

The LbL technique allows the spontaneous adsorption of molecules with precise thickness control during the film assembly. Here, poly(allylamine hydrochloride) (PAH) is the positive polyelectrolyte, while poly(sodium 4styrenesulfonate) (PSS) and AgNPs are the negative polyelectrolytes. Initially, a drop of PAH solution is applied onto the electrode surface for 8 minutes, followed by removal using a syringe and thoroughly washed with ultrapure water to eliminate loosely bound material. The surface is then dried for 10 minutes and the process is repeated for the opposite polyelectrolyte. This cycle is repeated until the desired number of deposited bilayers; (PAH/PSS)₁₅ denotes an LbL film composed of 15 deposited bilayers. Our sensor array comprises: i) a bare interdigitated electrode (IDE1), ii) an IDE covered with (PAH/PSS)₁₅ bilayers (IDE2), iii) an IDE covered with (PAH/PSS)₁₅ followed 100 by (PAH/AgNPs)₁₅ (IDE3), and iv) an IDE similar to IDE3 but with AgNPs ten times more concentrated, resulting in (IDE4).

C. Zeta potential

The surface charge characteristics from the AgNPs are assessed through the Zeta potential measurement, indicative of the electrical charge present within the nanoparticle's surrounding bilayer. It is conducted utilizing a Malvern ZSZe 3600 particle-size zeta Potential Analyzer. The AgNPs solution is appropriately diluted at a 1:200 ratio in DI water, and subsequently loaded into capillary cells featuring gold electrodes for examination. Measurements are performed in triplicate, and the acquired data are processed using the Zetasizer Software program (Malvern, UK).

D. Adsorption kinetics

The LbL adsorption kinetics of materials onto a solid substrate [62,63] is a crucial step, not always carried out, establishing the optimal adsorption time of the electrolytes on a substrate to achieve a uniform LbL coating. Briefly, AgNPs can electrostatically interact with an oppositely charged material (PAH). By keeping a fixed immersion time in PAH at 8 min, the adsorption kinetics can be obtained for varying immersion times in the AgNPs solution, as described elsewhere. After each immersion, the quartz plates are allowed to air dry for 15 minutes, resulting in a multilayered LbL structure. UV-Vis absorption spectroscopy is employed at each deposition step, confirming the material adsorption by the characteristic AgNP absorption band at 420 nm.

E. Microfluidic e-tongue setup

Briefly, as described in a previous publication, the microfluidic e-tongue setup consists of four IDEs linearly arranged on a gold-plated printed circuit board. Positioned along a single microchannel, these IDEs facilitate the propulsion of the analyte using a syringe pump. The integration and automation of this e-tongue device streamline data acquisition, reducing potential errors associated with manual operations and minimizing user contact with the analyte during data collection. A multiplexer switches data acquisition between IDEs during measurements performed in triplicate for statistical validation. Impedance data is acquired in a Solartron 1260A impedance analyzer within 1Hz - 10 MHz frequency, with an AC signal set at 25 mV, and a flow rate of 15 mL/h inside the microchannel. Following triplicate acquisitions for each analyte, the microchannel and IDEs are thoroughly washed with 10 mL of deionized water at moderate flow. This cleansing process not only maintains measurement integrity but also assesses any variations in

sensor impedance post-analyte interaction, thereby mitigating cross-contamination between samples.

F. Data analysis

The impedance data obtained from the e-tongue are analyzed by Principal Component Analysis (PCA), a statistical method that facilitates the identification of patterns and structures in raw data, unveiling relationships between variables and offering valuable insights for sample differentiation. In the context of e-tongue data, the PCA score plot typically shows clusters grouping similar samples. The k-means method is employed to determine these clusters, with their quality assessed by the silhouette coefficient (SC). Introduced by Kaufman and Rousseeuw, the silhouette coefficient serves as a quality index for clustering. SC values ranging from 1.00 to 0.71 indicate a very robust cluster structure, SC between 0.70 to 0.51 reflects a reasonably well-structured cluster, SC between 0.50 to 0.26 indicates a weak cluster structure, and SC \leq 0.25 suggests no discernible cluster structures. We use the open-source software Orange for data analysis and visualization.

III. RESULTS AND DISCUSSION

A. Synthesis of NPs

AgNPs exhibit a distinctive characteristic: the presence of a light extinction peak within 400 – 670 nm wavelength range. This peak arises from the plasmonic collective oscillation of electrons in phase with the incident radiation. Noble elements such as silver demonstrate d-d transition bands that lead to a shift in the plasmonic frequency to the visible part of the spectrum, giving a specific color to the NPs. The Lee and Meisel synthesis employing sodium citrate reduction typically yields nanoparticles with diameters ranging from 50 nm to 100 nm, featuring an absorption peak at 420 nm [70] that is observed in the UV-Vis absorption spectroscopy measurements, as shown in Figure 1a). In our case, the cohesion between layers in the LbL deposition is primarily driven by electrostatic forces. As we want to intercalate AgNPs layer with PAH, we have to be careful as the cationic or anionic behavior can be influenced by the pH. In our study, pH is fixed to 6.8 in the as-prepared AgNP solution. It is noteworthy to mention that altering the pH of the AgNPs solution resulted in the degradation of the AgNPs. At pH 6.8 the Zeta potential is - 24.56 mV, a specific condition selected to optimize the AgNPs stability, thus facilitating their intercalation in the LbL films. *B. Silver NP adsorption kinetics*

The UV-Vis absorption spectra following the deposition of each layer of AgNPs are depicted in Figure 2a), with an observed slight increase in the absorbance maximum between 400 and 500 nm after the deposition. Notably, a more pronounced peak appears at 486 nm, indicating a shift compared to the colloidal spectrum, which may be attributed to the agglomeration of AgNPs on the film surface, a phenomenon also observed in the TEM analysis (see Figure 1b). Figure 2b) presents the absorbance at 420 nm for each deposited bilayer as a function of the immersion time in the AgNPs solution. A change in the adsorption regime is observed at ~ 940 s (~ 15 min.) of immersion, indicating the optimal time for forming an AgNP monolayer on the quartz plate. In Figure 2c) we can clearly see the LbL absorbance for a 15 min. immersion, with the absorbance at 420 nm exhibiting a linear increase at each deposited bilayer. It

indicates that the same amount of material is deposited on the surface at each deposition step during the LbL assembly .

C. E-tongue characterization

The e-tongue applied to discern basic flavors yields a SC = 0.96, stating a robust cluster structure and excellent discrimination among different tastants. The high SC value suggests a successful differentiation between the basic flavors with a high degree of confidence. Furthermore, there are no signs of cross-contamination and the sensor also displayed no change in performance after a year of usage. The sensor ability to maintain consistent performance over a year without any special care demonstrates its reliability and durability. This is essential for practical applications where sensors may be deployed for extended periods without frequent maintenance or calibration. Figure 3a) illustrates the score plot of PC1 vs. PC2, capturing a total variance of 96.5%, with PC1 carrying 91.2% of the information and PC2 describing 5.3%. The e-tongue exhibits excellent performance in distinguishing samples having the umami flavor, achieving a robust SC of 0.96. Comparing this SC value with that obtained by Hensel et al. [that used physically synthesized Ag nanoparticles, demonstrates that this setup outperforms theirs in discriminating umami flavors. PC1 may visually suggest inadequate separation of the last five analytes; however, the projection of the data on PC1 facilitates the discrimination between L-glutamic acid and a commercially acquired food enhancer, while PC2 enables a complete discrimination of the latter. It's important to note that the SC is calculated based on the number of principal components (PCs) used in the PCA to reconstruct the original data. To further discriminate among the six food enhancers, we can also explore the score plot of PC2 vs. PC3, shown in Figure 3b). It clearly distinguishes between different samples, providing additional insight into the discrimination capabilities of the e-tongue. Our e-tongue is formed by sensing units varying the density of chemically synthesized AgNPs within LbL layers, and the e-tongues detailed by Mercante et al and Hensel et al are the closest to compare. The former employs AuNPs stabilized with PAH in layered LbL films, albeit without adjusting NP density as we have made. Additionally, their application focused on a distinct analyte, milk. In contrast, Hensel et al modulated LbL films by varying the AgNPs density, conducted umami measurements, and utilized SC analysis, facilitating a more pragmatic comparison.

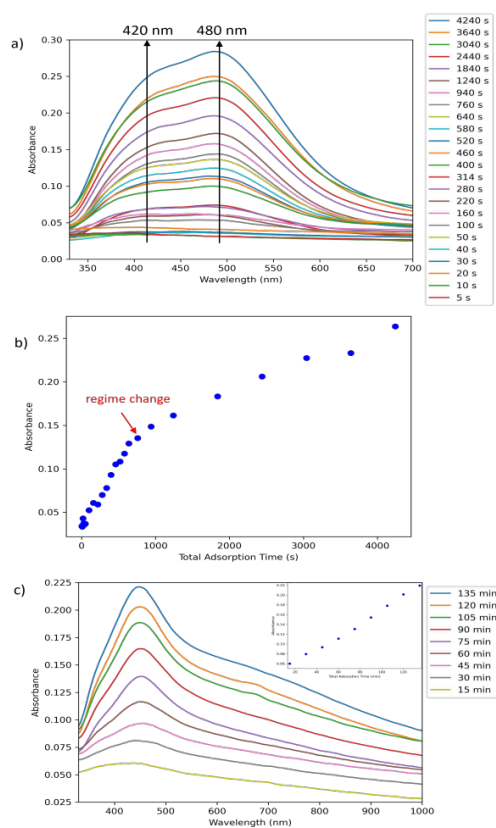


Figure 1. (a) UV-Vis absorption spectrum of AgNPs after the absorption of each layer on quartz slides. The two arrows indicate the growth of peaks at 420 and 486 nm. (b) NP absorbance at a wavelength of 420 nm, as a function of the total adsorption time for each bilayer. (c) Absorbance for a deposition using a 15 min. immersion time in the AgNPs solution.

Our device and Hensel's easily detect and distinguish food enhancers using a microfluidic e-tongue setup. Therefore, our current approach indicates a long-term usage of an e-tongue setup, and the LbL assembly expands compositional possibilities to form the sensing units. Concerning works found in the literature proposing the detection of umami, the comparison with our results is not straightforward as, overall, the sensors for umami can use specific or non-specific detection. To achieve high sensitivity and selectivity, some works present a certain degree of complexity for the complexation of compounds in the selective detection.

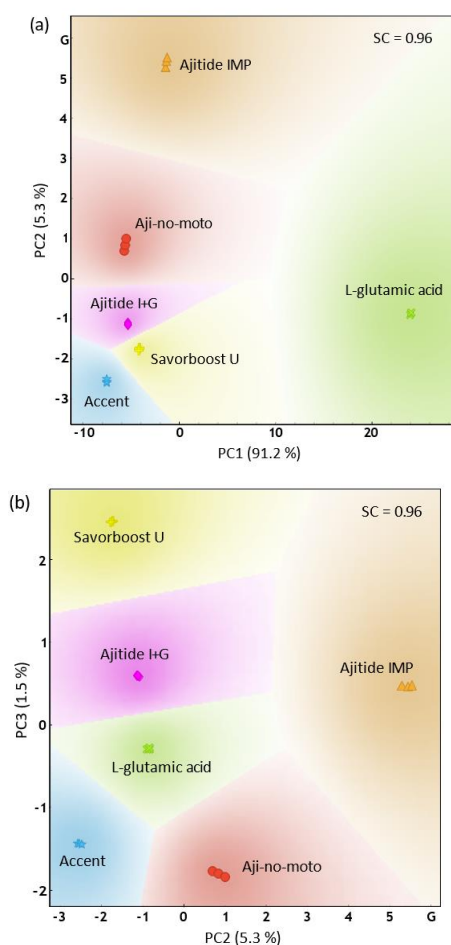


Figure 2. PCA score plots of the e-tongue used here to different umami samples across the entire frequency range.

IV. CONCLUSIONS

We explored here the incorporation of AgNPs into an LbL assemblies used as sensing units in a microfluidic e-tongue setup. Our results indicated absence of cross-contamination and long-term stability, proven to be robust and suitable for diverse real-world applications, offering reliable and consistent performance over a year. Our methodology of directly incorporating AgNP layers within a simple LbL structure offers a unique strategy with significant potential for expanding compositional possibilities in sensor applications. We emphasize also the importance of precise parameter control in the sensing units formation in impedimetric e-tongues.

ACKNOWLEDGMENTS

The Food Ingredients Division of Ajinomoto in Brazil for the umami samples. We thanks Igor Fier for multiplexed microfluidic setup development and the acquisition software.

REFERENCES

[1] Suárez et al., *Food Control* 2019, 100, 221-228. [2] Wang et al., *Food Chem.* 2020, 312, 126086. [3] Wu et al., *Food Anal. Methods* 2021, 14, 1298-1308. [4] de Oliveira et al., *J. Food Sci.* 2022, 87, 3138-3150. [5] Xiao et al., *Food Chem.* 2022, 372, 131264. [6] Souza et al., *Sens. Actuators B Chem.* 2021, 328, 129036. [7] Parra et al., *Sens. Actuators B Chem.* 2004, 101, 368-378. [8] Feng et al., *Food Chem.*

2021, 339, 127924. [9] Matsui et al., *Chemosensors* 2022, 10, 287. [10] Jung et al., *Biosens. Bioelectron.* 2022, 200, 113923. [11] Khalaf et al., *Food Chem.* 2021, 343, 128428. [12] Jiménez-Jorquera et al., *Talanta* 2010, 80, 1009-1018. [13] Chaiyo et al., *Chemosphere* 2022, 301, 134754. [14] Parra et al., *Talanta* 2013, 110, 367-373. [15] Lvova et al., *Anal. Chim. Acta* 2006, 572, 66-73. [16] Hassanien et al., *Sens. Actuators B Chem.* 2016, 234, 201-213. [17] Voza et al., *J. Food Sci.* 2019, 84, 3225-3233. [18] Yamanaka et al., *Food Control* 2016, 66, 363-370. [19] Abbas et al., *J. Food Sci.* 2020, 85, 2655-2662. [20] Wang et al., *Sens. Actuators B Chem.* 2019, 297, 126758. [21] Ye et al., *Food Control* 2020, 107, 106776. [22] Saeys et al., *Sensors* 2019, 19, 1296. [23] Shi et al., *Food Chem.* 2020, 307, 125589. [24] Su et al., *J. Agric. Food Chem.* 2017, 65, 7811-7818. [25] Wei et al., *Trends Food Sci. Technol.* 2019, 89, 316-332. [26] Zhang et al., *Food Chem.* 2021, 348, 129084. [27] Barbosa et al., *Sensors* 2019, 19, 4176. [28] Chen et al., *Food Chem.* 2021, 342, 128286. [29] Kozłowski et al., *Food Anal. Methods* 2020, 13, 456-465. [30] Silva et al., *J. Apic. Res.* 2021, 60, 109-119. [31] Lim et al., *Sensors* 2020, 20, 1475. [32] Anzai et al., *J. Agric. Food Chem.* 2019, 67, 12203-12211. [33] de Oliveira et al., *Food Res. Int.* 2020, 134, 109276. [34] Zhang et al., *J. Food Process Eng.* 2020, 43, e13396. [35] Masson et al., *Food Chem.* 2019, 279, 339-347. [36] Shu et al., *Food Anal. Methods* 2020, 13, 1660-1668. [37] Zheng et al., *J. Food Qual.* 2021, 2021, 5578396. [38] Mohammadi et al., *J. Food Sci. Technol.* 2020, 57, 3025-3034. [39] Vieira et al., *J. Food Sci.* 2021, 86, 1641-1652. [40] Tseng et al., *Food Chem.* 2021, 348, 129113. [41] Xu et al., *Food Chem.* 2019, 277, 631-637. [42] Cui et al., *Food Chem.* 2022, 371, 131125. [43] Wang et al., *J. Food Eng.* 2022, 314, 110748. [44] Zhao et al., *Food Chem.* 2022, 370, 131015. [45] He et al., *J. Agric. Food Chem.* 2019, 67, 4985-4994. [46] Yin et al., *Food Control* 2022, 139, 109086. [47] Li et al., *Food Chem.* 2021, 359, 129932. [48] Kim et al., *Food Res. Int.* 2021, 148, 110600. [49] Yu et al., *Talanta* 2019, 199, 466-473. [50] Liu et al., *Food Chem.* 2020, 305, 125492. [51] Hu et al., *Anal. Chim. Acta* 2021, 1167, 338543. [52] Chen et al., *J. Food Sci.* 2020, 85, 3683-3692. [53] Zheng et al., *J. Agric. Food Chem.* 2021, 69, 3290-3298. [54] Wang et al., *Food Chem.* 2019, 287, 80-88. [55] Liu et al., *Food Anal. Methods* 2020, 13, 1691-1701. [56] Feng et al., *Biosens. Bioelectron.* 2020, 165, 112408. [57] Han et al., *Food Chem.* 2022, 375, 131697. [58] Wang et al., *Food Chem.* 2019, 272, 543-548. [59] Zhou et al., *Food Chem.* 2021, 359, 129897. [60] He et al., *Sens. Actuators B Chem.* 2019, 291, 198-207. [61] Sun et al., *Talanta* 2022, 242, 123257. [62] Wang et al., *Food Chem.* 2020, 313, 126122. [63] Liu et al., *Food Chem.* 2022, 371, 131025. [64] Li et al., *Food Res. Int.* 2019, 116, 1185-1192. [65] Hu et al., *Food Chem.* 2020, 309, 125717. [66] Chen et al., *J. Food Sci.* 2019, 84, 1773-1780. [67] Yin et al., *Food Chem.* 2021, 344, 128638. [68] Wang et al., *Food Chem.* 2022, 370, 130965. [69] Wu et al., *Food Chem.* 2019, 294, 144-150. [70] Zhao et al., *Food Chem.* 2020, 307, 125610. [71] Liu et al., *Food Res. Int.* 2022, 155, 111072. [72] Chen et al., *Food Chem.* 2021, 338, 127971. [73] Wang et al., *Food Chem.* 2020, 319, 126536. [74] Zhou et al., *Food Chem.* 2022, 373, 131506. [75] Wässie et al., *Nanomaterials for Environmental and Agricultural Sectors*, Springer, 2023. [76] Caroleo et al., *Sensors* 2022, 22, 2649. [77] Mondal et al., *Heliyon* 2022, 8, e12207. [78] Chugh et al., *Nanosensors for Smart Agriculture*, Elsevier, 2022.

Development of microfluidic biosensors for studying epithelial cells processes by impedance spectroscopy

Ana Laura Tohmé
Instituto de Nanosistemas
Universidad Nacional de General San Martín
 Buenos Aires, Argentina
 atohme@unsam.edu.ar

Nicolás Saffioti
Instituto de Nanosistemas
Universidad Nacional de General San Martín
 Buenos Aires, Argentina
 nsaffioti@unsam.edu.ar

Diego Pallarola
Instituto de Nanosistemas
Universidad Nacional de General San Martín
 Buenos Aires, Argentina
 dpallarola@unsam.edu.ar

Abstract — Epithelial cells are crucial for the function of tissues and organs, defending against pathogens, enabling nutrient absorption, and maintaining homeostasis. The complex interactions between epithelial cells and the extracellular matrix (ECM) underpin epithelial physiology, while disruptions in these interactions contribute to numerous diseases, including bacterial infections and autoimmune disorders. Traditional *in vitro* methods to study these barriers fail to replicate the full complexity of the *in vivo* environment, limiting our understanding of cellular processes and our ability to dynamically monitor epithelial function. To address these limitations, we have aimed to develop innovative biosensors that permit simultaneous Electrochemical Impedance Spectroscopy (ECIS) and microscopic observation of epithelial cell interactions with their environment under biomimetic conditions.

In this work, we fabricated Indium Tin Oxide (ITO) microelectrodes with excellent transparency and characterized them through ECIS and cyclic voltammetry, demonstrating high sensitivity. We also developed an aligner to precisely integrate the microelectrodes with polydimethylsiloxane (PDMS) microfluidic devices, creating biomimetic conditions for epithelial culture. We optimized channel functionalization with ECM proteins and assessed the adhesion of Madin-Darby Canine Kidney (MDCK) cells, a model cell line for epithelium studies. Our ongoing work focuses on optimizing experimental conditions for direct monitoring of cell-to-ECM and cell-to-cell interactions using ECIS. This research presents a novel approach for studying the molecular basis of epithelial pathologies by enabling multiparametric monitoring of epithelial cell interactions.

Keywords— *Epithelial barrier integrity, microfabrication, microfluidics, electrochemistry, sensors, soft lithography, cell culture.*

I. INTRODUCTION

The epithelial barrier is fundamental to human health, serving as a critical frontline in the body's defense against environmental threats, pathogens, and the maintenance of homeostasis [1]. Epithelial cells, regulate the passage of substances between the internal and external media, playing a pivotal role in protecting tissues from infection and injury [2]. However, when these tight junctions are compromised, it can lead to increased permeability and the onset of various diseases, including inflammatory bowel disease, celiac disease, and other conditions that disrupt the body's delicate balance [3].

Traditional methods for studying epithelial barriers often lack the dynamism and complexity of the *in vivo* environment, limiting the understanding of barrier physiology and pathology. Addressing this gap, we introduce a novel approach employing an electrochemical microfluidic sensor capable of mimicking the epithelial microenvironment. These sensors are integrated with microfluidic devices for establishing precise conditions to closely replicate the epithelial natural setting, like constant nutrient supply and waste removal by the bloodstream, lumen flow and vessel architecture. Through the application of electrochemical impedance spectroscopy (EIS), our sensor could provide real-time, quantitative assessments of epithelial processes in response physiological and pathological processes.

II. BIOSENSOR FABRICATION AND CHARACTERIZATION

A. ITO microelectrode fabrication

ECIS is a non-invasive technique that allows monitoring cell processes, particularly the adhesion of cells to a substrate or the formation of cell-cell junctions [4]. ECIS relies on the use of electrodes on which cells could interact, adhere and grow. Moreover, transparent electrodes allow simultaneous implementation of microscopic observation providing multiparametric information of cell behavior.

Our group has strong experience in the design and fabrication of Indium Tin Oxide (ITO) transparent electrodes on glass surfaces to study cell interactions [5]. In order to obtain a biosensor for studying epithelial cells using ECIS we designed new ITO microelectrodes capable of reporting information from an epithelial monolayer and fabricated them in the clean room facilities.

Utilizing positive photolithography, our team has engineered interdigitated ITO microelectrodes (IDEs). Different designs were created by adjusting the width, spacing, and active area of the IDEs. These variants are being employed for optimizing the sensor's performance and sensitivity [6]. To characterize the electrode, Scanning Electron Microscopy (SEM) was applied (Figure 1). Image characterization showed an excellent resolution of electrode fabrication process providing adequate substrates for ECIS.

This work was financially supported by the European Union's Horizon 2020 Research and Innovation Programme under the Marie Skłodowska-Curie grant agreement no. 872869 Bio-TUNE project.

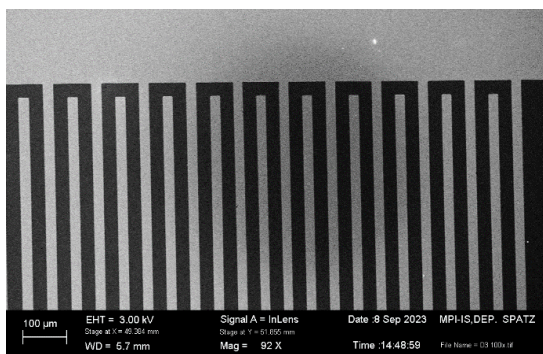


Fig. 1. Scanning Electron Microscopy (SEM) image of interdigitated microelectrode fabricated by positive photolithography. Finger width 20 µm, gap between electrodes 30 µm.

B. Coupling of ITO microelectrodes to microfluidic devices

To create a biomimetic sensor, we decided to integrate ITO microelectrodes with microfluidic devices. Microfluidics allows the creation of miniature channels for the precise manipulation of nanoliter volumes of fluid. We employed polydimethylsiloxane (PDMS) due to its low price, good biocompatibility and permeability to gases, high transparency and low fluorescent background and created microchannels that could be coupled with our ITO microelectrodes design. We aimed to combine ITO microelectrodes with PDMS microfluidic devices to develop platforms where cellular interactions can be accurately monitored under controlled experimental conditions. Given that both the microelectrodes and the microfluidic channels operate on the micrometer scale, an affordable, compact and portable aligner was developed to ensure precise alignment of ITO substrates with PDMS microfluidic chips [7]. This aligner (Fig. 2) is critical for the successful integration of these two components, facilitating the layered assembly required in microfabrication processes. The aligner was created following the open hardware philosophy, plans and instructions for its replication are available for other groups working in microfluidics interested in it.

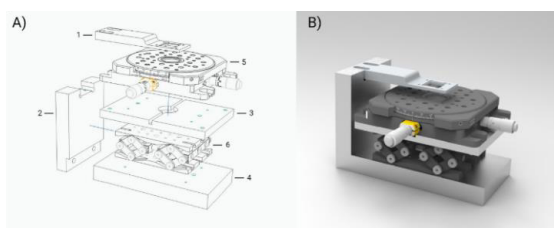


Fig. 2. In panel A, the image shows the exploded view of the aligner. The number indicate the constituting pieces: 1. Holding arm. 2. Arm support. 3. Stage adapter. 4. Base. 5. X/Y/θ-stage. 6. Z-stage. In panel B, the image shows a render of the assembled aligner.

Figure 3 presents a micrograph of the PDMS microfluidic chip precisely aligned and placed on top of the interdigitated ITO electrode. This image exemplifies the successful coupling of microfluidic channels with the electrodes, showcasing the seamless interface between the microfluidic channels and the underlying electrode structure. The careful alignment ensures optimal contact for

electrochemical measurements while maintaining the integrity of the fluidic pathways for precise sample delivery and manipulation.

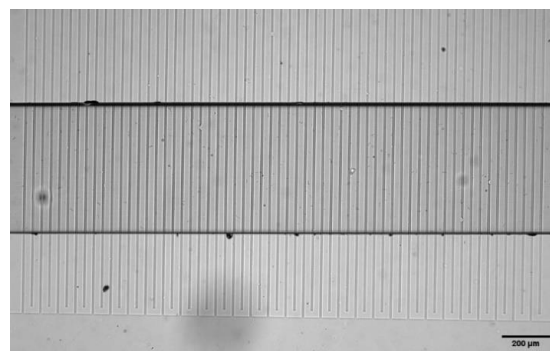


Fig. 3. Micrograph of the assembled microfluidic device with incorporated IDE. The image was obtained by bright field microscopy.

C. Cell culture in microfluidic chip

Following the successful integration of ITO microelectrodes with PDMS microfluidic devices, the next essential step is establishing cell cultures conditions inside these microfluidic devices. This setup allows for the maintenance of stable and homogenous culture conditions, which are critical for the growth and development of a healthy cell monolayer. Moreover, the transparency and biocompatibility of both ITO electrodes and PDMS chips ensure that cells can be monitored in real time using both ECIS and microscopic observation, without adversely affecting cell viability or function.

The cultivation of cells in the microfluidic chips utilizes the precise fluidic control offered by the PDMS microchannels allowing constant nutrient supply and waste removal. However, parameters such as surface treatment, coating with EM proteins, cell density, flow conditions, and bubble prevention in the channel are key aspects that we are currently optimizing. We employed Madin-Darby Canine Kidney (MDCK) cells, a model epithelial cell line, for these studies (Fig. 4). MDCK cells are known for their ability to form tight junctions, making them an excellent model for studying epithelial barrier function.

For the cell culture within the microfluidic channels, an essential step involved the functionalization of the channels with a fibronectin solution at a concentration of 20 µg/ml. This process entailed filling the channels with the fibronectin solution and allowing it to sit undisturbed overnight to ensure adequate coating of the surface. The following day, we introduced a cell suspension at a density of 3×10^6 cells/ml into the channels using a pressure-driven flow of 300 mbar. This specific pressure setting of 300 mbar was necessary to prevent the cells from decanting; without it, a lower concentration of cells would reach the channel, compromising the uniformity and integrity of the cell layer. After the cell infusion, the flow was halted to facilitate cell adhesion and spreading. After a period of 3 hours, to further promote cell attachment and the formation of a confluent monolayer, the flow was resumed at a continuous rate of 1 µl/min and maintained overnight. This meticulous procedure facilitated the formation of a robust

and uniform epithelial monolayer within a timeframe of 16 hours.

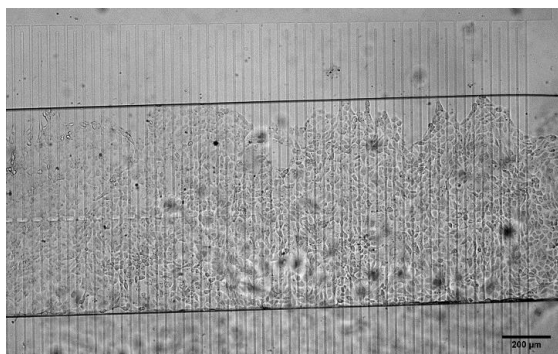


Fig. 4. Micrograph of MDCK monolayer on the microfluidic channel. The image was obtained by bright field microscopy.

D. Electrochemical characterization of biosensors

For the electrochemical characterization of our biosensors, we have conducted cyclic voltammetry measurements using the redox probe ferrocenemethanol (FcMeOH) at a 1 mM concentration in PBS buffer (pH 7.5 at 25°C), as shown in Figure 5. These measurements demonstrate the typical behavior of microelectrodes and confirm the successful integration of the interdigitated microelectrode design within the microfluidic channels. The observed electrochemical responses are indicative of the efficient electrode surface area and the effective diffusion of redox species within the microchannels, validating the functional performance of our microelectrodes in a fluidic environment.

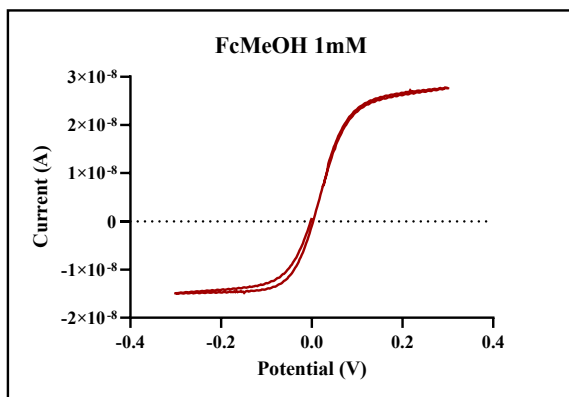


Fig. 5. Cyclic voltammetry performed on the ITO interdigitated microelectrode inside the microfluidic channel when the solution with FcMeOH 1 mM was injected.

III. FUTURE WORK

Currently, we are expanding our research to include ECIS as a tool to monitor cell adhesion and the formation of a monolayer of MDCK cells within the microfluidic device. Following the establishment of a stable monolayer, we are assaying different microelectrodes designs to find

the one with the best performance. Then, we plan to perform a calcium switch experiment by adding ethylenediaminetetraacetic acid (EDTA) to the media. This procedure is expected to disrupt the tight junctions between the cells, simulating a compromise in the epithelial barrier's integrity. The ability of our microfluidic device to detect such changes through impedance measurements would provide a powerful platform for studying epithelial barrier functions and their role in various physiological and pathological processes, such as the presence of bacterial toxins that disrupt epithelial barriers, the epithelial defense against cancer or the integration of implants. This part of our research is in progress, and we anticipate that the results will further demonstrate the versatility and applicability of our microfluidic system for advanced biological and electrochemical studies.

ACKNOWLEDGMENT

This work was financially supported by the European Union's Horizon 2020 Research and Innovation Programme under the Marie Skłodowska-Curie grant agreement no. 872869 Bio-TUNE project. PD acknowledges financial support from Max-Planck-Gesellschaft (Max Planck Partner Group Nanoelectronics for Cellular Interfaces INS/MPI-MR) and the National Agency for the Promotion of Science and Technology (ANPCyT, PICT-2019-00905). SNA acknowledges financial support from the National Agency for the Promotion of Science and Technology (ANPCyT, PICT-2019-03218). TAL acknowledges ANPCyT (PICT-2019-00905) for a doctoral scholarship. PD and SNA are staff researchers of CONICET.

REFERENCES

- [1] M. Gieryńska, L. Szulc-Dąbrowska, J. Struzik, M.B. Mielcarska, K.P. Gregorczyk-Zboroch, "Integrity of the Intestinal Barrier: The Involvement of Epithelial Cells and Microbiota—A Mutual Relationship," *Animals: An Open Access Journal from MDPI*, vol. 12(2), 2022, 145, <https://doi.org/10.3390/ani12020145>.
- [2] S. Panwar, S. Sharma, P. Tripathi, "Role of Barrier Integrity and Dysfunctions in Maintaining the Healthy Gut and Their Health Outcomes," *Frontiers in Physiology*, vol. 12, 2021, 715611, <https://doi.org/10.3389/fphys.2021.715611>.
- [3] D. Yazici, I. Ogulur, Y. Pat, H. Babayev, E. Barletta, S. Ardicli, et al., "The epithelial barrier: The gateway to allergic, autoimmune, and metabolic diseases and chronic neuropsychiatric conditions," *Seminars in Immunology*, vol. 70, 2023, 101846, ISSN 1044-5323, <https://doi.org/10.1016/j.smim.2023.101846>.
- [4] C.M. Lo, C.R. Keese, I. Giaefer, "Impedance analysis of MDCK cells measured by electric cell-substrate impedance sensing," *Biophysical Journal*, vol. 69(6), 1995, 2800–2807, [https://doi.org/10.1016/S0006-3495\(95\)80153-0](https://doi.org/10.1016/S0006-3495(95)80153-0).
- [5] D. Pallarola, A. Bochen, V. Guglielmotti, T.A. Oswald, H. Kessler, J.P. Spatz, "Highly Ordered Gold Nanopatterned Indium Tin Oxide Electrodes for Simultaneous Optical and Electrochemical Probing Cell Interactions," *Analytical Chemistry*, vol. 89(18), 2017, 10054–10062, <https://doi.org/10.1021/acs.analchem.7b02743>.
- [6] N.S. Mazlan, M.M. Ramli, M.M. Abdullah, D.S. Halin, S.S. Isa, L.F. Talip, N.S. Danial, & S.A. Murad, "Interdigitated electrodes as impedance and capacitance biosensors: A review," 2017.
- [7] V. Guglielmotti, N.A. Saffioti, A.L. Tohmé, M. Gambarotta, G. Corthey, D. Pallarola, "A portable and affordable aligner for the assembly of microfluidic devices," *HardwareX*, vol. 12, 2022, e00348, <https://doi.org/10.1016/j.ohx.2022.e00348>.

Optofluidic set up for production and measurement of Sodium-Alginate microdroplets

Rômulo Ferreira dos Santos
Department of Electrical Engineering
 University of Brasilia, Brasilia, Brasil
romulo.santos@ieec.org

Matheus Rotta Ribeiro
Department of Electrical Engineering
 University of Brasilia, Brasilia, Brasil
matheus.rotta.ribeiro@gmail.com

Daniel Orquiza de Carvalho
Department of Electrical Engineering
 University of Brasilia, Brasilia, Brasil
daniel.orquiza@ene.unb.br

Juliana de Novais Schianti
Department of Electrical Engineering
 University of Brasilia, Brasilia, Brasil
juliana.schianti@unb.br

Sebastien R. M. J. Rondineau
Department of Electrical Engineering
 University of Brasilia, Gama, Brasil
sebastien@unb.br

Abstract — In this work we present an optofluidic system to produce droplets with size measurements done in line by optical fiber connected perpendicularly to the system. The system has been applied to obtain sodium alginate microcapsules by gelation process. Sodium Alginate is a polysaccharide widely used in the food industry to encapsulate flavors and vitamins. The Biotechnology area also has interest in this type of microcapsule to conduct cells in different studies. In this way, we present a low-cost device to obtain droplets with controlled sizes, measured by optical fiber in the moment of droplets formation. Optical fiber offers a non-invasive method of measurement in line. In this system it was possible to obtain droplets with sizes varying from 320 up to 900 μm and the results were comparable to microscope images.

Keywords—*optofluidic, droplets, sodium alginate, optical fiber sensor*

I. INTRODUCTION

Microfluidic devices have been widely used to obtain droplets with a very high chemical and physical control [1-2]. When droplets are processed in microfluidic devices, they offer advantages such as small sizes with high homogeneity, economy of reagents and low costs compared to bulk systems [3-5]. In this way, real time measurements are a key factor in conduct decisions that could improve the material processed in these devices. Characteristics such as sizes, morphologies, frequency of production are pursued in different studies [6-7]. To measure these characteristics different methods have been applied involving electrical, optical and RF/Microwave sensors [8-9]. Among these methods, optical sensors offer a noninvasive way to obtain some parameters such droplet sizes, concentration, velocity, and frequency of droplets production [10-11].

Sodium Alginate is a polymer of acidic sugar residues, being a polysaccharide with chemical and physical characteristics useful for biotechnological applications [12-14]. The characteristics such as sustainable natural material, non-toxicity, excellent biocompatibility, biodegradability, and easy way to chemical functionalization have been attracted research in applied this biopolymer [15-16]. Na-Alginate in a contact to polyvalent ions such as Mg^{2+} and Ca^{2+} produce a type of gel in a crosslinking process called ionic gelation [17]. This gel could be performed as capsules, beads, thin films, nanoparticles, and nanofibers [18]. Alginate

capsules have been applied to encapsulate flavors, vitamins, and drugs in Pharmaceutical and Food Industries because of their porosity characteristic favoring a controlled release [19]. Besides, Na-Alginate also has been applied to encapsulate cells or even to produce 3D matrix for cell cultures in Biotechnology area. As nanofilms, Na-alginate has been used as electrochemical biosensor in strategies on immobilizing biomolecules.

In this way, this project has the purpose of obtaining Na-Alginate capsules with controllable sizes and in the future, implement cells encapsulation. The first step in this process is the obtention of Na-alginate droplets and perform the ionic gelation outside the microsystem. Our system is composed of an acrylic microfluidic device to obtain droplets and perform the droplet size measurement in line, using an optical fiber coupled perpendicularly on the chip (see Fig.1). The light signal is captured by a photodiode and translated by an Arduino control and software routine. By varying the concentration of Na-alginate solutions and flow rates we intend to produce different size capsules. These capsules will be applied to immobilize cells or nanoparticles in the future.

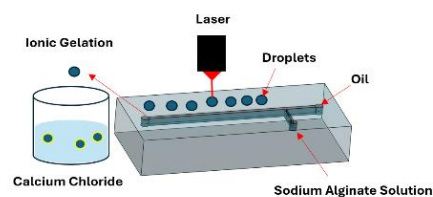


Fig1. Na-Alginate droplets in a microfluidic system

II. EXPERIMENTAL PROCEDURE

A. Device fabrication

A T-junction microfluidic device was fabricated to produce droplets. The main channel has 500 μm the side channel has 250 μm of width, and it was utilized an acrylic sheet of 300 μm -thick. The geometry was patterned using a CO_2 CNC laser router (Nagano, NCRL6040). A 2mm- thick acrylic cover sheet with inlet and outlet holes and a bottom sheet were connected to the channels using double side tape. A cylindrical holder for the optical fiber was also installed and connected to the system. Metallic connectors were glued

with epoxy resin to couple the plastic tubing to syringe pumps (New Era, NE-1000). The complete system is shown in Fig.2 (a).

B. Optical Set Up

The optical set up was composed by a laser diode to introduce light at 632.8 nm on the chip by optical fiber with a core diameter of 8.2 μm (SMF-28). The optical fiber was positioned perpendicular to the microfluidic device, and on the bottom chip it was connected a photodiode to detect the light signal and measure the droplets sizes. An Arduino control was implemented to analyze the response from photodiode. A zoom image from optical fiber area on the device is shown in Fig. 1b.

C. Fluid Phases and Droplet Sizes Measurements

Our first experiments were implemented using sunflower oil (Bunge Alimentos, Brazil) with 4 % of surfactant polyglycerol polyricinoleate (PGPR) and deionized water as fluid phases. On sequence, we utilized soybean oil as continuous phase and sodium alginate (Na-Alginate, Sigma Aldrich) with a concentration of 0.5 w/w in water to observe the formation of alginate microcapsules. The solidification of the core droplets was obtained with calcium chloride (CaCl_2 , Dinamica Co.) solution in a 4% of concentration in water. The continuous flow rate varied from 6 up to 45 mL/h and the dispersed flow rate was maintained in 3 mL/h. The droplet sizes were also measured using a microscope coupled to a camera and the photos obtained were analyzed by ImageJ to compare the droplet sizes with optical measurements.

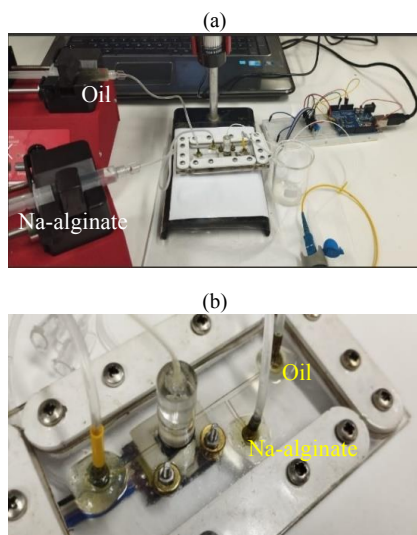


Fig.2 Experimental Set Up: (a) Optofluidic set up for droplets production and measurements and (b) optical fiber and photodiode region in zoom.

III. RESULTS AND DISCUSSIONS

A. Optical in line measurements

On sequence, it is presented the first alginate droplets measurements obtained with the top fiber device. On each graph we can observe the patterns obtained as the droplets cross the optical path, corresponding to the valleys on the curves. In the Fig 3 (a) it is presented the optical signal for a rate between dispersed flow and continuous flow of 1:2. In this situation we observed a droplet with a plug formate. In (b) the relation between phases was 1:5, in (c) 1:8 and in (d) 1:11. As expected, when the continuous flow increases it is possible to observe a reduction in the width indicating the reduction of the droplets sizes, and also it is possible to observe an increasing in droplets frequency production. We observed some instabilities on the measurements and droplets with polydispersity. For low fluid flows it was not possible to observe the formation of small droplets, probably because of Na-Alginate concentration in water. Adjustments in Na-Alginate and Surfactant concentrations must be executed to improve the droplets formation.

B. Droplets

In Fig. 4 it is shown the Na-alginate droplets formed without the gelation process. The images correspond to the relation between phases presented before on the graphs. After gelation process in CaCl_2 solution the capsule formed should be small. This reduction will be evaluated further. It is possible to observe droplets with sizes varying from 400 up to 1000 μm . The biggest droplets it was obtained in rate of 1:2 with a size of 930 μm (Fig. 4(a)), and as the rate between phases became bigger the droplets sizes became smaller, and it was possible to observe the obtention of satellite droplets with sizes of 100 μm . In this condition, the droplet did not have a round shape, and it is more considered like a plug inside the main channel. On other conditions, we have droplets with sizes as 570, 400 and 350 μm , respectively Fig.4 (b), (c) e (d).

C. Comparison between measurements

In Table 1 it is described the droplets size measurements obtained by the two methods, with optical fiber (Dopt) and with microscope (Dmic). The droplet diameter with optical fiber were obtained by getting the full width at half maximum on the peak, and calculated the diameter by informations of fluid flow rate and channels geometry. It is indicated the total flow rate Q_{total} (dispersed plus continuous phase), the Velocity based on total flow rate and the relation between phases ($Q_d:Q_c$). In the microscope measurement it was used a standard microscope ruler. The results showed a difference around 12%. Some reasons for this difference can be discussed, as operational errors and instabilities during droplets formation. Besides, it is possible that have occurred some droplets coalescence in the case of microscope measurements.

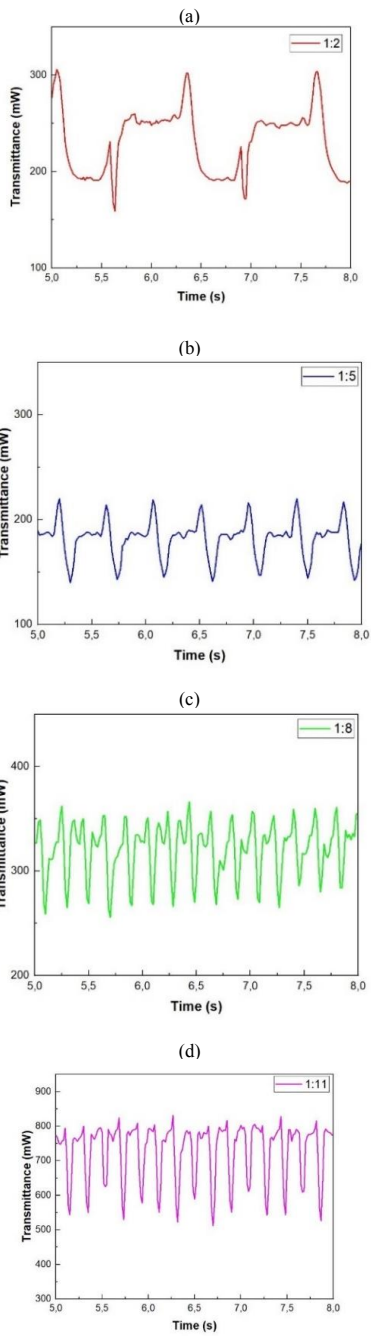


Fig.3 Optical measurements indicating the transmitted light over the time for different ratios between phases (dispersed and continuous, respectively): (a)1:2, (b) 1:5, (c) 1:8 and d) 1:11. The dispersed phase was maintained fixed in 3 ml/h.

TABLE I. DROPLETS DIAMETERS

Qd:Qc	Droplets Diameter			
	Q_{total} ml/h	Velocity m/s	D_{opt} μm	D_{mic} μm
1:2	9	0,02	930	1053
1:5	18	0,03	530	574
1:8	28	0,05	350	410
1:11	38	0,07	320	347

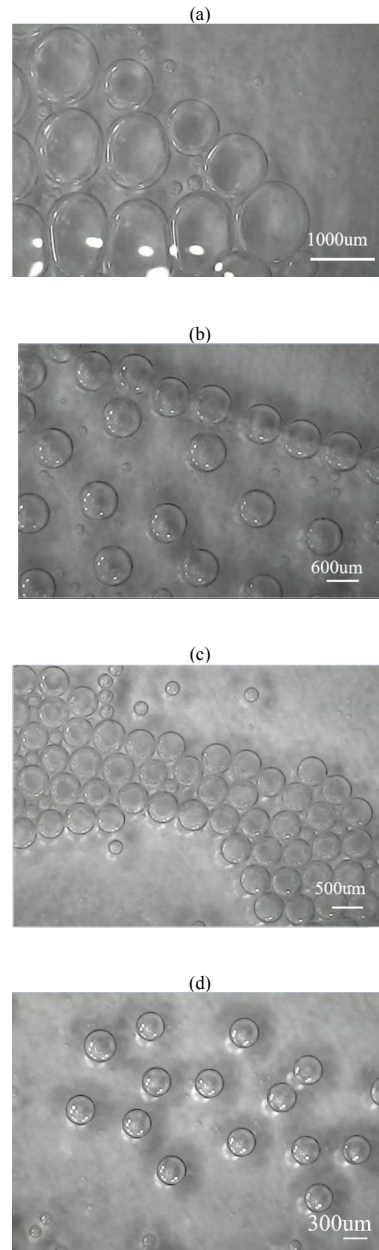


Fig. 4 Microscope images for different ratios between phases: (a) 1:2, (b) 1:5, (c) 1:8 and (d) 1:11. We have droplets with sizes of 1053, 570, 400 and 350 μm , respectively.

IV. CONCLUSIONS

We fabricated in acrylic substrate an optofluidic system to obtain droplets and measure their sizes in the moment of formation. This system was applied to produce sodium alginate droplets, with different values of flow rates. The results showed that the system was able to measure the droplets, and we obtain sizes varying from 350 up to 900 μm . Some adjustments in the sample concentrations must be made to improve the results. Also, the Sodium Alginate gelation in Calcium Chloride solutions to produce microcapsules, that have a rigid shape compared to droplets. In the future, these droplets will be used to encapsulate cells and nanoparticles.

ACKNOWLEDGMENT

The authors are grateful to Brazilian financial agencies: Conselho Nacional de Desenvolvimento Científico e Tecnológico (CNPq), grants number 102003/2022-0, and also Fundação de Apoio à Pesquisa do Distrito Federal (FAPDF) with grant number 271/2021-03/2021, 00193-00000923/2021-48.

REFERENCES

- [1] G. Eason, B. Noble, and I. N. Sneddon, "On certain integrals of Lipschitz-Hankel type involving products of Bessel functions," *Phil. Trans. Roy. Soc. London*, vol. A247, pp. 529–551, April 1955. (*references*)
- [2] J. Clerk Maxwell, *A Treatise on Electricity and Magnetism*, 3rd ed., vol. 2. Oxford: Clarendon, 1892, pp.68–73.
- [3] I. S. Jacobs and C. P. Bean, "Fine particles, thin films and exchange anisotropy," in *Magnetism*, vol. III, G. T. Rado and H. Suhl, Eds. New York: Academic, 1963, pp. 271–350.
- [4] K. Elissa, "Title of paper if known," unpublished.
- [5] R. Nicole, "Title of paper with only first word capitalized," *J. Name Stand. Abbrev.*, in press.
- [6] Y. Yorozu, M. Hirano, K. Oka, and Y. Tagawa, "Electron spectroscopy studies on magneto-optical media and plastic substrate interface," *IEEE Transl. J. Magn. Japan*, vol. 2, pp. 740–741, August 1987 [Digests 9th Annual Conf. Magnetics Japan, p. 301, 1982].
- [7] M. Young, *The Technical Writer's Handbook*. Mill Valley, CA: University Science, 1989.
- [8] Sun, Yuqiong et al. "Recent progress on performances and mechanisms of carbon dots for gas sensing." *Luminescence : the journal of biological and chemical luminescence* vol. 38,7 (2023): 896-908. doi:10.1002/bio.4306.
- [9] Li, Changxu et al. "A Review of Coating Materials Used to Improve the Performance of Optical Fiber Sensors." *Sensors (Basel, Switzerland)* vol. 20,15 4215. 29 Jul. 2020, doi:10.3390/s20154215.
- [10] Liu, Wenkai et al. "Micro-Droplets Parameters Monitoring in a Microfluidic Chip via Liquid-Solid Triboelectric Nanogenerator." *Advanced materials (Deerfield Beach, Fla.)* vol. 35,52 (2023): e2307184. doi:10.1002/adma.202307184.
- [11] Saucedo-Espinosa, Mario Alberto et al. "Continuous Electroformation of Gold Nanoparticles in Nanoliter Droplet Reactors." *Angewandte Chemie (International ed. in English)* vol. 62,5 (2023): e202212459. doi:10.1002/anie.202212459.
- [12] Morozkina, Svetlana et al. "The Fabrication of Alginate Carboxymethyl Cellulose-Based Composites and Drug Release Profiles." *Polymers* vol. 14,17 3604. 1 Sep. 2022, doi:10.3390/polym14173604.
- [13] Mota, Rita et al. "Cyanoflan: A cyanobacterial sulfated carbohydrate polymer with emulsifying properties." *Carbohydrate polymers* vol. 229 (2020): 115525. doi:10.1016/j.carbpol.2019.115525.
- [14] Ertesvåg, Helga. "Alginate-modifying enzymes: biological roles and biotechnological uses." *Frontiers in microbiology* vol. 6 523. 27 May. 2015, doi:10.3389/fmicb.2015.00523.
- [15] Zhang, Zhaoyu et al. "Research Progress of Chitosan-Based Biomimetic Materials." *Marine drugs* vol. 19,7 372. 27 Jun. 2021, doi:10.3390/md19070372.
- [16] Shrivastav, Prachi et al. "Bacterial cellulose as a potential biopolymer in biomedical applications: a state-of-the-art review." *Journal of materials chemistry. B* vol. 10,17 3199-3241. 4 May. 2022, doi:10.1039/d1tb02709c.
- [17] Zhao, Congxian et al. "Gelation of Na-alginate aqueous solution: A study of sodium ion dynamics via NMR relaxometry." *Carbohydrate polymers* vol. 169 (2017): 206-212. doi:10.1016/j.carbpol.2017.03.099.
- [18] Richardson, Joseph J et al. "Convective polymer assembly for the deposition of nanostructures and polymer thin films on immobilized particles." *Nanoscale* vol. 6,22 (2014): 13416-20. doi:10.1039/c4nr04348k.
- [19] Chen, Liang-Hsun et al. "Nanoemulsion-Loaded Capsules for Controlled Delivery of Lipophilic Active Ingredients." *Advanced science (Weinheim, Baden-Wuerttemberg, Germany)* vol. 7,20 2001677. 28 Aug. 2020, doi:10.1002/advs.202001677.
- [20] Andersen, Therese et al. "3D Cell Culture in Alginate Hydrogels." *Microarrays (Basel, Switzerland)* vol. 4,2 133-61. 24 Mar. 2015, doi:10.3390/microarrays4020133.
- [21] Schumacher, Heinz Martin et al. "Cryopreservation of Plant Cell Lines Using Alginate Encapsulation." *Methods in molecular biology (Clifton, N.J.)* vol. 2180 (2021): 639-645. doi:10.1007/978-1-0716-0783-1_34.
- [22] Chen, Jingyi et al. "A glucose biosensor based on glucose oxidase immobilized on three-dimensional porous carbon electrodes." *The Analyst* vol. 140,16 (2015): 5578-84. doi:10.1039/c5an00200a.
- [23] Lee, Dongkyu et al. "Fabrication of Microparticles with Front-Back Asymmetric Shapes Using Anisotropic Gelation." *Micromachines* vol. 12,9 1121. 17 Sep. 2021, doi:10.3390/mi12091121.

Proyectos de Microfluídica en el Departamento de Micro y Nanotecnología-CNEA-CAC

Claudio Ferrari
Departamento de Micro y
Nanotecnología-CNEA-CAC
Instituto de Nanociencia y
Nanotecnología (INN)
Buenos Aires, Argentina

Guido Berlin
Departamento de Micro y
Nanotecnología-CNEA-CAC
Instituto de Nanociencia y
Nanotecnología (INN)
Buenos Aires, Argentina

El departamento de micro y nanotecnología cuenta con un área limpia en la cual se desarrollan tareas relacionadas con diseño, fabricación y caracterización de micro dispositivos tanto para desarrollos de proyectos propios como para proyectos de nuestra institución, instituciones científicas nacionales e internacionales, universidades y también empresas privadas. En ese marco se busca desarrollar líneas de investigación referentes a sensores que utilizan técnicas de microfluídica. Esta presentación tiene como objetivo adentrarse en los fundamentos de los microfluidos, sus ventajas y sus amplias aplicaciones y presentar las líneas de investigación que se desarrollan en el departamento de micro y nanotecnología.

Keywords—Microfabricación, Lab-on-a-Chip, style, styling, insert (key words)

I. INTRODUCCIÓN

La microfluídica es la ciencia y tecnología de manipular fluidos a una escala pequeña [1]. En los últimos años ha surgido como una herramienta poderosa en varios campos, desde la biología y la química hasta la ingeniería y la medicina. Este campo aprovecha principios de física, química, ingeniería y biología para diseñar sistemas que pueden manejar volúmenes pequeños de fluidos con alta precisión.

A. Ventajas de la Microfluídica

1. **Miniaturización:** Al reducir el tamaño de los sistemas, la microfluídica ofrece volúmenes de muestra reducidos, tiempos de reacción más rápidos y una mayor sensibilidad.
2. **Alto Rendimiento:** Los dispositivos microfluídicos permiten el procesamiento paralelo de múltiples muestras simultáneamente, mejorando la eficiencia y el rendimiento.
3. **Integración:** Varias funciones, como mezcla, separación y detección, pueden integrarse en un solo chip microfluídico, optimizando los flujos de trabajo experimentales.
4. **Automatización:** Los sistemas microfluídicos pueden ser automatizados, minimizando la intervención manual y reduciendo el error humano.

5. **Rentabilidad:** La miniaturización reduce el consumo de reactivos y la generación de residuos, haciendo que los microfluidos sean una solución rentable para muchas aplicaciones.

B. Aplicaciones de la Microfluídica

Diagnóstico Biomédico: Los dispositivos microfluidicos se utilizan para diagnósticos en el punto de atención, permitiendo la detección rápida y precisa de enfermedades y patógenos.

Descubrimiento de Medicamentos: La microfluídica facilita el cribado de alto rendimiento de candidatos a fármacos, acelerando el proceso de descubrimiento de medicamentos.

Química Analítica: Los sistemas microfluidicos se emplean para separaciones cromatográficas, preconcentración de muestras y análisis químico con una sensibilidad mejorada.

Ingeniería de Tejidos: La microfluídica juega un papel crucial en la creación de construcciones de tejidos complejos al controlar precisamente el microambiente para el cultivo celular.

Monitoreo Ambiental: Los sensores microfluidicos se utilizan para la detección in situ de contaminantes, patógenos y contaminantes en el aire y el agua.

En definitiva, la microfluídica representa un cambio de paradigma en la manipulación de fluidos, ofreciendo un control y eficiencia incomparables en diversas aplicaciones. A medida que este campo continúa evolucionando, su impacto en la ciencia, la tecnología y la atención médica está destinado a expandirse, impulsando la innovación y el descubrimiento.

II. PROYECTOS

Un chip de microfluídica se puede describir como un dispositivo que permite procesar o visualizar una pequeña cantidad de líquido. El chip suele ser transparente y su tamaño suele ser de unos pocos centímetros. Los chips de microfluidos tienen microcanales internos aún más finos que

un cabello, están conectados al exterior mediante orificios en el chip llamados puertos de entrada/salida. Los chips de microfluidos están hechos de termoplásticos como acrílico, vidrio, silicona o un caucho de silicona transparente llamado PDMS. En el departamento principalmente trabajamos con dispositivos de PDMS-vidrio.

A. Magsens

El trabajo presentado se enmarca en un proyecto amplio, cuyo objetivo es el diseño, fabricación y validación de un lab-on-a-chip basado en el control de micro y nano partículas magnéticas funcionalizadas para la detección de biomoléculas por medio de sensores magnéticos [2-5].

La idea es diseñar y fabricar un dispositivo capaz de transportar de manera controlada nanopartículas superparamagnéticas (SPNP). Para ello se están realizando estudios teóricos y numéricos de la generación de campo magnético en el chip y de su interacción con las partículas, la construcción del sistema simulado y su fabricación y caracterización experimental.

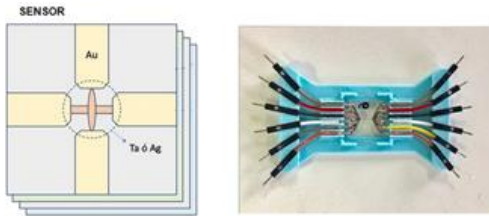


Fig. 1. Caracterización experimental de un sistema de transporte de nanopartículas magnéticas para su integración a un biosensor.

La Fig. 1 muestra un primer dispositivo que permite el transporte controlado de SPNPs y también un diseño multicapa preliminar de uno de los sensores magnéticos.

En la Fig. 2 se aprecian detalles de microfabricación del dispositivo.

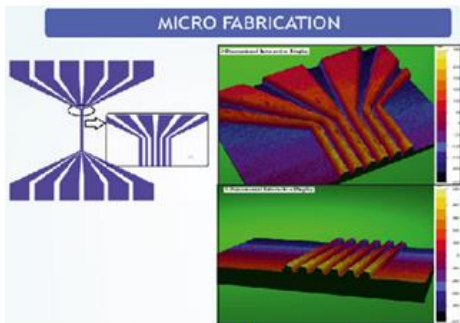


Fig. 2. Medición obtenida por perfilometría óptica

Este es un trabajo que comprende la colaboración de varios grupos de trabajo dentro de CNEA, que van desde la detección de campos magnéticos hasta el transporte de partículas magnéticas a través de microcanales.

B. dispositivos para la generación de microgotas

El objetivo del proyecto es el diseño, simulación, fabricación y caracterización de dispositivos para la generación pasiva de microgotas mediante dispositivos generados a partir de PDMS - vidrio, el cual se fabrica a través de un molde de fotoresina generado por técnicas de

fotolitografía. En los últimos años la generación controlada de microgotas ha experimentado un enorme crecimiento, como así también sus aplicaciones [6-10]. En ese contexto se estudia cómo afecta a los diferentes parámetros la presencia de obstáculos en un canal en forma de T. Se han hecho simulaciones y se han contrastado con experimentos lográndose un muy buen acuerdo.

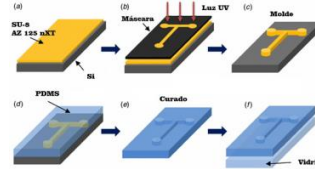


Fig. 3. Fabricación de dispositivo microfluidico PDMS-vidrio

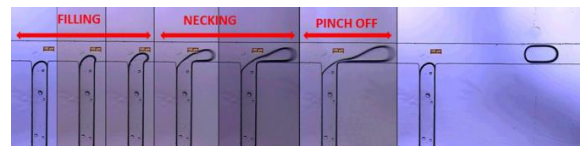


Fig. 4. Proceso de formación de gotas

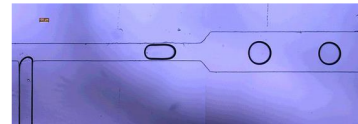


Fig. 5. Formación de gotas (canal en T)

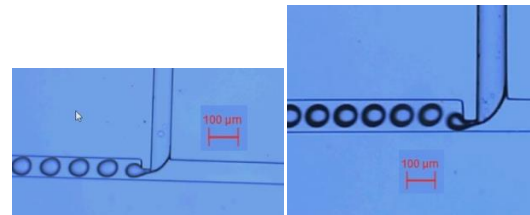


Fig. 6. Formación de microgotas con obstrucción de canal T

C. Ficeltar

Según la Organización Mundial de la Salud, el cáncer es la principal causa de muerte en el mundo. Durante el año 2020 se contabilizaron más de 19 millones de nuevos casos y casi 10 millones de muertes por culpa de esta patología, lo que representa un sexto de las defunciones de dicho año. La detección temprana de esta enfermedad mejora la respuesta al tratamiento, incrementa la probabilidad de supervivencia, disminuye la morbilidad y reduce los costos asociados a la terapia.

El proyecto FiCelTAR, Filtro de Células Tumorales Argentino, del Departamento Micro y Nanotecnología (CNEA), propone el desarrollo de un dispositivo basado en una membrana microporosa para la detección temprana del cáncer mediante el filtrado de una muestra de sangre periférica. El prototipo cuenta con una membrana metálica microfabricada por electroplating por medio de un molde fotolitográfico. Esta es soportada por mordazas de aleación

de aluminio con o-rings de caucho sintético. Dicho prototipo busca probar el funcionamiento mecánico, pero los materiales de su construcción no son adecuados para la aplicación final, que involucra la interacción con sistemas biológicos, se está trabajando en una segunda generación que cumpla con los requisitos mencionados.

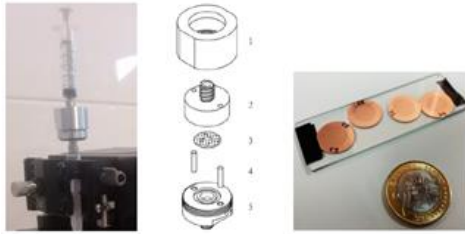


Fig. 7. Planos y prototipo del Ficeltar

- [1] Taberlin P. "Introduction to Microfluidics". Oxford University Press (2009)
- [2] Natteri M. Sudharsan, and Raju V. Ramanujan, "Magnetic Droplet Merging by Hybrid Magnetic Fields," IEEE MAGNETICS LETTERS, Volume 7 (2016).
- [3] Inga Ennena, Andreas Hüttena, "Magnetic nanoparticles meet microfluidics," NRW 2016
- [4] Vijaya Sunkara, Dong-Kyu Park and Yoon-Kyoung Cho, "Versatile method for bonding hard and soft materials," Cite this: RSC Advances, 2012, 2, 9066–9070 (2012).
- [5] Mark Tondra, Mike Granger, Rachel Fuerst, Marc Porter, Catherine Nordman, John Taylor, and Seraphin Akou., "Design of Integrated Microfluidic Device for Sorting Magnetic Beads in Biological Assays," IEEE Transactions on Magnetics (Volume: 37, Issue: 4, July 2001).
- [6] H. Viswanathan, "The Effect of Junction Gutters for the Upscaling of Droplet Generation in a Microfluidic T-Junction," Microgravity Science and Technology (2022) 34: 43
- [7] Tomasz Glowdel, Caglar Elbuken, and Carolyn L. Ren "Droplet formation in microfluidic T-junction generators operating in the transitional regime. II. Modeling" PHYSICAL REVIEW E 85, 016323 (2012)
- [8] Tomasz Glowdel, Caglar Elbuken, and Carolyn L. Ren, "Droplet formation in microfluidic T-junction generators operating in the transitional regime. I. Experimental observations" PHYSICAL REVIEW E 85, 016322 (2012)
- [9] Encyclopedia of Microfluidics and Nanofluidics, Prof. Dongqing Li, Department of Mechanical Engineering, Vanderbilt University
- [10] Xueying Wang, Antoine Riaud, "Pressure drop-based determination of dynamic interfacial tension of droplet generation process in T-junction microchannel" Springer-Verlag Berlin Heidelberg 2014

Oil spacer for droplet frequency control in 3D printer microfluidic device coupled to contactless detectors

Ismael Sánchez
Laboratory of Biosensors and Bioanalysis (LABB), Department of Biological Chemistry. IQUIBICEN, University of Buenos Aires and CONICET, CABA, Argentina. ismaelsanchez@qb.fcen.uba.ar

Federico Figueredo
Laboratory of Biosensors and Bioanalysis (LABB), Department of Biological Chemistry. IQUIBICEN, University of Buenos Aires and CONICET, CABA, Argentina. fericofigueredo@qb.fcen.uba.ar

Eduardo Cortón
Laboratory of Biosensors and Bioanalysis (LABB), Department of Biological Chemistry. IQUIBICEN, University of Buenos Aires and CONICET, CABA, Argentina. eduardo@qb.fcen.uba.ar

Abstract— Microfluidics represents a promising tool for the manipulation of fluids at the micrometer scale. The objective of this study is to evaluate the efficacy of 3D-printed microfluidic devices, particularly those incorporating spacers within their channels, for the generation and detection of droplets utilizing a contactless conductivity detector (C⁴D). This approach aims to enhance the precision and reliability of detection outcomes, while reducing the potential for errors commonly associated with traditional microfluidic techniques.

Keywords— microfluidics, microdroplets, 3D printing technology component

I. INTRODUCTION

Microfluidics is an emerging interdisciplinary field that studies the manipulation of fluids in micrometer channels. This approach has revolutionized areas such as chemical and biological analysis by enabling the miniaturization of systems, reducing the volume of samples and reagents, and facilitating the integration of high-precision sensors into devices known as microchips [1]. Notable applications include the separation and analysis of molecules, isolation of single cells, and assessment of cellular responses, underscoring their potential in diagnostics and cell biology studies [2].

Microchip fabrication by 3D printing has emerged as a promising alternative due to its accessibility, versatility and ability to produce customized devices at low cost [3]. This technology has enabled the development of microchips with diverse geometries, including those designed for the generation of droplets, fundamental in drug encapsulation and delivery studies [4].

In this study, we report the use of a 3D printed droplet microchip to evaluate the frequency of droplet formation and their respective peaks and their detection by a contactless conductivity detector (C⁴D). We explored microchips with and without spacers, observing how these configurations influence the signal amplitude, in addition we seek to avoid the possibility of the passage of two drops passing at the same time through the sensor electrode obtaining erroneous signals. We hypothesize that the inclusion of spacers improves the uniformity and accuracy of the signal, thus optimizing detection in advanced analytical applications.

II. MATERIAL AND METHODS

A. Materials

The following materials were used for this study: KCl (Sigma Aldrich, St. Louis, MO, USA), Span® 80 (Sigma Aldrich), mineral oil (EWE, Saladillo, Buenos Aires,

Argentina), and poly(lactic acid) (PLA) filament supplied by Printalot (Monte Grande, Buenos Aires, Argentina). Tempered glass syringes of 5 mL (Somimaco, Buenos Aires, Argentina) were used for the continuous phase and disposable syringes of 1 mL (Bremen Tools Argentina SA, Buenos Aires, Argentina) for the dispersed phase.

B. 3D printed microfluidic device fabrication

The microfluidic devices were fabricated using a 3D printer based on fused deposition modeling (FDM), following a protocol previously established by Duarte et al. [5]. The device design included two microchannels, one for the continuous phase and one for the dispersed phase, both with dimensions of 700 μm wide and 700 μm deep. The design was based on a T-junction configuration, where channel I was intended for the dispersed phase and channel II for the continuous phase. In addition, configurations with additional spacers were explored, incorporating a third channel 700 μm wide that was connected to the main channel for continuous phase (Fig. 1). This approach sought to optimize precision and uniformity in droplet generation.

C. Droplet generation

For the generation of droplets, a 33.5 mM KCl solution was prepared and injected into channel I, using a syringe as the source of the dispersed phase. In parallel, a mixture of mineral oil and 1% Span® 80 was introduced into channel II, acting as a continuous phase. Injections of both phases were performed simultaneously using syringe pumps (NE-300, New Era Pump Systems, USA and KdScientific, 101-CE, Holliston, MA, USA) operating at controlled flow rates of 5 μL min⁻¹ for the dispersed phase and 10 μL min⁻¹ for the continuous phase. The selected flow rates ensured stable droplet formation and were adjusted to maximize the reproducibility of the experiment, and it was verified with an electron magnifier that none of the droplets passed through any electrode at the same time.

D. Contactless Conductivity Detection (C⁴D)

The size of the droplets was monitored in real time using a C⁴D, based on the electronic principles described by Pinheiro et al [6]. The system employed a high-frequency sine wave with an amplitude of 7 Vpp, generated by a function generator (Standford Research Systems model

DS340). The induced current signal was captured by a receiving electrode, converted to voltage, rectified and amplified before being digitized using an A/D interface (National Instruments model NI-USB-6009). The frequency of the sine wave was optimized at 400 kHz to obtain the best analytical response in droplet detection, and the resulting signal was monitored and analyzed through software developed in LabVIEW™.

E. Data analysis

Data analysis focused on the correlation between the frequency of droplet formation and the amplitude of the detected signal, using statistical tools to evaluate the accuracy and reproducibility of the system.

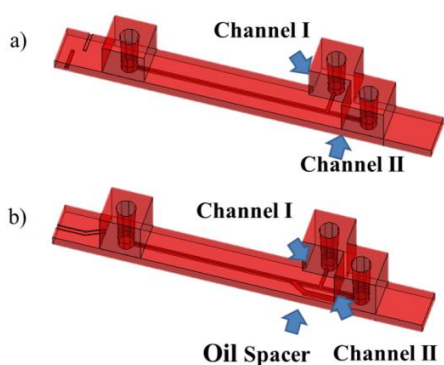


Fig. 1. Scheme showing the configuration of the microfluidic devices (a) without and (b) with spacer.

III. RESULTS

The frequency of droplet passage directly affects the response of the C⁴D and thus its sensitivity. To evaluate the influence of the microfluidic device design on droplet detection, signal amplitude and noise level were measured at a frequency of 400 kHz, keeping the voltage amplitude constant at 7 V_{pp}. Different values of signal-to-noise ratio (SNR), signal amplitude, percentage error and frequency of the recorded peaks were obtained for each type of device (Table 1).

The results show that the inclusion of a spacer in the microfluidic device significantly improves the signal amplitude, with a lower percentage error, compared to devices without a spacer (Fig. 2). In addition, it was observed that, at lower droplet frequencies, the signal is optimal, suggesting better detection of droplets under these conditions.

TABLE I. ANALYTICAL PARAMETERS OBTAINED WITH THE MICROFLUIDIC DEVICE TESTED IN THIS STUDY.

Microchip	Analytical parameters			
	Signal amplitude (mV)	RSD (%)	SNR	Droplet frequency (Hz)
T-junction	4.8 ± 0.9	20.1	7.4	0.288

T-junction + 700 μm channel width spacer	45.0 ± 2.0	4.4	69.7	0.059
--	------------	-----	------	-------

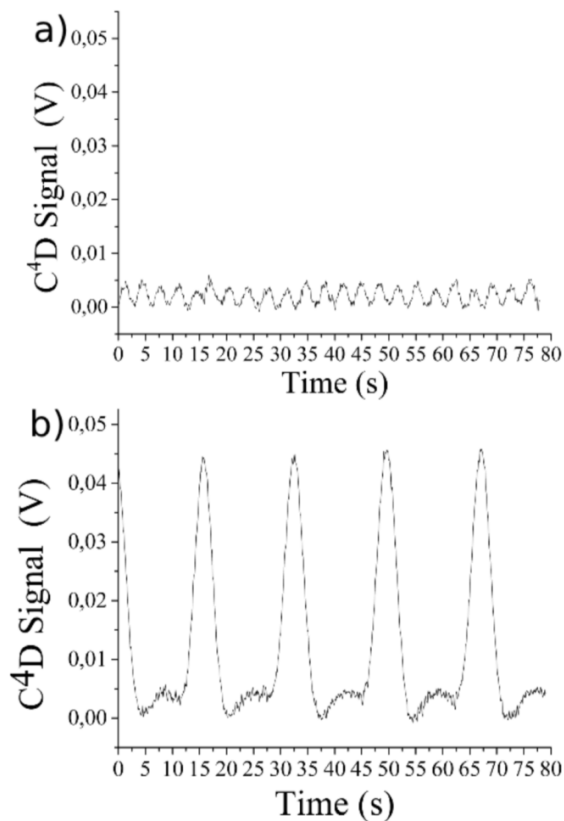


Fig. 2. Contactless conductivity measurements for droplet monitoring for the different microchips designed. Flow rate of continuous phase at 10 μL min⁻¹ and of dispersed phase 5 μL min⁻¹. Detection conditions: 400 kHz and 7 V_{pp}. a) T-junction b) T-junction + 700 μm channel width spacer

IV. DISCUSSION

The designed microfluidic device injects an oil phase into channel 1 and a 33.5 mM KCl solution into channel 2, thereby generating droplets that are monitored in real time by the C⁴D sensor. The results demonstrate that the incorporation of 700 μm spacers into the continuous phase channels markedly enhances the signal amplitude (45 ± 2 mV) in comparison to the channel devoid of a spacer (4.8 ± 0.9 mV). Moreover, the inclusion of spacers significantly reduces the error to 4.44%. The SNR exhibited a notable enhancement with the incorporation of spacers, attaining values of 69.76 for the 700 μm channels in comparison to 7.44 in the channel devoid of spacers. However, the frequency of droplet passage demonstrated a decline with the introduction of spacers.

The findings indicate that 3D-printed microfluidic devices with spacers enhance the precision of droplet detection and affect the frequency of droplet passage. This technology offers significant promise for the advancement of

sophisticated diagnostic systems and presents novel avenues for research in microfluidics and bioanalysis.

V. CONCLUSION

The results obtained suggest that the implementation of spacers on microfluidic chips improves the efficiency of the C⁴D for droplet detection. The higher signal amplitude and lower error rate observed with the use of spacers confirm the initial hypothesis that these components optimize device performance. This study opens new opportunities for the use of C⁴D detection in more complex applications, such as real-time monitoring of controlled drug release and pharmacokinetic studies, areas where precision in the detection of droplet size is crucial. In summary, the results confirm that the implementation of spacers on microchips improves the sensitivity and accuracy of the droplet detection system. These findings have important implications for the development of advanced microfluidic systems and suggest that future research should focus on optimizing materials and designs for specific applications.

ACKNOWLEDGMENT

The authors gratefully acknowledge financial support from the National Agency of Scientific and Technological Promotion (ANPCyT) (grant BID-PICT 2020-04023) and

National Council for Scientific and Technological Research (CONICET).

REFERENCES

- [1] L. C. Duarte, F. Figueredo, C. L. S. Chagas, E. Cortón, and W. K. T. Coltro, "A review of the recent achievements and future trends on 3D printed microfluidic devices for bioanalytical applications," *Anal Chim Acta*, vol. 1299, p. 342429, Apr. 2024, doi: 10.1016/j.aca.2024.342429.
- [2] F. Sala, C. Ficorella, R. Osellame, J. Käs, and R. Martínez Vázquez, "Microfluidic Lab-on-a-Chip for Studies of Cell Migration under Spatial Confinement," *Biosensors (Basel)*, vol. 12, no. 8, p. 604, Aug. 2022, doi: 10.3390/bios12080604.
- [3] A. K. Au, W. Huynh, L. F. Horowitz, and A. Folch, "3D-Printed Microfluidics," *Angewandte Chemie International Edition*, vol. 55, no. 12, pp. 3862–3881, Mar. 2016, doi: 10.1002/anie.201504382.
- [4] S. E. Alavi et al., "Microfluidics for personalized drug delivery," *Drug Discov Today*, vol. 29, no. 4, p. 103936, Apr. 2024, doi: 10.1016/j.drudis.2024.103936.
- [5] L. C. Duarte, C. L. S. Chagas, L. E. B. Ribeiro, and W. K. T. Coltro, "3D printing of microfluidic devices with embedded sensing electrodes for generating and measuring the size of microdroplets based on contactless conductivity detection," *Sens Actuators B Chem*, vol. 251, pp. 427–432, 2017, doi: 10.1016/j.snb.2017.05.011.
- [6] K. M. P. Pinheiro, K. C. A. Rezende, L. C. Duarte, G. F. Duarte-Junior, and W. K. T. Coltro, "Contactless conductivity detection on lab-on-a-chip devices: A simple, inexpensive, and powerful analytical tool for microfluidic applications," in *Handbook on Miniaturization in Analytical Chemistry: Application of Nanotechnology*, Elsevier, 2020, pp. 155–183. doi: 10.1016/B978-0-12-819763-9.00008-8.



3 |

Biosensores

Biosensors

Biossensores

Gold nanostars-based plasmonic platform for photoelectrochemical detection of C-reactive protein

Yeison Monsalve¹
yeisone.monsalve@udea.edu.co

Andrés F Cruz-Pacheco¹
andres.cruz1@udea.edu.co

Jahir Orozco¹
grupo.tandemnanobioe@udea.edu.co

¹Max Planck Tandem Group in Nanobioengineering, Institute of Chemistry, Faculty of Natural and Exact Sciences, University of Antioquia, Complejo Ruta N, Calle 67 No. 52-20, Medellín 050010, Colombia.

Abstract— This study introduces a novel photoelectrochemical (PEC) immunosensor using plasmonic nanomaterials to enhance the detection of C-reactive protein (CRP), an inflammation biomarker. The immunosensor employed disposable electrodes decorated with gold nanostars (AuNSs) and antibodies, enabling specific CRP detection via photocurrent generation at a fixed potential. The biointerfaces' chemical, PEC, morphological, and structural characterization and the detection assay's analytical performance assessment were achieved using microscopic, spectroscopic, chemical, and electrochemical techniques. Characterization showcased high sensitivity in detecting CRP within a linear range of 25 to 800 pg/mL and a limit of detection (LOD) of 13 pg/mL. The biosensor offered the potential for rapid, differential CRP detection, aiding in the early diagnosis of inflammatory diseases and improving patient care.

Keywords—Photoelectrochemical detection, plasmonic nanoparticle, inflammation biomarker, analytical performance

I. INTRODUCTION

Photoelectrochemical (PEC) biosensors are advancing rapidly as analytical tools for quantifying (bio)analytes in samples. PEC biosensors utilize light and photoactive materials to induce charge carriers, participating in redox reactions at the electrode/solution interface [1]. The PEC technique effectively isolates the excitation source (light) from the detection signal (current), substantially minimizing unwanted background noise and resulting in higher sensitivity for bioanalysis compared to conventional methods [2]. However, a limitation arises from the instability of biomolecules under high-energy ultraviolet light stimulation. Integrating plasmonic photoactive nanomaterials excited by near-infrared radiation is a promising strategy to address this issue. They enhance energy conversion efficiency, facilitate charge transfer processes, and minimize biomolecule photodamage, thereby improving the effectiveness of PEC detection. This work reports on a PEC platform using disposable electrodes decorated with nanostructured plasmonic materials to enhance photocurrent signals for detecting C-reactive protein (CRP), a key inflammation biomarker [3], as shown in Figure 1. The proposed biointerface featuring gold nanostars (AuNSs) and antibodies employed soft bioconjugation strategies [4]. While characterization involved microscopic, spectroscopic, chemical, and electrochemical techniques, selective CRP detection used chronoamperometry. This effort is a step toward developing versatile, specific, and sensitive PEC biosensors for clinical diagnosis, particularly biomarker monitoring, with potential applications in low-cost, energy-based point-of-care devices [5].

II. MATERIALS AND METHODS

The synthesis of gold nanoparticles was carried out using the conventional Turkevich method [6]. AuNSs were synthesized through a chemical reduction of gold chloride with ascorbic acid (AA) in the presence of silver nitrate and the previously synthesized gold nanoparticles. Characterization of the

AuNSs included X-ray diffraction (XRD), transmission electron microscopy (TEM), ultraviolet and visible (UV-Vis) spectroscopy, dynamic light scattering (DLS), and electrophoretic light scattering (ELS). The PEC behavior of the biosensing interface involved treating screen-printed carbon electrodes (SPCEs, Metrohm DropSens ref. DRP-110/Oviedo-Spain) by oxidation to generate carboxylic acid groups, followed by modification with AuNSs.

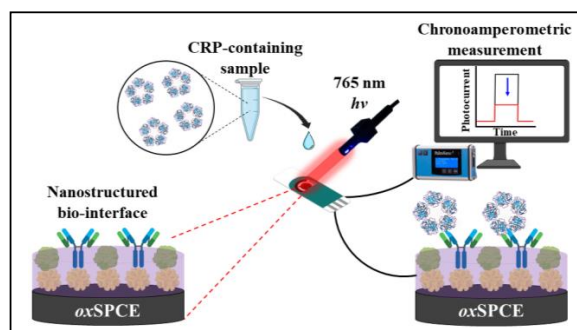


Figure 1. Schematic illustration of the modification of SPCE with AuNSs/anti-CRP to detect CRP by chronoamperometry in a PBS 1X pH 7.4 solution containing 10 mM of ascorbic acid under 765 nm illumination.

The PEC experiments were conducted using a UV LED Spot Curing System and a potentiostat/galvanostat, optimizing various parameters to achieve the best photocurrent signal. The immunosensor architecture was developed by establishing a biofunctional interface with AuNSs and anti-CRP antibodies. The functionalization of anti-CRP was optimized to determine the best time and concentration. Characterization of the biosensing interface included diffuse reflectance UV-vis spectroscopy (UV-vis DRS), Raman spectroscopy, field emission scanning electron microscopy (FE-SEM), atomic force microscopy (AFM), cyclic voltammetry (CV), and electrochemical impedance spectroscopy (EIS). The analytical performance of the immunosensor for detecting CRP was assessed, determining the linear range, sensitivity, specificity, selectivity, reproducibility, repeatability, and stability. The immunosensor's performance was tested in the presence of other related proteins to evaluate its specificity and selectivity. Stability was assessed through repeated measurements and long-term testing over several days.

III. RESULTS

A label-free nano-immunosensor based on AuNSs/SPCE nanobiocomposite was developed for the PEC detection of CRP. AuNSs were synthesized using the seed-assisted growth methodology. The nanoparticles (NPs) and the modified electrodes were characterized through UV-vis spectroscopy, TEM, XRD, DLS, ELS, UV-vis DRS, Raman, FE-SEM, AFM, CV and EIS. The detection of CRP involved monitoring changes in the charge of the redox probe at the electrode/solution interface using the PEC-based device to

evidence the anti-CRPs decorated nanostructured platform-CRP affinity reaction. The PEC transduction principle employed in this immunosensing assay utilized the localized surface plasmon resonance (LSPR) effect of AuNSs to enhance the photoelectric conversion efficiency of the electrode surface. Under 765 nm excitation light, the carbon surface generated electron-hole pairs, which were further amplified by the LSPR effect of the AuNSs, resulting in a substantial increase in the photocurrent response. AA served as a hole scavenger in this PEC immunosensing strategy. When the carbon surface, decorated with AuNSs, was irradiated with the 765 nm light source, photoinduced electrons were generated. These electrons were transferred to the electrode, while the photoinduced holes were scavenged by AA, leading to the generation of a photocurrent.

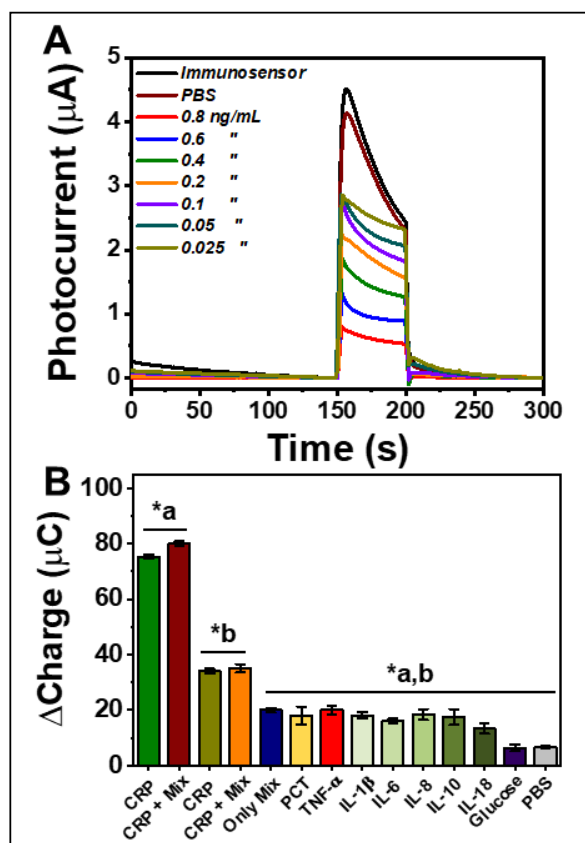


Figure 2. (A) Chronoamperometric signals of the label-free photoelectrochemical nano-immunosensor toward different concentrations of CRP. (B) Immunosenor specificity and selectivity when detecting 400 (a) and 25 pg/mL (b) of CRP, 400 pg/mL PCT, TNF- α , IL-1 β , IL-6, IL-8, IL-10, IL-18, and 100 μ g/mL glucose. * Indicates significant differences with $p < 0.05$ for all interferents and negative control.

The plasmonic PEC biosensing platform demonstrated simplicity, specificity, and selectivity in detecting CRP within a linear range of 25 to 800 pg/mL (Figure 2A), with a limit of detection (LOD) of 13 pg/mL. Moreover, the platform exhibited high specificity and selectivity in the presence of inflammatory biomarkers such as procalcitonin (PCT), tumor necrosis factor alpha (TNF- α), glucose, interleukin-1 β (IL-

1 β), interleukin-6 (IL-6), interleukin-8 (IL-8), interleukin-10 (IL-10), and interleukin-18 (IL-18), as shown in Figure 2B. Additionally, the PEC platform demonstrated acceptable stability over time, with insignificant variations in the signal over 10 days. These clinically significant results underscore the device's high sensitivity for monitoring slight variations in CRP concentration.

IV. CONCLUSION

The developed biosensor, utilizing plasmonic NPs from a PEC-based device, exhibited exceptional analytical performance and helped monitor CRP concentrations of clinical relevance, underscoring their potential for simple, rapid, and differential CRP detection. This approach supports early inflammatory disease detection, facilitates treatment evaluation, and enhances patient care, potentially reducing treatment costs and comprehensive medical care needs.

ACKNOWLEDGMENT

The authors acknowledge MinCiencias for funding the project Validation of a Nanobiosensor to detect SARS-CoV-2 rapidly (Cod. 111593092980). J.O acknowledges financial support from Minciencias, the University of Antioquia, and the Max Planck Society through the Cooperation Agreement 566-1, 2014. The authors also thank EPM and Ruta N for hosting the Max Planck Tandem Groups.

REFERENCES

- [1] X. Xu, Q. Xu, W. Li, F. Xiao, and H. Xu, "From engineered photoactive materials to detection signal amplification strategies in photoelectrochemical biosensing of pathogens: New horizons and perspectives," *Chem. Eng. J.*, vol. 480, no. December 2023, p. 147941, 2024, doi: 10.1016/j.cej.2023.147941.
- [2] R. Li, R. Yan, J. Bao, W. Tu, and Z. Dai, "A localized surface plasmon resonance-enhanced photoelectrochemical biosensing strategy for highly sensitive and scatheless cell assay under red light excitation," *Chem. Commun.*, vol. 52, no. 79, pp. 11799–11802, 2016, doi: 10.1039/c6cc05964c.
- [3] W. Ansar and S. Ghosh, "Inflammation and Inflammatory Diseases, Markers, and Mediators: Role of CRP in Some Inflammatory Diseases BT - Biology of C Reactive Protein in Health and Disease," W. Ansar and S. Ghosh, Eds., New Delhi: Springer India, 2016, pp. 67–107. doi: 10.1007/978-81-322-2680-2_4.
- [4] A. F. Cruz-Pacheco, Y. Monsalve, Y. Serrano-Rivero, J. Salazar-Uribe, E. Moreno, and J. Orozco, "Engineered synthetic nanobody-based biosensors for electrochemical detection of epidermal growth factor receptor," *Chem. Eng. J.*, vol. 465, no. December 2022, 2023, doi: 10.1016/j.cej.2023.142941.
- [5] J. Orozco, "Nanoscience, nanotechnology, and disruptive technologies in the context of precision medicine," *Rev. la Acad. Colomb. Ciencias Exactas, Fis. y Nat.*, vol. 47, no. 183, pp. 221–241, 2023, doi: 10.18257/raccefyn.1895.
- [6] B. V. Enüstün and J. Turkevich, "Coagulation of Colloidal Gold," *J. Am. Chem. Soc.*, vol. 85, no. 21, pp. 3317–3328, 1963, doi: 10.1021/ja00904a001.

Portable biosensing device for *in vitro* diagnostic

Melania Mesas Gómez
Grup of Sensors and Biosensors
Universitat Autònoma de Barcelona
Bellaterra, Spain
0000-0002-3297-1077

Jennifer Marfa
Grup of Sensors and Biosensors
Universitat Autònoma de Barcelona
Bellaterra, Spain
0000-0001-5321-3841

Rosanna Rossi
Grup of Sensors and Biosensors
Universitat Autònoma de Barcelona
Bellaterra, Spain
0000-0002-3656-2908

Anaïxis del Valle
Grup of Sensors and Biosensors
Universitat Autònoma de Barcelona
Bellaterra, Spain
0000-0001-5587-9081

Arnau Pallarès-Rusiñol
BioEcllosion SL
Edifici Eureka
Bellaterra, Spain
0000-0001-9990-148X

Mercè Martí
Institut de Biotecnologia i de
Biomedicina
Universitat Autònoma de Barcelona
Bellaterra, Spain
0000-0002-1846-0043

Juan Carlos Porras
Grup of Sensors and Biosensors
Universitat Autònoma de Barcelona
Bellaterra, Spain
JuanCarlos.Porras@autonoma.cat

Jofre Ferrer-Dalmau
BioEcllosion SL
Edifici Eureka, campus UAB
Bellaterra, Spain
0000-0002-7415-6222

María Isabel Pividori
Grup of Sensors and Biosensors
Universitat Autònoma de Barcelona
Bellaterra, Spain
0000-0002-5266-7873

Abstract— This study presents the development of a portable biosensing device designed for early and accurate disease identification through the quantification of various biomarkers. The device combines magnetic actuation and electrochemical biosensing within a battery-operated portable reader, offering a versatile and agnostic platform capable of quantifying a wide range of biomarkers. This adaptability allows the device to meet emerging diagnostic challenges. The method significantly reduces the time to results, enabling the detection of target biomarkers at low concentration ranges using a simplified analytical procedure for the end-user. This biosensing test is particularly valuable in low-resource settings, where access to gold-standard laboratory tests is limited, and in high-income countries, where it can substantially reduce turnaround times and costs. The proof of concept is validated in this study for a pathogenic bacterium, demonstrated in both immunosensing and genosensing formats.

Keywords— *In vitro* diagnostics (IVD), biosensing devices, biomarker quantification, magnetic actuation, electrochemical biosensing, personalized medicine.

I. INTRODUCTION

The recent pandemic of a communicable disease that spread across international borders globally in a matter of days highlighted the need for *in vitro* diagnostic (IVD) solutions able to provide prompt diagnosis and help implement security and prevention measures to interrupt the transmission chain. IVD also plays an important role not only in reducing disease burden by interrupting the transmission of communicable infectious agents but also in preventing the development of long-term complications in non-communicable diseases. Currently, and more than ever, these tests are a major research field of growing interest among researchers worldwide.

Beside the impact in good health and wellbeing, the global *in vitro* diagnostics (IVD) market was valued at USD 81.3 billion in 2020 and is expected to reach USD 124.6 billion by 2027, growing at a CAGR of 6.3% from 2020 to 2027 [1]. This growth is being driven by the increasing demand for point-of-care IVD devices. The pandemic has significantly increased awareness of the importance of disease diagnosis, while rising disposable income levels are further

fueling market growth. Consequently, there is a strong focus on research aimed at developing IVDs for use at the point of care. These innovations enable rapid screening of patients who require treatment, moving away from the traditional reliance on standard clinical diagnostics performed by highly qualified personnel in centralized laboratories.

For over two decades, the World Health Organization (WHO) has coined the term ‘ASSURED’ (Affordable, Sensitive, Specific, User-friendly, Rapid and Robust, Equipment-free, and Deliverable to end-users) to refer to the ideal characteristics of a diagnostic test for resource-limited settings [2]. Although the original ‘assured’ features remain relevant, with the emergence of digital technology and m-health, future diagnostics should incorporate these elements to create diagnostic platforms that can provide real-time disease control strategies, enhance the efficiency of health care systems, and ultimately improve patient outcomes.

Accordingly, it has been recently revised to include two additional criteria as ‘REASSURED’, including Real-time connectivity and Ease of specimen collection, to design future devices [3]. Although technology has progressed enough to create diagnostic tests that meet these criteria, the challenge remains in developing a ‘Reassured’ test, comparable in analytical performance to the most accurate laboratory tests based on benchtop equipment.

‘Reassured’ tests must have low complexity without any lost in diagnostic accuracy in a format which can be either used in low resource settings where high-quality gold-standard laboratory tests are not available, and in high-income countries to dramatically improve turnaround times for results to reduce costs [4]. The complexity of a test includes the need for user interpretation, the level of training necessary, the number of manual manipulations, the number of user intervention steps required, and the instrumentation requirement [5]. The FDA defines the characteristics that a simple diagnostic test should ideally have [6]. These features have been recently updated [7]. Low complexity for a test includes the end-user interpretation and level of training required, or the number of manual manipulations and intervention steps. In general, the analytical performance and

the quality of the result improve as the complexity for a diagnostic test remarkably increases from lateral flow (LFA), enzyme immunoassay (ELISA) and nucleic acid–amplification test (PCR). Unfortunately, the total assay time and the need for complex bench-top instrumentation which requires laboratory facilities and costly maintenance, also increase.

Three *key cross-cutting technological challenges* have been identified as bottlenecks in ‘Reassured IVD tests’:

(i) the detection of challenging targets, such as low-concentration and high-complexity molecules like nucleic acids (DNA, RNA, miRNA);

(ii) the isolation of these targets from complex specimens; and,

(iii) the development of instrumentation suitable for low-resource settings.

Among these three technological challenges, *the detection of nucleic acids* stands out as particularly difficult, as highlighted by the FDA [7].

During the recent pandemic, PCR [8] emerged as the state-of-the-art and dominant diagnostic test for infectious diseases [9], despite the rapid development of alternative technologies that argue nucleic acid amplification is not always necessary. Surprisingly, this quantitative technique has also been implemented for screening purposes, providing a simple YES/NO binary result, even though the turnaround time can range from hours to days. This demonstrates that nucleic acid amplification, despite its technical complexity and high costs, remains the optimal methodology for screening many pathogens, offering the best balance between maximum sensitivity and practical feasibility. This is a major issue for many diseases that are common in low-resource settings, where the lack of simple and easy-to-use nucleic acid diagnostic tests is a major barrier to timely treatment.

One of the main challenges to making these tests more widely available in low-resource settings is to avoid thermocyclers, which need infrastructure including reliable power supply. In order to solve this barrier, one approach is focused on putting PCR at the point-of-need, by designing a diagnostic kit that includes a hand-held PCR device operated by either batteries or solar energy [5], that can potentially be used to screen for communicable diseases that normally require PCR as a gold standard.

The second technological challenge, *the isolation of targets from complex specimens*, involves the use of direct, unprocessed samples such as capillary blood (fingerstick), venous whole blood, nasal swabs, throat swabs, or urine.

To overcome this challenge, solid-phase separation techniques, such as magnetic particles (MPs), can be employed. These particles bind to the targets of interest, allowing them to be concentrated before testing. This approach not only preconcentrates biomarkers from complex samples but also removes interfering matrices, thereby enhancing the sensitivity and specificity of IVDs. Since the early reports on magnetic separation technology [10], magnetic particles have been recognized as a powerful and versatile preconcentration tool in a wide range of analytical and biotechnology applications.

This technology has been widely incorporated for researchers worldwide in classical methods in biomolecular

tools and in benchtop instrumentation. Beside the amazing properties of MPs, the main drawback is that magnetic separation is usually performed in less than 1 mL of sample, due to i) the high cost of biological-modified MPs and ii) the issues related with the magnetic actuation of large volume of samples.

Regarding the third technological challenge related to *instrumentation requirements* [7], no electronic or mechanical maintenance beyond simple tasks, such as changing a battery or power cord, are amenable with low resource settings.

These features are compatible with biosensors based on electrochemical transducers. In recent years, electrochemical biosensors have gained popularity for their sensitivity, rapid analysis, and cost-efficiency. This sensitivity is particularly valuable for precise testing and early disease diagnosis, as it allows for the detection of low concentrations of biomolecules. Moreover, real-time connectivity can be easily achieved with this kind of device. However, despite extensive research in the field, only a few examples of these biosensors are currently available on the market, with the most popular being those based on enzymatic reactions, such as glucose biosensors. These devices allow untreated capillary blood (fingerstick) to be directly processed without the need for washing steps to remove excess reagents.

Although enzymatic biosensors are widely used and popular, significant improvements are still needed to achieve analytical simplification in immunosensors and DNA biosensors. This remains a major bottleneck and may limit their accessibility for end users in the developing world.

This study presents the development of an innovative biosensing device that effectively addresses the three key challenges in diagnostic testing. By combining magnetic actuation with electrochemical biosensing, the device can detect targets in complex specimens without compromising analytical performance or test accuracy. It offers a more efficient and cost-effective solution compared to traditional methods, with the flexibility to adapt to emerging challenges with minimal technological adjustments. The IVD platform is designed for versatile use, proving valuable in low-resource settings where high-quality gold-standard laboratory tests are unavailable, as well as in high-income countries to enhance turnaround times and reduce healthcare costs.

II. EXPERIMENTAL SECTION

A. Instrumentation

The platform to perform RDTs (Rapid Diagnostic test) composed by two components, as outlined in Fig 1 (and the procedure describes in PCT/EP2022/071078 ‘Device for Assay System, System and Method’)

- Disposable cartridge, including i) the sample holder containing all the reagents lyophilizate, including modified-magnetic particles with the bioreceptor, to preconcentrate the biomarker presents in the sample, and the HRP-labelling reagent, in which the reaction takes place in 15 min ii) the cartridge containing the microfluidic and the electrode and in which the magnetic actuation is performed, while the excess of sample and reagents are removed by capillarity.

- Digital reader, including the external magnet and the interface between the cartridge and the digital reader itself which allows the quantitative electrochemical readout (cathodic current obtained by applying a predetermined potential) in less than one minute, reporting the levels of biomarker in concentration units. Data may be collected directly from the display of the digital reader and sent by Bluetooth to the App. Accordingly, any potential target specifically attached to a magnetic particle and labelled with HRP in the sample holder, can be potentially quantified with this approach.

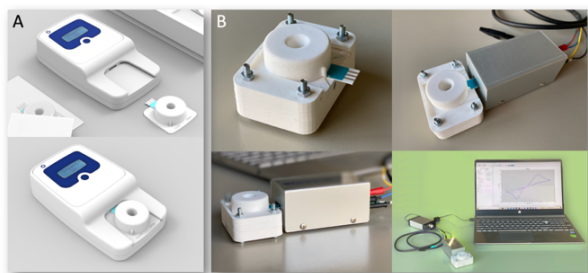


Fig. 1. Panel A. Biosensing device platform described in PCT/EP2022/071078. The figure shows the two components: i) Disposable cartridge and ii) Digital reader for the readout, including the external magnet. Data may be collected directly from the display of the digital reader and sent by Bluetooth to an App. Panel B. Laboratory proof of concept, containing a cartridge for the magnetic actuation. The cartridge is connected to a portable commercial bipotentiostat (DropSens, Spain). In the proof of concept, the electrochemical readout is performed in a laptop computer operated, under the DropView 2.2 software, in which the portable bipotentiostat is connected by a USB port.

B. Validation of the biosensing device at laboratory conditions

The biosensing device (cartridge and reader) is agnostic and can quantify a wide selection of biomarkers (Figure 2), regardless of their type, in a straightforward process for the end user. The specific reaction is performed in a sample holder, in a one-step incubation, in which the sample is added to the lyophilizate reagents (the magnetic particles and the conjugate). This process will be assessed using a wide range of biomarkers of different nature. In this instance, the pathogenic bacteria *Mycobacterium sp* is taken as a model, in immunosensing and genosensing approach.

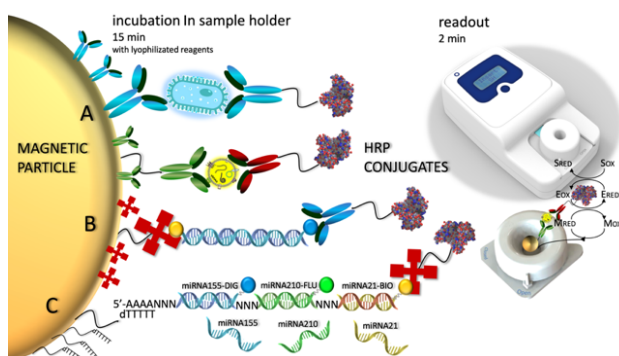


Fig. 2. Molecular strategies integrated in the core of the technology, showing the molecular detail for the specific reactions performed on the sample holder, involving magnetic particle reaction and HRP labelling, and the electrochemical readout on the IVD platform, which is common for all kind of targets, regardless of their nature.

III. RESULTS AND DISCUSSION

A. Electrochemical magneto immunosensing for the quantification of *Mycobacteria*

One of the main objectives of this study is to achieve analytical simplification, aimed at minimizing user intervention while maintaining analytical performance. This work is also focused on detecting *M. fortuitum* through an amperometric readout using a user-friendly handheld electrochemical device with an integrated internal potentiostat. The disposable cartridge encompasses both the microfluidic system and the electrode, enabling magnetic actuation and efficient removal of excess samples and reagents. Notably, the same solution serves a dual role in both washing and catalyzing the reaction through the HRP enzyme (referred to as the cartridge solution). As a result, the need for using multiple buffers is eliminated, streamlining the process and reducing time, making it simpler for the end-user. Additionally, the cartridge design allows for the use of a small solution volume, up to 300 μL .

Fig. 3. Panel A shows the calibration plot from 0 to 2.2×10^6 CFU mL^{-1} for the detection of the *M. fortuitum* in hemodialysis water with the electrochemical immunosensor. The data was fitted with a non-linear regression (Sigmoidal 4PL, GraphPad Prism Software v 10.0.1, $R^2 = 0.9987$) and the limit of detection (LOD) were calculated, resulting in a value of 4.3×10^3 CFU mL^{-1} , by processing 0.1 mL of sample.

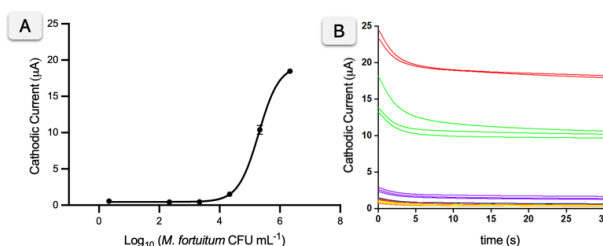


Fig. 3. Panel A. Calibration plot for the electrochemical biosensing of *M. fortuitum* from 0 to 2.2×10^6 CFU mL^{-1} with the magneto-actuated electrochemical immunosensor in water samples ($R^2 = 0.9987$). (n = 3). Panel B. Raw data obtained from the amperometric measurements, performed at applied potential = -0.150 V (vs. Ag/AgCl). The current value at the steady current (30 s) was used for the calibration plot.

To further improve the LODs, this work introduces a new approach that combines filtration with direct immunomagnetic separation (IMS), enabling the processing of larger sample volumes (up to 100 mL) by retaining and isolating bacteria on the filters for subsequent IMS, as outlined in Figure 4.

Selecting the appropriate filter material is crucial to ensure a swift filtration workflow, a good removing of the bacteria retained in the filters by the magnetic particles, while minimizing nonspecific adsorption of all the reagents (including the enzymatic conjugate) during the one-step incubation on the filters. The biosensor integrating the novel preconcentration method in a one-step incubation (by filtering 100 mL of sample), and further electrochemical immunosensor, shows LODs as low as 5 CFU mL^{-1} [11]. Compared with the electrochemical biosensor without the integration of the preconcentration method, an impressive 10^3 fold improvement was achieved.

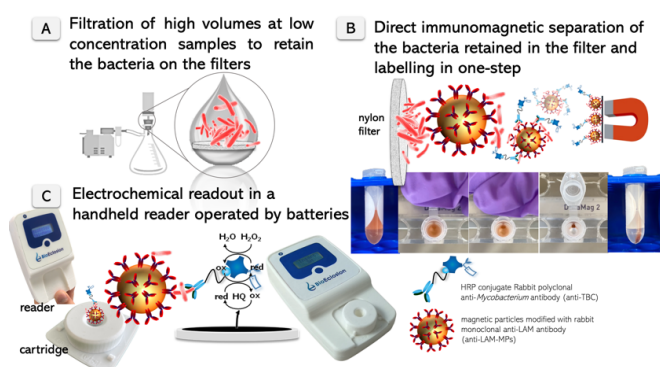


Fig. 4. Schematic representation of A) filtration, B) immunomagnetic separation of the bacteria retained in the filters and labelling in one-step, followed by C) electrochemical readout for the detection of *M. fortuitum* in hemodialysis water performed in a cartridge and handheld device. In Panel B, experimental details are presented, showing how the filter is positioned on the Eppendorf tube for immunomagnetic separation. The photos in Panel B were captured in 1-second frame sequences.

B. Electrochemical magneto genosensing for the quantification of Mycobacteria

To study the analytical performance of the electrochemical magneto-genosensor for the detection of *mycobacteria*, a calibration plot with attenuated samples of *M. bovis* BCG-Pasteur strain at different concentrations ranging from 0 to 2.6×10^7 were analyzed. To enhance sensitivity, this study focused on the genetic amplification of the bacterial genome on magnetic particles [12]. The initial exploration involved the double-tagging PCR method developed in our labs [12,13,14]. The results for the detection of the amplicons obtained after the double-tagging PCR with each set of primers *IS6110* (blue), and *gyrB* (red) were shown in Figure 4, Panel A and B, respectively.

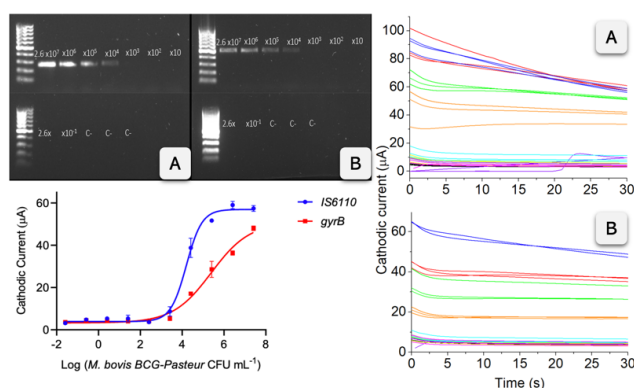


Fig. 5. Calibration plot for the electrochemical magneto-genosensing and gel electrophoresis of the amplicons obtained by the primers coding for *IS6110* (blue and A) and *gyrB* (red and B) by processing *M. bovis* BCG-Pasteur at different concentrations ranging from 0 to 2.6×10^7 CFU mL⁻¹. The error bars show the standard deviation for n=3.

The electrophoresis gel image shows the results for the detection of the *IS6110* and *gyrB* genes across various concentrations of the *M. bovis* BCG-Pasteur strain. In both panels A (*IS6110*) and B (*gyrB*), a unique clear band are observed at the expected MW corresponding to different bacterial concentrations, ranging from 2.6×10^7 down to 2 CFU. The negative controls (indicated as C-1) show no signal, ensuring that there was no non-specific amplification or primer dimer formation. The intensity of the bands decreases

as the bacterial concentration decreases, which is consistent with the expected results. Notably, the visual LOD appears to be at 10^4 CFU, as this is the lowest concentration where distinct bands are still visible for both genes. The raw data from the amperometric measurements, which correlate with these results, is detailed in Figure 4 (inset panels). The data were analyzed using a nonlinear regression, the four-parameter logistic curve (Sigmoidal 4-PL, GraphPad Prism Software, v.8.0) with values of $R^2= 0.9909$ and $R^2= 0.9815$, employing the *IS6110* and *gyrB* amplicons, respectively. The LOD was calculated for each calibration curve by processing of the negative controls (n=20) leading a promising LODs as low as 117 CFU mL⁻¹ for *gyrB* gene, and 518 CFU mL⁻¹ for *IS6110*.

IV. CONCLUDING REMARKS

The innovative aspects of the device presented in this study integrate key components aimed at achieving simplification and portability while maintaining outstanding analytical performance. The method offers a robust preconcentration strategy using magnetic particles, facilitating the efficient capture and concentration of targets. This approach significantly enhances the detection capabilities, especially in complex matrices. The user-friendly cartridge design minimizes user intervention, improving ease of use and reproducibility, which is critical for consistent results in diverse settings. The study also highlights the successful integration of both immunosensing and genosensing approaches into the platform. Additionally, the handheld electrochemical readout, powered by batteries, enables on-site and point-of-care testing, marking a significant advancement in electrochemical biosensing applications. This portability is especially beneficial in low-resource settings where traditional laboratory infrastructure may be lacking.

ACKNOWLEDGMENT

This research was funded by the Ministry of Science, Innovation and Universities, Spain (Projects PID2019-106625RB-I00/AEI/10.13039/501100011033 and PID2022-136453OB-I00) and from Generalitat de Catalunya (2017-SGR-220, 2021SGR-00124).

REFERENCES

- [1] Global In Vitro Diagnostics Market - Forecasts from 2022 to 2027 (14/01/23) Retrieve from <https://www.researchandmarkets.com/reports/5576462/global-in-vitro-diagnostics-market-forecasts#product--toc>.
- [2] Mabey D et al, 2004. Nat Rev Microbiol 2:231-40
- [3] Land KJ et al, 2019. Nat Microbiol 4, 46–54.
- [4] Smith S et al, 2018. RSC Adv 8, 34012–34.
- [5] LaBarre P et al, 2011. PLoS ONE 6:e19738.
- [6] Food and Drug Administration, 2008. Clinical Laboratory Improvement Amendments of 1988 (CLIA) Waiver Applications for Manufacturers of In Vitro Diagnostic Devices.
- [7] Food and Drug Administration, 2020. Recommendations for Clinical Laboratory Improvement Amendments of 1988 (CLIA) issued on January 30, 2008.
- [8] Mullis K et al, 1987. Methods Enzymol 155:335–50.
- [9] Millat-Martinez P et al, 2021. Lancet Infect Dis 21: 629–36.
- [10] Rembaum A. et al, 1982. J Immunol Methods 52:341-51.
- [11] Mesas Gómez, M. et al, 2024. Sensors and Actuators B: Chemical 403: 135211.
- [12] Lermo A et al, 2007. Biosens Bioelectron 22:2010-17.
- [13] Lermo A et al, 2008. Biosens Bioelectron 23,1805-11.
- [14] Brasil PR et al, 2009. Anal Chem 81, 1332–39.

Traffic light-based point-of-care test for the rapid stratification of fever syndromes

Melania Mesas Gómez
Grup of Sensors and Biosensors
Universitat Autònoma de Barcelona
Bellaterra, Spain
0000-0002-3297-1077

Anaïxis del Valle
Grup of Sensors and Biosensors
Universitat Autònoma de Barcelona
Bellaterra, Spain
0000-0001-5587-9081

Arnau Pallarès-Rusiñol
BioEcllosion SL
Edifici Eureka, campus UAB
Bellaterra, Spain
0000-0001-9990-148X

Mercè Martí
Institut de Biotecnologia i de Biomedicina
Universitat Autònoma de Barcelona
Bellaterra, Spain
0000-0002-1846-0043

Bàrbara Baró
IsGlobal, Hospital Clínic
Universitat de Barcelona
Barcelona, Spain
0000-0001-7780-1744

Jofre Ferrer Dalmau
BioEcllosion SL
Edifici Eureka, campus UAB
Bellaterra, Spain
0000-0002-7415-6222

Quique Bassat
IsGlobal, Hospital Clínic
Universitat de Barcelona
Barcelona, Spain
0000-0003-0875-7596

Mària Isabel Pividori
Grup of Sensors and Biosensors
Universitat Autònoma de Barcelona
Bellaterra, Spain
0000-0002-5266-7873

Abstract— Recent evidence highlights the significance of sTREM-1 and Ang-2 as quantitative biomarkers for assessing disease severity, treatment response, and outcomes in various conditions, including malaria, pneumonia, COVID-19, among others fever syndromes. Elevated sTREM-1 levels have shown strong correlations with disease severity, multiple organ dysfunction, and mortality. To aid in risk stratification, patients in this study were classified into three groups based on their sTREM-1 levels using the WHO-proposed traffic light color system. A threshold value of 239 pg mL⁻¹ represented the ‘green light’, indicating low risk, while levels exceeding 629 pg mL⁻¹ were designated as ‘red light’, signifying an urgent need for admission. An intermediate ‘yellow light’ indicated further monitoring. In this paper, we present a rapid test integrating magnetic separation and electrochemical biosensing on a portable device operated by batteries. Within less than one minute, the digital reader provides quantitative readout of the biomarker levels in pg mL⁻¹, which is then displayed on the device's screen and transmitted to the accompanying App via Bluetooth. The device's performance in classifying sTREM-1 levels is presented, demonstrating excellent readout results with a short 15-minute incubation step and a swift 1-minute readout process. This innovative point-of-care test holds great promise for aiding clinicians in rapid risk stratification and timely decision-making, potentially enhancing child survival outcomes and improving patient management in a variety of fever syndromes and specific diseases.

Keywords— Fever, infection, triage, clinical trial, rapid screening test, hand-held reader, sTREM-1, Ang2

I. INTRODUCTION

The number of child deaths is rapidly decreasing worldwide, from over 17 million annual deaths in the 1970's to around 5.2 million in 2019 [1]. However, such impressive progress needs to be nuanced, as significant differences according to geographical regions remain. Child mortality reductions have been comparatively modest in low- and middle- income countries, which now account for up to 99% of all child deaths [2,3], a striking reminder of the many inequities that impair global health. In this context, infectious

diseases remain a leading cause of death among children under the age of 5, particularly in Sub-Saharan Africa and Southern Asia, accounting for nearly 2/3 of all global child deaths (5 %) [4]. Currently, the most common infectious causes of child mortality are pneumonia (15 % of all under 5 deaths), diarrheal diseases (8.3 %), malaria (5 %), neonatal sepsis (7 %), meningitis (2 %), and measles (2 %), all of which are readily preventable (through vaccines or other preventive measures), or curable (with antibiotics or antimalarials). Indeed, most infectious diseases are not fatal if they are recognized early in the course of illness and rapidly treated once detected by the health system. However, the ongoing failure to effectively manage infections in low-income settings continues to result in the death of a child every 10 seconds [2]. The cardinal signal of most infectious diseases is fever, one of the most common symptoms that lead people to seek health care and hospital admission, with > 1 billion annual episodes globally. When triaging sick patients, and beyond assessing clinical severity, efforts have traditionally focused on identifying the underlying pathogen (etiological diagnosis), to better target therapeutic interventions. In low-income countries, where therapeutic resources are limited, this "focus on the pathogen" has been driven by the necessity to identify the most lethal infections, such as bacterial infections and malaria, that are most likely to respond to specific treatments including antibiotics and antimalarials. Indeed, target product profiles have been developed for this purpose [5]. Moreover, and in the context of the global problem of antibiotic overuse, pathogen-based diagnostic approaches do not reduce antibiotic prescription and may even increase their inappropriate use [6].

The host response plays a crucial role in determining both the onset and outcome of severe infections. A growing body of evidence indicates that life-threatening infections share common pathways in the host response, where the function and integrity of the endothelium are compromised (microvascular dysfunction), ultimately leading to end-organ dysfunction and death [7]. The endothelium is the largest interconnected organ in the human body, linking all vital

organs. Endothelial cell activation and subsequent loss of integrity is a common pathway of injury induced by multiple life-threatening infections such as malaria, pneumonia (including COVID-19), toxic shock, dengue, sepsis, among many others [8]. Thus, these dysregulated host responses to infection, which trigger microvascular injury regardless of the infection's cause (i.e., pathogen-agnostic mechanisms of disease) [8], appear to be a common phenomenon linking various diseases. Strong evidence suggests that measuring mediators of these pathways at the initial clinical presentation (as levels of sTREM-1 or Ang-2) can reliably identify individuals at risk of severe and fatal infections. Thus, the breakthrough is to use the host immune and endothelial activation as an 'in-vivo biosensor' to guide triage and management decisions, with more accuracy than previously used approaches. The novelty lies here in the possibility to connect diagnosis and treatment through the same biological pathway, to both anticipate outcome and guide management decisions, bypassing inefficiencies in current triaging practices.

These markers have already been integrated into a 'near patient' 1-hour multiplex diagnostic platform (Ella™) [9], demonstrating clear potential for early identification of at-risk sick children who are most likely to benefit from intensive care, antimicrobials, and potentially novel therapeutic agents. However, this approach is costly and requires significant laboratory infrastructure, making it unsuitable for many low-resource settings. To overcome these challenges, triaging aids must specifically address all these critical gaps.

We propose the use of a point-of-care (PoC) biosensor for detecting 'severity biomarkers' of endothelial and immune activation as a risk-stratification strategy. By quantifying these prognostic biomarkers, this biosensor could effectively risk-stratify fever syndromes from all causes, accurately identifying patients with severe illness or those at risk of progressing to life-threatening conditions. This approach could significantly enhance fever management globally, leading to a substantial reduction in mortality, disability, and healthcare costs (Figure 1).

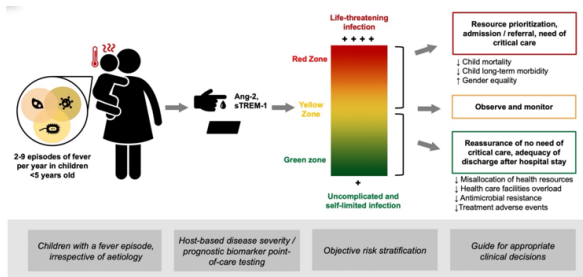


Fig. 1. Conceptual framework for a Rapid Triage Test to risk-stratify sick children.

II. EXPERIMENTAL SECTION

A. Instrumentation

The RDT platform (and the procedure describes in PCT/EP2022/071078 'Device for Assay System, System and Method') is composed by two components: A) Disposable cartridge, including i) the sample holder containing antibody-modified magnetic particles and labelled-antibody which binds the biomarker (sTREM-1) in 15 minutes, and ii) the

cartridge containing the microfluidic and the screen-printed electrode and in which the magnetic actuation is performed, while the excess of sample and reagents are removed by capillarity, as disclaimed in PCT/EP2022/071078. B) Digital reader: including the external magnet and the interface between the cartridge and the digital reader itself which allows the electrochemical readout in less than one minute. The output of the device provides a traffic light-based system for risk stratification. The quantitative data may be collected directly from the display of the digital reader and sent by Bluetooth to the App.

B. Antibodies

Various commercial reagents targeting the sTREM-1 has been selected and experimentally tested. The TREM1 Mouse anti-Human (Clone 193015, R&D Systems™) is a monoclonal antibody specific for human sTREM-1, and it was employed as the capture antibody to immobilize sTREM-1 from samples onto magnetic particles. A Recombinant Rabbit Monoclonal Anti-TREM1 (Abcam) served as a detection antibody, with its specificity and different species origin offering the advantage of preventing cross-reactivity. Additionally, a Human TREM-1 Antibody, Polyclonal Goat IgG (R&D Systems™), could serve as either a capture or detection antibody in a sandwich ELISA format. Moreover, a Human TREM-1 Biotinylated Antibody, Polyclonal Goat IgG (R&D Systems™), was used due to the typical pairing of biotinylated antibodies with streptavidin-HRP for the detection of captured antigens.

III. RESULTS AND DISCUSSION

A. Immobilization of commercial antibodies on magnetic carriers

Antibodies were covalently immobilized onto the surface of Dynabeads® M450 tosylactivated magnetic particles (MPs) in a procedure designed improve the antibody-antigen interactions, as shown in Figure 2.

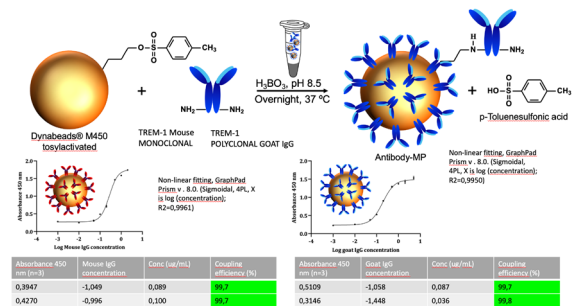


Fig. 2. Study of the efficiency for the covalent immobilization of antibodies on tosylactivated magnetic particles. The figure presents the results for the successful covalent immobilization of mouse monoclonal and goat polyclonal antibodies against TREM-1 onto Dynabeads® M450 magnetic particles. The graphs display the non-linear fitting (sigmoidal, 4PL model) of antibody concentration versus absorbance at 450 nm, with R-squared values of 0.9961 and 0.9950 for mouse and goat antibodies, respectively. The high coupling efficiencies (99.7% for mouse IgG and 99.8% for goat IgG) demonstrate the efficacy of the immobilization process under the optimized conditions of pH 8.5 at 37 °C, with the specific interactions resulting in stable, covalently attached antibodies on the particle surface, ready for subsequent applications. N=3.

The tosyl groups on the MPs, due to their electrophilic nature, can form stable covalent bonds with nucleophilic

amine groups present on antibodies. These amine groups are typically located on the lysine residues alongside the antibody structure. The immobilization process is optimized by conducting the reaction in a basic environment (pH 8.5) using a boric acid buffer and allowing the reaction to proceed at 37°C, commonly overnight, to maximize binding efficiency. The remaining antibodies were quantitatively analyzed through non-linear regression using a 4 Parameter Logistic (4PL) model, yielding sigmoidal curves that represent the binding affinity and saturation of the antibodies on the MPs. The absorbance was measured at 450 nm, with the mouse monoclonal IgG and goat polyclonal IgG showing nearly complete coupling efficiencies of 99.7% and 99.8%, respectively. These high efficiencies indicate that almost all the antibodies were successfully bound to the MPs, confirming the effectiveness of the immobilization procedure.

B. Design of the assay format

The rational design of an immunoassay is critical for enhancing diagnostic accuracy and sensitivity. Combining monoclonal, polyclonal, and recombinant antibodies broadens the spectrum of epitope recognition, markedly improving the assay sensitivity and the probability of detecting antigens, even those present at minimal concentrations, as is the case of TREM-1 target. Such an approach is crucial when dealing with low-abundance biomarkers, where signal amplification becomes essential. The integration of the biotin-streptavidin system, especially when using polyHRP, escalates the signal manifold, a key factor for the assay lower limit of detection. The versatility provided by these formats enables assays to be tailored for a specific sensitivity, specificity, and efficiency. Thus, the strategic selection of antibody formats and conjugation methods allows for the crafting of highly adaptable ELISA platforms, accommodating a wide range of diagnostic requirements for the point-of-care design.

Figure 3 illustrates different formats of commercial reagents employed in the magneto-ELISA platform, using a combination of antibodies for capturing and detecting the target proteins.

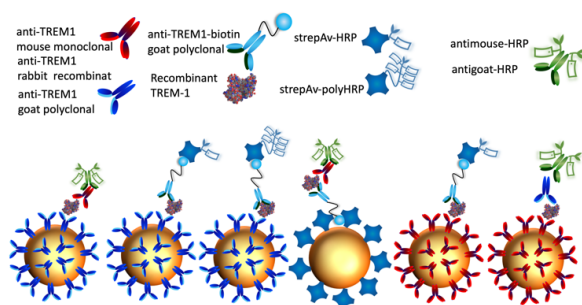


Fig. 3. Different formats evaluated for the detection of TREM-1 using commercial reagents in the magneto-ELISA platform.

These different formats enable the development of a robust, sensitive, and specific assay for the detection of sTREM-1, crucial for the proposed point-of-care test performance. The use of these commercial reagents and formats suggests a sandwich ELISA-type approach on a magneto-ELISA platform, aiming for high-throughput and accurate detection of biomarkers in various sample types. Among the different formats outlined in Figure 3, the one showing superior analytical performance, as illustrated by the Figure 4, employs a combination of anti-TREM1 antibodies

and streptavidin-polyHRP (streptavidin conjugated to polymeric horseradish peroxidase) for the detection of sTREM-1. In this optimized assay, recombinant anti-TREM1 rabbit monoclonal antibodies are used as capture antibodies, providing high specificity due to their monoclonal nature. The detection is conducted using goat polyclonal antibodies biotinylated to interact with the streptavidin-polyHRP, enhancing the signal due to the multiple HRP enzymes on each streptavidin molecule. This allows for a robust amplification of the signal, facilitating the detection of lower antigen concentrations. The optimized conditions for the magneto-ELISA assay, involve the use of a recombinant anti-TREM1 rabbit monoclonal antibody for capturing sTREM-1 proteins at a concentration of 10^6 magnetic particles (MPs) per assay. For the detection of captured proteins, a biotinylated anti-TREM1 goat polyclonal antibody is used at 0.2 μg per assay. The signal is then amplified by streptavidin-polyHRP, which is used at an amount of 2 ng per assay, indicating a highly sensitive assay configuration that maximizes signal output while minimizing reagent use.

C. Optimization of the point of care device

The reduction of time and simplification of the analytical procedure in diagnostic assays are critical features in the development of PoC testing platforms. The significance of these improvements lies in their direct impact on patient care and workflow efficiency in healthcare settings:

- Rapid decision-making: shorter assay times facilitate quicker clinical decision-making, which is crucial in acute and emergency care settings. faster results enable prompt initiation of appropriate treatments, potentially leading to improved patient outcomes.

- Increased throughput: simplifying and accelerating the testing process allows for a greater number of samples to be processed within the same timeframe, thereby increasing the throughput of diagnostic laboratories.

- Accessibility: simplified assays that can be conducted rapidly are more accessible to smaller clinics or resource-limited settings where complex equipment and specialized personnel may not be available.

- Quick turnaround times for test results can improve patient experience and compliance, particularly for outpatient procedures or in community health programs.

Beside the optimization of reagent concentration, selection of reagents and formats, in this study, three different assay timings were compared: "60-60-30," "15-30," and "15-10," which represent the incubation times in minutes for various steps in the immunoassay process.

In conclusion, the "15-10" format would be expected to provide a substantial increase in efficiency, making it a favorable option for PoC applications. It suggests that the necessary interactions between antibodies and antigens, along with the subsequent signal development, can occur effectively in a significantly reduced timeframe. Implementing such optimized protocols in clinical settings can transform patient care by providing timely diagnoses and enabling immediate clinical response, which is critical for conditions requiring urgent intervention.

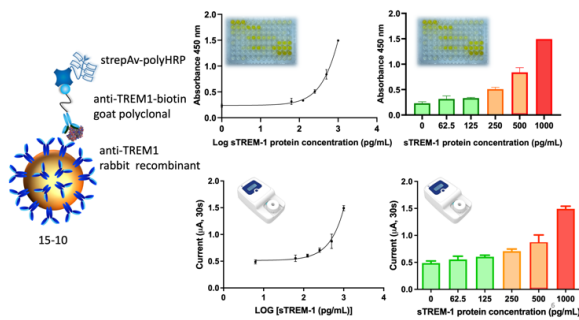


Fig. 4. Comparative analysis of optimized assay conditions in magneto-ELISA and PoC platforms. This figure illustrates the optimized conditions for the detection of soluble triggering receptor expressed on myeloid cells 1 (sTREM-1) using both magneto-ELISA and PoC platforms. The assay employs anti-TREM1-biotin goat polyclonal antibodies for detection and anti-TREM1 rabbit recombinant antibodies for capturing sTREM-1, combined with streptavidin-polyHRP for signal amplification. The "15-10" designation indicates the reduced incubation periods (in minutes) for each step, significantly decreasing overall assay time while maintaining high analytical performance. The upper graphs show ELISA absorbance results across a log range of sTREM-1 protein concentrations, while the lower graphs display corresponding PoC electrochemical detection, with current measured in microamperes (μA). The robust increase in signal with higher antigen concentrations validates the efficacy of the optimized "15-10" assay for quick and sensitive sTREM-1 detection, able to detect the concentration of clinical interest. $N=3$

D. Evaluation on different matrix

Figure 5 describes an experimental validation of a diagnostic assay performed before the optimization phase, where various biological matrices—PBS (phosphate-buffered saline), serum, plasma, and whole blood—were tested to assess the assay's performance. A standard addition, often referred to as 'spiking', was used to evaluate the assay's ability to detect recombinant soluble TREM-1 (sTREM) across these different sample types. In this context, 'spiked' refers to the intentional addition of a known quantity of recombinant sTREM-1 to the biological samples to create a controlled increase in analyte concentration. This approach is often used to simulate the presence of the analyte in real-world samples and to validate the sensitivity and accuracy of the assay. The performance is quantified by measuring the cathodic current (in microamperes, μA) which is directly related to the concentration of the detected analyte.

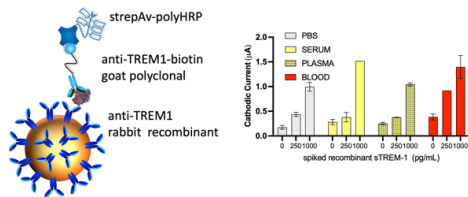


Fig. 5. Pre-optimization validation of sTREM detection assay in biological matrices. This figure shows the results of a diagnostic test ability to detect varying concentrations of spiked recombinant sTREM-1 in different biological matrices: PBS, serum, plasma, and whole blood. The bar graph illustrates the cathodic current response, measured in microamperes (μA), corresponding to the assay's performance at each sTREM-1 concentration level. Notably, the assay demonstrates a robust ability to identify sTREM-1 with excellent performance across all matrices, including the complex matrix of whole blood. $N=3$.

IV. CONCLUDING REMARKS

In this study, we have demonstrated the potential of a novel PoC platform based on electrochemical biosensing for

the rapid and sensitive detection of sTREM-1, key biomarkers associated with severe infections and disease outcomes. The platform enables swift risk stratification, providing crucial information in low-resource settings. The traffic light-based system and Bluetooth-enabled digital reader facilitate easy interpretation and immediate decision-making, which is critical in clinical settings. The results highlight the efficiency of the antibody immobilization process on magnetic particles, ensuring high coupling efficiencies for both mouse and goat antibodies, confirming the efficacy of the immobilization procedure. Furthermore, the strategic selection and combination of antibodies in different formats have demonstrated superior analytical performance, especially using a sandwich immunoassay. This approach ensures high throughput and accurate detection of sTREM-1, even in low-concentration samples. Future studies will focus on integrating the current 15-10 min assay steps into a single 15-minute procedure by producing custom monoclonal antibodies modified with polyHRP, which are not commercially available. This advancement aims to streamline the process, further reducing the assay time while maintaining high sensitivity and specificity. Additionally, further research will include the study of Ang-2 alongside sTREM-1, exploring the potential for multiplexing these two biomarkers. This approach could provide a more comprehensive risk stratification tool, enhancing the diagnostic capabilities of the point-of-care device in detecting severe infections and guiding timely clinical interventions. By providing clinicians with quick and reliable stratification data, this platform can significantly improve patient outcomes, especially for conditions requiring urgent intervention.

ACKNOWLEDGMENT

EChLiBRiST – Enhancing Children's Lives with Biomarkers for Risk Stratification and Triage, is a consortium of 13 institutions from Europe, Africa and North America convened to develop and clinically validate a quantitative point-of-care test for the measurement of severity biomarkers to improve risk stratification of fever syndromes and thus, enhance child survival. Project funded under the European Union's Horizon Europe research and innovation programme under the HORIZON-HLTH-2021-DISEASE-04 call (Project reference 101057114) The Ministry of Science, Innovation and Universities, Spain (Projects PID2019-106625RB-I00/AEI/10.13039/501100011033 and PID2022-136453OB-I00) and from Generalitat de Catalunya (2017-SGR-220, 2021SGR-00124) are also acknowledged.

REFERENCES

- [1] United Nations Inter-agency Group for Child Mortality Estimation (UN IGME), Levels & Trends in Child Mortality. Report 2019. Estimates developed by the UN Inter-agency Group for Child Mortality Estimation (Accessed on 11.01.2020, at <https://childmortality.org/reports>). 2019: New York.
- [2] Global Burden of Disease Child Mortality Collaborators. Lancet, 2016. 388(10053): p. 1725-1774.
- [3] Lawn, J.E., et al. Lancet, 2014. 384(9938): p. 189-205.
- [4] Liu, L., et al. The Lancet, 2015. 385(9966): p. 430-440.
- [5] Dittrich, S., et al. PloS one, 2016. 11(8): p. e0161721.
- [6] Rao, S., et al. JAMA Netw Open, 2021. 4(6): p. e2111836.
- [7] Ghosh, C.C., et al. Proc Natl Acad Sci U S A, 2016. 113(9): p. 2472-7.
- [8] Mikacenic, C., et al. PloS one, 2015. 10(10): p. e0141251
- [9] Chang, J.L., et al. Am J Trop Med Hyg, 2018. 99(4): p. 1080-1088.

Laccase electrochemical biosensor based on carbon nanotubes modified with diazonium salt

María Belén Piccoli
 Departamento de Físicoquímica, Fac.
 Cs. Químicas, UNC
 INFIQC (CONICET)
 Córdoba, Argentina
 belen.piccoli@unc.edu.ar

Raquel Viviana Vico
 Departamento de Química Orgánica,
 Fac. Cs. Químicas, UNC
 INFIQC (CONICET)
 Córdoba, Argentina
 raquel.vico@unc.edu.ar

Nancy Fabiana Ferreyra
 Departamento de Físicoquímica, Fac.
 Cs. Químicas, UNC
 INFIQC (CONICET)
 Córdoba, Argentina
 nfferreyra@unc.edu.ar

Abstract—We develop an enzymatic biosensor for phenolic compounds based on the immobilization of the enzyme Laccase on glassy carbon electrodes modified with single-walled carbon nanotubes functionalized with diazonium salt. The biosensor allowed for obtaining fast, stable, and sensitive electroanalytical responses to various polyphenolic compounds and was successfully employed in the determination of the total content of polyphenolic compounds in lemon verbena extract.

Keywords: Laccase, carbon nanotubes, diazonium salt polyphenols, electrochemical biosensor.

I. INTRODUCTION

In recent decades, nanobiotechnological developments have been focused on the design of biosensors to achieve devices with a better analytical performance by exploiting the synergistic properties of hybrid nanomaterials (HNM), obtained by combining nanomaterials, functionalizing agents (organic groups or molecules, ligands, polymers, etc.) and biomolecules (enzymes, lectins, antibodies, DNA, etc.). In this sense, the application of carbon nanotubes (CNT) in electrochemical biosensors has made it possible to significantly reduce the detection limits and improve the sensitivity of these devices due to their high response amplification capacity, their electro-catalytic properties and high area/volume ratio [1]. Adequate surface functionalization allows altering the π -conjugated interactions between the nanotubes, thus overcoming their tendency to agglomerate, improving their compatibility with the solvent, and allowing the incorporation of functional groups for anchoring biomolecules. Covalent modification of CNTs includes functionalization of the side walls, edges, ends, and defects. One of the most important methods for modifying the walls of CNTs is the coupling of diazonium salts (DS). This strategy allows for achieving materials with an adequate degree of functionalization and consequently greater dispersibility in solvents compatible with biomolecules [2].

In this work, we develop an enzymatic biosensor to quantify phenolic compounds based on the immobilization of the enzyme Laccase on glassy carbon electrodes (GCE) modified with single-walled carbon nanotubes (SWCNT) functionalized with DS. Laccase is a benzene diol oxidoreductase belonging to the polyphenol oxidase family of enzymes and is capable of oxidizing a variety of substrates (phenols and their derivatives, dyes, ketones, amines, and anions such as phosphate and ascorbate), in presence of molecular oxygen as an electron acceptor, producing water

as the final product of the reaction. These characteristics have led to the development of biosensors for use in the food industry, for example in the detection of polyphenols in fruit juices, wine, and tea, and to detect fungal contamination in grape musts [3]. Due to the wide range of substrates that it can oxidize, it has also been used in contaminated water source treatment and in monitoring pesticides and hormones [4]. A disadvantage of this protein is its instability in solution. Consequently, its application requires optimizing the immobilization on the transducer materials and evaluating their stability over time. The biosensor we propose allowed for obtaining fast, stable, and sensitive electroanalytical responses to diverse polyphenolic compounds and was successfully employed in the amperometric determination of the total content of polyphenols in lemon verbena extract (LVE).

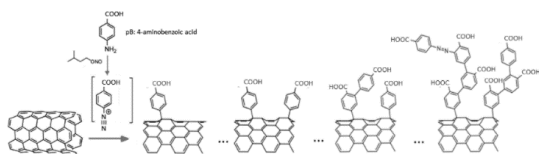
II. MATERIALS AND METHODS

A. Reactives

SWCNT of chirality (7, 6) containing more than 77% of nanotubes with (0.7 to 1.1) nm of diameter (704121-16), 4-aminobenzoic acid (pBA), anhydrous *N,N*-dimethylformamide (DMF), acetonitrile and isopentyl nitrite, Laccase from *Trametes versicolor* (oxygen oxidoreductase, EC 1.10.3.2), *N*-hydroxysuccinimide and *N*-etil-*N'*-(3-dimetilaminopropil) carbodiimide hydrochloride were from Sigma-Aldrich. All reactives were of analytical degree. All solutions were prepared with ultrapure water (18 M Ω cm).

B. Functionalization of SWCNT

SWCNT were functionalized with the DS obtained from the 4-aminobenzoic acid (p-BA), as shown in scheme 1. Briefly, 200.7 mg de SWCNT (16.725 mmol) were dispersed in 50 mL of DMF in an ultrasonic bath (Heischer model UP400S) for 1 h and then with an ultrasonic probe (VCX 130W probe from Sonics and Materials with a 6 mm diameter titanium alloy micro-tip) for 30 min using cycles of 30 s with amplitude of 60% in an ice bath. Then 2.7455 g (20.02 mmol) of p-BA were dissolved in 50 mL of deoxygenated DMF and added to the dispersion of SWCNT under N₂ flow. To produce the DS, 2 mL of isopentyl nitrite were added and the reaction was allowed to proceed for 17 h at 60 °C under stirring. The reaction product was exhaustively washed with DMF and dimethyl ether, filtered under vacuum and dried in an oven to constant weight. The product obtained is named SWCNTs-pBA. This nanomaterial was characterized using different techniques, as described below. From thermogravimetry analysis, a loss of mass of 23 % was determined that corresponds to the amount of organic material attached to the nanotubes (not shown).



Scheme 1: SWCNT functionalization reaction.

C. Equipment

Spectrophotometric determinations were carried out with a Shimadzu UV-2600 spectrophotometer and a 0.1 cm optical path quartz cuvette. Raman spectra were obtained with a Horiba Jobin Yvon Model HR 800 UV Raman microscope with laser of 632.8 nm and 514.5 nm of wavelength. 100X or 50X objective lens were used to focus the laser beam and collect the scattered Raman signal. The power of the laser used to analyze the solid samples and GCE/SWCNT-pBA was 0.33 and 0.12 mW, respectively at $\lambda=632.8$ nm, and 0.09 and 0.04 mW at $\lambda=514.5$ nm, respectively. The acquisition time was 5 seconds for an average of 5 spectra per sample. These conditions were selected to avoid inducing heating damage of the samples. FTIR spectra were recorded with a Thermo Scientific Nicolet iN10 infrared Microscope between 400 and 4000 cm^{-1} (64 scans, 4 cm^{-1} resolution); Zeta potential was measured using a Zsizer SZ-100Z, provided with a semiconductor laser excitation solid-state (532 nm, 10 mW) and using the laser-Doppler velocimetry technique. Cyclic voltammetry (CV) and chronoamperometry (CA) were performed with an Autolab PGSTAT128N and a Teq4 potentiostat, respectively. A GCE of 3 mm diameter (CHI104, CH Instruments), a Pt wire, and an Ag/AgCl, 3M NaCl electrode (RE-5B, BAS) was used as working, counter and reference electrode, respectively [5]. All reported potentials are referred to this reference electrode. All the experiments were performed at room temperature.

D. Obtention of SWCNT-pBA dispersion

0.50 mg of SWCNTs-pBA were dispersed in 1 milliliter of a mixture of ethanol/water 50/50 % V/V by sonication with the ultrasonic probe for 20 min, followed by ultracentrifugation at 15000 rpm to decant impurities and agglomerated nanotubes. The effectiveness of the method and the colloidal stability over time were evaluated by measuring the absorbance at 254 nm of 1/10 dilutions of the supernatant. The colloidal dispersion was stable for at least 60 days after preparation (not shown).

E. Surface modification

GCE were cleaned by polishing with alumina powder 0.05 μm for 2 min, followed by sonication in deionized water for 30 s. The electrodes were electrochemically treated applying fifteen consecutive cycles of potential between -0.30 V and 0.80 V at 0.100 Vs^{-1} in 0.10 M, pH 7.0 phosphate buffer (PBS). The electrodes were then modified by drop coating with 10 μL of the SWCNT-pBA dispersion and the solvent was allowed to evaporate at 60 $^{\circ}\text{C}$ for 20 min. The electrode is named GCE/SWCNT-pBA.

F. Preparation of lemon verbena extracts

The extracts were obtained from 1.0 g of dry leaves in 10 mL of ultrapure water, heating at 80 $^{\circ}\text{C}$ for 25 minutes. The extracts were filtered with an acetate filter of 0.22 μm . The

total contain of polyphenols (TCP) was determined by the Folin-Ciocalteu (FC) method [6]. Calibration curve was obtained by mixing a volume of a stock solution of 3,4,5-trihydroxybenzoic acid gallate (gallic acid, GA) with 0.25 mL of FC reactive and water. The final volume was adjusted to 5.0 mL with ultrapure water to obtain standard concentrations between 1.0 – 20.0 mg/L. After 8 min, 1.7 mL of Na_2CO_3 7.5 % P/V was added, the reaction was allowed to proceed for 30 min at room temperature and the absorbance was measured at 765 nm. The same procedure was performed using 25 μL of LVE instead of GA.

G. Chronoamperometrical measurements and statistical analysis of the response

CA experiments were carried out under convective conditions, achieved by magnetic stirring. The transient current was allowed to decay to a steady state value before the addition of a given amount of the polyphenol and the subsequent generated current was monitored as a function of time, calibration curves were thus obtained. The sensitivity, S, of the biosensor was determined from the slope of the fitting line of the linear portion of the calibration curve. The detection (LOD) and quantification (LOQ) limit were calculated as $3.3 \times \text{SD}/S$ or $10 \times \text{SD}/S$, respectively, where SD is the standard deviation of the background current. The response of the biosensor towards catechol (CAT), hydroquinone (HQ), resorcinol (RES), GA, and bisphenol A (BPA) was analyzed. The potential for the CA experiments was selected for each substrate according to their electrochemical response evaluated from CV at the working pH (pH =5.0), being 0.200 V, 0.050 V, 0.100 V for CAT, HQ, RES, respectively and 0.000 V for GA and BPA.

III. RESULTS AND DISCUSSION

A. Abbreviations and Acronyms

Hybrid nanomaterials (HNM), carbon nanotubes (CNT), diazonium salts (DS), lemon verbena extract (LVE), 4-aminobenzoic acid (p-BA), glassy carbon electrodes (GCE), N-hydroxysuccinimide (NHS) and N-ethyl-N'-(3-dimethylaminopropyl) carbodiimide (EDC), single-walled carbon nanotubes pristine (SWCNT) and SWCNT modified with p-BA DS (SWCNT-pBA), cyclic voltammetry (CV), chronoamperometry (CA), total contain of polyphenols (TCP), Folin-Ciocalteu (FC), gallic acid (GA), catechol (CAT), hydroquinone (HQ), resorcinol (RES), GA and bisphenol A (BPA), gallic acid equivalent (GAE), detection limit (LOD) and quantification limit (LOQ), gallic acid equivalent (GAE).

B. SWCNT-PBA characterization

Table 1 shows the ratio of D and G intensity bands (I_D/I_G) of the Raman spectra of the nanomaterial, the values are the average of 5 independent measures. Solid samples of pristine and functionalized SWCNT as well as the spectra of modified electrodes GCE/SWCNT-pBA were analyzed. The functionalized nanomaterial shows a notorious increase of I_D/I_G compared to SWCNT, with values dependent on the wavelength used, in agreement with previous reports [7]. Similar I_D/I_G values are observed for the SWCNT-pBA before and after ultrasonic treatment and deposition on GCE,

pointing that this energetic treatment does not produce significant structural modifications in the nanomaterial.

TABLE I. RAMAN CHARACTERIZATION OF SWCNT-pBA

Material	I _D /I _G λ=632.8 nm	I _D /I _G λ=514.5 nm
SWCNT	(0.0474±0.0006)	(0.0484±0.0006)
SWCNT-pBA	(0.48±0.01)	(0.68±0.03)
GCE/SWCNT-pBA	(0.396±0.006)	(0.69±0.02)

The nature of the functional groups incorporated into the SWCNT was identified by XPS and FTIR spectroscopy. Fig. 1A shows the XPS high-resolution spectra for C_{1s} and O_{1s}. Some changes in the contributions of C_{1s} are observed after chemical modification of the nanotubes, the contribution of C-O bond from alcohols, phenols, and ethers increased 6.3% and appears a new contribution due to the C=O bond of the -COO⁻ groups incorporated. Additionally, the modified nanotubes present an increase in the percentage of oxygen content (6.2 % for SWCNT and 10.3 % for SWCNT-pBA), and a noticeable change in the relative proportion of C-O and C=O bonds in the O_{1s} spectra (plots c and d).

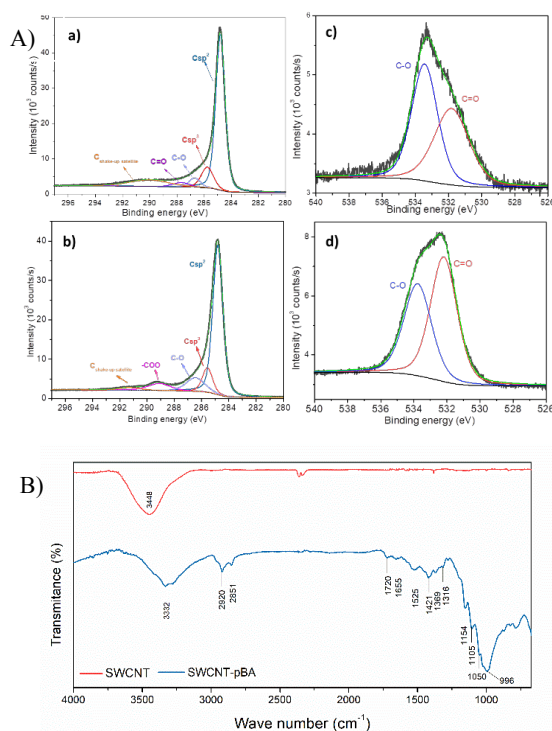


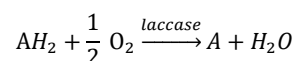
Fig. 1. A) High-resolution XPS spectra of C_{1s} (a and b), O_{1s} (c and d) of SWCNT (a and c) and SWCNT-pBA (b and d). B) FTIR spectra of SWCNT and SWCNT-pBA.

Fig. 1 B shows the FTIR spectra, SWCNT exhibits only a broad band in the region of 3500 cm⁻¹ probably due to adsorbed water or other impurities, in agreement with

the XPS results that showed the presence of O contributions. The introduction of chemical functionalities leads to the disruption of π-π interactions, producing more intense bands than those detected in the spectra of the original material. SWCNT-pBA shows peaks at 3332 cm⁻¹ and 1316 cm⁻¹ from νO-H and νC-O of the carboxylic acid groups, 3072 cm⁻¹ from the aromatic νC-H, 2920 and 2850 cm⁻¹ of asymmetric and symmetric νC-H sp³ respectively, 1720 cm⁻¹ of νC=O of carboxylic acid group, 1655 and 1525 and 1420 cm⁻¹ from aromatic νC-C bond overlapped with the asymmetric and symmetric stretching vibration of carboxylate group, a signal at 1370 cm⁻¹ from δO-H. The increase in the O content and the signals identified in the FTIR spectra evidences the presence of carboxylic groups, among other oxygenated functions, on the surface of the nanomaterial. These functional groups provide the nanotubes with pH-dependent surface charges that allow the stable dispersion of the nanomaterial in the solvent used. In this sense, the zeta potential increases from around 0V at pH 4 to -40 mV at pH 9 (not shown). The presence of the functional groups was also analyzed by electrochemical characterization of the SWCNT-pBA response (no shown).

C. Laccase immobilization

Lac can catalyze the oxidation of *o*-, *m*-, and *p*-benzenediols and phenol to *o*-, *m*-, *p*-quinones or radical species in the presence of molecular oxygen according to the reaction:



where AH₂ and A are reduced and oxidized states of phenol, in this work CAT, HQ, RES, GA, and BPA. The product of the enzyme oxidation is subsequently reduced at the electrode working at the appropriate potentials [3]. The advantage of this enzyme is that it does not require any cofactor for the catalytic reaction, but it could be unstable after immobilization, causing a decrease in the sensitivity of the biosensor over time. Thus, the first step in the construction of the enzymatic electrochemical biosensor was to achieve adequate immobilization of the protein, which would allow the connection between the electrode and the substrates of the enzyme, maintaining its activity without releasing it into the solution or producing significant denaturation during its immobilization. We employed two methods to select the best condition for the immobilization of Lac on GCE/SWCT-pBA: 1) physisorption (phys) for 60 min from a Lac solution 2.0 mg/mL avoiding solvent evaporation, and 2) covalent bonding (cov) by cross-linking to activated carboxylic groups of the nanotubes. In the second method, the activation was performed using 100 mM equimolar solution of EDC and NHS for 20 min, followed by Lac adsorption under the same conditions of method 1. The response towards catechol of both biosensors was compared and the variation in sensitivity with successive uses and over storage time was evaluated. Fig. 2A shows a CA response of catechol at GCE/SWCT-pBA/Lac_{phys} and the corresponding calibration curve (inset) from whose slope we determined the sensitivity of the electrode. Fig 2B presents the variation of the biosensor's sensitivity as a function of storage time.

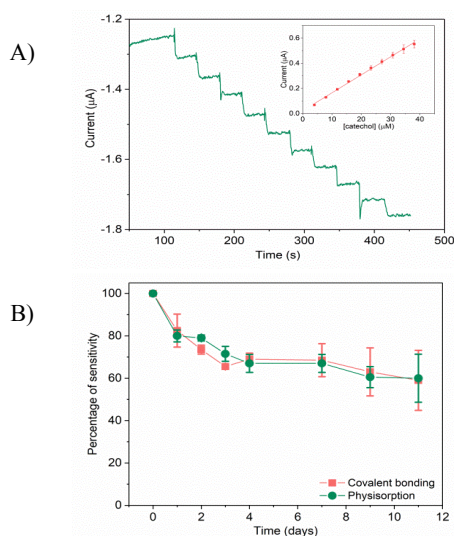


Fig.2. A) CA response of GCE/SWCNT-pBA/Lac_{phys}. Inset shows the corresponding calibration plot. B) Variation of the sensitivity as a function of the storage time for Lac physisorbed or covalently bonded to GCE/SWCNT-pBA. Sensitivity was determined from calibration plots for catechol at a potential of 0.200 V as average of two independent measurements. Supporting electrolyte: acetate buffer 0.1 M pH 4.5.

The sensitivity value of recently prepared biosensor was $(13.8 \pm 0.2) \mu\text{A mM}^{-1}$ and $(12.9 \pm 0.6) \mu\text{A mM}^{-1}$ for Lac physisorbed and covalently bonded, respectively. For both methods, the bioelectrode response shows almost the same decrease of their initial response after 11 days, $(60 \pm 11) \%$ and $(59 \pm 14) \%$ for physisorption and covalently bonded enzyme, respectively. Considering these results, physisorption was selected for the following experiments because requires less preparation time and reduces the reagents needed. The biosensor response to the other polyphenols was also evaluated in different supporting electrolytes, and pH selecting the most appropriate one. Table 2 shows the analytical parameters obtained for the best conditions.

TABLE II. ANALYTICAL PARAMETERS OF THE BIOSENSOR

Substrate	Sensitivity* ($\mu\text{A mM}^{-1}$)	K_M' (μM)	LOD/LQO (μM)
CAT	(17.8 ± 0.7)	(111 ± 9)	0.6/2
HQ	$(7 \pm 1).10$	(37 ± 1)	0.2/0.5
RES	(0.150 ± 0.007)	$(6.4 \pm 0.2).10^3$	140/400
GA	(13.4 ± 0.8)	180 ± 2	1/3
BPA	(4.0 ± 0.4)	ND	4/11

*Supporting electrolyte 0.10 M Britton-Robinson buffer pH=5.0

D. Bioelectrochemical determination of TCP in lemon verbena extracts

TCP in LVE was determined by the standard addition method. Fig. 3 shows the calibration curve, as average of 5 independent measures, obtained with GCE/SWCNT-pBA/Lac_{phys}. From the calibration curve a TCP = $(12.9 \pm 0.6) \text{ mM}$, or $(22 \pm 1) \text{ mM}$ of gallic acid equivalent (GAE) was determined. From FC method a TCP = $(14.1 \pm 0.7) \text{ mM}$ or $(24 \pm 1) \text{ mM}$ GAE was determined. These results evidence a good agreement between both methodologies.

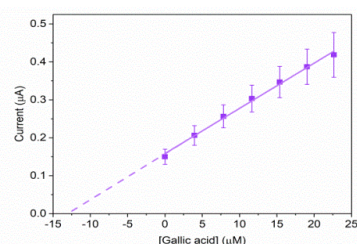


Fig. 3. Calibration plot of LVE quantification by standard addition of GA acid. $E_{ap} = 0.000 \text{ V}$. Supporting electrolyte: acetate buffer 0.1 M pH 5.0.

IV. CONCLUSIONS

Single-walled carbon nanotubes were functionalized by grafting with diazonium salt from 4-aminobenzoic acid. The chemical groups at the surface of the nanomaterial provided them with pH-dependent surface charges that allowed obtaining reproducible and stable colloidal dispersion for more than 60 days. The glassy carbon electrodes modified with the nanomaterial were a suitable platform to immobilize the laccase enzyme through physisorption. The biosensors maintain 60% of their initial response even after 10 days. With the optimized design, the detection of different polyphenols, that may be present in food samples, was feasible. Additionally, the biosensor shows an acceptable response to bisphenol A, a contaminant usually found in wastewater. The enzymatic biosensor was successfully validated for the detection of total content of polyphenol in lemon verbena extracts. These results suggest this biosensor could be an alternative or complementary method for the determination of antioxidants in beverages or for polyphenols quantification in contaminated water.

ACKNOWLEDGMENT

The authors thank SECyT-UNC, and Agencia Nacional de Promoción Científica y Tecnológica (ANPCYT) [PICT-2020-2524] for the financial support. M. B. Piccoli, thanks CONICET for the fellowship.

REFERENCES

- [1] Kny E.; Hasler R.; Luczak W.; Knoll W.; Szunerits S.; Kleber C. State of the Art and Future Research Directions of Materials Science Applied to Electrochemical Biosensor Developments, *Anal. Bioanal. Chem.*, **2024**, 416, 2247–2259.
- [2] Oskın P.; Demkina I.; Dmitrieva E.; Alferov S. Functionalization of Carbon Nanotubes Surface by Aryl Groups: A Review, *Nanomaterials*, **2023**, 13, 1–21.
- [3] Castrovilla M.C.; Tempesta E.; Cartoni A.; Plescia P.; Bolognesi P.; Chiarinelli J.; Calandra P.; Cicco N.; Verrastro M.F.; Centonze D.; Gullo L.; Del Giudice A.; Galantini L.; Avaldi L. Fabrication of a New, Low-Cost, and Environment-Friendly Laccase-Based Biosensor by Electrospray Immobilization with Unprecedented Reuse and Storage Performances, *ACS Sustain. Chem. Eng.*, **2022**, 10, 1888–1898.
- [4] Villalba-Rodríguez A.M.; Parra-Arroyo L.; González-González R.B.; Parra-Saldivar R.; Bilal M.; Iqbal H.M.N. Laccase-Assisted Biosensing Constructs – Robust Modalities to Detect and Remove Environmental Contaminants, *Case Stud. Chem. Environ. Eng.*, **2022**, 5, 100180.
- [5] Selzer S.M.; Vico R. V.; Ferreyra N.F. Immobilization of Concanavalin A on Iron Oxide Magnetic Nanoparticles. Effect of Bovine Serum Albumin in the Recognition Interactions of the Lectin, *Surfaces and Interfaces*, **2022**, 30, 101908.
- [6] Nikolaeva T.N.; Lapshin P. V.; Zagoskina N. V. Method for Determining the Total Content of Phenolic Compounds in Plant Extracts with Folin–Denis Reagent and Folin–Ciocalteu Reagent: Modification and Comparison, *Russ. J. Bioorganic Chem.*, **2022**, 48, 1519–1525.
- [7] Ojha A.K.; Heise H.M. Material analysis using raman spectroscopy: A comparative study of graphite, single- and multi-walled carbon nanotubes, Springer International Publishing, **2019**

Coacervates Improve Nucleotide Biosensors through Sequestration

Christopher M. Green
Center for Bio/Molecular Science and
Engineering Code 6900, U.S. Naval
Research Laboratory.
Washington, D.C. 20375, USA
christopher.green@nrl.navy.mil

Rein V. Ulijn
Nanoscience Initiative at Advanced
Science Research Center, Graduate
Center of the City University of New
York
New York, NY 10031, USA.
rulijn@gc.cuny.edu

Deborah Sementa
Nanoscience Initiative at Advanced
Science Research Center, Graduate
Center of the City University of New
York
New York, NY 10031, USA.
dsementa@gc.cuny.edu

Sebastián A. Díaz*
Center for Bio/Molecular Science and
Engineering Code 6900, U.S. Naval
Research Laboratory
Washington, D.C. 20375, USA
sebastian.diaz@nrl.navy.mil

Igor L. Medintz
Center for Bio/Molecular Science and
Engineering Code 6900, U.S. Naval
Research Laboratory.
Washington, D.C. 20375, USA
igor.medintz@nrl.navy.mil

Coacervates, also known as molecular condensates are peptide-based membraneless liquid-liquid phase separated domains. As coacervates must maintain charge equilibration, they are adept at sequestering and concentrating molecules from solution. We have demonstrated that coacervates provide a simple and biocompatible medium to improve nucleic acid biosensors through sequestration; sequestration results in increasing the local concentration within the coacervate. Using positively charged polypeptides such as polyarginines along with ATP as a counter ion we form coacervates capable of improving FRET-based nucleotide biosensors. Within the coacervates the limit of detection was lowered, the signal to noise was improved, and the kinetics were faster. We also show that the order of addition does not modify the improvement.

Keywords—Coacervate, Molecular Condensate, DNA, Biosensing, FRET

I. INTRODUCTION

Detecting RNA and DNA is crucial for identifying viral, bacterial, and mycotic infections, with emerging potential in biomarker applications for various human diseases[1]. Oligonucleotide based probes, such as fluorescent molecular beacons (MBs), are popular for their ease of synthesis and readout[2]. Hairpin (HP) form DNA probes, single stranded (ss) DNA with a stem-loop secondary structure, are effective in conjunction with Förster resonance energy transfer (FRET)-based fluorescent readouts. MBs labeled with fluorescent dyes show efficient donor-acceptor energy transfer in the HP form, resulting in changes in fluorescent emission ratios upon target binding and rearrangement of the MB structure.

Peptide-based coacervates, also referred to as molecular condensates, have gained attention as a biomaterial with diverse applications, from biosensing to drug delivery[3]. These liquid-liquid phase-separated domains form micrometer-scaled structures, creating a condensed phase rich in biomolecules, separating from the original aqueous solution but having no actual membrane[4]. Coacervates exhibit varying degrees of supramolecular order within a mostly disordered system[5]. The continuous aqueous environment enables steady exchange between phases, crucial for biosensing applications. Due to their charge equilibration, modified hydrophobicity, and dielectric constant, coacervates can sequester and concentrate molecules from the solution[6].

Simple peptide-derived coacervates have been shown to recruit nucleotides into the condensed phase, resembling proteins enlisting DNA or RNA within membraneless compartments within cells[7].

By combining these two approaches, we recently demonstrated that nucleotide based probes such as MBs sequester, or colocalize, into the coacervates increasing local concentrations[8]. This resulted in considerable improvements in the limit of detection (LOD), as well as the signal to noise. Furthermore, we observed an increase in kinetics, the end-point of the sensing occurring on average 4.4 times faster[8]. The question arose, whether this was due to destabilization of the HP MB within the coacervates. To test this hypothesis we inverted the order of addition, having either the MB or the target already sequestered into the coacervate and then adding the other component, and observed reaction kinetics. In a aqueous buffer condition the order of addition did not modify the kinetics nor the form of the signal. Yet in the case of the coacervate system, the kinetics appeared to be unmodified and the final signal are similar, but the spectral changes are unique depending on the order of addition. This implies that if destabilization of the HP form is occurring it is very fast as well as that intake of the MB into the coacervate strongly changes dye fluorescence.

II. MATERIALS AND METHODS

Peptides (polyarginine, R₉) were purchased with the trifluoroacetic acid removed from Biosynthesis, while DNA was purchased from IDT. All other reagents purchased from Sigma Aldrich and used as is. The utilized buffer was 10 mM Tris-HCl, 15 mM KCl, 0.5 mM MgCl₂, pH 7.6.

Coacervates were formed as detailed previously[5]. In brief, stock solutions of the peptide, ATP, and DNA, along with the buffer solution were prepared in deionized water. The peptide was added to the buffer in an Eppendorf tube so that 400 μ M would be the final concentration and then ATP was added subsequently, at 750 μ M final concentration, and mixed through pipetting. The DNA, MB or target, was then added at 250 nM concentration and allowed to sequester for 20 minutes at RT before the complementary strand was added.

Solution based fluorescence spectra were measured at 20 °C using a TECAN Spark plate reader exciting from above on a 384-microwell plate. An excitation wavelength of 520 nm

was used to excite the sample and the fluorescence emission was measured from 540-725 nm with 5 nm steps when collecting the entire spectra, or the Cy3 and Cy5 peaks were followed at 570 and 670 nm, respectively.

Confocal fluorescence microscopy was performed as reported previously[8]. Briefly, 20 μ l of sample was imaged on a Leica TCS SP8 STED 3X with a 60X objective lens (with oil immersion). Excitation at 520 nm with the emission range collected (540-740 nm) for total intensity.

FRET is the non-radiative energy transfer through dipole-dipole coupling of an excited donor molecule to the ground state of an acceptor molecule. FRET is efficient on the nm scale and can be followed through changes in fluorescence intensity, making it an optimal tool for determination of DNA rearrangement. An in depth description of FRET is beyond the scope of this manuscript but many excellent reviews are available[9].

III. RESULTS

A. Biosensor improvement through utilization of coacervates.

The chosen MB was a 24 nucleotide length ssDNA with a Cy3 dye on the 3' end as a FRET donor and a Cy5 dye on the 5' end as a FRET acceptor. The sequence of the MB was 5Cy5/CTACTATTTGATGAGATAGTA/3Cy3 with the target strand we wished to detect a 16 nucleotide ssDNA, TCTACTATCTCATCAA, complementary to the section in bold in the MB. In the absence of target strand the MB would fold into a HP shape (see Fig. 1) placing the Cy3 and Cy5 in close proximity resulting in high FRET. Upon binding of the target the MB took a more linear form, separating the dyes and decreasing the FRET. The dsDNA form was determined to have a melting temperature of 48 ± 2 °C, indicating that the binding of the target was generally irreversible at the 20 °C we worked at[8]. This was demonstrated in both an aqueous buffer as well as in a solution containing the coacervates.

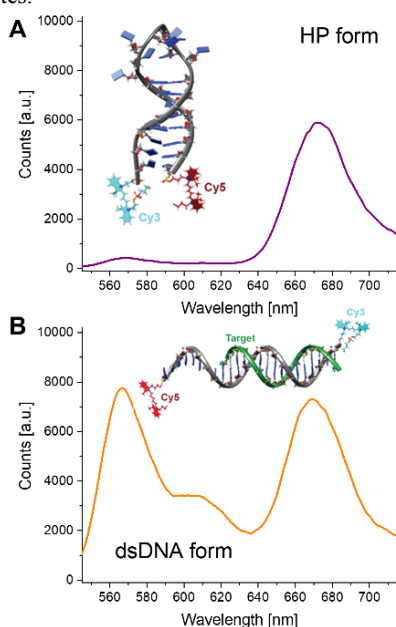


Fig. 1. Schematic and fluorescence emission spectra of MB in (A) HP form and (B) ds DNA form.

Sequestration of nucleotides within coacervates has been observed in cellulo, principally RNA was observed as it is more prevalent in the cytosol[10]. While Liu et al were able to demonstrate in vitro a 40000-fold increase in local concentration of nucleotides into coacervates using a polymer-oligopeptide hybrid to form the coacervate[6]. Our own work quantified that more than 99.6% of the DNA was found within our R₉-ATP coacervates using centrifugation and microscopy (see Fig. 2)[8].

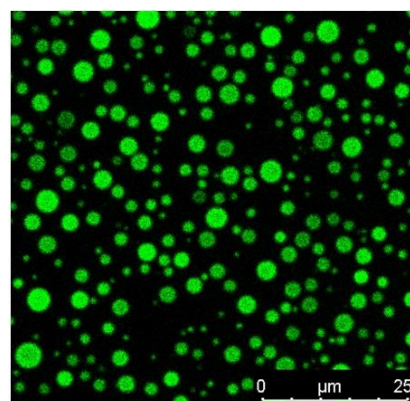


Fig. 2. Confocal fluorescence image showing the MB colocalized into the coacervate interior. Excitation at 520 nm and emission collected from 540-740 nm.

One could represent the coacervate as reducing the solution volume by orders of magnitude, we estimate at least 100-fold, allowing the target and MB to interact at a greater rate[8]. By following the change in Cy5/Cy3 emission ratio we were able to demonstrate a 20-fold decrease in LOD of our MB for target DNA by including coacervates in our solution (see Fig. 3). It was also observed that the colocalization of the organic dyes, Cy3 and Cy5, within the coacervate increased their fluorescent quantum yield (QY) due to the increased viscosity of the medium[11]. This in turn results in an improved signal to noise as observed in the uncertainties seen in Fig. 3.

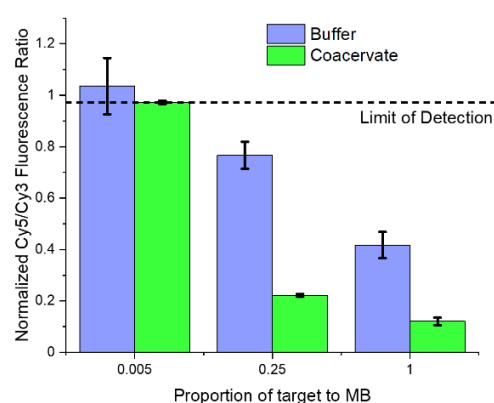


Fig. 3. Fluorescence emission ratio normalized to no target addition in buffer (blue) and coacervate (green) conditions. Uncertainties arise from triplicate experiments. The limit of detection was determined as 3 times the standard deviation of a sample with no target addition.

B. Effect of order of addition.

Due to the strong charge distribution of the R₉ polypeptide (strong positive charge) and the DNA (negative charge), it was expected that the biopolymers would interact. In fact, in previous work from the lab, it was observed that if the peptide concentration was insufficient to form the coacervate it would complex the MB and deactivate its functionality as a biosensor[8]. The hypothesis arose that the coacervate could be destabilizing the HP structure of the MB. To test this hypothesis we undertook an experiment in which the order of addition of the MB and target was inverted to test what appearance the fluorescence ratio had over the time course of the experiment. We prepared samples that contained either: buffer only or included coacervates in the solution, and then either added the MB only, the target only, or no DNA and then pipetted these into a 384-well plate. We subsequently waited 20 minutes and then added the complementary DNA (i.e. added target to the MB wells and MB to the target wells) or the preformed dsDNA in the case of the wells that had no previous DNA using a multipipetter and began following the Cy5/Cy3 fluorescence ratio (see Fig. 4). For this experiment, the proportion of target to MB was kept at 1:1.

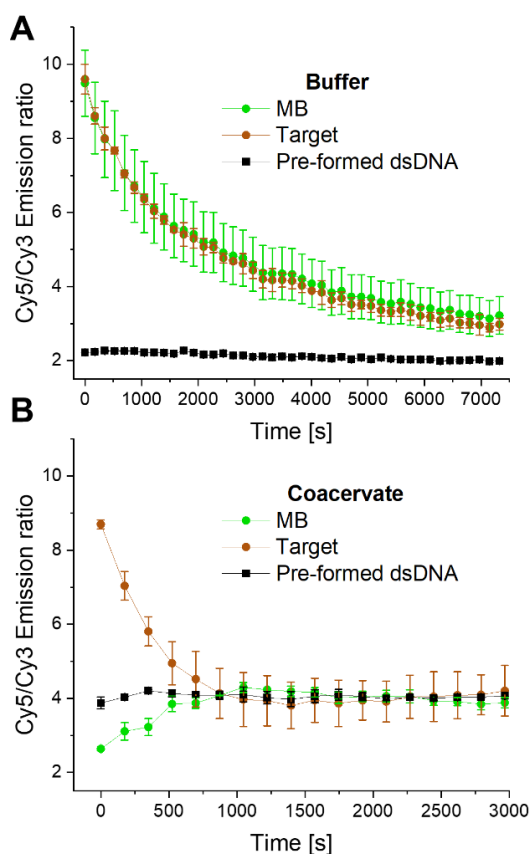


Fig. 4. Time trace of Cy5/Cy3 emission ratio where the DNA in the legend is added at t_0 . The complementary strand is already found in the solution. (A) Buffer condition. (B) Coacervates. Uncertainties arise from duplicate experiments.

As can be observed in Fig. 4A the effect of order addition within buffer solution is null. In the case of the coacervates it was observed that the kinetics of the reaction were, at least, 7 times faster (note the difference in the scale of the x-axis); it is not readily apparent if the buffer conditions had reached the end-point. Though within the coacervate condition it did not appear as if the order of addition mattered, in as far as the time required to reach an end-point, both reaching the end-point at around 900 s. This suggests that if the coacervate is destabilizing the HP form of the MB, this occurs quicker than the diffusion kinetics of the DNA within the coacervate.


What is unique about the order of addition in coacervates is that due to the changes in fluorescent QY of the dyes the relative signal change is inverted when adding the target or the MB. If the MB is already within the coacervate then the addition of the target causes the Cy5/Cy3 ratio to decrease as target diffuses into the coacervate and transforms it from the HP to dsDNA form, consistent with a decrease in FRET efficiency. If the target is within the coacervate and the MB is added second, we actually observe an increase of the Cy5/Cy3 ratio. This is counterintuitive since the FRET efficiency of the system has gone down. What was subsequently realized is that though the FRET decreased from 96% to 32%, the increase of the dye QYs from 0.16 to 0.62 in the case of Cy3 and from 0.28 to 0.36 for Cy5, actually outweighs the decrease in FRET.

IV. CONCLUSIONS

In summary, peptide based coacervates are an optimal way to sequester nucleotides, including MBs. Through sequestration, the local concentration is enhanced and the LOD is improved. Coacervates provide additional benefits, including an environment that enhances the fluorescence QY of cyanine dyes located in their interior. This effect improves the signal-to-noise of the bioassay, but does make it possible that the observed signal may depend on the order of addition. Making it paramount that a proper experimental design be implemented and followed. We show in this work that the end-result is not modified upon the order of addition, so if we only look at the fluorescence ratio, for example at the 30 min mark, than any approach is valid. Finally, in this manuscript we show that if the enhanced kinetics are in part driven by the destabilization of the HP form of the MB, this occurs on a scale that is quicker than our experiment could detect, and therefore the order of addition is not crucial to the kinetics enhancement. We conclude that any HP destabilization occurs faster than the diffusion time of the nucleotide into the coacervates.

REFERENCES

- [1] M. Mukhtar, S. Sargazi, M. Barani, H. Madry, A. Rahdar, and M. Cucchiari, "Application of nanotechnology for sensitive detection of low-abundance single-nucleotide variations in genomic DNA: A review," *Nanomaterials*, vol. 11, pp. 1384, 2021.
- [2] A. Tsourkas, M. A. Behlke, S. D. Rose, and G. Bao, "Hybridization kinetics and thermodynamics of molecular beacons," *Nucleic Acids Res.*, vol. 31, pp. 1319-1330, 2003.
- [3] R. S. Fisher and S. Elbaum-Garfinkle, "Tunable multiphase dynamics of arginine and lysine liquid condensates," *Nat. Commun.*, vol. 11, pp. 4628, 2020.
- [4] D. Sementa, D. Dave, R. S. Fisher, T. Wang, S. Elbaum-Garfinkle, and R. V. Uljin, "Sequence-tunable phase behavior and intrinsic fluorescence in dynamically interacting peptides," *Angew. Chem. Int. Ed.*, vol. 62, pp. e202311479, 2023.

- 
- [5] A. Jain, S. Kassem, R. S. Fisher, B. Wang, T.-D. Li, T. Wang, et al., "Connected peptide modules enable controlled co-existence of self-assembled fibers inside liquid condensates," *J. Am. Chem. Soc.*, vol. 144, pp. 15002-15007, 2022.
- [6] J. Liu, F. Zhorabek, T. Zhang, J. W. Y. Lam, B. Z. Tang, and Y. Chau, "Multifaceted cargo recruitment and release from artificial membraneless organelles," *Small*, vol. 18, pp. 2201721, 2022.
- [7] Y. Huang and X. Huang, "Biomolecule-based coacervates with modulated physiological functions," *Langmuir*, vol. 39, pp. 8941-8951, 2023.
- [8] C. M. Green, D. Sementa, D. Mathur, J. S. Melinger, P. Deshpande, S. Elbaum-Garfinkle, et al., "Sequestration within peptide coacervates improves the fluorescence intensity, kinetics, and limits of detection of dye-based DNA biosensors," *Commun. Chem.*, vol. 7, pp. 49, 2024.
- [9] D. Mathur, S. A. Díaz, N. Hildebrandt, R. D. Pensack, B. Yurke, A. Biaggne, et al., "Pursuing excitonic energy transfer with programmable DNA-based optical breadboards," *Chem. Soc. Rev.*, vol. 52, pp. 7848-7948, 2023.
- [10] D. P. Mascotti and T. M. Lohman, "Thermodynamics of oligoarginines binding to rna and DNA," *Biochem.*, vol. 36, pp. 7272-7279, 1997.
- [11] M. E. Sanborn, B. K. Connolly, K. Gurunathan, and M. Levitus, "Fluorescence properties and photophysics of the sulfoindocyanine cy3 linked covalently to DNA," *J. Phys. Chem. B*, vol. 111, pp. 11064-11074, 2007.

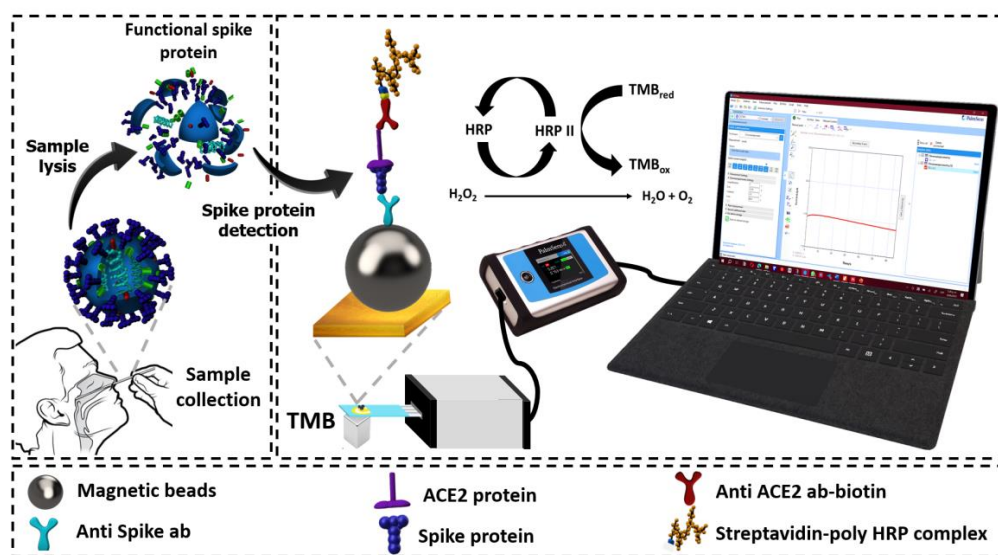
Development of an electrochemical immunosensor for SARS-CoV-2 detection and clinical validation

Viviana Vásquez Fonseca
*PhD Student, Max Planck Tandem Group in
 Nanobioengineering
 University of Antioquia
 Medellín, Colombia
 viviana.vasquez@udea.edu.co*

Jahir Orozco Holguín
*Group Leader, Max Planck Tandem Group in
 Nanobioengineering
 Faculty of Natural and Exact Sciences
 University of Antioquia
 Medellín, Colombia
 Grupo.tandemnanobioe@udea.edu.co*

Abstract— After the crisis generated by the COVID-19 pandemic, countries around the world, especially developing countries, are seeking sovereignty over their health systems. Sovereignty can be achieved through research and technological development of new and improved strategies for detecting, diagnosing, prognosis, and predicting the course of established, current, or emerging diseases. Biosensors can contribute to this need by providing detection tools that are highly sensitive, specific, and easy to implement at the point of care. However, transitioning these technologies to society requires evaluation in different environments related to each device's technological readiness level (TRL). This work reports on an electrochemical immunosensor for detecting SARS-CoV-2, tested it in a relevant decentralized environment. For this purpose, an electrochemical immunosensor based on magnetic beads was developed to detect the spike-ACE2 protein complex by enzymatic amplification and a redox reaction that could be measured in a sensitive and specific way by chronoamperometry. This device was validated with 150 samples (101 samples from infected patients and 49 from healthy individuals), demonstrating a high clinical performance with a clinical sensitivity of 96.04 % and a clinical specificity of 87.75 %, correlated with polymerase chain reaction (RT-PCR) as the gold standard. Finally, its technological applicability was demonstrated in a relevant decentralized environment by analyzing thirty previously validated samples, where 93.33 % of them did not show statistically significant differences with respect to the data from our laboratory. The grade o maturity of the device achieved demonstrate the potential of biosensors for detecting infectious pathogens.

Keywords— *Clinical validation, SARS-CoV-2, spike protein, immunosensor, magnetic beads, electrochemical biosensor.*



I. INTRODUCTION

Emerging infectious diseases constitute a serious health problem due to their rapid spread and their impact on patients, who may respond differently to infection, leading to serious infectious processes and sometimes even death [1][2]. Events such as the COVID-19 pandemic have shown that there is still a long way to go in addressing emerging infectious diseases. Nanobiosensors emerge as promising detection tools for this

purpose. These devices can take advantage of biorecognition molecules' high affinity and nanomaterials' unique properties for the rapid, specific, and highly sensitive detection of biomarkers at different molecular levels, offering a smart solution to the limitations of conventional methods. [3][4].

The development of this type of device paves the way for the sovereignty of the health systems of each country so that when faced with another possible health emergency, they would not depend on the technological production of other countries but

would instead have the capacity to rapidly develop their own diagnostic and prognostic tools with adequate analytical services for the detection and screening of the population at the point of care and in the shortest possible time.

In this work, we developed an electrochemical immunosensor for detecting the SARS-CoV-2 Spike protein. The proof of concept was first analytically characterized, showing high performance. Subsequently, the device was clinically validated under laboratory conditions by analyzing 150 samples, 101 samples from patients infected with COVID-19 and 49 healthy individuals, previously analyzed by RT-PCR as a gold standard. Finally, it was validated in a relevant environment, outside our laboratory, by analyzing thirty of the previously validated samples and statistically comparing the differences of the measurements in both environments.

II. METHODOLOGY

A. Materials

Dynabeads™ MyOne™ carboxylic acid (Ref. 65011) was obtained from Thermo Fisher Scientific. SARS-CoV-2 (2019-nCoV) spike antibody, rabbit PAb (Ref. 40591-T62); SARS-CoV-2 (2019-nCoV) spike S1-His recombinant protein (Ref. 40591-V08H) were obtained from Sino Biological.

N-(3-dimethylaminopropyl)-N'-ethylcarbodiimide hydrochloride (EDC) (Ref. E6383-5G), N-hydroxysuccinimide (NHS) (Ref. 130672-5G) and 2-(N-morpholino) ethanesulfonic acid sodium salt (MES), were purchased from Sigma-Aldrich. Potassium hydrogen phosphate (K_2HPO_4) and disodium hydrogen phosphate (Na_2HPO_4) were acquired from PanReac AppliChem. Potassium dihydrogen phosphate (KH_2PO_4), potassium chloride (KCl), and sodium chloride (NaCl) were obtained from J.T. Baker®. Sulphuric acid (H_2SO_4) was purchased from Honeywell Fluka™. Human ACE2 biotinylated antibody (Ref. BAF933) was obtained from R&D systems. Soluble TMB (Ref. 613544-100ML) was obtained from Merck. Streptavidin-poly-HRP-80 (Ref. 65R-S105PHRP) was obtained from Fitzgerald.

25 mM MES buffer pH 6.5 was used to activate carboxylic groups and conjugate anti-spike antibodies. In addition, 0.15 M Phosphate-buffered saline 1X pH 7.4 (PBS) was used to conjugate the spike protein. ChemCruz radioimmunoprecipitation lysis buffer (RIPA, Ref. sc-24948), containing 1% phenylmethylsulphonyl fluoride (PMSF), 1% sodium orthovanadate, and 2% protease inhibitor cocktail, was used for lysing viral particles and samples.

B. Immunosensor assembly

The immunosensor design consists of carboxylated submicrometer magnetic beads decorated with a capture antibody that pre-concentrates the spike protein from patient samples and interacts with angiotensin-converting protein 2 (ACE2). A sandwich with a biotinylated anti-ACE2 signal antibody interacts with the streptavidin-poly 80 (HRP) enzyme complex. In the presence of hydrogen peroxide and a mediator, this enzyme produces an electrochemical signal on the surface of a screen-printed electrode that correlates with changes in protein concentration, recorded on a portable potentiostat by chronoamperometry. Electrochemical measurements were performed using a three-electrode SPAuE

cell on a PalmSens4 potentiostat with PS Trace analysis software [5].

C. Clinical validation

150 samples from people in Medellin, Antioquia, Colombia, with COVID-19-related symptoms were collected between November 2022 and May 2023 by nasopharyngeal swabs and tracheal aspirates and analyzed by RT-PPCR, measuring the viral load of the 2N and E genes of SARS-CoV-2. By this technique, 101 of the samples were found to be positive and 49 negative. These samples were lysed with RIPA lysis buffer and analyzed with the electrochemical immunosensor. This work was endorsed for validation in human samples by the bioethics committee of the University of Antioquia with approval act N° 22-04-986 on June 15, 2022.

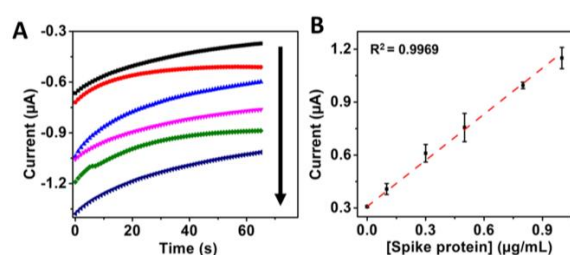


Fig. 1. A) Immunosensor electrochemical response with increasing concentrations of 0, 0.1, 0.3, 0.5, 0.8, and 1 mg/mL of the spike protein amplified with streptavidin-HRP (poly) 80 and B) Corresponding calibration curve (current absolute value).

D. Validation in a relevant environment

Of the 150 validated samples, 30 were selected (20 positive and 10 negative) and analyzed with the immunosensor under conditions outside the laboratory in a diagnostic center in Medellin, Antioquia, Colombia, and the measured signals were compared with the data obtained during validation.

III. DISCUSSION AND RESULTS

A. Immunosensor assembly

The immunosensor developed takes advantage of the high affinity of the SARS-CoV-2 spike protein for ACE2 protein, which has been reported to be 10-20 times higher than that evidenced by SARS-CoV-1. In addition, its design is based on magnetic beads, which allow the spike protein to be pre-concentrated directly from the sample, facilitating washes and reducing the effects of interferents present in biological matrices. In addition, the biosensor implements a streptavidin-poly 80 (HRP) enzymatic complex as an amplification system to generate a redox reaction in the presence of TMB and H_2O_2 , which can be measured by chronoamperometry. The parameters involved in the development of the immunosensor were rapidly screened by spectrophotometry, obtaining the highest absorbance signal and the lowest signal-to-noise ratio by conjugating the capture antibody in MES buffer at pH 6.0 for 2 hours, with 1% casein as blocking agent, 20 µg of magnetic beads, and with concentrations of 12 µg/mL for the capture antibody, 2 µg/mL of ACE2 protein and anti-ACE2 antibody, and 50 µg/mL of streptavidin-poly 80 (HRP). The optimal values of each parameter were used in the electrochemical detection, showing a high correlation [5].

For the calibration curve, commercial spike protein concentrations from 0 to 1 $\mu\text{g}/\text{mL}$ were evaluated, demonstrating a sensitivity of $0.83 \mu\text{A} \cdot \text{mL}/\mu\text{g}$, a LOD of 22.55 ng/mL, and $R^2 = 0.997$ (see Figure 1), characteristics comparable with other literature reports, and clinically relevant. Next, the immunosensor was evaluated between 1 and 10^6 copies/mL of artificially assembled pseudovirions, demonstrating a sensitivity of $1.28 \mu\text{A} \cdot \text{mL}/\text{copies}$, a LOD of 0.12 copies/mL, and high linearity, i.e., $R^2 = 0.982$. But when evaluated against viral particles cultured from an infected patient inactivated by UV-light exposure for 30 min, a low sensitivity $6.0 \times 10^{-7} \mu\text{A} \cdot \text{mL}/\text{copies}$ and worst LOD of 4.17×10^4 copies/mL ($R^2 = 0.987$) in a range between 1 to 5×10^5 copies/mL was observed. It is due to damage caused by UV light, which decreases the functionality of the structural proteins and, consequently, the ability of the spike protein to bind to the ACE2 protein.

The immunosensor was also evaluated against SARS-CoV-2 homologous viruses such as SARS-CoV-1 and MERS-CoV, as well as another glycoprotein (β -1.4-GALT-5) due to the nature of the spike protein. In this, the sensor demonstrated high specificity and selectivity with statistically significant differences in all interferents ($p < 0.05$) (see Figure 2) [5]. Finally, the immunosensor demonstrated stability of up to 20 days at 4°C and high reproducibility with less than 10 % signal differences.

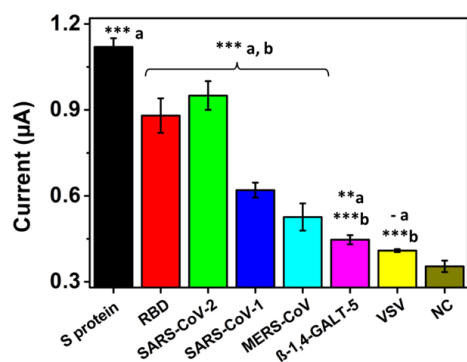


Fig. 2. Immunosensor specificity when detecting 1 $\mu\text{g}/\text{mL}$ spike, RBD and β -1,4-GALT-5 proteins and 1×10^5 copies/mL MERS, SARS-CoV-1, SARS-CoV-2 and VSV pseudovirions supernatants. Statistically significant differences with respect to (a) the negative control and (b) the commercial spike protein, ***($p < 0.001$), **($p < 0.01$), *($p < 0.05$) and - ($p > 0.05$).

B. Clinical validation

Due to the need to obtain the functional spike protein from the viral particles, we used a RIPA lysis buffer that breaks the virus membrane and leaves the structural proteins free without affecting their functionality. Dilutions of 1:1 and 1:10 of the biological sample in RIPA buffer were evaluated, showing a higher signal at a 1:10 ratio (in a final volume of 50 μL). 150 samples from patients with symptoms related to COVID-19 were analyzed using this methodology (see Figure 3). When calculating the analytical characteristics of the immunosensor, we observed a clinical sensitivity of 96.04 % and a clinical specificity of 87.75 %. We calculated the area under the curve from the receiver operating characteristic (ROC) curve with a value of 0.83 related to high accuracy. Finally, the current values obtained by the immunosensor were correlated with the CT values of the q-

PCR gold standard. A high dispersion of the data was observed, which is related to the sample collection technique, showing higher linearity in those samples collected by nasopharyngeal swabs ($R^2 = 0.797$) compared to tracheal aspirates ($R^2 = 0.662$), which showed greater variability in the final sample volume. In addition, it may be related to the SARS-CoV-2 variants, which, according to reports in the literature, have different affinities between the spike protein and the ACE2 protein.

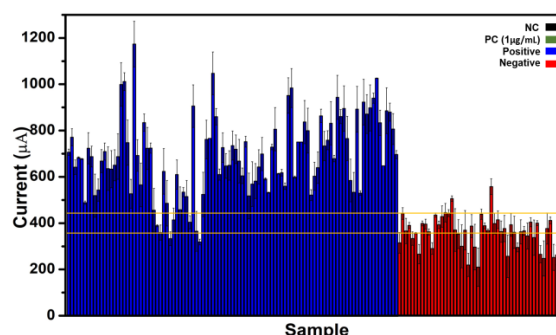


Fig. 3. Current values were obtained from the immunosensor in the detection of 101 positive and 49 negative samples by chronoamperometry at a potential of -150 mV, compared to a positive control (PC) and a negative control (NC) in the presence or absence of commercial spike protein, respectively. Both samples and controls were lysed in RIPA buffer before measurements ($n = 3$). The yellow lines correspond to the standard deviation of the negative control in RIPA buffer spiked with saliva (nasopharyngeal-like sample). Please note that all negative and positive samples were defined by q-PCR results.

C. Validation in a relevant environment

Thirty patient samples were measured in a relevant decentralized environment, and data were correlated with the values obtained in our laboratory, showing high linearity ($R^2 = 0.979$). 93.33% of the samples did not present significant differences between the data obtained in both environments ($p > 0.05$). However, they did require longer stabilization time of the current signal due to the low environmental temperature, which must be considered when measuring in different environments.

IV. CONCLUSIONS

The electrochemical immunosensor developed in this work showed a high potential to detect SARS-CoV-2 in a sensitive, selective, and specific manner with high reproducibility, without the need for RNA extraction, complex and robust equipment, or specialized personnel compared to RT-PCR, and with only 5 μL of the sample. In addition, the device showed a high clinical sensitivity of 96.04 %, a clinical specificity of 87.75 %, and the ability to differentiate between different viral loadings under laboratory conditions and relevant decentralized conditions outside our laboratory. Therefore, this detection platform achieved a technology readiness level of TRL-6. It could serve as a basis for developing biosensors to detect other emerging viruses to reduce the detection time and screening of infected patients, isolating them at the right time and reducing the possibility of spreading and thus facing future crises such as the COVID-19 pandemic.

ACKNOWLEDGMENT

The authors acknowledge MinCiencias for funding the project Validation of a Nanobiosensor to detect SARS-CoV-2 rapidly (Cod. 111593092980). J.O acknowledges financial support from the Minciencias, the University of Antioquia, and the Max Planck Society through the Cooperation Agreement 566-1, 2014. The authors thank Luz Elena Valencia and Xiomara Espinal Bedoya from Adilab (Medellín) for donating patient samples and sample data. The authors thank the PECET and the Immunovirology Group from the University of Antioquia for donating patient samples, viral particles, and Vero cells, respectively, and CECOLTEC for the Sensit Smart pocket potentiostat donation. The authors also thank the technical assistance of Maria Camila Lopez-Osorio and Melissa Montoya-Guzman of the Gastrohepatology Group from the University of Antioquia and EPM and Ruta N for hosting the Max Planck Tandem Groups. The authors want to acknowledge Gary Whittaker at Cornell University for providing the plasmids needed for the pseudovirion system.

REFERENCES

- [1] J. Wan *et al.*, "Human-IgG-Neutralizing Monoclonal Antibodies Block the SARS-CoV-2 Infection," *Cell Rep.*, vol. 32, no. 3, p. 107918, Jul. 2020, doi: 10.1016/j.celrep.2020.107918.
- [2] J. R. Rohr *et al.*, "Emerging human infectious diseases and the links to global food production," *Nature Sustainability* 2019 2:6, vol. 2, no. 6, pp. 445–456, Jun. 2019, doi: 10.1038/s41893-019-0293-3.
- [3] P. Diez Sánchez, R. Villalonga Santana, and J. M. Pingarrón Carrazón, "Nuevos nanomateriales para el diseño de Biosensores Electroquímicos y Sistemas de liberación controlada," [Tesis doctoral] España, Universidad Complutense de Madrid p. 479, 2016. Recuperado de: <https://hdl.handle.net/20.500.14352/22788>.
- [4] N. Debnath and S. Das, "Nanobiosensor: Current trends and applications," in *NanoBioMedicine*, Springer Singapore, 2020, pp. 389–409. doi: 10.1007/978-981-32-9898-9_16.
- [5] V. Vásquez, M.-C. Navas, J. A. Jaimes, and J. Orozco, "SARS-CoV-2 electrochemical immunosensor based on the spike-ACE2 complex," *Anal Chim Acta*, vol. 1205, p. 339718, May 2022, doi: 10.1016/J.ACA.2022.339718.

Desarrollo de biosensores basados en ácidos nucleicos para la detección de genes implicados en la degradación de xenobióticos en ambientes contaminados

1st Agustín Nahuel Juárez

Laboratorio de Microbiología Ambiental y Nanotecnología.
(Departamento de Química Biológica, FCEN-UBA)
CABA-Bs. As-Argentina
ajuarez@qb.fcen.uba.ar

2nd Maria Eugenia Cardillo

Laboratorio de Microbiología Ambiental y Nanotecnología.
(Departamento de Química Biológica, FCEN-UBA)
CABA-Bs. As-Argentina
mariaeugeniocardillo@gmail.com

3rd Laura Judith Raiger Iustman

Laboratorio de Microbiología Ambiental y Nanotecnología.
(Departamento de Química Biológica, FCEN-UBA)
IQUBICEN (UBA-CONICET)
CABA-Bs. As-Argentina
lri@qb.fcen.uba.ar

4th Natalia Jimena Sacco

Laboratorio de Microbiología Ambiental y Nanotecnología.
(Departamento de Química Biológica, FCEN-UBA)
IQUBICEN (UBA-CONICET)
CABA-Bs. As-Argentina
nsacco@qb.fcen.uba.ar

Abstract—En el desarrollo de genosensores electroquímicos es importante disponer de una superficie conductora eléctrica con posibilidad de retener el DNA. Para lograr una mejor sensibilidad y un mayor rango de concentración de trabajo, la superficie del electrodo se puede modificar con diferentes materiales como nanotubos de carbono de paredes múltiples (MWCNTs) sin oxidar u oxidados (MWCNTs ox) y quitosano (CHI), entre otros. En este trabajo se estudió el diseño de una plataforma para un genosensor electroquímico, donde los procesos fueron estudiados mediante voltametría cíclica. Se realizaron electrodos de carbono modificados con una dispersión de MWCNTs ox en ácido acético y quitosano. Se seleccionó el gen alk B para ser detectado dado que codifica para una enzima involucrada en la degradación de hidrocarburos, teniendo fuerte relevancia a nivel ambiental, se diseñaron sondas específicas de ssDNA para ser inmovilizadas covalentemente sobre el electrodo de trabajo. Además, se realizó la optimización de glutaraldehído como agente entrecruzante y suero albumina bovina (BSA) para bloquear la superficie. Para la etapa de bioreconocimiento se ensayaron diferentes condiciones (temperatura ambiente y 50°C) obteniendo una disminución de aproximadamente 12% de la señal, dando claro ejemplo de la especificidad del sensor construido.

Index Terms—Genosensores, Electroquímica, Hidrocarburos, MWCNTs ox

I. INTRODUCCIÓN

Los biosensores son por definición dispositivos que permiten la detección de un compuesto deseado, utilizando una base biológica, la cual sufre alguna modificación de su estado basal para su función pudiendo ser esta detección cuantitativa o no. La base biológica del reconocimiento suele estar en íntimo contacto con un transductor el cual es el encargado de transformar la modificación del material biológico en una señal

que puede ser interpretada por otro dispositivo, por ejemplo, una señal eléctrica. Durante el desarrollo de un biosensor se busca que el mismo tenga alta sensibilidad, selectividad y con un tratamiento sencillo de la muestra pudiéndose ser utilizados in situ [1].

Dentro del universo de los biosensores se los puede clasificar de acuerdo al elemento de reconocimiento a utilizar, siendo un tipo los denominados genosensores, en los cuales el material biológico a determinar es un gen de interés. La idea tras estos sensores se basa en la hibridación de cadenas de ssDNA que sean complementarias y mediante un transductor lograr identificar esta modificación. Llevar a cabo la construcción entonces del dispositivo requiere la elección de la plataforma y el transductor a utilizar. En este sentido, la construcción de un biosensor electroquímico es una buena alternativa a los métodos de detección más tradicionales como puede ser una PCR. Una sonda de ácidos nucleicos se inmoviliza sobre una superficie de trabajo y al enfrentarla a la muestra deseada, de existir complementariedad se hibridarán y esto se verá reflejado en el cambio de señal del biosensor; una disminución significativa de la señal frente al control negativo se lo considerara entonces un resultado positivo [2].

En la actualidad existen electrodos conocidos como *screen-printed electrodes* (SPCE por sus siglas en inglés) los cuales tienen la ventaja de su construcción a gran escala y bajo costo; además, debido a la alta sensibilidad que pueden tener, es posible utilizar únicamente microlitros de muestra. Estos dispositivos poseen 3 electrodos integrados, uno de trabajo, uno de referencia y otro llamado contra electrodo. En el de trabajo es en donde va a ocurrir el proceso de bioreconocimiento.

Un campo importante para el desarrollo de los biosensores es el de las ciencias ambientales. Los microorganismos, en especial las bacterias, cumplen un rol fundamental en la remediación de zonas contaminadas. Un claro ejemplo es la acción de los derrames de petróleo en donde las bacterias pueden degradarlo o transformarlo en compuestos más solubles. Este es el caso de la *Pseudomona extremaustralis* 14,3 la cual posee una alcano-monooxigenasa (AlkB), dicha enzima tiene la capacidad de oxidar hidrocarburos transformándolos en compuestos más biodisponibles para su degradación [3]. La presencia entonces de esta enzima en ambientes naturales es un buen indicio tanto del estado de situación como de la capacidad de biorremediación que posee un sitio.

En el presente trabajo se diseñaron y optimizaron las diferentes etapas para la construcción de un genosensor electroquímico capaz de detectar la presencia del gen alkb.

II. DISEÑO EXPERIMENTAL

Se utilizaron electrodos serigrafiados (SPCE) (Battaglini, INQUIMAE) con electrodo de trabajo (ET) y contraelectrodo (CE) de carbón y electrodo de referencia (RE) Ag/AgCl. Se realizaron 5 suspensiones diferentes para estudiar su efecto en la nanoestructuración de la superficie del ET. Para ello se utilizaron nanotubos de carbono de pared múltiple (MWCNTs) (Sigma-Aldrich), MWCNTs oxidados (MWCNTs ox), quitosano (CHI) (Sigma-Aldrich) en ácido acético glacial (Anedra). En todos los casos, la concentración de las dispersiones de MWCNTs y la solución de quitosano fue 5 mg/ml en ácido acético 2 M. Para el diseño del genosensor, se inmovilizaron sondas de ssDNA sobre el ET. Para el diseño de dichas sondas se seleccionó el gen alkb. Se utilizaron primers previamente diseñados para la detección de dicho gen en muestras ambientales [4] [5] a los cuales se les adiciono una modificación en el extremo 5' para facilitar la unión covalente del DNA sonda al electrodo. Se ensayaron 2 concentraciones distintas de glutaraldehído (GA) (Sigma-Aldrich) (0,25 y 2,5)% v/v como enlazador para la formación de uniones covalentes. Se ensayaron 3 concentraciones distintas de BSA (Sigma-Aldrich) (0,5; 1 y 2)% p/v para bloquear la superficie libre del ET luego de inmovilizar la sonda de ssDNA y evitar el pegado inespecífico del ssDNA blanco. Para la etapa de bioreconocimiento, luego de desnaturalizar el ssDNA blanco (región de 100 pb del gen alkb la cual posee una secuencia complementaria al ssDNA sonda) a 95°C por 10 minutos, se ensayaron diferentes condiciones de incubación: a 50 °C y a temperatura ambiente por 2 minutos. Como control negativo se utilizó un fragmento de ssDNA de 100 pb con zonas no complementarias a la sonda de ssDNA inmovilizada. Todos los ensayos se realizaron por triplicado. El análisis estadístico fue realizado en GraphPad. En la figura 1 puede observarse el protocolo de armado del genosensor en forma esquemática.

III. CARACTERIZACIÓN ELECTROQUÍMICA DE LOS ELECTRODOS.

Se utilizó una solución salina tamponada con fosfato (PB) (pH 7,0) de 5 mM como electrolito de soporte para el

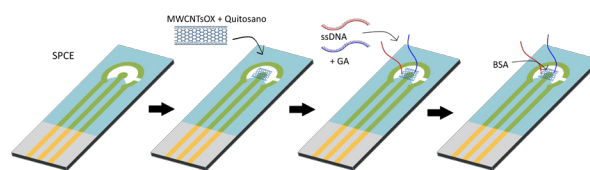


Fig. 1. Protocolo esquemático de la modificación de los electrodos.

pretratamiento electroquímico de SPCE. El pretratamiento electroquímico se realizó mediante voltamperometría cíclica (VC): 15 ciclos, a una velocidad de escaneo de 100 mV/s entre (0 y 1,5) V vs. Ag/AgCl, utilizando un potenciostato Squidstat Solo (Admiral Instrument). Las áreas de superficie electroquímica (ECSA) se calcularon mediante VC utilizando como electrolito la solución de $[\text{Fe}(\text{CN})_6]^{3-}$ 5 mM en 1 M KCl, 3 ciclos a una velocidad de escaneo de 50 mV/s entre 0,3 y 0,7 V. El principio de detección que se utilizará se basa en la exploración de cambios de estas propiedades de interfase del electrodo con el marcador redox $[\text{Fe}(\text{CN})_6]^{3-} / [\text{Fe}(\text{CN})_6]^{4-}$, utilizando mediciones de voltametría cíclica (VC). A través del uso de esta técnica podemos determinar la variable a cuantificar (I_p , corriente pico) debido a los cambios en la corriente no faradaica, sin la necesidad de elementos de marcaje extras. Luego de cada modificación al ET y de cada paso de optimización para el armado del biosensor se realizaron VC a fin de determinar la corriente pico anódica (I_{pa}). Para ello, se realizaron VCs: 3 ciclos, a una velocidad de escaneo de 50 mV/s entre 0 y 0,6 V vs. Ag/AgCl utilizando la sonda redox de ferri:ferrocianuro: 5 mM $[\text{Fe}(\text{CN})_6]^{3-} + [\text{Fe}(\text{CN})_6]^{4-} + 0,1$ M KCl en PB 50 Mm. Todas las mediciones electroquímicas se realizaron a temperatura ambiente.

IV. RESULTADOS Y DISCUSIÓN

A. Caracterización del proceso electroquímico

En la primera etapa se investigó el efecto de la nanoestructuración de la superficie del ET con diferentes dispersiones de MWCNTs, MWCNTs ox y CHI para luego realizar la caracterización electroquímica mediante VC. Los resultados demuestran que hay diferencias entre las distintas dispersiones en parámetros como la I_{pa} registrada y el ECSA (Tabla I y figura 2).

TABLE I
VALORES DEL ECSA E I_{pa} PARA LAS DIFERENTES DISPERSIONES.

Dispersión	ECSA (cm ²)	I_{pa} (μA)
MWCNTs	0,741±0,064	100,00±10,10
MWCNTs ox	0,593±0,076	50,38±4,27
CHI	0,531±0,098	73,49±7,17
MWCNTs+CHI	0,809±0,094	85,18±11,72
MWCNTs ox+CHI	1,016±0,035	107,30±12,05

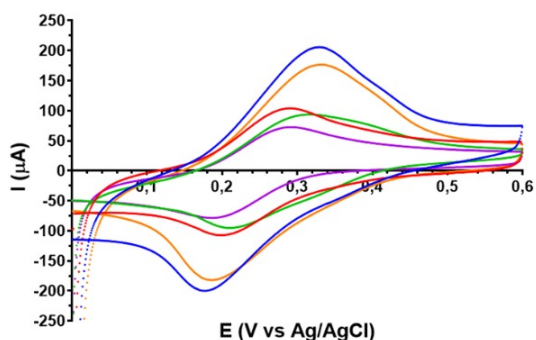


Fig. 2. Voltamogramas para electrodos modificados con distintas suspensiones. MWCNTs ox+CHI (azul), MWCNTs+CHI (rojo), CHI (verde), MWCNTs ox (violeta) y MWCNTs (naranja).

Los valores del ECSA varían para las distintas modificaciones que se ensayaron, presentando un área electroquímicamente activa mayor al área geométrica del electrodo de trabajo ($0,119 \text{ cm}^2$) en todos los casos, siendo la modificación con MWCNTsox + CHI la mayor además de menor dispersión en los datos, lo cual le da mayor reproducibilidad a las mediciones. Esto implica que la modificación de los ET aumentan el área superficial sobre la cual ocurre el proceso redox de la sonda evaluada. Además, a mayor ECSA, mayor será el recubrimiento de la biomolécula de reconocimiento (ssDNA, en este caso) y por ende mayor la probabilidad de detección del analito (también ssDNA) lo que permite aumentar la sensibilidad del biosensor. Al calcular la corriente de pico anódicas (Ipa) se obtuvo que los valores de corriente más altos registrados corresponden a electrodos modificados con las dispersiones de MWCNTs ox+CHI (Tabla I y Figura 2). Dado que el principio de detección del genosensor se basa en los cambios en la corriente de pico en presencia/ausencia de ssDNA complementario a la sonda, se busca obtener un sistema donde la sonda redox genere una corriente pico mayor, para obtener un rango lineal de análisis lo más amplio posible. Por todo lo anteriormente mencionado, seleccionamos para la modificación de la superficie del ET utilizado en el biosensor, la dispersión de MWCNTs ox + CHI. Se estudió la estabilidad de electrodos modificados con esta dispersión seleccionada almacenados a 4°C . Se analizaron las I_p y se encontró que el valor de la misma permanece constante hasta después del día 7. Ésto indicaría que los electrodos de trabajo modificado son estables en estas condiciones de almacenamiento durante dicho lapso de tiempo. Pasados los 14 días, se encontró una disminución del valor de la I_p de entre un 14,5% y un 21,7%.

B. Optimización del protocolo de armado del genosensor

Se estudió el agregado de glutaraldehído (GA) como enlazador para la unión covalente de la sonda de ssDNA a la superficie del ET modificada con la dispersión MWCNTs ox+CHI. En primer lugar se estudió si su agregado de GA (2,5% v/v) durante la inmovilización de la sonda afectaba la

señal detectada (I_{pa}) frente a un control sin GA. Al agregar GA en el momento de la inmovilización la corriente detectada es considerablemente menor, además de que los potenciales de los picos (E_p) se separan. Lo contrario sucedió con el control sin GA, la I_p no se ve alterada significativamente y la forma del gráfico no parecería variar de forma apreciable (figura 3).

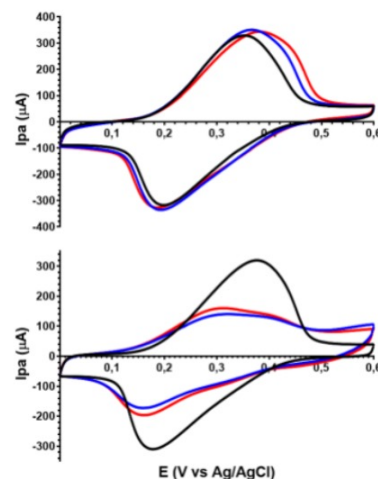


Fig. 3. Voltamograma de los electrodos modificados con suspensión de MWCNTs ox+CHI, inmovilizando sin GA (arriba) y con GA (abajo). Las mediciones se realizaron luego de la modificación (negro), inmovilización (azul) y bloqueo (rojo)

Se procedió por lo tanto a optimizar su uso, estudiando su efecto a distintas concentraciones, (0,25 y 2,5)% v/v. Se registró la I_p de electrodos modificados, y se observó que la I_{pa} media registrada para electrodos tratados con GA 2,5% v/v es menor a la de los electrodos tratados con 0,25% v/v (Tabla II). Se realizó un ANOVA de dos factores y se encontró que la interacción entre los factores tratamiento y concentración no es significativa y que no hay un efecto significativo del tratamiento, mientras que sí lo hay de la concentración. Esto significa que la concentración de GA influye significativamente en la I_{pa} registrada, siendo ésta mayor cuando la concentración del entrecruzante es menor.

TABLE II
MEDIA MAS DESVIO DE LA I_{PA} PARA ELECTRODOS INMOVILIZADOS CON DISTINTAS CONCENTRACIONES DE GA.

[GA] (%v/v)	Media
0,25	163,400±3,941
2,5	90,800±4,897

Se pudo observar en ambos casos que los picos del voltamograma realizados con la sonda redox $[\text{Fe}(\text{CN})_6]^{3-} / [\text{Fe}(\text{CN})_6]^{4-}$ se ensanchan y las corrientes registradas disminuyen de forma considerable. El ensanchamiento de picos se podría deber a que al modificar la superficie del electrodo se ve afectada la cinética de la reacción [6]. Por otro lado, la disminución de la corriente de pico se debe a un aumento de

la repulsión electrostática entre los grupos fosfato del ssDNA inmovilizado y los iones ferricianuro, impidiendo que este se acerque a la superficie del electrodo y transfiera sus electrones. Siguiendo con el diseño del protocolo de armado del biosensor, se ensayaron 3 concentraciones de BSA diferentes (0, 5, 1 y 2 % p/v en PB, pH 7,4). Está proteína se utiliza como bloqueador de la superficie libre del ET una vez inmovilizada la sonda de ssDNA. Pudimos determinar que la mejor condición para realizar el bloqueo de la superficie del ET es con BSA al 1% p/v en PB a pH 7,4. Como paso final para comprobar la utilidad del genosensor, se procedió a optimizar la etapa de biorreconocimiento, para ello se colocó una alícuota de DNA blanco sobre el ET y se ensayaron diferentes condiciones de incubación: a 50 °C y a temperatura ambiente por 2 minutos. En la Figura 4 se muestran las corrientes pico calculadas para cada etapa del diseño experimental incluyendo la etapa de biorreconocimiento donde se observó la señal (I_{pa}) disminuye un 11,65% respecto al paso anterior de bloqueo cuando el electrodo se incubaba a 50°C y un 2,03% cuando se hace a temperatura ambiente. En el caso del control negativo no se obtuvieron disminuciones significativas de la señal, lo que demuestra que no es reconocido por la sonda de ssDNA utilizada y por lo tanto que es reconocimiento del genosensor es específico.

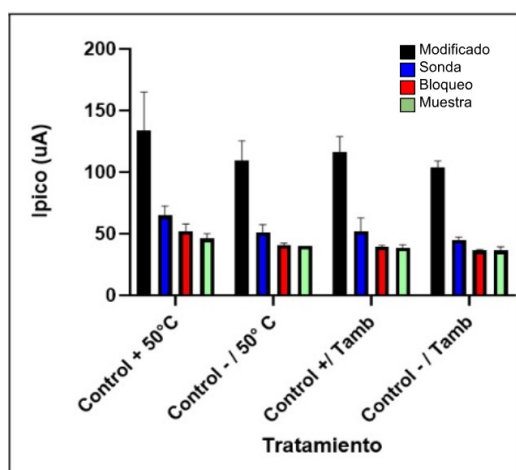


Fig. 4. Promedio de las I_{pa} obtenidas en las diferentes etapas ya optimizadas para el armado del genosensor.

V. CONCLUSIONES

En cuanto a la sensibilidad del electrodo, se pudieron observar diferencias significativas entre las distintas suspensiones siendo la más estable la de MWCNTs ox y quitosano. Además se pudo determinar que el ECSA es significativamente mayor cuando se modifica el ET con dicha dispersión. En cuanto al protocolo de inmovilización, se puede concluir que el GA es necesario para que la sonda de ssDNA se una covalentemente a la superficie nanoestructurada del biosensor, manteniendo su estabilidad y que la mejor condición para realizar el bloqueo de la superficie del ET es con BSA al 1% p/v en PB a pH 7,4. Se logró obtener y purificar el DNA blanco mediante el uso de los primers diseñados para tal fin, los cuales se modificaron para ser utilizados con sonda de ssDNA. Se llevó a cabo la prueba de concepto demostrando que es posible el reconocimiento del DNA blanco mediante la metodología planteada, pudiendo observarse una disminución de aproximadamente 12% de la I_p. Actualmente se está comenzando a trabajar en la determinación de la sensibilidad del genosensor para el gen de interés además de comenzar los ensayos con muestras de DNA genómico y de muestras ambientales.

REFERENCES

- [1] M. N. Velasco-García and T. Mottram, "Biosensor technology addressing agricultural problems," *Biosystems Engineering*, vol. 84, no. 1, pp. 1–12, Jan. 2003. doi:10.1016/s1537-5110(02)00236-2
- [2] N. Zhu, Z. Chang, P. He, and Y. Fang, "Electrochemical DNA biosensors based on platinum nanoparticles combined carbon nanotubes," *Analytica Chimica Acta*, vol. 545, no. 1, pp. 21–26, Jul. 2005. doi:10.1016/j.aca.2005.04.015
- [3] P. M. Tribelli, C. Di Martino, N. I. López, and L. J. Raiger Iustman, "Biofilm lifestyle enhances diesel bioremediation and biosurfactant production in the Antarctic polyhydroxyalkanoate producer *Pseudomonas extremaustralis*," *Biodegradation*, vol. 23, no. 5, pp. 645–651, Feb. 2012. doi:10.1007/s10532-012-9540-2
- [4] Kloos, K., Munch, J. C., & Schloter, M. (2006). "A new method for the detection of alkane-monoxygenase homologous genes (alkB) in soils based on PCR-hybridization." *Journal of microbiological methods*, 66(3), 486–496. <https://doi.org/10.1016/j.mimet.2006.01.014>
- [5] S. M. Powell, S. H. Ferguson, J. P. Bowman, and I. Snape, "Using real-time PCR to assess changes in the hydrocarbon-degrading microbial community in Antarctic soil during bioremediation," *Microbial Ecology*, vol. 52, no. 3, pp. 523–532, Aug. 2006. doi:10.1007/s00248-006-9131-z
- [6] S. Kim, D. Kim, G. Hwang, and J. Jeon, "A bromide-ligand ferrocene derivative redox species with high reversibility and electrochemical stability for aqueous redox flow batteries," *Journal of Electroanalytical Chemistry*, vol. 869, p. 114131, Jul. 2020. doi:10.1016/j.jelechem.2020.114131

Avances y desafíos en el desarrollo de un aptasensor electroquímico para atrazina

Andrea M. Monroy
 Área Química, Instituto de Ciencias
 Universidad Nacional de General
 Sarmiento
 Buenos Aires, Argentina
 amonroy@campus.ungs.edu.ar

Griselda L. Sosa
 Área Química, Instituto de Ciencias
 Universidad Nacional de General
 Sarmiento
 Buenos Aires, Argentina
 glosa@campus.ungs.edu.ar

Helena M. Ceretti
 Área Química, Instituto de Ciencias
 Universidad Nacional de General
 Sarmiento
 Buenos Aires, Argentina
 hceretti@campus.ungs.edu.ar

Silvana A. Ramírez
 Área Química, Instituto de Ciencias
 Universidad Nacional de General
 Sarmiento
 Buenos Aires, Argentina
 sramirez@campus.ungs.edu.ar

M. Belén Ponce
 Área Química, Instituto de Ciencias
 Universidad Nacional de General
 Sarmiento
 Buenos Aires, Argentina
 mponce@campus.ungs.edu.ar

Abstract— Se presentan los avances en el desarrollo de un aptasensor para atrazina empleando espectroscopia de impedancia electroquímica para la generación de la señal de reconocimiento. Si bien en bibliografía se encuentran trabajos que logran límites de detección en la escala sub-nanomolar para este analito, las estrategias label-free empleadas implican construcciones elaboradas. Esta propuesta pretende realizar contribuciones en la dirección de simplificar la construcción del aptasensor. En este trabajo presentamos los resultados obtenidos para el reconocimiento de atrazina empleando el aptámero seleccionado por Williams et al inmovilizado sobre electrodos de oro serigrafados vía interacción oro-azufre. Las curvas de reconocimiento obtenidas muestran la posibilidad de reconocer y detectar la presencia de atrazina en un ensayo label-free sencillo y desde un punto de vista cuantitativo sugieren un rango lineal cuyo límite superior está en el orden micromolar.

Keywords— aptasensor – atrazina – Espectroscopia de impedancia electroquímica – Electrodos serigrafados – Estrategia label-free

I. INTRODUCCIÓN

Los aptasensores se basan en el reconocimiento molecular entre una hebra simple cadena de ADN o ARN y un analito. La buena estabilidad térmica, la posibilidad de conjugación con diferentes moléculas sin afectar la afinidad, la detección de sustancias tóxicas o especies con baja inmunidad, entre otros atributos, han despertado el interés para su aplicación en diversos campos como el diagnóstico médico (*point of care*) y el monitoreo ambiental [1].

En cuanto a los métodos de detección, han sido desarrollados protocolos para la detección electroquímica de secuencias de ADN (genosensores), moléculas pequeñas y proteínas. Un factor clave es la cantidad de hebras de ADN simple cadena a inmovilizar sobre la superficie para lograr una señal cuantificable. Los electrodos serigrafados (*screen-printed electrodes*, SPE) ofrecen una plataforma versátil para el diseño de dispositivos debido a la posibilidad de modificar la superficie con nanomateriales, polímeros conductores, etc. Asimismo, la electrodeposición de oro sobre la superficie de carbono (AuSPE) permite el anclaje directo vía quimisorción de hebras de ADN tioladas. La técnica de impedancia (EIS) ha sido ampliamente utilizada para detectar los cambios

sucesivos que tienen lugar sobre la superficie luego de cada etapa de ensamblado del sensor. Esta técnica electroquímica presenta la ventaja de no requerir modificaciones químicas adicionales para la generación de la señal. La misma también resulta adecuada para detectar el reconocimiento molecular entre el aptámero anclado a la superficie y su analito [2]. Sin embargo, en el caso de moléculas pequeñas (masa molar < 1000 Da) la detección conlleva el desafío de magnificar un pequeño cambio.

La atrazina (2-cloro-4-etilamin-6-isopropilamin-s-triazina, ATZ, masa molar 215,68 Da) es un herbicida del grupo de las triazinas, usado para la eliminación de malezas en diversos cultivos. En Argentina, es el tercer compuesto más usado junto con el glifosato, y se ha detectado en muestras de suelo ($7-66 \mu\text{g kg}^{-1}$) y agua de lluvia ($0,22 - 26,9 \mu\text{g L}^{-1}$) de áreas urbanas de la pampa argentina [3][4]. Se considera un disruptor endocrino y ha sido relacionado con carcinogénesis [5]. La EPA recomienda una cantidad máxima de atrazina en agua potable de $3 \mu\text{g L}^{-1}$ ($0,014 \mu\text{M}$) [6].

Si bien diversos autores han logrado límites de detección en la escala nanomolar para ATZ, las estrategias *label-free* propuestas implican construcciones elaboradas [7][8][9][10]. Esta propuesta pretende realizar contribuciones en la dirección de simplificar la construcción del aptasensor. En este trabajo presentamos los resultados obtenidos para el reconocimiento de ATZ empleando el aptámero seleccionado por Williams et al [11]. Se utilizaron AuSPE sobre los que se inmovilizó el aptámero vía interacción oro-azufre. La detección del reconocimiento se realiza por EIS.

II. MATERIALES Y MÉTODOS

Se empleó el aptámero que reconoce atrazina [11] modificado en su extremo 5' con un grupo disulfuro para la inmovilización sobre oro vía un enlace S-Au. El mismo fue provisto por IDT, purificado por HPLC y su secuencia es: 5'-(CH₂)₆-S-S-(CH₂)₅-TTTTTACTGTTTGCCTGGCGGATTTAGCCAGTCA GTG.

Se realizó una electrodeposición de oro a corriente controlada sobre electrodos serigrafados de carbono ($A = 0,07 \text{ cm}^2$) [12] utilizando un baño de oro comercial (espesor 24 KTS, Vm 316). Los AuSPE obtenidos se caracterizaron por voltametría cíclica (CV) y EIS en presencia de $\text{K}_4\text{Fe}(\text{CN})_6$ 5 mM en buffer

Hepes 50 mM pH 7,2 / NaCl 300 mM (Buffer 1), empleando un electrodo de referencia de Ag/AgCl. La electrodeposición de Au sobre los electrodos serigrafados se verificó mediante microscopía electrónica de barrido (SEM) y análisis por EDS (*Energy Dispersive X-Ray Spectroscopy*) (LAMEI).

Para la modificación de los AuSPE con el aptámero se empleó un procedimiento ya probado en nuestro laboratorio [13]. Brevemente, se redujo el puente disulfuro utilizando Tris(2-carboxietil) fosfina (TCEP) 1,5 mM durante 2 h, en oscuridad. Luego se diluyó en buffer Tris 25 mM pH 8,2 / NaCl 300 mM / MgCl₂ 10 mM (Buffer 2), hasta alcanzar una concentración de 100 nM. A continuación, se depositó una gota de 25 µL de dicha solución (Apt-SH) sobre los electrodos por 1 h a temperatura ambiente. Se lavaron con Buffer 2, se secaron bajo corriente de N₂ y se depositó una gota de 25 µL de 6-mercaptop-1-hexanol (MCH) 1 µM en Buffer 2, por 30 min a temperatura ambiente. Se lavaron con Buffer 2, se secaron con N₂ y se caracterizaron por CV y EIS.

Se determinó la densidad superficial de aptámero por cronocoulombimetría utilizando (Ru(NH₃)₆)³⁺ [14].

Una vez modificados los AuSPE, se procedió al reconocimiento de ATZ por inmersión de los electrodos durante 1 h, a temperatura ambiente, en soluciones de ATZ (0,01 - 1 µM) en Buffer 2. Se caracterizaron por CV y EIS, previo lavado con Buffer 2 y secado en corriente de N₂.

III. RESULTADOS

A fin de seleccionar un conjunto de electrodos AuSPE con comportamiento similar (en general $n \geq 3$) se empleó K₄Fe(CN)₆ 5mM como sonda redox y CV y EIS como técnicas de control. Se tomaron los parámetros característicos de separación de los picos anódico y catódico en la CV (ΔE_p) y la resistencia a la transferencia de carga (R_{tc}) en EIS, como criterio de selección. Las Fig. 1A y B muestran la respuesta electroquímica de un conjunto seleccionado de AuSPE ($n=5$). Se observa una respuesta de reproducibilidad aceptable. Desde un punto de vista electroquímico, se considera que esta sonda presenta un comportamiento reversible cuando el ΔE_p es de 60 mV/n. Sin embargo, los valores experimentales de ΔE_p son de (98 ± 4) mV, lo que sugiere que la reversibilidad de la respuesta se ve afectada en esta superficie.

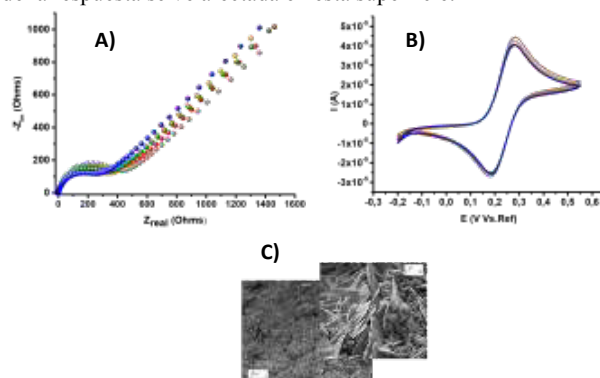


Fig. 1. Respuesta de AuSPE por EIS (A) y CV (B) en K₄Fe(CN)₆ 5mM en Buffer 1 para 5 electrodos. Cada color representa un electrodo diferente. Imágenes obtenidas por SEM (C) para un AuSPE (aumento 1000x y 10000x).

Las imágenes obtenidas por SEM y el análisis por EDS, confirman la electrodeposición de Au sobre la base de carbono de los electrodos serigrafados. Se observa una superficie heterogénea en la microescala (Fig. 1C).

Si bien la técnica de CV se emplea frecuentemente para evaluar la reproducibilidad de la respuesta electroquímica, su sensibilidad no es alta. En efecto, la respuesta de los cinco electrodos anteriores por EIS (Fig. 1A) muestra aún cierta variabilidad en los valores de la R_{tc} , (346 ± 49) ohm. Empleamos dicha técnica como un segundo criterio de control de reproducibilidad de respuesta superficial.

Una vez modificados los AuSPE con la secuencia del aptámero, se realizó el tratamiento con MCH. El mismo tiene como objetivo cubrir la superficie libre y orientar las secuencias de ADN. Se evaluó la modificación comparando los resultados de EIS.

La Fig. 2 muestra el gráfico de Nyquist antes y después de modificar la superficie de los AuSPE con el aptámero y el MCH. El aumento en la R_{tc} y la mayor respuesta capacitiva evidencian la modificación del electrodo. Además, empleando cronocoulombimetría en solución de (Ru(NH₃)₆)³⁺ se evaluó el cubrimiento superficial, el valor obtenido, (4,7 ± 0,7) × 10¹² moléculas/cm², está en concordancia con los datos reportados en bibliografía [14].

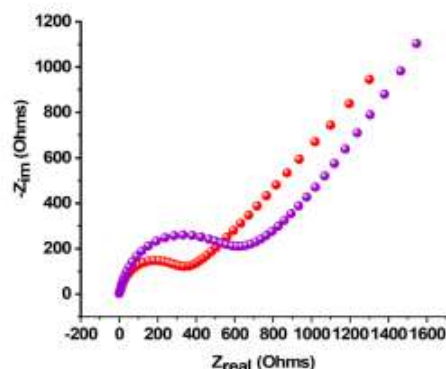


Fig 2. Representación de Nyquist para un electrodo AuSPE, sin modificar (rojo), modificado con el Apt-SH + MCH (violeta). Sonda redox: K₄Fe(CN)₆ 5 mM en Buffer 1.

Para evaluar el efecto de la presencia de ATZ, se midió la respuesta por CV y EIS de los AuSPE modificados antes y después de ser expuestos a soluciones de ATZ en el rango micromolar. Los resultados obtenidos para ATZ 1 µM se muestran en la Fig. 3. La representación de Nyquist no mostró un cambio correlacionable con la concentración de ATZ. Se decidió, por lo tanto, emplear el gráfico de BODE, módulo de la impedancia (Z) vs frecuencia, para los datos experimentales.

La impedancia total (Mod Z) se calculó usando la siguiente fórmula:

$$\text{Mod } Z = (R^2 + X^2)^{0,5} \quad (\text{ec. 1})$$

donde R es la componente real y X se refiere a la componente imaginaria de la impedancia.

A altas frecuencias, la impedancia se debe únicamente a la resistencia de la solución que se mantiene constante independientemente de la modificación de la superficie y/o de

la presencia del analito. A bajas frecuencias, se hace evidente el comportamiento capacitivo. A frecuencias intermedias (inset Fig. 3), contribuyen tanto la capacidad de la doble capa como la resistencia del electrolito y es donde los cambios son más significativos. Como puede observarse en la Fig. 3, la exposición a ATZ conduce a una disminución en la señal de impedancia a frecuencias intermedias. Esto sugiere que el ingreso de ATZ a la capa de reconocimiento modifica las características de la componente capacitiva del sistema de detección. Estas diferencias se hacen más significativas en la zona de 100 Hz.

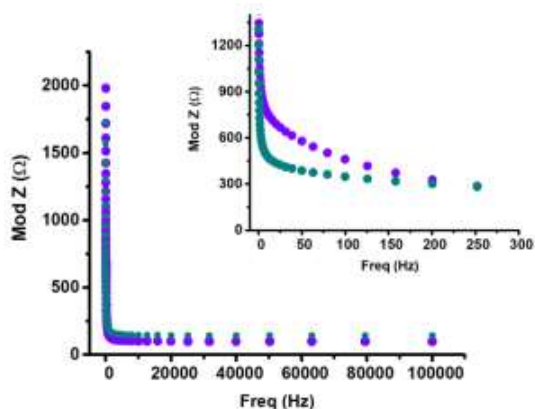


Fig. 3. Módulo de Z vs Frecuencia para AuSPE modificado con el Apt-SH + MCH (violeta) y expuesto a ATZ 1 µM (verde). Sonda redox: $K_4Fe(CN)_6$ 5 mM en Buffer 1.

La Fig. 4 muestra el efecto de la exposición a ATZ para el aptámero inmovilizado sobre AuSPE (n=6). En estas curvas de reconocimiento del analito, se graficó la diferencia relativa de Z, considerando como blanco (Z_0) la señal obtenida en ausencia de ATZ. Se observa una curva de respuesta típica, que se ameseta, evidenciando la posible saturación de la capa de reconocimiento. La presencia de variabilidad en la construcción se hace evidente a través de la magnitud de las barras de error.

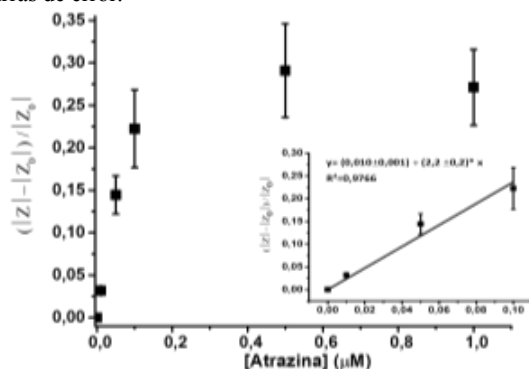


Fig. 4. Curva de reconocimiento de ATZ. El inserto muestra la región lineal.

En cuanto a su utilidad para la detección y cuantificación de ATZ en muestras acuosas, la región lineal de la curva de reconocimiento se extiende hasta concentraciones en torno a 0,1 µM. Los valores límites establecidos por EPA se encuentran en la zona del límite de detección/cuantificación de nuestra curva, lo que indica que es necesario ampliar el rango lineal hacia concentraciones más bajas. En cambio, la

región de altas concentraciones podría ser de utilidad para la cuantificación en las muestras de agua de lluvia, disponiéndose así de un dispositivo transportable a campo.

IV. CONCLUSIONES

Los resultados obtenidos muestran la posibilidad de reconocer y detectar la presencia de ATZ en un ensayo label-free sencillo empleando un aptámero inmovilizado sobre electrodos serigrafados que emplean oro como material de anclaje. La curva de reconocimiento sugiere un rango lineal cuyo límite superior está en el orden micromolar.

La deposición electroquímica de nanopartículas de oro de distintas geometrías, junto con el uso de secuencias doble cadena en una estrategia de desplazamiento por el analito, son aspectos a explorar para la modificación superficial con el objetivo de mejorar la magnitud de la señal en la región de concentraciones nanomolares.

AGRADECIMIENTOS

A la Organización para la Prohibición de las Armas Químicas (OPCW, Proyecto L/ICA/ICB-103/21) y a la Universidad Nacional de General Sarmiento por el financiamiento.

REFERENCIAS

- [1] Z. Taleati, A. Khoshroo, y M. Mazloum-Ardakani, "Screen-printed electrodes for biosensing: a review (2008-2013)", *Microchim. Acta* 181, 865-891, 2014.
- [2] S. Trashin, M. de Jong, T. Breugelmans, S. Pilehvar y K. DeWael, "Label-free impedance aptasensor for major peanut allergen ARA H1", *Electroanalysis* 27, 32-37, 2015.
- [3] H. Obana, M. Okihashi, K. Akutsu, Y. Kitagawa y S. Hori, "Determination of acetamiprid, imidacloprid, and nitenpyram residues in vegetables and fruits by high-performance liquid chromatography with diode-array detection", *J. Agr. Food Chem.* 50, 4464-4467, 2002.
- [4] L. L. Alonso, P. M. Demetrio, M. A. Etchegoyen y D. J. Marino, "Glyphosate and atrazine in rainfall and soils in agroproductive areas of the pampas region in Argentina", *Science of Tot. Environ.* 645, 89-96, 2018.
- [5] M. Wang, J. Chen, S. Zhao, J. Zheng, K. He, W. Liu, W. Zhao, J. Li, K. Wang, Y. Wang, J. Liu y L. Zhao, "Atrazine promotes breast cancer development by suppressing immune function and upregulating MMP expression", *Ecotox. Environ. Safety* 253, 114691, 2023.
- [6] EPA. Atrazine. 2017. <https://www.epa.gov/ingredients-used-pesticide-products/atrazine>
- [7] L. Fan, C. Zhang, W. Yan, Y. Guo, S. Shuang, C. Dong y Y. Bi, "Design of a facile and label-free electrochemical aptasensor for detection of atrazine", *Talanta* 201, 156-164, 2019.
- [8] L. Madianos, E. Skotadis, G. Tsekis, L. Patsiouras, M. Tsigourakos y D. Tsoukalas, "Impedimetric nanoparticle aptasensor for selective and label-free pesticide detection", *Microelectron. Eng.* 189, 39-45, 2018.
- [9] L. Madianos, G. Tsekis, E. Skotadis, L. Patsiouras y D. Tsoukalas, "A highly sensitive impedimetric aptasensor for the selective detection of acetamiprid and atrazine based on microwires formed by platinum nanoparticles", *Biosens. Bioelectron.* 101, 268-2674, 2018.
- [10] Z. Qi, P. Yan, J. Qian, L. Zhu, H. Li y L. Xu, "A photoelectrochemical aptasensor based on CoN/G-C3N4 donor-acceptor configuration for sensitive detection of atrazine", *Sens. Act. B Chem.* 387, 133792, 2023.
- [11] R. M. Williams, C. L. Crihfield, S. Gattu, L. A. Holland y L. J. Sooter, "In vitro selection of a single-stranded DNA molecular recognition element against atrazine", *Int. J. Mol. Sci.* 15, 14332-14347, 2014.
- [12] G. Priano, G. González, M. Günther y F. Battaglini, "Disposable gold electrode array for simultaneous electrochemical studies", *Electroanalysis* 20, 91, 2008.
- [13] H. Ceretti, B. Ponce, S. A. Ramirez y J. M. Montserrat, "Adenosine reagentless electrochemical aptasensor using a phosphorothioate immobilization strategy", *Electroanalysis* 22, 147-150, 2010.
- [14] A. B. Steel, T. M. Herne y M. J. Tarlov, "Electrochemical quantitation of DNA immobilized on gold", *Anal. Chem.* 70, 4670-4677, 1998.

An Automated Low-Cost SPR Sensor for Glyphosate Detection in Potable Water

1st Matheus Rotta Ribeiro
Dept. Electrical Engineering
University of Brasilia(UnB)
 Brasilia, Brazil
 matheus.rotta.ribeiro@gmail.com

2nd Juliana de Novais Schianti
Dept. Electrical Engineering
University of Brasilia (UnB)
 Brasilia, Brazil
 juliana.schianti@unb.br

3rd Daniel Vieira Neves
Dept. of Cellular Biology
University of Brasilia (UnB)
 Brasilia, Brazil
 210041498@aluno.unb.br

4th Renata Vieira Bueno
Dept. of Cellular Biology
University of Brasilia (UnB)
 Brasilia, Brazil
 buenorvieira@gmail.com

5th Rômulo Ferreira dos Santos
Dept. of Electrical Engineering
University of Brasilia (UnB)
 Brasilia, Brazil
 romulo.santos@ieee.org

6th João Alexandre R. G. Barbosa
Dept. of Cellular Biology
University of Brasilia (UnB)
 Brasilia, Brazil
 joaobarbosa@unb.br

7th Josaphat Desbas
Dept. Electrical Engineering
University of Brasilia (UnB)
 Brasilia, Brazil
 desbasj007@yahoo.fr

8th Daniel Orquiza de Carvalho
Dept. Electrical Engineering
University of Brasilia (UnB)
 Brasilia, Brazil
 daniel.orquiza@ene.unb.br

Abstract—In this paper, a low cost Surface Plasmon Resonance (SPR) automated platform using the Kretschmann configuration is presented. It consists of a custom mechanical system, optic system, and a controller. The mechanical system incorporates two automated anti-backlash goniometers. Mechanical supports for prism and flow cell heads were produced in 3D Printer and the flow cell was fabricated using PDMS polymer. The SPR set up were tested using different solutions with a very small refraction index range and with a resolution of 0.01 degree. This system it is under development and will be applied to the detection of herbicide concentration in potable water. Some initial results with soy herbicide (glyphosate) and an immobilized biosensor are presented showing the viability of the set up.

Index Terms—surface plasmon resonance, biosensor, microfluidics, glyphosate, low-cost

I. INTRODUCTION

Glyphosate is an herbicide with phosphorous in its composition and is widely used in world agriculture to control weeds in soybeans, cotton, coffee, and other large plantations [1]. In Brazil, glyphosate is the most consumed herbicide, as the country is one of the largest soybean exporters in the world. Many different studies have identified the use of glyphosate as a possible cause of different cancers and other long-term illnesses in addition to being the cause of instant deaths due to poisoning with high exposure to the herbicide [2] [3]. Different detection methods have been studied to

detect the presence of glyphosate such as chromatographic, electrochemical, and spectroscopic methods [1]. Because of its characteristics such as composition, solubility in water and low mass, glyphosate detection is considered a challenge [1]. In this way, Surface Plasmon Resonance (SPR), a spectroscopic technique, is being studied in this work in order to exploit its advantages such as being label free and able to perform real time measurements.

Surface plasmon resonance (SPR) refers to the excitation of electromagnetic surface waves that occur at the interface between a dielectric and a metallic medium due to the incidence of p-polarized light. These excitations give rise to surface plasmons, which resonate with the reflected light. This resonance creates a fringe region or dark band where the intensity of reflected light reaches a minimum at a specific angle or frequency, which can then be correlated to changes in the local refractive index. [4] The most common configuration for biosensing applications is the Kretschmann configuration [5], which consists of a prism, a nanometal film, and a sensing layer.

Although an effective technique for real-time, label-free biomolecular interactions [7], most commercial setups utilize complex optics, microfluidics, and electronics systems, making them, as of present, very costly. [8] - [10] In this paper a low-cost surface plasmon resonance sensor system with a detecting EPSPS (5-enolpyruvylshikimate-3-phosphate synthase) protein biosensor is presented. The target analyte chosen is glyphosate, which is one of the world's most-

Conselho Nacional de Desenvolvimento Científico e Tecnológico (CNPq), grants number 102003/2022-0, and also Fundação de Apoio à Pesquisa do Distrito Federal (FAPDF) with grant number 271/2021-03/2021, 00193-00000923/2021-48. IBERSENSOR 2024

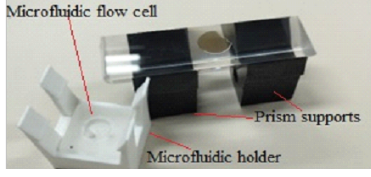


Fig. 1. Experimental set up, in detail: microfluidic flow cell and holder, prism supports, BK7 prism and golden chip

used herbicides.

This paper is organized as follows: Section II presents the theory of surface plasmon resonance, in Section III the process of fabricating the Au films and microfluidic device embedded in our system are shown, and in Sections IV, V the final remarks and conclusion of the tests, and overall sensor performance.

II. THEORY

A. Surface plasmon resonance theory

Surface plasmon resonance can be described as a charge collective-density oscillation at the interface of two mediums with opposite dielectric constant signs. That charge density oscillation is associated to a surface plasmon wave (SPW) that is TM polarized and parallel to the interface plane. The propagation constant of the SPW at a semi-infinite dielectric, metal follow the given expressions [6] [7]

$$\beta_{SP} = \frac{2\pi}{\lambda} \sqrt{\frac{\epsilon_m \epsilon_d}{\epsilon_m + \epsilon_d}} \quad (1)$$

$$\beta_{pr} = \frac{2\pi}{\lambda} n_p \sin(\theta) = \text{Re}\{\beta_{SP}\} \quad (2)$$

Where, $\epsilon_m, \epsilon_d, n_p$ are the metal film, sample permittivities, and prism refraction index. λ the free-space wavelength, and β_{sp}, β_{pr} , are the propagation constants for impinging light at the dielectric metal interface and at the prism-metal interface, respectively.

III. MATERIALS AND METHODS

A. Au and Ti deposition

Round glass slides were utilized as substrate for the SPR sensor. The slides were cleaned using RCA standard recipes to prepare for RF magnetron sputtering deposition of metal films. After the simulations, a film of 5 nm of titanium adhesion layer was deposited on the glass surface, and on the sequence, 50 nm of gold was deposited. The deposition parameters were power of 150 W, chamber pressure of 1 mTorr, and Argon flow of 60 sccm.

B. Supports, Chip Holder and Flow Cell

The SPR golden chip was connected to the prism by two supports, a chip holder, and a flow cell. The support and chip holder was produced using PLA(polylactic acid) polymer in a filament 3D-Printer Tevo Tornado. All pieces were printed with 50% filling using a 0.4 mm nozzle. A mold for the microfluidic

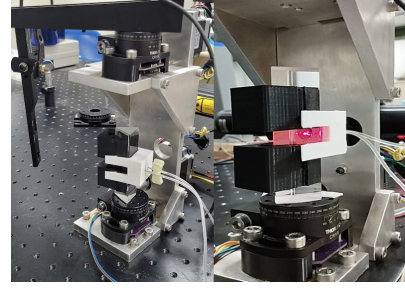


Fig. 2. SPR experimental set up in operation on the goniometer. Left picture: The spr sensor in custom-designed aluminium chassis. Right picture: Sample Holder.

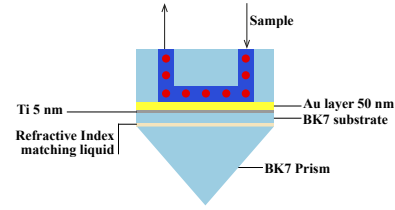


Fig. 3. Description of the SPR sensors transducer layers.

device was also produced under the same configurations. The flow cell design was reproduced with PDMS(polydimethylsiloxane) polymer. The microfluidic device is a well of 8 mm in diameter and 3.6 mm in height. The total volume of the well was about 0,180 mL. All pieces were designed using FUSION 360 (Autodesk, San Francisco) and the software IDEAMAKER (Raise3d, Shanghai) to prepare the slicing for the 3D Printer. All parts are shown in detail in Fig. 1, and in Fig. 2, the setup in operation.

C. SPR Sensor Optical Setup

The transducer configuration can be seen in Fig. 3. It consists of a prism(DWNTZ, Shenzhen) followed by a thin film of refraction index matching fluid, followed by a glass slide (BK7 substrate) where an adhesion titanium layer and a gold layer are deposited on top. On the gold layer, a microfluidic well transports the sample material.

The experimental setup is described in Figure 4. It comprises of an isosceles prism made of BK7 glass ($n \approx 1.5151$), two anti-backlash motorized goniometers (Thorlabs, CR1M) that are aligned by their rotating axis, an arm for holding a photodetector (Thorlabs, PM100) and a custom-designed rotating arm analyzer, that assembles the parts together.

To place the glass slides on the prism, first a small drop of refractive index (RI) matching oil is placed on the glass slide. Following, it is placed gently on the prism face forming a thin film between the prism and slide surface. The droplet size is chosen such that all of the space gets filled with RI-matching oil without spilling over.

To illuminate the gold film, a HeNe laser ($\lambda = 632.8$ nm) with a power of 20 mW (CW) was used (1135P,

JDS Uniphase). The laser was fixed at a p-polarization configuration, followed by a polarizing beam splitter (PBS102, Thorlabs). Additionally, two mirrors are added in typical *walking the beam* configuration to simultaneously control beam direction and height. This arrangement enables the reflectivity measurements at oblique angles in a θ - 2θ configuration. The whole system is controlled via a custom-made Matlab script.

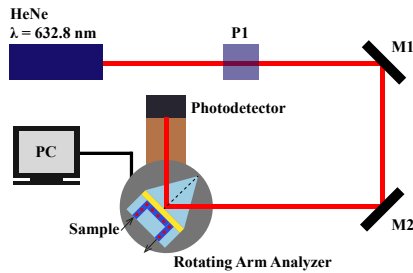


Fig. 4. Optical setup for SPR angle interrogation. M1, M2: mounted mirrors. P1: polarizer.

D. Solutions preparation and SPR Measurements

Different concentrations of water solution combined with calcium chloride ($CaCl_2$) were utilized to evaluate the SPR system (Fig 6). The solutions have concentrations varying from 0 to 5 % in weight of salt. The golden chip was cleaned using Piranha solution ($4H_2SO_4 : 1H_2O_2$), and a refractive index (RI) matching oil was utilized between the chip and prism. The solutions were injected using a syringe pump (NE-1000) with a flow rate maintained in 0.1 mL/min.

Besides the described tests, preliminar characterization was performed with biological application of this SPR set up. The solutions used for immobilization of the EPSPS developed protein was nickel and buffer solution. After cleaned in Piranha solution the golden chip remained overnight in a solution of NTA-SAM in order to prepare for immobilization. On sequence, it was introduced a set of solutions for immobilization treatment, being water, nickel, buffer, protein and buffer solution again using the same fluid flow rate for all substances. After this, the chip is ready to test the presence of glyphosate on water sample solutions.

IV. RESULTS AND DISCUSSION

A. Refractive index calibration

Fig. 5 shows the curves of the power reflectance (mW) against resonance degree for different concentrations of calcium chloride solutions. The samples were calibrated with a ST 335a digital refractometer (Nanning Bokun, Guangxi). For the water solution, represented by a black curve, it was obtained a resonance angle of 75.80° an expected value for the water solution. As the salt concentration increased, it was possible to observe that other curves were shifted to the right, with resonance angles varying from each

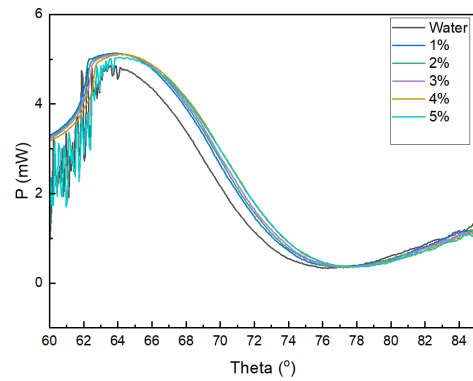


Fig. 5. Resonance angles for calcium chloride solutions in different concentrations

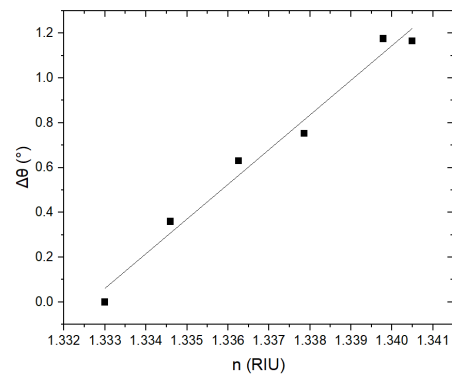


Fig. 6. Curve of resonance angles by measured refractive index of calcium chloride solutions in different concentrations.

concentration around 0.3° . The concentration of 5%, for instance, has a resonance angle of 77.85° . For angles around 60.0° , some signal noise was observed possibly due to instabilities on the detector during measurements. Each measurement was conducted three times, and the average data was plotted on the picture. In Fig. 6 a plot of the measured refractive index of the chloride solutions versus the resonance angle obtained for the SPR minima for each concentration is presented. It is possible to observe that the system has a sensitivity of around 159.72 degrees per refractive index unit change.

B. First biological tests

The SPR set up was designed to evaluate the presence and concentration of glyphosate herbicide in potable water solution through the use of an immobilized detecting protein. The first test of protein EPSPS immobilization on the golden surface was conducted and the results are shown below on Fig.7. The immobilization treatment starts after a cleaning process. The sequence of solutions was conducted inside the SPR set up, and each measurement was done three times.

The SPR curves shows very small differences between each solution measured, around 1° differences. One possible reason for this small variation could be

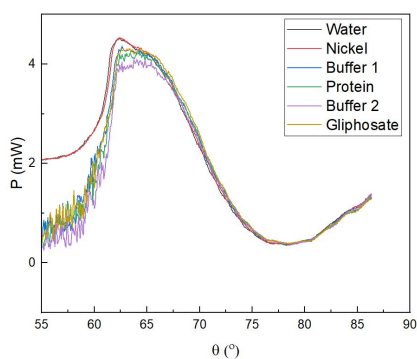


Fig. 7. SPR curves of surface treatment solutions sequenced by the first glyphosate detection.

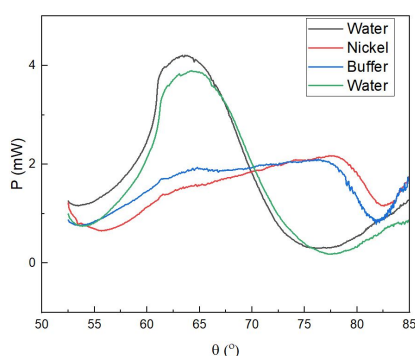


Fig. 8. SPR curves of surface treatment solutions in a non biofunctionalized chip.

the thickness of the layer beneath the bioreceptor. All of these angles were very close to the SPR angle obtained for a pure water solution. In this way, SPR measurements were conducted to obtain information about the set of solutions used in protein immobilization procedures. Fig. 8 shows the angular scan for water, nickel, and buffer solution. In this procedure, the golden chip was also cleaned by Piranha solution and no biological procedure was completed. In this case, it is possible to observe that for nickel and buffer solution the resonance angle shifts around 50° and presents a considerable reduction in reflected power signal. The second water solution was flowing in the system to observe if some residues were left on the golden chip. As it is possible to observe, the resonance angle was around 75° on the first water solution, and around 77.0° on the final water solution, which was passed through the flow cell after nickel and buffer solution, indicating that some residue was kept on the golden surface.

In this context, more measurements with glyphosate solutions should be carried out and at different concentrations. Some doubts remain regarding the functionalization of the surface and some biological tests need to be carried out, however, it is clear that the sensor operates with good sensitivity. This work is in

development and other results will be published further.

V. CONCLUSION

In this work an SPR set up built with the purpose of detecting the presence of herbicides in potable water solutions is presented. Prism supports and cell flow heads was produced in 3D printer facilitating the SPR sensors manipulation. The mechanical and electrical control was produced with low costs devices. The SPR system was able to detect very small differences in terms of refraction index and has a resolution of 0.01° . Initial tests for herbicide detection have been carried out and more tests need to be done and publish further. However, the results are promising and indicate the viability of the system.

ACKNOWLEDGMENT

This study was financed in part by the Coordenação de Aperfeiçoamento de Pessoal de Nível Superior - Brasil (CAPES) - Finance Code 001. The authors are grateful to brazilian financial agencies: Conselho Nacional de Desenvolvimento Científico e Tecnológico (CNPq), grants number 102003/2022-0, and also Fundação de Apoio à Pesquisa do Distrito Federal (FAPDF) with grant number 271/2021-03/2021, 00193-00000923/2021-48.

REFERENCES

- [1] A. L. Valle, F. C. C. Mello, R. P. Alves-Balvedi, L. P. Rodrigues, and L. R. Goulart, "Glyphosate detection: methods, needs and challenges," *Environmental Chemistry Letters*, vol. 17, no. 1, pp. 291–317, Sep. 2018, doi: <https://doi.org/10.1007/s10311-018-0789-5>
- [2] C. A. Damalas and I. G. Eleftherohorinos, "herbicide Exposure, Safety Issues, and Risk Assessment Indicators," *International Journal of Environmental Research and Public Health*, vol. 8, no. 5, pp. 1402–1419, May 2011, doi: <https://doi.org/10.3390/ijerph8051402>.
- [3] International Agency for Research on Cancer, "IARC Monographs Volume 112: evaluation of five organophosphate insecticides and herbicides," Lyon, France, Mar. 2015.
- [4] B. A. Prabowo, A. Purwidyantri, and K.-C. Liu, "Surface Plasmon Resonance Optical Sensor: A Review on Light Source Technology," *Biosensors*, vol. 8, no. 3, Aug. 2018, doi: <https://doi.org/10.3390/bios8030080>.
- [5] E. Kretschmann and H. Raether, "Notizen: Radiative Decay of Non Radiative Surface Plasmons Excited by Light," *Zeitschrift für Naturforschung A*, vol. 23, no. 12, pp. 2135–2136, Dec. 1968, doi: <https://doi.org/10.1515/zna-1968-1247>.
- [6] Homola J., S. S. Yee, and G. Gauglitz, "Surface plasmon resonance sensors: review," *Sensors and Actuators B: Chemical*, vol. 54, no. 1–2, pp. 3–15, Jan. 1999, doi: [https://doi.org/10.1016/s0925-4005\(98\)00321-9](https://doi.org/10.1016/s0925-4005(98)00321-9).
- [7] J. Homola, "Surface Plasmon Resonance Sensors for Detection of Chemical and Biological Species," *Chemical Reviews*, vol. 108, no. 2, pp. 462–493, Feb. 2008, doi: <https://doi.org/10.1021/cr068107d>.
- [8] D. Capelli, V. Scognamiglio, and R. Montanari, "Surface plasmon resonance technology: Recent advances, applications and experimental cases," *TrAC Trends in Analytical Chemistry*, vol. 163, pp. 117079–117079, Jun. 2023, doi: <https://doi.org/10.1016/j.trac.2023.117079>.
- [9] Bionavis, "Bionavis products" 2024. [online]. <https://www.bionavis.com/en/products/>
- [10] Cytiva/Biacore, "SPR instruments for label-free analysis of biomolecular interactions for research, discovery, or screening", 2024. [online]. Available: <https://www.cytivalifesciences.com/en/us/shop/protein-analysis/spr-label-free-analysis/spr-systems>

Development of a real-time toxicity biosensor based on bacterial motility.

Melina Nisenbaum
*Institute of Food and Environmental
 Science and Technology (INCITAA),
 National University of Mar del Plata
 CONICET*
 Mar del Plata, Argentina
 ORCID: 0000-0002-6661-4430

Estefany Cujano Ayala
*Bioengineering Lab, Institute of
 Scientific and Technological Research
 in Electronics (ICYTE), National
 University of Mar del Plata
 CONICET*
 Mar del Plata, Argentina
 Email: estefany.cujano@gmail.com

Marcelo Nicolás Guzmán
*Bioengineering Lab, Institute of
 Scientific and Technological Research
 in Electronics (ICYTE), National
 University of Mar del Plata
 CONICET*
 Mar del Plata, Argentina
 ORCID: 0000-0002-4258-6615

Gustavo Javier Meschino
*Bioengineering Lab, Institute of
 Scientific and Technological Research
 in Electronics (ICYTE), National
 University of Mar del Plata
 CONICET*
 Mar del Plata, Argentina
 ORCID: 0000-0003-3835-7745

Silvina Agustinelli
*Institute of Food and Environmental
 Science and Technology (INCITAA)
 National University of Mar del Plata
 CONICET*
 Mar del Plata, Argentina
 ORCID: 0000-0001-8276-7827

Silvia Elena Murialdo
*Institute of Food and Environmental
 Science and Technology (INCITAA),
 National University of Mar del Plata
 CIC*
 Mar del Plata, Argentina
 ORCID: 0000-0002-0331-2240

Abstract— This article presents the first studies for the development of a toxicity biosensor based on bacterial motility. The study proposes that microorganisms, in the presence of toxic compounds in water, present differentiated patterns of movement and cellular distribution that are quantifiable through calculation algorithm techniques applied to dynamic laser speckle image processing, which could be used for the development of a real-time water quality biosensor. The biospeckle technique, a tool widely used to evaluate the temporal evolution of various phenomena, allows the identification of qualitative differences in bacterial motility resulting from the presence of different substrates in the liquid medium. We worked with a known concentration of motile bacteria, which were exposed to different pure contaminants and a rich substrate. As controls, a sterile physiological solution (culture diluent) and a bacterial culture without toxic additions were used. Each sample was individually trans-illuminated with an expanded laser and attenuated from the bottom through a ground glass diffuser. The videos were recorded at different times and subsequently processed using different algorithms, obtaining speckle activity values that represent the level of activity (related to bacterial motility) within each sample. Preliminary results highlight the potential of this technique and suggest the suitability of the bacteria used as a bioindicator. This study represents a significant step towards the development of a rapid, high-resolution biosensor, which could find various applications in health, the environment and food quality control.

Keywords— *Laser, Biospeckle, Bacteria, Biosensor.*

I. INTRODUCTION

A bioindicator is an organism or biological response that reveals the presence of contaminants through measurable responses. These organisms or communities of organisms provide information about alterations in the environment or the amount of environmental pollutants through physiological, chemical or behavioral changes [1, 2].

Microbes (e.g., algae, bacteria and yeast) offer a good alternative in the manufacturing of biosensors because they can be mass-produced through cell culture [3]. Furthermore, compared to cells from higher organisms (such as plants,

animals and humans) microbes are easier to manipulate and have better viability and stability in vitro, which can greatly simplify the manufacturing process and improve the performance of the products [4].

Biological responses that reflect damage to living organisms are crucial for pollution assessment as they provide information on the ecological consequences of contaminants in aquatic environments [5]. The need for simple, rapid and relatively inexpensive tests to evaluate water toxicity has influenced the expansion of research in this area. Biological early warning systems (BEWSs) have been developed for continuous monitoring of water quality, allowing direct and continuous detection of a wide range of contaminants or toxic conditions based on the physiology and behavior of organisms [6, 7].

Bacterial movement is related to the survival strategy under environmental stress [8], ensuring environments high in nutrients and low in toxicity [9]. Movement is especially advantageous when nutrients are limited, as it positions cells away from competing bacteria. There are numerous investigations on changes in the population dynamics of different unicellular organisms caused by pollutants or effluents [10, 11, 12], however, there are no reports to date of the use of bacterial mobility as a toxicity sensor, except as described in [13] for *Spirillum volutans*.

The values of motility parameters can be modified by cells and the environment [9]. Swimming speed has been reported to change in response to variations in the presence or absence of nutrients in the environment [8, 14, 15], as well as in response to various environmental conditions such as high temperature, high salt concentrations, high concentrations of carbohydrates or high concentrations of low molecular weight alcohols [16]. Some of the most commonly studied bacteria include *Bacillus subtilis*, *Escherichia coli*, *Salmonella typhimurium*, *Streptococcus* sp., and *Rhodobacter sphaeroides* among others [9].

Bacterial bioassays are generally carried out in aqueous samples because their locomotion is facilitated in this medium [18], and they are used in the control of wastewater and the efficiency of industrial treatment plants [19]. This project

This research was partially funded by grants UNMdP15/G634ING638/21, UNMdP15/G634ING691/23 and PICT- 2020-SERIEA-02571

initially proposes to study microbial activity in aqueous samples in order to apply it directly to water control.

Dynamic Speckle Laser (DLS) or Biospeckle is a phenomenon characteristic of biological samples generated when illuminating the sample with a beam of coherent light, creating an interference pattern. This pattern consists of areas with varying intensity, commonly referred to as "speckles." If the sample exhibits activity that leads to fluctuations in its refractive index over time, these speckle patterns will dynamically evolve, resulting in what is known as a dynamic speckle pattern.

The DLS provides an interesting, fast, non-destructive, and non-invasive tool for the study of biological samples. Biospeckle has found applications in various areas, including the detection of bacterial chemotaxis and differentiation between fungal and bacterial growth in semi-solid medium [20-21]. Recently, it has been applied in real-time monitoring of bacterial kinetics [22] to estimate effectiveness in water disinfection [23] and to estimate bacterial concentration in aqueous samples [24].

When animated scatterers, such as bacteria, are moved by deliberate swimming movements, fluctuations in the speckle pattern occur. If the swimming action is irregular and random, the frequency spectrum of the speckle fluctuations will be qualitatively similar to that of Brownian motion, but with a timescale appropriate for swimming speed [25]. The spectrum will be continuous, containing all frequencies up to an upper limit, determined by the size of the speck and the swimming speed.

This paper presents the first studies for the development of a toxicity biosensor based on bacterial mobility in conjunction with the biospeckle technique. The study proposes that microorganisms, in the presence of toxic compounds in water, present differentiated patterns of movement and cellular distribution that are quantifiable through calculation algorithm techniques applied to dynamic laser speckle image processing, which will be used for the development of a water quality biosensor.

II. MATERIALS AND METHODS

A. Microbial Culture

Pure cultures of *Pseudomonas aeruginosa* were used as bioindicators (PS) [10] in the exponential growth phase. These cultures were maintained in Luria-Bertani (LB) broth at 25°C and stirred at 150 rpm. A known low concentration of cells was prepared using sterile saline solution (NaCl 0.9% (v/v)) as a diluent, as defined according to previous work [26, 27]. Five milliliters of the culture to be measured were placed in a Petri dish with a diameter of 55 mm. Prior to this, a nutrient (citrate) or toxic compound (dodecene, 2-4-5-trichlorophenol, 2-4-6-trichlorophenol, 2-4-5-6-tetrachlorophenol, pentachlorophenol, kerosene, undecene) was added and manually shaken.

The selection of compounds was based on previous knowledge indicating that this bacterial strain is attracted or repelled by them [26, 27], which can induce changes in their swimming behaviour. The experiment was conducted in triplicate for each substrate. The speckle activity of bacteria without substrate was used as a control. Speckle activity of the substrates without bacteria were also used as blank controls.

B. DLS Video Acquisition Protocol

A forward-scattering configuration was employed for the acquisition and storage of bio-speckle patterns. The sample was illuminated from the bottom through a ground glass diffuser with a HeNe Uniphase 1135P laser (maximum output power of 20 mW and wavelength of 632.8 nm), expanded. A CCD camera (Imaging Source DMK23G618) connected to a PC recorded the sequence of 8-bit gray scale images with a resolution of 640 x 480 square pixels. Video captures were taken at 1, 3 and 5 minutes after adding the substrate to the plate containing the bacterial culture.

To evaluate the dynamics of the phenomenon during stationary periods, image sequences of 400 frames were recorded with an exposure time of 1/30 s and a recording speed of 30 frames per second, totaling 13.33 seconds of recording time. The aperture and gain of the CCD camera, along with the distance to the sample, were adjusted to achieve a well-resolved speckle grain size. A gain of 0 dB was chosen in the camera to minimize electronic noise, which affects the exposure time due to the loss of brightness. From the image sequences of the speckle patterns generated by the samples, time series corresponding to the intensity level of each pixel were extracted.

The activity level of each pixel's time series (x, y) in the acquired video was calculated using Fuzzy Granularity (FG) descriptor (1) [28] which quantifies the time intensity variations. The discrete signal is transformed into a set of fuzzy granules (G) characterized by three levels of intensity (k), light, medium and dark. The intensity levels are range values overlapped in the sense of fuzzy sets.

$$FG = \sum_{k=1}^3 \frac{|suc_{n,k}(G(x_n,k))|}{N} \quad \text{with } n = 2,3, \dots, N \quad (1)$$

Where

$$suc_{n,k} = \begin{cases} 1 & \text{if } G(x_{n-1},k) \text{ is true and } G(x_n,k) \text{ is false} \\ 0 & \text{in other case} \end{cases}$$

Based on this computed value, a matrix is created for each video the mean value of the matrix is calculated and is called the activity level of the sample.

III. RESULTS

Eighteen algorithms were evaluated, of which the Fuzzy algorithm obtained the greatest significant difference between the samples and the best correlation between the results provided by this algorithm and by other methods previously tested for this purpose [21, 26, 27].

Fig. 1 displays the activity values of the Fuzzy descriptor for the videos obtained from the samples processed one minute after the addition of the substrate to the medium with bacteria. The measurements were carried out one minute after adding the sample to the measurement plate to avoid interferences due to turbulence generated in the solution. Variations in bacterial activity can be observed when exposed to different toxic substrates, distinguishing them from samples with citrate (a rich substrate) and without substrate (water, control). These preliminary findings provide evidence that

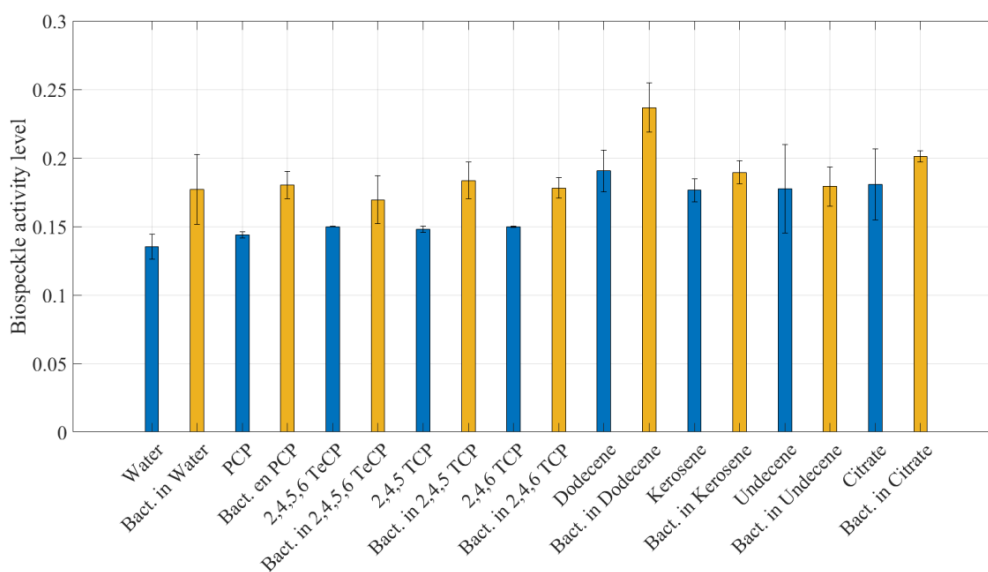


Fig. 1. Fig. 1. Level of biospeckle activity presented by bacteria in the presence of different substrates (yellow), and activity measured by controls (substrates in water without bacteria, blue). The measurements were carried out one minute after adding the sample to the measurement plate to avoid turbulence of the medium.

dynamic analysis of the speckle pattern, or biospeckle, can effectively discern changes in PS behavior depending on the specific exposure, yielding both quantitative and qualitative data. Moreover, this bacterial strain is known to be chemotactic towards these substrates and capable of degrading some of them [21, 26, 27], further supporting its potential as an efficient bioindicator of toxicity. Building upon these results, our research group is exploring the development of a toxicity biosensor for liquid matrices based on PS as a bioindicator and the biospeckle technique as a sensor. This technique offers several advantages, including objectivity, sensitivity, and rapid data acquisition and processing, with results obtained in less than 15 minutes. Such methodology holds promise as a reliable biosensor for environmental pollution assessment and water resource health monitoring, among other potential applications. Currently, other analytical studies are underway to correlate these activity values with other techniques. The ability of this approach to provide rapid and accurate assessments makes it a valuable tool in various fields, including environmental monitoring and biomedicine.

IV. CONCLUSION

Biospeckle techniques have demonstrated high efficiency in characterizing bacterial activity in semisolid media [20, 21]. Furthermore, some studies have explored the application of biospeckle in detecting motile activity in larger microorganisms, including protozoa, rotifers and algae [25]. The ability of this technique to detect variations in the speed of movement of bacteria, which typically measure approximately 2 microns, has been convincingly demonstrated.

Building on this premise, a preliminary technique was introduced to evaluate the variation in PS motility by subjecting the bacteria to various toxic substances. The results provided evidence of the potential of the analysis technique to detect changes in microbial motility. However, further research is warranted to advance the study.

Additional experiments are currently underway to determine variations in the behavior of PS in liquid medium using other laboratory techniques. This is being done in order to correlate these activity data with various motility parameters and evaluate the appropriate exposure times to capture speckle patterns more effectively. Repeating the experiments under different conditions will provide a more comprehensive understanding of the capabilities and limitations of the technique, ultimately leading to a refined and robust methodology. This research will significantly contribute to the development of this promising biospeckle-based approach for detecting changes in microbial motility and its potential applications in ecotoxicity and environmental biomonitoring studies.

ACKNOWLEDGMENT

The researchers express their gratitude for the support provided by the National Scientific and Technical Research Council (CONICET), the Scientific Research Commission of Buenos Aires (CIC), and the National University of Mar del Plata, Argentina, in facilitating the execution of this work. Additionally, they extend their appreciation to PhD Mario Cisneros of the UNMdP for his valuable technical advice on intellectual property.

REFERENCES

- [1] D.W. Jeffrey and B. Madden, *Bioindicators and environmental management*. London: Academic Press, 1991.
- [2] B. A. Markert, A. Breure and H. Zechmeister, "Bioindicators & Biomonitors: Principles, Concepts and Applications", *Trace Metals and Other Contaminants in the Environment*, vol. 6, 2003.
- [3] L. Su, W. Jia, C. Hou and Y. Lei, "Microbial biosensors: A review", *Biosens. Bioelectron.*, vol 26, pp. 1788–1799, 2011.
- [4] B. Jiang, et al., "Whole-cell bioreporters for evaluating petroleum hydrocarbon contamination", *Crit. Rev. Environ. Sci. Technol.*, vol 0, pp. 1–51, 2020.

- [5] T. Harald and D. Hader, "Fast examination of water quality using the automatic biotest ECOTOX based on the movement behavior of a freshwater flagellate", *Water Research*, vol. 33, pp. 426-432, 1999.
- [6] A. Gerhardt, "Bioindicator species and their use in biomonitoring", In: *Environ. Monit. Encycl. Life Support Syst.*, vol. 49, Charlotte : Eolss 2002.
- [7] A. Ortega, et al., "Tecnologías de Biosensores en la medida de la calidad de agua", IV Jornadas de Ingeniería del Agua, La precipitación y los procesos erosivos, Córdoba, 21 and 22 de Octubre 2015.
- [8] S. Umehara, A. Hattori, I. Inoue, K. Yasuda, "Asynchrony in the growth and motility responses to environmental changes by individual bacterial cells", *Biochem. Bioph. Res. Comm.*, vol. 356, pp. 464-469, 2007.
- [9] J.G. Mitchell and K. Kogure, "Bacterial motility: links to the environmental driving force for microbial physics", *FEMS Microbiol. Ecol.*, vol. 55, pp. 3-16, 2005.
- [10] M. Espigares, I. Roman, J.M. Gonzales Alonso, B. de Luis, F. Yeste and R. Galvez, "Proposal and application of an ecotoxicity biotest based on *Escherichia coli*", *J. Appl. Toxicol.*, vol. 10, pp. 443-446, 1990.
- [11] S. Paissé, et al., "How a Bacterial Community Originating from a Contaminated Coastal Sediment Responds to an Oil Input", *Environ. Microbiol.*, vol. 60, pp. 394-405, 2010.
- [12] R. Tecon, and J. R. Van Der Meer, "Bacterial biosensors for measuring availability of environmental pollutants", *Sensors*, vol. 8, pp. 4062-4080, 2008.
- [13] J.H. Bowdre, N.R. Krieg, "Water quality monitoring: bacteria as indicators" Virginia Water Resources Research Center. Virginia Polytechnic Institute and State University. Blacksburg, Virginia, 1974.
- [14] J.G. Mitchell, L. Pearson, A. Bonazinga, S. Dillon, H. Khouri, and R. Paxinos, "Long lag times and high velocities in the motility of natural assemblages of marine bacteria", *Appl. Environ. Microbiol.*, vol. 61, pp. 877-882, 1995.
- [15] S. Khan, and D.R. Trentham, "Biphasic excitation by leucine in *Escherichia coli* chemotaxis", *J. Bacteriol.*, vol. 186, pp. 588-592, 2004.
- [16] C. Li, C.J. Louise, W. Shi and J. Adler, "Adverse conditions which cause lack of flagella in *Escherichia coli*", *J. Bacteriol.*, vol. 175, pp. 2229-2235, 1993.
- [17] S. Girotti, E.N. Ferri, M.G. Fumo, E. Maiolini, "Monitoring of environmental pollutants by bioluminescent bacteria", *Anal. Chim. Acta*, vol. 608, pp. 2-29, 2008.
- [18] G.A. Nils Ekelund and Donat P. Häder, "Environmental Monitoring Using Bioassays", In: "Bioassays: Advanced Methods and Applications", 419-37, 2018.
- [19] M.J. Bae and Y.S. Park, "Biological early warning system based on the responses of aquatic organisms to disturbances: A review", *Sci. Total Environ.*, vol. 466-467, pp. 635-649, 2014.
- [20] S.E. Murialdo, L.I. Passoni, M.N. Guzman, G.H. Sendra, H. Rabal, M. Trivi, "Discrimination of motile bacteria from filamentous fungi using dynamic speckle", *Journal of Biomedical Optics*, vol. 17, 056011, 2012.
- [21] M. Nisenbaum, G. H. Sendra, G.A. Cerdá Gilbert, M. Scagliola, J.F. González and S.E. Murialdo, "Hydrocarbon biodegradation and dynamic laser speckle for detecting chemotactic responses at low bacterial concentration", *Journal of Environmental Sciences*, vol. 25, pp. 613-625, 2013.
- [22] H. Loutfi, et al., "Real-time monitoring of bacterial growth kinetics in suspensions using laser speckle imaging", *Sci. Rep.*, vol 10, pp. 408, 2020.
- [23] D.C. Viana, J.F. Pires and R.A. Braga, "Biospeckle laser technique applied for estimating disinfection accomplishment of wastewaters subjected to chlorination", *Process Safety and Environmental Protection*, vol. 109, pp. 670-676, 2017.
- [24] M.N. Guzmán, M. Nisenbaum, S.E. Murialdo and G.J. Meschino, "Determinación de la Carga Microbiana en Agua por Medio del Análisis de Patrones de Speckle Dinámico, Number: 9769, SABI2022. XXIII Congreso Argentino de Bioingeniería y XII Jornadas de Ingeniería Clínica. 13 al 16 de Setiembre 2022 - San Juan - Argentina.
- [25] J. A. Cole and M.H. Tinker, "Laser speckle spectroscopy - A new method for using small swimming organisms as biomonitors", *Bioimaging*, vol. 4, pp. 243-253, 1996.
- [26] M. Nisenbaum, A. Bouchet, M.N. Guzmán, J.F. González, G.H. Sendra, J. Pastore and M. Trivi, S.E. Murialdo, "Dynamic laser speckle and fuzzy mathematical morphology applied to studies of chemotaxis towards hydrocarbons", *International Journal of Environment and Health*, vol 7, pp. 58-69, 2014.
- [27] E. Okada, M. Nisenbaum, J. Martínez Arca and S.E. Murialdo, "Chemotaxis detection towards chlorophenols using video processing analysis", *Journal of Microbiological Methods*, vol 142 (June), pp. 15-19, 2017.
- [28] G. H. Sendra, A. Dai Para, L. I. Passoni and H. Rabal. "Biospeckle descriptors: A performance comparison", *Proceedings of SPIE - The International Society for Optical Engineering* · September 2010

Rapid screening test for *Streptococcus agalactiae* neonatal infections combining portable PCR and electrochemical genosensing

Anaïxis del Valle
Grup of Sensors and Biosensors
Universitat Autònoma de Barcelona
Bellaterra, Spain
0000-0001-5587-9081

Melania Mesas Gómez
Grup of Sensors and Biosensors
Universitat Autònoma de Barcelona
Bellaterra, Spain
0000-0002-3297-1077

Arnau Pallarès-Rusiñol
BioEcllosion SL
Edifici Eureka, campus UAB
Bellaterra, Spain
0000-0001-9990-148X

Mercè Martí
Institut de Biotecnologia i de Biomedicina
Universitat Autònoma de Barcelona
Bellaterra, Spain
0000-0002-1846-0043

Bàrbara Baró
IsGlobal, Hospital Clínic
Universitat de Barcelona
Barcelona, Spain
0000-0001-7780-1744

Jofre Ferrer-Dalmau
BioEcllosion SL
Edifici Eureka, campus UAB
Bellaterra, Spain
0000-0002-7415-6222

Quique Bassat
IsGlobal, Hospital Clínic
Universitat de Barcelona
Barcelona, Spain
0000-0003-0875-7596

Maria Isabel Pividori
Grup of Sensors and Biosensors
Universitat Autònoma de Barcelona
Bellaterra, Spain
0000-0002-5266-7873

Abstract— *Streptococcus agalactiae* (Group B *Streptococcus*, GBS) is the leading cause of neonatal infections, impacting both pregnant mothers and specially their offspring. This infection affects 18% of the pregnant women worldwide, leading to a spectrum of diseases, including maternal infection, stillbirth, and sepsis in newborns. Current detection methods rely on culturing techniques, resulting in long turnaround times for results and sophisticated laboratory infrastructure and training. In response to these limitations, this work presents the development of a point-of-care (PoC) rapid screening test based on a hand-held thermocycler to perform double tagging end-point PCR in combination with electrochemical genosensing, specifically targeting the GBS *fbxA* gene. The results demonstrate a simple, specific, and highly promising system for detecting the presence of GBS in pregnant mothers and newborns.

Keywords— perinatal infections, Group B *Streptococcus* (GBS), rapid screening test, hand-held thermocycler, genosensing devices

I. INTRODUCTION

In the absence of a rapid point-of-care (PoC) diagnostic test, infectious diseases are often managed using clinical algorithms based on the presence of symptoms and local disease prevalence estimations. While this approach effectively identifies most patients who require treatment (high sensitivity), it also leads to the unnecessary treatment of patients with alternative diagnoses who might recover without intervention (poor specificity). Syndromic management of diseases typically results in the overuse of limited antimicrobials and inadequate treatment, which in turn contributes to the development of drug resistance [1]. The accurate identification of patients who truly require treatment remains a significant challenge in infectious disease control. The burden of infectious diseases could be substantially reduced if appropriate diagnostic tests were readily available [2].

Group B *Streptococcus* (GBS) is a bacterium commonly found in the gastrointestinal and genital tracts. Although there is significant geographical variation, it is estimated that up to 18 % of pregnant women globally are asymptomatic carriers of GBS [3]. Maternal rectovaginal colonization with GBS is the primary pathway for GBS transmission, leading to disease in the mother, fetus, and newborn. Maternal infections and subsequent vertical transmission of GBS during pregnancy and childbirth contribute significantly to the burden of perinatal disease, with GBS responsible for an estimated 409,000 maternal, fetal, and infant cases and 147,000 stillbirths and infant deaths annually [4]. For this reason, identifying pregnant women who are infected with GBS is crucial for implementing targeted antimicrobial preventive strategies that minimize the risk of perinatal infections in the fetus and newborn. Based on this rationale, many countries have integrated systematic screening of pregnant women during the third trimester into antenatal care. Women who test positive in the culture of rectovaginal swabs are treated with antibiotics during labor to reduce the risk of GBS transmission and subsequent infections in the newborn. his strategy has led to a significant decrease in the incidence of GBS disease in high-income countries. However, implementing this approach in low-income settings is challenging due to the limited availability of laboratory support needed for microbiological analyses [5]. Disease caused by GBS most commonly includes bacteremia, sepsis, pneumonia, and meningitis in newborns [6], and survivors often develop long-term sequelae, such as neurodevelopmental disabilities. GBS is a global problem, but its impact is particularly severe in African populations, which account for 54% of estimated cases and 65% of all fetal and infant deaths. Additionally, up to 3.5 million preterm births may be attributable to GBS, leading to significant additional indirect morbidity and mortality.

Early identification of maternal GBS carriage or confirmation of its presence in normally sterile bodily fluids

is crucial for the timely implementation of preventive or therapeutic life-saving interventions. Currently, the diagnosis of GBS infection relies on conventional microbiological culture of bodily fluids (such as blood, cerebrospinal fluid, and amniotic fluid), which can take days to confirm. A PoC rapid screening test, applicable near the patient, to detect GBS infections in both mothers and newborns would be a groundbreaking approach, particularly in low-income countries where the challenges of implementing microbiological cultures are significant. Previous attempts to develop such screening tools have been hindered by the poor sensitivity of the rapid tests. In this study, a robust molecular methodology is proposed for the rapid and PoC screening of GBS infections in pregnant women and infants, designed to be feasible in low-resource settings.

Since the early reports on the amplification of target nucleic acid sequences using polymerase chain reaction (PCR) [7], this technique has found widespread application in various areas of genetic analysis, including forensic science and the diagnosis of genetic and infectious diseases. PCR can generate billions of DNA copies from a single target molecule within a few hours [8]. The primary advantages of PCR include a significant improvement in test sensitivity—up to 100-fold over antigen detection—and much faster turnaround times compared to classical culturing methods. Additionally, PCR allows for multiplexing and real-time detection, further enhancing its utility in diagnostic applications.

During the COVID-19 pandemic, PCR has proven to be the state-of-the-art and dominant diagnostic test for infectious diseases [9], despite the rapid development of alternative technologies. RT-PCR is now widely regarded as the gold standard for detecting communicable diseases. Surprisingly, this quantitative technique has also been used for screening individuals, providing a simple YES/NO binary result, despite its long turnaround time—ranging from hours to days—and the requirements for specialized instrumentation, trained personnel, and infrastructure, including a reliable power supply. This demonstrates that DNA/RNA amplification, despite its technical complexity and high costs, remains the optimal methodology for screening many pathogens, offering an excellent balance between maximum sensitivity and feasibility for pathogen detection.

Since the initial report on the integration of PCR with electrochemical genosensing devices [10], our group has explored various PCR-based strategies to amplify the analytical signal and increase the sensitivity of the readout. A double-tagging PCR amplification strategy with electrochemical readout was developed in our labs [11-13]. In this approach, a set of double-tagged primers labeled with small tags (such as biotin, digoxigenin, fluorescein, among others) is used during amplification to enable immobilization on the platform and subsequent readout. This method not only achieves DNA amplification but also double labels the amplicon to enhance readout sensitivity. Additionally, this approach can be easily multiplexed to detect up to three pathogens simultaneously. Our group demonstrated the simultaneous electrochemical biosensing of *Salmonella*, *Listeria* and *E. coli* [14,15]. Even improved analytical features were achieved by combining double-tagging amplification with immunomagnetic separation (IMS) [16,17]. Our group also demonstrated a comparable sensitivity achieved with two RDT (rapid diagnostic test) platforms for

the detection of double-tagged amplicons: electrochemical biosensing and lateral flow [18].

The first generation of nucleic-acid amplification technologies based on PCR cannot feasibly be incorporated into rapid diagnostic tests due to the need for thermocycling platforms, trained personnel, and infrastructure, including a reliable power supply—factors that pose a significant barrier to the use of PCR in resource-limited settings [19]. To address this challenge, our group has developed RDTs based on isothermal amplification techniques, such as rolling circle amplification (RCA) and padlock probes [20-22], which eliminate the need for thermocyclers. However, isothermal amplification requires multiple reagents and involves several steps, limiting its practical implementation in low-resource settings. The goal of this study is therefore to bring PCR to the point of need by designing a diagnostic kit that includes a hand-held PCR device and a portable RDT prototype. This system has the potential to be used for screening communicable diseases that typically require PCR as the gold standard, directly at the point of care.

II. EXPERIMENTAL SECTION

A. Instrumentation

The AmpliFAST test is considered an *in-vitro* diagnostic test (IVD) which is a PoC rapid test based on a RDT platform and a portable thermocycler for the rapid detection of Group B *streptococcus* in a total time within 40 minutes and at low cost. The test is mainly composed by two components (as schematized in Figure 1): 1) portable hand-held thermocycler operated by batteries, in which the sample is amplified in 30 min by cycling the temperature at fixed condition (no programming is allowed for the final user). 2) RDT platform for the electrochemical genosensing.

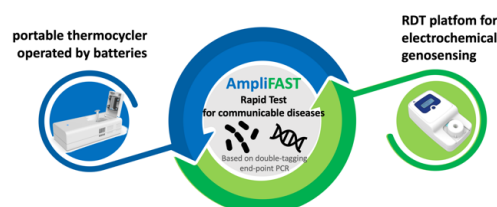


Fig. 1. Schematic diagram of the two components of the AmpliFast test including the portable thermocycler, based on a double-tagging amplification of the bacteria and the RDT platform for the readout based. First application envisaged is the detection of Group B *streptococcus* perinatal infections.

The RDT platform (as described in PCT/EP2022/071078 ‘Device for Assay System, System and Method’) consists of two main components:

A) Disposable cartridge: i) Sample holder: Contains streptavidin magnetic particles and a labeled antibody that binds to the amplified double-tagged DNA from the bacteria within 10 minutes. ii) Cartridge: Includes the microfluidic system and the screen-printed electrode where magnetic actuation occurs, while excess sample and reagents are removed by capillarity.

B) Digital reader: This includes the external magnet and the interface between the cartridge and the digital reader, enabling the electrochemical readout in less than one minute. The device provides a binary YES/NO response, with data that can be directly viewed on the digital reader's display and transmitted via Bluetooth to an accompanying app.

B. Strains and primers

This study focuses on *Streptococcus agalactiae* (NCTC 8181), with efforts toward the amplification of specific genetic sequences for the inclusion in the AmpliFast test. This bacterium is typically cultured under aerobic conditions at 37°C. The study targets the *fbSA* gene, crucial to the bacterium virulence, utilizing primers designed for its precise amplification. The forward primer sequence GCGTTTGAGACGCAATGAA and the reverse primer AGCACCTACGATAGCAACGG allow for the amplification of a 265 base pair product. Furthermore, the 16S rRNA sequence is employed as a reliable positive control, with primers GAGTACGACCGCAAGTTGA and CCCAACATCTCACGACACGA amplifying a 202 base pair product. The specificity study used a selection of bacterial strains to ascertain the precision of the developed rapid diagnostic test for Group B *Streptococcus* (GBS). The strains included *Pseudomonas aeruginosa* (ATCC 15442), *Klebsiella pneumoniae* (ATCC BAA-1705), *Enterobacter spp.*, *Escherichia coli* (ATCC 10536), and *Salmonella choleraesuis* (ATCC 13311). These strains were chosen to provide a comprehensive cross-reactivity profile for the *fbSA* primer, by confirming that no amplification occurred with these non-GBS bacteria. Each strain was carefully selected for its relevance in clinical diagnostics and its potential to act as a confounder in GBS detection, thereby reinforcing the specificity of the AmpliFast diagnostic tool.

C. Double-tagging PCR and electrochemical genosensing

The prototype combining PCR amplification with an RDT platform was tested in this study to address PoC neonatal sepsis caused by GBS as a first model, aiming to meet the highest standards of sensitivity and specificity while considering analytical simplification. To enhance sensitivity, this study focused on the genetic amplification of the bacterial genome on magnetic particles [11]. The initial exploration involved the double-tagging PCR method developed in our labs [11,12,13] (Figure 2).

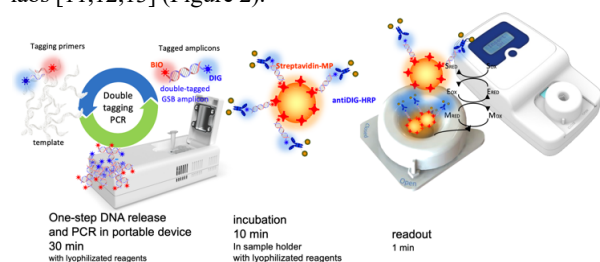


Fig. 2. Molecular strategy which are the core of the technology, showing the molecular detail of the double tagging end-point PCR which will be performed in a portable thermocycler, followed by the reagent mixture, and the readout perform on the RDT platform.

This approach was previously demonstrated in lab conditions for the single or multiplex detection of genomic DNA of foodborne pathogens (including *E. coli*, *Salmonella* [11,12,13], *Listeria* [14-16], zoonotic tuberculosis, and lately to detect transcripts of inflammatory biomarkers (IFN- γ) by double-tagging RT-PCR, in which the RT is performed on poly(dT)-MPs [17]. The lysis of the bacteria was integrated as an initial heating cycle during PCR [14,16], and the released DNA was simultaneously amplified and labeled by an end-point double-tagging PCR in the portable thermocycler

prototype by using a double tagged set of primer labelled with biotin and digoxigenin. Furthermore, different strategies for room-temperature-storable PCR mixes were evaluated, as well as compared with commercial options (Kerafast, FLUOROGENICS™, among others). The double-tagging-PCR approach was firstly demonstrated in our labs for the detection of ATCC strains and clinical isolates obtained from Hospital Clinic (Barcelona), taking as a model of GBS diseases, and perinatal sepsis due to GBS.

D. Biosafety considerations

The experiments were conducted in compliance with Biosafety Class 2 requirements for handling all the studied strains. All biological waste generated from the experiments was disposed of in accordance with local regulations for handling biohazards.

III. RESULTS AND DISCUSSION

A. Study of PCR performance on different *Streptococcus agalactiae* serotypes

Figure 3 shows the PCR results for the detection of various serotypes isolated from clinical samples of *Streptococcus agalactiae* using *fbSA* primers, demonstrating that the assay successfully amplified the target gene across multiple clinical isolates. The lysis method employed was heat shock, the enzyme used was SolisFAST master mix, and the primer concentration was set at 250 nM. The PCR used 2 μ l of lysate, and strain 8181 from the ATCC served as the positive control. The gel electrophoresis results display distinct bands for each serotype, affirming the efficacy of the primers, with DNA concentrations in the samples ranging from 73.3 ng μ L⁻¹ to 121.5 ng μ L⁻¹. It's noted that the amplicon size for the *fbSA* gene is consistent with the expected molecular weight, confirming the specificity and accuracy of the PCR.

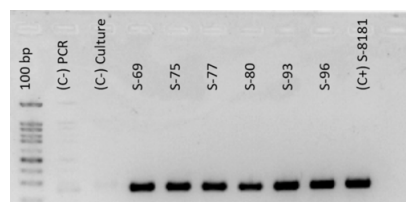


Fig. 3. Electrophoresis of *fbSA*-targeted PCR for *Streptococcus agalactiae* Serotypes. Clear bands demonstrate the efficiency of the primers in amplifying *fbSA* gene across different clinical isolates with sample DNA concentrations ranging from 73.3 to 121.5 ng μ L⁻¹. The amplicon size is consistent across samples, indicating reliable detection. S8181 serves as the positive control.

B. AmpliFast test performance and specificity study

Figure 4 displays the specificity of the *fbSA* primers in the detection of GBS using a portable thermocycler and a RDT. The results are quantified by amperometry, showing cathodic current measurements in microamperes (μ A). High cathodic current values are observed for GBS, which indicates a strong signal and successful amplification of the *fbSA* gene. In contrast, other bacteria such as *Pseudomonas aeruginosa*, *Klebsiella pneumoniae*, *Enterobacter spp.*, *Escherichia coli*, and *Salmonella choleraesuis* show significantly lower currents, highlighting the specificity of the primer to GBS without cross-reactivity with these non-target species.

Figure 4, right panel shows a control assay using 16S rRNA primers, which serve as a general bacterial marker. Here, uniform cathodic currents across all tested bacterial species are observed, validating the assay ability to detect bacterial DNA in general. These results, obtained with the portable thermocycler and a RDT, demonstrate the specificity of the *fb*sA primers to GBS even in the presence of other bacterial strains, reinforcing the potential use of this assay in a PoC setting to accurately diagnose GBS infections.

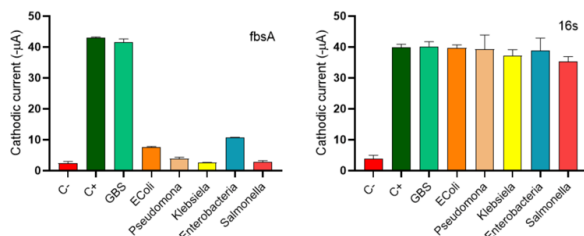


Fig. 4. Specificity study of *fb*sA and 16S primers using electrochemical genosensing. The results confirm the *fb*sA primer specificity for GBS using a portable thermocycler and rapid diagnostic test (RDT) platform.

The results present evidence of the *fb*sA primer high specificity for detecting GBS via a portable thermocycler and RDTs, with electrochemical genosensing showing substantial cathodic current for GBS, indicative of robust signal generation and effective gene amplification. In contrast, the significantly lower currents for other tested bacterial species such as *Pseudomonas aeruginosa*, *Klebsiella pneumoniae*, *Enterobacter spp.*, *Escherichia coli*, and *Salmonella choleraesuis* highlight the primer selectivity, avoiding cross-reactivity which is crucial for accurate diagnostics. Furthermore, the results for 16S rRNA primers, indicates the capability to detect a wide range of bacteria, thus presenting the 16S rRNA-based assay as a promising candidate for a RDTs for sepsis. The consistent reaction of all species to the 16S rRNA primers could pave the way for the development of a rapid, universal sepsis screening tool, which would be relevant for early and broad-spectrum bacterial infection diagnosis. Such a test would be particularly valuable in clinical settings where rapid identification of a bacterial infection can lead to timely and life-saving treatment interventions.

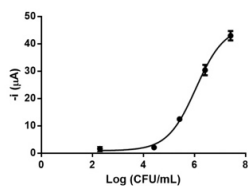


Fig. 5. Calibration plot for the AmpliFast test. The graph shows amperometric responses across various concentrations of GBS (measured in logarithmic Colony Forming Units (CFUs/mL)), with an LOD of 1.34×10^4 . This translates to an approximate LOD of 2415 CFUs per swab. These findings affirm the sensitivity of the AmpliFast test for GBS detection when using a portable thermocycler and a RDT platform.

Figure 5 illustrates the Limit of Detection (LOD) of the AmpliFast test for detecting Group B *Streptococcus* (GBS). The results are measured through amperometry, showing cathodic current in microamperes (μ A). The minimum detectable value is found to be 1.61×10^4 CFUs/mL, indicating a LOD of approximately 2415 CFUs/swab. This underscores the potential utility in PoC scenarios for precise GBS infection compared to commercial devices [23].

IV. CONCLUDING REMARKS

In conclusion, these findings support the use of the *fb*sA primer for targeted GBS detection while also proposing the future potential of 16S rRNA primers for the development of a rapid, point-of-care sepsis test. This could improve sepsis diagnostics, as the wide array of bacteria that show positive reactions with the 16S primers includes many common strains of sepsis. Thus, this RDT could potentially provide healthcare providers with a powerful tool for the prompt recognition and treatment of this serious condition.

The innovative aspects of the test presented here integrates key components aiming to achieve simplification and portability while maintaining outstanding analytical performance. In conclusion, the method offers a DNA preconcentration strategy amenable with low resource settings. The user-friendly cartridge and reader design minimizes user intervention, enhancing ease of use and reproducibility. Moreover, the handheld electrochemical readout powered by batteries enables on-site and point-of-care testing, marking a significant advance in electrochemical biosensing applications.

ACKNOWLEDGMENT

This research was funded by the AmpliSens project, under the project reference CPP2021-008459. This initiative is part of the "Proyectos en Colaboración Pública-Privada 2021". Ministerio de Ciencia e Innovación, Spain, coordinated by BioEclon S.L. and in collaboration with partners UAB, ISGlobal, and Eurecat. The Ministry of Science, Innovation and Universities, Spain (Projects PID2019-106625RB-I00/AEI/10.13039/501100011033 and PID2022-136453OB-I00) and from Generalitat de Catalunya (2017-SGR-220, 2021SGR-00124) are also acknowledged.

REFERENCES

- [1] Amexo M et al, 2004. Lancet 364:1896-8.
- [2] Zachariah R et al, 2011. Trop Med Int Health. 16:37-41
- [3] Russell NJ et al, 2017. Clin Infect Dis. 65:S100-S111
- [4] Seale AC et al, 2017. Clin Infect Dis. 65: S125-S132.
- [5] Madrid L, et al, 2017. Clin Infect Dis.65:S160-S172.
- [6] Centers for Disease Control and Prevention. Active Bacterial Core Surveillance Report, Emerging Infections Program Network, Group B Streptococcus, 2018.
- [7] Mullis K et al, 1987. Methods Enzymol 155:335-50
- [8] Saiki RK et al, 1988. Science 239:487-91
- [9] Millat-Martinez P et al, 2021. Lancet Infect Dis 21: 629-36
- [10] Pividori MI et al, Electroanal 15:1815-23.
- [11] Lermo A et al, 2007. Biosens Bioelectron 22:2010-17.
- [12] Lermo A et al, 2008. Biosens Bioelectron 23,1805-11.
- [13] Brasil PR et al, 2009. Anal Chem 81, 1332-39
- [14] Brandão D et al, 2015. Biosens Bioelectron 74:652-9.
- [15] Liébana S et al, 2016. Anal Chim Acta 904:1-9. (Feature article)
- [16] Liébana S et al, 2009. Anal Chem 81, 5812-20.
- [17] Carinelli S et al, 2018. Biosens Bioelectron 117:183-90
- [18] Ben Aissa A et al, 2017. Biosens Bioelectron 88:265-72.
- [19] Urdea MI et al, 2006. Nature 444 S1, 73-9.
- [20] Nilsson M et al, 1994. Science 265:2085-8
- [21] Carinelli S et al, 2017. Biosens Bioelectron 93:65-71.
- [22] Ben Aissa A et al, 2021. Sensors 21, 1749.
- [23] <https://www.cepheid.com/es-ES/tests/blood-virology-womens-health-sexual-health/xpert-xpress-gbs.html>



4 |

Sensores químicos

Chemical sensors

Sensores químicos

Sensores electroquímicos

Electrochemical sensors

Sensores eletroquímicos

Sensores optoquímicos

Optochemical sensors

Sensores optoquímicos

DetECCIÓN DE DROGAS DE ABUSO EMPLEANDO MATRICES DE SENSORES VOLTAMÉTRICOS Y PRINCIPIOS DE LENGUA ELECTRÓNICA

Xavier Cetó
Grup de Sensors i Biosensors
 Universitat Autònoma de Barcelona
 Bellaterra, Barcelona, Spain
 xavier.ceto@uab.cat

Elena Rodríguez-Franch
Grup de Sensors i Biosensors
 Universitat Autònoma de Barcelona
 Bellaterra, Barcelona, Spain
 elena.rodriguez@uab.cat

Roger Serentill-Grau
Grup de Sensors i Biosensors
 Universitat Autònoma de Barcelona
 Bellaterra, Barcelona, Spain
 roger.serentill@uab.cat

Manel del Valle *
Grup de Sensors i Biosensors
 Universitat Autònoma de Barcelona
 Bellaterra, Barcelona, Spain
 manel.delvalle@uab.cat

Resumen— Se describe la aplicación de sensores voltamétricos para el análisis de drogas ilícitas con ayuda de diferentes herramientas de aprendizaje automático e inteligencia artificial con el objeto de lograr su identificación y cuantificación. Para ello se obtienen los voltamogramas completos de diferentes sensores como huella dactilar de la sustancia en cuestión, los cuales se procesan con la ayuda de herramientas de reconocimiento de patrones. Con su ayuda se obtiene un perfil único para cada sustancia, en lugar de centrarse en los picos individuales de oxidación. Para ello se utilizan diferentes sensores modificados con nanocomponentes o catalizadores redox, los cuales se emplean para analizar las muestras mediante la técnica de voltamperometría de onda cuadrada (SWV). La identificación de las diferentes drogas y sustancias habituales de corte se logró mediante el análisis de componentes principales (PCA) y el análisis de discriminante lineal (LDA), mientras que su cuantificación se logró mediante un modelo de mínimos cuadrados parciales (PLS). El sistema desarrollado tiene un gran interés para la identificación de drogas confiscadas a nivel forense o de aduana, mediante sensores de un solo uso y de bajo coste.

Palabras clave— sensores voltamétricos, análisis de componentes principales, aprendizaje automático, lengua electrónica, opioides, agentes de corte.

I. INTRODUCCIÓN

El tráfico y el consumo de drogas ilícitas se han convertido en los últimos años en una carga mundial bien conocida [1, 2]. No sólo preocupa desde el punto de vista de la salud (efectos físicos y mentales) y económico, sino también por sus consecuencias en la sociedad (por ejemplo, traficantes, aumento de la violencia, economía sumergida, etc.). Para poder actuar sobre tales actividades fraudulentas y salvaguardar al público, las agencias de seguridad y aplicación de la ley requieren de métodos rápidos y portátiles que les permitan identificar de una manera rápida y confiable una posible droga tras su interceptación [3].

La baja precisión de las pruebas de color, o el alto costo y la complejidad de las pruebas instrumentales, son algunos de los inconvenientes de los procedimientos in situ utilizados actualmente para la identificación de drogas ilícitas. Además, los tests de color están dirigidos a una sustancia concreta, requiriendo el uso de un test diferente para cada droga que se

sospecha, mientras que a su vez sólo están disponibles para las drogas más comunes. Como alternativa, es sabido que los métodos de prueba basados en espectroscopía y/o espectrometría de masas son un enfoque más potente [3]. Sin embargo, siguen siendo costosos (tanto el equipo como los consumibles), requieren tiempo y pueden requerir un paso de pretratamiento de la muestra; por lo tanto, tampoco resuelven por completo el problema. En este sentido, los sensores electroquímicos ofrecen información rápida y precisa con un coste reducido. Además, presentan ventajas como sensibilidad, amplio rango lineal, mínimo requerimiento de energía, potencial para miniaturización y portabilidad, instrumentación simple y facilidad de operación. Todo ello les hace adecuados para el desarrollo de dispositivos manuales, compactos y de fácil operación para análisis in situ [4].

Sabido que la mayoría de las drogas de abuso son electroactivas junto con las ventajas mencionadas anteriormente, la determinación electroquímica simultánea de muestras incautadas aún podría ser un desafío dada su complejidad y la similitud de respuesta entre algunas drogas y agentes de corte. Un posible inconveniente es que se produzca el solapamiento entre picos cuando se analizan mezclas; también se ha descrito la supresión de algunos picos para determinadas combinaciones de sustancias [5]. En este sentido, el acoplamiento con el procesamiento quimiométrico permite extraer la máxima información química de estos datos complejos. Con este enfoque es posible desconvolucionar respuestas electroquímicas superpuestas complejas y lograr la identificación y cuantificación simultánea de varios analitos. Si además se usa una serie de sensores modificados químicamente, en lugar de depender de un solo electrodo desnudo, aún es posible mejorar las prestaciones del sistema; este enfoque es el que se conoce como lengua electrónica [6].

Con este objeto, este trabajo presenta algunos de los logros alcanzados hasta el momento en la detección de drogas ilícitas y agentes de corte comunes con los principios de la lengua electrónica (Fig. 1). Dada la complejidad del escenario, el análisis de opioides se ha tomado como primer caso de estudio, con experimentos planificados en orden creciente de complejidad. En primer lugar, se investigó el uso de diferentes electrodos para la generación de huellas dactilares voltamperométricas, seguido de la identificación cualitativa de las diferentes drogas en concentraciones fijas y variables.

Investigación respaldada por los proyectos PID2019-107102RB-C21 y PID2022-136709OB-C21, financiados por AEI/10.13039/501100011033/ Unión Europea NextGenerationEU/PRTR.

A continuación, también se intentó la identificación de drogas mezcladas con diferentes agentes de corte, en lo que representa un escenario más realista. Finalmente, se evaluó la cuantificación simultánea de mezclas de tres drogas diferentes, tanto en ausencia como en presencia de diferentes agentes adulterantes.

II. EXPERIMENTAL

A. Matriz de sensores

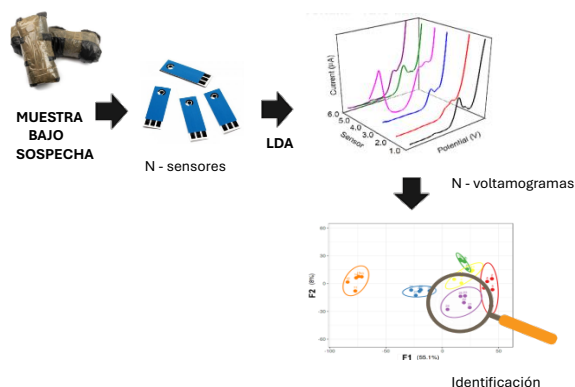


Fig. 1. Esquema de la aproximación propuesta para la identificación de drogas ilícitas en muestras forenses.

Se prepararon diversos sensores voltamétricos utilizando diferentes modificadores como nanotubos de carbono, grafeno, ftalocianina de cobalto (II) (CoPH), azul de Prusia, polipirrol, así como nanopartículas de paladio (Pd) o nanopartículas de óxido de cobre, bismuto, titanio, zinc y estaño. Esos modificadores se seleccionaron teniendo en cuenta estudios previos con ET en otros campos [7]. De esta manera, se evaluaron electrodos serigrafados (SPE) modificados con diferentes tintas de carbono. Brevemente, el procedimiento para su elaboración fue el siguiente: para la modificación de sensores serigrafados comerciales (Metrohm-Dropsens C110) se preparó una tinta de poliestireno mezclando 58% de grafito, 10% del modificador específico y 32% de poliestireno en polvo con 250 μL de mesitileno. A continuación, se vertió 1 μL de la solución obtenida sobre el electrodo y se secó a 40°C durante 1 h.

B. Medidas electroquímicas

Las mediciones voltamperométricas de onda cuadrada (SWV) se realizaron a temperatura ambiente utilizando un potenciostato PalmSens MultiEmStat de 4 canales (Houten, Países Bajos) controlado con el paquete de software MultiTrace. De esta manera, las muestras de drogas se analizaron con los conjuntos de sensores mencionados anteriormente colocando una gota de la solución sobre los electrodos y registrando un único barrido de oxidación para cada una de las muestras y electrodos. El barrido se realizó entre -0.2 y +1.5 V, con un escalón de 5 mV, amplitud de 25mV y frecuencia 10 Hz. Para evitar cualquier efecto de contaminación en los electrodos y tener que realizar una regeneración física de su superficie, se realizó una medición de un blanco entre cada muestra.

C. Tratamiento de datos

El análisis quimiométrico se realizó mediante scripts implementados en MATLAB (MathWorks, Natick, MA, EE.

UU.), utilizando sus correspondientes toolboxes estadísticas. Concretamente, se utilizaron algoritmos genéticos (GA) como herramienta de selección de características para reducir la cantidad de entradas alimentadas a los modelos quimiométricos cuantitativos dada la gran dimensionalidad de los datos voltamétricos [8]. A continuación, se realizó un análisis cualitativo mediante análisis de componentes principales (PCA) que permitió evaluar patrones iniciales en los datos y evaluar (des)similitudes de las muestras, mientras que a continuación se utilizó un análisis discriminante lineal (LDA) para construir el modelo clasificador que permitió categorización de las diferentes muestras. Finalmente, el análisis cuantitativo de mezclas de drogas se logró mediante regresión de mínimos cuadrados parciales (PLS). Esta elección se justifica por el afán de conseguir el modelo más simple posible capaz de cumplir la tarea deseada. En este sentido, la elección de GA como herramienta de selección de características proporciona una doble ventaja ya que, por un lado, permite reducir significativamente el procesamiento informático, mientras que, por otro lado, permite mejorar el rendimiento del modelo y la capacidad de generalización alcanzada. De manera similar, se prefirió PLS a las redes neuronales artificiales (ANN) debido a su simplicidad y menores requisitos computacionales.

III. RESULTADOS

Para ilustrar el potencial del enfoque propuesto, se realizaron aproximaciones de complejidad creciente; a saber, la identificación de diferentes opioides sin/con la presencia de agentes de corte y la cuantificación de mezclas de opioides, sin/con la presencia de agentes de corte. Para cada uno de ellos, se preparó y midió un conjunto diferente de muestras con los sensores propuestos, sometiendo posteriormente las respuestas obtenidas al modelo apropiado dependiendo de si se buscaba una respuesta cualitativa o cuantitativa. Para todos los modelos desarrollados, se adoptó una estrategia de validación cruzada, en el que el conjunto de muestras se dividió en dos subconjuntos: subconjunto de entrenamiento (utilizado para ajustar el modelo) y subconjunto de prueba (utilizado para evaluar su rendimiento).

A. Identificación de drogas

El primer paso fue la caracterización analítica de las respuestas voltamétricas de los diferentes electrodos hacia las diferentes drogas considerados, para asegurar que existe respuesta, y que estas respuestas resultan diferenciadas entre los diferentes electrodos. A continuación, se enviaron los voltamogramas a PCA y la bondad de la agrupación observada se utilizó para seleccionar el conjunto de sensores óptimo para cada escenario [9].

Por ejemplo, la Fig. 2 muestra las respuestas voltamétricas para tres SPE modificados, en este caso concreto usando una matriz con un sensor de carbono no modificado, y electrodos modificados con ftalocianina de cobalto y nanopartículas de Pd, donde se puede ver cómo cada uno genera señales diferenciadas. La composición de la matriz de sensores fue optimizada en paralelo a dichos experimentos (resultados no mostrados). El resultado del análisis en componentes principales de estos datos se muestra en la Fig. 3, donde se ve una clara agrupación de cada sustancia, lo que confirma que se obtienen diferentes huellas dactilares para cada caso. De forma significativa, incluso cuando se varía la concentración de las sustancias, el algoritmo aún puede identificarla correctamente, puesto que la señal se normaliza previamente.

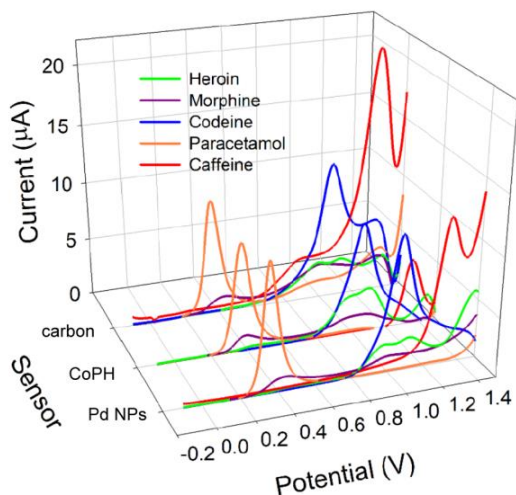


Fig. 2. Muestra de señales voltamétricas obtenidas con la matriz de sensores propuesta y diferentes drogas de abuso y agentes de corte.

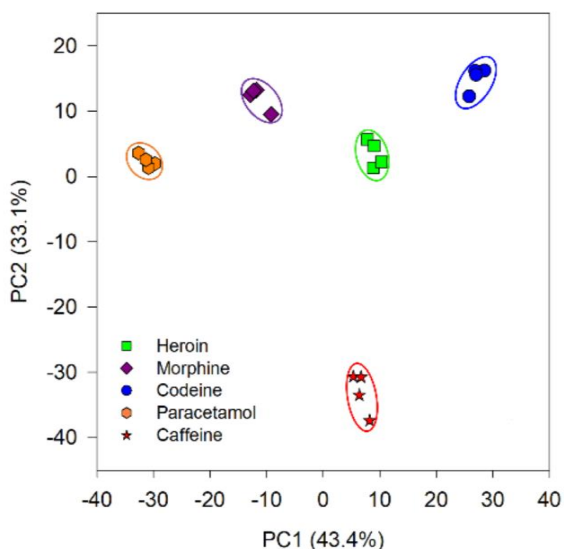


Fig. 3. Diagrama de "scores" obtenido tras el análisis de componentes principales (PCA) de las medidas voltamétricas obtenidas con la matriz de sensores anterior, al realizar medidas con diferentes drogas opiáceas y agentes de corte.

B. Identificación de drogas mezcladas con agentes de corte

En un segundo caso cualitativo, se intentó la identificación y clasificación de cuatro fármacos diferentes cuando se mezclaban con diferentes agentes de corte. Para ello, se analizó un nuevo conjunto de muestras con los diferentes sensores, y se modelaron las respuestas con ayuda del análisis de discriminante lineal (LDA) como método supervisado para conseguir la clasificación en 5 grupos diferentes: uno para cada uno de los fármacos considerados (mezclados o no con agentes de corte) y uno para todos los diferentes agentes de corte. Nuevamente, se obtuvieron unos agrupamientos evidentes para cada una de las clases consideradas, logrando un porcentaje de éxito de clasificación para el subconjunto de prueba del 100 %.

C. Cuantificación de drogas (puras) en mezclas

A continuación, se evaluó la cuantificación simultánea de mezclas de las tres drogas opiáceas consideradas en III.A. Para ello, se preparó un conjunto de muestras, se midieron con el conjunto de sensores y luego se construyó el modelo cuantitativo empleando algoritmos genéticos y mínimos cuadrados parciales (GA-PLS). Para visualizar las prestaciones de respuesta del modelo de cuantificación, se construyeron gráficos comparativos de las concentraciones previstas vs. las esperadas (Fig. 4), a partir de las cuales también se calcularon los parámetros de regresión lineal. Como se puede visualizar, se obtuvieron tendencias satisfactorias para cada una de las drogas y subconjuntos, con líneas de regresión cercanas a las ideales, estando los valores ideales de pendiente, correlación e intercepción dentro de los intervalos de confianza obtenidos.

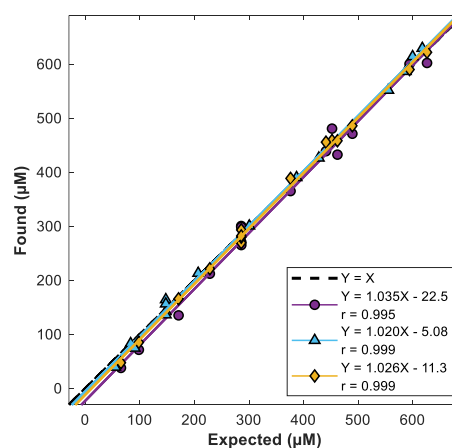


Fig. 4. Bondad del modelado cuantitativo en la resolución de mezclas de (●) heroína, (▲) morfina y (◆) codeína en el rango de 0-700 µM. Información correspondiente a la comparativa concentración calculada vs. concentración esperada para el conjunto externo de prueba. La comparación de referencia ($y=x$) se muestra como referencia. El modelo final utiliza algoritmos genéticos para selección de información significativa y mínimos cuadrados parciales para el cálculo (GA-PLS).

D. Cuantificación de mezclas de drogas y adulterantes

Por último, se utilizó el enfoque anterior, pero utilizando un conjunto diferente de muestras, para lograr la cuantificación de situaciones donde se encuentran los mismos tres opiáceos en presencia de dos agentes de corte (paracetamol y cafeína). Como antes, se utilizó GA-PLS para construir el modelo de cuantificación que permitió no solo la cuantificación de las diferentes drogas, sino también la de los agentes de corte. Nuevamente, con una tendencia satisfactoria y parámetros de regresión cercanos a los valores ideales.

Con estos cuatro casos que se muestran, se intuye que los sistemas basados en detección electroquímica y contribución de herramientas de inteligencia artificial pueden ser en un futuro los detectores de posibles alijos de drogas interceptados. Como ventaja es posible enumerar una manipulación mínima, una determinación rápida y sencilla, y un coste reducido, que posibilita un esquema de sistema sensor de un solo uso. Como observación adicional, se puede comentar como el sistema es posible implementarlo con

sistemas de telecomunicación encriptados, de forma que el operario solamente recoge las medidas, estas son enviadas a un modelo de identificación en la nube, y por internet se recibe el resultado. Una operativa de este tipo permitiría además un refinamiento continuo del modelo, si los múltiples usuarios confirmasen los resultados con análisis de referencia.

IV. CONCLUSIONES

La combinación de sensores voltamétricos modificados con diferentes herramientas de aprendizaje automático e inteligencia artificial ha demostrado ser un enfoque útil para el análisis de drogas de abuso, en este caso opiáceos. Aunque el ejemplo mostrado se reduce a morfina y compuestos derivados, estos principios son igualmente válidos para otras drogas de abuso (por ejemplo, cocaína, ketamina o metanfetamina), con la única condición que la sustancia sea electroactiva. Para ampliar el conjunto de sustancias detectadas sería recomendable reconsiderar la matriz de sensores utilizada, para lo que se despone de una metodología que permite definir un conjunto de sensores optimizado para una aplicación dada [9]. En el caso aquí mostrado, se han obtenido resultados satisfactorios tanto en la discriminación cualitativa de sustancias como en su cuantificación simultánea, incluso en mezclas de diferentes drogas y/o diferentes agentes de corte. En consecuencia, teniendo en cuenta el rendimiento demostrado en este resumen y las ventajas inherentes de los métodos electroquímicos, como su simplicidad, bajo costo y portabilidad, se confirma la idoneidad del enfoque actual para el desarrollo de sistemas portátiles para análisis descentralizados, en aplicaciones forenses y de examen en aduanas.

REFERENCIAS

- [1] M. Singer, "Drugs and development: The global impact of drug use and trafficking on social and economic development," *Int. J. Drug Policy*, vol. 19, no. 6, pp. 467-478, 2008.
- [2] L. Degenhardt and W. Hall, "Extent of illicit drug use and dependence, and their contribution to the global burden of disease," *Lancet*, vol. 379, no. 9810, pp. 55-70, 2012.
- [3] D. Vearrier, J. A. Curtis, and M. I. Greenberg, "Biological testing for drugs of abuse," in *molecular, clinical and environmental toxicology. experientia supplementum*, vol. 100, A. Luch, Ed. Basel: Birkhäuser Basel, 2010, pp. 489-517.
- [4] J. Wang, "Portable electrochemical systems" *Trends Analytical Chem*, vol. 21, no. 4, pp. 226-232, 2002.
- [5] M. de Jong, A. Florea, J. Eliaerts, F. Van Durme, N. Samyn, and K. De Wael, "Tackling poor specificity of cocaine color tests by electrochemical strategies" *Anal. Chem.* vol. 90, no. 11, pp. 6811-6819, 2018.
- [6] M. del Valle, "Electronic tongues employing electrochemical sensors" *Electroanalysis*. vol. 22, no. 14, pp. 1539-1555, 2010.
- [7] J. M. Gutiérrez, L. Moreno-Barón, M. I. Pividori, S. Alegret, and M. del Valle, "A voltammetric electronic tongue made of modified epoxy-graphite electrodes for the qualitative analysis of wine" *Microchim. Acta*, vol. 169, pp. 261-268, 2010.
- [8] X. Cetó, F. Céspedes, and M. del Valle, "Comparison of methods for the processing of voltammetric electronic tongues data" *Microchim. Acta*, vol. 180, pp. 319-330, 2013.
- [9] M. Sarma, N. Romero, X. Cetó, and M. del Valle, "Optimization of sensors to be used in a voltammetric electronic tongue based on clustering metrics" *Sensors*, vol. 20, no. 17, p. 4798, 2020.

An IoT Electrochemical Sensor based on a Conductive Polymer-modified Electrode for Levofloxacin Determination

Bryan E. Alvarez-Serna

Instituto de Ingeniería

Universidad Nacional Autónoma de México

Ciudad de México 04510, México

BAlvarezS@iingen.unam.mx

Roberto G. Ramírez-Chavarría

Instituto de Ingeniería

Universidad Nacional Autónoma de México

Ciudad de México 04510, México

RRamirezC@iingen.unam.mx

Abstract—In this paper, we introduce a low-cost system of screen-printed electrodes (SPE) modified with poly(methylene blue) (PMB) as an electrochemical sensor for levofloxacin (LVX) determination with Internet of Things (IoT) connectivity. Developing new electrochemical devices with IoT connectivity to modify, validate, and measure within a single system represents a significant advancement in creating accessible IoT platforms for drug detection. The proposed SPE/PMB sensor was tested using LVX solutions prepared in phosphate buffer. As a result, the sensor achieved a detection limit of 1.4 mg/L within a concentration range of 0 to 50 mg/L, proving its potential to quantify drugs at low concentrations in liquid samples and its integration into IoT measurement systems.

Index Terms—Conductive polymer, screen-printed electrodes, electropolymerization, internet of things, levofloxacin

I. INTRODUCTION

Levofloxacin (LVX) is one of the most commonly used antibiotics in treating infectious diseases of the respiratory tract, urinary tract, skin, and soft tissues [1]. However, the excessive abuse of antibiotics worldwide poses a significant danger as it can lead to antibiotic resistance. It constitutes a serious public health and environmental problem, as levofloxacin residues return to the environment through untreated and treated water discharges, contaminating sources of drinking and irrigation water [2]. Therefore, detecting LVX is crucial to curb its spread and prevent human consumption of contaminated water and food.

Detection and quantification of LVX require sophisticated analytical techniques such as high-performance liquid chromatography [3], capillary electrophoresis [4], and paramagnetic resonance [5], to mention only a few. These techniques require complex bench-top equipment, sample pretreatment, and long-time operation for analysis. Currently, electrochemical sensors have become an attractive alternative to conventional analytical techniques for the detection of drugs [6]. Electrochemical sensors offer advantages such as high sensitivity,

low detection limits, selectivity, portability, easy manufacturing, and rapid response. Electrochemical transduction is based on a redox reaction that produces changes in an electrical signal proportional to the concentration of the analyte. Among the various electrochemical sensors, amperometric sensors allow continuous measurements over time, with high sensitivity and low detection limits when an electroactive species is involved, suitable for developing portable and accessible detection devices [7]. Amperometric sensors conventionally use a three-electrode electrochemical cell, which includes a reference electrode, an auxiliary electrode, and a working electrode. Conventional electrodes are typically pencil-type, which are difficult to modify due to their size and fragility. A powerful alternative is to use screen-printed electrodes (SPE), which are compact, require no pretreatment or recalibration, and contain all three electrodes on the same substrate [8]. The SPE allows integration into portable devices, minimizing the reaction volume compared to classical vials or tubes and providing specificity by modifying the working electrode surface. The most popular techniques of modification are chemical, thermal, and electrochemical. Notably, electrochemical modification offers a simple, fast, and accessible process using electro-analytical methods, namely electrodeposition. This technique produces homogeneous functionalization of the working electrode to enhance its electrical conductivity, ion absorption, and chemical stability, to name a few [9]. Electrochemical sensors based on modified electrodes still have two main limitations. Firstly, modified electrodes require advanced materials such as nanomaterials [10], biomolecules [11], or metal-organic frameworks [12], to mention only a few. Secondly, although the specificity and performance of modified sensors are impressive, their manufacturing cost and preparation are not easy to replicate in resource-limited environments.

The modification based on conductive polymers has emerged as an attractive and cost-effective alternative for developing electrochemical sensors. These sensors present several advantages, such as simple synthesis processes, corrosion resistance, reproducibility, and stability [13]. Among the wide variety of conductive, poly(methylene blue) (PMB),

This work was supported by SECTEI-CDMX project 1564c23 "e-SAST". BE Alvarez-Serna acknowledges CONACYT for the PhD studies grant (CVU 1004078).

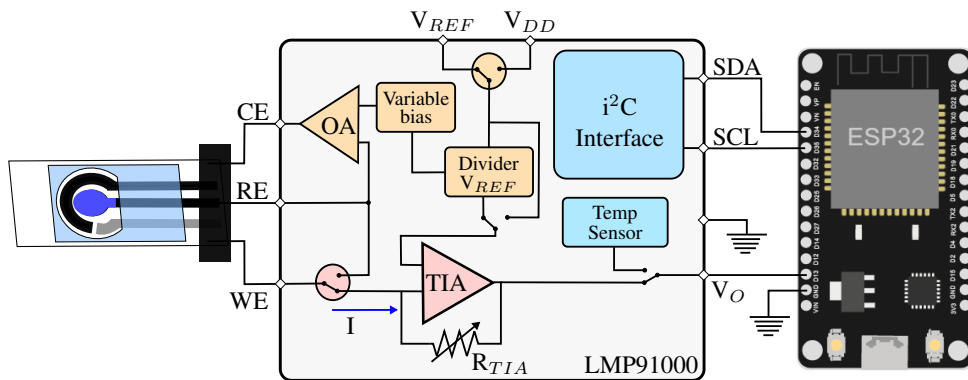


Fig. 1: Schematic diagram of the instrumentation system with Internet of Things connection, called iioT-Stat.

obtained from methylene blue (MB) monomer, is an electroactive polymer that generates reactions at low electrical potential [14]. Additionally, MB has a high electron transfer efficiency, can be polymerized on solid substrates, and is highly reactive to organic molecules, adequate for drug detection. Today, the development of economical and high-performance electrochemical sensors and their integration into wireless or autonomous monitoring systems poses a global scientific challenge [15]. For this reason, this study has developed an instrumentation system under the Internet of Things (IoT) approach. IoT is a technological trend that allows us to connect an electrochemical sensor to the internet to exchange data and control message traffic. Additionally, an IoT sensor can be integrated into networks with other sensors using protocols and data analysis algorithms, including artificial intelligence [16]. These platforms allow remote access to real-time data and enable experimenters to take preventive or corrective actions on experiment parameters in an automated manner. Therefore, this study demonstrates the advantages of modifying SPE electrodes with PMB using a simple yet effective methodology and their integration into an accessible IoT instrumentation system with minimal hardware for quantifying LVX in liquid samples. The aim is to contribute to the establishment of a solid framework for developing new IoT electrochemical sensors to quantify LVX, or any antibiotic, with high sensitivity and low detection limits.

II. METHODS

A. Materials

Levofloxacin (98 %, ACS reagent) was purchased from Sigma-Aldrich (St. Louis, USA). Isopropyl alcohol (91 %, v/v), hydrochloric acid (38 %, w/v), hydrogen peroxide (30 %, w/w), methylene blue (98 %, w/v), phosphate buffer at pH 7.4, and distilled water were acquired from Meyer (Mexico City, Mexico). Additionally, we used an electrochemical cell based on screen-printed electrodes purchased from Metrohm DropSens (Oviedo, Spain) model C110. The sensor has a reference electrode made of silver paste. In contrast, the

counter and working electrodes were made of carbon paste. However, the working electrode was modified with PMB to enhance the sensor's sensitivity for LVX detection.

B. Measurement system for IoT

In Fig. 1, the schematic diagram of the IoT instrumentation system, named iioT-Stat, is depicted. The system allows for electrode modification, validation of its operation, and levofloxacin quantification using the same configuration but different electrochemical techniques. The iioT-Stat consists of the SPE/PMB sensor connected to the LMP91000 integrated circuit from Texas Instruments, which is controlled by a development board with system-on-chip technology from the ESP32 family. The LMP91000 is a compact potentiostat for electrochemical applications that can be configured for different electrochemical techniques using an i²C communication protocol. Additionally, it features temperature compensation and a polarization current regulator connected to an operational amplifier (OA) to bias the sample using the RE and CE electrodes. The electrochemical technique is configured with the ESP32 board, where input parameters are adjusted.

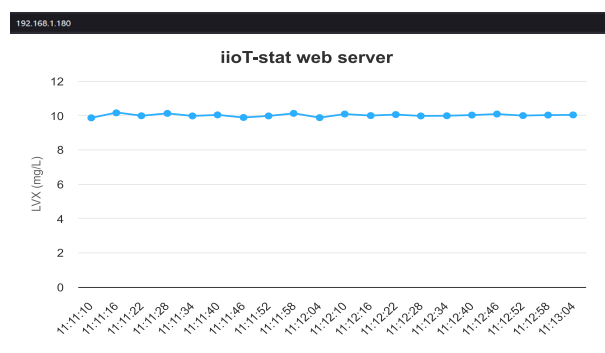


Fig. 2: Preview of the web server displaying real-time levofloxacin concentration over time.

Subsequently, the current, I , generated between the working electrode and the analyte is measured using a transimpedance amplifier (TIA) to convert the current into an output voltage, V_O , which is proportional to the input current by a feedback resistor, R_{TIA} , such that $V_O = V_{REF} - R_{TIA} I$. The V_O is digitized by a 12-bit analog-to-digital converter within the ESP32 board. Voltammograms for modifying, validating, and calibrating the sensor were obtained on a personal computer. Finally, taking advantage of the fact that the board has a built-in WiFi module, we send the data over the internet to a website programmed in HTML, which is hosted within the board. These data can be viewed on a web server from any device using an IP address. Fig. 2 shows the server with a Highcharts graph, which is a JavaScript-based software library for graphics, illustrating the concentration of LVX over time.

C. Modification of the SPE with PMB

The three electrodes of the SPE sensor are on a plastic substrate with dimensions of $3.4 \times 1.0 \times 0.05$ cm. The WE has an active surface area of 12.57 mm^2 and was modified to increase its sensitivity for quantifying LVX. The modification process consists of three stages. Firstly, the surface of the sensor was activated with a solution containing hydrochloric acid (HCl), hydrogen peroxide (H_2O_2), and distilled water at a 1:1:3 ratio (v/v) for 2 minutes. Subsequently, a $50 \mu\text{L}$ drop of a phosphate buffer at pH 7.4 and 0.01 M of MB solution was placed, and 20 continuous cycles of cyclic voltammetry (CV) were applied. Finally, the sensor was rinsed with distilled water and dried at room temperature.

III. RESULTS

A. Electrochemical modification and validation of the SPE/PMB

Fig. 3(a) illustrates the electropolymerization process using 20 cycles of CV. This process is carried out within a potential range of -0.5 to 1.5 V with a scan rate of 50 mVs^{-1} to deposit PMB onto the WE surface. The first voltammogram, depicted in red, illustrates the redox reaction of the monomer with its cathodic and anodic peaks at -0.38 and 0.47 V, respectively. On the other hand, the voltammograms in blue show the remaining nineteen cycles of the PMB electropolymerization process. There, the amplitude of the oxidation and reduction current peaks increases and decreases, respectively, depending on the number of cycles. This gradual increase in current makes sense as the electroactivity of the polymer increases with the number of cycles, indicating the proper electropolymerization of PMB.

Subsequently, we studied the electrochemical response of the sensor before and after modification with PMB to detect LVX. Experimentally, we prepared a solution of 40 mg/L LVX in phosphate buffer and measured it using CV in a potential range of -0.4 to 0.4 V with a scan rate of 50 mVs^{-1} . Fig. 3(b) displays the black voltammogram with the sensor without PMB (SPE), where it can be observed that the current amplitude is less than $8 \mu\text{A}$, and although it exhibits the behavior of a redox reaction, it is not easy to define the values of the oxidation and reduction peaks. On the other

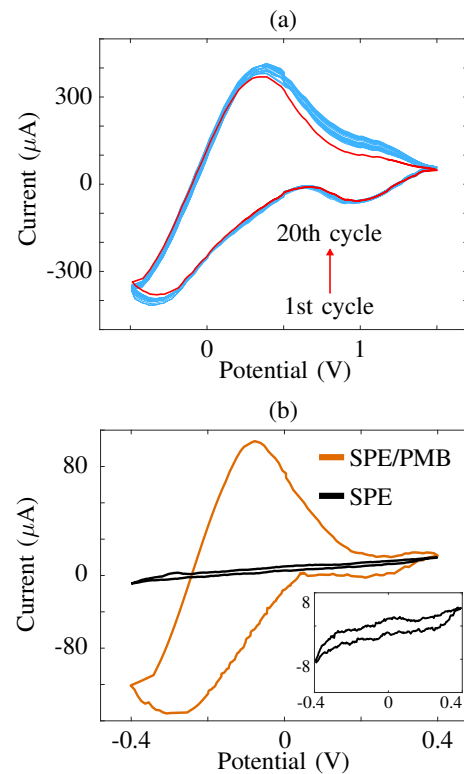


Fig. 3: (a) Electropolymerization process of PMB by cyclic voltammetry in phosphate buffer at pH 7.4 and 0.01 M methylene blue. (b) Cyclic voltammograms of the sensor with PMB (SPE/PMB) and the sensor without PMB (SPE) to detect 40 mg/L of LVX prepared in phosphate buffer.

hand, the orange voltammogram with the sensor with PMB (SPE/PMB) shows a cathodic current peak greater than $80 \mu\text{A}$, indicating that the PMB enhances the sensor response in the presence of LVX. Based on these results, we demonstrate that the PMB deposited on the electrode undergoes a redox reaction, increasing the current amplitude without altering the potential range.

B. Amperometric detection of LVX

To further investigate the sensor's ability to quantify LVX, we applied the amperometry technique with a potential of 0.5 V for six hours. In the first hour, we measured in phosphate buffer without LVX; subsequently, we gradually increased the concentration in 10 mg/L increments every 10 minutes. Fig. 4(a) shows the amperometric response of the sensor for 0, 10, 20, 30, 40, and 50 mg/L of LVX in phosphate buffer. The graph demonstrates that the current amplitude consistently increases with each successive elevation of LVX concentration. Additionally, the current measurements at each interval maintain their value with variations of less than 5% from their average, indicating repeatability in the measurements.

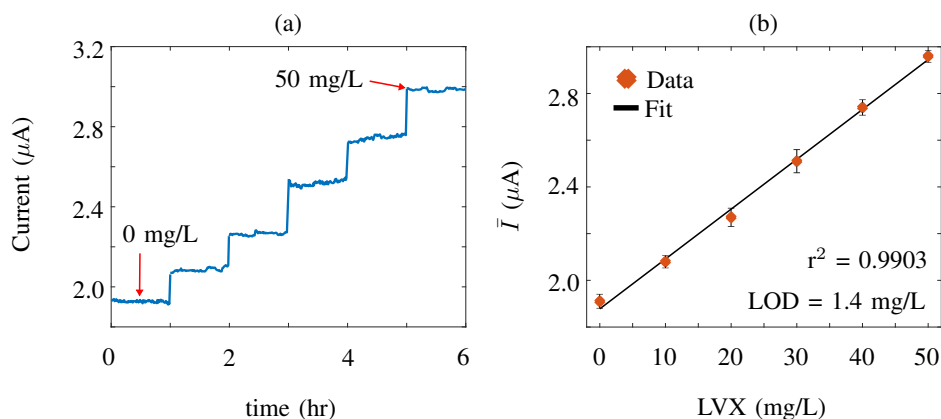


Fig. 4: (a) Amperometric response of the SPE-PMB sensor upon adding different concentrations of LVX at an applied potential of 0.5 V. (b) Calibration curve of the average current \bar{I} as a function of the LVX concentration.

Finally, we calculated the average current, \bar{I} , value for each concentration. With this value, we established the calibration curve to quantify LVX, as shown in Fig. 4(b). The calibration curve displays the experimental data (black dots), the standard deviation (vertical lines) for three measurements, and the linear model (solid line) in a range from 0 to 50 mg/L of LVX. As expected, the \bar{I} has a directly proportional relationship with the LVX concentration, showing a coefficient of determination close to 99 % and a detection limit (LOD) of 1.4 mg/L, which is in the same order of magnitude as previous reports [17].

IV. CONCLUSIONS

We have developed a cost-effective electrochemical sensor based on a system of modified screen-printed electrodes (SPE) with poly(methylene blue) (PMB) for levofloxacin (LVX) determination in liquid samples. Our work combines the electropolymerization process, validation, and amperometric measurements in a single electrochemical device with Internet of Things (IoT) connectivity. The modification process demonstrates the ability to electrodeposit PMB onto an electrode for electrochemical determination of LVX with high sensitivity. Our sensor showcased its capacity to quantify LVX with a low detection limit of 1.4 mg/L. Following these findings, the development of this sensor aims to demonstrate a simple, low-cost, and accessible methodology for designing modified electrochemical sensors for drug detection and their integration into IoT platforms.

REFERENCES

- [1] L. Saya, V. Malik, D. Gautam, G. Gambhir, W. R. Singh, S. Hooda *et al.*, "A comprehensive review on recent advances toward sequestration of levofloxacin antibiotic from wastewater," *Sci. Total Environ.*, vol. 813, p. 152529, 2022.
- [2] M. S. de Ilurdoz, J. J. Sadhwani, and J. V. Reboso, "Antibiotic removal processes from water & wastewater for the protection of the aquatic environment-a review," *J. Water Process. Eng.*, vol. 45, p. 102474, 2022.
- [3] Y. He, Z. Ma, and L. B. Junior, "Distinctive binary g-c3n4/mos2 heterojunctions with highly efficient ultrasonic catalytic degradation for levofloxacin and methylene blue," *Ceram. Int.*, vol. 46, no. 8, pp. 12364–12372, 2020.
- [4] R. Řemínek and F. Foret, "Capillary electrophoretic methods for quality control analyses of pharmaceuticals: A review," *Electrophoresis*, vol. 42, no. 1-2, pp. 19–37, 2021.
- [5] X. Zhang, Y. Tian, L. Zhou, L. Wang, J. Zhang, Y. Liu, and J. Lei, "Efficient degradation of levofloxacin using a g-c3n4@ glucose-derived carbon catalyst with adjustable n content via peroxymonosulfate activation," *Chemosphere*, vol. 314, p. 137684, 2023.
- [6] Q. Wang, Q. Xue, T. Chen, J. Li, Y. Liu, X. Shan, F. Liu, and J. Jia, "Recent advances in electrochemical sensors for antibiotics and their applications," *Chin. Chem. Lett.*, vol. 32, no. 2, pp. 609–619, 2021.
- [7] R. Rajapaksha, U. Hashim, S. C. Gopinath, N. A. Parmin, and C. Fernando, "Nanoparticles in electrochemical bioanalytical analysis," in *Nanoparticles Anal. Med. Devices*. Elsevier, 2021, pp. 83–112.
- [8] P. Kelišková, O. Matvieiev, L. Janíková, and R. Šešlovská, "Recent advances in the use of screen-printed electrodes in drug analysis: A review," *Curr. Opin. Electrochem.*, p. 101408, 2023.
- [9] E. Senokos, M. Rana, C. Santos, R. Marcilla, and J. J. Vilatela, "Controlled electrochemical functionalization of cnt fibers: structure-chemistry relations and application in current collector-free all-solid supercapacitors," *Carbon*, vol. 142, pp. 599–609, 2019.
- [10] D. Tonelli, E. Scavetta, and I. Gualandri, "Electrochemical deposition of nanomaterials for electrochemical sensing," *Sensors*, vol. 19, no. 5, p. 1186, 2019.
- [11] I. R. Suhito, K.-M. Koo, and T.-H. Kim, "Recent advances in electrochemical sensors for the detection of biomolecules and whole cells," *Biomedicines*, vol. 9, no. 1, p. 15, 2020.
- [12] X. Zhang, K. Wan, P. Subramanian, M. Xu, J. Luo, and J. Fransaer, "Electrochemical deposition of metal-organic framework films and their applications," *J. Mater. Chem. A.*, vol. 8, no. 16, pp. 7569–7587, 2020.
- [13] S. Tajik, H. Beitollahi, F. G. Nejad, I. S. Shoaie, M. A. Khalilzadeh, M. S. Asl, Q. Van Le, K. Zhang, H. W. Jang, and M. Shokouhimehr, "Recent developments in conducting polymers: Applications for electrochemistry," *RSC advances*, vol. 10, no. 62, pp. 37834–37856, 2020.
- [14] L. Abad-Gil and C. M. Brett, "Poly (methylene blue)-ternary deep eutectic solvent/au nanoparticle modified electrodes as novel electrochemical sensors: Optimization, characterization and application," *Electrochim. Acta*, vol. 434, p. 141295, 2022.
- [15] I. Yaroshenko, D. Kirsanov, M. Marjanovic, P. A. Lieberzeit, O. Korostynska, A. Mason, I. Frau, and A. Legin, "Real-time water quality monitoring with chemical sensors," *Sensors*, vol. 20, no. 12, p. 3432, 2020.
- [16] S. L. Ullo and G. R. Sinha, "Advances in smart environment monitoring systems using iot and sensors," *Sensors*, vol. 20, no. 11, p. 3113, 2020.
- [17] K. Rudnicki, K. Sipa, M. Brycht, P. Borgul, S. Skrzypek, and L. Poltorak, "Electrochemical sensing of fluoroquinolone antibiotics," *TrAC Trends Anal. Chem.*, vol. 128, p. 115907, 2020.

Electrochemical performance of a hybrid material of $\text{Ce}(\text{OH})\text{CO}_3$ and carbon nanotubes

Fernando F. Muñoz
UNIDEF, CONICET, MINDEF,
Departamento de Investigaciones en
Sólidos
CITEDEF
Buenos Aires, Argentina
fmunoz@citedef.gob.ar

Ana L. Rinaldi
Departamento de Ciencias Químicas,
Facultad de Farmacia y Bioquímica
Universidad de Buenos Aires
Buenos Aires, Argentina
ana-r-88@hotmail.com

Romina R. Carballo
Departamento de Ciencias Químicas,
Facultad de Farmacia y Bioquímica
Universidad de Buenos Aires
IQUIFIB-CONICET, Facultad de
Farmacia y Bioquímica
Universidad de Buenos Aires
Buenos Aires, Argentina
romina.carballo191278@gmail.com

Santiago Cosci
Departamento de Ciencias Químicas,
Facultad de Farmacia y Bioquímica
Universidad de Buenos Aires
Buenos Aires, Argentina
santiago.cosci@gmail.com

Paula C. Dabas
Departamento de Ciencias Químicas,
Facultad de Farmacia y Bioquímica
Universidad de Buenos Aires
Buenos Aires, Argentina
paulic.dabas@gmail.com

M. Celina Bonetto
IQUIFIB-CONICET, Facultad de
Farmacia y Bioquímica
Universidad de Buenos Aires
Buenos Aires, Argentina
celinatt@yahoo.com.ar

J. Iván González Jorge
Departamento de Ciencias Químicas,
Facultad de Farmacia y Bioquímica
Universidad de Buenos Aires
IQUIFIB-CONICET, Facultad de
Farmacia y Bioquímica
Universidad de Buenos Aires
Buenos Aires, Argentina
jigonzaalez930209@gmail.com

Santiago Sobral
IQUIFIB-CONICET, Facultad de
Farmacia y Bioquímica
Universidad de Buenos Aires
Buenos Aires, Argentina
ssobral.teq@gmail.com

Abstract—Cerium hydroxycarbonate and multiwalled carbon nanotubes ($\text{Ce}(\text{OH})\text{CO}_3$ and CNT respectively), drop-casted onto a glassy carbon (GC) electrode and electrochemically treated ($\text{tCe}(\text{OH})\text{CO}_3/\text{CNT}$) has been obtained as a new hybrid material, characterized through SEM and electrochemical techniques. The charge transfer resistance (R_{CT}) value of $\text{tCe}(\text{OH})\text{CO}_3/\text{CNT}$ was up to two orders of magnitude lower than the R_{CT} of bare GC electrodes.

Keywords—*Electrochemical pretreatment; Cerium hydroxycarbonate; Carbon nanotubes; Dopamine; Differential pulse voltammetry.*

1. INTRODUCTION

The nature of an electrode material plays a crucial role in the construction of high-performance electrochemical sensors. Biomolecules on conventional electrodes usually display broad peaks and often present sensitivity and selectivity problems due to their sluggish surface kinetics. [1,2].

Electrochemical pretreatments like amperometric or voltammetric oxidations and/or reductions can enhance the performance of modified electrodes producing active sites with high density of electronic states and/or a large amount of oxygen containing functional groups. That way, huge potential drops can be favored, as well as quick electron transfer kinetics for the analyte and a background current decrease (*i.e.* electrochemical treatment of CNTs in acidic conditions can partially convert them into graphene like materials improving the electron transfer rate) [3-4]. Cerium dioxide-based compounds have abundant intrinsic structural defects (*i.e.*, oxygen vacancies), and are widely applied in catalysis, oxygen sensors, water gas shift

reactions, fuel cells, and biomedicine [5-6]. In the solid phase, it displays a rapid and reversible interconversion between Ce^{3+} and Ce^{4+} , which gives this oxide extraordinary catalytic and electrocatalytic properties [7]. Its combination with a conductive component such as carbon can improve the redox ability of Ce and provide additional functionality as high electrical conductivity, mechanical strength, chemical stability, and surface to volume ratio [8].

Few reports are found on the electrochemical properties of $\text{Ce}(\text{OH})\text{CO}_3$, a compound in the cerium-based family that is usually obtained as a precursor while synthesizing its oxides. Nevertheless, it has been found adequate for its use as an electrode for lithium ion batteries [9] or as electromagnetic wave absorber with high conductivity [10]. Several $\text{Ce}(\text{OH})\text{CO}_3$ syntheses rely on urea hydrolysis [11], rising the pH reaction media by NH_3 release. Many studies aimed towards controlled morphology propose that finely tuned urea decomposition provide a balanced NH_3 release, a condition where distinct morphologies arise, from rods or dumbbells to fully formed spheres [12]. The present work aims to study the influence of electrochemical pretreatments (7 voltammetric cycles from -1 to 1.1 V) applied to modified electrodes with $\text{Ce}(\text{OH})\text{CO}_3$ and CNTs, and the impact on its overall electrochemical performance.

2. EXPERIMENTAL

2.1 Reagents

KCl, NaOH, NH_4Cl , $(\text{NH}_4)_2\text{SO}_4$, K_2HPO_4 , HCl, H_2SO_4 96%, $\text{K}_3[\text{Fe}(\text{CN})_6]$, $\text{K}_4[\text{Fe}(\text{CN})_6]$, $\text{Ce}(\text{SO}_4)_2$, $\text{Ce}_2(\text{SO}_4)_3$, $\text{Ce}(\text{NO}_3)_3 \cdot 6\text{H}_2\text{O}$, HAc 99.7%, NaAc, ethanol and urea, were used as received.

CNTs (> 98% carbon basis, 10 nm outer diameter, 4.5 nm inner diameter and 3.5 μm length), were purchased from Merck.

All chemicals were of analytical grade, and deionized water was used to prepare the solutions.

$\text{Ce}(\text{OH})\text{CO}_3$ precursor was synthesized via the low temperature urea homogenous precipitation method [13].

2.2. Preparation of $\text{Ce}(\text{OH})\text{CO}_3/\text{CNT}$ modified electrodes and electrochemical measurements

0.25 g L^{-1} of CNT or 0.25 g L^{-1} CNT + 7 g L^{-1} $\text{Ce}(\text{OH})\text{CO}_3$, were both added to a 0.1 mol L^{-1} H_2SO_4 solution in ethanol (eH_2SO_4) and ultrasonically dispersed for 120 min.

The GC electrodes (1 mm diameter) were polished with alumina powder (0.3 μm) on a wet cloth, obtaining a mirror-like surface, then rinsed with deionized water. In modified electrodes, 5 μL of dispersions were deposited onto a pretreated GC electrode, followed by drying at 30 $^\circ\text{C}$ for 1h. CNT or $\text{Ce}(\text{OH})\text{CO}_3/\text{CNT}$ modified electrodes were electrochemically treated applying 7 cycles of cyclic voltammetry (CV) at 50 mV s^{-1} from -1 to +1.1 V vs $\text{Ag}/\text{AgCl}/\text{KCl}$ saturated in each respective dispersion. The resulting modified electrodes were named tCNT and t $\text{Ce}(\text{OH})\text{CO}_3/\text{CNT}$, and both were washed thoroughly before use.

All electrochemical measurements were made with a standard three-electrode system. A glassy carbon bare electrode (GC, Structure Probe, Inc. PA, USA), or modified ones with ntCNT, tCNT, nt $\text{Ce}(\text{OH})\text{CO}_3/\text{CNT}$ or t $\text{Ce}(\text{OH})\text{CO}_3/\text{CNT}$ were assayed as working electrodes. A Pt wire was used as counter electrode and $\text{Ag}/\text{AgCl}/\text{KCl}$ saturated as reference electrode.

All measurements were performed at room temperature with freshly prepared solutions.

2.3 Electrochemical measurements

All measurements were carried out in KCl 0.1 mol L^{-1} unless otherwise stated. Differential pulse voltammetry (DPV) experiments were carried out using 50mV pulse amplitude, 0.05s pulse width, 5mV step size and 0.35s pulse period.

A frequency range of 100 kHz to 0.1 Hz was used for electrochemical impedance spectroscopy (EIS) measurements, done in $[\text{Fe}(\text{CN})_6]^{3-/4-}$ in 0.1 mol L^{-1} KCl , with an amplitude of oscillation set to 10 mV and the working potential to +130mV.

2.4. Apparatus

CV and DPV detection were performed with a purpose built potentiostat (TEQ-Argentina) containing a digital signal generator implemented for different electrochemical techniques. EIS was recorded using a potentiostat TEQ4-Z (TEQ-Argentina) with a frequency response analyzer. Phase identification of the $\text{Ce}(\text{OH})\text{CO}_3$ sample was carried out by conventional X-ray diffraction (XRD) analysis using a Panalytical Empyrean diffractometer.

3. RESULTS AND DISCUSSION

3.1. $\text{Ce}(\text{OH})\text{CO}_3$ precursor characteristics

$\text{Ce}(\text{OH})\text{CO}_3$ was obtained with a distinct morphology. A relatively simple process was chosen, via heating a closed vessel at normal pressure, relying on the thermally aided hydrolysis of urea, with the crucial difference being its high molar ratio respective to Ce^{3+} , *i.e.* 10 to 1. That assures a very high number of nucleation centers, due to the slow hydrolysis of urea and thus a slow, restrained liberation of NH_3 and steady pH rise, two facts that provide a very controlled $\text{Ce}(\text{OH})\text{CO}_3$ particle growth and a final dumbbell's morphology with unique textural, disaggregated properties, crucial to electrocatalytic sensors.

3.2. Physicochemical characterization of modified electrodes

Through pretreatment methods, several desired effects can be obtained on electrodes, *i.e.* rougher surface, microstructure change, and new edge plane sites of the graphitic structure [3]. In this work, SEM assays were made to evaluate the physicochemical changes produced in the modified electrodes after electrochemical pretreatment.

Pristine $\text{Ce}(\text{OH})\text{CO}_3$ consisted on dumbbells made up of many gathered rods, with an average width of 6-10 μm (each rod being between 400-100 nm wide) (Fig. 1a). After sonication in eH_2SO_4 , these dumbbells were disassembled into individual rods. After the electrochemical pretreatment, clear differences were seen between $\text{Ce}(\text{OH})\text{CO}_3$ morphologies in Figs. 1b and c. Remarkably, Fig. 1c (t $\text{Ce}(\text{OH})\text{CO}_3/\text{CNT}$) shows that after pretreatment, CNTs were clearly connected to both $\text{Ce}(\text{OH})\text{CO}_3$ particles and the GC surface through some kind of slurry.

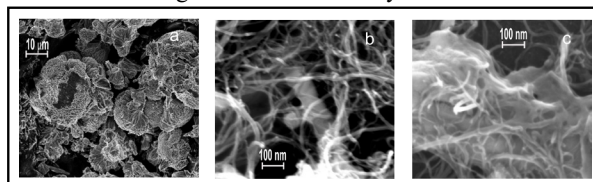


Figure 1: SEM images of solid $\text{Ce}(\text{OH})\text{CO}_3$ (a), $\text{ntCe}(\text{OH})\text{CO}_3/\text{CNT}$ (b), or $\text{tCe}(\text{OH})\text{CO}_3/\text{CNT}$ (c).

Since the slurry is always nearby the $\text{Ce}(\text{OH})\text{CO}_3$ particles, we propose that it comes from them, but at the same time CNTs seem essential for the attachment to the GC surface. Regarding the adhesion mechanism that took place, $\text{Ce}(\text{OH})\text{CO}_3$ can be used as a sacrificial template, where the OH^- and CO_3^{2-} from its structure are substituted by specific and desired counter anions, in a substitution/digestion process while retaining, partially or wholly, the original morphology [14]. In parallel, there are several studies that show that the pretreatment step with successive oxidation and reduction cycles could induce partial openings and of oxygen defects into the CNT [15]. Hence, these oxygenated functional groups would take the role of those desired counter anions, and replace CO_3^{2-} and OH^- anions, all within the solid $\text{Ce}(\text{OH})\text{CO}_3$ phase, effectively immobilizing the rods onto the CNT slurry which is itself attached to the GC.

3.3. Electrochemical performance of $Ce^{3+/4+}$ and $[Fe(CN)_6]^{3-/4-}$ assays

The voltammograms obtained in the electrochemical treatment (7 cycles of cyclic voltammetry, CV) of CNT modified electrodes along with the voltammograms obtained in the electrochemical treatment of $Ce(OH)CO_3/CNT$, clearly points to oxidation and reduction peaks related to the $Ce^{3+/4+}$ redox couple at around 690/790 mV obtained in the latter case (Fig. 2a).

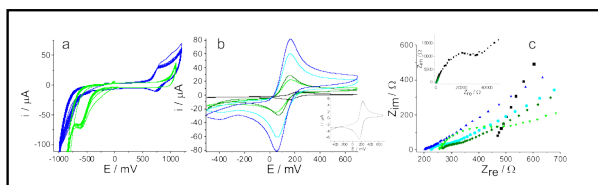


Figure 2: a) 7 CV cycles of $Ce(OH)CO_3/CNT$ (blue) or CNT (light green) modified electrodes in their respective dispersions (a). Cyclic voltammograms (b) and Nyquist plots (c) employing 5 mmol L^{-1} $[Fe(CN)_6]^{3-}$ in 0.1 mol L^{-1} phosphate buffer. Measurements were made with bare GC electrode (black) or GC electrodes modified with ntCNT (light green); tCNT (green); nt $Ce(OH)CO_3/CNT$ (cyan); or t $Ce(OH)CO_3/CNT$ (blue). A zoom in the GC curve is shown in the inset of figure c.

Such crucial feature arises as a consequence of the electrochemical treatment and not before (not seen in nt $Ce(OH)CO_3/CNT$), since in the solid precursor, Ce presents a very low tendency to redox cycling from its nominal $3+$ oxidation state, by virtue of the crystal structure of the hydroxycarbonate that hinders the $4+$ state [16].

Thus, having established a deliberately induced modification that introduces the $Ce^{3+/4+}$ equilibria, the modified electrodes electrochemically treated, were assayed through CV using the $[Fe(CN)_6]^{3-/4-}$ redox probe, and EIS using $[Fe(CN)_6]^{3-/4-}$ (Figs. 2b and c respectively) to evaluate their performance compared with bare GC or modified electrodes not electrochemically treated (ntCNT or nt $Ce(OH)CO_3/CNT$).

$[Fe(CN)_6]^{3-/4-}$ is a classical example of an inner-sphere electrode reaction probe with surface-sensitive response [17], therefore we studied the behavior of bare GC, and modified ntCNT, tCNT, nt $Ce(OH)CO_3/CNT$ and t $Ce(OH)CO_3/CNT$ electrodes through CV studies in its presence. It was observed that even when nt $Ce(OH)CO_3/CNT$ and ntCNT exhibited an acceptable ΔE_p with good redox peak currents, t $Ce(OH)CO_3/CNT$ exhibited the best performance in $[Fe(CN)_6]^{3-/4-}$ solution with the lowest ΔE_p and the nearest to 1 peak current ratio (i_{pc}/i_{pa}), both signs of good reversibility (Fig 2b).

Furthermore, the electroactive surface area (ECSA) was calculated for bare GC and modified electrodes by using the Randles-Sevcik equation (1) assuming mass transport only by diffusion processes, a broadly used method in electrochemical sensors applications [18]:

$$i_p = 2.69 * 10^5 n^{3/2} A D^{1/2} C v^{1/2} \quad (1)$$

where D is the $[Fe(CN)_6]^{3-/4-}$ diffusion coefficient ($\text{cm}^2 \text{ s}^{-1}$), i_p is the anodic peak current (A), C is the $[Fe(CN)_6]^{3-/4-}$ concentration (mol cm^{-3}), A is the electroactive area (cm^2), n is the number of transferred electrons and $v^{1/2}$ is the square

root of scan rate (V s^{-1}). The constant value of $2.69 * 10^5$ has units of $\text{C mol}^{-1} \text{ V}^{-1/2}$.

The modification of GC electrodes with CNT increased the ECSA value of bare GC electrodes in one-fold (from 0.059 to 0.384 cm^2), while the further addition of $Ce(OH)CO_3$ and the electrochemical pretreatment that yields t $Ce(OH)CO_3/CNT$ triplicates the area of CNT electrodes (from 0.044 to 0.127 cm^2), giving evidence of an overall process needed to achieve an adequate final hybrid material. Lastly, EIS using $[Fe(CN)_6]^{3-/4-}$ was chosen to further evaluate the capacity for electron transfer of the modified electrodes; the obtained Nyquist plots are presented in Fig. 2c. The R_{CT} values, determined by fitting the data using an appropriate equivalent circuit, show the enhancement of electron transfer rate (*i.e.* an R_{CT} decrease) with the electrochemical pretreatment of CNT (a 10 times R_{CT} decrease in comparison with GC), and a markedly great improvement with the addition of $Ce(OH)CO_3$ and the subsequent electrochemical pretreatment of these electrodes (more than 200 times R_{CT} decrease in comparison with GC). It has to be taken into account that the addition of $Ce(OH)CO_3$ to CNT, without electrochemical pretreatment, already improves the R_{CT} of the modified electrodes when compared with ntCNT, proving the extent of the influence of cerium in the electrocatalytic properties. It is also observed that the electrochemical treatment improves the electron transfer rate of the tCNT electrodes, implying that the CNTs were favorably modified electrochemically, as previously mentioned.

In accordance with the ΔE_p and ECSA results, the Nyquist plots show higher electrocatalytic performance for t $Ce(OH)CO_3/CNT$ as confirmed by the drop of R_{CT} , as the semicircle in the Nyquist plot of this modified electrode is practically absent, a strong indicator that only mass transfer effects are present. In this context, this implies a better electrocatalytic activity for this redox couple, and also the desired synergy between the precursor materials [19].

3.4. Dopamine electrochemical determinations

The GC electrodes display the highest oxidation peak potentials (E_{pa}) for DA, while tCNT and t $Ce(OH)CO_3/CNT$ modified electrodes clearly improved the determination of DA showing lower E_{pa} potentials (Fig. 3).

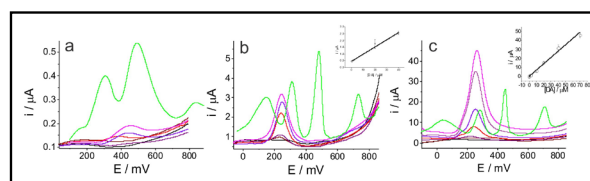


Figure 3: DPV measurements showing a DA calibration curve (from 2 to 70 μmol L^{-1}) and simultaneous determination of AA, DA, UA, Trp (green curve) in concentrations: $500, 20, 100, \text{ and } 15 \text{ μmol L}^{-1}$ respectively, using a bare GC electrode (a), or tCNT (b) or t $Ce(OH)CO_3/CNT$ modified electrodes.

The biggest difference between modified electrodes, either electrochemically treated or not, is observed between CNT and $Ce(OH)CO_3/CNT$. The addition of $Ce(OH)CO_3$ improves DA sensitivity values (*i.e.* ten times higher). The treatment which yields t $Ce(OH)CO_3/CNT$ electrodes do not impact significantly in the E_{pa} values for DA if the results

are compared with $\text{ntCe(OH)CO}_3/\text{CNT}$, but it really improves the linear range for DA ($0.4\text{-}40 \mu\text{mol L}^{-1}$ for $\text{ntCe(OH)CO}_3/\text{CNT}$ and $0.1\text{-}40 \mu\text{mol L}^{-1}$ for $\text{tCe(OH)CO}_3/\text{CNT}$).

The limits of detection (LOD) and quantification (LOQ) were calculated for each electrode at study for DA using the formula $3*SD*b^{-1}$ or $10*SD*b^{-1}$ respectively, where SD is the standard deviation of 3 consecutive readings of the blank response and b is the slope of the analyte calibration. The LOD values of $\text{tCe(OH)CO}_3/\text{CNT}$ are in the range of the best DA values reported in literature (LOD: $0.003 \mu\text{mol L}^{-1}$ and LOQ: $0.001 \mu\text{mol L}^{-1}$).

4. CONCLUSIONS

In this work, non-expensive materials (Ce(OH)CO_3 and CNT) and eco-friendly processes (a hard sacrificial template synthesis and electrochemical treatments) were employed to satisfactory develop a hybrid $\text{Ce(OH)CO}_3/\text{CNT}$ modified GC electrode. The addition of CNT and Ce(OH)CO_3 to GC electrodes show better activity towards DA determination, but the fully electrochemically treated material with both precursors presents the higher improvement. These electrodes displayed the best LOD and LOQ for DA, in very good agreement with literature values.

ACKNOWLEDGMENTS

This work was supported by the University of Buenos Aires, the National Council for Scientific and Technological Research (IQUIFIB-CONICET) and the ANPCyT (Préstamo BID, PICT 2021 GRF TI-00269).

REFERENCES

- [1] R.L. McCreery, Advanced carbon electrode materials for molecular electrochemistry, *Chem. Rev.* 108 (2008) 2646-2687.
- [2] P. Chen, R.L. McCreery, Control of electron transfer kinetics at glassy carbon electrodes by specific surface modification, *Anal. Chem.* 68 (1996) 3958-3965.
- [3] A. Rana, N. Baig, T.A. Saleh, Electrochemically pretreated carbon electrodes and their electroanalytical applications - A review, *J. Electroanal. Chem.* 833 (2019) 313-332.
- [4] M.C. Bonetto, F.F. Muñoz, V.E. Diz, N.J. Sacco, E. Cortón, Fused and unzipped carbon nanotubes, electrochemically treated, for selective determination of dopamine and serotonin, *Electrochim. Acta* 283 (2018) 338-348.
- [5] T. Montini, M. Melchionna, M. Monai, P. Fornasiero, Fundamentals and catalytic applications of CeO_2 -based materials. *Chem. Rev.* 116 (2016) 598713.
- [6] A.B. Shcherbakov, V.V. Reukov, A.V. Yakimansky, E.L. Krasnopeeva, O.S. Ivanova, A.L. Popov, V.K. Ivanov, CeO_2 Nanoparticle-containing polymers for biomedical applications: A review, *Polymers* 13 (2021) 924.
- [7] B.M. Reddy, Chapter 8 - Redox properties of metal oxides, in J.L.G. Fierro (ed.), *Metal oxides chemistry and applications*, 1st edition, CRC Press, Boca Raton, 2006, pp.: 215-246.
- [8] S. Agarwal, B.L. Mojet, L. Lefferts, A.K. Datye, Chapter 2 - Ceria nanoshapes-structural and catalytic properties, in Zili Wu, Steven H. Overbury (eds.), *Catalysis by materials with well-defined structures*, 1st edition, Elsevier, Oxford, 2015, pp.: 31-70.
- [9] F. Hrizi, H. Dhaouadi, F. Touati, Cerium carbonate hydroxide and ceria micro/nanostructures: Synthesis, characterization and electrochemical properties of CeCO_3OH . *Ceram. Int.* 40 (2014) 25-30.
- [10] H. Wei, X. Wang, G. Tong, B.X. Fan, X. Wang, W. Wu, Morphology, size, and defect engineering in Ce(OH)CO_3 hierarchical structures for ultra-wide band microwave absorption. *J. Mater. Chem. C* 10 (2022) 281.
- [11] M.Z. Wu, Q.H. Zhang, Y.M. Liu, Q.Q. Fang, X.S. Liu, Hydrothermal preparation of fractal dendrites: Cerium carbonate hydroxide and cerium oxide, *Mater. Res. Bull.* 44 (2009) 1437.
- [12] R. Suarez Anzorena, F.F. Muñoz, P. Bonelli, A.L. Cukierman, S.A. Larrondo, Hierarchical, template-free self-assembly morphologies in CeO_2 synthesized via urea-hydrothermal method, *Ceramics Int.* 46 (2020) 11776-11785.
- [13] J. Šubr, V. Štengl, S. Bakardjieva, L. Szatmary, Synthesis of spherical metal oxide particles using homogeneous precipitation of aqueous solutions of metal sulfates with urea, *Powder Technol.* 169 (2006) 33-40.
- [14] A.M. Kaczmarek, K. Van Hecke, R. Van Deun, Nano- and micro-sized rare-earth carbonates and their use as precursors and sacrificial templates for the synthesis of new innovative materials, *Chem. Soc. Rev.* 44 (2015) 2032-2059.
- [15] S. Pei, H.-M. Cheng, The reduction of graphene oxide, *Carbon* 50 (2012) 3210-3228.
- [16] P. Kim, A. Anderko, A. Navrotsky, R.E. Riman, Trends in structure and thermodynamic properties of normal rare earth carbonates and rare earth hydroxycarbonates, *Minerals* 2018, 8, 106.
- [17] A.J. Bard, L.R. Faulkner, Chapter 3, *Electrochemical Methods, Fundamentals and Applications*, John Wiley & Sons, Texas, 2001.
- [18] J. Krejci, Z. Sajdlova, V. Nedela, E. Flodrova, R. Sejnohova, H. Vranova, R. Plicka, Effective surface area of electrochemical sensors. *J. Electrochem. Soc.* 161 (2014) 147-150.
- [19] A.L. Rinaldi, M.C. Bonetto, S. Sobral, R. Carballo, Evaluation of the synergistic effects of a novel organic-inorganic nickel hybrid nanocomposite as electrocatalyst toward glucose oxidation, *J. Electroanal. Chem.* 863 (2020) 114039.

Sensor electroquímico compuesto de grafito modificado con quitosano y Azure-A para el monitoreo in-situ de la frescura en pescado

Brenda Beleiro

Departamento de Química. Facultad de Ciencias Naturales y Ciencias de la Salud. Universidad Nacional de la Patagonia "San Juan Bosco". IIDEPYS-GSJ.
Comodoro Rivadavia, Argentina.
bbeleiro@gmail.com

Silvia Miscoria

Departamento de Química. Facultad de Ciencias Naturales y Ciencias de la Salud. Universidad Nacional de la Patagonia "San Juan Bosco". (IIDEPYS-GSJ).
Comodoro Rivadavia, Argentina
silviamiscoria@unpata.edu.ar

Reartes Daiana Fernanda

INFIQC, Departamento de Físicoquímica,
Facultad de Ciencias Químicas, Universidad Nacional de Córdoba
Córdoba, Argentina
daiana.reartes@unc.edu.ar

Rodríguez Marcela Cecilia

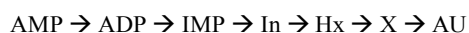
INFIQC, Departamento de Físicoquímica,
Facultad de Ciencias Químicas, Universidad Nacional de Córdoba
Córdoba, Argentina
marcela.rodriguez@unc.edu.ar

Resumen—Se empleó como estrategia un material compuesto de grafito (CPE) modificado por adsorción de quitosano (QS) y Azure A (AzA) CPE/QS/AzA para el diseño de un sensor electroquímico dirigido a la cuantificación y especiación altamente sensible y selectiva de hipoxantina (Hx), xantina (X) y ácido úrico (AU). Se llevó a cabo el estudio de diversos parámetros de análisis del sistema empleando la estrategia de acumulación de los analitos a potencial de circuito abierto (OCP), para la determinación simultánea de Hx, X y AU, procedentes de la vía de degradación y catabolismo de las purinas. Estos analitos son indicadores asociados con la pérdida de la frescura del pescado para su consumo ya que sus niveles se incrementan en los procesos de degradación cárnica.

Palabras clave— compuesto de grafito, quitosano, Azure A, hipoxantina, xantina, ácido úrico.

I. INTRODUCCION

Las purinas son moléculas que revisten un especial interés ya que, al igual que las pirimidinas, son constituyentes estructurales fundamentales del ADN y el ARN [1]. El catabolismo de las purinas comienza por la degradación del ATP en ciertas condiciones metabólicas y deriva en la formación de ácido úrico (AU) como producto final en el ser humano, o bien, en alantoína para aquellos que poseen la enzima uricasa como el pescado y ciertos primates. El mecanismo



general cuyo producto es el AU puede describirse como sigue:

Donde AMP es monofosfato de adenosina, ADP es

difosfato de adenosina, IMP es monofosfato de inosina e In es inosina.

De esta vía, es importante remarcar que en condiciones fisiológicas la enzima xantina oxidasa (XOD), cataliza la conversión sucesiva de Hx a X e inmediatamente a AU, como se muestra en la Figura 1. [2]

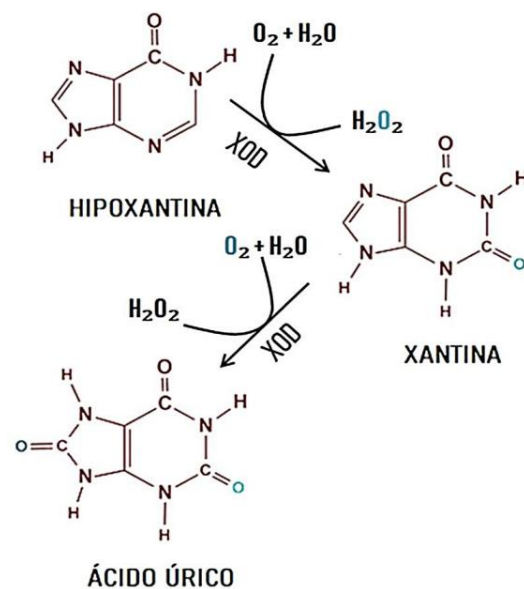


Figura 1- Esquema simplificado del mecanismo de acción de la XOD.

Si bien la concentración de Hx varía de acuerdo con diferentes parámetros biológicos como especie, composición de macronutrientes y reserva de glucógeno, entre otros; es considerada como uno de los

principales parámetros relacionados con la evolución del deterioro del tejido en el tiempo transcurrido desde su muerte. En lo que respecta a la X, su contenido es bajo en el músculo de pescado debido a la acción de la XOD que rápidamente la oxida a AU. Este último por su parte podría constituir el parámetro final de la oxidación de la Hx. Sin embargo, al considerar la rápida transformación de la Hx en sus derivados oxidados, resulta interesante la medición de los tres parámetros en simultáneo, ya que brinda información del estado de frescura [3-5].

En este sentido, el desafío es diseñar metodologías que permitan la especiación y cuantificación *in situ* de los tres analitos de modo rápido, simple, sensible y selectivo. Esta determinación es de importancia central en la industria pesquera como fuente de recursos alimenticios y económicos, ubicándose Argentina en el puesto N°20 dentro de los principales países productores [6]. En la actualidad, el monitoreo individual de Hx, X y AU se realiza por técnicas tediosas que además de ser costosas, requieren preparación previa de la muestra, siendo compleja la cuantificación simultánea de los tres analitos. Por lo expuesto previamente, las técnicas de elección son cromatografía líquida de alta performance (HPLC), espectrofotometría-UV y métodos de fluorescencia [7]. En este contexto, el empleo de sensores electroquímicos constituye una alternativa simple, portable y rentable en la cuantificación de estas biomoléculas, permitiendo realizar determinaciones *in situ* sin necesidad de tratamientos previos de la muestra.

Desde el punto de vista de los materiales de electrodo, el grafito presenta múltiples ventajas como su bajo costo y buena conductividad eléctrica. Los materiales compósitos de grafito a su vez presentan también gran versatilidad al ser maleables lo que proporciona una gran facilidad de renovación superficial a diferencia de los electrodos sólidos. Este material compósito otorga además la posibilidad de incorporar nanomateriales y biomoléculas que mejoren la sensibilidad y selectividad [8,9]. El quitosano (Qs) es un biopolímero obtenido a partir de la desacetilación de la quitina, es soluble en ácidos orgánicos diluidos, adquiriendo cargas positivas por la presencia de grupos amino. Presenta además características mucoadhesivas que le confieren una gran capacidad de para interactuar con biomoléculas [10]. Por otro lado, el Azure A (N', N' dimethylphenothiazin-5-ium-3,7-diamine), es un compuesto perteneciente a la familia de las fenotiazinas derivado del Azul de metileno (MB). La estructura de anillos aromáticos altamente conjugados le confiere electronegatividad y comportamiento electroactivo bajo ciertas condiciones experimentales.

En este trabajo se diseñó un sensor electroquímico basado en un compósito de grafito empleando partículas de grafito y como aglutinante aceite mineral en una

relación 70/30, respectivamente. Este material de electrodo fue posteriormente modificado mediante adsorción secuencial con Qs y AzA. Esta plataforma fue caracterizada desde el punto de vista electroquímico, estudiando el comportamiento de los tres analitos Hx, X y AU, mediante voltamperometría cíclica (VC), y voltamperometría de pulso diferencial (DPV). Una vez optimizado el sistema se llevó a cabo el ensayo de cuantificación y especiación de los analitos mediante acumulación a potencial de circuito abierto (OCP) con una posterior etapa de transducción de la señal de oxidación de las moléculas adsorbidas empleando DPV.

II. MATERIALES Y MÉTODOS

A. Materiales

Quitosano desacetilado en un 75%, Azure A, glutaraldehído (GA), aceite mineral, hipoxantina, xantina y ácido úrico fueron provistos por Sigma Aldrich. El fosfato de sodio dibásico anhidro y fosfato de sodio monobásico se obtuvieron de Baker. El grafito se obtuvo de Thermo Fisher; y ácido acético glacial e hidróxido de sodio de Biopack. Todas las soluciones se prepararon con agua ultrapura ($\rho = 18,0 \text{ M}\Omega \text{ cm}^{-1}$) obtenida de un equipo Millipore-MilliQ. Todos los experimentos fueron realizados a temperatura ambiente.

B. Aparatos

Para realizar los ensayos electroquímicos se emplearon workstations Epsilon (BAS) y ParaSTAT (AMETEK); las acumulaciones a OCP se realizaron mediante convección forzada a 600 rpm. En los ensayos electroquímicos se empleó una celda convencional de 3 electrodos: electrodo de referencia de Ag/AgCl/Cl⁻, contraelectrodo: alambre de platino (Pt) y el electrodo de trabajo: compósito de grafito modificado con quitosano y Azure-A (CPE/Qs/AzA).

III. RESULTADOS Y DISCUSIÓN

A. Construcción de la plataforma

Empleando VC se llevó a cabo el monitoreo de las modificaciones del CPE por adsorción de 1 mM Qs y 1,0 mM AzA, ambos en buffer acetato (BAC) 0,20 M pH 5,00. Además, se ensayó la incorporación de 1,0% de GA como potencial agente favorecedor del anclaje del AzA en la matriz de Qs. En esta etapa se emplearon los tres analitos en estudio en una concentración de 1,0 mM con un tiempo de acumulación de 5 minutos mediante OCP.

Se estudió la adsorción de Qs y AzA para los tiempos de 10 y 20 minutos para cada uno sobre el CPE. En primer lugar, se evaluó el tiempo de adsorción de AzA sobre CPE (CPE/AzA). Posteriormente, se estudió el tiempo de Qs y AzA sobre CPE (CPE/Qs/AzA). La selección de las condiciones óptimas se basó en una evaluación conjunta de los parámetros de corriente de

pico (I_p), tiempo y reproducibilidad de los resultados, tal como se muestra en la Figura 2.

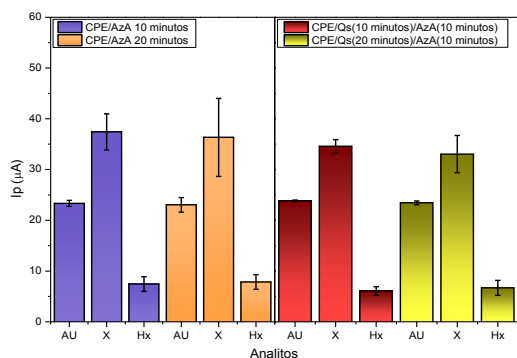


Fig. 2: Comparación de las respuestas de I_p obtenidas sobre CPE/AzA y CPE/Qs/AzA para 1 mM de AU, X y Hx, respectivamente, para tiempos de adsorción de Qs y AzA de 10 y 20 minutos en BAc 0,20 M pH 5,00.

Es importante remarcar que en los ensayos empleando la plataforma CPE/Qs ningún analito demostró respuesta, por lo que el Qs no favorece el comportamiento electroquímico de Hx, X y AU. Sin embargo, en presencia de AzA (CPE/AzA), se observan tres señales claramente definidas a diferentes valores de potencial de los tres analitos en simultáneo. De acuerdo con los resultados obtenidos, se observa que en ausencia de Qs para un tiempo de adsorción de AzA de 10 min (CPE/AzA) se observa una mayor reproducibilidad (dada por la desviación estándar de los resultados) en comparación con tiempos mayores de adsorción, por lo que se seleccionó 10 minutos como tiempo óptimo de adsorción para AzA. Para la plataforma CPE/Qs/AzA se llevó a cabo el estudio del tiempo de adsorción de Qs para 10 y 20 minutos. En este caso, se encontró una mayor reproducibilidad para tiempos de 10 minutos de Qs en referencia con tiempos mayores. En presencia de Qs y AzA (CPE/Qs/AzA) la respuesta para Hx, X y AU demuestra un claro perfil en las señales de los analitos mejorando significativamente la reproducibilidad de las mismas. Estos resultados indicarían que la presencia de Qs es fundamental en la plataforma para mejorar la adsorción del AzA en la superficie del sensor tal como se ha reportado previamente[11]. Asimismo, el empleo de GA como agente favorecedor de la interacción Qs/AzA no demostró cambios significativos en la respuesta de los analitos con respecto a CPE/Qs/AzA. En consecuencia, para los ensayos posteriores se seleccionó la plataforma CPE/Qs/AzA.

Sobre la plataforma óptima se efectuó el estudio del tiempo de acumulación a OCP para AU, X e Hx, con el fin de evaluar la respuesta electroquímica de los analitos de interés. En esta etapa, se seleccionaron tiempos de 5 y 10 minutos y se trabajó con una concentración de 1,0 mM de cada analito. Se analizaron los valores de corriente de pico máximos para cada tiempo de acumulación, los resultados obtenidos se muestran en la

Figura 3. En comparación con los resultados para 5 minutos se observa que luego de 10 minutos de acumulación a OCP hay una marcada disminución en la respuesta. Es importante resaltar que el proceso de acumulación a OCP procede en condiciones de agitación a 600 rpm y probablemente el comportamiento observado se debe a una desorción parcial de los analitos a tiempos prolongados. Por lo tanto, se seleccionó 5 minutos a OCP para llevar a cabo el análisis de AU, X e Hx.

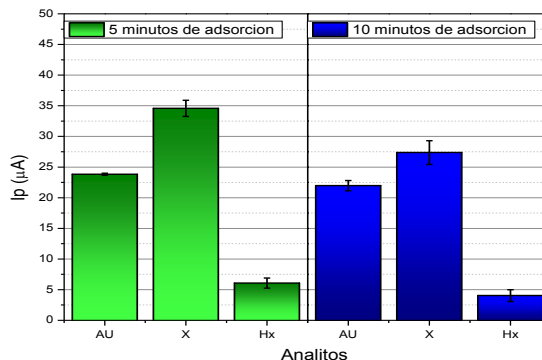


Figura 3: Respuestas de I_p obtenidas para AU, X e Hx sobre CPE/Qs/AzA con tiempos de acumulación a OCP de 5 y 10 minutos en BAc 0,20 M pH 5,00.

Teniendo en cuenta el tiempo óptimo de OCP se llevó a cabo el estudio de la dependencia de la respuesta electroquímica de los analitos en función de la naturaleza del electrolito soporte. Con este objetivo se emplearon soluciones de buffer fosfato (PBS) 0,10 M pH 7,40 y buffer acetato (BAc) 0,20 M pH 5,00 pH, como se muestra en la Figura 4. De lo resultados obtenidos se puede inferir que la mejor respuesta se obtiene empleando PBS pH 7,40. Asimismo, estos resultados son congruentes con el pH fisiológico de la muestra real, lo que evitaría llevar a cabo pretratamientos de la muestra para efectuar la determinación de la frescura *in situ*. Por lo tanto, se seleccionó PBS pH 7,40 como condición óptima de trabajo.

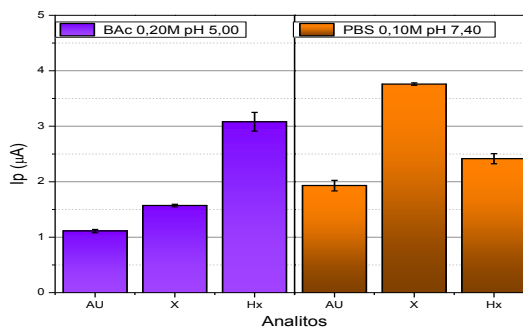


Figura 4: Respuestas de I_p obtenidas sobre CPE/Qs/AzA con acumulación de 5 minutos a OCP para 1 mM de AU, X y Hx.

B. Estudio del comportamiento electroquímico de los analitos.

Una vez optimizadas las condiciones operativas de la

plataforma, se evaluó el efecto de la velocidad de barrido en el sistema empleando VC en una ventana de potencial de -0,200 a +1,700 V, registrándose los valores de corriente de pico (I_p) para 1,0 mM de Hx, X y AU, respectivamente en PBS 0,10 M pH 7,40. Las velocidades de barrido ensayadas fueron: 0,010; 0,025; 0,050; 0,075; 0,100; 0,200 y 0,250 Vs^{-1} . A partir del análisis de los resultados obtenidos se observó una relación lineal de las corrientes de oxidación en función de la velocidad de barrido, indicando que los procesos de oxidación de los analitos de estudio están controlados por difusión.

C. Estudio del desempeño analítico del sensor CPE/QS/AzA

Una vez optimizadas todas las condiciones de trabajo se efectuó el estudio del desempeño analítico del sensor empleando DPV. Para determinar los parámetros analíticos del sensor se realizaron ensayos para cada analito por separado y en mezcla, empleando un amplio intervalo de concentraciones de 0,0 μM a 100,0 μM . Asimismo, se realizó el estudio de mezclas de los analitos variando la concentración de uno de los analitos, manteniendo constante la concentración de los otros dos.

En la Figura 5 se observa que fue posible determinar concentraciones tan bajas como 5,0 μM , mostrando señales distintivas e independientes para cada uno de los analitos en una mezcla. Esto demuestra la capacidad del sensor para realizar la especiación de los tres bioindicadores en un único ensayo, lo que refuerza su potencial para aplicaciones analíticas *in situ* donde se requiere alta sensibilidad y selectividad, además de versatilidad y bajo costo.

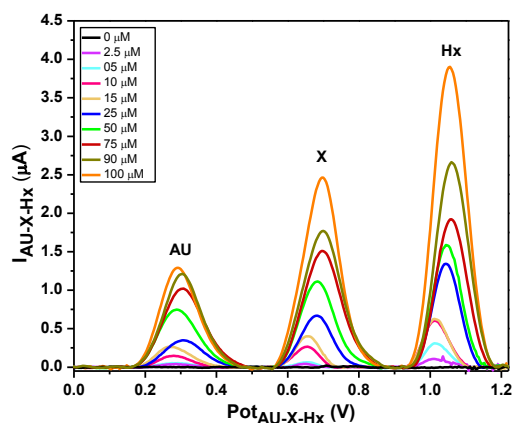


Fig. 5: Respuesta de I_p para mezclas de los analitos AU, X e Hx en PBS 0,10 M pH 7,40 en un intervalo de concentración de 2,50; 5,00; 10,0; 15,0; 25,0; 50,0; 75,0; 90,0 y 100,0 μM

IV. CONCLUSIONES

En este trabajo fue posible obtener una plataforma sensora (CPE/Qs/AzA) por adsorción

secuencial de Qs y AzA en etapas de 10 minutos respectivamente que permite cuantificar y especificar de forma sencilla, simultánea, altamente sensible y selectiva de tres bioindicadores: xantina, hipoxantina y ácido úrico, a niveles micromolares y en un amplio intervalo de concentraciones. Es importante resaltar que, el límite permitido de xantina, hipoxantina y ácido úrico debe mantenerse por debajo de 60 μM para asegurar un adecuado nivel de frescura del pescado para consumo humano. Este desarrollo abre las puertas para el diseño de un sensor que permita la determinación de la frescura del pescado *in situ* aplicable a muestras reales en los sitios de recolección, transporte y comercialización.

V. AGRADECIMIENTOS

Las autoras agradecen el apoyo económico de CONICET, SECyT-UNC, Ministerio de Ciencia, Tecnología e Innovación de la Nación y ANPCyT.

DFR y BB agradecen la Beca doctoral otorgada por CONICET.

VI. REFERENCIAS

- [1] O. Soria Arteché, J. Péres Villanueva, J. F. Palacios Espinosa and J. F. Cortés Benítez, "Bases de la química heterocíclica aplicada a la obtención de compuestos orgánicos de interés farmacéutico", División de Ciencias Biológicas y de la Salud, ISBN: 978-607-28-1887-3, Ciudad de México, 2020.
- [2] E. Watanabe, K. Ando, I. Karube, H. Matsuoka and S. Suzuki, "Determination of hypoxanthine in fish meat with an enzyme sensor", Journal of Food Science, Vol. 48, pp. 496-500, 1983.
- [3] H. H. Huss, "Quality and quality changes in fresh fish", FAO, Fisheries Technical Paper 384, Rome, 1995.
- [4] B. Dey, W. Ahmad, G. Sarkhel, G. H Lee and A. Clouthury, "Fabrication of niobium metal organic frameworks anchored carbon nanofiber hybrid film for simultaneous detection of xanthine, hypoxanthine and uric acid", Microchemical Journal 186, 2023.
- [5] R. Jones, J. Murray, E. I Livingston and C. K Murray, "Rapid estimations of hypoxanthine concentrations and indices of the freshness of chill-stored fish", J. Sci. Fd. Agric. 15:763, 1964.
- [6] Organización de las Naciones Unidas para la Alimentación y la Agricultura, "Estado de la Pesca y la Acuicultura", Roma, 2022. ISBN 978-92-5-136464-2.
- [7] A. Woyewoda, S. J. Shaw, P. J. Ke and B. G. Burns, "Recommended laboratory methods for assessment of fish quality", Tech. Rep. FISH. Aquat. Sci 1448, 1968.
- [8] I. Svancara, K. Vytras, I. Barek and J. Zima, "Carbon paste electrodes in modern electroanalysis", Critical Reviews in Analytical Chemistry, Vols. 31 (4) 311-345, 2001.
- [9] S. Miscoria, G. Barrera and G. Rivas, "Enzymatic biosensor based on carbon paste electrodes modified with gold nanoparticles and polyphenol oxidase", Electroanalysis, No. 17, 2005.
- [10] S. Khattak, F. Wahid, L. Liu, S. Jia, L. Chu, Y. Xie and Z. Li, "Applications of cellulose and chitin/chitosan derivatives and composites as antibacterial materials: current state and perspectives", Mini-Review, Applied Microbiology and Biotechnology, 103:1989-2006, 2019.
- [11] Tangkaram, Tanin, et al. "Highly stable amplified low-potential electrocatalytic detection of NAD⁺ at azure-chitosan modified carbon electrodes". Sensors and Actuators B: Chemical, 2007, vol. 121, no 1, p. 277-281.

A laser biospeckle sensor applied to processes in the fishing industry: a highly sensitive monitor solution.

Marianina Perez Cenci
*Institute of Food and Environmental
 Science and Technology (INCITAA)*
National University of Mar del Plata
 CONICET
 Mar del Plata, Argentina
 email: mperezcenci@gmail.com
 ORCID: 0000-0002-1359-5408

Marcelo Nicolás Guzmán
*Bioengineering Lab, Institute of
 Scientific and Technological Research
 in Electronics (ICYTE), National
 University of Mar del Plata*
 CONICET
 Mar del Plata, Argentina
 ORCID: 0000-0002-4258-6615

Alejandra Tomac
*Institute of Food and Environmental
 Science and Technology (INCITAA),
 National University of Mar del Plata*
 CONICET
 Mar del Plata, Argentina
 ORCID: 0000-0003-3391-6771

Melina Nisenbaum
*Institute of Food and Environmental
 Science and Technology (INCITAA),
 National University of Mar del Plata*
 CONICET
 Mar del Plata, Argentina
 ORCID: 0000-0002-6661-4430

Silvia Elena Murialdo
*Institute of Food and Environmental
 Science and Technology (INCITAA),
 National University of Mar del Plata*
 CIC
 Mar del Plata, Argentina
 ORCID: 0000-0002-0331-2240

Silvina Agustinelli*
*Institute of Food and Environmental
 Science and Technology (INCITAA)
 National University of Mar del Plata*
 CONICET
 Mar del Plata, Argentina
 ORCID: 0000-0001-8276-7827 email:
 silagustinelli@fi.mdp.edu.ar

Abstract— This paper presents the results obtained from the development of a non-invasive optical sensor for monitoring quality and changes in fish species during different processing stages. The laser biospeckle (BSL) methodology was applied at various stages of fish product development. A back-scatter measurement system was configured with a low-power laser and CCD camera to analyze changes "in situ". The results demonstrate that the BSL technique is sensitive and has high potential for detecting changes in samples related to different applied treatments. It allows differentiation between immersion times in hake samples treated with polyphosphates solution and also the level of hurdle dosis applied to extend shelf life of stripped weakfish samples treated with ionizing radiation. The BSL technique is suitable for detecting changes in the fish muscle matrix, being non-invasive and providing real-time measurements, making it suitable for monitoring the quality and safety of fish products.

Keywords— *Laser, Biospeckle patterns, Fish products, Quality*

I. INTRODUCTION

Fish products are a naturally healthy source of food due to the nutritional richness of their matrix: high biological value proteins, polyunsaturated Omega 3 fatty acids, vitamins and minerals. Their development involves processing stages from fish species that require thorough and reliable controls due to their high perishability [1,2]. Assessing quality in terms of safety involves the quantification of volatile bases, microbial counting, pathogen detection, changes in physicochemical parameters, texture and sensory attributes [2,3].

While the methodology for quantifying and evaluating quality is objective and reproducible, it has limitations in sample handling, risk of contamination, processing times, and the use of reagents. These factors can extend study duration or require increased resources and human input to complete them efficiently. This makes the focus on the development and application of new tools and

methodologies easy to handle and use, with an immediate response time, to anticipate and reduce negative impacts.

It has been demonstrated that changes in biological samples can be detected through their surface interaction with a light source [4, 5, 6]. Among these methodologies the Laser Biospeckle (BSL) technique is emerging. By illuminating a surface with coherent laser light, a time-varying granular pattern called dynamic speckle is generated. This phenomenon occurs when light is scattered by objects exhibiting some degree of activity, resulting in images with bright and dark regions. The BSL technique is a non-invasive, inexpensive, and easily applicable method for the contactless analysis and monitoring of industrial and biological phenomena of practical interest.

It has been applied successfully in numerous studies evaluating biological and structural changes in various food matrices. Among them is the viability analysis of seeds, the monitoring of fruit ripening [7,8,9], and the detection of damages to fruits and vegetables [10]. In meat it was analyzed the application of BSL to assess the aging of beef [11], while in pork and chicken muscle tissue BSL pattern analysis was used to evaluate textural and cellular changes following the slaughter during refrigerated storage [12]. BSL has been also used in the detection of bacterial chemotaxis and differentiation between fungal and bacterial growth in semi-solid medium [6, 13].

In this study, the applications of BSL as a sensor to monitor the developmental stages of different fish products are presented. In this way, BSL is applied as a simple and effective tool to study changes in the quality of fish products.

II. MATERIALS AND METHODS

A. Fish samples

The study focused on fish species captured in the Argentine Sea, such as hake (*Merluccius hubbsi*), as well as on underexploited or bycatch species like striped weakfish (*Cynoscion striatus*). They were analyzed based on the types of processing stages. In the first, samples of hake filets were immersed in sodium tripolyphosphate (STP) solution. STP is a food-grade chemical agent used in the fishing industry to

This research was partially funded by grants UNMdP15/G667-ING616/21, UNMdP15/G667-ING671/23 and PICT- 2020- SERIEA-1610

improve water retention properties during freezing and thawing stages. The samples were immersed in a 4% STP solution at a ratio of 1:5 (fish: solution) at $15 \pm 0.5^\circ\text{C}$. By this treatment, the fish water samples content are affected and so texture parameters too. Like salt, phosphates increase the ionic strength of fish proteins. Alkaline phosphates also increase pH and move proteins away from their isoelectric point. These changes at the molecular level increase the fish muscle's retention capacity and reduce moisture loss during the various stages of processing. However, its improper use promotes excessive moisture absorption which can lead to economic fraud to the consumer [14].

In the second test, the focus was on the effect of treating samples with different dosis of ionizing energy on striped weakfish filets: 0, 4, and 8 kGy, using a ^{60}Co source (600,000 Curies) at the Ezeiza Atomic Center (CNEA), and they were stored at $4 \pm 1^\circ\text{C}$ for one month. Ionizing radiation is a safe and efficient preservation method, the application of which in fish and shellfish began in the sixties and continues today [2,15]. Untreated samples served as the control group for the experiments.

B. BSL system set up

The BSL system was configured with a coherent laser light source and a CCD camera. The laser beam was directed onto the surface of the fish samples, inducing dynamic speckle patterns. The CCD camera captured these patterns in real-time. The setup ensured that the laser beam was aligned properly and that the camera had a clear view of the sample surface. Additionally, appropriate filters and lenses were used to optimize the quality of the captured speckle patterns. The system was calibrated to ensure accurate and consistent measurements. Data acquisition and analysis software were employed to process the captured images and extract relevant information about the dynamic speckle patterns. Overall, the BSL system was designed to provide non-invasive, real-time monitoring of changes in the fish samples' quality. In order to quantify the detected activity, mathematical descriptors were used. From the statistical point of view, the simplest method to detect variations in a signal is the standard deviation (SD), which is a measurement of the spread of the variations in the signal [16]. While the weighted generalized differences (DGP) descriptor is based on the time domain calculations, normalized by the quantity of sample division [16].

III. RESULTS AND DISCUSSION

The BSL activity detected on hake and stripped weakfish samples exposed to different production processes is visualized in Figures 1 and 2, respectively.

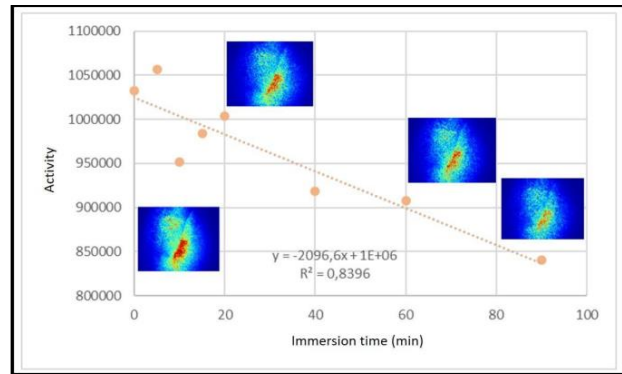


Fig 1. Activity detected in hake samples immersed in STP solution

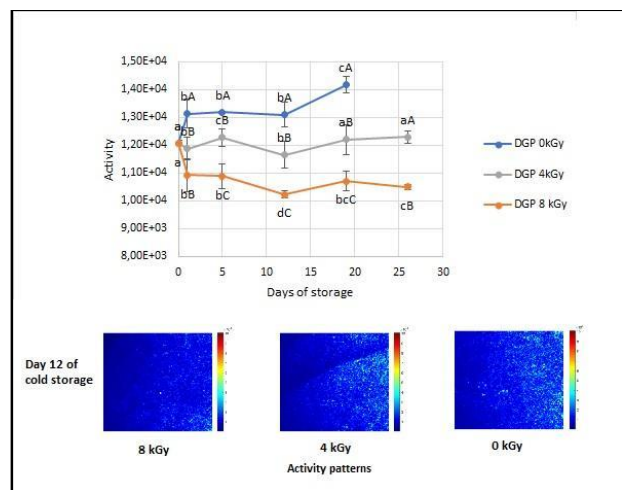


Fig 2. Activity detected in striped weakfish filets treated with ionizing energy at different doses. Speckle pattern images on day 12.

According to the obtained results, it was observed that the response of the interaction between the samples and the laser light is sensitive to the treatments to which fish muscle can be exposed. This quantified response allowed differentiation between immersion times in the assays conducted on hake and between radiation applied to stripped weakfish samples, considering also the effect of refrigeration storage time. Regarding this last assay, it was detected that in the control stripped weakfish filets (0 kGy), the activity showed significantly higher values during storage compared to samples treated with radiation. The samples treated with 8 kGy remained without significant changes and below the control sample and 4 kGy treated samples response. The changes induced by these treatments on the fish muscle are generally imperceptible to the human eye and require the application of exhaustive techniques with a large amount of sample, which must be reduced in size to generate homogeneity representing the analyzed batch, as well as long incubation times, reagents, a sensory panel, sophisticated equipment, among others [1-3].

Given the non-invasive nature of the BSL technique, its avoidance of direct contact with the sample in terms of manipulation and size reduction, and ultimately the real-time measurement value obtained, it defines it as a suitable technique for monitoring fish products while safeguarding their safety and the integrity of the samples.

IV. CONCLUSION

The laser biospeckle methodology proved to be favorable for use as a monitoring sensor for fish samples at different processing stages. The studies conducted reflect the potential of the BSL technique to be used in the fishing industry. Given the urgency of acquiring such analysis techniques in both production lines and raw material control, as well as in institutions that oversee and promote food safety, it is essential to continue deepening the studies conducted so far.

ACKNOWLEDGMENT

The researchers thank the National Scientific and Technical Research Council (CONICET) and the National University of Mar del Plata (UNMdP), Argentina, for their financial support.

REFERENCES

- [1] S.P. Agustinelli, M.I. Yeannes, Effect of Frozen Storage on Biochemical Changes and Fatty Acid Composition of Mackerel (*Scomber japonicus*) Muscle. *J Food Res*, 4(1): 135-147. 2015
- [2] A. Tomac & M.I. Yeannes. Gamma radiation effect on quality changes in vacuum-packed squid. *Int J Food Sci Tech*. 47 (7). 1550.1557.2012
- [3] M. Czerner, S.P. Agustinelli, S. Guccione, M.I. Yeannes. Effect of different preservation processes on chemical composition and fatty acid profile of anchovy (*Engraulis anchoita*). *International Journal of Food Sciences and Nutrition*, 66(8): 887-894. 2015
- [4] H. Rabal and R. Braga. *Dynamic Laser Speckle and applications*. CRC Press. Boca Raton, FL, USA 2008
- [5] R. Pandiselvam, V.P. Mayoorkha, Anjineyulu Kothakota, S.V. Ramesh, Rohit Thirumdas, Praneeth Juvvi, Biospeckle laser technique – A novel non-destructive approach for food quality and safety detection, *Trends in Food Science & Technology*, V 97: 1-13, 2020.
- [6] S.E. Murialdo, L.I. Passoni, M.N. Guzman, G.H. Sendra, H. Rabal, M. Trivi, "Discrimination of motile bacteria from filamentous fungi using dynamic speckle", *Journal of Biomedical Optics*, vol. 17, 056011, 2012.
- [7] Z. Ansari & AK Nirala, Assessment of bio-activity using the methods of inertia moment and absolute value of the differences. *Optik*, 124 (6): 512-516. 2013
- [8] L. Baranyai & M. Zude. Analysis of laser light propagation in kiwifruit using backscattering imaging and Monte Carlo simulation. *Comput. Electron Agr.* 69:33–39. 2009
- [9] G.G. Romero, C.C. Martinez, E.E. Alanis, G.A. Salazar, V.G. et al.. Bio-speckle activity applied to the assessment of tomato fruit ripening. *Biosyst. Eng.* 103:116–119. 2009
- [10] C. Abou Nader, J.M. Tualle, E. Tinet, D.A. Etori. New Insight into Biospeckle Activity in Apple Tissues. *Sensors* 19, 497. 2019.
- [11] CA, Isis, RA, Braga, E. Jr., Ramos, A.L., Ramos & E.A.R. Roxael. Application of biospeckle laser technique for determining biological phenomena related to beef aging. *Journal of Food Engineering*, 119(1), 135–139. 2013.
- [12] P. Oleksandr, L.I. Muravsky & M.I. Berezuk. Application of biospeckles for assessment of structural and cellular changes in muscle tissue. *Journal of Biomedical Optics*, 20(9) 0950061-7. 2015.
- [13] M. Nisenbaum, A. Bouchet, M.N. Guzmán, J.F. González, G.H. Sendra, J. Pastore and M. Trivi, S.E. Murialdo, "Dynamic laser speckle and fuzzy mathematical morphology applied to studies of chemotaxis towards hydrocarbons", *International Journal of Environment and Health*, vol 7, pp. 58-69, 2014.
- [14] CONICET (2020). "Relevamiento de aspectos técnicos de pH y otros parámetros de calidad establecidos por Brasil para el ingreso de productos pesqueros congelados. Valores de referencia para la Merluza común (*Merluccius hubbsi*)". Informe Final, agosto 2020. Grupo ADhOC "Ph en Pescado". Red de Seguridad Alimentaria. Disponible en: <https://rsa.conicet.gov.ar/wp-content/uploads/2020/08/Informe-RSA-ASPECTOS-TECNICOS-pH-pescado-AC.pdf>
- [15] A. Tomac, M. C. Cova, P. Narvaiz, M. I. Yeannes, Sensory acceptability of squid rings gamma irradiated for shelf-life extension, *Radiation Physics and Chemistry*, V 130: 359-361. 2017
- [16] G. H. Sendra, A. Dai Para, L. I. Passoni and H. Rabal. "Biospeckle descriptors: A performance comparison", *Proceedings of SPIE - The International Society for Optical Engineering* · September 2010

A proof of concept for a porous silicon-polymer hybrid sensor

Ignacio Gómez Vargas¹, Federico Fookes², Natalia Casis^{3,5}, Diana Estenez^{3,5}, Claudio Berli³, Luisa Cencha^{4,5}, and Raul Urteaga^{4,5}

¹IMAL (Universidad Nacional del Litoral-CONICET), RN N° 168 Km 0, 3000 Santa Fe, Argentina.

²Instituto de Investigaciones en Ciencias de la Salud, Facultad de Ciencias de la Salud, Universidad Católica de Santa Fe, Cngo. Echagüe 7151, 3000, Santa Fe, Argentina.

³INTEC (Universidad Nacional del Litoral-CONICET), Ruta Nacional N° 168, Km 0, 3000, Santa Fe, Argentina.

⁴IFIS-Litoral (Universidad Nacional del Litoral-CONICET), Guemes 3450, 3000 Santa Fe, Argentina.

⁵Facultad de Ingeniería Química (Universidad Nacional del Litoral), Santiago del Estero 2829, 3000, Santa Fe, Argentina.

August 2, 2024

Abstract—In this work, we describe a fabrication method for a sensor to be used in chemical and biological detection. This sensor consists of a porous photonic crystal whose internal surface is covered by a given functionalized polymer specially designed to detect a given analyte, capturing both the high sensitivity of the photonic crystal and the high specificity offered by the polymer. Here, we used porous silicon photonic crystals and polystyrene. The proposed method of fabrication consists of the infiltration of the polymer into the nanopores, monitored in real-time through an interferometric method.

Keywords—photonic crystals, functionalized polymers, microfluidic, biosensors

I. INTRODUCTION

In recent years, the development of photonic crystals (PCs) has gained a lot of impulse because of the numerous fields of applications for which they have been employed, such as telecommunications, energy production, design of optical devices, quantum technologies, and ultimately, sensing [1]. PCs are a rather heterogeneous group of macroscopic arrays with the shared property of having a periodic dielectric function which generates a photonic gap, this is, a region of wavelengths in which light propagation within the material is prohibited. This attribute allows the design of high-sensitive measuring devices, often relying on changes of some sort of optical signal in response to the presence of a given analyte. Unfortunately, PCs by themselves often lack the specificity achieved by some other types of sensors [2]. On the other hand, it is generally possible to craft polymers with a good degree of specificity to some target molecule by several different methods of synthesis and use them in combination with PCs to design chemical sensors. However, identifying and quantifying the interaction having place between the polymer and its analyte may present a difficult task, compromising sensibility [3].

This work builds on previous research in the field of microfluidics in porous materials and aims to apply this

knowledge to the development of a PC-polymer hybrid sensor. Here, a porous silicon membrane acting as a photonic crystal is partially filled with a model polymer (polystyrene).

II. WORKING PRINCIPLE

Porous silicon is obtained through the anodization of silicon wafers. During this electrochemical etching, silicon atoms are dissolved from the wafer into the solvent and the intensity of applied current pulses can be controlled in such a way as to generate a series of layers, each of a given porosity, which spans from the surface (exposed to the electrolyte) to the bulk of the silicon wafer.

By carefully designing an adequate pattern of porous layers on a silicon membrane, it is possible to obtain films transmitting or reflecting light in very particular ways, behaving as 1D photonic crystals. References on porous silicon fabrication as well as its optical properties abound, see for example [4]. When the porous layers of a silicon sample resemble those shown in Fig. 1a, alternating between two values of porosities, i.e. two values of effective refractive index, and having a defect layer consisting of a thicker layer in the middle (we refer to this pattern as a microcavity), its reflectance spectrum exhibits great reflectance values in a given region of wavelengths together with an abrupt minimum [1].

This sharp minimum in the reflectance spectrum can be chosen to be centered at a given wavelength value λ_0 (by tuning the porosity and length of each layer) and might be used to build up a sensor in the following way. First, the functionalized polymer, responsive to a given target analyte, is obtained and casted to form films. Then, the polymer film is placed on the top of the silicon membrane, which is set at a given temperature $T > T_g$, where T_g is the glass transition temperature of the polymer. The polymer is rapidly heated up, and able to flow. Consequently, it starts to infiltrate the pores of the material (see Fig. 2), increasing the effective refractive index of each layer and causing a right-shift in

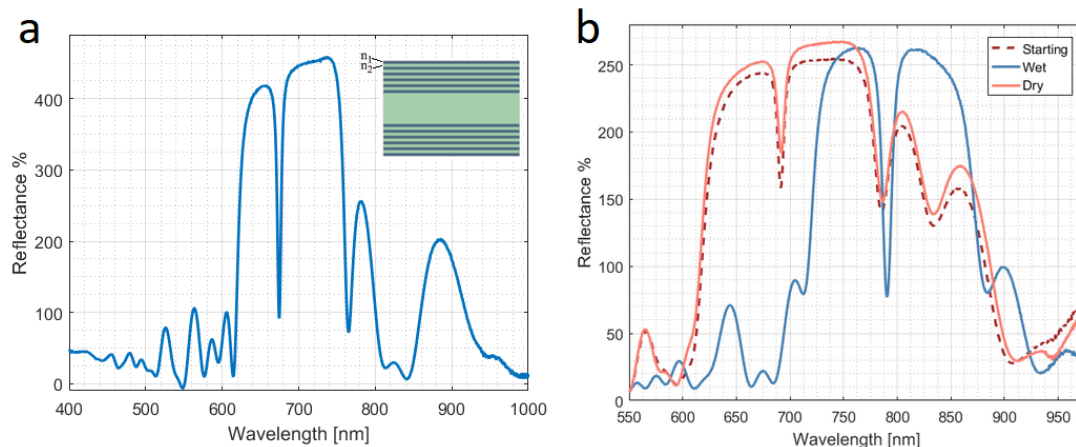


Fig. 1. (a) Reflectance spectrum belonging to a porous silicon membrane with layers having two different refractive indexes n_1 and n_2 , as depicted in the inset. (b) Spectra taken at room temperature belonging to the same porous silicon sample partially filled with polystyrene (starting), filled until completion with ethanol (wet), and after being left to dry for 12 minutes (dry).

the entire reflectance spectrum of the PC (and, in particular, in the reflectance minimum). If this infiltration process is stopped midway, so the pores of the material are only partially occupied by the polymer, then the solution to be tested can be introduced in the space left. What one could hope to be happening inside the pores in the first infiltration is that melted polystyrene diffuses not as a sudden and flat fluid front but to exhibit what is known as a *prewetting layer*. This consists of a polymer melt fraction that surpasses the rest of the fluid by traveling through the walls of the material's pores. The reason this prewetting layer is desirable is that it should increase the exposed surface of the polymer to the target analyte in a partially filled silicon membrane, thus increasing the effect that the interaction polymer-analyte could have on the optical signal. References pointing to evidence on the existence of such prewetting layer in this setting are [5], [6].

The net result in this case -even after evaporation of the solution-, would be an even further right-shift in the reflectance minimum, indicating the presence of the analyte in the tested solution. Working on this hypothesis, a series of experiments were designed and executed to verify the feasibility of such an arrangement. Information on the used materials as well as details on the experimental setups are given in the next section.

III. METHODS AND MATERIALS

Porous silicon membranes. The mesoporous silicon membranes were made by electrochemical anodization of crystalline silicon, p-type, boron dopant, orientation [100], and resistivity 1-5 m Ω -cm, provided by Topsil Semiconductor Materials SA, USA. The silicon acts as the anode of an electrochemical cell, where the electrolyte is a solution of fluorhydric acid and ethanol (1 HF(50%):2 EtOH). The porosity and mean pore size of the membranes are defined by the current density used during anodization, whereas the anodization time defines the thickness of the films. Two different values of current densities were used, 10 and 50

mA/cm², which gave 45 and 70% porosity, respectively.

Thermoplastic Polymer Films. The polymer used to infiltrate the pores was polystyrene (PS). Commercial grade (polydisperse) polystyrene of molecular weight 2.79×10^4 g/mol and dispersity 1.38 was mainly used for this purpose. For some experiments, monodisperse polystyrenes of molecular weights ranging from 0.71 and 27.5×10^4 g/mol were employed. Polymer films were obtained by pressing polymer powder (some tens of mg) between two glass slides and heating at 200 °C in an oven for 5 min; thus, films of less than 100 μ m thickness were obtained.

Interferometric Technique. The experimental setup consists of a UV-vis-NIR spectrometer (Ocean Optics HR4000) with an R400-7-SR fiber-optic reflection probe and a temperature-controlled plate. The porous silicon membrane is placed over the heater, and when a thin layer of polymer is deposited on its surface, the measurement of the reflectance spectra begins at regular intervals. Temperatures used in this work ranged between room temperature and 180°C. The optical

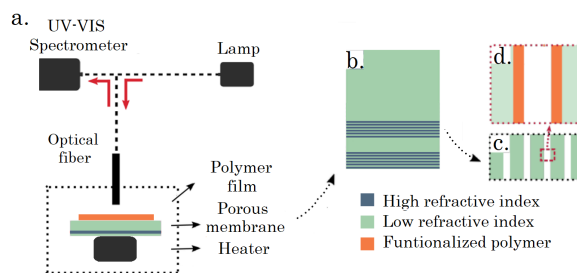


Fig. 2. (a) Optical setup. (b) The pattern of porous layers imprinted in the silicon membrane. (c) Zoom in over the pores. (d) Functionalized polymer partially covering the silicon pores after infiltration.

fiber guides the light from the lamp to the porous silicon membrane and collects the reflected light, taking it back to the spectrometer (see Fig. 2). When the polymer begins to infiltrate the pores by capillary action, the reflectance peaks move to the right as a consequence of the increase in the refractive index. All reflectance spectra shown in this work were taken as percentages relative to the reflectance of a single silicon wafer.

IV. RESULTS AND DISCUSSION

A. First tests with polystyrene

This first round of measurements was conducted at 180 °C and using the polydisperse polystyrene to infiltrate the porous silicon PCs. Fig. 3 exhibits the shift of the initial reflectance spectrum of a silicon sample -consisting of a uniform layer plus a microcavity, as shown in the inset of this figure- as a function of time. Again, the explanation for this phenomenon is that while the polystyrene begins to fill the membrane pores, the refractive index of the material increases, which causes the interference pattern of light traveling in its interior to shift towards greater wavelengths. Despite its simplicity, these measurements confirmed that the selected test polymer does fill the pores and produces the desired effect on the optical signal, in a way that allows a real-time assessment of the degree of infiltration by measuring the amount of shift in λ_0 at a particular time.

B. Partial filling with polystyrene and completion with ethanol

While it is possible to estimate the degree of infiltration with the employed method, it is also possible to control the speed of the filling process by modifying the temperature of the experiment. Furthermore, withdrawing the sample from the heater stops the infiltration of the polymer, enabling to obtain membranes partially filled. In Fig. 1b, the spectrum belonging to one of these partially filled samples was acquired at three different states: the initial state, where a fraction of the pores contains polystyrene, a second state in which the partially filled PC was completely filled with ethanol, and the last one (taken approximately 12 minutes after the previous one), when the alcohol was evaporated from the membrane. Notice the final reflectance spectrum is quite similar to the original one, meaning that after evaporation of ethanol the PC's optical behavior returns to the initial state.

The described experiment was a success in showing that the idea behind the proposed sensor is feasible, as it is possible to obtain partially filled samples with polymer and to complete the filling with a solution to be tested. Of course, this should be checked empirically with each combination of photonic crystal, polymer, and target solution as the interactions between these can severely modify the nature of the filling process at a point where no infiltration at all could take place.

C. Microcavity and uniform layer filling curves

Although the sensor's fabrication method was considered successful, there are still some questions to be answered in regard to the specific manner in which polystyrene travels

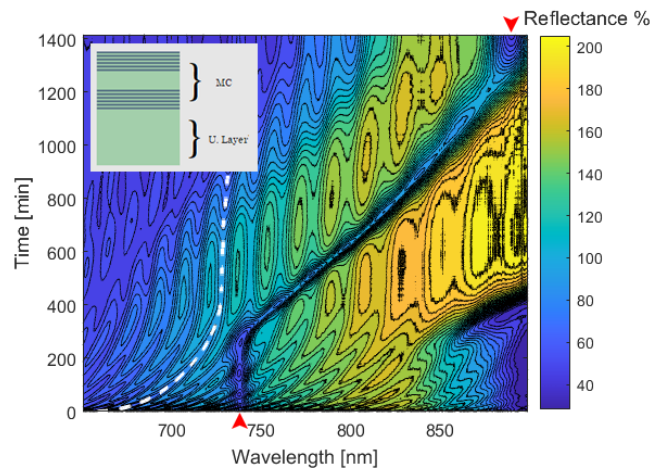


Fig. 3. Reflectance spectra as a function of time for a porous silicon sample with a 6 μm uniform layer plus a MC (see inset) put in contact with a polystyrene film at 180°C. Red arrows indicate the initial and final values of λ_0 . The white dotted line displays the wavelength shift on the underlying spectrum having place before the change on λ_0 .

through the silicon pores. Complex fluids transport in porous media is a complex topic and comprises a subject of its own, existing a wide variety of models and equations that could explain the way melted polystyrene diffuses into the material [7]. As previously stated in Section II, a desirable feature of this diffusion would be the existence of a prewetting layer.

To characterize the infiltration of the polystyrene into the porous silicon, measurements were made with a batch of porous silicon PCs having a uniform thick layer before the MC (see the inset on Fig. 3). The introduced layer had a porosity of around 45% and a thickness of 6 μm . As the polystyrene is put in contact with the surface of the membrane starting with this layer, it must initially travel through it before reaching the MC (which causes the reflectance minimum at λ_0), resulting in a right-shift of the underlying oscillations before the minimum is affected, as can be seen on the measurement shown on Fig. 3 (observe here the white dotted line). Using this figure, it is possible to obtain the curves $\Delta\lambda_0$ (representing the change in wavelengths of λ_0) and $\Delta\lambda_{UL}$ (representing the change in wavelengths of the underlying oscillations associated to the uniform layer) as a function of time. These curves were acquired using polystyrenes with different values of molecular weight, they were normalized with respect to the filling time (i.e., the time it takes to whether λ_0 or λ_{UL} to reach their final values) and they were plotted together in Fig. 4. This figure shows that the shift in λ_0 seems to start at approximately the same time the shift associated with the uniform layer stops when the samples are heated at 180°C in contact with the different films of polystyrene, however, some overlapping between the two can be seen (meaning there could be a prewetting layer forming inside the pores). From this figure, we also know the time it takes to fill a porous silicon PC with polystyrene of a given molecular

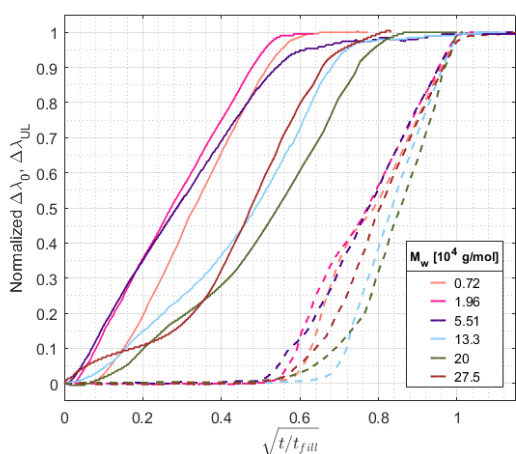


Fig. 4. Normalized values of $\Delta\lambda_0$ (dotted lines) and $\Delta\lambda_{UL}$ (solid lines) for samples with a uniform layer of $6\ \mu\text{m}$ length and varying molecular weights M_w (expressed in units of $10^4\ \text{g/mol}$) as a function of $\sqrt{t/t_{fill}}$, where t is time of measurement and t_{fill} . The temperature of this experiment was 180°C .

weight. Moreover, by studying both wavelength shifts $\Delta\lambda_0$ and $\Delta\lambda_{UL}$ simultaneously it is possible to know where to stop the infiltration in each case, providing great versatility in the sensor's fabrication with different polymer chain sizes.

D. Filling times vs polystyrene molecular weights

Based on the results shown in Fig. 4, the filling time for each polymer was determined. Fig. 5 displays both the MC filling times and the uniform layer filling times versus the molecular weight of the employed polystyrene, where it can be seen a progressive increase in the filling time as the polymer chains become bigger. Interestingly, this increase seems not to be linear, as a clear break in the behavior can be appreciated between the second and the third samples. This change in slope is attributed to the bigger degree of confinement the polymer chains are experiencing while moving inside the silicon pores [4].

V. CONCLUSIONS AND FUTURE WORK

As described in this essay, a proof of concept of a novel porous silicon-polystyrene sensor was successfully developed, with many of its fundamental pillars - including the actual infiltration of polystyrene into the pores, the ability to perform real-time assessment using the chosen interferometric technique, and the subsequent possibility of partial fillings with polymer and completion with a target solution - functioning just as expected. At present, further research is ongoing for better characterization of the fluid front of melted polystyrene, but the primary objective of future work lies in the actual testing of a fully functioning sensor.

Since the use of porous silicon as the photonic crystal in these initial tests was considered positive, forthcoming tests will likely retain this component of the sensor while coupling it with an appropriate pair of polymer and target analyte to

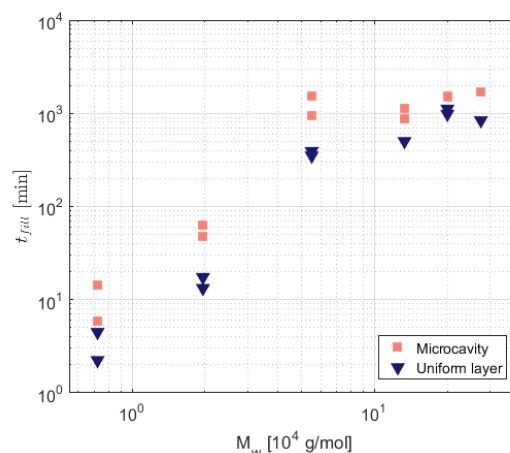


Fig. 5. Filling times for both the uniform layer and the MC versus molecular weight M_w of the infiltrated polystyrene at 180°C for samples with a fixed uniform layer of $6\ \mu\text{m}$ length.

attempt detecting their interaction in situ. We are evaluating the use of functionalized polystyrene to detect clonazepam [8]. Additionally, it is worth noting that the simplicity of the proposed sensor makes it suitable for adaptation to function as a lab-on-a-chip. Furthermore, due to the possibility of designing specific color-based readability, it could even be integrated into smartphone apps using tools such as those presented in [9].

ACKNOWLEDGMENT

The authors acknowledge the funding support received from the "Consejo Nacional de Investigaciones Científicas y Técnicas", Grant No. PIP-2020-1049, Universidad Nacional del Litoral, Grant No. CAID 2020-50620190100114L, Argentina.

REFERENCES

- [1] Joannopoulos, J. D. "Photonic crystals: Molding the flow of light" (Princeton University Press, 2008), 2 edn.
- [2] Nair, R. V. & Vijaya, R. "Photonic crystal sensors: An overview". *Progress in Quantum Electronics* **34**, 89–134 (2010).
- [3] Chen, W., Meng, Z., Xue, M. & Shea, K. J. "Molecular imprinted photonic crystal for sensing of biomolecules". *Molecular Imprinting* **4**, 1–12 (2016).
- [4] Cencha, L. G., Urteaga, R. & Berli, C. L. "Interferometric technique to determine the dynamics of polymeric fluids under strong confinement". *Macromolecules* **51**, 8721–8728 (2018).
- [5] Cencha, L. G., Dittrich, G., Huber, P., Berli, C. L. & Urteaga, R. "Precursor film spreading during liquid imbibition in nanoporous photonic crystals". *Physical Review Letters* **125** (2020).
- [6] Dittrich, G. et al. "Polymeric liquids in mesoporous photonic structures: From precursor film spreading to imbibition dynamics at the nanoscale". *The Journal of Chemical Physics* **160** (2024).
- [7] Lu, G., Wang, X.-D. & Duan, Y.-Y. "A critical review of dynamic wetting by complex fluids: From newtonian fluids to non-newtonian fluids and nanofluids". *Advances in Colloid and Interface Science* **236**, 43–62 (2016).
- [8] An, J., Wang, X., Li, Y., Kang, W. & Lian, K. "Polystyrene nanofibers as an effective sorbent for the adsorption of clonazepam: Kinetic and thermodynamic studies". *RSC Advances* **12**, 3394–3401 (2022).
- [9] Schaumburg, F. et al. "A free customizable tool for easy integration of microfluidics and smartphones". *Scientific Reports* **12** (2022).

Fluorescent Probe-Based Detection and Quantification of Polylactic Acid (PLA) Nanoparticles

M. Andrea Molina Torres
Departamento de Química Orgánica,
Facultad de Ciencias Químicas,
Universidad Nacional de Córdoba
INFIQC-CONICET
Córdoba, Argentina
amolinatorres@unc.edu.ar

Janet Chinellato Díaz
Departamento de Química Orgánica,
Facultad de Ciencias Químicas,
Universidad Nacional de Córdoba
IPQA-CONICET
Córdoba, Argentina
janet.chinellato@unc.edu.ar

Facundo Mattea
Departamento de Química Orgánica,
Facultad de Ciencias Químicas,
Universidad Nacional de Córdoba
IPQA-CONICET
Córdoba, Argentina
fmattea@unc.edu.ar

Marcelo R. Romero
Departamento de Química Orgánica,
Facultad de Ciencias Químicas,
Universidad Nacional de Córdoba
IPQA-CONICET
Córdoba, Argentina
marcelo.ricardo.romero@unc.edu.ar

Natalia L. Pacioni
Departamento de Química Orgánica,
Facultad de Ciencias Químicas,
Universidad Nacional de Córdoba
INFIQC-CONICET
Córdoba, Argentina
n.lpacioni@unc.edu.ar

Abstract— An analytical strategy using rhodamine 6G as a chemical sensor was validated for detecting and quantifying polylactic acid nanoparticles in aqueous systems, with limits of detection and quantification in the picomolar order. The recovery assays in spiked river samples demonstrated the accuracy of the analytical method with 95% confidence.

Keywords— PLA, nanoparticles, rhodamine 6G, fluorescence quenching

I. INTRODUCTION

The widespread use of petroleum-based plastics has led to the accumulation of plastic waste in the environment. This waste includes fragments like microplastics (MPL), and smaller particles known as nanoplastics (NPL), now a major concern for aquatic ecosystems [1]. Poly (lactic acid) (PLA) is an alternative to conventional plastics, a synthetic polymer with excellent mechanical properties, biodegradability, biocompatibility, and recyclability. These properties have led to a growing demand for PLA in various industries, such as agriculture, automotive, textile, food packaging, and medical sciences [2]. However, as PLA waste is also likely to increase, it can contribute to forming MPL and NPL particles in the environment. Although PLA is biodegradable, it requires specific conditions for degradation, which may not always be present in the environment. Recent studies have shown that even biodegradable polymers such as PLA can adversely affect aquatic organisms, including the growth of the benthic community [1-2]. Therefore, it is necessary to develop analytical methods to detect PLA MPLs and NPLs in various organisms and ecosystems and establish concentration-effect relationships. Within this frame, this work proposes a method for quantifying PLA nanoparticles (N-PLA) using the fluorescence quenching of rhodamine-6G (R6G) in aquatic systems.

II. MATERIALS AND METHODS

A. Reagents and materials

Rhodamine 6G (Rh6G, Aldrich), acetone (CH_3COCH_3 , Taurus), potassium monobasic phosphate (KH_2PO_4 , Merck),

sodium chloride (NaCl, Taurus), potassium chloride (KCl, Merck), and potassium bromide (KBr, Merck) were analytical grade and were used as received. MilliQ water was obtained from a Millipore instrument (resistivity, 25 °C: 18.2 M Ω cm). Polylactic acid was synthesized with a MW: 4000.

B. Instrumentation

Absorption spectra were acquired using a UV-vis Shimadzu 1800 spectrophotometer within the 200–800 nm wavelength range, using quartz cells with a path length of 1 cm. pH measurements were conducted using an Orion (Boston, MA, USA) model 720 A pH-meter equipped with a Ross combination pH electrode. Calibration of the pH meter was done using standard buffers at pH values of 4.008 and 6.994. Centrifugation were carried out using an Eppendorf Centrifuge 5804. Fluorescence measurements were conducted employing a Cary Eclipse fluorescence spectrophotometer (Agilent), with a Peltier temperature controller set at 25.0 °C. Data analysis was run using Origin®, Version 2021 by OriginLab Corporation, Northampton, MA, USA, or PAST 4.02.

C. Synthesis of PLA nanoparticles

First, 25 mg of polylactic acid (PLA) were dissolved in 5 mL of acetone and heated at 45°C for 2 hours, followed by gradual cooling to room temperature. Then, the PLA nanoparticles (PLA-NP) were obtained by nanoprecipitation utilizing an automated micro syringe specially designed for this purpose. The procedure involved the controlled addition of microdroplets, dispensed at a rate of 5 mL/h, containing the PLA in acetone, into MilliQ water, and kept at constant stirring. Subsequently, acetone was removed from the nanoparticle suspension via rotary evaporation under reduced pressure at ambient temperature.

D. Calibration curves

A stock solution of Rh6G was prepared in water and stored at 4 °C until use. The solution was shielded from light exposure using aluminum foil to prevent photodegradation. Prior to conducting fluorescence experiments, the Rh6G concentration was determined by UV-visible spectroscopy.

All the fluorescence measurement were recorded at 25.0 °C, employing quartz cells with a path length of 1.0 cm.

Rh6G solutions (0.40 μM) in 0.01 M phosphate buffer at pH 6.94 (PBS) were excited at 526.5 nm with 2.5 nm slit widths for both excitation and emission, in the absence and presence of PLA-NP (47.7-334 μM). The fluorescence spectra were recorded at 1 and 5 minutes after adding the PLA-NP to the R6G solutions. The pH of the PBS solution was adjusted to 6.94, although, for practical purposes, in here the pH is expressed as 7.0.

E. Recovery assays in surface river water

Surface river water was collected at a sampling point along the Villa General Belgrano stream, Córdoba, Argentina (31°58'48.9"S 64°33'26.4"W). The samples were stored in clean polyethylene bottles and used without any pretreatment. Blank solutions did not show any signal for PLA-NP. Then, solutions of PLA-NP at different levels of concentrations and containing 5% (v/v) of river water and Rh6G (0.40 μM) were prepared by triplicate and their fluorescence spectra were recorded and analyzed. The concentration levels were chosen to cover the suitable analyte region by testing the method accuracy, mainly at two critical points: near the quantitation limit and near the upper limit of the dynamic range.

III. RESULTS AND DISCUSSIONS

A. Characterization of PLA-NP

The PLA nanoparticles were synthesized and characterized via Scanning Electron Microscopy (SEM), Zeta potential, and Dynamic Light Scattering (DLS). Spherical nanoparticles with an average diameter of 60 nm (Fig. 1) and a polydispersity index of 0.4 were obtained.

B. R6G as a molecular sensor for PLA-NP

The fluorescence emission of R6G was measured in the presence of PLA-NP at various concentrations. A concentration of 0.4 μM of Rh6G was selected to maintain the absorbance value below 0.05 while ensuring a dependable fluorescence intensity. PLA-NP quenched the luminescent signals of Rh6G (Fig. 2). Interestingly, the degree of fluorescence quenching at certain nanoparticle concentrations was observed to be influenced by the measuring time of the spectrum. Monitoring the maximum fluorescence intensity of Rh6G (552 nm) over time revealed a consistent pattern: a decline in fluorescence within the first 5 minutes, followed by stabilization or an increase, particularly at higher NP concentrations. Consequently, fluorescence measurements within the initial 5 minutes were chosen for analysis.

Furthermore, the Stern-Volmer plot (F_0/F vs. [PLA-NP]) showed the linear relationship whose fit corresponded to Equation (1), where F_0 and F represent the emission fluorescence in the absence and presence of PLA-NP, respectively, and K_{SV} denotes the Stern-Volmer constant (Fig. 3). Notably, K_{SV} also indicates the calibration sensitivity.

$$F_0/F = 1 + K_{SV}[PLA-NP] \quad (1)$$

The sensitivity of Rh6G to PLA-NP was $(2.34 \pm 0.04) \times 10^9 \text{ M}^{-1} \text{ y}$ $(4.4 \pm 0.1) \times 10^9 \text{ M}^{-1}$, at 1 and 5 minutes, respectively. Therefore, at 5 minutes, the sensitivity of R6G was 1.88 times higher than at 1 minute. Thus, we decided to set the measurement time at 5 minutes as an analytical strategy to continue with the method validation.

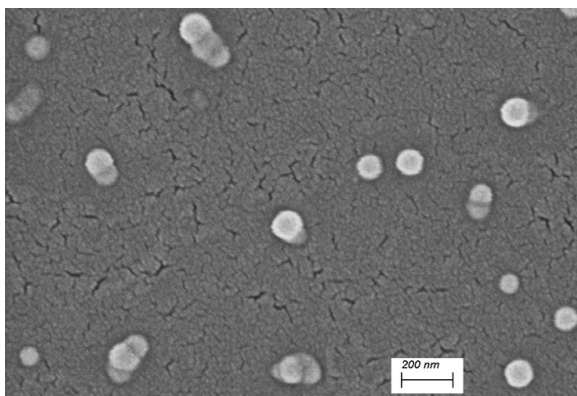


Fig. 1. Representative SEM image for the PLA-NP at 50kX in a microscope working at 5 kV.

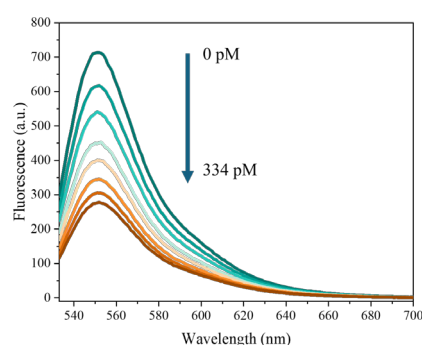


Fig. 2. Fluorescence spectra of Rh6G in the presence of different concentrations of PLA-NP measured at 5 minutes.

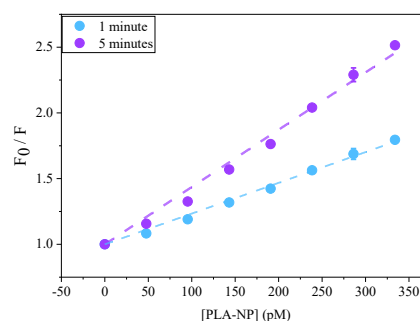


Fig. 3. Stern-Volmer plots for Rh6G in the presence of PLA-NP at different recording times and 25.0 °C.

C. Analytical parameters

According to the current IUPAC recommendations, the limits of detection (LOD) and quantification (LOQ) were determined using Equations 2 and 3, respectively:

$$LOD = \frac{3.3s_x}{SEN} \sqrt{1 + h_0 + \frac{1}{I}} \quad (2)$$

$$LOQ = \frac{10s_x}{SEN} \sqrt{1 + h_0 + \frac{1}{I}} \quad (3)$$

$$h_0 = \frac{[PLA-NP]_{cal}^2}{\sum_{i=1}^I ([PLA-NP]_i - [PLA-NP]_{cal})^2} \quad (4)$$

Where s_x , h_0 , and I correspond to the blank or residual standard deviation, the leverage for the blank sample (Equation 4), using $[\overline{PLA - NP}]_{cal}$ as the mean calibration concentration and $[PLA - NP]_i$ at each nanoparticle concentration used in the curve, and the number of calibration samples, respectively.

The LOD and LOQ were 26.5 pM equivalent to 1.59×10^{13} particles L^{-1} , and 80.7 pM (4.86×10^{13} particles L^{-1}), respectively.

Currently, other techniques under development for detecting micro and nanoplastics include Scanning Transmission X-ray microscopy (STXM) [3], Correlative SEM-Raman microscopy [4], Pyrolysis/Gas Chromatography-Mass Spectrometry (PYR/GC-MS) [5], and Inductively Coupled Plasma-Mass Spectrometry (ICP-MS) [6]. The LOD and LOQ obtained using ICP-MS and the modulation of a fluorescent molecular rotor are around $10^5 - 10^{12}$ particles L^{-1} [6-7]. Although our analytical approach exhibits LOD higher than those reported for other NPL, it is noteworthy that our methodology remains simple and fast and does not require highly specialized equipment or trained personnel.

D. Recovery assays

Given the current trend towards using biodegradable polymeric nanoparticles, it is highly likely that they will end up in the aquatic environment, like other NPL. Therefore, their quantification in these kinds of matrices becomes relevant. The analytical procedure was validated through a recovery test performed on spiked matrices of surface water from the Villa General Belgrano stream in the city of Córdoba. Considering the influence of the matrix in the fluorescence emission of Rh6G, a new calibration curve was performed incorporating 5% v/v surface river water, and the sensitivity was recalculated accordingly. Table 1 shows the obtained results, demonstrating the accuracy of the method at 95% significance.

IV. CONCLUSIONS

In summary, an analytical strategy based on the fluorescence quenching of rhodamine 6G can detect and quantify 60 nm PLA-NP at low picomolar levels. The method is accurate at 95% significance and represents a fast and straightforward way to analyze this sort of nanoplastics.

TABLE I. APPARENT RECOVERIES FOR PLA-NP IN SURFACE RIVER WATER

Concentration added (pM)	Concentration found ^a (pM)	Recovery (%) ^b	RSD (%) ^b
223.6	246.6	110	2
313.0	330.5	106	3
372.7	351.3	94	1

^a Using the $K_{sv} = (23.0 \pm 0.5) \times 10^8 M^{-1}$ obtained in the presence of surface river water

^b Average recovery and relative standard deviation (RSD) obtained by triplicate.

ACKNOWLEDGMENT

J.C.D. thanks for the CONICET scholarship. F.M, M.R.R and N.L.P are research members of CONICET. We also thanks fundings to: SECYT-UNC, PRIMAR TP: 32520170100384CB, ANPCyT for PICT 2021-GRFT1-00728 and PICT-2021-FRFT1-00426.

REFERENCES

- [1] M. Shen, B. Song, G. Zeng, Y. Zhang, W. Huang, X. Wen, and W. Tang, "Are biodegradable plastics a promising solution to solve the global plastic pollution?," *Environ. Pollut.*, 2020., vol. 263, pp. 114469.
- [2] N. M. Ainali, D. Kalaronis, E. Evgenidou, G. Z. Kyzas, D. C. Bobori, M. Kaloyianni, et al., "Do poly(lactic acid) microplastics instigate a threat? A perception for their dynamic towards environmental pollution and toxicity," *Sci. Total Environ.*, 2022, vol. 832, pp. 155014.
- [3] A. Foetisch, M. Filella, B. Watts, L.-H. Vinot, and M. Bigalke, "Identification and characterisation of individual nanoplastics by scanning transmission X-ray microscopy (STXM)," *J. Hazard. Mater.*, 2022, vol. 426, pp. 127804.
- [4] R. Schmidt, M. Nachtnebel, M. Dienstleder, S. Mertschnigg, H. Schroettner, A. Zankel, et al., "Correlative SEM-Raman microscopy to reveal nanoplastics in complex environments," *Micron* 2021, vol. 144, pp.103034.
- [5] Y. Xu, Q. Ou, M. Jiao, G. Liu, and J. P. van der Hoek, "Identification and Quantification of Nanoplastics in Surface Water and Groundwater by Pyrolysis Gas Chromatography–Mass Spectrometry," *Environ. Sci. Technol.*, 2022, vol. 56, pp. 4988–4997.
- [6] J. Jiménez-Lamana, L. Marigliano, J. Allouche, B. Grassi, J. Szpunar, and S. Reynaud, "A Novel Strategy for the Detection and Quantification of Nanoplastics by Single Particle Inductively Coupled Plasma Mass Spectrometry (ICP-MS)," *Anal. Chem.*, 2020, vol. 92, pp. 11664-11672.
- [7] A. Moraz, and F. Breider, "Detection and Quantification of Nonlabeled Polystyrene Nanoparticles Using a Fluorescent Molecular Rotor," *Anal. Chem.*, 2021, vol. 93, pp. 14976-14984.

Optimización de un sensor no enzimático para la determinación impedimétrica de glucosa salival

Ana Laura Rinaldi
Departamento de Ciencias Químicas
Facultad de Farmacia y Bioquímica
Universidad de Buenos Aires
CABA, Argentina
alrinaldi@ffyb.uba.ar

María Celina Bonetto
IQUIFIB-CONICET
Facultad de Farmacia y Bioquímica
Universidad de Buenos Aires
CABA, Argentina
celinatt@yahoo.com.ar

Santiago Sobral
IQUIFIB-CONICET
Facultad de Farmacia y Bioquímica
Universidad de Buenos Aires
CABA, Argentina
ssobral.teq@gmail.com

José Iván González Jorge
Departamento de Ciencias Químicas
IQUIFIB-CONICET
Facultad de Farmacia y Bioquímica
Universidad de Buenos Aires
CABA, Argentina
jjgonzalez930209@gmail.com

Santiago Cosci
Departamento de Ciencias Químicas
Facultad de Farmacia y Bioquímica
Universidad de Buenos Aires
CABA, Argentina
santiago.cosci@gmail.com

Romina Carballo
Departamento de Ciencias Químicas
IQUIFIB-CONICET
Facultad de Farmacia y Bioquímica
Universidad de Buenos Aires
CABA, Argentina
rocar@ffyb.uba.ar

Resumen—En este trabajo presentamos GlucoZETA un sensor no enzimático para la cuantificación de glucosa en el rango de concentración esperada para muestras no invasivas de saliva. GlucoZETA funciona bajo el principio de la oxidación directa de la glucosa en contacto con una superficie sensora constituida por nanopartículas de oro recubiertas por óxido/hidróxido de níquel ($\text{Ni}(\text{OH})_2/\text{AuNp}/\text{SPE}$). El sensor propuesto fue caracterizado mediante SEM y técnicas de espectroscopia de impedancia electroquímica (EIS). Las mediciones de EIS a una única frecuencia revelan que los valores de la componente capacitiva del sensor (Zimaginaria) presentan la mejor respuesta lineal para concentraciones de glucosa en el rango de 0,10 a 2 mM (1,80 a 36,4 mg/dL), a 0,1 Hz y +0,400 V vs Ag/AgCl. La curva de calibración de $1/Z_{\text{Im}}$ en función de la concentración de glucosa en saliva artificial fue obtenida con una pendiente de $0,4003 \text{ K}\Omega^{-1} \text{ mM}^{-1}$, $R^2=0,9924$ y un límite de detección de 0,04 mM de glucosa. GlucoZETA resulta ser un sensor no enzimático que supera las desventajas del uso de modificadores biológicos y aplica una metodología electroquímica altamente sensible, permitiendo la cuantificación directa de glucosa sin requerir muestra de sangre.

Palabras claves—glucosa, sensor no enzimático, impedancia a una sola frecuencia.

I. INTRODUCCIÓN

La cuantificación de glucosa resulta ser una problemática siempre vigente debido al impacto de su determinación en diferentes áreas (industria alimenticia, biotecnología, diagnóstico clínico). En particular, en el control y manejo de los niveles de glucosa en pacientes diabéticos, la principal motivación reside en la exploración de metodologías no invasivas alternativas a la clásica toma de muestra de sangre (pinchazo o extracción venosa) que contribuyen a lograr una mejor adhesión del paciente al monitoreo de su enfermedad [1]. Asimismo, determinar la relación existente entre los niveles de glucosa en sangre y en otros fluidos corporales (saliva, lágrimas, sudor) es esencial para el desarrollo de métodos más simples para el control de la diabetes. Algunos estudios reportan que los niveles de glucosa salival en el rango de 10 a 32 mg/dL (0,55 a 1,8 mM de glucosa) se correlacionan con los valores de glucosa en sangre (120 a 261 mg/dL) en pacientes diabéticos, mientras que valores más bajos (4,3 a

12,9 mg/dL, equivalentes a 0,24 a 0,72 mM) son obtenidos en pacientes no diabéticos [2, 3].

El desarrollo de sensores no enzimáticos de glucosa (NEGS) requiere de la investigación de fases de reconocimiento molecular que permitan, en cierto modo, compensar la pérdida de selectividad causada por la eliminación de la enzima del diseño del sensor. Entre los (nano)materiales más utilizados para la construcción de estos sensores se encuentran los derivados del ácido borónico, nanopartículas metálicas (de oro, platino), óxidos e hidróxidos de metal (níquel, cobre, cobalto), polímeros biomiméticos, nanotubos de carbono, materiales híbridos [4]. En el caso de los NEGS basados en $\text{Ni}(\text{OH})_2$, la oxidación electrocatalítica de glucosa es mediada por la cupla redox $\text{Ni}^{\text{(II)}}/\text{Ni}^{\text{(III)}}$ en medio alcalino, y en trabajos previos hemos discutido el efecto sinérgico del oro para la generación de especies catalíticas, fuertemente oxidantes, de NiOOH [5].

La elección de la técnica de transducción de la señal es fundamental para el desarrollo exitoso de un sensor, y los sensores no enzimáticos de glucosa no escapan a esta generalidad. En el diseño de sensores electroquímicos la adquisición de corriente y/o potencial genera una respuesta amperométrica, potenciométrica o impedimétrica. Claramente, una de las técnicas de mayor crecimiento de los últimos años ha sido la espectroscopia de impedancia electroquímica (EIS), cuya principal ventaja es su elevada sensibilidad frente a los eventos de reconocimiento en la superficie del electrodo, y que permite analizar toda la complejidad del sistema de manera sencilla, en un único experimento, sin las limitaciones o condicionantes de la medición DC. Sin embargo, la mayor dificultad de estos sensores impedimétricos reside en la necesidad de procesar la información en todo el rango de frecuencias para finalmente obtener el ajuste de los datos a un circuito equivalente y poder representar los valores de resistencia de transferencia de carga (Rct) en función de la concentración del analito de interés. Como alternativa, hemos desarrollado una metodología que consiste en el análisis de impedancia electroquímica a una única frecuencia, basada en la optimización previa del parámetro de la impedancia compleja (módulo, Zimaginaria, Zreal, fase) que mejor correlaciona con la concentración de analito [6].

En este trabajo, presentamos los avances del prototipo y la optimización de un sensor no enzimático de glucosa, GlucoZETA, construido sobre electrodos impresos de grafito (SPE) de fabricación nacional modificados con nanopartículas de oro recubiertas por óxido/hidróxido de níquel ($\text{Ni}(\text{OH})_2/\text{AuNp}/\text{SPE}$). GlucoZETA es un sensor impedimétrico, en el cual la medición de la impedancia electroquímica a una única frecuencia permite la cuantificación de glucosa en los rangos de concentración esperados para el analito en muestras de saliva (0,10 a 2 mM de glucosa).

II. EXPERIMENTAL

A. Materiales, equipamiento y metodologías

Todos los reactivos utilizados fueron de grado analítico, provisto por Merck y Sigma-Aldrich y utilizados tal como se recibieron, sin realizar ningún tipo de purificación. Para la preparación de todas las soluciones se utilizó agua desionizada. Los SPE fueron fabricados en nuestro laboratorio. Los mismos consisten en un electrodo de trabajo de grafito (7 mm² de área superficial), un electrodo de referencia de Ag/AgCl y un contraelectrodo de grafito. La modificación con nanopartículas de oro y el depósito de níquel fueron realizados según el procedimiento descrito en [5, 7]. En forma resumida, las nanopartículas de oro se generaron a corriente constante (-100 μA , 300 s) sobre los SPE empleando una solución de AuCl_4H 0,5 mM. La electrodeposición de las nanopartículas de níquel se llevó a cabo mediante la aplicación de un potencial de -1,3 V vs Ag/AgCl por 60 segundos a partir de una solución de $\text{Ni}(\text{NO}_3)_2 \cdot 6\text{H}_2\text{O}$ 10 mM.

Las mediciones de voltametría cíclica (VC) fueron realizadas con un potenciostato (TEQ-Argentina), con un generador de señal digital para la implementación de diferentes técnicas electroquímicas. Los espectros EIS fueron registrados utilizando un potenciostato TEQ4-Z (TEQ-Argentina) con un analizador de frecuencia. El análisis de los datos y la optimización de los parámetros de EIS fueron realizados con un software de desarrollo propio graf_v3 (https://github.com/jgonzalez930209/graf_v3/releases).

La microscopía electrónica de barrido (Zeiss DSM982 GEMINI SEM con pistola de emisión de campo) fue utilizada para caracterizar la morfología y estructura de los electrodos

Todos los experimentos fueron llevados a cabo en KOH 0,1 M a temperatura ambiente y por triplicado. En los experimentos de EIS se utilizó el rango de frecuencias de 100 kHz a 0,1 Hz. La amplitud de oscilación (AC) fue de 10 mV_{RMS}. El potencial de trabajo óptimo fue ajustado a +0,400 V (vs Ag/AgCl), para las mediciones de glucosa.

Las soluciones de trabajo para la curva de calibración se prepararon adicionando estándar de glucosa (0, 0,23, 0,45, 0,70, 1, 1,25 y 2 mM) a la saliva artificial (fórmula de Ringer: para 1 L: 9 g de NaCl, 0,4 g de KCl, 0,2 g de $\text{CaCl}_2 \cdot \text{H}_2\text{O}$ y 0,2 g de NaHCO_3) [8]. En el momento de la medición, 5 μL de KOH 5 M fueron agregados a 1000 μL de dichas soluciones. Los posibles interferentes también fueron considerados en concentraciones fisiológicas.

III. RESULTADOS Y DISCUSIÓN

A. Caracterización y comportamiento electroquímico de $\text{Ni}(\text{OH})_2/\text{AuNp}/\text{SPE}$ frente a glucosa

Los electrodos impresos de grafito fueron modificados con hidróxido de níquel, previa inmovilización de nanopartículas de oro (AuNp) a fin de obtener $\text{Ni}(\text{OH})_2/\text{AuNp}/\text{SPE}$. En la Fig. 1, las imágenes de SEM de este sensor revelan una distribución homogénea de nanopartículas esféricas de 85 nm de diámetro promedio cuando el níquel es electrodepositado sobre las AuNp. Sin embargo, las AuNp no solo condicionan la morfología de la superficie sensora sino que los sustratos de oro también tienen un efecto sinérgico sobre los óxidos de níquel favoreciendo la formación de sitios activos estables hacia la oxidación catalítica de glucosa, aumentando significativamente la respuesta electroquímica.

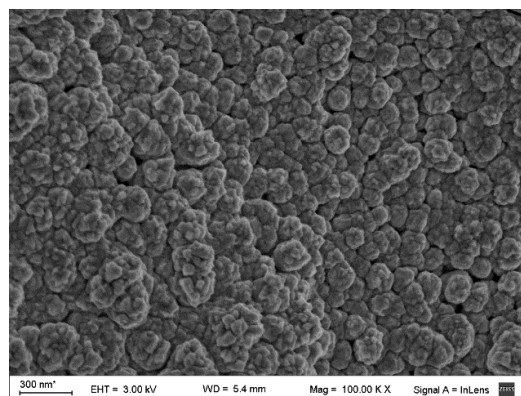
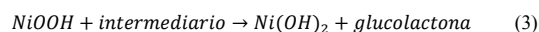
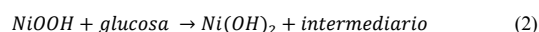
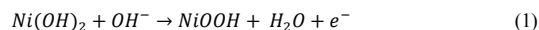
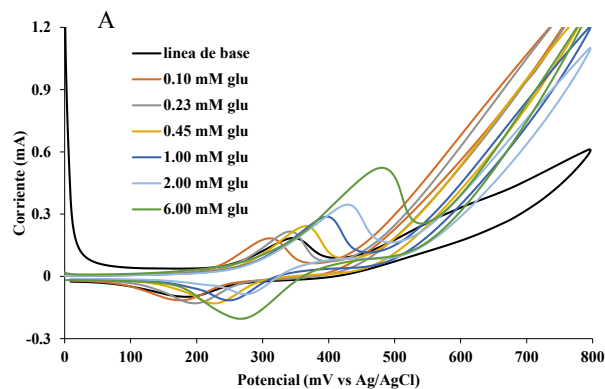


Fig. 1. Imagen SEM correspondiente a la electrodeposición de níquel sobre AuNp/SPE (magnificación 100000 x).

La respuesta del sensor $\text{Ni}(\text{OH})_2/\text{AuNp}/\text{SPE}$ frente a glucosa (Fig. 2 A) y la selectividad del mismo en presencia de sustancias interferentes (Fig. 2 B), han sido estudiadas mediante experimentos de VC. El comportamiento electrocatalítico de $\text{Ni}(\text{OH})_2/\text{AuNp}/\text{SPE}$ hacia la oxidación de glucosa en KOH 0,1 M se explica de acuerdo a las siguientes reacciones (1), (2) y (3):



Este mecanismo contempla la adsorción de glucosa y de sus intermediarios y la posible acumulación de los mismos pero solo en condiciones de alta concentración de analito (mayores a 2 mM) [5]. Por otra parte, los experimentos de VC también revelan que la respuesta del sensor a glucosa no se ve modificada en presencia de ácido ascórbico y de dopamina en concentraciones 0,08 mM y 0,05 mM, respectivamente.



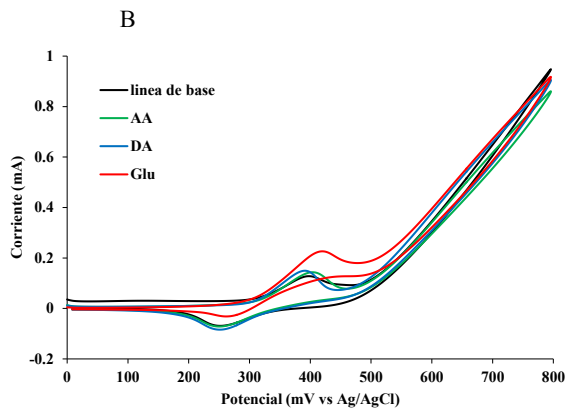


Fig. 2. (A) VC de Ni(OH)₂/AuNp/SPE frente a agregados crecientes de glucosa en KOH 0,1 M (de 0,10 a 6 mM). (B) VC de Ni(OH)₂/AuNp/SPE en presencia de posibles interferentes: ácido ascórbico (0,08 mM), dopamina (0,05 mM) y finalmente glucosa (2 mM). Los analitos fueron agregados secuencialmente a la misma solución de KOH 0,1 M

B. Mediciones de espectroscopía de impedancia electroquímica empleando Ni(OH)₂/AuNp/SPE frente a glucosa. Optimización de GlucoZETA

Con el fin de evaluar y proponer un nuevo sensor impedimétrico de glucosa basado en Ni(OH)₂/AuNp/SPE, denominado GlucoZETA, se realizaron mediciones de espectroscopía de impedancia electroquímica en KOH 0,1 M frente a diferentes concentraciones de glucosa. Se obtuvieron los gráficos de Nyquist, y el ajuste al circuito eléctrico equivalente mostrado en la Fig. 3 se corresponde con la existencia de un proceso de adsorción de intermediarios de reacción, tal como se indicó previamente (CPE_{ads}, R_{ads}) [5]. Sin embargo, a bajas concentraciones de glucosa esos intermediarios no se acumulan dado que su oxidación es más rápida que su generación.

El desempeño analítico de GlucoZETA hacia la cuantificación de glucosa en saliva artificial fue evaluado empleando el método de impedancia a una única frecuencia. Para ello, la determinación de la frecuencia y el parámetro óptimo de la impedancia compleja fueron obtenidos analizando la mejor pendiente y coeficiente de correlación (R²) [6]. El software graf_v3 desarrollado en nuestro laboratorio fue aplicado para dicho análisis. Los resultados indican que son los valores de la impedancia imaginaria (Z_{Im}) a 0,1 Hz los que mejor representan la respuesta lineal del sensor propuesto frente a la glucosa en un rango de concentración de 0,10 a 2 mM del analito, a +0,400 V (vs Ag/AgCl) (Fig. 4 A). Sin dudas, la impedancia imaginaria se relaciona con la señal capacitiva del sensor que refleja los cambios en la superficie del modificador, especialmente a bajas concentraciones del analito y en el rango esperado para la glucosa salival. Teniendo en cuenta estas condiciones experimentales para GlucoZETA, se obtuvo la curva de calibración del parámetro 1/Z_{Im} en función de la concentración de glucosa en saliva artificial con una pendiente de 0,4003 KΩ⁻¹ mM⁻¹, R²=0,9924 y un límite de detección de 0,04 mM (Fig. 4 B).

Finalmente, se desarrolló un prototipo de GlucoZETA a escala laboratorio, el cual fue aplicado en la determinación de

glucosa en 6 muestras de saliva artificial. Se obtuvieron valores de recuperación aceptables (entre el 97,4 y 106 %) con una desviación relativa estándar (RSD) menor al 5% para los niveles de glucosa ensayados. Los resultados se presentan en la Tabla 1.

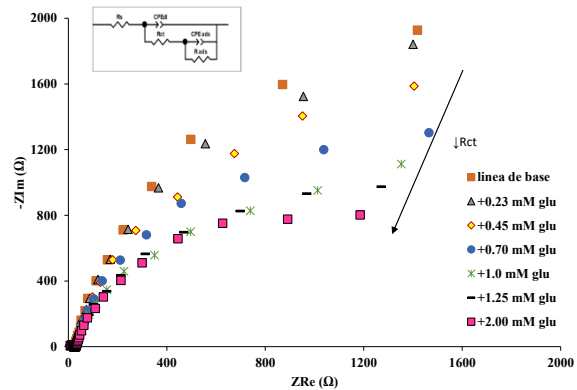


Fig. 3. Gráfico de Nyquist para Ni(OH)₂/AuNp/SPE frente a concentraciones crecientes de glucosa en el rango de 0 a 2 mM, en KOH 0,1 M. El recuadro muestra el correspondiente circuito eléctrico equivalente.

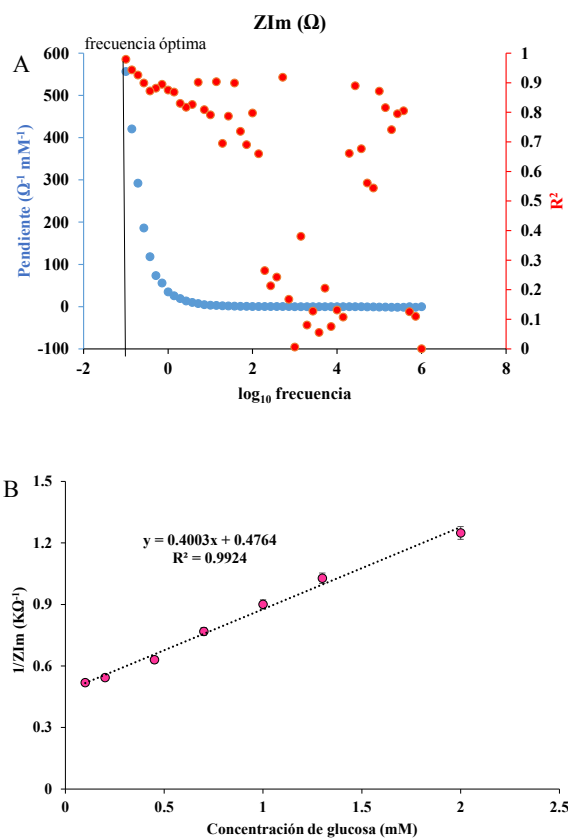


Fig. 4. (A) Superposición de los valores de pendiente y R² correspondientes al parámetro de la impedancia imaginaria (Z_{Im}) para determinar la frecuencia óptima de la respuesta a glucosa empleando el sensor GlucoZETA. (B) Curva de calibración para 1/Z_{Im} en función de la concentración de glucosa salival a 0,1 Hz y +0,400 V vs Ag/AgCl (n=3).

TABLA 1. RESULTADOS DE LA DETERMINACION DE GLUCOSA EN SALIVA ARTIFICIAL EMPLEANDO GLUCOZETA

Muestra ^a	Concentración de glucosa agregada (mM)	Concentración medida con GlucoZETA (mM)	Recuperación (%)	RSD (% n=3)
1	0,23	0,24	102,0	4,7
2	0,45	0,48	106,7	4,5
3	0,76	0,74	97,4	3,8
4	0,90	0,93	103,3	4,0
5	1,23	1,25	101,6	3,3
6	1,86	1,83	98,4	4,1

^a Muestras de saliva artificial según la fórmula de Ringer [8]

IV. CONCLUSIONES

En este trabajo hemos evaluado un sensor no enzimático para la cuantificación de glucosa, de fabricación nacional, basado en nanopartículas de oro recubiertas con óxido/hidróxido de níquel (Ni(OH)₂/AuNp/SPE). La optimización de la medición de un parámetro de la impedancia compleja (Z_{im}) a una única frecuencia (0,1 Hz) y a +0,400 V vs Ag/AgCl que mejor correlaciona con la concentración del analito fue posible mediante la aplicación del software graf_v3. Finalmente, GlucoZETA se presenta como un prototipo de sensor impedimétrico adecuado para la determinación de glucosa en el rango de concentración de 0,10 a 2 mM del analito, compatible con el estudio en muestras biológicas no invasivas.

AGRADECIMIENTOS

Los autores agradecen los financiamientos otorgados por UBA (UBACyT2023 Mod I 20020220200052BA) y ANPCyT (PICT 2021 GRF T1 00269). J. I. G. J. agradece a CONICET por la beca doctoral.

REFERENCIAS

- [1] A. Salek-Maghsoudi, F. Vakhshiteh, R. Torabi, S. Hassani, M.R. Ganjali, P. Norouzi, M. Hosseini, and M. Abdollahi, "Recent advances in biosensor technology in assessment of early diabetes biomarkers", *Biosens. Bioelectron.*, vol. 99, pp. 122–135, 2018.
- [2] S. Gupta, S.V. Sandhu, H. Bansal, and D. Sharma, "Comparison of salivary and serum glucose levels in diabetic patients", *J. Diabetes Sci. Technol.*, vol. 9, pp. 91–96, 2015.
- [3] H. Elmongy, and M. Abdel-Rehim, "Saliva as an alternative specimen to plasma for drug bioanalysis: a review", *Trends Anal. Chem.*, vol. 83, pp. 100–108, 2016.
- [4] H. Zhu, L. Li, W. Zhou, Z. Shao, and X. Chen, "Advances in non-enzymatic glucose sensors based on metal oxides", *J. Mater. Chem. B*, vol. 4, pp. 7333–7349, 2016.
- [5] A. Rinaldi, and R. Carballo, "Impedimetric non-enzymatic glucose sensor based on nickel hydroxide thin film onto gold electrode", *Sensors Actuators B Chem.*, vol. 228, pp. 43–52, 2016.
- [6] M. E. Strong, J. R. Richards, M. Torres, C. M. Beck, and J. T. La Belle, "Faradaic electrochemical impedance spectroscopy for enhanced analyte detection in diagnostics", *Biosens. Bioelectron.*, vol. 177, 112949, 2021.
- [7] G. Martínez-Paredes, M.B. González-García, and A. Costa-García, "In situ electrochemical generation of gold nanostructured screen-printed carbon electrodes. Application to the detection of lead underpotential deposition", *Electrochim. Acta*, vol. 54, pp. 4801–4808, 2009.
- [8] H. Othman, and N. Ettayeb, "Electrochemical comporment of Ni–Ti alloys immersed in two types of artificial saliva", *J. Biomed. Mater. Res. B*, vol. 105B, pp. 778–784, 2017.

Electrodos de grafito modificados para la detección electroquímica de glifosato en agua

Ana Janeiro
Área de Química
Instituto de ciencias, UNGS
Los Polvorines, Bs. As., Argentina
ajaneiro@campus.ungs.edu.ar

Camila Romero
Área de Química
Instituto de ciencias, UNGS
Los Polvorines, Bs. As., Argentina
cam123191@hotmail.com

Mariana Hamer
CONICET
Área de Química
Instituto de ciencias, UNGS
Los Polvorines, Bs. As., Argentina
mhamer@campus.ungs.edu.ar

Abstract— En este trabajo se desarrolla la preparación y caracterización de electrodos de grafito modificados con films poliméricos de Cu(II) porfirina y su utilización en la determinación de glifosato por técnicas electroquímicas.

Keywords— Glifosato, cobre, porfirina, sensor

I. INTRODUCCIÓN

El glifosato (N-fosfonometilglicina) GLY, es uno de los herbicidas organofosforados no selectivos más utilizados para inhibir el crecimiento de plantas de hoja ancha y pastos en la producción agrícola y el mantenimiento del paisaje. Existe una creciente inquietud por los peligros que conlleva su uso para el medio ambiente y la salud de las personas debido a la exposición excesiva.

Los métodos actuales de detección de glifosato incluyen ensayos ELISA [1], métodos cromatográficos [2], y espectroscopía de masa [3], que requieren equipamiento costoso, pasos de derivatización y protocolos complejos. Así mismo la muestra tiene que ser transportada al laboratorio y requiere pretratamientos.

La detección electroquímica de GLY tiene las ventajas de que permite diseñar dispositivos de bajo costo, transportables, miniaturizables, sencillos de utilizar y que arroja resultados de fácil interpretación [4].

En este trabajo se propone aprovechar la capacidad complejante del GLY para coordinar iones Cu (II) [5]. Para ello se modificaron electrodos de grafito con films poliméricos de porfirinas de cobre y se analizó la señal electroquímica de soluciones de GLY de distintas concentraciones. El sensor construido muestra una buena conductividad y detección de GLY en muestras acuosas.

II. MATERIALES Y MÉTODOS

Reactivos: Cu(II) 5,10,15,20-[meso-tetra(N-sulfato fenil) porfirina] (Cu-TPPS; Fig. 1), KNO₃ (sigma), Glifosato (sigma), NaOH (Merck), Ferrocenometanol (Aldrich), NaH₂PO₄ (Merck), Na₂HPO₄ (Merck).

Materiales: minas de lápiz HB 0,7 mm Staedtler; celda electroquímica de 4 mL con tapón de teflón.

Los ensayos electroquímicos se realizaron con un sistema de tres electrodos: electrodos de trabajo de grafito; electrodo de referencia Ag/AgCl y electrodo auxiliar de platino; empleando un potenciostato TEQ 4.0 con módulo de impedancia.

PICTO-UNGS (PICTO 2021-UNGS 00002) y PICT-2021-GRF-00035.

El film de porfirina de cobre sobre los electrodos de trabajo se obtuvo por electropolimerización de Cu-TPPS en NaOH 0,1 M. Para ello se hicieron de 15 a 20 voltametrías cíclicas (VC) entre 0 y 1400 mV (Fig. 2).

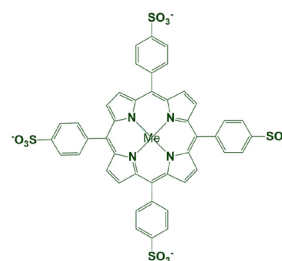


Fig. 1: Estructura del complejo Cu(II) 5,10,15,20-[meso-tetra(N-sulfato fenil) porfirina] (Cu-TPPS). Me: Cu.

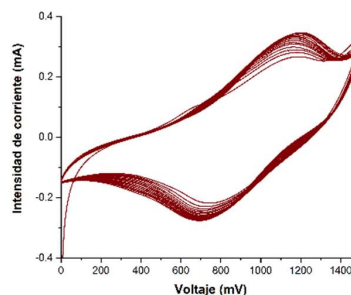


Fig. 2: VC polimerización de Cu-TPPS en NaOH 0,1M sobre la superficie de grafito.

Las imágenes SEM del polímero de CuTPP fueron tomadas con un equipo Zeiss LEO1450VP y los análisis de energía dispersiva de los estudios de espectroscopía de rayos X(EDS) se realizaron en un EDAX Genesis 2000. Las muestras se colocaron sobre cinta adhesiva de carbón recubierta de oro.

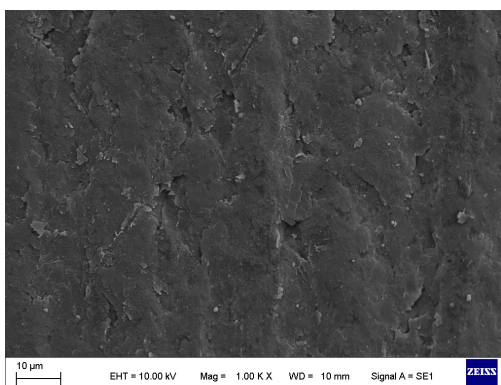
Los espectros Raman se recogieron en un equipo de microscopia confocal Renishaw Via Reflex equipado con un detector CCD de 1024 × 256 píxeles, una rejilla holográfica de 2400 ranuras/mm y un láser Ar de 50 mW de longitud de onda de 532 nm como fuente de excitación.

III. RESULTADOS

Las superficies de los electrodos de trabajo se modificaron con un film polimérico de Cu-TPPS empleando VC entre 0 y 1400 mV.

Los aspectos morfológicos del film depositado se evaluaron por microscopía SEM (Fig. 3). Se observó que el recubrimiento abarca una amplia área superficial con presencia de agregados globulares, que podrían incrementar los sitios de unión del Cu [6,7]. Las interacciones de estos sitios con el GLY podrían mejorar el proceso de detección selectiva, aumentando la sensibilidad del sensor electroquímico.

A



B

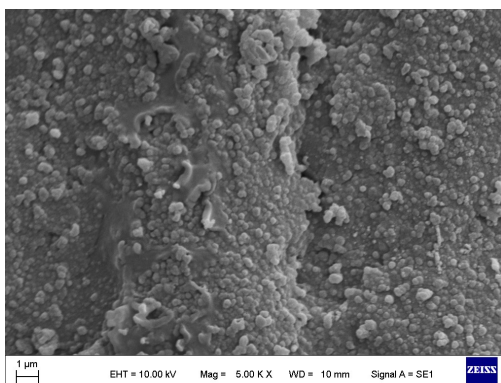


Fig. 3: Imagen SEM A) electrodo de grafito. B) film polimérico cobre Cu-TPPS sobre los electrodos de grafito.

Asimismo, se realizó el análisis elemental de los electrodos modificados por EDS, lo que permitió observar la composición del material depositado. En la Tabla I se muestra esta información.

Tabla I. EDS electrodos de grafito modificados con Cu-TPPS

Elementos	%Peso	%Atómico
C K	79.29	89.16
O K	10.34	8.73
P K	1.30	0.56
Cl K	0.39	0.15
K K	2.42	0.84
Cu K	0.80	0.18
S K	5.45	0.37
Total	100	

Además, se comprobó la presencia del film de porfirinas por espectroscopia RAMAN de las superficies modificadas

excitando a 532 nm. Los espectros RAMAN de los films muestran los picos de absorción característicos de los esqueletos de anillos porfirínicos (Fig. 4). Como se observa, el pico a $\sim 390 \text{ cm}^{-1}$ es sensible al cambio de la conformación del anillo porfirínico. Por otro lado, las bandas a $\sim 1000 \text{ cm}^{-1}$ y a $\sim 1360 \text{ cm}^{-1}$ se corresponden con el modo de vibración del anillo porfirínico y de respiración de las uniones C-N pirrólicos, haciendo referencia a una vibración no simétrica del esqueleto porfirínico, respectivamente. La Tabla II resume las asignaciones.

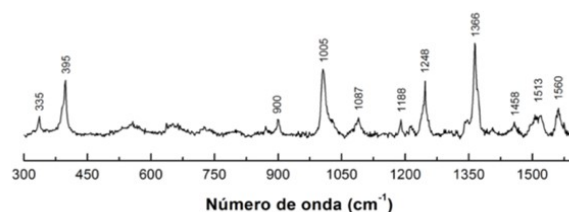


Fig. 4. Espectro Raman de las superficies estudiadas. Excitación a 532 nm.

Tabla II. Asignaciones de las bandas que se observan en la Fig. 4.

CuTPPS	Asignación [8]
335	δ porfirina
395	γ porfirina
1005	ν porfirina
1087	δ C β - H
1248	δ porfirina
1366	ν C α -N
1513	ν sim C-C + δ asim porfirina
1560	ν porfirina

ν , stretching; γ , folding out of the plane; δ , flexion

Se evaluó el comportamiento electroquímico del electrodo antes y después de la modificación con Cu-TPPS. Para ello se analizó la transferencia electrónica frente al sistema $\text{Fe}(\text{CN})_6^{3-}/\text{Fe}(\text{CN})_6^{4-}$ en KNO_3 0,1 M. La respuesta de voltametría cíclica (VC) del $\text{Fe}(\text{CN})_6^{3-}$ resultó casi reversible para todos los electrodos. La corriente máxima anódica y catódica aumentó linealmente con la raíz cuadrada de las velocidades barrido lo que indica un proceso controlado por difusión (Fig. 5). Se cumple la ecuación de *Randles-Sevcik* que relaciona la corriente con la velocidad de barrido de potencial (a 298 K) según [9]:

$$I_p = 2,69 \times 10^5 \times n^2 \times A \times C_i^* \times D_i^{1/2} \times v^{1/2}$$

Ecuación 1: I_p corriente de pico, n número de electrones intercambiados, A el área del electrodo, C_i^* concentración de la especie electroactiva, D_i coeficiente de difusión, V velocidad de barrido.

La diferencia entre las pendientes obtenidas para el electrodo modificado y sin modificar indica una disminución del coeficiente de difusión debido al cambio en la superficie del electrodo.

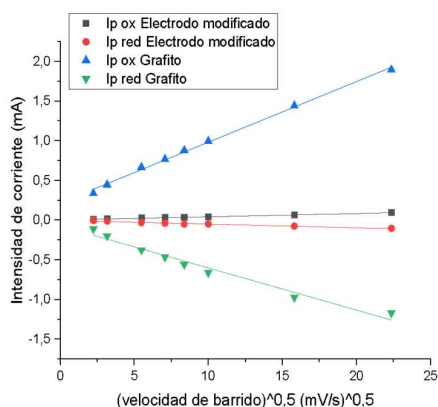


Fig. 5: Intensidad de corriente en función de la velocidad de barrido. $\text{Fe}(\text{CN})_6^{3-}/\text{Fe}(\text{CN})_6^{4+}$ 25 mM en KNO_3 0,1 M.

También se analizó la transferencia electrónica por VC para los electrodos en buffer 25 mM fosfato pH 7.20 en presencia y ausencia de GLY (Fig 6). Se observó mayor transferencia electrónica sobre el electrodo modificado y una mayor intensidad de corriente en presencia de GLY.

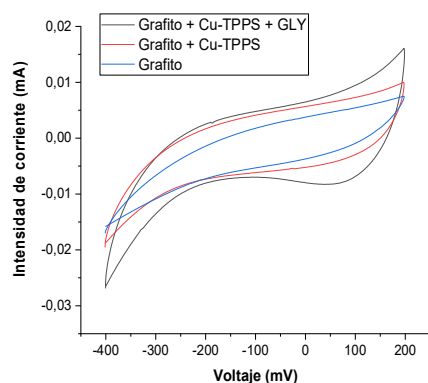


Fig 6: VC en buffer fosfato, azul: electrodo de grafito, rojo: electrodo modificado con Cu-TPPS, negro: electrodo modificado + GLY.

Se analizó el funcionamiento del electrodo como sensores para GLY utilizando las técnicas de amperometría y DPV.

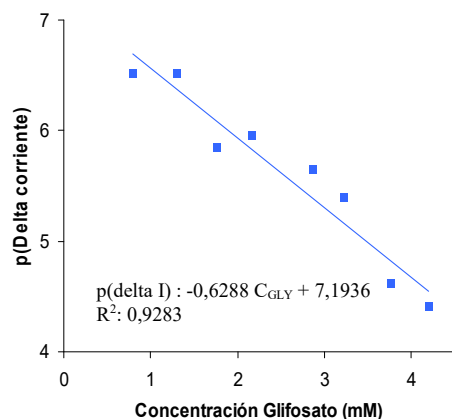


Fig 7 Relación entre la corriente medida por amperometría y la concentración de GLY.

Sobre 4 mL de buffer 25 mM fosfato pH 7.20 se hicieron agregados sucesivos de una solución 10 mM de GLY (Fig. 7).

Se midió la corriente tras cada agregado aplicando un potencial de 100 mV por 1800 s. Obteniéndose una relación proporcional entre la corriente medida y la cantidad de GLY agregada.

Por otro lado se prepararon muestras acuosas de concentración creciente, entre 5 y 200 $\mu\text{mol L}^{-1}$, de GLY en PBS 0,1 M que se analizaron cuantitativamente por DPV. La intensidad de corriente resultó ser máxima en ausencia de GLY. Al aumentar la concentración de GLY la corriente disminuyó gradualmente en forma proporcional al logaritmo de la concentración (Fig. 8).

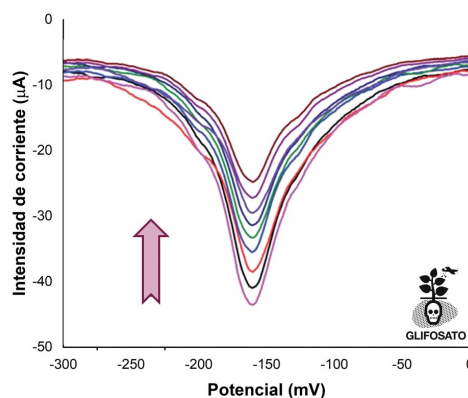


Fig. 8: Respuesta por DPV para concentraciones crecientes de 5 a 200 $\mu\text{mol L}^{-1}$ de GLY (5, 10, 25, 50, 75, 100, 125, 150, 200 $\mu\text{mol L}^{-1}$).

En las condiciones ensayadas, utilizando soluciones acuosas de GLY, el sensor presentó un rango lineal frente a concentraciones crecientes de 5 a 185 $\mu\text{mol L}^{-1}$ con un límite de detección de 1 $\mu\text{mol L}^{-1}$ (S/N = 3) (Fig. 9).

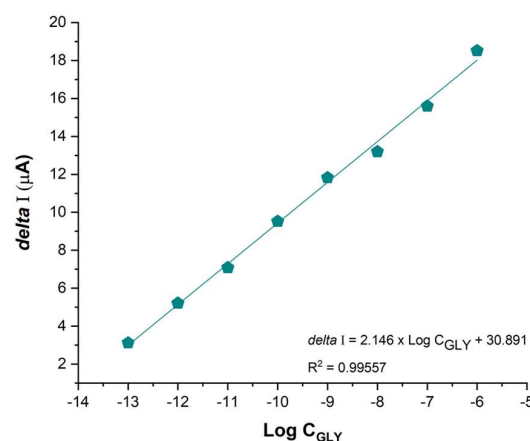


Fig. 9: Curva de concentración para soluciones acuosas de distintas concentraciones de GLY en PBS 0,1 M.

IV. CONCLUSIONES

El electrodo de grafito fue modificado exitosamente con el polímero Cu-TPPS. Esto pudo observarse por diferentes

técnicas ópticas y electroquímicas. Por otro lado, el electrodo modificado pudo ser utilizado como sensor para detectar GLY en agua. Se espera que estos electrodos puedan ser utilizados en matrices complejas tanto en el laboratorio como en estudios de campo al diseñar un dispositivo portátil.

V. AGRADECIMIENTOS

Se agradece a la Agencia Nacional de Promoción Científica y Tecnológica y a la UNGS por la financiación de este trabajo a través del programa PICTO-UNGS (PICTO 2021-UNGS 00002) y PICT-2021-GRF-00035. M.H es miembro del CONICET.

VI. REFERENCIAS

- [1] H. Liu, P. Chen, Z. Liu, J. Liu, J. Yi, F. Xia, and C. Zhou, "Sensor de luminiscencia electroquímica basado en doble supresión para la detección de glifosato de alta sensibilidad" *Sensors and Actuators B: Chemical*, (2020), 304, 127364.
- [2] R. Exterkoetter, D.E. Rozane, W.C. da Silva, A. Theodoro Toci, G. A. Cordeiro, S. F. Benassi and M. Boroski, "Potential of terracing to reduce glyphosate and AMPA surface runoff on Latosol". *J Soils Sediments* (2019), 19, 2240.
- [3] E. Junqué, P. Fernández, I. Filippi and J. O. Grimalt, "Determination of glyphosate and its derivative, aminomethylphosphonic acid, in human urine by gas chromatography coupled to tandem mass spectrometry and isotope pattern deconvolution". *Journal of Chromatography Open* (2023), 4, 100087.
- [4] H. Z. T. Johnson, N. Jared, J. K. Peterson, J. Li, E. A. Smith, S. A. Walper, S. L. Hooe, J. C. Breger, I. L. Medintz, C. Gomes, and J. C. Claussenamer, "Enzymatic laser - induced graphene biosensor for electrochemical sensing of the herbicide glyphosate". *Global Challenges* (2022), 6, 2200057.
- [5] M. Regiart, A. Kumar, J. M. Gonçalves, G. J. Silva Junior, J. C. Masini, L. Angnes and M. Bertotti, "An electrochemically synthesized nanoporous copper microsensor for highly sensitive and selective determination of glyphosate". *ChemElectroChem* (2020), 7, 1558.
- [6] M. Hamer, R.R. Carballo, I.N. Rezzano, "Electrocatalytic reduction of hydrogen peroxide by nanostructured bimetallic films of metalloporphyrins". *Electroanalysis* (2009) 19, 2133.
- [7] R. Jiang , Y-H. Pang, Y-Q. Yang, C-Q. Wan, X-F. Shen, *Sens and Act B: Cheml*, 358 (2022) 131492.
- [8] M. Hamer and I.N. Rezzano, "Copper porphyrin metal-organic framework modified carbon paper for electrochemical sensing of glyphosate". *Inorg Chem*, (2016), 55, 8595.
- [9] Bard, A. J., Faulkner, L. R "Electrochemical methods. Fundamentals and applications". 2da edición. (2001). Capítulo 6. ISBN: 0-471-04372-9.

Mejoras en las Producción Agrícola y Reducción del Impacto Ambiental en la Industria Agrícola en Suelos de Diferente Tipología Mediante el Uso de Sondas de Nutrición

Eva Arasa-Puig
Grupo de Sensores y Biosensores
(GSB)
Universidad Autónoma de Barcelona
(UAB)
Bellaterra, España
eva.arasa@uab.es

Óscar González
Grupo de Sensores y Biosensores
(GSB)
Universidad Autónoma de Barcelona
(UAB)
Bellaterra, España
Oscar.GonzalezR@autonoma.cat

Julián Alonso-Chamarro
Grupo de Sensores y Biosensores
(GSB)
Universidad Autónoma de Barcelona
(UAB)
Bellaterra, España
julian.alonso@uab.es

Abstract— El aumento de la población mundial ha supuesto una demanda creciente de alimentos. Por eso es necesario aumentar el rendimiento y la producción de las tierras de cultivo mediante la adición de fertilizantes. El uso excesivo de fertilizantes, sin embargo, implica sobrecostes innecesarios e importantes daños medioambientales. La monitorización del estado nutricional del suelo es de vital importancia para la agricultura, solo de esta manera se puede predecir la cantidad adecuada de fertilizante que es necesario aplicar.

En este trabajo se evalúan las tendencias del estado nutricional del nitrato en suelos de diferente tipología. También se estudia cómo varía este comportamiento con el pH para conocer las condiciones ideales de trabajo y así evitar lixiviaciones masivas de nutrientes hacia el subsuelo. Con este fin se realizan una serie de adiciones de KNO_3 y de agua, simulando adiciones de fertilizante y el riego o la lluvia, y se monitoriza la respuesta del suelo utilizando una sonda Nutrisens.

Keywords— agricultura de precisión, nitrato, monitorización suelos, solución del suelo, lixiviación

I. INTRODUCTION

El aumento de la población mundial ha supuesto una creciente demanda de alimentos cuya obtención depende en gran medida de la producción agrícola. Esta viene limitada por la disponibilidad de terrenos cultivables, así como el acceso a un recurso muy escaso como el agua, muy afectado por el cambio climático. Para contrarrestar estos problemas resulta de gran importancia maximizar el rendimiento de los terrenos cultivables. Este uso intensivo del suelo agota los nutrientes naturales que tienen que ser suplidos por el agricultor idealmente en la proporción que sea necesaria.

La fertilización en exceso representa un gasto económico innecesario y genera un enorme impacto ambiental negativo. Uno de los nutrientes más fácilmente asimilados por los cultivos es el ion nitrato. La capacidad del suelo para retener este ion en la capa cercana a la superficie donde se encuentran las raíces es limitada debido a que generalmente suele presentar una mayor cantidad de cargas negativas. Esto favorece su lixiviación hacia los acuíferos y los ríos produciendo la eutrofización de las aguas [1]. Por otro lado, un defecto de fertilización impacta negativamente en el rendimiento y la calidad de los cultivos agrícolas.

Conocer las características edafológicas del suelo, así como otros parámetros que puedan influir en el cultivo, como

factores climáticos, es necesario para poder aportar el tipo y cantidad correcta de fertilizante en cada una de las etapas fenológicas del cultivo.

La planta toma los nutrientes por contacto físico entre la superficie mineral del suelo y las raíces de las plantas que absorben los nutrientes de la solución del suelo (no directamente de la estructura del suelo). La concentración de nutrientes en suelo disminuye con la ingesta por parte del cultivo. El reemplazo de estos nutrientes en la solución del suelo es resultado de reacciones químicas y biológicas que tienen lugar en el suelo. La habilidad de un suelo para recuperar la concentración del nutriente en la solución del suelo se llama capacidad tampón (CB). Esta capacidad depende del pH y viene regulada por los minerales que se pueden disolverse del suelo para pasar a la solución del suelo por reacciones microbianas y, principalmente, por la capacidad de intercambio del suelo o de la materia orgánica usada en los sustratos agrícolas.

La capacidad de intercambio es un proceso reversible donde cationes y aniones adsorbidos en la superficie del suelo es intercambiado por otro catión o anión de la solución del suelo. El origen de la superficie cargada es fundamental para entender la disponibilidad de los nutrientes y su retención en el suelo. Además, la capacidad del suelo para retener agua en solución también tiene impacto en la CB [2]. No obstante, los suelos son altamente complejos y los nutrientes y la forma en que estos son aportados al suelo durante el proceso de fertilización provoca que estos puedan quedar retenidos en fracciones de suelo no lábiles y, por lo tanto, no disponibles, al menos de forma inmediata, para ser asimilados por las plantas.

En conclusión, para estimar la disponibilidad real de nutrientes en suelo es de gran importancia conocer los nutrientes que quedan en solución y la CB del suelo.

Comercialmente, existe una gran variedad de lisímetros (sondas succión), que se utilizan para determinar la concentración de nutrientes en el agua del suelo, pero no son capaces de dar información sobre la CB. En este trabajo se propone el uso de una sonda potenciométrica (Nutrisens) [3] basada en electrodos selectivos de iones (ESIs) que, instalada directamente en el suelo, suministra datos en continuo y en tiempo real tanto de la evolución de la concentración de los nutrientes en la solución del suelo como de la influencia de la CB de este en dicha evolución. Este tipo de sondas proporcionan información relativa al ion al que son

selectivas en forma libre en fase acuosa [4]. Estas formas iónicas de los nutrientes son las que tienen interés agronómico ya que son las que las plantas pueden asimilar.

En este trabajo, se presentarán los resultados proporcionados por la sonda de Nitrato tras la adición de este ion a suelos de diferente tipología y su posterior lavado con disoluciones de diferente pH. El estudio pretende establecer la capacidad que posee el suelo, en función del pH, para mantener el nitrato en la solución del suelo (lisímetro), la capacidad para (fijar) adsorber nitrato en la estructura del suelo (Nutrisens) y determinar las condiciones en las que se minimice la lixiviación del nitrato hacia profundidades de campo alejadas de la zona asimilación de las raíces del cultivo.

II. EXPERIMENTAL

A. Descripción de las muestras

Se han utilizado muestras de sustratos agrícolas tanto sintéticos como naturales, siendo estos últimos más complejos y heterogéneos que los suelos sintéticos.

Como sustrato sintético se utiliza perlita expandida previamente saturada con nitrato. La perlita se caracteriza por tener un exceso de cargas positivas en su estructura y por una elevada capacidad para retener agua en su estructura. Se caracteriza por ser homogéneo, poroso y poco denso.

Como sustratos naturales se han estudiado un suelo arenoso y otro arcilloso. Los suelos arcillosos, en general, se caracterizan para una mayor capacidad para retener nutrientes tanto en la estructura del suelo como en la solución de suelo que un suelo arenoso. La complejidad de un suelo arcilloso suele ser superior también a la de un suelo arenoso.

Las muestras de suelo de origen natural se han secado durante 24 h a 80 °C y se han tamizado para tener un diámetro de partícula inferior a 1 mm.

B. Montaje experimental

Para realizar este estudio se fabrican *ad hoc* unas celdas con drenaje incorporado que se efectúa haciendo el vacío con una jeringa de 50 mL. Estas celdas incorporan una pieza mecanizada de metacrilato a modo de filtro para separar la muestra del suelo de la base del recipiente. Se recorta un filtro de papel del mismo tamaño para evitar la colmatación del filtro mecanizado. En caso que fuera necesario, se puede utilizar el agitador para homogeneizar la solución excedente con el suelo.

En la celda se introduce la muestra de suelo junto a la sonda Nutrisens y el lisímetro. Las lecturas de potencial del Nutrisens se registran conectando la sonda a un potenciómetro portátil fabricado *ad hoc* (SDIAN6, TMI, España) y controlado por un ordenador. El montaje experimental esquematizado se muestra en la figura 1.

Las medidas registradas son:

- Capacidad del nitrato de quedar adsorbido en la superficie del suelo utilizando la sonda Nutrisens. La sonda suministra variaciones de potencial descendentes al aumentar la concentración de ion, aunque para visualizarlos datos se ha invertido el sentido de variación observándose un crecimiento del potencial con la concentración.
- Solución del suelo: Se utiliza un lisímetro (Rizhosphere, Países Bajos). La solución de nitrato extraída se

mide con un analizador portátil (HORIBA LAQUAtwin, Japón). [5]

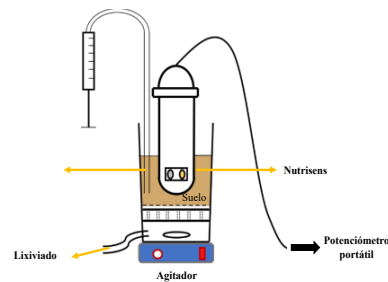


Fig 1. Esquema del montaje experimental

- Lixiviación: Las aguas de drenaje se recogen y se determina el nitrato con un analizador portátil (HORIBA LAQUAtwin, Japón).

C. Metodología de trabajo

Se pesan 80 g de muestra de suelo natural. En el caso de la perlita, debido a sus características, se pesan 8 g.

Se realizan adiciones de 35 mL de disolución de agua y de nitrato a diferentes concentraciones. Pasados 10 minutos, en caso de que sea necesario y dependiendo del tipo de suelo, se retira el exceso de líquido haciendo el vacío con la jeringa incorporada en la zona de lixiviado. A continuación, se toma una muestra con el lisímetro para medir concentración de nitrato en la solución del suelo.

Para estudiar el comportamiento del suelo frente a las adiciones de nutrientes, se realizan adiciones de agua Milli-Q y de patrones de 50, 150, 300 i 500 ppm de NO_3^- en este mismo orden ajustado a pH 4, pH 5 y pH 8, respectivamente.

A continuación, se realizan 5 adiciones de agua Milli-Q (pH 4, pH 5 y pH 8) para simular el riego o la lluvia en el campo. Estos pH han sido escogidos por ser el rango de pH más habitual en suelos.

III. RESULTADOS Y DISCUSIÓN

A continuación, se muestran los resultados obtenidos con la adición de nitrato y posterior lavado en suelos de diferente tipología (perlita saturada, suelo arenoso y arcilloso).

A. Adición nitrato

Los datos relativos a la adición de nutrientes se muestran en la figura 2.

En el caso de la perlita, esta había sido previamente saturada de nitrato. Este nitrato parece quedar retenido en la estructura de la perlita dejando sin posiciones donde unirse los nuevos aportes de nutrientes (puntos azules). Se observa, tras la saturación del material, que nuevos aportes de nutriente no quedan retenidos por el material y el nitrato queda en la solución del suelo. En esta disolución, la concentración de nutriente es prácticamente idéntica a la de la disolución que se adiciona. En este caso, destaca el comportamiento a pH 5 (rojo), donde el aporte de nutrientes conlleva una disminución de la señal del Nutrisens, lo que implica que se está lavando el nitrato previamente retenido en la matriz de perlita. Eso

ADICIÓN NITRATO

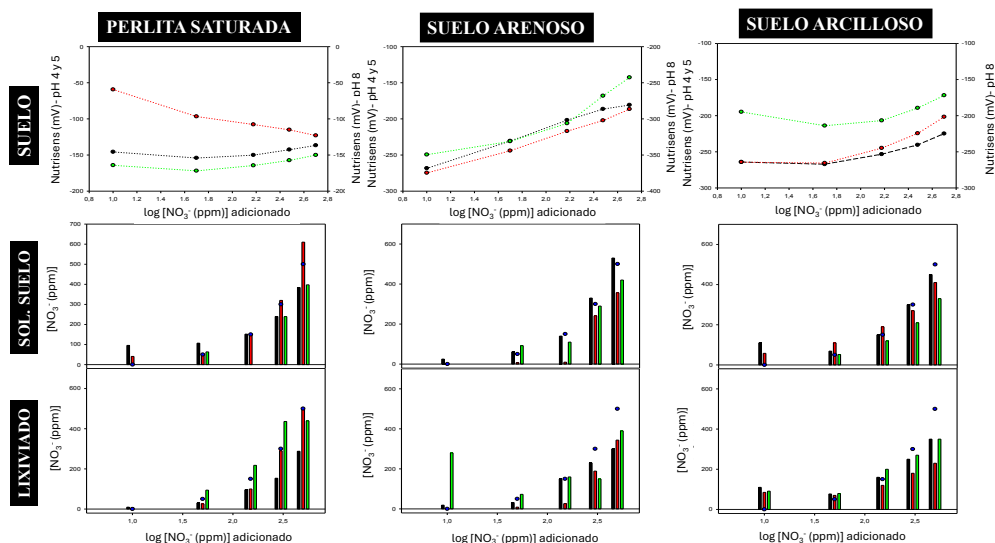


Fig 2. Respuesta obtenida en suelos de diferente tipología a la adición de nitrato, solución de suelo y lixiviación (negro: adiciones realizadas a pH 4, rojo: adiciones realizadas a pH 5, verde: adiciones realizadas a pH 8).

LAVADO

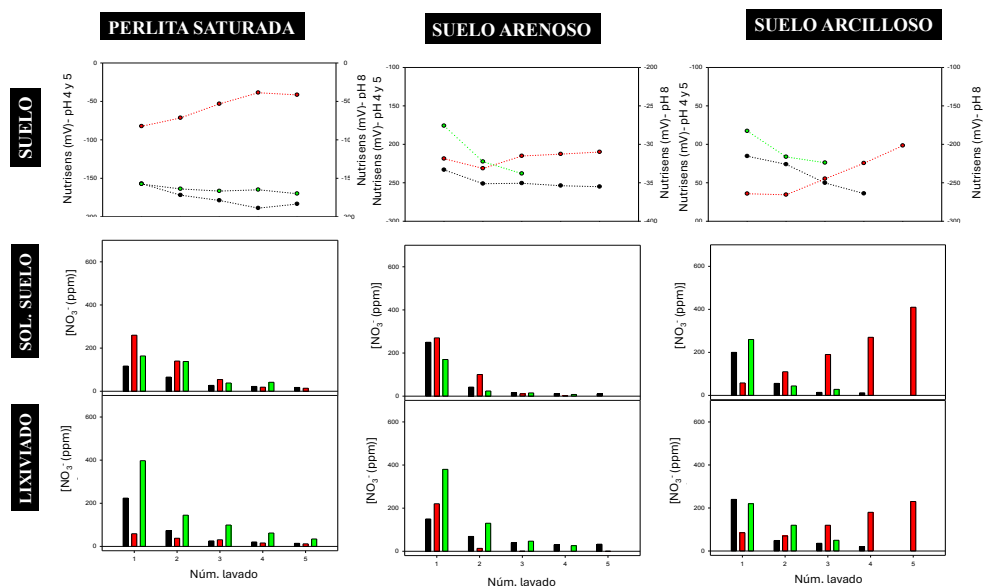


Fig 3. Respuesta obtenida en suelos de diferente tipología al lavado, solución de suelo y lixiviación (negro: adiciones realizadas a pH 4, rojo: adiciones realizadas a pH 5, verde: adiciones realizadas a pH 8).

comporta una mayor concentración en la solución del suelo (el que se aporta más el que se lava).

En el caso del suelo arenoso, un aporte de nutrientes conlleva un aumento del nitrato que presente en el suelo. A pH 5 (rojo), se observa que apenas hay nitrato en la solución del suelo y este tampoco se encuentra en la lixiviación. Más adelante se va a discutir con más profundidad este aspecto.

En el suelo arcilloso, por sus características intrínsecas, puede tener una mayor concentración de nitrato adsorbido en su estructura. Eso provoca que la señal se mantenga estable en las primeras adiciones, indicando que lo que se aporta es inferior a lo que se encuentra adsorbido en el suelo. A pH 5

(rojo), en general, se observa una mayor tendencia a que el nitrato quede en la solución del suelo a nivel de raíces y, por lo tanto, este se encuentra en menor proporción en la lixiviación.

Referente a la lixiviación, y tal como era de esperar, se observa una mayor lixiviación en el caso de la perlita y una menor en el caso de la arcilla. Destaca la lixiviación del nitrato del suelo arenoso que se observa a pH 8 (verde) con la primera adición.

B. Lavado

Los datos relativos al comportamiento con el lavado de los diferentes suelos se muestran en la figura 3.

En el caso de la perlita saturada, a pH 4 (negro) y 8 (verde) se observa una ligera bajada del nitrato que se encuentra en el suelo. Con los lavados, también disminuye la concentración de nitrato que se encuentra en la solución del suelo y en el lixiviado. Destaca la lixiviación que se observa a pH 8. En cambio, a pH 5 (rojo), se observa un incremento de la concentración de nitrato que hay en el suelo con los lavados, indicando que, de alguna manera, en estas condiciones, estamos liberando el nitrato que se encontraba retenido en fracciones no lábiles del suelo. Este nitrato se encontraría ya en mayor disposición para poder ser asimilado por las plantas.

En el suelo arenoso, se muestra una disminución del nitrato fijado en el suelo con los lavados consecutivos a pH 4 y 8. En cambio, a pH 5, después de una primera bajada empieza a subir el nitrato en el suelo. Con la adición de nutrientes (ver figura 2) a este pH, el nitrato se encontraba en una menor concentración en la solución del suelo y en lixiviación que en el resto. No se observó una mayor sensibilidad en la respuesta comparado con el resto de pHs evaluados, por lo que probablemente este nitrato se ha quedado fijado en fracciones de suelo menos lábiles que no son detectables con el Nutrisens. Bajo ciertas condiciones, el nitrato previamente fijado en estas fracciones se puede movilizar hacia fracciones del suelo más accesibles para las plantas. Esto provoca un el incremento del nitrato fijado en la estructura del suelo en estas fracciones más lábiles.

En el caso de este suelo arenoso, destaca la lixiviación que se observa a pH 8 (verde). Se observa una mayor disminución del nitrato adsorbido en el suelo a este pH, indicando también la liberación del nitrato fijado en el suelo, en este caso de fracciones más lábiles que sí son detectadas con el Nutrisens.

Finalmente, en el suelo arcilloso se observa una disminución del nitrato adsorbido en el suelo tanto a pH 4 (negro) como 8 (verde). En cambio, a pH 5 (rojo), con los primeros lavados se mantiene estable el nitrato adsorbido en el suelo y en solución de suelo. La concentración del lixiviado es inferior que para el resto de pHs evaluados. Con los siguientes lavados, parece que se moviliza en nitrato fijado en estructuras del suelo menos lábiles hacia fracciones más disponibles que son detectadas con el Nutrisens. Al mismo tiempo aumenta la concentración en la solución del suelo y en la disolución lixiviada.

IV. CONCLUSIONS

Para maximizar la producción agrícola de alimentos son necesarias condiciones en las que se pueda mantener una concentración adecuada de nutrientes en la solución del suelo

a nivel de raíces y/o suelos con una elevada capacidad tampón. Al mismo tiempo se quiere minimizar la lixiviación para evitar problemas medioambientales.

En el caso de la perlita del estudio, su capacidad de retención de nutrientes viene dado por la elevada capacidad de mantener el nitrato en solución.

En el caso del suelo arenoso, la aplicación de fertilizantes/riegos a pH 5 comporta una menor concentración de nitrato en la solución del suelo. No obstante, este se esta fijando a fracciones del suelo poco accesibles para las plantas. Bajo ciertas condiciones se puede revertir esta situación y movilizarlo para favorecer su asimilación por parte de las plantas.

El suelo arcilloso en estudio, en cambio, muestra una mayor tendencia a mantener el nitrato en solución del suelo a pH 5 y una menor capacidad de retención en la estructura del suelo a pH 8.

Desde el punto de vista de la lixiviación, se debería evitar los riegos con pH básicos en el suelo arenoso en estudio y a pH 5 en el caso del suelo arcilloso, ya que tienden a la lixiviación. En el caso del suelo arenoso, esto se produce por desadsorción del nitrato fijado en las fracciones más accesibles del suelo mientras que en el suelo arcilloso se produce una movilización del nitrato a fracciones más accesibles.

AGRADECIMIENTOS

Los autores quieren agradecer por su contribución económica al Ministerio Español de Ciencia e Innovación a través del proyecto PID2020-117216RB-I00, al Govern de la Generalitat de Catalunya a través del proyecto 2021SGR00124 y a la empresa VerdeSmart por la cesión de diferentes materiales.

REFERENCIAS

- [1] E. Nakao, Y. Kitazumi, K. Kano and O. Shirai, "Pollution control of nitrate-selective membrane by the inner solution and on-site monitoring of nitrate concentration in soil" *Analytical Sciences*, vol 37, pp. 887-891, 2021.
- [2] Havlin, J.L.; Tisdale, S.L.; Nelson, W.L.; Beaton, J.D. (2017). *Soil fertility and fertilizers: an introduction to nutrient management*. Pearson. ISBN-978-93-325-7034-4
- [3] PCT/ES2016/070853, Continuous monitoring probe in real time of chemical parameters of interest directly in soils and system for continuous monitoring and in real time of said chemical parameters of interest.
- [4] C.M.A. Brett, "Electrochemical sensors for environmental monitoring. Strategy and examples" *Pure Appl. Chem*, vol 73 (12), pp. 1969-1977, 2001.
- [5] <https://www.horiba.com/esp/water-quality/pocket-meters/>

Hacia un Sensor Electroquímico Basado en Carbohidratos de *Leishmania*

Carolina Sofía Touloumdjian
Departamento de Ingredientes Activos
y Biorrefinería
Instituto Nacional de Tecnología
Industrial
San Martín, Buenos Aires, Argentina
ctouloumdjian@inti.gob.ar

Federico José Williams
Instituto de Química Física de los
Materiales, Medio Ambiente y Energía
CONICET
Ciudad Universitaria, Buenos Aires,
Argentina
fwilliams@qi.fcen.uba.ar

Eleonora Elhalem
Departamento de Ingredientes Activos
y Biorrefinería
Instituto Nacional de Tecnología
Industrial / CONICET
San Martín, Buenos Aires, Argentina
eelhalem@inti.gob.ar

Santiago Esteban Herrera
Instituto de Química Física de los
Materiales, Medio Ambiente y Energía
CONICET
Ciudad Universitaria, Buenos Aires,
Argentina
sherrera@qi.fcen.uba.ar

María Julieta Comin
Gerencia Operativa de Desarrollo
Tecnológico e Innovación
Instituto Nacional de Tecnología
Industrial / CONICET
San Martín, Buenos Aires, Argentina
jcomin@inti.gob.ar

Lucía Gandolfi Donadio
Departamento de Ingredientes Activos
y Biorrefinería
Instituto Nacional de Tecnología
Industrial / CONICET
San Martín, Buenos Aires, Argentina
lgandolfi@inti.gob.ar

Abstract— La leishmaniasis es un problema de salud pública que afecta particularmente a la región norte de nuestro país. En la actualidad, es deseable contar con un método de diagnóstico específico, económico y accesible incluso en zonas aisladas y de bajos recursos. En este trabajo se presentan los avances en el desarrollo de un sensor impedimétrico basado en hidratos de carbono constitutivos de glicolípidos superficiales de *Leishmania*. Se utilizaron oligosacáridos sintéticos que se inmovilizaron sobre un electrodo de oro a través una de reacción de acoplamiento con tioles ácido-terminales autoensamblados. La unión de los azúcares a la superficie se confirmó por espectroscopía de impedancia electroquímica (EIS) y espectrometría fotoelectrónica de rayos X (XPS). La respuesta del sensor se basó en los cambios registrados en la resistencia de transferencia de carga y en la capacidad de doble capa eléctrica para el par $\text{Fe}(\text{CN})_6^{4-}/\text{Fe}(\text{CN})_6^{3-}$ mediante mediciones de EIS luego de incubar el electrodo en una matriz dada. El sistema desarrollado se puso a prueba en un ensayo de reconocimiento de anticuerpos séricos anti-glicano de pacientes con leishmaniasis tegumentaria americana. El método utilizado mostró indicios de ser capaz de distinguir sueros infectados de no infectados.

Palabras clave— *Leishmania*, sensor electroquímico, espectroscopía de impedancia.

I. INTRODUCCIÓN

El lipofosfoglicano (LPG) y los glicoinositolfosfolípidos (GIPLs) de *Leishmania* son glicolípidos de superficie muy abundantes e inmunogénicos [1–4] lo que los hace biomoléculas relevantes para el desarrollo de tests de diagnóstico específicos. En Argentina, *L. braziliensis* es el principal agente causante de la leishmaniasis tegumentaria americana (LTA), enfermedad endémica en la región. En el caso de *L. braziliensis*, los glicolípidos de superficie contienen unidades de galactofuranosa (Gal_f), residuo presente en microorganismos, pero no en mamíferos, que ha sido reportado como antigénico [5,6].

Las alternativas de diagnóstico que involucran sensores electroquímicos presentan una alta sensibilidad, su fabricación es de bajo costo y su empleo no requiere reactivos adicionales como, por ejemplo, sistemas de marcación (en el caso del ELISA, anticuerpos unidos a enzimas) [7]. En particular, la espectroscopía de impedancia electroquímica

(EIS, por sus siglas en inglés) permite detectar pequeños cambios en la composición superficial de electrodos, tales como la adsorción específica de biomoléculas. Asimismo, existen antecedentes de aplicación de esta técnica para la detección eficaz de lectinas[8] y microorganismos [9,10] utilizando hidratos de carbono como sondas.

El presente trabajo propone el desarrollo de un sistema electroquímico para diagnóstico, conformado por un electrodo funcionalizado con azúcares antigénicos de membrana de *Leishmania*. Se seleccionaron cinco fragmentos constitutivos del LPG y los GIPLs de *Leishmania braziliensis* que contienen galactofuranosa (Fig. 1, compuestos 1-5) para ser utilizados como elementos de reconocimiento de anticuerpos anti-glicano circulantes en sueros infectados.

Con el fin de acceder a compuestos puros y debidamente caracterizados de las estructuras seleccionadas, se recurrió a la síntesis química (Fig. 1). Se añadió un motivo 5-aminopentilo en el extremo reductor de los azúcares para inmovilizarlos mediante una reacción de acoplamiento a una monocapa de tioles autoensamblados sobre un electrodo de

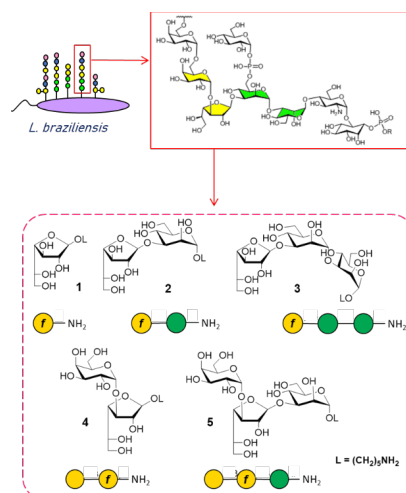


Fig. 1. Galactofuranósidos de membrana de *Leishmania* 1-5 obtenidos por síntesis química.

oro. Los electrodos fueron caracterizados con técnicas de análisis de superficies a fin de confirmar la unión de los azúcares.

Recientemente, el grupo del Dr. Igor Almeida de la Universidad de Texas reportó que el compuesto **2** mostró inmunorreactividad en un ensayo de ELISA en presencia de sueros de pacientes positivos de LTA [11]. Se eligió, entonces, este fragmento para poner a prueba el sistema desarrollado. Luego de modificar la superficie con el glicósido, se midió la respuesta electroquímica por EIS frente a la incubación con pools de sueros positivos y negativos de LTA.

II. DESARROLLO

A. Funcionalización de la superficie de Au

Los electrodos utilizados fueron superficies ultraplanas (rugosidad cuadrática media de 0.6 nm) de Au obtenidas mediante la técnica de desmolde en plantilla de Si/SiO₂ [12]. Sobre los mismos, se depositó una monocapa de tioles mixtos autoensamblados (SAM): ácido 11-mercaptopundecanoico (MUA) y 6-mercaptohexanol (MH). La posibilidad de fijar la relación molar entre un tiol reactivo frente al grupo amino (el MUA) y uno inerte (el MH) permitió modular la proporción de azúcares en la superficie. Seguidamente, los grupos carboxilos de la SAM se activaron por tratamiento con EDC/NHS, y luego se expusieron al aminoglicósido elegido para formar la unión amida. Por último, para bloquear aquellas posiciones que no hubieran reaccionado se realizó una incubación con etanolamina.

B. Caracterización superficial

La progresión de las reacciones de superficie durante la funcionalización se monitoreó por EIS. Las mediciones se realizaron en una celda de teflón de tres electrodos utilizando Ag/AgCl como electrodo de referencia, una malla de Pt como contraelectrodo y una solución 1:1 de [Fe(CN)₆]³⁻/[Fe(CN)₆]⁴⁻ en KNO₃ como cupla redox en solución. Los espectros obtenidos se ajustaron al circuito equivalente de Randles (Fig. 2) para obtener la resistencia de transferencia de carga (R_{ct}) y la capacidad de doble capa eléctrica (C_{dl}) del sistema.

Por otro lado, la incorporación de los glicósidos fue evaluada mediante espectrometría fotoelectrónica de rayos X (XPS, por sus siglas en inglés). Para ello, tres soportes independientes se trataron con: (a) MUA; (b) MUA, EDC/NHS y el monosacárido **1**; (c) MUA, EDC/NHS y el trisacárido **5**. Los espectros obtenidos se procesaron e integraron y se analizaron las regiones características de S2p, N1s, C1s y O1s.

C. Evaluación de la respuesta del sensor impedimétrico frente a sueros humanos positivos y negativos de leishmaniasis tegumentaria americana

Se utilizaron muestras archivadas de suero de individuos diagnosticados por distintas técnicas (ELISA, PCR y frotis) como positivos o negativos para leishmaniasis tegumentaria americana (LTA). Las mismas fueron provistas por el Dr. J. Diego Marco del Instituto de Patología Experimental de la Universidad Nacional de Salta.

Partiendo de 16 muestras de suero humano se obtuvieron dos pools: uno consistente de 8 sueros de individuos con diagnóstico positivo para LTA (pool positivo, LTA+) y otro de 8 sueros individuales de diagnóstico negativo (pool

negativo, LTA-). Para los ensayos se utilizaron diluciones seriadas en PBS 1x entre 1:2560 y 1:160 de cada uno de ellos.

Se prepararon dos electrodos independientes modificados con el compuesto **2**. Luego, se incubaron por 20 minutos con cada una de las diluciones del pool positivo o del pool negativo, yendo de menores a mayores concentraciones, realizando mediciones de EIS entre ellas. Como control de especificidad se preparó un electrodo sin azúcar, en el que los ácidos carboxílicos activados se hicieron reaccionar únicamente con etanolamina. Luego, se evaluó la respuesta frente a la incubación con el pool de sueros positivos.

Como medida de la respuesta electroquímica del sistema, se empleó la relación entre los parámetros de ajuste de los espectros antes (dilución infinita) y después de la exposición al pool de sueros (LTA+ o LTA-).

III. RESULTADOS Y DISCUSIÓN

El glicósido **1** se utilizó como modelo para la puesta a punto del protocolo de funcionalización de los electrodos de oro. La superficie se trató según lo descrito en la sección II.A y la progresión de las reacciones de funcionalización se monitoreó por EIS. Las curvas de Nyquist obtenidas luego de cada uno de los pasos se muestran en la Fig. 2. Los valores obtenidos a partir del ajuste de las curvas de S1 (Au), S2 (Au con tioles) y S3 (Au con tioles y **1**), esto es, la resistencia de la solución (R_s), R_{ct} y C_{dl}, se muestran en la tabla 1.

Los parámetros C_{dl} y R_{ct} se correlacionan con el grado de recubrimiento de la superficie. En el caso R_{ct}, un aumento en su valor indica un mayor grado de recubrimiento. En la tabla 1 se observa que este parámetro aumenta entre la medida realizada al oro limpio (S1) y la realizada luego de la incubación con la mezcla de tioles (S2), lo cual es consistente con la formación de la SAM sobre la superficie. Cuando existen grupos expuestos cargados negativamente, como es el caso del ácido carboxílico, la resistencia a la transferencia de carga es mayor por efecto de la repulsión eléctrica entre los grupos -COO⁻ y los aniones [Fe(CN)₆]³⁻/[Fe(CN)₆]⁴⁻. Por consiguiente, la disminución del valor de R_{ct} luego de exponer

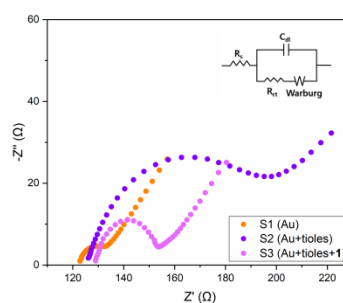


Fig. 2. Espectros de impedancia registrados a lo largo de la funcionalización de un electrodo de oro con **1**.

TABLA I. VALORES DE AJUSTE DE LOS ELEMENTOS DEL CIRCUITO EQUIVALENTE DE LOS ESPECTROS DE IMPEDANCIA REGISTRADOS A LO LARGO DE LA FUNCIONALIZACIÓN.

Espectro	R _s (Ω)	R _{ct} (Ω)	C _{dl} (μF)
S1	122.3	13.3	38.5
S2	125.8	77.6	37.1
S3	129.7	47.3	3.0

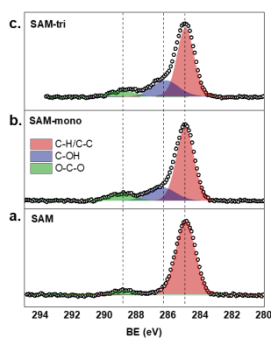


Fig. 3. Espectros de XPS de superficies de oro funcionalizadas con: (a) MUA, (b) MUA y **1** y, (c) MUA y **5**.

al electrodo a EDC/NHS y el glicósido **1** (S3) demuestra que el azúcar se encuentra anclado en superficie.

Para confirmar la incorporación efectiva de los glicósidos, se estudió la composición atómica de las superficies modificadas mediante XPS. Se registraron los espectros de tres superficies: (a) Au tratado con MUA; (b) Au tratado con MUA, EDC/NHS y el monosacárido **1** y; (c) Au tratado con MUA, EDC/NHS y el trisacárido **5**. En la Fig. 3 se presentan las señales observadas en la región del C. Los datos de S, N y O también fueron analizados (no disponibles en este resumen).

La superficie que no fue funcionalizada con los azúcares (Fig. 3.a) mostró señales a 285 y 289 eV correspondientes a los metilenos de la cadena de tiol y los carbonos carboxílicos, respectivamente, en una relación cercana a 1:10 consistentes con la unión de MUA (11 carbonos) a Au. Adicionalmente, en la región de O1s se registró un pico ancho, típico del grupo ácido. Luego, en la región de C1s de la superficie tratada con el glicósido **1** (Fig. 3.b) se observaron señales a 285 y 289 eV junto con un pico adicional a 286 eV, característico de átomos de C unidos a grupos hidroxilo. Asimismo, la región de N1s mostró un pico en 400 eV que sumó evidencia a la incorporación exitosa del azúcar. Por último, el espectro de la superficie tratada con **5** mostró los mismos picos en la región N1s y C1s, con mayor proporción de C característicos del azúcar (286 y 289 eV) respecto de los CH₂ (285 eV) mayoritarios en los alcanotioles (Fig. 3.c). La información obtenida fue consistente con la unión del trisacárido **5** a la superficie de oro.

Habiendo confirmado la efectividad del protocolo de modificación de superficie aplicado, se estudió la respuesta de un electrodo funcionalizado con **2** frente a sueros de pacientes con leishmaniasis tegumentaria americana. Para esta prueba, se utilizaron dos pools de sueros: un pool de sueros positivos (LTA+) y otro de sueros negativos (LTA-). Dos electrodos independientes se incubaron por 20 minutos con diluciones seriadas entre 1:160 y 1:2560 de LTA+ ó LTA- y, luego de cada incubación, se registraron los espectros de impedancia. Los valores de R_{ct} (R) y $R_{ct,C_{dl}}$ (R.C) obtenidos a partir de los ajustes realizados utilizando el circuito equivalente de la Fig. 2 se compararon con los valores registrados a dilución infinita (R_0 y $(R.C)_0$, respectivamente) (Fig. 4).

Al analizar ambas curvas, se observa que a diluciones mayores a 1:1000 la respuesta frente al suero positivo (color verde) fue baja y muy similar a la registrada con el suero negativo (color gris). Al aumentar la concentración, en cambio, se observó un aumento de hasta un 19% en el cociente

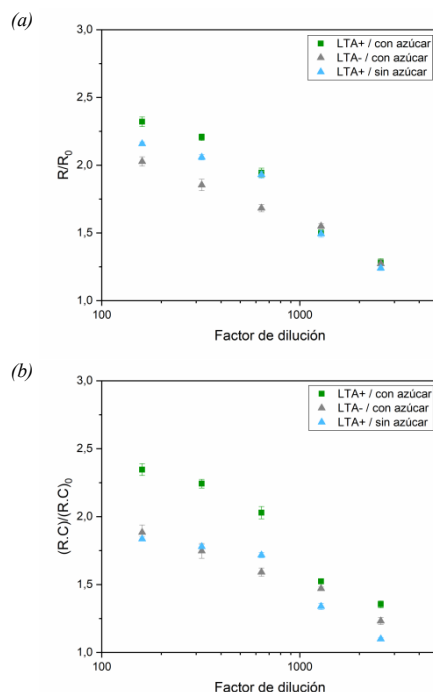


Fig. 4. Respuesta electroquímica registrada por EIS de electrodos funcionalizados con **2** e incubados con un pool de sueros negativos (LTA-, color gris) o pool de sueros positivos (LTA+, color verde) en función de la dilución. También se muestran los resultados de un electrodo control sin **2** expuesto al pool de sueros positivos (LTA+, color celeste). (a) Relación entre valores de R_{ct} antes (R_0) y después (R) de la incubación en función del factor de dilución. (b) Relación entre valores de $R_{ct,C_{dl}}$ antes ($(R.C)_0$) y después (R.C) de la incubación en función del factor de dilución. Las barras de error representan un desvío estándar luego de 3 mediciones consecutivas.

R/R_0 (dilución 1:320) y un 28% en el cociente $(R.C)/(R.C)_0$ (misma dilución, Fig. 5).

Para evaluar si el cambio registrado en la señal se debía a la interacción específica del pool positivo con el azúcar, se utilizó un electrodo control bloqueado en su totalidad con etanolamina (sin azúcar). Luego de cada incubación se registraron los espectros por EIS, las curvas de Nyquist se ajustaron y los parámetros obtenidos se procesaron y compararon con los datos obtenidos anteriormente. De ser específica la interacción, el electrodo control debía dar una señal comparable a la registrada con el electrodo funcionalizado con **2** e incubado con el suero negativo.

En el gráfico de R/R_0 (Fig. 4.a) no se evidenció una diferencia entre la respuesta del sistema ante sueros infectados respecto de la registrada en los controles. Sin embargo, esto no fue así cuando se eligió el cociente $(R.C)/(R.C)_0$ como indicador de respuesta (Fig 4.b). En este caso, a diluciones menores a 1:1000 el método muestra indicios de poder discriminar sueros infectados de sueros no infectados con *Leishmania* por interacción específica de las muestras con el glicósido **2**.

IV. CONCLUSIONES

Se modificaron electrodos de oro con fragmentos de hidratos de carbono de superficie de *L. braziliensis*. El protocolo de funcionalización elegido resultó adecuado para ese fin, como pudo comprobarse a partir de los estudios

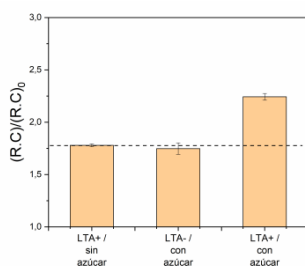


Fig. 5. Valores del cociente $(R.C)/(R.C)_0$ obtenidos en el estudio de la respuesta electroquímica (EIS) de un electrodo funcionalizado con **2** frente a la incubación con una dilución 1:320 del pool de sueros positivos (LTA+) o del pool de sueros negativos (LTA-). A la izquierda se muestra el valor obtenido del electrodo control sin azúcar incubado con sueros positivos (LTA+). Las barras de error representan un desvío estándar luego de 3 mediciones consecutivas.

realizados por EIS y XPS. Al evaluar por EIS la respuesta de un electrodo modificado con **2** frente a sueros de pacientes diagnosticados como positivos o negativos para LTA se observó que, al utilizar R.C como medida de la respuesta electroquímica, era posible diferenciar ambas muestras. Este resultado es coincidente con lo observado por ELISA. Para comprobar la eficacia del sistema de detección y, por lo tanto, la capacidad del azúcar de superficie de actuar como sonda en el reconocimiento de anticuerpos séricos, resta realizar un ensayo de reproducibilidad de la técnica.

El presente trabajo representa un gran avance en la aplicación de hidratos de carbono en sistemas electroquímicos, un área que hasta el momento ha sido poco estudiada. La técnica desarrollada junto con la selección adecuada de un elemento de reconocimiento específico puede representar una estrategia efectiva para el diagnóstico de la leishmaniasis tegumentaria americana, con vistas a la adaptación de esta tecnología a la detección de otras patologías.

AGRADECIMIENTOS

Este trabajo recibió financiación externa a través del PICT 2017-2569 (FONCYT, Agencia I+D+i).

REFERENCIAS

- [1] L. U. Buxbaum, "Leishmania mexicana Infection Induces IgG to Parasite Surface Glycoinositol Phospholipids that Can Induce IL-10 in Mice and Humans", *PLoS Negl. Trop. Dis.*, vol. 7, e2224, 2013.
- [2] J. L. Avila, M. Rojas, A. Acosta, "Glycoinositol phospholipids from American Leishmania and Trypanosoma spp: partial characterization of the glycan cores and the human humoral immune response to them", *J. Clin. Microbiol.* vol. 29, pp. 2305–2312, 1991.
- [3] W. K. Tonui, P. A. Mbatia, C. O. Anjili, A. S. Orago, S. J. Turco, J. I. Githure, D. K. Koech, "Transmission blocking vaccine studies in leishmaniasis: I. Lipophosphoglycan is a promising transmission blocking vaccine molecule against cutaneous leishmaniasis", *East Afr. Med. J.*, vol. 78, pp. 84–89, 2001.
- [4] C.-L. Forestier, Q. Gao, G.-J. Boons, "Leishmania lipophosphoglycan: how to establish structure-activity relationships for this highly complex and multifunctional glycoconjugate?", *Front. Cell. Infect. Microbiol.*, 4:193, 2015.
- [5] M. V. Arruda, W. Colli, B. Zingales, "Terminal beta-D-galactofuranosyl epitopes recognized by antibodies that inhibit Trypanosoma cruzi internalization into mammalian cells", *Eur. J. Biochem.*, vol. 182, pp. 413–421, 1989.
- [6] J. E. Bennett, A. K. Bhattacharjee, C. P. J. Glaudemans, "Galactofuranosyl groups are immunodominant in Aspergillus fumigatus galactomannan", *Mol. Immunol.*, vol. 22, pp. 251–254, 1985.
- [7] A. Hushegyi, J. Tkac, "Are glycan biosensors an alternative to glycan microarrays?", *Anal. Methods*, vol. 6, pp. 6610–6620, 2014.
- [8] A. Hushegyi, T. Bertok, P. Damborsky, J. Katrlík, J. Tkac, "An ultrasensitive impedimetric glycan biosensor with controlled glycan density for detection of lectins and influenza hemagglutinins", *Chem. Commun.*, vol. 51, pp. 7474–7477, 2015.
- [9] X. Guo, A. Kulkarni, A. Doepke, H. B. Halsall, S. Iyer, W. R. Heineman, "Carbohydrate-based label-free detection of escherichia coli ORN 178 using electrochemical impedance spectroscopy", *Anal. Chem.*, vol. 84, pp. 241–246, 2012.
- [10] F. Cui, Y. Xu, R. Wang, H. Liu, L. Chen, Q. Zhang, X. Mu, "Label-free impedimetric glycan biosensor for quantitative evaluation interactions between pathogenic bacteria and mannose", *Biosens. Bioelectron.*, vol. 103, pp. 94–98, 2018.
- [11] S. M. Viana, A. L. Montoya, A. M. Carvalho, B. S. de Mendonça, S. Portillo, J. J. Olivares, N. H. Karimi, I. L. Esteveao, U. Ortega-Rodríguez, E. M. Carvalho, W. O. Dutra, R. A. Maldonado, K. Michael, C. I. de Oliveira, I. C. Almeida, "Serodiagnosis and therapeutic monitoring of New-World tegumentary leishmaniasis using synthetic type-2 glycoinositolphospholipid-based neoglycoproteins", *Emerg. Microbes Infect.*, vol. 11, pp. 2147–2159, 2022.
- [12] E.A. Weiss, G. K. Kaufman, J. K. Kriebel, Z. Li, R. Schalek, G. M. Whitesides, "Si/SiO₂-templated formation of ultraflat metal surfaces on glass, polymer, and solder supports: Their use as substrates for self-assembled monolayers", *Langmuir*, vol. 23, pp. 9686–9694, 2007.

Sensor electroquímico para la evaluación de la corrosión de estructuras de hormigón armado

Gustavo S. Duffó
 Depto. Corrosión – CNEA
 CONICET – UNSAM
 Av. Gral. Paz 1499
 (1650) San Martín – Argentina
 duffo@cnea.gov.ar

Silvia B. Farina
 Depto. Corrosión – CNEA
 CONICET – UNSAM
 Av. Gral. Paz 1499
 (1650) San Martín – Argentina
 farina@cnea.gov.ar

Resumen — Una de las causas más frecuentes de deterioro de las estructuras de hormigón armado es la corrosión de los refuerzos. Por ese motivo, en el Depto. Corrosión de la Comisión Nacional de Energía Atómica (CNEA – Argentina) se desarrolló un sensor con el cual es posible medir adecuadamente varios parámetros asociados con dicho proceso, y con los cuales el especialista, utilizando normas o recomendaciones vigentes, puede conocer el estado de la estructura y tomar decisiones respecto a la necesidad de aplicar estrategias de remediación, en caso de ser necesarias. En el presente trabajo se describen las distintas aplicaciones que se le ha dado al sensor mencionado y que ha sido instalado tanto en estructuras nuevas como en preexistentes. Los resultados obtenidos muestran la ventaja del empleo de dichos sensores para evaluar el estado de una estructura de hormigón armado desde el punto de vista de la corrosión de los refuerzos.

Keywords— *Hormigón armado, sensores, corrosión*

I. INTRODUCCIÓN

Las estructuras civiles tales como puentes, represas hidroeléctricas y edificios requieren enormes esfuerzos de construcción, grandes inversiones y una vida útil considerable. Tales estructuras son vitales para los estándares de vida de la población y sus roturas prematuras y/o inesperadas suelen ser catastróficas en términos de tiempo, dinero y, en algunos casos, vidas. Esto lleva a la necesidad de la utilización de sistemas (no destructivos, en lo posible) de evaluación de dichas estructuras. Previo a la posibilidad del monitoreo *in-situ* de la corrosión de las barras de acero de refuerzo en un hormigón armado, el análisis del estado de tales estructuras se hacía por medio de la toma de muestras de hormigón o por medio del uso de técnicas invasivas (destructivas). Sin embargo, la posibilidad del empleo de sensores embebidos es menos invasiva, y permite la medición de señales analógicas que pueden ser obtenidas empleando dispositivos electrónicos externos a la estructura [1].

La complejidad de los diversos tipos de corrosión hace que este monitoreo sea dificultoso. La temperatura y la concentración de especies disueltas tales como el cloruro, afectan dramáticamente tanto el tipo de corrosión como su velocidad de propagación. Además, los parámetros controlantes pueden modificarse con el tiempo, requiriendo mediciones periódicas en tiempo real. Un sistema de medición de corrosión integrado debe ser capaz de medir adecuadamente, no sólo los parámetros electroquímicos relacionados con el proceso corrosivo en sí (resistencia de polarización, por ejemplo), sino también otros importantes parámetros medioambientales tales como temperatura,

concentración de iones cloruro, conductividad eléctrica del hormigón y disponibilidad de oxígeno. Una vez medidos dichos parámetros, el especialista puede recurrir a normas o recomendaciones para poder conocer la situación de la estructura y tomar decisiones respecto a la necesidad de aplicar estrategias de remediación, en caso de ser necesarias.

Con el objetivo de determinar el estado de una estructura de hormigón armado desde el punto de vista de la corrosión de sus armaduras, deben ser considerados los siguientes parámetros [2-4]:

* *Potencial de corrosión.* Este valor es la diferencia de potencial entre un electrodo fabricado con el mismo acero de refuerzo empleado en la estructura y un electrodo de referencia. El valor medido, analizado bajo ciertas normas, provee información cualitativa del estado de la barra de refuerzo cercana al lugar de la medición.

* *Velocidad de corrosión.* Este parámetro es generalmente medido basado en la técnica de la resistencia de polarización lineal. La medición se efectúa empleando un electrodo fabricado con el mismo acero de refuerzo, un electrodo de referencia y un contraelectrodo inerte, generalmente de acero inoxidable

* *Resistividad eléctrica del hormigón.* Este valor es uno de los factores más importantes que controlan la velocidad de corrosión del acero, ya que está directamente relacionado con el contenido de humedad. Se suele obtener a partir de la medición de la resistencia eléctrica entre electrodos inertes y es posteriormente convertida a resistividad empleando una constante de calibración correspondiente al arreglo geométrico de electrodos empleado.

* *Transporte de oxígeno.* Este es otro de los parámetros importante que controla la velocidad de corrosión del refuerzo. Se lo mide con una combinación de dos electrodos inertes y un electrodo de referencia, determinando la denominada *densidad de corriente límite de oxígeno*.

* *Contenido de cloruro.* Se mide a partir de la medición de la diferencia de potencial entre un electrodo específico de cloruros y un electrodo de referencia, para luego convertirlo en concentración de cloruro a partir de una curva de calibración. Los sistemas que detectan cambios en el contenido de cloruro dentro del hormigón suelen ser utilizados como alerta temprana para predecir deterioros en la estructura.

* *Temperatura.* Puesto que todos los procesos químicos, electroquímicos y de transporte son, en mayor o menor medida, térmicamente activados, la corrosión del acero

dependerá de la temperatura y por ende, es de fundamental importancia conocer su valor dentro de la estructura considerada.

Sensores embebibles capaces de medir todos estos parámetros están disponibles en el mercado internacional, pero con precios prohibitivos para el mercado local, debido a su alto grado de sofisticación (muchas veces, innecesaria). En el presente trabajo se presenta un sensor desarrollado en el Depto. Corrosión de la Comisión Nacional de Energía Atómica. Este sensor, embebido permanentemente en una estructura de hormigón armado, se puede emplear para el seguimiento del deterioro de una estructura, ya sea nueva o preexistente, por medio de la medición de los parámetros mencionados más arriba. Con estos parámetros el especialista puede tomar decisiones respecto a la durabilidad de la estructura analizada. Por supuesto que hay variadas técnicas para el seguimiento del proceso de corrosión, pero las empleadas en el sensor desarrollado son las más simples y económicas y las que proveen la mayor exactitud y reproducibilidad en los resultados. En el presente trabajo se describen las distintas aplicaciones que se le ha dado al sensor mencionado y que ha sido instalado tanto en estructuras nuevas como en preexistentes. Los resultados obtenidos muestran la ventaja del empleo de dichos sensores para evaluar el estado de una estructura de hormigón armado desde el punto de vista de la corrosión de los refuerzos.

II. DESARROLLO Y APLICACIONES

El sensor consta de diversos electrodos, los cuales, juntamente con un termómetro de platino (Pt100) son embebidos en una resina especial, resistente al medio alcalino del hormigón (Fig. 1). La parte expuesta de los electrodos (y el termómetro envainado) son luego recubiertos con un mortero poroso y el conjunto es montado sobre las armaduras para el caso de una construcción nueva o embebido en una estructura ya existente por medio de la realización de una perforación y su posterior cobertura con mortero de reparación. En la figura 2 se muestran los electrodos con su función específica, y la forma de incluirlo en la estructura a analizar.

Las mediciones con este sensor se efectúan con potenciostatos-galvanostatos de uso común en laboratorios de corrosión o en campo, de manera de obtener los parámetros deseados. En cuanto a los métodos de medición, la temperatura, el potencial de corrosión y el potencial del electrodo específico de cloruros se determinan en forma pasiva a partir de datos generados por el sensor; mientras que, para las mediciones de la resistividad eléctrica del hormigón, el flujo de oxígeno y la densidad de corriente de corrosión es necesario generar una señal que perturbe al sensor y lo que se mide es la respuesta a esta perturbación [1].

La primera aplicación del sensor desarrollado fue para determinar la susceptibilidad a la corrosión de una estructura de hormigón armado correspondiente a un proyecto tendiente a seleccionar al material más idóneo para la fabricación de un contenedor de residuos radioactivos de nivel bajo de actividad, cuya durabilidad debe ser mayor que 300 años [5].



Fig. 1. Sensor previo a ser cubierto con mortero de reparación

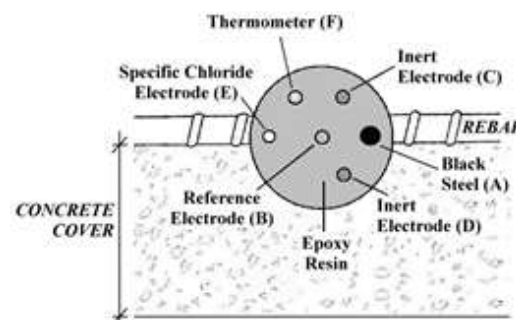


Fig. 2. Esquema de los electrodos del sensor y forma de instalación en la estructura a analizar.

Posteriormente, y a pedido de concesionarios de diversas represas hidroeléctricas del país (Piedra del Águila, Alicurá y Cabra Corral) se instalaron estos sensores para determinar el estado de tendones de acero embebidos en material cementíceo, ya sea correspondientes a tendones de anclaje como de estructuras postensadas. Los resultados de las mediciones, hasta el momento, revelaron que las velocidades de corrosión son consistentes con la vida útil prevista para las centrales mencionadas [6, 7].

Por una invitación cursada por la Comisión de Energía Atómica de Bélgica (SCK) y subsidiada por un Proyecto Europeo de Cooperación (ESV-Euridice-GV), se instrumentó un prototipo de supercontenedor de residuos radioactivos de alta actividad, que se construyó en el Laboratorio Magnel de la Universidad de Ghent. Dicho proyecto involucró la participación de varios grupos internacionales, de manera de poder contrastar diversas técnicas de medición. Los sensores desarrollados en el grupo fueron los únicos que proveyeron datos cuantitativos en tiempo real de la evolución del proceso de corrosión a medida que el hormigón de la estructura se hidrataba [8].

Ante el requerimiento de NASA (Nucleoeléctrica Argentina Sociedad Anónima) se instrumentó un silo de almacenamiento en seco de combustibles nucleares quemados de la Central Nuclear Atucha I. Dicho silo es un depósito transitorio de combustibles gastados, y debido a las altas dosis radiactivas presentes, tiene un espesor de pared de hormigón y una densidad de armaduras poco frecuente.

Se instalaron varios sensores y se están tomando datos desde el mismo inicio de la colada del hormigón. Por otro lado, también se instrumentó el reactor nuclear CAREM 32 (Central Argentina de Elementos Modulares) cuya construcción se viene llevando a cabo en las cercanías de los reactores nucleares Atucha I y II.

También se han empleado en un prototipo de contenedor de residuos radioactivos de bajo nivel de actividad fabricado con hormigones de alta performance, (Fig. 3) [9, 10]. Se puede apreciar cómo el sensor detecta el decrecimiento de la velocidad de corrosión a medida que las reacciones de hidratación de hormigón tienen lugar, y el efecto que los cambios de temperatura debidos a las diferentes estaciones del año, tienen sobre la velocidad de corrosión. Idéntico comportamiento se ha obtenido al medir la resistividad eléctrica del hormigón y el flujo de oxígeno.

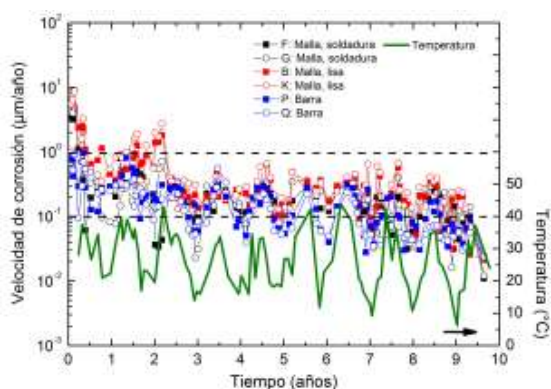


Fig. 3. Resultados obtenidos con el sensor desarrollado embebido en un prototipo de contenedor de residuos radioactivos.

También se destaca el empleo de estos sensores en diversos trabajos llevados a cabo en cooperación con otros grupos, tales como los ensayos realizados con Centro de Construcciones del INTI; el LEMIT (Laboratorio de Entrenamiento Multidisciplinario para la Investigación Tecnológica) en una estación experimental de Mar del Plata y en un trabajo de cooperación internacional con el Instituto Eduardo Torroja de Ciencias de la Construcción, auspiciado por el Consejo Superior de Investigaciones Científicas (CSIC) del Reino de España, donde se están comparando resultados de diversos sensores y de técnicas de medición de los parámetros requeridos para determinar el estado de una estructura de hormigón armado.

En la actualidad, se están realizando modificaciones sobre el sensor, de manera de poder medir independientemente la velocidad de corrosión a partir del análisis de la corriente galvánica generada entre dos electrodos. Los resultados obtenidos al presente muestran que esta técnica también es promisoría para estimar la velocidad de deterioro de una estructura de hormigón armado.

III. CONCLUSIONES

Luego de más de 15 años del desarrollo del sensor de corrosión para estructuras de hormigón armado, llevado a cabo en el Depto. Corrosión de la Gerencia Materiales de la Comisión Nacional de Energía Atómica, se puede establecer que su empleo en diversas áreas (energía nuclear, energía hidroeléctrica, estructuras civiles, etc.) ha sido exitoso.

La utilización de estos sensores en la determinación de parámetros relacionados con la corrosión de armaduras es una de las herramientas más promisorias y económicas de predecir la vida útil de una estructura de hormigón armado. Su ventaja es el bajo costo y la posibilidad de emplearlo tanto en estructuras en construcción o en estructuras preexistentes.

AGRADECIMIENTOS

Los autores agradecen los subsidios recibidos por parte del FONCYT (Ministerio de Ciencia, Tecnología e Innovación, Argentina) y el CONICET (Consejo Nacional de Investigaciones Científicas y Técnicas).

REFERENCIAS

- [1] G.S. Duffö and S.B. Farina, "Development of an embeddable sensor to monitor the corrosion process of new and existing reinforced concrete structures", *Construction and Building Materials*, 23, (2009), 2746-2751.
- [2] J. McCarter and Ø. Vennesland, "Sensor systems for use in reinforced concrete structures", *Construction and Building Materials*, 18, (2004), 351-358.
- [3] J.P. Broomfield, K. Davies and K. Hladky, "The use of permanent corrosion monitoring in new and existing reinforced concrete structures", *Cement Concrete Comp.*, Vol. 24 (2002), 27-34.
- [4] P. Pedferri, R.B. Polder, L. Bertolini and B. Elsener, "Corrosion of Steel in Concrete: Prevention, Diagnosis, Repair", Wiley-VCH, Weinheim (2004).
- [5] G.S. Duffö, E.A. Arva, F.M. Schulz and D.R. Vazquez, "Durability of a reinforced concrete designed for the construction of an intermediate-level radioactive waste disposal facility", *Journal of Nuclear Materials*, 420, (2011), 382-387.
- [6] A.L. Burkart, G.S. Duffö and P. Castro, "Corrosion Monitoring for Integrity Assessment of Post-Tensioned Strands at Piedra del Aguila Spillway", *Hydropower and Dams International Journal*, 6, (2014), 64-70.
- [7] G.S. Duffö, A.L. Burkart y D. Aguiar, "Evaluación de integridad de anclajes y monitoreo de la corrosión en el aprovechamiento hidroeléctrico AES-Alicura". *Proceeding Congreso CONAMET-SAM 2015 – XV Congreso Internacional de Metalurgia y Materiales. Concepción (Chile) 17 al 20 de noviembre de 2015.*
- [8] B. Kursten, F. Druyts, L. Areias, Y. van Ingelgem, D. De Wilde, G. Nieubourg, G. S. Duffö and C. Bataillon, "Preliminary results of corrosion monitoring studies of carbon steel overpack exposed to supercontainer concrete buffer", *Corrosion Engineering, Science and Technology*, 49, (2014), 485-491.
- [9] D. R. Vazquez, Y. Villagran Zacardi, C. Zega, M. E. Sosa and G. S. Duffö, "Implementation of different technics for the monitoring of reinforced concretes corrosion applied to rebar embedded in concretes with ordinary and pozzolanic Portland cement", *Procedia Materials Science*, 8, (2015), 73-81.
- [10] D.R. Vazquez, "Corrosión del refuerzo en el hormigón. Análisis de diversas variables involucradas y de las técnicas de detección", Tesis Doctoral, Instituto Sabato (CNEA-UNSAM) (2023).

Biofuncionalización de electrodos de carbono serigrafiados para la detección de arsénico (III)

Reartes Daiana Fernanda
INFIQC, Departamento de Físicoquímica,

Facultad de Ciencias Químicas, Universidad Nacional de
Córdoba,
Córdoba, Argentina
daiana.reartes@unc.edu.ar

Rodriguez Marcela Cecilia
INFIQC, Departamento de Físicoquímica,
Facultad de Ciencias Químicas, Universidad Nacional de
Córdoba
Córdoba,
Córdoba, Argentina
marcela.rodriguez@unc.edu.ar

Resumen—En este trabajo, se presenta un enfoque innovador que utiliza una bioplataforma nanoestructurada basada en quitosano (Qs) y nanopartículas de oro (NPsAu) para lograr una detección sensible y selectiva de arsénico lo que lo convierte en una herramienta prometedora para la monitorización rápida y efectiva de la contaminación por arsénico en el agua potable. El objetivo de este trabajo es obtener un nanosensor portátil capaz de detectar de manera sensible y selectiva bajas concentraciones de arsénico como indicador de alto impacto en el ámbito clínico y ambiental, empleando voltamperometría de pulso diferencial (DPV). Para lograr este objetivo, se realizó un pretratamiento electroquímico de la superficie del electrodo para optimizar su respuesta y estabilidad. Luego, se procedió a la modificación de la superficie mediante el cubrimiento de un biocompósito de nanopartículas de oro y quitosano. Una vez que se establecieron todos los parámetros necesarios, se evaluó la respuesta de la plataforma electroquímica para diferentes concentraciones de arsénico, así como frente a potenciales interferentes que podrían estar presentes en las muestras. Esta plataforma funcionalizada promueve el adecuado reconocimiento del analito y contribuye a la detección altamente sensible y selectiva de arsénico (III), aún en presencia de altas concentraciones de potenciales interferentes como plomo, cadmio y cromo.

Palabras clave: nanosensor electroquímico, arsénico (III), nanopartículas de oro, quitosano

I. INTRODUCCIÓN

Los sensores para la detección de arsénico tienen aplicaciones importantes en la monitorización ambiental y la salud pública. Se han realizado estudios para evaluar estos sensores en la detección eficiente de contaminación por arsénico y en la prevención de enfermedades relacionadas con la exposición a este agente tóxico. La exposición prolongada al arsénico, principalmente a través del agua y alimentos contaminados, puede tener efectos graves en la salud. La toxicidad del arsénico está relacionada con su capacidad para interferir con procesos biológicos esenciales en el organismo humano, como la síntesis de proteínas y el metabolismo celular. [1]. La exposición prolongada al arsénico, principalmente a través del agua y alimentos contaminados, puede tener efectos graves en la salud, de allí la importancia del monitoreo de sus niveles ambientales en poblaciones urbanas [1]. El uso de metodologías electroquímicas se presenta como una prometedora herramienta que facilita la detección en bajos niveles de concentración, permitiendo la prevención de efectos perjudiciales a través de mediciones simples y de bajo costo [2]. La utilización de nanomateriales funcionalizados o compósitos de nanomateriales y (bio)polímeros es una opción altamente interesante para lograr la detección exitosa de este indicador debido a sus propiedades

físicoquímicas distintivas. En los últimos años se ha trabajado en el desarrollo de (bio)sensores portátiles y de bajo costo que puedan ser utilizados en el campo para la detección rápida de arsénico en agua potable. Estos dispositivos son especialmente importantes en áreas donde la contaminación por arsénico es un problema grave.

En este trabajo, se propone una bioplataforma nanoestructurada basada en el uso de nanopartículas de oro (NPsAu) y Quitosano (Qs) para llevar a cabo la cuantificación sensible y selectiva de arsénico (III). La estrategia de detección se basa en la fuerte interacción que se establece entre el arsénico y las NPsAu. El objetivo del presente trabajo es obtener un nanosensor portátil de dimensiones mínimas para la detección sensible y selectiva de arsénico como indicador de alto impacto tanto en el ámbito clínico como ambiental empleando la técnica de DPV.

II. MATERIALES Y MÉTODOS

A. Materiales

Quitosano Fluka ($C_s \geq 95\%$ desacetilado, 150–275 kDa, viscosidad 100–200 mpa.s disuelto en ácido acético al 1,0%). Benzoquinona (BQ), cloruro de potasio (KCl), hexacianoferrato de potasio (III) ($K_3[Fe(CN)_6]$), hexacianoferrato(II) de potasio trihidrato ($K_4[Fe(CN)_6]$), trihidrato de ácido tetracloroáurico(III) El 99 %, citrato de sodio, se obtuvo de Sigma-Aldrich. Se usó una solución de 0,020 M de tampón fosfato (PBS) pH 7,40 para disolver BQ.

B. Aparatos

Las mediciones electroquímicas fueron llevadas a cabo en el Epsilon Workstation (BAS) [3-4]. Las condiciones de trabajo de técnica voltamperometría de pulso diferencial (DPV) empleadas fueron: Potencial inicial: -0,50 V. Potencial final: 1,0V. Scan rate: 20,0 mV. Step: -4,0 mV. Pulse Width: 50 ms. Pulse period: 200 ms. Pulse amplitude: 50,0 mV. Pulse Type: Voltamperometry. Para voltamperometría cíclica se realizó un barrido de potencial desde -0,60 V a 0,80 V empleando una solución de buffer fosfato 0,050 M pH 7,40 a una velocidad de barrido de 0,050 V/s.

Para las determinaciones electroquímicas se utilizaron electrodos de carbono serigrafiados comerciales provistos por Metrohm DropSens (DRP-110) [5]. Estos electrodos serigrafiados (SPE) constituyen una microcelda electroquímica en sí misma de 34 mm de longitud, 10 mm de ancho y 0,5 mm de espesor. Están compuestas por un electrodo de trabajo de carbono (4 mm de diámetro), un electrodo auxiliar de carbono y un electrodo de pseudo referencia de plata, impresos en un sustrato de cerámica. Estos SPE son aptos para el uso de microvolúmenes (pueden

trabajar con el volumen de una gota), para ensayos descentralizados o para desarrollar sensores específicos [6]. Se empleó una solución de $K_3[Fe(CN)_6]/K_4[Fe(CN)_6]$ 0,050 M en KCl 1,0 M como sonda redox en los ensayos electroquímicos.

Los registros espectrales UV-Vis (entre 350 nm y 750 nm) de este trabajo se obtuvieron con un espectrofotómetro Shimadzu UV-2600 utilizando una celda de cuarzo de 0,100 cm a temperatura ambiente [4,7].

III. RESULTADOS Y DISCUSIONES

A. Caracterización óptica

La síntesis del compuesto de Qs con NPsAu se estudió empleando espectroscopia UV-vis, y los registros obtenidos se muestran en la Figura 1. En la curva espectral (a) se puede observar un máximo en la intensidad de pico en la zona de 530-540 nm que indica la presencia de la banda de plasmón superficial típica de NPsAu esféricas. Con los datos obtenidos del espectro y empleando la ecuación propuesta por el grupo de Haiss [8] se estimó el tamaño de las NPsAu. El tamaño promedio obtenido fue de 50 nm, valor congruente con los datos reportados por la bibliografía [9]. Para el espectro UV-vis de una solución de nanopartículas de oro recubiertas con quitosano (NPsAu-Qs) (b) se evidencia un claro pico de absorción, pero con menor intensidad, indicando que la interacción del quitosano con las NPsAu afecta las propiedades ópticas de estas.[10].

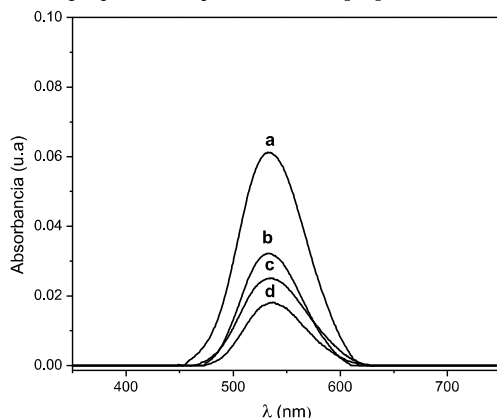


Figura 1: Espectros UV-vis de (a) NPsAu, (b) NPsAu-Qs, (c) NPsAu - Qs-As (III) 0,001ppm, (d) NPsAu -Qs-As(III) 0,1ppm

También se realizó el seguimiento del compuesto obtenido NPsAu-Qs en presencia del analito, observándose una disminución de la intensidad de la señal a medida que aumenta la concentración del mismo (c y d). Esto se debe a que las NPsAu, que forman parte del compuesto, en presencia de arsénico forman aglomerados que producen una disminución en la señal óptica debido a la baja disponibilidad de estas. Se han reportado previamente resultados similares que relacionan la disminución de la intensidad de banda del plasmón superficial como consecuencia de la agregación de NPsAu recubiertas inducida por la presencia de As (III) [9]. Por lo tanto, la interacción del compuesto con el arsénico conduce a cambios en el entorno de las nanopartículas y provoca la agregación de las mismas debido a la adsorción del arsénico en su superficie.

B. Activación del electrodo de carbono serigrafiado y modificación con el compuesto

Se llevó a cabo un pretratamiento de la superficie del electrodo portátil serigrafiado de carbono (SPE) aplicando diferentes potenciales anódicos: 1,0 V; 1,2 V; 1,4 V y 1,6V empleando una solución de buffer fosfato (PBS) 0,050 M pH 7,40 durante 60 segundos. El objetivo de este procedimiento es mejorar el comportamiento redox de la superficie del electrodo de trabajo con respecto a la respuesta de un electrodo sin pretratar. En este proceso se empleó voltamperometría cíclica (VC) utilizando como analito soporte 1-4 benzoquinona (BQ) empleando una solución de PBS 0,050 M pH 7,40 como electrolito soporte[5].

TABLA I. RESPUESTA DE BQ EN FUNCIÓN DEL PRETRATAMIENTO DE LA SUPERFICIE DEL ELECTRODO SERIGRAFIADO (SPE)

Superficie SPE			
	Potencial aplicado (V)	Epa (V)	Ipa/Ipc
Sin pretratamiento	-	0,16	0,45
Con pretratamiento	1	0,10	0,50
	1,2	0,07	0,65
	1,4	-0,08	0,80
	1,6	-0,07	0,80

De acuerdo con los resultados reportados en la Tabla I se puede observar que, entre los potenciales 1,40 V y 1,60 V no se registraron cambios significativos tanto en el potencial de pico anódico (Epa) para BQ como en la relación de corrientes de pico anódica y catódica (Ipa/Ipc), lo que permite concluir que el potencial óptimo para realizar la activación de la superficie del electrodo de trabajo es 1,40 V; durante 60 segundos en una solución de buffer fosfato 0,050 M pH 7,40; evitando el empleo de potenciales mayores, estos resultados coinciden con reportes previos de la literatura [5]. Posteriormente, la superficie del SPE pretratado se modificó con el compuesto AuNPs-Qs, seguido del tratamiento a temperatura y tiempo controlados (50°C durante 15 minutos) para asegurar la adhesión de la plataforma (AuNPs-Qs/SPE).

C. Estudio del efecto del tiempo y del potencial de acumulación de As

El efecto del tiempo y del potencial de acumulación de arsénico se llevó a cabo sobre SPE/AuNPs-Qs a través de experimentos de DPV, utilizando soluciones estándar de arsénico (III) 1,0 ppm empleando como electrolito soporte HCl 1,0M. En primera instancia, se realizó el estudio del tiempo de acumulación del analito mediante convección forzada (400 rpm). En la Figura 2 puede observarse un aumento gradual en el valor de la Ip a medida que se incrementa el tiempo de acumulación hasta 180 s. Tiempos mayores no producen incrementos significativos en la respuesta demostrando mayor dispersión en los valores de Ip obtenidos. Por lo tanto, se seleccionó como tiempo óptimo de acumulación 180 s en condiciones de convección forzada a 400 rpm.

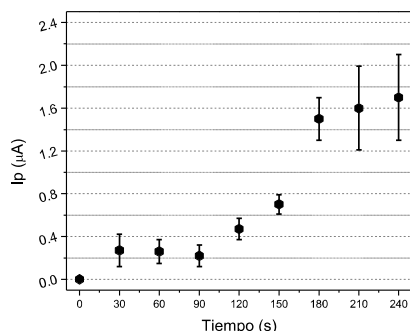


Figura 2: Respuesta de I_p obtenida de ensayos de DPV empleando una solución estándar de As (III) empleando HCl 1,0 M como electrolito soporte para diferentes tiempos de acumulación.

Una vez seleccionado el tiempo óptimo de trabajo, se procedió a una segunda optimización variando el potencial de acumulación ya que es un factor determinante en la detección de arsénico en ensayos electroquímicos.

En la Figura 3 se observa que a partir de $-0,100$ V y hacia potenciales más negativos hay un ligero incremento de la I_p hasta alcanzar un valor de potencial de $-0,500$ V en donde la respuesta crece notablemente. Potenciales más negativos que $-0,500$ V no produjeron cambios significativos, por lo que este valor de potencial fue seleccionado como el óptimo para la acumulación de arsénico.

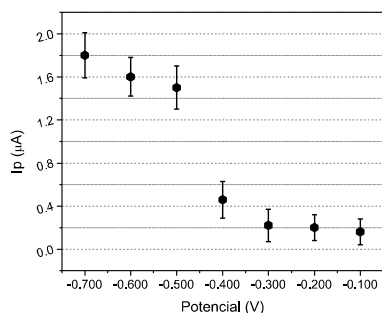


Figura 3: Respuesta de DPV de soluciones de As (III) en HCl 1M a diferentes potenciales de acumulación

D. Determinación de los parámetros analíticos

Para evaluar el desempeño analítico del sensor se realizó la correspondiente curva de calibración para distintas concentraciones de arsénico (Figura 4). El comportamiento de la plataforma está relacionado directamente con la aglomeración de las NPsAu, dando origen a las interacciones de afinidad que presenta el compuesto NPsAu con As (III) [11]. A medida que la concentración disminuye se produce una mayor aglomeración de NPsAu, aumentando la especificidad de interacción de la plataforma electroquímica en presencia del analito. Como consecuencia, se obtiene un incremento en la respuesta de corriente [12]. En cambio, en

altas concentraciones de As (III) la superficie electroquímica se encuentra saturada y se desfavorecen las interacciones del arsénico produciendo una menor respuesta electroquímica similar a la del blanco.

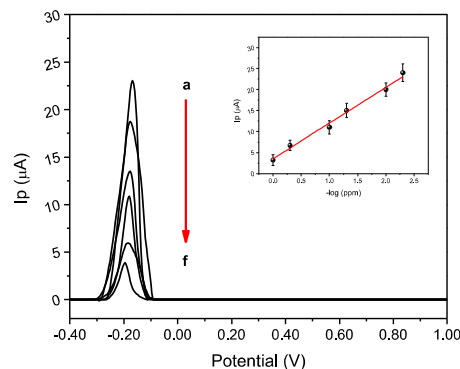


Figura 4: Respuestas de corriente del As (III) en un amplio intervalo de concentraciones desde 5ppb hasta 1000ppb. Con un tiempo de acumulación de 180s a -500 mV en condiciones de convección forzada. Inset: Grafico de $-\log$ de la concentración.

Por otra parte, para realizar el estudio de la selectividad se emplearon soluciones estándar de Pb(II), Cd(II) y Co(II) a una concentración de 10 ppb como potenciales interferentes de la plataforma electroquímica de estudio. (figura 5).

Los resultados obtenidos demuestran que la plataforma electroquímica presenta una gran selectividad frente al arsénico (III) incluso en presencia de interferentes, pudiendo detectar concentraciones menores al límite de 10 ppb establecido por la Organización Mundial de la Salud (OMS) en aguas de consumo humano.

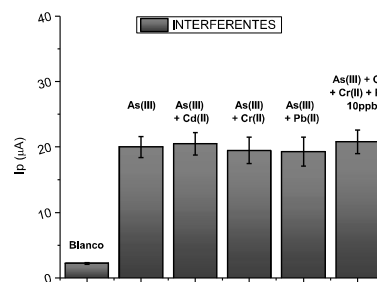


Figura 5: Respuestas de la superficie electroquímica de soluciones de As(III) en presencia de interferentes de estándar de Pb(II), Cd(II) y Co(II) a una concentración de 10 ppb.

IV. CONCLUSIONES

Se obtuvo un método de pretratamiento óptimo para la activación de la superficie del electrodo de trabajo y se demostró que la bioplataforma obtenida (SPE/NPsAu-Qs/As(III)) presenta una gran sensibilidad, cuantificando

concentraciones en el rango de 5 a 1000ppb, por debajo del límite de 10ppb establecido por la Organización Mundial de la Salud (OMS). Con las caracterizaciones ópticas se demostró que la presencia As (III) modifica la distribución de las NPs Au produciendo una disminución de absorbancia en presencia de concentraciones bajas de arsénico. En lo que respecta a los resultados electroquímicos, se determinaron condiciones óptimas de tiempo y potencial de acumulación para la detección de As (III) y se concluyó que esta bioplataforma presenta una interacción sensible y eficiente para As(III). También se demostró que, conforme aumenta la presencia de As(III) en la superficie, se produce una disminución de la señal de corriente hasta obtener respuestas similares al blanco. También se realizaron pruebas con diversos interferentes demostrando una gran selectividad de la plataforma hacia As(III) en presencia de potenciales interferentes tales como Cd(II), Co(II) y Pb(II). Esta novedosa plataforma abre las puertas para el desarrollo de sensores descentralizados que permiten el monitoreo del arsénico como indicador ambiental en poblaciones urbanas donde los niveles de arsénico son un problema grave.

V. AGRADECIMIENTOS

Las autoras agradecen el apoyo económico de CONICET, SECyT-UNC, Ministerio de Ciencia, Tecnología e Innovación de la Nación y ANPCyT.

DFR agradece la Beca doctoral otorgada por CONICET.

REFERENCIAS

- [1] Rodríguez, Marcela C., et al. "Applications of Carbon Nanotubes-Based Electrochemical Sensing Strategies for Heavy Metals and Arsenic Quantification. *In Pure and Functionalized Carbon Based Nanomaterials*. CRC Press, 2020. p. 197-227.
- [2] Ramírez, María L., et al. "Cysteine functionalized bio-nanomaterial for the affinity sensing of Pb (II) as an indicator of environmental damage". *Microchemical Journal*, 2018, vol. 141, p. 271-278.
- [3] Jalit, Y., Moreno, M., Gutierrez, F. A., Sanchez Arribas, A., Chicharro, M., Bermejo, E., ... & Rodríguez, M. C. "Adsorption and electrooxidation of nucleic acids at glassy carbon electrodes modified with multiwalled carbon nanotubes dispersed in polylysine" *Electroanalysis*, 2013, vol. 25, no 5, p. 1116-1121.
- [4] Gallay, P., López Mujica, M., Bollo, S., & Rivas, G. " Genosensing Applications of Glassy Carbon Electrodes Modified with Multi-Walled Carbon Nanotubes Non-Covalently Functionalized with Polyarginine" . *Micromachines*, 2022, vol. 13, no 11, p. 1978.
- [5] Moreno, M., Arribas, AS, Bermejo, E., Chicharro, M., Zapardiel, A., Rodríguez, MC, ... & Rivas, GA (2010). "Detección selectiva de dopamina en presencia de ácido ascórbico utilizando electrodos serigrafiados modificados con nanotubos de carbono". *Talanta* , 80, vol. 5, pp. 2149-2156.
- [6] Metrohm, *Electrodo serigrafiado de carbono 110*. (Oline). Disponible: https://www.metrohm.com/es_es/products/110/110.html
- [7] Gutierrez, Fabiana Andrea, María Dolores Rubianes, and Gustavo Adolfo Rivas. "New bioanalytical platform based on the use of avidin for the successful exfoliation of multi-walled carbon nanotubes and the robust anchoring of biomolecules. Application for hydrogen peroxide biosensing." *Analytica Chimica Acta*, 2019, vol. 1065, p. 12-20.
- [8] Haiss, W., Thanh, N. T., Aveyard, J., & Fernig, D. G. (2007). "Determination of size and concentration of gold nanoparticles from UV-Vis spectra". *Analytical chemistry*, 79, vol. 11, pp. 4215-4221.
- [9] Harisha, K. S., Narayana, B., & Sangappa, Y. (2021). "Highly selective and sensitive colorimetric detection of arsenic(III) in aqueous solution using green synthesized unmodified gold nanoparticles". *Journal of Dispersion Science and Technology*, 2023, vol. 44, no 1, pp. 132-143.
- [10] Huang, L., Zhai, M., Peng, J., Xu, L., Li, J., & Wei, G. (2007). "Synthesis, size control and fluorescence studies of gold nanoparticles in carboxymethylated chitosan aqueous solutions." *Journal of colloid and interface science*, 316(2), 398-404.
- [11] Boruah, B. S., Daimari, N. K., & Biswas, R. (2019). "Functionalized silver nanoparticles as an effective medium towards trace determination of arsenic (III) in aqueous solution". *Results in Physics*, vol. 12, pp. 2061-2065.
- [12] Kim, S., Lee, S., Kim, S., Shin, J., Cha, B. S., Lee, E. S., & Park, K. S. (2024). "Colorimetric detection of arsenite using Tris-mediated gold nanoparticle aggregation and chitosan lateral flow strip-based signal enhancement". *Sensors and Actuators B: Chemical*, 2024, vol. 407, pp. 13546.

A Simplified Do-It-Yourself Protocol for Manufacturing Dual-Detection Paper-Based Analytical Devices for Saliva-Based Diagnostics

Lucas R. Sousa
Instituto de Química
Universidade Federal de Goiás
 Goiânia, GO, Brazil and
Laboratório de Biosensores y Bioanálisis (LABB), Departamento de Química Biológica e IQUIBICEN-CONICET, Facultad de Ciencias Exactas y Naturales
Universidad de Buenos Aires
 CABA, Argentina
 l.rod.sousa@gmail.com

Karoliny A. Oliveira
Instituto de Química
Universidade Federal de Goiás
 Goiânia, GO, Brazil
 karoliny.almeida@gmail.com

Habdias A. Silva-Neto
Instituto de Química
Universidade Federal de Goiás
 Goiânia, GO, Brazil
 habdiasneto@hotmail.com

Eduardo Cortón
Laboratorio de Biosensores y Bioanálisis (LABB), Departamento de Química Biológica e IQUIBICEN-CONICET, Facultad de Ciencias Exactas y Naturales
Universidad de Buenos Aires
 CABA, Argentina
 eduardo@qb.fcen.uba.ar

Wendell K. T. Coltro
Instituto de Química
Universidade Federal de Goiás
 Goiânia, GO, Brazil
 wendell@ufg.br

Lucas F. Castro
Instituto de Química
Universidade Federal de Goiás
 Goiânia, GO, Brazil
 lucas_decastro2015@hotmail.com

Federico Figueredo
Laboratorio de Biosensores y Bioanálisis (LABB), Departamento de Química Biológica e IQUIBICEN-CONICET, Facultad de Ciencias Exactas y Naturales
Universidad de Buenos Aires
 CABA, Argentina
 figueredofederico@yahoo.com

Abstract — This work presents the development of dual microfluidic paper-based analytical devices (μ PADs) integrating both colorimetric and electrochemical detection modules. The μ PADs were fabricated using a commercial 3D pen with acrylate photopolymer for carbon ink and hydrophobic barriers, the dual- μ PADs offer a low-cost, versatile platform for point-of-care diagnostics. The device was tested for lactate, pH, nitrite, and salivary amylase (sAA) in saliva samples from both healthy individuals and those with periodontitis. Results showed that individuals with periodontitis had elevated levels of nitrite and sAA, lower pH, and minimal lactate compared to healthy individuals. The dual- μ PADs demonstrated a limit of detection of $10.7 \mu\text{mol L}^{-1}$ for nitrite, 94.16 U mL^{-1} for sAA, and 0.06 mmol L^{-1} for lactate, proving effective for early diagnosis of periodontal disease. The proposed method offers a simple and affordable approach to manufacturing μ PADs, costing approximately \$0.05 per device.

Keywords — μ PADs, saliva, colorimetric detection, electrochemical detection, periodontitis.

I. INTRODUCTION

Microfluidic paper-based analytical devices (μ PADs) have garnered significant attention for point-of-care testing (POCT) due to their advantages, including affordability, sensitivity, specificity, and accessibility to end-users. [1,2] Additionally, the ease of integrating various detection techniques with this type of instrumentation makes them viable for different target analytes. While colorimetric detection is often highlighted as the pioneering approach [3], there are also reports of using other techniques such as electrochemistry [4], fluorescence [5], and mass spectrometry [6].

Currently, μ PADs can be fabricated using a variety of techniques and can be applied across diverse fields such as

clinical diagnostics, food quality control, environmental monitoring, biotechnology, materials science, and petrochemistry. [1,7] From a clinical perspective, the literature reveals the use of μ PADs for screening and prognosis of various socially impactful diseases, utilizing different biological fluids.[8]

Saliva, for example, can be useful for a different systematic diseases and oral cavity-related diseases. Several works reported before the use of saliva samples to evaluate the health status of patients for preventive diagnosis or even for prognosis of oral diseases such as periodontitis or gingivitis.[9,10]

Periodontitis is a chronic inflammatory disease leading to periodontal tissue destruction and tooth loss, that affects 5–20% of adults in the world. Due to the variability in salivary biomarkers among individuals with different medical histories and risk factors, multiplex analysis is essential for early diagnosis. While microbiological tests are time-consuming, recent studies highlight other salivary biomarkers, such as biomolecules, inorganic compounds, and enzyme activity, as being correlated with periodontitis. [9]

In this study, we developed a μ PAD incorporating both colorimetric and electrochemical modules for clinical analysis in saliva. The primary aim of this device is to detect the presence of target analytes, including lactate, pH, nitrite, and salivary amylase, to monitor bacterial levels in the saliva of both healthy individuals and patients with periodontitis.

Our preliminary studies indicate that μ PADs designed for dual detection demonstrate a significant analytical response for each of these analytes, paving the way for further investigation into the diagnostic performance of these devices in clinical settings.

II. MATERIALS AND METHODS

A. μ PADs fabrication

The μ PAD was fabricated using a commercial 3D pen filled with an acrylate photopolymer, which was used both for the carbon ink to create the electrodes and for the paper microfluidic barriers. The electrodes were fabricated using a stencil-printing technique, while a pen-on-paper drawing strategy was employed to create hydrophobic barriers. The device integrates electrochemical and colorimetric modules, with electrodes and microfluidic channels created on paper substrates using low-cost materials and without the need for any electrical equipment. The colorimetric modules were developed by impregnating specific reagents for nitrite, sAA, and pH into their respective detection zones. After fabricating the microfluidic channels, solutions containing the reagents were precisely deposited using micropipettes to ensure uniform distribution. The devices were cured with a UV light flashlight (wavelength = 400 nm) before being sealed with adhesive films to prevent contamination and evaporation. The performance of the colorimetric detection was evaluated by spiking artificial saliva with known concentrations of each analyte, followed by visual and software-assisted analysis to quantify the color intensity changes. Fig. 1 shows the fabrication steps of the μ PAD, including the colorimetric and electrochemical modules.

B. Colorimetric and electrochemical detection

Colorimetric data were analyzed using the Photometrix® app, which is available for free download on the Apple Store.[11] To capture images under ambient light conditions, a smartphone was positioned 5 cm above the μ PAD with the aid of a 3D-printed support. Electrochemical detection was performed using a bipotentiostat/galvanostat model μ Stat400 (DropSens, SL, Oviedo, Spain) monitored by DropView software.

The colorimetric reagents were pre-impregnated in the detection zones in the following order: for nitrite, the modified Griess reaction was used with sulfanilamide and NED; for sAA, a mixture of povidone/potassium iodide and starch was used; and for pH, bromothymol blue indicator was employed. For the electrochemical detection of lactate, the working electrode surface was modified with Prussian blue nanocubes and the enzyme lactate oxidase (LOx).

C. Saliva analysis

To demonstrate the clinical feasibility of diagnosing salivary biomarkers, unstimulated saliva samples were collected from five volunteers, including both healthy individuals and those with periodontal diseases, in accordance with ethical principles approved by the ethical committee of the Federal University of Goiás (CAAE n° 68,271,817.9.0000.5083). The samples, used without prior treatment, were analyzed for lactate, nitrite, pH, and α -amylase concentrations using the proposed dual- μ PADs. Standard solutions were prepared with artificial saliva, and the results were compared with those from a reference method.

D. Calibration method

The calibration method involved spiking an artificial saliva sample with standard solutions of nitrite, sAA, and lactate, in concentration ranges of 25-30 $\mu\text{mol.L}^{-1}$, 200-100 U.mL^{-1} , and 0.2-1.0 mmol.L^{-1} , respectively. For pH calibration, the sample was spiked with sodium acetate buffer (pH 3.7) and adjusted with PBS buffer (pH 7.2). After spiking, different concentrations within these ranges were measured using the corresponding method for each analyte. Evaluation was performed using a colorimetric app for nitrite, sAA, and pH, and chronoamperometry for lactate. Measurements were taken in quintuplicate to obtain the calibration curve.

III. RESULTS

The dual detection μ PADs have been employed to detect different target analytes and also used to determine important disease biomarkers in body fluids. However, traditional fabrication methods of these devices often require heavy equipment such as ovens or heaters, and many involve costly printers. Additionally, wax printers are no longer available. This creates a pressing need for alternative, simpler fabrication methods suitable for point-of-care applications. In this regard, the do-it-yourself (DIY) approach has gained traction, allowing for the inexpensive and straightforward production of μ PADs. This DIY concept can also be adapted to other dual- μ PAD detection modes, making them more accessible for point-of-care use

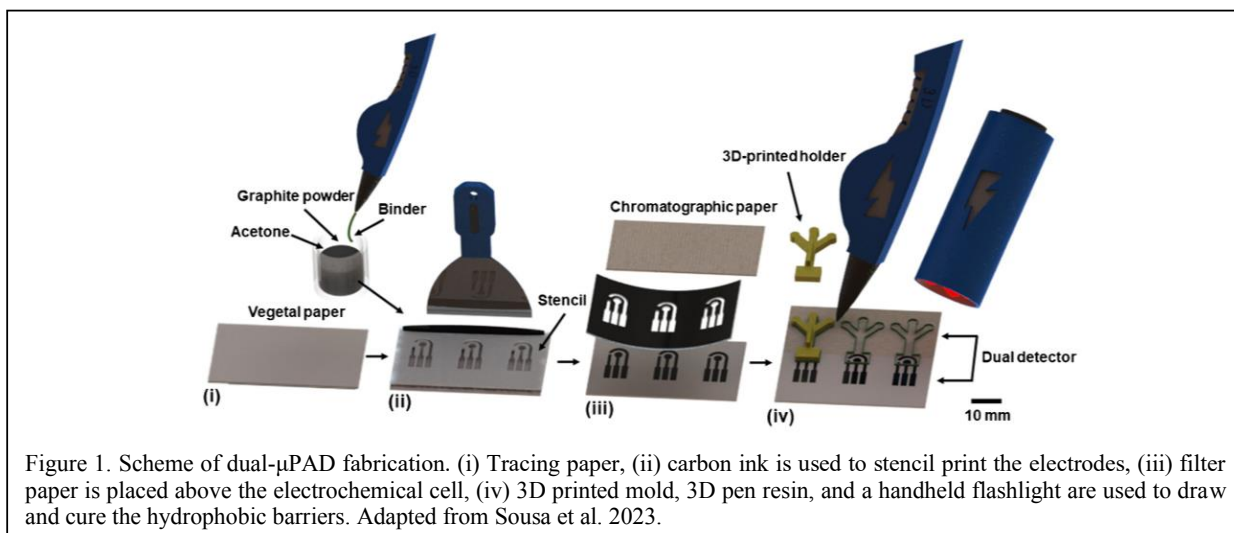


Figure 1. Scheme of dual- μ PAD fabrication. (i) Tracing paper, (ii) carbon ink is used to stencil print the electrodes, (iii) filter paper is placed above the electrochemical cell, (iv) 3D printed mold, 3D pen resin, and a handheld flashlight are used to draw and cure the hydrophobic barriers. Adapted from Sousa et al. 2023.

To address reproducibility problems concerning manual fabrication, a 3D-printed mold was used to create microfluidic channels and detection zones. Due to the viscous nature of the polymer resin, complete penetration into the paper surface took about 5 minutes when applied on one side. For each analysis, a volume of 130 μL , using was sufficient to cover the colorimetric detection zones and conduct electrochemical measurements.

A. Electrodes fabrication and modification

The conductive ink was made by mixing graphite powder with a polymer solution from a 3D pen, using acetone as a diluent, in ratios of 60:40, 50:50, and 40:60 (polymer to graphite). Higher polymer content increased electrical resistance due to its insulating properties, leading to reduced conductivity and decreased Faradaic current. The 40:60 ratio provided optimal performance with a peak-to-peak separation of ~ 250 mV and comparable results to screen-printed electrodes. The electroactive area of the 40% polymer electrodes was 6.58×10^{-2} cm^2 . Variations in electrode geometric area were noted, but reproducibility tests showed no significant statistical differences.

To perform the lactate detection, the electrodes were modified with Prussian Blue (PB) and lactate oxidase (LOx). This modification was based on previously reported work by Sgobbi et al. (year).[12] Through chronoamperometric analysis and studies using scanning electron microscopy (SEM), we observed that the modification was sufficient for conducting the analysis of the target analyte.

B. Analytical clinical evaluation

The analytical performance of the device was simultaneously evaluated for lactate, pH, nitrite and salivary amylase (sAA) analysis. The colorimetric sAA analysis protocol on paper analytical devices is reported here for the first time. The limit of detection (LOD) calculated by the colorimetric analytical curve was $10.7 \mu\text{mol.L}^{-1}$ for nitrite, 94.16 U.mL^{-1} for sAA and a 0.5 units of resolution for pH. For electrochemical detection, amperometric measurements for lactate were recorded achieving limit of detection of 0.06 mmol.L^{-1} . Saliva samples collected from both healthy individuals and those with periodontitis were employed to test the dual- μPAD .

As can show in Table individuals with periodontitis showed high levels of nitrite and sAA ($>94 \mu\text{mol.L}^{-1}$ and $> 610 \text{ U.mL}^{-1}$) in comparison with healthy individuals ($\leq 16 \mu\text{mol.L}^{-1}$ and 545 U.mL^{-1}). Moreover, periodontitis saliva resulted in acid pH and almost null lactate levels. The recovery tests obtained values between 85 and 120% for all tests. Based on the data presented, it can be seen that the increase in bacterial biomarkers in saliva leads to increased sAA concentrations and decreased lactate levels. These results were expected since nitrite is directly associated with the presence of bacteria that produce this compound. Consequently, the presence of bacteria also reduces the levels of pH and nutrients present in saliva, which explains the increase in available sAA and the decrease in lactate. In addition, these values were compared with reference methods to compare the reliability of the dual- μPAD s.

TABLE 1. VALUES OF BIOMARKERS FOUND IN SALIVA SAMPLES EMPLOYING THE DUAL- μPAD S AND REFERENCE METHOD^a

Samples	Nitrite (μM)		sAA (U/mL)		pH		Lactate (mM)	
	μPAD	Referen ce method	μPAD	Referen ce method	μPAD	Referen ce method	μPAD	Referen ce method
Control #1	<LD	<LD	429.6 ± 1.3	440.4 ± 0.1	7.2 \pm 0.1	7	0.8 \pm 0.1	0.92 ± 0.1
Control #2	<LD	<LD	380.1 ± 1.4	373.3 ± 0.1	7.2 \pm 0.1	7	0.7 \pm 0.1	0.65 ± 0.1
Control #3	15.8 ± 1.6	16.7 ± 0.1	544.6 ± 5.1	540.9 ± 0.1	6.4 \pm 0.2	6	0.7 \pm 0.1	0.60 ± 0.1
Periodontit is #1	94.5 ± 3.8	94.6 ± 0.1	610.5 ± 2.1	606.5 ± 0.1	6.3 \pm 0.1	6	<LD	0.003 7 \pm 0.1
Periodontit is #2	106.1 ± 2.1	103.3 ± 0.1	641.1 ± 1.2	655.4 ± 0.1	5.5 \pm 0.1	6	<LD	0.001 2 \pm 0.1

^a Adapted from Sousa et al. 2023

IV. CONCLUSION


The proposed protocol provides a simple and cost-effective method for the fabrication of dual- μPAD s, which are versatile platforms for the sensitive detection of salivary biomarkers essential for point-of-care diagnostics in clinical settings. This method features a simplified manufacturing process that requires minimal equipment and no power supply, making it accessible and practical for widespread use. Each device costs approximately \$0.05, demonstrating its affordability. The integration of a 3D pen polymer to create both hydrophobic barriers and conductive ink highlights the innovation of this approach. The dual- μPAD s have been successfully validated for the detection of lactate, sAA, nitrite, and pH, demonstrating reliable analytical performance. The simplicity, cost-effectiveness, and versatility of this method position it as a promising tool for global implementation in point-of-care diagnostics.

ACKNOWLEDGMENT

The authors gratefully acknowledge financial support from the National Agency of Scientific and Technological Promotion (ANPCyT) (grant BID-PICT 2020-04023), CNPq (grants 307554/2020-1, 405620/2021-7 and 382604/2022-9), FAPEG (grant 202310267000258) and INCTBio (grant 465389/2014-7) and National Council for Scientific and Technological Research (CONICET). We would also like to thank the Faculty of Dentistry at the Federal University of Goiás.

REFERENCES

- [1] T. Ozer, C. McMahon, and C. S. Henry, "Advances in Paper-Based Analytical Devices," *Annual Review of Analytical Chemistry*, vol. 13, pp. 85–109, June 2020.
- [2] H. A. Silva-Neto, I. V. S. Arantes, A. L. Ferreira, G. H. M. do Nascimento, G. N. Meloni, W. R. de Araujo, T. R. L. C. Paixão, and W. K. T. Coltro, "Recent advances on paper-based microfluidic devices for bioanalysis," *TrAC Trends in Analytical Chemistry*, vol. 158, 116893, January 2023..
- [3] A. W. Martinez, S. T. Phillips, M. J. Butte, and G. M. Whitesides, "Patterned Paper as a Platform for Inexpensive, Low-Volume, Portable Bioassays," *Angewandte Chemie International Edition*, vol. 119, no. 8, pp. 1340–1342, February 2007.
- [4] J. Mettakoonpitak, K. Boehle, S. Nantaphol, P. Teengam, J. A. Adkins, M. Srisa-Art, and C. S. Henry, "Electrochemistry on Paper-based Analytical Devices: A Review," *Electroanalysis*, vol. 28, no. 7, pp. 1420–1436, July 2016.
- [5] S. Patel, R. Jamunkar, D. Sinha, Monisha, T. K. Patle, T. Kant, K. Dewangan, and K. Shrivastava, "Recent development in nanomaterials fabricated paper-based colorimetric and fluorescent sensors: A

- 
- review," *Trends in Environmental Analytical Chemistry*, vol. 31, September 2021
- [6] S. Chen, Q. Wan, and A. K. Badu-Tawiah, "Mass Spectrometry for Paper-Based Immunoassays: Toward On-Demand Diagnosis," *Journal of the American Chemical Society*, vol. 138, no. 20, May 2016
- [7] S. Chen, Q. Wan, and A. K. Badu-Tawiah, "Mass Spectrometry for Paper-Based Immunoassays: Toward On-Demand Diagnosis," *Journal of the American Chemical Society*, vol. 138, no. 20, May 2016.
- [8] S. Rink and A. J. Baeumner, "Progression of Paper-Based Point-of-Care Testing toward Being an Indispensable Diagnostic Tool in Future Healthcare," *Analytical Chemistry*, vol. 95, no. 3, pp. 1785–1793, 2023.
- [9] L. R. Sousa, H. A. Silva-Neto, L. F. Castro, K. A. Oliveira, F. Figueredo, E. Cortón, and W. K. T. Coltro, "Do it yourself" protocol to fabricate dual-detection paper-based analytical device for salivary biomarker analysis," *Analytical and Bioanalytical Chemistry*, vol. 415, pp. 4391–4400, 2023
- [10] T. W. Pittman, D. B. Decsi, C. Punyadeera, and C. S. Henry, "Saliva-based microfluidic point-of-care diagnostic," *Theranostics*, vol. 13, no. 3, pp. 1091–1108, Jan. 2023.

Use of peanut shell biochar in the formulation of inks for screen-printed electrodes

Florencia Bernassani
LABB, Laboratorio de Biosensors y Bioanálisis, Departamento de Química Biológica e IQUIBICEN-CONICET Facultad de Ciencias Exactas y Naturales, Universidad de Buenos Aires
 CABA, Argentina
fbernassani@qb.fcen.uba.ar

Federico Figueredo
LABB, Laboratorio de Biosensors y Bioanálisis, Departamento de Química Biológica e IQUIBICEN-CONICET Facultad de Ciencias Exactas y Naturales, Universidad de Buenos Aires
 CABA, Argentina
federicofigueredo@qb.fcen.uba.ar

Pablo Arnal
Centro de Tecnología de Recursos Minerales y Cerámica (CETMIC), CONICET-UNLP-CICPBA Facultad de Ciencias Exactas, Universidad Nacional de La Plata)
 La Plata, Argentina
arnal@quimica.unlp.edu.ar

Mónica Mosquera Ortega
BioAnalytical Chemistry Lab, Department of Agri-food, Environment and Animal Sciences (DiAA), University of Udine Udine, Italy.
monica.mosquera@uniud.it

Eduardo Cortón
LABB, Laboratorio de Biosensors y Bioanálisis, Departamento de Química Biológica e IQUIBICEN-CONICET Facultad de Ciencias Exactas y Naturales, Universidad de Buenos Aires
 CABA, Argentina
eduardo@qb.fcen.uba.ar

Abstract— The design of screen-printed electrodes (SPE) for compact, low-cost, and disposable electrochemical sensors has garnered significant attention from the scientific community in recent years. However, to achieve industrial scalability, it is crucial to address the cost of conductive inks and ensure their environmentally friendly disposal. A promising option that meets sustainability criteria is the use of biochar, pyrolyzed biomass waste, as a carbon source to replace conventional materials. In this study, SPEs were designed with varying concentrations of biochar. It was found that SPEs with a 15% mass loading still retained the properties of graphite electrodes. At higher concentrations, a decrease in performance was observed. Additionally, three different chemical treatments were employed to activate the biochar and enhance its properties. It was observed that employing a basic treatment improved electrochemical performance. These findings encourage further research to enhance the physicochemical properties of biochars and their implementation in sustainable electrodes for electroanalytical applications.

Keywords— biochar, peanut shell, screen-printed electrodes, electroanalysis.

I. INTRODUCTION

The development of compact and disposable electrochemical sensors, such as SPEs, has received increasing attention in recent decades. The screen-printing technique has been widely used in the field of electroanalysis, enabling the development of new high-performance sensing platforms. [1]. Besides, the design of sensors is attractive because they are cost-effective, easy to produce, compatible with miniaturized systems, have low reagent consumption, and are extremely versatile [2].

The production of cost-effective electrochemical sensors is highly dependent on the formulation of conductive inks, which represents significant challenge for the large-scale manufacturing of analytical devices [3]. This limitation has motivated researchers to produce conductive inks, particularly carbon-based inks such as graphite, graphene, and carbon nanotubes [4]–[6].

Nevertheless, the depletion of natural resources and, consequently, the increasing importance of environmental conservation are also reflected in the development of devices. The quest for scientific methodologies or eco-friendly and cost-effective materials is becoming increasingly evident and relevant. This is especially crucial for regions where technological advancements do not yet support the use of costly and sophisticated techniques [7]. A promising alternative is the use of biochar or biocharcoal, a cost-effective material derived from renewable resources or waste products, such as peanut shells. This material is of significant interest as it retains some properties of conventional carbons while adhering to principles of circular economy and sustainability. In this context, the objective of this study was to design SPEs incorporating biochar derived from peanut shells within the ink formulation. Furthermore, the study examined the impact of various chemical treatments on the electrochemical performance of the biochar.

II. MATERIALS AND METHODS

A. Materials

Biochar (BC) derived from peanut shells (a local producer) was obtained through an incomplete burning process previously described in [8]. Graphite (Gr) was purchased from Grafitos Coloidales Juan Carlos Espiñeira Loeda. Vulcan XC-72 carbon black (CB) was acquired from Fuel Cell Store. Nail polish was obtained from a local producer. Acetone, potassium chloride, potassium hydroxide, nitric acid (concentrated), and potassium ferricyanide of analytical grade were purchased from Sigma Aldrich, Argentina. All solutions were prepared using distilled water.

B. Biochar modifications

The removal of aromatic hydrocarbons was performed according to a previously published protocol [9]. 1 g of BC was added to 75 mL of acetone. The mixture was stirred for one hour, then filtered and dried at 80°C overnight. The BC

was then ground and sieved (53-micron mesh). The resulting powder will be referred to as BCL. Subsequently, acidic or basic activation was carried out.

A basic treatment was performed following a protocol adapted from [10]. 300 mg of BCL was immersed in 50 mL of KOH (3M). The suspension was heated to 80°C for 2 h with constant stirring. The content was then filtered through a fritted glass funnel and washed with distilled water until a neutral pH. The powder obtained was dried at 80°C overnight. The resulting biochar activated in an alkaline medium will be referred to as BCB.

The acidic treatment was based on a modified protocol from [11]. 300 mg of BCL was immersed in 50 mL of HNO₃ (5M) in a flask. The suspension has been driven in a reflux system at 60°C for 3 h. Post-reaction, the suspension was filtered through a fritted glass funnel and washed with distilled water until a neutral pH. The obtained powder were dried at 80°C overnight. The biocarbon activated by acid will be referred to as BCA.

C. Preparation of SPE

The preparation of the conductive ink was carried out by adding 300 mg of carbon powder (Table I) to 300 mg of nail polish. To achieve the required viscosity, 500 µL of acetone was added. The SPE were prepared by spreading the conductive ink on pouch film that contained an adhesive glossy mask with the cutout of the three-electrode system prepared by using a cutting printer (Silhouette model Cameo 4). The ink was deposited onto the adhesive masks and spread in a single direction. Immediately, the masks were removed, and the device was allowed to dry for 24 h at room temperature. Subsequently, the detection area was delineated with nail polish.

TABLE I. POWDER MASS COMPOSITION (%) OF SPE

SPE	Gr	BCX (x = -, L, A, B)	CB
Control	85	0	15
BCX10	75	10	15
BCX15	70	15	15
BCX25	60	25	15
BCX50	35	50	15

D. Electrochemical characterization

All electrochemical characterizations were conducted by cyclic voltammetry (CV) with the produced SPEs. The working electrode diameter used was 0.4 cm, resulting in a geometric area of 0.125 cm². Measures were carried out using a Gamry Interface 1010 B potentiostat (Gamry, Warminster, PA, USA). For this purpose, 200 µL of a potassium ferricyanide 5 mM solution in KCl (0.1M) was placed in the detection area.

III. RESULTS

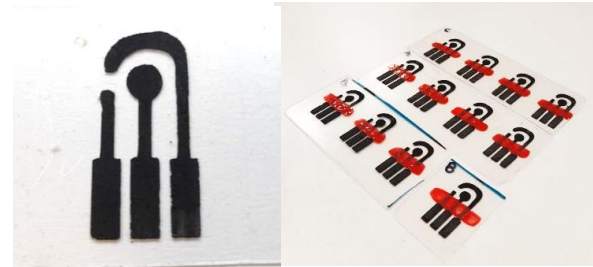


Fig. 1. Digital image of the fabricated SPEs

The obtained SPEs are shown in Fig. 1. The electrochemical response of these SPEs was investigated using CV with potassium ferricyanide as probe reaction. CV studies revealed typical redox peaks associated with the ferricyanide/ferricyanide redox couple in all evaluated SPEs. As shown in Fig 2.A, the addition of BC to the ink resulted in an increase in capacitance. Fig. 2.B indicates that increasing the proportion of BC in the SPEs led to performance comparable to the control up to 15% BC in the ink (BC15%). Beyond this concentration, a decrease in the current peak was observed.

The effect of the treatments applied to BC was evaluated at the most optimal proportion (BC-15%). As detailed in Table II, washing with acetone and KOH 3M led to improved performance (BCL15% and BCB15%), relative to BC-15%, by removing surface oils and, in the case of the basic treatment, inorganic substances such as Si and its derivatives..

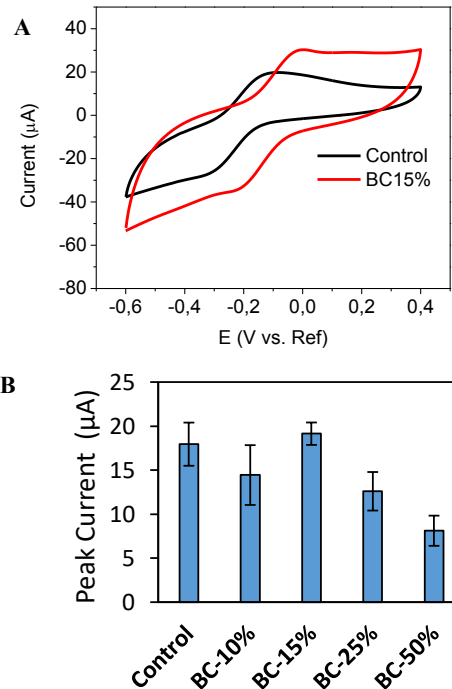


Fig. 2. A) CV of control and BC15% SPE in potassium ferricyanide 5 mM in KCl (0.1M) at a scan rate of 0.01 V/s. B) Cathodic peak current intensity.

This was not observed with the acidic activation (BCA15%), although an increase in capacitance was noted. This effect may be attributed to a higher concentration of acidic functional groups, increased surface defects, or enhanced porosity. Further physicochemical studies are required to supplement the obtained results.

TABLE II. FERRICYANIDE CATHODIC PEAK CURRENT

SPE	Peak current (μA)
Control	18 ± 3
BC-15%	19 ± 1
BCL15%	22 ± 2
BCB15%	24 ± 3
BCA15%	20 ± 2

IV. CONCLUSION

These results suggest that peanut shell biochar can serve as a modifier for screen-printed electrodes and has the potential to replace conventional carbon materials from a more sustainable perspective. Additionally, the implementation of post-synthesis treatments, such as organic and basic treatments, proves effective in enhancing the material's performance. Nonetheless, further investigation is needed to explore the properties of biochar and the impact of these treatments, as well as to continue optimizing the SPEs to achieve better electrochemical performance. This underscores the need for future research in this area.

ACKNOWLEDGEMENT

The authors gratefully acknowledge financial support from the National Agency of Scientific and Technological

Promotion (ANPCyT) (grant BID-PICT 2020-04023) and CONICET.

REFERENCES

- [1] L. A. Pradela-Filho *et al.*, "Glass varnish-based carbon conductive ink: A new way to produce disposable electrochemical sensors," *Sensors Actuators, B Chem.*, vol. 305, 2020.
- [2] K. C. Honeychurch and J. P. Hart, "Screen-printed electrochemical sensors for monitoring metal pollutants," *TrAC - Trends Anal. Chem.*, vol. 22, no. 7, pp. 456–469, 2003..
- [3] W. Yang and C. Wang, "Graphene and the related conductive inks for flexible electronics," *J. Mater. Chem. C*, vol. 4, no. 30, pp. 7193–7207, 2016..
- [4] F. E. Galdino *et al.*, "Graphite Screen-Printed Electrodes Applied for the Accurate and Reagentless Sensing of pH," *Anal. Chem.*, vol. 87, no. 23, pp. 11666–11672, 2015..
- [5] E. P. Randviir, D. A. C. Brownson, J. P. Metters, R. O. Kadara, and C. E. Banks, "The fabrication, characterisation and electrochemical investigation of screen-printed graphene electrodes," *Phys. Chem. Chem. Phys.*, vol. 16, no. 10, pp. 4598–4611, 2014.
- [6] H. Menon, R. Aiswarya, and K. P. Surendran, "Screen printable MWCNT inks for printed electronics," *RSC Adv.*, vol. 7, no. 70, pp. 44076–44081, 2017.
- [7] C. Kalinke *et al.*, "State-of-the-art and perspectives in the use of biochar for electrochemical and electroanalytical applications," *Green Chem.*, vol. 23, no. 15, pp. 5272–5308, 2021.
- [8] L. A. Long and P. M. Arnal, "Conversion of Wood into Hierarchically Porous Charcoal in the 200-Gram-Scale using Home-Built Kiln**," *Chemistry-Methods*, vol. 1, no. 11, pp. 477–483, 2021.
- [9] X. Shui, C. A. Frysz, and D. D. L. Chung, "Solvent cleansing of the surface of carbon filaments and its benefit to the electrochemical behavior," *Carbon N. Y.*, vol. 33, no. 12, pp. 1681–1698, 1995.
- [10] T. Huggins, H. Wang, J. Kearns, P. Jenkins, and J. Ren, "Biochar as a sustainable electrode material for electricity production in microbial fuel cells," 2014.
- [11] P. R. de Oliveira, C. Kalinke, J. L. Gogola, A. S. Mangrich, L. H. M. Junior, and M. F. Bergamini, "The use of activated biochar for development of a sensitive electrochemical sensor for determination of methyl parathion," *J. Electroanal. Chem.*, vol. 799, pp. 602–608, 2017.

Enhanced performance of plastic electrodes dopped with chemically activated biochar from peanut shells

Monica Mosquera Ortega
*BioAnalytical Chemistry Lab,
 Department of Agri-food, Environment
 and Animal Sciences (Di4A), University
 of Udine*
 Udine, Italy
 monica.mosquera@uniud.it
<https://orcid.org/0000-0003-3542-3495>

Federico Figueredo
 Laboratory of Biosensors and
 Bioanalysis (LABB), Department of
 Biological Chemistry and IQUIBICEN.
 Faculty of Sciences, University of
 Buenos Aires and CONICET, Ciudad
 Universitaria
 Buenos Aires City, Argentina
<https://orcid.org/0000-0002-7220-5609>

Florencia Bernassani
 Laboratory of Biosensors and
 Bioanalysis (LABB), Department of
 Biological Chemistry and IQUIBICEN.
 Faculty of Sciences, University of
 Buenos Aires and CONICET, Ciudad
 Universitaria
 Buenos Aires City, Argentina
<https://orcid.org/0000-0001-5318-004X>

Eduardo Cortón
 Laboratory of Biosensors and
 Bioanalysis (LABB), Department of
 Biological Chemistry and IQUIBICEN.
 Faculty of Sciences, University of
 Buenos Aires and CONICET, Ciudad
 Universitaria
 Buenos Aires, Argentina
<https://orcid.org/0000-0003-1897-4666>

Sabina Susmel
 BioAnalytical Chemistry Lab,
 Department of Agri-food, Environment
 and Animal Sciences (Di4A),
 University of Udine
 Udine, Italy
<https://orcid.org/0000-0002-6916-7373>

Abstract— In this work, we presented the analytical performance of biochar obtained from peanut shells. Large amounts of biomass were produced using kiln-home pyrolysis. The investigation was focused on chemical activation of the biochar through treatment with chitosan and a strong base, obtaining biochar-chitosan composite electrodes. Physical-chemical characterization techniques were used to evaluate the resulting biochar powders, and as well as the electrodes. The resulting plastic electrodes were electrochemically tested and applied as a proof of concept for the electrochemical detection.

Keywords— *Biochar from peanut shells, Biocarbon-chitosan composite activation, Ion heavy metals SWSAV detection*

I. INTRODUCTION

Due to their efficient and promising applications in electrochemistry, carbon-based materials have been the subject of intense and interesting studies for several years. Its low cost, almost inert electrochemistry, and its particular interaction with electrolytes and redox systems have made it a versatile and ideal electrode material for the detection of organic and inorganic substances in both aqueous and non-aqueous media [1,2].

Ongoing innovation in the development of new carbon-based electrode materials includes advanced chemical treatments to decorate their structure [3,4,5]. In this way, functional groups are strategically incorporated into the carbon structure or in its surface to optimise the redox interactions between the analyte and the electrode [6,7,8]. Biochar (Bc) is a promising material with potential applications in electrochemistry [9,10]. Bc retains the porosity of the original material with a porous structure (macro, micro and mesoporous), this characteristic provides it with a high surface area which facilitates mass transfer. Likewise, its characteristics and physicochemical properties depend on the

type of raw material, the pyrolysis conditions, and on the preparation of the material before and/or after the pyrolysis process such as size reduction, cleaning, exfoliation or/ and chemical activation. The latter has generated a link between the innovation of new electrode materials and the use of natural resources [11].

In this work, we show for the first time the production of plastic electrodes manufactured from graphite (GP) and a new activated biochar-chitosan composite (Bc-CS) obtained from peanut shells using a novel and sustainable home-built kiln method. The new Bc-CS was physicochemical characterized, and used to test its robustness as a new electrode material, thus linking these new materials to the application of green chemistry.

II. EXPERIMENTAL

New Bc was obtained from peanut shells through a home-built kiln [12] which yielded a significant amount of material in a sustainable manner (86 g, 43% yield). Bc-CS was obtained by treating 500 mg Bc with 10 mL of chitosan (CS) (2% prepared in acetic acid) using an ultrasonic probe coupled to microtip (60 min: 2 min ON/ 1 min OFF, 30% amplitude and temperature ≤ 10 °C). Finally, the stable dispersion was treated with 100 mL of NaOH 1% to obtain the new Bc-CS activated.

Plastic electrodes were manufacture with a blend of GP and the dry powder Bc-CS in relation 3:1 (GP₇₅:Bc-CS₂₅) using the method reported by [6].

New materials Bc and Bc-CS were characterised by means of a scan electron microscope (SEM) using an FEI Scios 2 field emission microscope (FESEM) with a Schottky emitter. Specific surface area and pore size distribution were acquired by nitrogen desorption/adsorption (ASAP2020, Micromeritics, USA). Elemental distribution on the material surface was analyzed by X-ray photoelectron spectroscopy

(XPS, SPECS Flexmod, Germany) using a monochromatic Al K α X-ray source (1486,61 eV), 100w potency and a potential difference of 10 kV. Functional groups were analyzed by Fourier transform infrared spectra (FTIR) in ATR mode (Agilent tech. Cary 630).

All electrochemical experiments were carried out utilizing a commercial electrochemical workstation (Gamry, model Interface 3000). Cyclic voltammetry (CV) test were realized in KCl 0.1M as a supporting electrolyte and K₄Fe(CN)₆ / K₃Fe(CN)₆ 1mM as an electroactive probe. A steel bar and an Ag/AgCl were used as counter and reference electrode, respectively.

III. RESULTS AND DISCUSSION

A. Morphologic, structure and chemical characterization

Bc and Bc-CS powders morphology is shown in Fig. 1(a-b). SEM image of Bc shows an irregular surface and diverse porous sizes, typical of biochars, in which the most predominant size corresponds to macropores (1-50 μ m). This original structure changes noticeably after Bc treatment with CS and NaOH, which can be corroborated by the reduction in surface area shown in Fig. 2 corresponding to the BET analysis. This original structure changes noticeably after Bc treatment with CS and NaOH, which can be corroborated by the BET analysis, in which is possible to detect the reduction in surface area from 39.7 m²/g (Bc) to 10.57 m²/g (Bc-CS).

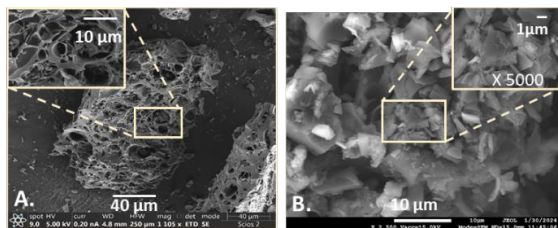


Figure 1. Scanning electron microscopy (SEM) images of (A) Bc and (B) Bc-CS.

The elemental composition analysis shows the effect of the CS treatment on Bc and the subsequent activation with NaOH (Table 1). Bc-CS composite shows a decreased C content (80.4%), while N (4.1%) and O (15.5%) increased respect at the Bc (C 94.1%, N 0.67%, and O 4.99%).

TABLE I. ELEMENTAL COMPOSITION ANALYSIS OF Bc AND Bc-CS

Element	% (abundance)	
	Bc	Bc-CS
Carbon	94.13	80.4
Sulfur	0.20	ND
Nitrogen	0.67	4.1
Oxygen	4.99	15.5

FTIR spectra of Bc, Bc-CS and CS are displayed in Fig. 2. The Bc-CS composite shows some peaks at 3300 cm⁻¹ (stretch -NH), and the methylene stretching vibrations at 2905 cm⁻¹ (C-H) attributed to the CS layer, indicating the coated surface of Bc by CS and its structure modification.

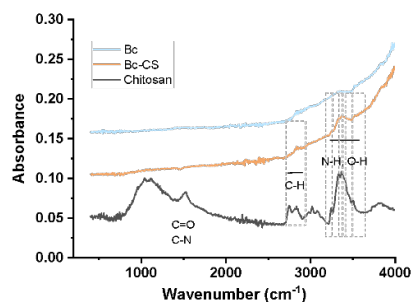


Figure 2. ATR-FTIR analysis of Bc, Bc-CS, and chitosan powders.

B. Electrochemical characterization

Electrochemical properties of the following plastics electrodes GP₁₀₀, GP₇₅Bc₂₅ and GP₇₅Bc-CS₂₅ were tested separately using CV with Fe(CN)₆^{3-/4-} redox system and KCl 0.1M as a support electrolyte. CV was accomplished using a potential window between -0.2 to 0.7 V in which GP₁₀₀ and GP₇₅Bc-CS₂₅ show a reversible behaviour of the redox couple with a defined and intense reduction and oxidation peaks (Fig. 3).

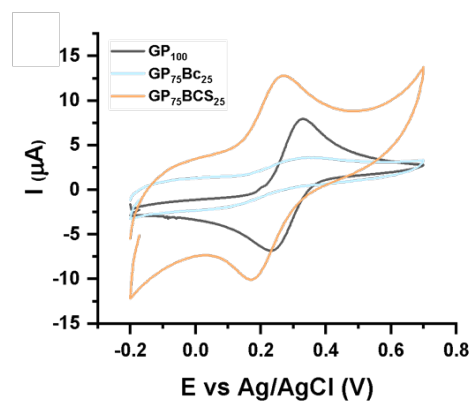


Figure 3. Cyclic voltammetry of Fe(CN)₆^{3-/4-} redox system] (1 mM in 0.1M KCl at 50 mV/s) at plastic electrodes manufactured using Bc100 and mixtures of GP₇₅Bc₂₅ and GP₇₅BcCS₂₅.

GP₇₅Bc-CS₂₅ (I_{pa}=13.86 μ A, Δ E_p=0.096 V) as a working electrodes, enhanced the electrochemical response for the reversible Fe(CN)₆^{3-/4-} redox system in comparison with GP₁₀₀ (GP₁₀₀, I_{pa}=7.29, Δ E_p=0.092V) electrodes in this specific proportion (25%). On contrary, electrodes manufactured just with Bc in the same proportion that Bc-CS not showed a quantifiable redox response.

These results indicate a significant improvement in the electrochemical efficiency of the composite, highlighting its potential for advanced electron transfer applications.

IV. CONCLUSIONS

Peanut shell biochar was obtained and characterized to manufacture plastic electrodes.. Activation with NaOH and treatment with chitosan improved the inherently poor electrical conductivity of the biochar powder. This has led to an improvement in the performance of the new biochar composite electrode by 25% concerning graphite. This new

material is versatile and promotes the green chemistry application process.

ACKNOWLEDGMENT

- Interreg Italy-Croatia Programme 2021-2027 for funding this research, conducted as part of the Standard project BRIGANTINE (ID ITHR0200237).
- University of Buenos Aires (UBA), the National Council for Scientific and Technological Research (CONICET) and National Agency of Scientific and Technological Promotion (ANPCyT) [grant number BID-PICT 2020-04023].
- We thank Dr. Pablo Arnal and his group National University of La Plata, Argentina for kindly providing the biochar material.

REFERENCES

- [1] Karnan, M., Subramani, K., Srividhya, P., & Sathish, M. Electrochemical Studies on Corn cob Derived Activated Porous Carbon for Supercapacitors Application in Aqueous and Non-aqueous Electrolytes. *Electrochimica Acta*, 2017, 228, pp. 586-596.
- [2] Lu, Y., Jao, W., Tai, C., & Hu, C. A comprehensive review on the electrochemical activation for non-aqueous carbon-based supercapacitors. *Journal of the Taiwan Institute of Chemical Engineers*, 2023, 154, pp. 104978.
- [3] Eivazzadeh-Keihan, R., Bahojb Noruzi, E., Chidar, E., Jafari, M., Davoodi, F., Kashtiaray, A., Ghafori Gorab, M., Masoud Hashemi, S., Javanshir, S., Ahangari Cohan, R., Maleki, A., & Mahdavi, M. Applications of carbon-based conductive nanomaterials in biosensors. *Chemical Engineering Journal*, 2022, 442, pp. 136183.
- [4] Wu, B., Yeasmin, S., Liu, Y., & Cheng, L. Sensitive and selective electrochemical sensor for serotonin detection based on ferrocene-gold nanoparticles decorated multiwall carbon nanotubes. *Sensors and Actuators B: Chemical*, 2022, 354, pp. 131216.
- [5] Oliveira, T. M., Ribeiro, F. W., Sousa, C. P., Salazar-Banda, G. R., De Lima-Neto, P., Correia, A. N., & Morais, S. . Current overview and perspectives on carbon-based (bio)sensors for carbamate pesticides electroanalysis. *TrAC Trends in Analytical Chemistry*, 2020, 124, pp. 115779.
- [6] Ben-Aissa, S., de Marco, R., & Susmel, S. (2023). POM@PMO plastic electrode for phosphate electrochemical detection: a further improvement of the detection limit. *Microchimica*, 2023, 190(4), pp. 1–10.
- [7] Figueredo, F., Jesús González-Pabón, M., & Cortón, E. Low Cost Layer by Layer Construction of CNT/Chitosan Flexible Paper-based Electrodes: A Versatile Electrochemical Platform for Point of Care and Point of Need Testing. *Electroanalysis*, 2018, 30(3), pp. 497–508.
- [8] Ye, W., Li, Y., Wang, J., Li, B., Cui, Y., Yang, Y., & Qian, G. Electrochemical detection of trace heavy metal ions using a Ln-MOF modified glass carbon electrode. *Journal of Solid State Chemistry*, 2019, 281, pp. 121032.
- [9] Ding, Y., Wang, T., Dong, D., & Zhang, Y. Using Biochar and Coal as the Electrode Material for Supercapacitor Applications. *Frontiers in Energy Research*, 2020, 7, pp. 495488.
- [10] Rahman, M. Z., Edvinsson, T., & Kwong, P. Biochar for electrochemical applications. *Current Opinion in Green and Sustainable Chemistry*, 2020, 23, pp. 25-30.
- [11] Kalinke, C., de Oliveira, P. R., Bonacin, J. A., Janegitz, B. C., Mangrich, A. S., Marcolino-Junior, L. H., & Bergamini, M. F. State-of-the-art and perspectives in the use of biochar for electrochemical and electroanalytical applications. *Green Chemistry*, 2021, 23(15), pp. 5272–5301
- [12] Long, L. A., & Arnal, P. M. Conversion of Wood into Hierarchically Porous Charcoal in the 200-Gram-Scale using Home-Built Kiln**. *Chemistry - Methods*, 2021, 1(11), pp. 477–483.

Towards new colorimetric detection strategies to detect loop-mediated isothermal amplification products in the Point-of-Care

Sandra Vlachovsky
Laboratory of Biosensors
and Bioanalysis (LABB),
Department of Biological
Chemistry. IQUIBICEN,
University of Buenos Aires
and CONICET, CABA,
Argentina

ORCID: 0009-0009-4147-
9146

Adrián Vojnov
Instituto de Ciencia y Tecnología Cesar
Milstein
ICT-Milstein-CONICET
CABA, Argentina
aavojnov@gmail.com

Lucas R. Sousa
Laboratory of Biosensors
and Bioanalysis (LABB),
Department of Biological
Chemistry. IQUIBICEN,
University of Buenos Aires
and CONICET, CABA,
Argentina
lrodsousa@gmail.com

Eduardo Cortón
Laboratory of Biosensors and
Bioanalysis (LABB), Department of
Biological Chemistry. IQUIBICEN,
University of Buenos Aires and
CONICET, CABA, Argentina
eduardo@qb.fcen.uba.ar

Pablo Di Ielsi
Laboratory of Biosensors
and Bioanalysis (LABB),
Department of Biological
Chemistry. IQUIBICEN,
University of Buenos Aires
and CONICET, CABA,
Argentina
pablodielsi@gmail.com

Fabiana Stolowicz
Instituto de Ciencia y
Tecnología Cesar Milstein
ICT-Milstein-CONICET
CABA, Argentina
fstolowicz@gmail.com

Federico Figueredo
Laboratory of Biosensors and
Bioanalysis (LABB), Department of
Biological Chemistry. IQUIBICEN,
University of Buenos Aires and
CONICET, CABA, Argentina
federicofigueredo@qb.fcen.uba.ar

Abstract - Colorimetric reactions are one of the most used strategies for the detection of the reaction products of loop-mediated isothermal amplification (LAMP) reactions, since they provide a simple and economical reading method, which can be used both in reactions in solution as in paper-based analytical devices. This work shows the development of paper microfluidic devices for the colorimetric detection of LAMP reactions, based on an adaptation of the ammonium molybdate technique in acidic medium to measure pyrophosphate. Through adaptations of this technique, visual detection of the pyrophosphate generated during genomic amplification is achieved, since it reacts with molybdate producing a blue color. The device is manufactured with inexpensive materials and reagents in the order of microliters, thus providing a simple and economical alternative method of colorimetric detection that can be coupled in the development of portable devices.

Keywords— LAMP, colorimetric detection, paper devices

I. INTRODUCTION

LAMP (loop-mediated isothermal amplification) was first introduced in 2000 by Notomi et al. [1] and was optimized with additional primers for accelerated amplification by Nagamine et al. [2]. LAMP has become the predominant nucleic acid amplification techniques (NAAT) today due to its features such as high specificity, high sensitivity, and simplicity. This technique has been applied for the clinical diagnosis of infectious diseases [3] and in plant virology [4], and its use has also extended to other areas such as environmental monitoring [5] and food quality control [6].

Because a high number of amplicons ($\sim 10^9$) are produced in a short period of time (< 1 h), LAMP allows rapid target detection with very high sensitivity. Furthermore, the reaction occurs at a constant temperature (60–65 °C), eliminating the need to use equipment to produce complex thermal cycles.

These characteristics make it an ideal technique to be used in the development of Point of Care (POC) devices, which allow the diagnosis to be made at the time and place where the patient receives care. This eliminates the complexity of transporting biological samples to laboratories, allowing for early stage diagnosis and rapid medical decisions. Due to its simplicity, a LAMP module can be integrated into a microfluidic chip and coupled to a simple detection system, such as colorimetric detection. This type of devices have been developed for the detection of pathogens such as African swine fever virus [7] or for the multiple detection of human immunodeficiency virus (HIV), hepatitis B (HBV), and hepatitis C virus (HCV), using the camera of a smartphone to read the result [8].

Among the multiple detection methods developed for LAMP, colorimetric detection is qualitative, which represents a disadvantage if the pathogen needs to be quantified, but at the same time, its low cost and simplicity are advantages in this type of devices.

In this work, a paper-based analytical device (μ PAD) has been developed for the detection of pyrophosphate produced during the amplification of genetic material in a LAMP reaction. Based on the classic ammonium molybdate reaction for the determination of phosphate [9], modifications have been made to adapt the measurement to a paper microfluidic device. During the reaction, ammonium molybdate in an acidic medium (generally sulfuric acid) forms a complex with the phosphate, which, when reduced, gives a blue color. Sulfuric acid has been replaced by toluene sulfonic acid to reduce paper oxidation, and 2-mercaptoethanol has been used as a reducer, since it was reported as the best reducer for the specific detection of pyrophosphate [10].

This type of rapid test is very useful for clinical diagnosis using human biological samples, but its use also represents an advantage in other areas such as agriculture. So, we have done the proof of concept of the device to read the result of LAMP

reactions for Huanglongbing (HLB) disease, also known as citrus greening or sadness. This is considered the most devastating disease of plants of the citrus genus worldwide, caused mainly by the bacteria *Candidatus Liberibacter asiaticus*. Once a plant is infected with HLB, there is no alternative to restore its health, so it inevitably dies [11].

The disease is transmitted through the transport of infected propagation material (buds or plant parts), or through its insect vector called *Diaphorina citri*, which prevails in America and Asia. Disease prevention programs are based on the early detection of infected material and its eradication, with the aim of preventing its spread [12].

II. MATERIALS AND METHODS

A. Chemical and materials

Ammonium molybdate, 2-mercaptoethanol, toluenesulfonic acid and sodium pyrophosphate decahydrate were acquired from Sigma-Aldrich (St. Louis, MO, USA). Stock and analytical solutions were prepared using ultrapure water processed through a water purification system (18 M Ω .cm, Merck Millipore, MA, USA)

A solution of 3 mM ammonium molybdate in 1 M toluenesulfonic acid was prepared.

LAMP positive samples were simulated by dissolving sodium pyrophosphate decahydrate in LAMP reaction mix, prepared with tris-HCl (pH 8.8, 20 mmol L⁻¹), KCl (10 mmol L⁻¹), (NH₄)₂SO₄ (10 mmol L⁻¹), MgSO₄ (8 mmol L⁻¹), Betaine (800 mmol L⁻¹), Tween 20 (0.1% v⁻¹), dNTP's (1.4 mmol L⁻¹). Pyrophosphate solutions 0.5, 1, 2.5, 5 and 10 mM were prepared. Real samples of LAMP amplifications to test citrus disease were used. The result was tested by the HNB method and by runs on agarose gels.

B. Fabrication of Paper Device

To manufacture the paper devices, Whatman™ quantitative filter paper (grade 1) was used. The paper was laminated and Silluette Cameo 3 cutting machine was used for cutting devices with the design shown in Fig. 1. The reagents were loaded into the device and allowed to dry; 0.5 μ l of ammonium molybdate 3 mM in toluenesulfonic acid 1M was placed in the detection zone and 0.5 μ l of 2-mercaptoethanol in the intermediate zone. For measurement, 5 μ l of LAMP reaction sample or mock samples were placed in the sample loading zone. The result was read 15 minutes after loading the sample.

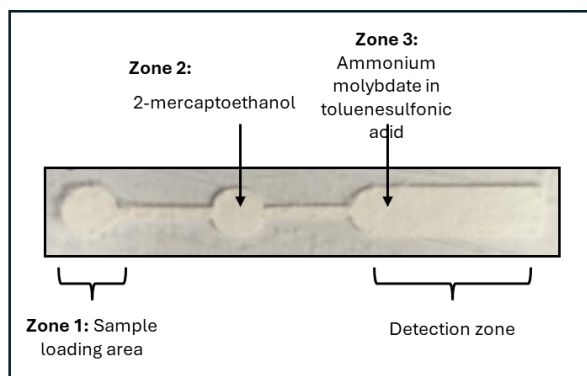


Fig. 1 Paper device for detecting pyrophosphate. The loading areas of the reagents, the sample and the detection area are indicated.

III. RESULTS

The devices were tested with simulated positive and negative samples, containing different amounts of pyrophosphate in the LAMP reaction mix. A result was obtained in the form of a blue band in the detection zone of the device for all pyrophosphate concentrations tested (0, 0.5, 1, 2.5, 5 and 10 mM). To simulate the negative samples, LAMP reaction mix without dissolved pyrophosphate was used. The testing of real samples was carried out with LAMP reactions for the diagnosis of citrus disease, the results of which were previously tested using agarose gels and with colorimetric methods. Fig. 2 shows the result of the testing of both the simulated and real samples.

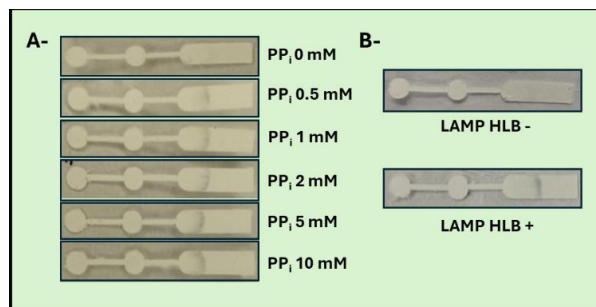


Fig. 2 The devices show the colorimetric detection of pyrophosphate (PPi) in solutions of different concentrations (A, simulated samples) and the detection of pyrophosphate produced in LAMP reactions for the diagnosis of Huanglongbing (HLB) disease (B, real samples). The positive result is displayed as the appearance of a blue band in the detection zone and the negative result as the absence of a band.

A widely used strategy in portable devices is to analyze the result of a colorimetric reaction using a smartphone application. With the aim of making the device compatible with this strategy, a 3-zone device was designed and tested, similar to the first but in which the third zone was replaced by a circular area similar to zones 1 and 2. The aim is to obtain a color homogeneous in area 3 so that the phone can take a photo of this area and analyze the color intensity. These devices were tested with 0, 1 and 5 mM pyrophosphate solutions. These devices were tested with 0, 1 and 5 mM pyrophosphate solutions and with LAMP samples for HLB (Fig. 3). Blue coloration was observed in area 3 for both the pyrophosphate solutions and the positive LAMP samples. In the case of pyrophosphate solutions, the color intensified at the edges while the positive LAMP showed a different pattern, covering only the right half of zone 3.

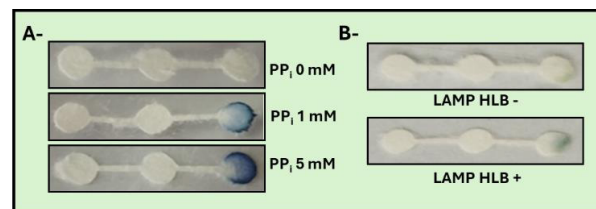


Fig. 3 The devices show the colorimetric detection of pyrophosphate (PPi) in solutions of different concentrations (A, simulated samples) and the detection of pyrophosphate produced in LAMP reactions for the diagnosis of Huanglongbing (HLB) disease (B, real samples). The positive result is

displayed as the appearance of a blue color in the detection area and the negative result as the absence of color.

IV. DISCUSSION

In the first device tested, in which the result is displayed as the presence or absence of a blue band in the detection area, it worked well for both real and simulated samples, obtaining a band with an intensity appropriate to be observed with the naked eye. This type of detection, used for example in pregnancy tests, has the advantage of being very simple and fast, but has the disadvantage that the result may not be clear if the intensity of the band is weak. This could lead to incorrect interpretation by the user, so some other checkpoint needs to be added. In the case of LAMP reactions, the amount of pyrophosphate produced is in the order of 1 to 5 mM, but it could happen that a negative sample has some lower concentration of pyrophosphate coming from the degradation of dNTPs or coming from the biological fluid from which amplification is performed. Although these concentrations would be negligible compared to those produced in a positive LAMP reaction, they could produce interference, producing a weak blue coloration. In this case it would be appropriate to read the result using a smartphone application that can decide if the result is positive or negative depending on the intensity of the color obtained. For this purpose, it is necessary that the detection area of the device has a homogeneous color. In the case of the second device tested, the appearance of color was adequate in the range of concentrations tested but the so-called "coffee grounds effect" was obtained, so a homogeneous coloration was not obtained. It will be necessary to modify the detection zone with some inert compound for the molybdate reaction, which produces a uniform diffusion of the color obtained.

REFERENCES

- [1] Notomi, T., Okayama, H., Masubuchi, H., Yonekawa, T., Watanabe, K., Amino, N., & Hase, T. (2000). Loop-mediated isothermal amplification of DNA. *Nucleic acids research*, 28(12), e63-e63.
- [2] Nagamine, K., Hase, T., & Notomi, T. J. M. C. P. (2002). Accelerated reaction by loop-mediated isothermal amplification using loop primers. *Molecular and cellular probes*, 16(3), 223-229.
- [3] Das, D., Lin, C. W., & Chuang, H. S. (2022). LAMP-based point-of-care biosensors for rapid pathogen detection. *Biosensors*, 12(12), 1068.
- [4] Panno, S., Matic, S., Tiberini, A., Caruso, A. G., Bella, P., Torta, L., ... & Davino, S. (2020). Loop mediated isothermal amplification: principles and applications in plant virology. *Plants*, 9(4), 461.
- [5] Liew, P. S., Lertanantawong, B., Lee, S. Y., Manickam, R., Lee, Y. H., & Surareungchai, W. (2015). Electrochemical genosensor assay using lyophilized gold nanoparticles/latex microspheres label for detection of *Vibrio cholerae*. *Talanta*, 139, 167-173.
- [6] Ali, A., Kreitlow, A., Plötz, M., Normanno, G., & Abdulmawjood, A. (2022). Development of loop-mediated isothermal amplification (LAMP) assay for rapid and direct screening of yellowfin tuna (*Thunnus albacares*) in commercial fish products. *PLoS one*, 17(10), e0275452.
- [7] Zhu, Y. S., Shao, N., Chen, J. W., Qi, W. B., Li, Y., Liu, P., ... & Tao, S. C. (2020). Multiplex and visual detection of African Swine Fever Virus (ASFV) based on Hive-Chip and direct loop-mediated isothermal amplification. *Analytica Chimica Acta*, 1140, 30-40.
- [8] Xie, C., Chen, S., Zhang, L., He, X., Ma, Y., Wu, H., ... & Zhou, G. (2021). Multiplex detection of blood-borne pathogens on a self-driven microfluidic chip using loop-mediated isothermal amplification. *Analytical and Bioanalytical Chemistry*, 413, 2923-2931.
- [9] Worsfold, P. J., Gimbert, L. J., Mankasingh, U., Omaka, O. N., Hanrahan, G., Gardolinski, P. C., ... & McKelvie, I. D. (2005). Sampling, sample treatment and quality assurance issues for the determination of phosphorus species in natural waters and soils. *Talanta*, 66(2), 273-293.
- [10] Putnins, R. F., & Yamada, E. W. (1975). Colorimetric determination of inorganic pyrophosphate by a manual or automated method. *Analytical Biochemistry*, 68(1), 185-195.
- [11] Bové, J. M. (2014). Huanglongbing or yellow shoot, a disease of Gondwanan origin: Will it destroy citrus worldwide?. *Phytoparasitica*, 42(5), 579-583.
- [12] Spann, T. M., Atwood, R. A., Dewdney, M. M., Ebel, R. C., Ehsani, R., England, G., ... & Stelinski, L. L. (2010). IFAS guidance for huanglongbing (greening) management. *Horticultural Sciences Department, Florida Cooperative Extension Service, Institute of Food and Agricultural Sciences, University of Florida*.



5 |

Diseño y tecnología de sensores

Design and technology of sensors

Design e tecnologia de sensores

Study of the maximum 2D-Silicon-based particle size that can be internalized by living cells.

Marta Duch
Micro- and Nanotools group
Institute of Microelectronics of
Barcelona
Cerdanyola del Vallés, Spain,
marta.duch@imb-cnm.csic.es

Patricia Vázquez
Molecular Biomedicine
Center for Biological Research
Margarita Salas)
Madrid, Spain
pvazquezcib@gmail.com

Juan Pablo Aguil
Micro- and Nanotools group
Institute of Microelectronics of
Barcelona
Cerdanyola del Vallés, Spain,
juanpablo.aguil@imb-cnm.csic.es

Héctor Zamora-Carreras
Molecular Biomedicine
Center for Biological Research
Margarita Salas
Madrid, Spain
hector.zamora@cib.csic.es

Ana Fernández-Escribano
Molecular Biomedicine
Center for Biological Research
Margarita Salas)
Madrid, Spain
ana.fenandez@cib.csic.es

Teresa Suárez
Molecular Biomedicine
Center for Biological Research
Margarita Salas
Madrid, Spain
teresa@cib.csic.es

Mariano Redondo Horcajo
Molecular Biomedicine
Center for Biological Research
Margarita Salas)
Madrid, Spain
marecib@cib.csic.es

Ana Sánchez
Micro- and Nanotools group
Institute of Microelectronics of
Barcelona
Cerdanyola del Vallés, Spain,
ana.sanchez@imb-cnm.csic.es

María Isabel Arjona
Micro- and Nanotools group
Institute of Microelectronics of Barcelona
Cerdanyola del Vallés, Spain
isabel.arjona@ijm.fr

Jose Antonio Plaza
Micro- and Nanotools group
Institute of Microelectronics of
Barcelona
Cerdanyola del Vallés, Spain
joseantonio.plaza@imb-cnm.csic.es

Adrián Rodríguez
Micro- and Nanotools group
Institute of Microelectronics of
Barcelona
Cerdanyola del Vallés, Spain,
adrian.rodriguez@imb-cnm.csic.es

Sergi Sánchez
Micro- and Nanotools group
Institute of Microelectronics of
Barcelona
Cerdanyola del Vallés, Spain,
sergi.sanchez@imb-cnm.csic.es

Abstract— Cell internalization is a common biological process by which micro- and nanoparticles are introduced into the cell. The biological mechanisms of internalization are reported for particles well below the mitotic size of the cells and are size-[1] and shape-dependent [2]. However, a question arises: Which is the maximum size of an external particle that can be internalized by a specific cell? Although, it is initially curiosity-driven question, the answer has relevant implications to discover new cellular internalization processes in fundamental cell biology, in the fields of micro- and nanoparticle applications, and in the emerging field of intracellular chips for nanobiomedicine.

Keywords— Intracellular chips, Silicon, Micro- and Nanoparticles, Cell viability, Cell internalization.

I. INTRODUCTION

Micro- and nanotechnologies derived from the microelectronic techniques offer an extensive opportunity to produce highly reproducible and versatile micro- and nanodevices. Compared with chemical synthesis methods to produce micro and nanoparticles, the techniques based on photolithographic processes lead to the possibility of a high control of shapes and dimensions and materials coming from the MEMS and NEMS fields.

Thus, these devices open the venue of a new field: chips for intracellular applications. Large intracellular chips have been reported as wireless radio frequency identification (RFID) devices[3], intracellular mechanical sensors[4] and even actuators[5]. These devices present large dimensions at cellular scale, with maximal surface area, thus providing a new platform that would allow the integration of multiple functionalities in the same particle to perform diverse functions. Consequently, they motivate and open questions related to the maximum size of a particle for its internalization. In our previous work, we observed that polysilicon 23.5- μm -diameter discs were internalized by cells with mitotic radii about 20 μm [5].

Here we aim to analyze which is the largest size a cell can internalize disc-shaped chips, using 500-nm-thick discs with diameters up to 40 μm , which are co-cultivated with different cell lines. This includes cell lines with different cell sizes to study the dependence of maximum internalized disc versus the size of the cell. These cell lines also include non-professional phagocytic cells[6] (HeLa and ARPE-19 cells), and professional activated macrophages (THP-1, DC2.4 and RAW 264.7 cells) to compare cell size and phagocytic capability (Figure 1).

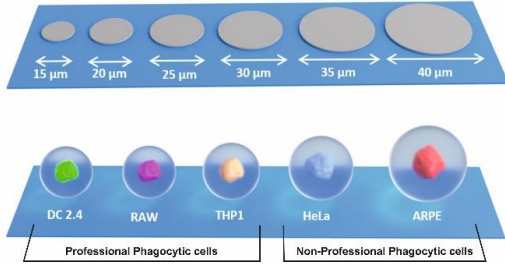


Figure 1: Schematic view of the diameter comparison of the fabricated devices and the equivalent diameter of the professional phagocytic cells (DC2.4, RAW 264.7, THP-1 cells) and the non-professional phagocytic cells (HeLa and ARPE-19 cells).

These studies are fundamental for several key topics as:

- Intracellular Chips: The size of these devices is a challenge for the integration of functionalities or even multiple functionalities in a single device. Thus, maximizing the area could allow advanced functionalities on a single device.
- Cell viability of the cells with internalized objects: The internalization of large objects, especially 2D objects, could induce adverse cell viability effects or even induce cell death as reported in a previous work of the group[5], with high interest for the field of nanomedicine.
- Cell internalization: Few studies focused on the internalization of large devices are reported, thus their biological mechanism involved in this process are not clearly understood.

II. FABRICATION PROCESS OF THE DEVICES

Silicon technologies offer the possibility of producing devices with a high control of their dimensions at the micro- and nanoscale and assuring biocompatibility. In this work, devices are produced by standard microelectronics techniques, Figure 2. The fabrication process is similar to the previously reported for intracellular chips[5, 7]. Polysilicon was selected as a structural material due its proven biocompatibility[8] and the capability of mass production with a high reproducibility dimensions. Low-stress and low-roughness polysilicon layers are required to avoid the initial bending of the devices or a high roughness that could affect the internalization process. A 1- μm -thick silicon oxide layer was grown on a silicon wafer, as a sacrificial layer, Figure 2.a). Then a 500-nm-thick polysilicon layer, as structural layer, was deposited by low-pressure chemical vapours deposition Figure 2.b). A photolithographic step and subsequent polysilicon dry etching patterned the devices, Figure 2.c-f). Finally, the devices are released from the substrate by etching the silicon oxide sacrificial layer by hydrofluorhydric acid (HF), Figure 2.g). The freestanding devices are collected and washed 3 times in 96% ethanol in order to avoid the sample contamination with HF traces, which we previously tested, were hazardous for cells experiments.

The number of devices per Eppendorff has to be controlled and homogeneous; the number of devices is always counted to assure the right device:cell ratio (~ 0.3) to shun the over internalization of devices in a single cell.

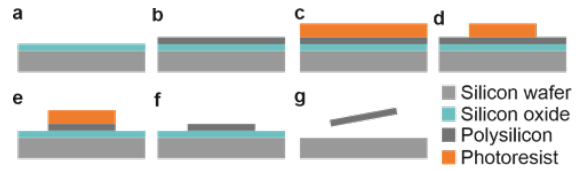


Figure 2: Technology for the fabrication of the devices. **a**, a sacrificial 1- μm -thick silicon oxide layer is deposited on the top of silicon wafer, **b**, a 0.5- μm -thick polysilicon layer is deposited, **c**, a 1.2- μm -thick photoresist is spun on the wafer and (**d**) the photolithographic process performed, **e**) a RIE process defined the chips, **f**), the remaining photoresist is removed, and, finally, **g**), the sacrificial layer is removed to collect the devices in an Eppendorf tube

III. DEVICE DESIGNS

In previous works, it has been demonstrated the capability of HeLa and MCF7 cells to internalize 500-nm-thick and 23.7- μm - Φ polysilicon disc-devices in the order of their mitotic diameter. In this study, we investigate the maximum size of these devices that can be internalized in living cells. For this purpose, we designed two sets of 500-nm-thick discs devices. Set 1 has devices with diameters of 15 μm , 20 μm and 25 μm which are in the range of the equivalent diameter of the studied cell lines. Set 2 is included to investigate the maximum device size that can be internalized by the different cell lines with devices of 30 μm , 35 μm and 40 μm in diameter (Figure 3). The geometrical and physical characteristics of the fabricated devices are summarized in Table 1.

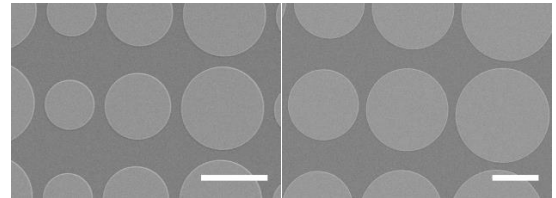


Figure 3: SEM images of the fabricated devices at the wafer level: (Left) Set 1, 15 μm , 20 μm and 25, and (Right) Set 2, 30 μm , 35 μm and 40 μm . Scale bars: 20 μm .

Table 1: Geometrical and physical characteristics of the fabricated devices. Diameter (Φ), thickness (Th), area (A), volume (V).

Φ (μm)	Th (μm)	A (μm^2)	V (μm^3)
15	0.5	377	88
20	0.5	659	157
25	0.5	1021	245
30	0.5	1460	353
35	0.5	1979	481
40	0.5	2576	628

IV. CELL LINES

We have chosen two epithelial non-professional phagocytes cell lines, a standard human cell line as HeLa and a large cell

line as ARPE-19[9], derived from the retinal pigmented epithelium. The study also includes three professional phagocytes, RAW 264.7[10], which are murine macrophages, THP-1[11], macrophages derived from the human monocyte cell line, and DC 2.4[12], murine dendritic cells. Macrophages and the dendritic cell line, DC 2.4, were selected for their phagocytic abilities and size diversity. All cell lines were cultured in their specific conditions and co-incubations with chips followed our published work [5]. In all experiments, RAW 264.7 AND THP-1 cell lines were activated to their inflammatory phenotypes, to increase their phagocytic capacities [10-11].

V. MAXIMUM SIZE OF INTERNALIZED DISCS

First, we estimated the volume of the cells from in vivo time-lapse experiments (diameter) and from confocal images (area) (Table 2). Typically, the cell volume was estimated from the diameter of the cells during mitosis. However, THP-1 and RAW 264.7 cell lines under inflammatory conditions display low cell division rates as a consequence of the differentiation process. In these cell lines, we integrated the area from the confocal images considering the z-step. After obtaining the volume, we estimate the equivalent diameter, Φ_{eq} , assuming this volume for a sphere

Table 2: Calculated volume, V , of the different cell lines and their equivalent diameter, Φ . ($8 \leq n \leq 29$). SD means standard deviation.

	ARPE-19	HeLa	THP-1	RAW 264.7	DC 2.4
V (μm^3)	8102	4893	3406	2686	2498
SD (μm^3)	3212	1267	821	884	743
Φ_{eq} (μm)	24.5	21.0	18.6	17.1	16.7
SD (μm)	1.7	1.6	0.7	0.9	1.6

We first incubated all cell lines with the set 2 of devices (the largest ones). Interestingly, as expected, ARPE-19 cell line, the biggest cell used in our work, easily internalized all of the largest discs. On the contrary THP-1 and DC 2.4 did not internalize any chip of Set 2 ($\Phi \geq 30 \mu\text{m}$). According to these results, we extended the study to the smallest devices of Set 1, except for ARPE 19 cells, which we found positive internalization of all sizes.

Figure 4 shows the size distribution percentage of internalized chips, meaning the percentage of internalized discs of each size considering only the cells with internalized discs for each set.

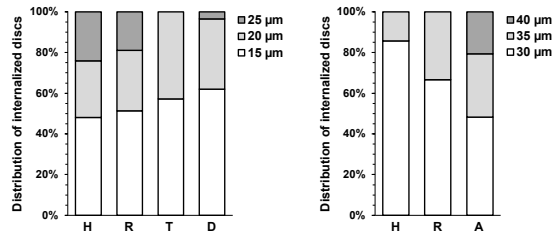


Figure 4: Percentage of each disc-size of internalized discs in the different cell lines. Cells with internalized discs were counted in in vivo time-lapse experiments, except for the ARPE-19 and THP-1 cell lines, that were counted on fixed slides. Cell lines: HeLa (H), RAW 264.7 (R), THP-1 (T), DC 2.4 (D) and ARPE-19 (A). Number of cells for Set 1, $n=14-$

29, and for Set 2, $n=3-7$.

As expected, the fraction of internalized chips diminished as the disc size increased, probably as a consequence of cell geometric and mechanical concerns, thus the number of cells with big discs inside is very small.

Comparing macrophage and non-macrophage cell lines, activated RAW 267.4 macrophages, with half the estimated volume of a HeLa cell can internalize chips of the same size, $35 \mu\text{m}$. That would indicate that the macrophages have higher capability to internalized large devices compared to their volume.

By only considering the phagocytic cell lines, the activated THP-1 did not internalized $\Phi \geq 25 \mu\text{m}$ discs, in spite that they have larger volume than RAW 264.7 which internalize disc up to $\Phi 35 \mu\text{m}$. Moreover, the smaller dendritic cells DC 2.4 could internalize discs up to $\Phi 25 \mu\text{m}$, though quite inefficiently, in the same conditions. This result would show that the cell volume is not the most relevant limitation for the internalization of large devices, which would suggest different internalization process for the different professional phagocytic cell lines. Figures 5 and 6 show some examples of the different cells lines with internalized discs.

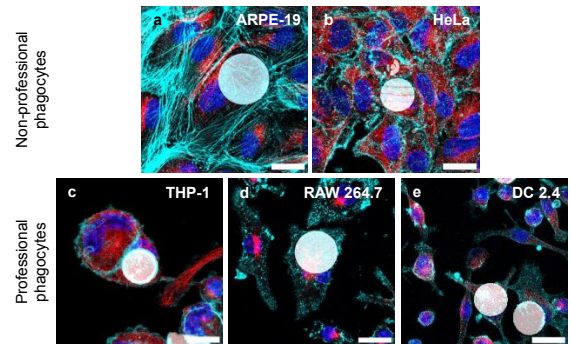


Figure 5: Internalized 2D silicon discs in different cell lines. Confocal images (max. projection) showing tubulin (red), nuclei (blue), 2D disc (white) and actin (cyan). ARPE-19 shows an internalized $\Phi 30\text{-}\mu\text{m}$ disc, RAW 264.7 shows a $\Phi 25\text{-}\mu\text{m}$ one and THP-1, HeLa and DC 2.4 show $\Phi 20\text{-}\mu\text{m}$ discs inside. Scale bars: $20 \mu\text{m}$.

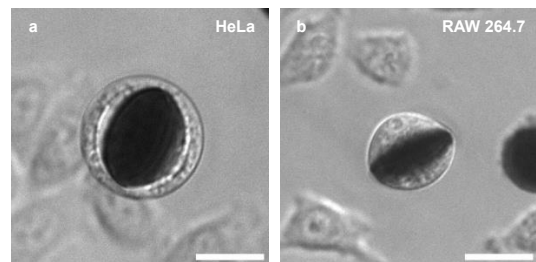


Figure 6: HeLa and RAW 264.7 cells with internalized discs. Optical images from time-lapse experiments showing a HeLa cell with a $\Phi 30\mu\text{m}$ disc and a RAW 264.7 cell with a $\Phi 25 \mu\text{m}$ one. Scale bar: $20 \mu\text{m}$.

VI. INTERNALIZATION EFFICIENCY OF A DISC ON INTIMATE CONTACT WITH A CELL

In order to dismiss the contribution of the cell migration behavior or cell mobility of the different cell lines to the estimation of the internalization ability, we determined the cell's efficiency for internalizing silicon discs. To accomplish this, we only considered the population of cells which were in intimate contact with the discs and counted the discs that are finally internalized by the cells. Internalization frequencies have been calculated from in vivo experiments (HeLa, RAW 267.4 and DC2.4 cell lines) or from confocal images (THP-1 and ARPE-19).

As a general observation, the efficiency of internalization diminishes as the size of the device increases (Table 3). HeLa cells are very efficient internalizing smaller discs, as previously described[5], and the professional phagocytes RAW 267.4 and DC 2.4 also showed competent internalization of Set 1 (Table 3). ARPE-19 cells showed no difficulty internalizing the largest devices of Set 2 according to its estimated size and volume (Tables 2 and 3).

Regarding the frequency of internalization of Set 2, it is rather interesting that HeLa cells, being non-professional phagocytes were more efficient in the uptake than RAW 264.7 cells, 28.5% vs. 4.6% for Φ 30 μm discs and 12.5 vs 5.6%, for Φ 35 μm discs. This behavior changed for the smallest devices of Set 1, Φ 15 μm , where RAW 264.7 showed larger internalization rates, 73.1 % vs. 54.5 for the HeLa cells, as expected from a professional phagocyte.

There could be multiple explanations for this fact, first, our conditions to activate RAW 264.7 cells to their inflammatory phenotype[10] could affect the internalization efficiency and might not exactly mimic the physiological ones. Second, even if RAW 264.7 can internalize Φ 35 μm discs, cell size might be important for internalization efficiency and HeLa cells are bigger (Table 2). And third, it has been described that cells can eat dead cells by other mechanisms, like when entosis[13] takes place, this mechanism which could be at work when internalizing these 2D devices with sizes over the cell diameters.

Table 3: Internalization efficiency of discs on intimate contact with a cell. Smaller discs are internalized more efficiently.

	15 μm		20 μm		25 μm		30 μm		35 μm		40 μm	
	n	%	n	%	n	%	n	%	n	%	n	%
HeLa	22	54.5	18	38.9	15	40.0	21	28.6	8	12.5	12	0
RAW 264.7	26	73.1	29	37.9	25	28.0	22	4.6	18	5.6	21	0
THP-1	38	21.1	53	11.3	39	0	1	0	1	0	1	0
DC 2.4	18	43.4	18	36.8	30	0	1	0	1	0	1	0
ARPE-19	-	-	-	-	-	-	29	48.3	22	40.9	23	26.1

VII. DISCUSSION

The study reports unexpected findings where non-professional phagocytic cells could internalize larger disc-shaped chips than phagocytic cells, probably due to their large volume. Another unanticipated finding is that among the phagocytic cells the largest one is not the cell line that

allows the larger device internalization, which could show that unknown factors play a role during phagocytosis.

Finally, we have to consider that this work is focused on the maximum size that can be mechanically internalized by different cells lines. It has to be considered that these large devices could cause cell death or mitotic arrest when cells start cell division, due to mechanical constraints[5].

We envision that these type of studies are of high value for the future nanomedicine and nanobiotechnology.

ACKNOWLEDGMENT

This work was supported with funds from the Spanish Government Grant PID2020-115663GB-C3 funded by MCIN and by FEDER "EU ERDF, a way of making Europe". The authors thank the clean-room staff of IMB-CNM for fabrication of the devices. The authors at CIB Margarita Salas are deeply indebted with the "Confocal Laser and Multidimensional Microscopy" in vivo in-house facility for their excellent work and professional collaboration.

REFERENCES

- [1] Rennick J.J., Johnston A.P.R., Parton R.G. "Key principles and methods for studying the endocytosis of biological and nanoparticle therapeutics." *Nat. Nanotech* 16.3 (2021): 266-276.
- [2] Gratton S.E.A., et al. "The effect of particle design on cellular internalization pathways." *PNAS* 105.33 (2008): 11613-11618.
- [3] Yang M.X., et al. "Intracellular detection and communication of a wireless chip in cell." *Sci. Rep.* 11.1 (2021): 1-8.
- [4] Gómez-Martínez R., et al. "Silicon chips detect intracellular pressure changes in living cells." *Nat. Nanotech.* 8.7 (2013): 517-521.
- [5] Arjona, M.I., et al. "Intracellular Mechanical Drugs Induce Cell-Cycle Altering and Cell Death." *Adv. Mater.* 34.17 (2022): 2109581.
- [6] Seeberg J.C., et al "Non-professional phagocytosis: a general feature of normal tissue cells". *Sci. Rep.* 9 (1) (2019):11875.
- [7] Duch, M., et al. "Tracking intracellular forces and mechanical property changes in mouse one-cell embryo development." *Nat. Mater.* 19, 1114–1123 (2020).
- [8] Shao Y., Fu J. "Integrated micro/nanoengineered functional biomaterials for cell mechanics and mechanobiology: a materials perspective." *Adv. Mater.* 2014, 26, 1494.
- [9] Dunn K.C., Aotaki-Keen A.E., Putkey F.R., Hjelmeland L.M. "ARPE-19, a human retinal pigment epithelial cell line with differentiated properties." *Exp. Eye Res.* 62(2):155-69, 1996.
- [10] Wu T.T., Chen T.L., Chen R.M. "Lipopolysaccharide triggers macrophage activation of inflammatory cytokine expression, chemotaxis, phagocytosis, and oxidative ability via a toll-like receptor 4-dependent pathway: Validated by RNA interference." *Toxicol. Lett.* 191, 195–202 (2009).
- [11] Genin M., Clement F., Fattaccioli A., Raes M., Michiels C. "M1 and M2 macrophages derived from THP-1 cells differentially modulate the response of cancer cells to etoposide." *BMC Cancer.* 8;15:577 (2015).
- [12] Shen Z., Reznikoff G., Dranoff G., Rock K.L. "Cloned dendritic cells can present exogenous antigens on both MHC class I and class II molecules." *J. Immunol.* 1997 15;158(6):2723-30.
- [13] Yuan J., Kroemer G. "Alternative cell death mechanisms in development and beyond." *Genes Dev.* 24(23):2592-602 (2010).

Piezoelectric impact sensor and infrared array sensor: comparative study for precision seeders.

Sebastián Rossi
*Department of Industrial
 Product Engineering
 National Institute of
 Industrial Technology
 INTI*
 Rosario, Argentina
 0000-0002-9005-3215

Ignacio Rubio Scola
*Department of Industrial
 Product Engineering
 National Institute of
 Industrial Technology
 INTI - CONICET - UNR*
 Rosario, Argentina
 0000-0001-9477-5242

Gastón Bourges
*Department of Industrial
 Product Engineering
 National Institute of
 Industrial Technology
 INTI - UNR*
 Rosario, Argentina
 0000-0002-6034-1697

Jorge Eliach
*Department of Industrial
 Product Engineering
 National Institute of
 Industrial Technology
 INTI*
 Rosario, Argentina
 0009-0005-9526-968X

Eglė Jotautienė
*Department of Agricultural
 Engineering and Safety
 Vytautas Magnus
 University Agriculture Academy*
 Kaunas, Lithuania
 0000-0003-1692-4032

Egidijus Šarauskis
*Department of Agricultural
 Engineering and Safety
 Vytautas Magnus
 University Agriculture Academy*
 Kaunas, Lithuania
 0000-0001-9339-769X

Davut Karayel
*Department of Agricultural Machinery
 and Technologies Engineering
 Faculty of Agriculture,
 Akdeniz University
 Antalya, Turkey*
 0000-0002-6789-2459

Abstract—The aim of this study is to present a comparison of two seed sensors for detecting and counting seeds in pneumatic precision seeders. First, an impact plate sensor, consisting of a plate and a microphone is introduced. When a seed impacts the sensor, the vibrations are reported by a microphone, and its corresponding software translates the impact moment. Secondly, an infrared sensor, which consists of a horizontal array of two infrared emitters facing an array of seven infrared receivers is introduced. When a seed passes, it generates a shadow, which is translated into a passing moment through specific software. Finally, statistics are presented showing the performance of each sensor. The research results of this study showed that both estimated errors were lower with the infrared sensor.

Index Terms—seed detection, impact plate sensor, infrared array sensor, pneumatic seeders, precision agriculture

I. INTRODUCTION

For optimum germination and initial growth, seeds must be properly placed in the furrow during sowing. A seeder should place seeds uniformly at a predetermined distance and depth. However, significant deviations from the desired seed placement often occur in practice. Precision seeders, also known as precision seed drills, are intended to overcome this challenge by planting seed precisely in the furrow. Disc plates are generally used to address the problem of precise seed metering. These plates convey seeds to holes that are located at a specific distance from the center of the plate, ensuring equal spacing between seeds. Each hole contains a single seed, which is released into the furrow at a precise time as the plate rotates. Accurate seeding practices have many benefits, including seed preservation, reduced labor intensity, improved operational efficiency, and increased farmer income.

Advances in precision seeding include monitoring seeding rate and creating a map of seeding status during the process. In precision seeding, the seeding rate index is currently obtained mainly indirectly by tracking changes in the number of seeds within the seed hopper or by calculating the seeder speed and the number of holes. Research on seed flow detecting devices for precision seed metering is necessary to assure seeding rate monitoring, identify missing seedings, enable real-time reseeding throughout the precision seeding process, and boost the overall control of precision seeding. From a different point of view, achieving uniform seed distribution in a furrow increases the growing area of each plant and improves yield by reducing competition between nearby plants. In addition, uniform seed placement facilitates the weeding process.

ISO (International Organization for Standardization) standard establishes standards for test methods and evaluation of precision seed drills. This standard describes the concepts of acceptability, coefficient of variation, multiple deliveries, and missing or lost seeds [1]. The ISO standard begins with the idea that ideal locations in a furrow are separated by a given reference distance. When the separation between consecutive seeds is less than 50% of the reference distance, they are defined as multiple seeds. On the other hand, it considers missing seeds when the distance between seeds is greater than 50% of the reference distance. In addition, an acceptable location is determined when the distance between seeds is within these limits. The percentages of multiple seeds, acceptable seeds, and missing seeds are denoted as M, D, and A, respectively. The coefficient of variation (C) is also obtained by calculating the distances between acceptable seeds.

Xie et al. chose three different types of sensors for testing: two infrared optoelectronic sensors and one high-frequency radio wave sensor [2]. The tests measure the accuracy of the sensors used to monitor the seeding parameters of the precision metering device at different seeding rates and spacings. Nardon and Botta reviewed approaches for measuring and evaluating seed row spacing to evaluate technical options for collecting seed mapping information for corn crop planting in precision agriculture applications [3].

The benefits of the photoelectric sensor include its high sensitivity, low cost, simple signal processing, and precise detection. But because of its sensitivity to dust, fertilizer residues, and other elements, it needs to be maintained regularly and with increased protection [4].

Piezoelectric sensors are simple to install, but their signal processing is more complex than photoelectric sensors because the signal shape is not a simple pulse, and a specific detection method is required [5].

II. MATERIALS AND METHODS

The impact plate sensor is based on a piezoelectric sensor which records impacts on the attached plate, which is shown in Fig. 1. A specific software identifies the impact moment. This sensor, presented and evaluated in [5] and [6], enables faster and more cost-effective seeding quality determination than grease belt test benches.



Fig. 1. Impact plate sensor. A piezoelectric sensor is glued to the fiberglass plate.

On the other hand, an infrared sensor consists of an array of infrared emitters faced to infrared receptors. These receptors are placed on one side of the U-shaped aluminum frame, shown in Fig. 2. Spacing between sensors is 4 mm. The diameter of each sensor is 3 mm. The infrared emitters placed in front of them are spaced 20 mm apart. The distance between the emitters and receivers is 200 mm. Rossi et al. proposed to treat the signals from the infrared sensors as an image [7]. The width of the image is based on an array of infrared sensors. The signal provided by the sensors array through time, creates an image where the number of sensors defines the width. Then, the image height is the test time elapsed. A simple threshold results in a binary matrix. Each seed pass is identified by searching connected pixels.

Seed meters are tested under typical sowing circumstances on a stationary test bench. An electric motor drives the vacuum-style pneumatic precision seed meter used. The electric motor has a Hall sensor, whose signal is collected to



Fig. 2. Infrared sensor frame. Two infrared emitters on the left (red) and seven infrared receivers on the right (blue).

confirm the proper dosage speed and utilized to control the motor's angular speed. A Kimo CP110 pressure transmitter, which has a voltage output from 0 to 10V and is designed to measure from 0 to 100mbar, is used to measure the vacuum pressure inside the meter. Similarly, the impact plate is located underneath a frame containing an array of seven aligned infrared sensors near the discharge tube's exit. A Fastec TS5-S high-speed camera is used to record the experiments. The camera is set at 500 frames per second, 8 bits of color depth, and 800x600 pixel resolution for these tests. A frame of the camera is illustrated in Fig. 3.

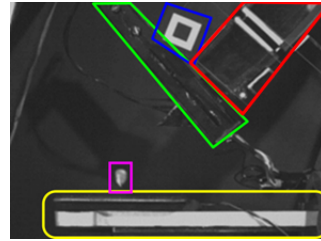


Fig. 3. A frame recorded by the high speed camera. The impact plate sensor in yellow, the infrared sensor in green, the end of the seed tube in red, a seed in violet and a reference for image stabilization in blue.

A data acquisition HBM QuantumX MX1615B is used to record electrical signals. It has 16 channels. The recorded signals are the pressure transmitter, the motor's Hall sensor, the infrared phototransistors and the piezoelectric at the end of the seed tube, and trigger time of each frame.

Each video is run through, frame by frame, registering on a spreadsheet the number of frames in which each seed passed through the infrared sensor frame in one column and in which it impacts against the plate in another. In addition, in a third column the cases in which a seed re-impacts the plate and observations, such as seeds not impacting the plate, were recorded.

III. EXPERIMENTS

A complete randomized experiment with 3 replications for each treatment is carried out for 3 types of seeds: corn, soybean and sunflower. The factor evaluated is the seed dosage rate, considering 2 levels depending on the type of seed. For corn and sunflower, seeds are dosed at 6.5 and 13.5 seeds per second. In the case of soybean, it was 33.3 and 66.7 seeds per second.

Each treatment of the experiment consists of running the seed meter under normal operating conditions mounted on a

static test bench, for a period, so that the filming includes from the first seed dosed to the last one. In this experiment, the camera is placed at approximately 1.5 m to capture the measurement area with both sensors.

For each trial, each sensor detection is compared with each manually recorded pass or impact. Two types of error are then counted. The number of passes not detected by the software is called *MissedPasses*, when computed as a normalized percentage it is called ND (Not Detected) and is defined in (1).

$$ND[\%] = 100 \frac{MissedPasses}{TR} \quad (1)$$

where *TR* is the number of Total Recorded Passes.

The number of detections that do not correspond to any pass in the manual record are called *MultiplePasses*. Extra detections are defined as ED (Extra Detections) and are calculated as the number of *MultiplePasses* in a normalized percentage in (2).

$$ED[\%] = 100 \frac{MultiplePasses}{TR} \quad (2)$$

Finally, ACC (Accuracy) is defined in normalized percentage in (3).

$$ACC[\%] = \frac{100}{1 + \frac{ND}{100} + \frac{ED}{100}} \quad (3)$$

Results obtained by applying (1), (2) and (3) are presented as boxplots. Fig. 4 shows the ND values for each seed, grouped by forward speed, and colored by kind of sensor. Similarly, Fig. 5 and Fig. 6 present ED and ACC values respectively. Note that in Fig. 4, 5 and 6, red and blue boxes represent, respectively, infrared and piezoelectric sensor data.

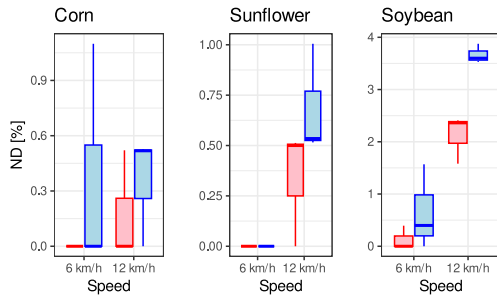


Fig. 4. Not detected percentage comparison.

The ND obtained with infrared sensor was better than piezoelectric ND. The highest difference is seen with soybean at 12 km/h. Piezoelectric sensor had more extra detections than IR. Infrared extra detections occurred only for sunflower seeds. For corn and sunflower seeds, both sensor results are acceptable, being over 99% accuracy. On the other hand, for soybean seeds accuracy is lower, and IR sensor showed a better response, considering that in the experiment setup the seed flow for soybean is greater than corn and sunflower flows.

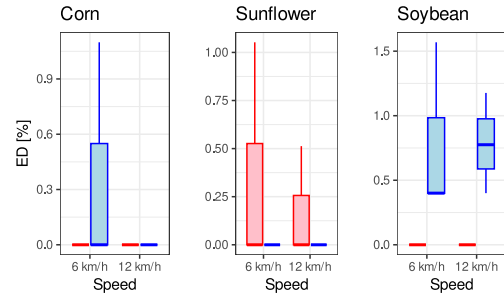


Fig. 5. Extra detection percentage comparison.

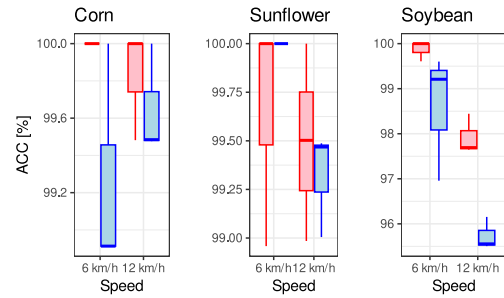


Fig. 6. Accuracy comparison.

When two or more seeds pass or impact the sensor close in time, detection methods compute only one pass. This is due that the signal shape of two close seeds and one seed are similar. To study the incidence of this phenomenon on errors presented here, histograms are plotted. The x-axis represents the elapsed time between each seed pass, registered whether detected or not, and the previous pass. For better graphic representation, this time is limited to 0.1s. Above 0.1s, all seeds are well detected, and no errors occurred.

In Fig. 7, 8 and 9, well detected seeds of corn and sunflower, by infrared sensor, are plotted on top. In the middle plot, not detected cases are presented upward for piezoelectric and downward for infrared. Similarly, the bottom plot corresponds to extra detections obtained, where just one occurred with piezoelectric and no extra detection with infrared. Except for one case in sunflower not detected, errors are found for low differential times between seeds. Not detections for the infrared sensor are concentrated between 0 and 4ms, while not detections for the piezoelectric sensor are more spread in histograms, between 0 and 10ms, with few cases over that range. Extra detections appear also in low differential time. In the piezoelectric sensor case, it could be related to the detection method, that identifies two peaks in one impact signal and computes two passes. In the infrared sensor, only 2 extra detections were found, both for sunflower seeds. The reason for these extra detections could be the elongated shape of the sunflower seeds. This special shape can generate a spread shadow with nonconnected components and the software can compute two shadows.

IV. CONCLUSIONS

This work presents a comparison of two seed sensors for detecting and counting seeds in pneumatic precision seeders. A complete randomized experiment was carried out for 3 types of seeds: corn, soybean, and sunflower.

The research results of this study showed that both estimated errors were smaller using an infrared sensor. A shorter differential time between the seeds affected the quality of the infrared sensor compared to the piezoelectric one. In the case of corn and sunflower, both sensor results are acceptable, being over 99% accuracy. Regarding soybean seeds, accuracy is lower in piezoelectric sensor, and IR sensor showed a better response.

In the case of double (or multiple) seeds, limitations are observed in the detection method with both sensors. An alternative method will be evaluated for these cases as future work.

ACKNOWLEDGMENT

This research was conducted with the financial support of Proyectos Interinstitucionales en Temas Estratégicos (PITES-33) MINCyT (Argentina).

REFERENCES

- [1] Standard, I. S. O. 7256/1-1984 : "Sowing equipment-Test methods Part 1: Single seed drills (precision drills)". Geneva, Switzerland: International Organization for Standardization, 1984
- [2] Xie, C., Zhang, D., Yang, L., Cui, T., Yu, T., Wang, D., & Xiao, T. "Experimental analysis on the variation law of sensor monitoring accuracy under different seeding speed and seeding spacing". *Computers and Electronics in Agriculture*, 2021, Vol 189, pp 106369.
- [3] Nardon, G., Botta, G. "Prospective study of the technology for evaluating and measuring in-row seed spacing for precision planting: A review". *Spanish Journal of Agricultural Research*, 2022, vol. 20, no 4, pp. e02R01.
- [4] Gierz, Ł., Kruszelnicka, W., Robakowska, M., Przybył, K., Koszela, K., Marciniak, A., Zwiachel, T. "Optimization of the sowing unit of a piezoelectrical sensor chamber with the use of grain motion modeling by means of the discrete element method. Case Study: Rape Seed". *Appl. Sci.* 2022, 12, 1594.
- [5] Rossi, S., Rubio Scola, I., Bourges, G., Šarauskis, E., Karayel, D. "Improving the seed detection accuracy of piezoelectric impact sensors for precision seeders. Part I: A comparative study of signal processing algorithms". *Computers and Electronics in Agriculture*, 2023, Volume 215, 108449.
- [6] Rossi, S., Rubio Scola, I., Bourges, G., Šarauskis, E., Karayel, D. "Improving the seed detection accuracy of piezoelectric impact sensors for precision seeders. Part II: Evaluation of different plate materials". *Computers and Electronics in Agriculture*, 2023, Volume 215.
- [7] Rossi, S., Rubio Scola, I., Eliach, J., Bourges, G., Šarauskis, E., Karayel, D. "Seed Detection Accuracy With Infrared Sensors Array In Precision Seeders". VIII Congreso Argentino de Ingeniería Mecánica - III Congreso Argentino de Ingeniería Ferroviaria, 2023.

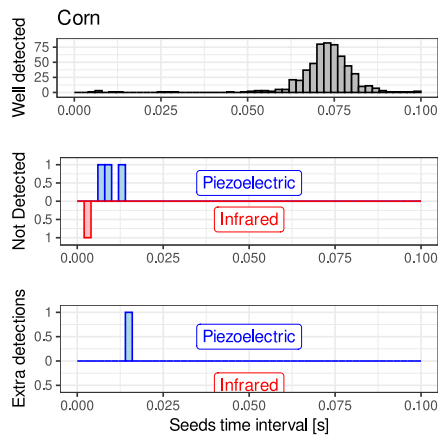


Fig. 7. Histograms of differential time between consecutive seed passes or impacts of corn seeds.

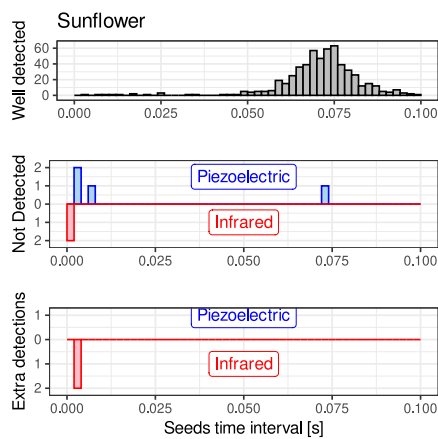


Fig. 8. Histograms of differential time between consecutive seed passes or impacts of sunflower seeds.

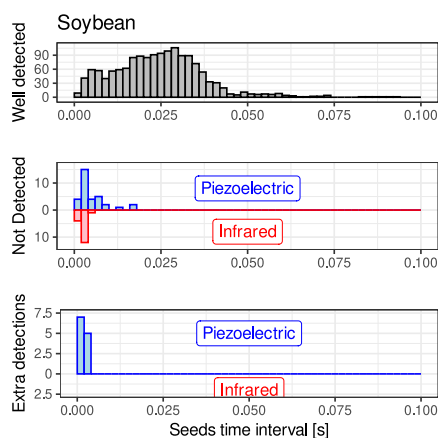


Fig. 9. Histograms of differential time between consecutive seed passes or impacts of soybean seeds.

Challenges in bottom cladding planarization of a waveguide for electrophotonic sensors

J. E. Zamudio-Interian
Electronics Department
Instituto Nacional
de Astrofísica, Óptica
y Electrónica (INAOE)
 Puebla, México
 0009-0006-5866-7694

D. Estrada-Wiese
Electronics Department
Instituto Nacional
de Astrofísica, Óptica
y Electrónica (INAOE)
 Puebla, México
 0000-0002-6245-7765

Alfredo A. González-Fernández
Electronics Department
Instituto Nacional
de Astrofísica, Óptica
y Electrónica (INAOE)
 Puebla, México
 0000-0002-9944-7923

Mariano Aceves-Mijares
Electronics Department
Instituto Nacional
de Astrofísica, Óptica
y Electrónica (INAOE)
 Puebla, México
 0000-0002-4668-2479

Abstract—The integration of electrophotonic (Eph) systems into the microelectronic industry has gained relevance with the advent of new light-emitting materials compatible with silicon technology. Early efforts have led to the development of a monolithic integrated Eph system comprising a silicon-based light-emitting capacitor (LEC), a waveguide, and a photodetector to explore unique on-chip sensing applications. However, challenges persist in the manufacturing and planarization sequences of the waveguide within an Eph system to ensure efficient light transmission. This study focuses on addressing one of these challenges through the fabrication of an imperative buried bottom cladding for the waveguide and explores planarization techniques to mitigate losses. Conventional silicon oxide (SiO_2) cavity filling techniques alongside mechanical polishing, a standard in semiconductor manufacturing, are investigated. Our results reveal effective cavity filling but highlight difficulties in achieving uniform planarization. The influence of the polishing parameters on material removal rates is examined, emphasizing the need for high-efficiency planarization techniques. Overall, this research contributes to the advancement of Eph systems by addressing fabrication challenges for enhancing efficient light transmission. By doing so, it paves the way for the widespread use of such systems in diverse sensing applications.

Keywords—electrophotonic system, waveguide bottom cladding, total internal reflection, planarization, mechanical polishing, bird's beak.

I. INTRODUCTION

In sensing and biosensing applications, Eph systems could play an important role. By harnessing the power of light for signal generation, transmission, and detection, these systems have the potential to permit rapid and noninvasive measurements of diverse variables in real-time. These capabilities can be used to achieve enhanced sensitivity, accuracy, and efficiency in sensing various variables, ranging from physical parameters to chemical compositions [6], [8]. In an Eph system both electronic and photonic components are integrated within a single platform, representing a cutting-edge technological advancement. Monolithic integration of these devices enables the potential miniaturization of lab-on-chip systems. The use of silicon-rich oxide (SRO) as electroluminescent material has allowed the development of silicon-based light-emitting capacitors (LECs) [7], which can be monolithically integrated into Eph systems as the light sources are compatible with

standard integrated circuits fabrication techniques [7]. The simplest of the Eph systems comprises an integrated light source (LEC), a waveguide, and a photodetector. This scheme has been used in the past as a liquid analyte sensor [9].

The cited previous studies have demonstrated the feasibility of fabricating Eph systems by achieving a successful coplanar integration and good communication between the LEC and the photodiode (Fig. 1a) [6]. However, to fully harness the advantages of the LEC, it is necessary to minimize light losses during transmission to the photodetector. Since the approach of this scheme involves the use of standard silicon substrates, the waveguide, consisting of a silicon nitride (Si_3N_4) core and a SiO_2 cladding, requires the latter to be buried into the silicon substrate, as depicted in Fig. 1a. This is not a trivial matter, as the fabrication methods employed significantly impact the final topography, which on its turn, will affect light transmission through the waveguide, since an uneven bottom cladding translates into an equally irregular Si_3N_4 core, resulting in light dispersion and losses. Hence, our research addresses the challenges of achieving a completely planar waveguide bottom cladding. We present a methodology where a single cavity in the silicon substrate is filled with SiO_2 (Fig. 1b) and explore an alternative planarization process distinct from the methods used in previous works [6]. Our aim is to mitigate losses and streamline the fabrication of Eph systems for enhanced efficiency and performance.

II. WAVEGUIDE BOTTOM CLADDING

The waveguide is a crucial element in the Eph scheme, as it confines and transmits the electromagnetic waves from the emitter to the photodetector. Such confinement can be modelled in a simplified way by the total internal reflection phenomenon [2]. Considering this, changes in the structure and materials of a waveguide significantly affect how the light is transmitted. This is what is taken advantage of for the development of optical sensors, as the placement of specific analytes in a particular section of the structure will modify the light transmission, and if such modification is quantified, it can then be related to the characteristics of such analyte.

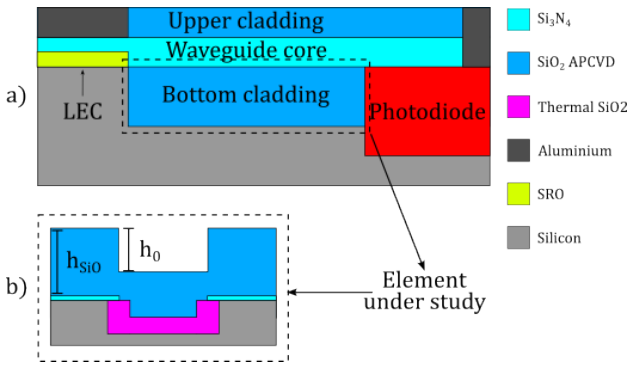


Fig. 1. Schematic illustration of a) an integrated Eph system leveraging a LEC device as a light emitter, alongside a waveguide and a photodiode (not on scale). The bottom cladding of the waveguide is buried within the substrate to achieve coplanar integration. Additionally, b) shows the proposed filling methodology, where h_0 represents the initial step height of SiO_2 after APCVD, and h_{SiO_2} represents the thickness of the SiO_2 layer.

In this case, waveguides serve as crucial components in the operation of Eph systems.

Considering a typical waveguide composed of a Si_3N_4 core and a SiO_2 cladding, the structure meets the initial conditions required for effective light transmission, since the refractive index of Si_3N_4 is higher than the one of SiO_2 . However, the fabrication process of integrating the waveguide on silicon substrates for Eph systems encounter significant challenges, as the SiO_2 bottom cladding needs to be buried to assure coplanarity of light source and waveguide (Fig. 1a). Burying the waveguides bottom cladding within the substrate introduces variations to the device's topography, disrupting the ideal design of the waveguide, leading to difficulties in maintaining consistent light propagation, which manifests as losses. Therefore, the general topography of the planar structure should be as smooth as possible, meaning the fabrication must seek the elimination of sudden height changes (unlevels). Of course, the structure still must have adequate dimensions to ensure the complete confinement of light within the core-cladding structure, and avoid leakage to the substrate, so the challenges of filling the cavity for the buried bottom cladding with SiO_2 must simultaneously be addressed. The latter requires exploring various oxide fabrication techniques, such as atmospheric pressure chemical vapor deposition (APCVD), sputtering, spin-on-oxide (SOX), and thermal oxidation. Each method has its inherent disadvantages and limitations (e.g., bird's beak effect or limitations on deposition thickness), which are essential to consider in order to achieve optimal results through their mitigation during the fabrication process [5]. For this reason, here we propose the employment of a combination of two techniques: first a thermal growth of SiO_2 followed by an APCVD deposition.

In the case of the planarization of the bottom cladding, common techniques like reflow of doped glasses (e.g., borotetraethylene orthosilicate (BTEOS) [6], boro-phosphosilicate glass (BPSG)) [1], and etchback, are available options. How-

ever, these methods can be relatively intricate to implement. Planarization methods, such as chemical etching, often result in undesired and excessive elimination of bottom cladding in some sections of the waveguide [10]. In contrast, planarization processes based on chemical mechanical polishing (CMP), while have being standard in semiconductor manufacturing since the 1980s [1], facilitate the global planarization of substrate surfaces in a single step, offering advantages in various applications like shallow trench isolation (STI), interlayer dielectric (ILD) planarizations, and contact formation [1]. A different option to CMP is the mechanical polishing, which becomes an attractive alternative due to its ease of implementation and comparatively reduced costs for achieving a smooth surface over the bottom cladding.

Our proposed methodology addresses the constraints associated with the different filling techniques of the cavities, and explores the potential use of mechanical polishing as a planarization technique of the bottom cladding of a waveguide by investigating the influence of the constituent parameters of mechanical polishing on the overall system.

A. Fabrication of the buried bottom cladding

N-type silicon wafers of (100) orientation were selected as substrates for potential Eph systems. The buried bottom cladding fabrication methodology (Fig. 1b) begins with the deposition of a 100 nm layer of Si_3N_4 film by low-pressure chemical vapor deposition (LPCVD). This Si_3N_4 layer protects the substrates surface and prevents cavity damage during subsequent polishing steps. This is patterned using a lithography followed by dry etching with tetrafluoromethane (CF_4). The Si_3N_4 film then acts as a masking layer during wet etching of 1.2 μm silicon bulk using 45% potassium hydroxide (KOH) at 40°C. Due to the anisotropic nature of KOH etching and the crystallographic orientation of the substrate, the resulting cavities exhibit sidewalls inclined at 54° [3]. Subsequently, the cavities are filled with SiO_2 using two different processes. First, a 700 nm layer of thermal SiO_2 is grown through wet oxidation (using water vapor) at 1100°C, followed by annealing at the same temperature. Approximately 44% of the silicon substrate is consumed during the oxidation process to form the SiO_2 film [3], resulting in partial cavity filling with SiO_2 (approximately 400 nm) and an increase in depth (nearly 1.5 μm). Second, a 1 μm layer of SiO_2 is deposited by APCVD, followed by annealing at 1100°C. It is noteworthy that the deposition of thicker SiO_2 films by APCVD may lead to cracks inside the cavities, which is why a combined filling methodology was implemented here. Through this methodology, we achieved complete cavity filling with SiO_2 , as shown in the Scanning Electron Microscopy (SEM) image of Fig. 2.

B. Planarization process

The peaks and troughs resulting from cavity filling techniques, which hereafter will be referred to as "unlevels", create irregularities around the substrates surface reference level (Fig. 2). These unlevels are planarized using a mechanical

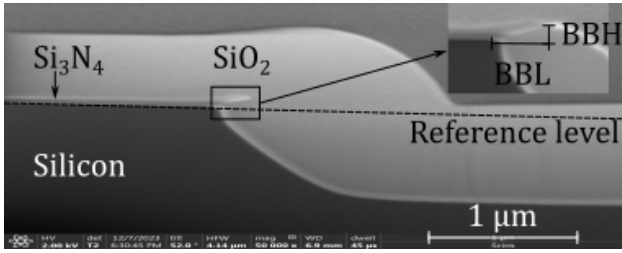


Fig. 2. SEM image of the fully SiO_2 filled cavity as the waveguides bottom cladding. Following the oxidation step, a phenomenon known as the bird's beak effect occurs, characterized by the bird's beak length (BBL) and height (BBH).

polishing process, which involves three main elements: a polishing machine, a polishing pad, and a slurry (typically consisting of a colloidal suspension). The surface of the substrate undergoes smoothing and planarization through the dynamic interplay of frictional forces between the sample, the polishing pad, and the abrasive particles suspended in the slurry, complemented by various physical parameters [1]. The presence of the Si_3N_4 layer serves to protect the cavity during the mechanical polishing process, with the process ideally ceasing upon reaching this layer. Optimal planarization results are anticipated to resemble those depicted in Fig. 3a.

A key challenge in the mechanical polishing process lies in optimizing the conditions, including material removal rates (MRR), selectivities, uniformity, and machine parameters. In our process, we utilize two types of polishing pads: an electronic-grade high-density polyurethane pad (P1) and a viscose-polyester pad (P2). Additionally, we employ three different slurries, each containing particles with unique abrasive properties: zirconium oxide (ZrO_2), cerium oxide (CeO), and alumina (Al_2O_3). Table I provides detailed characteristics of these slurries. Once planarization is complete, the Si_3N_4 film is removed by wet etching using 85% phosphoric acid at 90°C.

TABLE I
CHARACTERISTICS OF SLURRIES USED DURING MECHANICAL POLISHING

Slurry	S1	S2	S3	S4	S5	S6
Solvent	Deionized water			Isopropyl alcohol		
Solute	ZrO_2	CeO	Al_2O_3	ZrO_2	CeO	Al_2O_3
Average particle size (nm)	1400	500	50	1400	500	50
Proportion	5%	10%	25%	5%	10%	25%
pH	5-6	8-9	9-10	6-7	8-9	9-10

III. RESULTS

The SEM images show that the fabrication methodology employed for filling the cavity with SiO_2 effectively reduces cracks and voids within the structure (Fig. 2). However, this methodology bears resemblance to techniques like STI and local oxidation of silicon (LOCOS) [5], where the oxidation step introduces an undesirable phenomenon known as the

“bird’s beak”, attributed to the stress resulting from the mismatch in thermal expansion coefficients between Si_3N_4 and the substrate [4]. The bird’s beak is the main source of unlevels in the bottom cladding. Measurements reveal the dimensions of the bird’s beak effect, with a height (BBH) of 140 nm, a length (BBL) of 390 nm (inset in Fig. 2). The dimensions of the bird’s beak are influenced by the duration of the oxidation.

Profilometry measurements reveal an approximately 800 nm initial step height (h_0 in Fig. 1b) in the SiO_2 film covering the cavity prior to planarization. Notably, over the cavity, there is approximately 300 nm of SiO_2 protruding above the reference level, whereas the SiO_2 film over the Si_3N_4 film measures 1 μm in thickness (h_{SiO} in Fig. 1b). Following the mechanical polishing process, the observed polishing rates exhibited variable dependence on the material being removed and the specific conditions applied. The MRR in mechanical polishing can be represented by 1, which offers a simplified prediction based on parameters such as h_{SiO} and process time (t). Additionally, polishing rates have consistently shown a direct correlation with plate polishing velocity and pressure applied. Moreover, factors including pad type, slurry composition, and grain size also exert influence on the MRR.

$$MRR = h_{SiO}/t \quad (1)$$

We conducted mechanical polishing under constant machine parameters (plate polishing velocity was set at 80 rpm, with an applied pressure of 1 kgf/cm^2) and explored various combinations of slurries (outlined in Table I) and pads (P1 and P2) to remove 1 μm of SiO_2 . The obtained MRR (Table II) demonstrated increased values with larger particle sizes, higher slurry concentrations and higher pad hardness. The use of isopropyl alcohol as a solvent (increasing the pH) increased the MRR of slurries containing CeO and Al_2O_3 , while reducing the MRR of the slurry with ZrO_2 . Table II shows that some combinations of slurries and pads resulted in higher or lower MRR. However, despite employing various combinations for global planarization, the typical outcome results in uniform removal rates both on the sample’s surface and within the cavity. This results in conformal polishing of the SiO_2 layer, where the step height (h_s in Fig. 3b) after mechanical polishing approximates the h_0 , maintaining the original shape and features of structures, while the thickness of the SiO_2 layer tends to approach zero ($h_{SiO} \rightarrow 0$).

TABLE II
MRR (NM/MIN) OF 1 μm OF SiO_2 AS A FUNCTION OF SLURRY AND PAD TYPES. PLATE POLISHING VELOCITY WAS SET AT 80 RPM, WITH AN APPLIED PRESSURE OF 1 kgf/cm^2 .

	S1	S2	S3	S4	S5	S6
P1	200.0	20.0	18.2	66.7	100.0	25.0
P2	241.2	83.3	40.0	83.4	143.9	50.0

In Fig. 1a, we utilized a Si_3N_4 film as the waveguide core. However, the mechanical properties of Si_3N_4 makes it an attractive option not only as a waveguide core, but

also as a protective film. As expected, Si_3N_4 film exhibits a higher polishing rate than SiO_2 during the mechanical polishing. Nonetheless, during planarization, there is evidence of overpolishing in the cavity reaching the Si_3N_4 film surface, leading to partial removal of SiO_2 as depicted in Fig. 3b. This phenomenon results in h_s ranging between 600 nm to 900 nm at different polishing conditions.

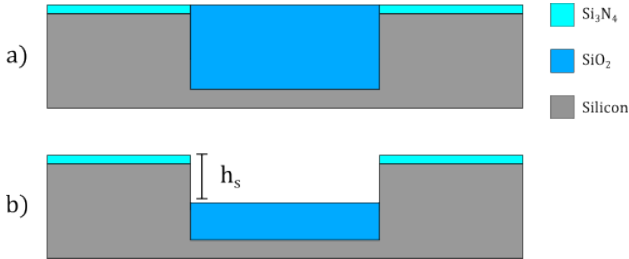


Fig. 3. Schematic diagram illustrating a) ideal mechanical polishing reaching the Si_3N_4 film and the b) obtained overpolishing effects within the cavity due to conformal planarization, where h_s represents the step height of overpolishing after mechanical polishing.

IV. CONCLUSIONS

The integration of Eph systems into the microelectronic industry holds significant promise, particularly with the advent of new light-emitting materials compatible with standard integrated circuit technology. While early efforts have led to the development of monolithic integrated Eph systems, challenges persist in manufacturing and planarization sequences, crucial for ensuring efficient light insertion and transmission.

This work addresses the challenges of producing integrated Eph systems by focusing on the fabrication of the buried bottom cladding of in such systems and exploring alternative planarization techniques to mitigate losses. Our results highlight effective cavity filling with SiO_2 by combining different filling techniques (thermal oxidation and APCVD). However, the processes used introduce unlevels that significantly impact the conformal deposit of a waveguide core over the cavity, potentially resulting in losses in the Eph system linked to the extent and magnitude of these irregularities. Through meticulous investigation of polishing parameters of a simple mechanical polishing technique to achieve a smooth

and homogeneous bottom cladding surface, we observed that the procedure tends to yield conformal outcomes featuring unlevels of approximately 800 nm high ($h_s \approx h_0$). In such cases, the MRR, height and smoothness of resulting steps (h_s) are contingent upon the properties of the slurry and pad utilized.

Addressing these unlevels opens future investigations towards optimized nonconformal polishing techniques or the integration of an additional step during the here proposed methodology. The present work sheds light on possible avenues for improving the fabrication process of efficient Eph systems, contributing to the advancement of novel Eph sensors.

ACKNOWLEDGMENT

The authors thank the microelectronics laboratory and the optics workshop of the Institute of Astrophysics, Optics and Electronics (INAOE).

REFERENCES

- [1] Suryadevara Babu, "Advances in chemical mechanical planarization (CMP)," Second Edition, Woodhead Publishing, 2021.
- [2] Novotny, L. and Hecht, B., "Principles of nano-optics," Cambridge University Press, 2006.
- [3] Wolf, S., "Microchip manufacturing," Latrice Press, 2003.
- [4] Van Zant, P., "Microchip fabrication: a practical guide to semiconductor processing," Sixth Edition, McGraw Hill LLC, 2013.
- [5] Campbell, S.A., "Fabrication engineering at the micro and nanoscale," Oxford University Press, 2013.
- [6] González-Fernández, A. A., Juvert, J. and Aceves-Mijares, M. and Domínguez, C., "Monolithic integration of a silicon-based photonic transceiver in a CMOS process," *IEEE Photonics Journal*, vol. 8, no. 1, pp. 1-13, 2016.
- [7] González-Fernández, Alfredo A., Aceves-Mijares, Mariano and Pérez-Díaz, Oscar and Hernández-Betanzos, Joaquin and Domínguez, Carlos, "Embedded silicon nanoparticles as enabler of a novel CMOS-compatible fully integrated silicon photonics platform," *Crystals*, vol. 11, no. 6, 2021.
- [8] L. Zhuang and A. J. Lowery, "Electro-photonics: An emerging field for photonic integrated circuits," in *Smart Photonic and Optoelectronic Integrated Circuits XX*, S. He, E.-H. Lee, and S. He, Eds. United States of America: SPIE, 2018, vol. 10536.
- [9] González-Fernández, A. A., Hernández-Montero, W. W., Hernández-Betanzos, J., Domínguez, C., and Aceves-Mijares, M. (2019). "Refractive index sensing using a Si-based light source embedded in a fully integrated monolithic transceiver." *AIP Advances*, 9(12), 125215.
- [10] Avilés Bravo J. J., "Investigación y desarrollo de procesos tecnológicos para la obtención de emisores de luz y guías de onda para la integración en sistemas electrofotónicos," M.S. thesis, National Institute of Astrophysics, Optics and Electronics, Santa María Tonanzintla, Puebla, México, 2019, unpublished.

Low-cost microwave sensor for detecting the first generation of microplastic in aqueous media

1st Josaphat Desbas
Dept. Electrical Engineering
University of Brasilia (UnB)
Brasília DF, Brazil
josaphat.desbas@aluno.unb.br

2nd Juliana de Novais Schianti
Dept. Electrical Engineering
University of Brasilia (UnB)
Brasília DF, Brazil
juliana.schianti@unb.br

3rd João Pedro Moreno de Oliveira
Dept. Electrical Engineering
University of Brasilia (UnB)
Brasília DF, Brazil
190128488@aluno.unb.br

4th Matheus Rotta Ribeiro
Dept. Electrical Engineering
University of Brasilia (UnB)
Brasília DF, Brazil
matheus.rotta.ribeiro@gmail.com

5th Mateus I. O. Souza
Dept. Electrical Engineering
University of São Paulo (USP)
São Carlos SP, Brazil
mateusafk@usp.br

6th Vinicius M. Pepino
Dept. Electrical Engineering
University of São Paulo (USP)
São Carlos SP, Brazil
vinicius.pepino@usp.br

7th Ben-Hur Viana Borges
Dept. Electrical Engineering
University of São Paulo (USP)
São Carlos SP, Brazil
benhur@sc.usp.br

8th Daniel Orquiza de Carvalho
Dept. Electrical Engineering
University of Brasilia (UnB)
Brasília DF, Brazil
daniel.orquiza@ene.unb.br

9th Achilles F. da Mota
Dept. Electrical Engineering
University of Brasilia (UnB)
Brasília DF, Brazil
achiles.mota@ene.unb.br

Abstract—The escalating environmental and health concerns associated with microplastic pollution have led to the development of accurate methods to monitor their environmental presence. In this sense, we propose using an interdigital microwave sensor tailored to analyze microplastic presence in liquid environments and capable of monitoring water quality. The presence of the microplastics in the sensor provoked a shift at the resonance factor of ($\Delta f = 570MHz$) when compared to the unload scenario. Our results show that the sensor is highly sensitive to the presence of microplastic. Therefore, this research constitutes a step forward in developing innovative technologies to mitigate the pervasive issue of microplastic pollution in aquatic ecosystems.

Index Terms—microwave sensor, microplastics, microfluidic channels, interdigital resonators

I. INTRODUCTION

Over the last decade, the surge in global plastic production reached a staggering 320 million tons annually [1] [2], which resulted in a substantial waste challenge with several consequences for human health. Approximately 8 million tons of plastic enter the oceans annually, accumulating in terrestrial and marine environments due to poor degradation and limited recovery options [3] [4].

In aquatic ecosystems, plastic undergoes degradation, leading to the formation of microplastics (particles smaller than 5 millimeters) through processes like microbiological activity, radiation, and mechanical stress [4] [5]. These microplastics, originating from various sources, pose profound threats to ecosystems, human health, and water quality [1] [3] [6].

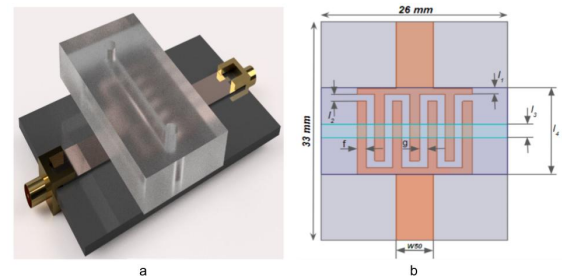


Fig. 1. (a) shows the proposed interdigital circuit coupled with the microfluidic channel, and (b) shows the top view of the sensor.

Studies reveal that microplastics have infiltrated the food chain, entering the human diet through seafood, salt, and even drinking water [7], emphasizing their prevalence in freshwater systems [8] [9], which turn this issue into a global concern and the need for urgent solutions. This pervasive issue demands international collaboration and innovative technologies to address the far-reaching consequences of microplastic pollution [10] [11].

In this context, sensors to detect and measure microplastic concentrations are extremely relevant. Given the pervasive nature of microplastic pollution and its potentially severe consequences, precise monitoring of its concentration in aquatic

ecosystems is essential for assessing the extent of the problem and devising effective mitigation strategies. Several approaches have been proposed, such as using optical and electrical microscopies, spectroscopy detection methods such as Fourier Transform Infrared Spectroscopy and Raman [12], mass spectroscopy [13], and techniques that evaluate electrical properties from microplastics considering impedance and capacitance changes [15]. Microscopy and spectroscopy methods measure microplastics' quantity, size, morphology, and composition; however, they require sophisticated equipment that is not readily available and is restricted in size detection.

Also, the slight difference in refraction index from water to microplastics became a challenge in optical methods [14]. Mass spectroscopies require pre-prepared samples, which are time-consuming and limited by a high heterogeneity of polymers. Electrochemical detection sensors have been applied with successful results regarding sensitivity and precise data. However, producing the electrode requires complex and expansive procedures [15]. By integrating these diverse approaches, researchers can develop comprehensive sensing systems that accurately assess microplastic pollution levels in aquatic ecosystems. These sensors are pivotal in advancing our understanding of microplastic contamination and developing effective mitigation strategies to protect environmental and human health. One cheap alternative that can be used to detect microplastics at aqueous media is by means of microwave sensors. These sensors are easily fabricated, with a small cost, and can have high sensitivity to the presence of microplastics.

In this regard, we propose using an interdigital resonator operating in a microwave regime to detect the presence of microplastics in an aqueous medium. The sensor is coupled with a microfluidic channel that can be linked to any water source for real-time water quality monitoring. We show that the resonance frequency of our devices shifts approximately 570 MHz when the microplastic passes through the microfluidic channel, representing a high sensitivity.

The paper is organized as follows: In section II, we present

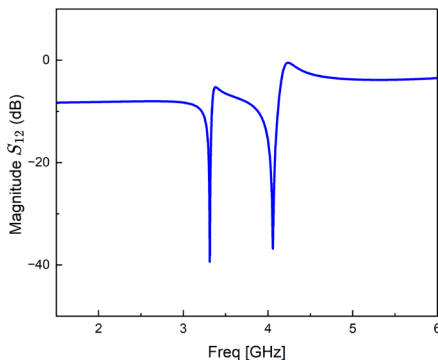


Fig. 2. Simulated transmission coefficient of the unloaded sensor.

the design optimization of the interdigital resonator and the simulation results with the presence of water inside the microchannel. In section III, we present the measurements and finish with some concluding remarks in section IV.

II. INTERDIGITAL SENSOR OPTMIZATION

The proposed sensor with the microfluidic channel is presented in Fig. 1 (a), where the microstrip is connected with an SMA connector, and the interdigital resonator is under a Polydimethylsiloxane (PDMS) block, where we built the microchannel. We utilized 0.75mm thick Rogers 5880 substrate, with permittivity of 2.2 and tangent loss of 0.0009. As well known, if the water directly touches the interdigital sensor, the ions present in the water create a current between the fingers, drastically reducing the sensor's quality factor. To solve this issue, we have added a 0.1 mm glass plate isolating the water from the fingers. Moreover, the interdigital dimensions (as shown in Fig. 1 (b)) were fine-tuned using quasi-Newton's method to achieve band-stop resonance at 4 GHz, with a high-quality factor, and the results can be seen in table I.

It is important to notice that the channel was empty during this optimization. The simulated transmission (S_{21}) as a function of the frequency can be seen in Fig. 2. As can be seen, the system presents two resonances, one at 3.313 GHz and a second at 4.057 GHz, with a corresponding quality factor of 47.41. In addition, a characteristic of the interdigital configuration is a high insertion loss, as seen by the high insertion loss of approximately -9 dB. As we increase the frequency, the insertion loss reduces to -5 dB at 6 GHz. However, despite some insertion loss, both resonances present a high-quality factor, which is required for detecting small-sized plastic inside the microfluid channels.

A. Characterization

After designing the interdigital sensor, we proceeded to characterize its operation and later presented some results when measuring its response to a microplastic presence.

III. RESULTS

We initially placed the microfluidic channel atop the sensor to start the characterization. The microfluidic channels to conduct microplastic sample fluids over the RF sensor were microfabricated in PDMS polymer (polydimethylsiloxane, Silicon Silgard 184 – Dow Corning) by the soft lithography technique. The first step was designing the molds with the desired geometry. It used a single straight channel with 2 mm of width

TABLE I
DIMENSIONS OF THE PROPOSAL INTER-DIGITAL SENSOR.

Dimensions	values [mm]
$W50$	5.1
$l1$	0.962
$l2$	1.301
$l3$	2
$l4$	6.292
f	1.301
g	1.144

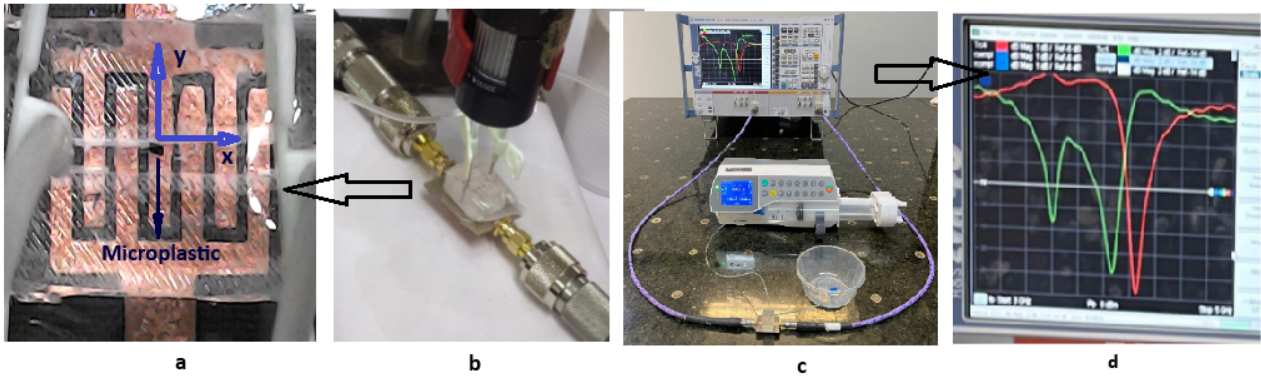


Fig. 3. Complete measurement setup; Proposed fabricated sensor under test

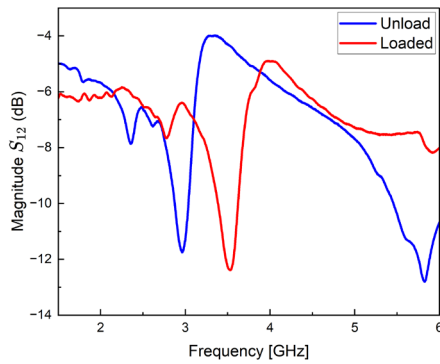


Fig. 4. Measured S_{21} with (red line) and without (blue line) the presence of the microplastic.

and 1 mm of height, designed in FUSION 360 (Autodesk). The molds were printed using a TEVO TORNADO 3D (Tower A, Sunac Zhihui Building, Shangfen Minzhi ,Longhua District, Shenzhen Guangdong, 51800) printer using PLA filament. In sequence, the PDMS was prepared in a proportion of 12:1 (PDMS: Additive) and introduced in the mold. The curing agent (additive) used for PDMS is Methylvinylcyclosiloxane, a chemical that facilitates the formation and solidification of silicone-based materials by linking various parts of the polymer chain together during the curing process. After the curing process, the polishing procedure was straightforward. We used wet sandpaper to polish the device for approximately 5 minutes. This step ensured a smooth and even surface, crucial for the device's performance. After heating at 85 C for 2 hours, the device was removed from the mold, and some polishing procedure was conducted to reduce the rugosity created by the filament on the surface.

After gluing the PDMS on the glass plate, using a precision pump, we could control the microplastic position (in the x-axis), placing it in any position of the channel as desired, as shown on the top view in Fig. 3 (a). We inserted the water flow

using the precision pump connected to the sensor by a 0.1 mm diameter silicone tube, as seen in Fig. 3 (b). In Fig.3 (c), we present the complete measurement setup of S_{11} in red and S_{21} in green. Finally, We connected the SMA connectors to a Rohde Schwarz ZVA40 vector network analyzer (Bedfordshire, UK), focusing on a zoomed-in frequency range of 2 GHz to 4 GHz. in Fig. 3 (d). As for the microplastic, we have utilized a ground-tire rubber (GTR) with dimensions of approximately 0.3 x 0.3 x 0.3 mm and permittivity of $\epsilon = 3.65 - 0.60j$ [6], as it represents a common type of microplastic found in aquatic environments.

To check if the microplastic can change the transmission, we initially measured S_{21} with (red line) and without (blue line) the presence of the microplastic, and the curves are shown in Fig. 4. The testing revealed a significant shift in the resonance frequency. Specifically, the resonance frequency changed from 2.96 GHz when unloaded to 3.53 GHz for the loaded condition, which is a substantial shift of approximately 570 MHz. Furthermore, a profound change in transmission at 3.53 GHz can also be noticed, representing a good frequency point for further exploration of microplastic detection. Finally, the quality factor is also slightly changed, from 8.41 when the sensor is empty to 14.13 for the loaded scenario. Note a degradation of the quality factor compared to the simulation due to the presence of water.

To improve the understanding of the optimum operation frequency, 5 shows the difference between S_{21} with and without the presence of the microplastic. As can be seen, there are two frequencies where the transmission difference is prominent, at 2.96 GHz and 3.53 GHz the difference is 5 and 8 dB, respectively. Therefore, both resonances can be used for microplastic detection.

Finally, we also swept the microplastic position inside the channel to study the shift in resonance frequency. Given the sensor's symmetrical nature, we charted the resonance frequency from its center to one end (as shown in Fig. 2). This insightful analysis allows us to discover the best position of the microplastic inside the fluidic channel. These results are shown in Fig 6 As can be seen, when the microplastic is above

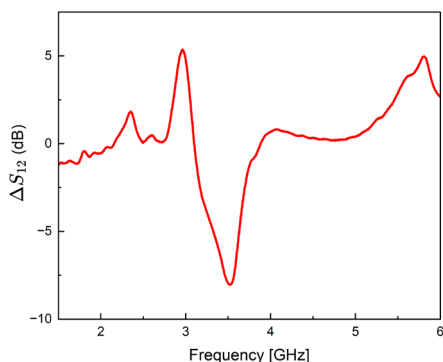


Fig. 5. Measured difference between the transmission S_{21} with and without the presence of the microplastic.

the 3rd finger, the resonance shift is higher. In conclusion, as the microplastic passes through the channel, the resonance frequency shifts and, consequently, the transmission. In this sense, it is possible to have a signature in time for each microplastic, enabling the differentiation of several types of microplastics and dimensions.

IV. CONCLUSION

In conclusion, our investigation demonstrates noteworthy shifts in the resonance frequency (Δf) when transitioning between the unloaded and loaded states of the interdigital microwave sensor. These shifts are compelling evidence of the sensor's ability to detect and quantify microplastic concentrations in liquid environments precisely. The results show promise and ongoing research will yield valuable insights. During the conference, we expect to refine these results, and present results for different types and dimensions of microplastic, highlighting the sensor's ability to detect and measure

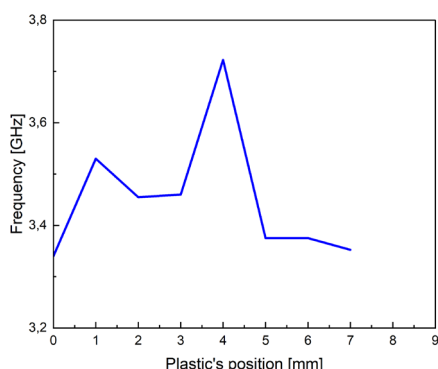


Fig. 6. Measured resonant frequency of the sensor as the microplastic flow inside the channel

them. Ultimately, this progress will contribute significantly to developing more effective monitoring and mitigation strategies to combat the widespread issue of microplastic pollution in aquatic ecosystems.

V. ACKNOWLEDGMENT

Fundação de Apoio à Pesquisa do Distrito Federal (FAPDF) with grant number 271/2021-03/2021, 00193-00000923/2021-48, 00193-00000849/2021-60. This study was financed in part by the Coordenação de Aperfeiçoamento de Pessoal de Nível Superior – Brazil (CAPES) – Finance Code 001 and Conselho Nacional de Desenvolvimento Científico e Tecnológico (CNPq), grants number 102003/2022.

REFERENCES

- [1] From oceans to dinner plates: The impact of microplastics on human health <https://doi.org/10.1016/j.heliyon.2023.e20440>
- [2] A. Ragusa, A. Svelato, C. Santacroce, P. Catalano, V. Notarstefano, O. Carnevali, F. Papa, M.C.A. Rongioletti, F. Baiocco, S. Draghi, Placentica: first evidence of microplastics in human placenta, *Environ. Int.* 146 (2021), 106274.
- [3] L.M.R. Mendoza, M. Balcer, Microplastics in freshwater environments: a review of quantification assessment, *TrAC, Trends Anal. Chem.* 113 (2019) 402–408.
- [4] A.B. Silva, A.S. Bastos, C.I. Justino, J.P. da Costa, A.C. Duarte, T.A. Rocha-Santos, Microplastics in the environment: challenges in analytical chemistry-A review, *Anal. Chim. Acta* 1017 (2018) 1–19.
- [5] C. Wang, J. Zhao, B. Xing, Environmental source, fate, and toxicity of microplastics, *J. Hazard Mater.* 407 (2021), 124357.
- [6] Plastics and microplastics: A threat to environment: <https://doi.org/10.1016/j.eti.2019.100352>.
- [7] Human Consumption of Microplastics: <https://doi.org/10.1021/acs.est.9b01517>
- [8] Reaching New Heights in Plastic Pollution— Preliminary Findings of Microplastics on Mount Everest <https://doi.org/10.1016/j.oneear.2020.10.020>
- [9] Microplastic and microfiber fluxes in the Seine River: Flood events versus dry periods : <https://doi.org/10.1016/j.scitotenv.2021.150123>.
- [10] <https://www.who.int/news-room/events/detail/2023/11/08/default-calendar/who-health-dialogue-plastics-in-health-care>.
- [11] Microplastics in freshwater and terrestrial environments: Evaluating the current understanding to identify the knowledge gaps and future research priorities: <https://doi.org/10.1016/j.scitotenv.2017.01.190>
- [12] Iri, A.H., Shahrah, M.H.A., Ali, A.M. et al. Optical detection of microplastics in water. *Environ Sci Pollut Res* 28, 63860–63866 (2021). <https://doi.org/10.1007/s11356-021-12358-2>
- [13] Junjie Zhang, Dongdong Fu, Huan Feng, Ye Li, Shuyi Zhang, Chu Peng, Yudi Wang, Hongwen Sun, Lei Wang, Mass spectrometry detection of environmental microplastics: Advances and challenges, *TrAC Trends in Analytical Chemistry*, Vol. 170, 2024, 117472, <https://doi.org/10.1016/j.trac.2023.117472>.
- [14] Benjamin O. Asamoah, Boniphace Kanyathare, Matthieu Roussey, Kai-Erik Peiponen, A prototype of a portable optical sensor for the detection of transparent and translucent microplastics in freshwater, *Chemosphere*, Vol. 231, 2019, Pages 161–167, <https://doi.org/10.1016/j.chemosphere.2019.05.114>.
- [15] Kamel, Ayman H. and Hefnawy, A. and Hazeem, Layla J. and Rashdan, Suad A. and Abd-Rabboh, Hisham S. M., Current perspectives, challenges, and future directions in the electrochemical detection of microplastics, *RSC Adv.*, vol. 14, n.3, 2134–2158, 2024. <http://dx.doi.org/10.1039/D3RA06755F>
- [16] Pérez-Campos, R.; Fayos-Fernández, J.; Monzó-Cabrera, J.; Martín Salamanca, F.; López Valentín, J.; Catalá-Civera, J.M.; Plaza-González, P.; Sánchez-Marín, J.R. Dynamic Permittivity Measurement of Ground-Tire Rubber (GTR) during Microwave-Assisted Devulcanization. *Polymers* 2022, 14, 3543. <https://doi.org/10.3390/polym14173543>

Elaboración de sensores finos de posición en Argentina

Martha Díaz Salazar
Departamento Energía Solar
Comisión Nacional de Energía Atómica
(CNEA)
Instituto de Nanociencia y
Nanotecnología
CNEA-Consejo Nacional de
Investigaciones Científicas y Técnicas
Buenos Aires, Argentina
marthadiazsalazar@cnea.gov.ar

Analía Moreno
Departamento Energía Solar
Comisión Nacional de Energía Atómica
(CNEA)
Instituto de Nanociencia y
Nanotecnología
CNEA-Consejo Nacional de
Investigaciones Científicas y Técnicas
Buenos Aires, Argentina
analiaveronicamoreno@cnea.gov.ar

Nadia Kondratiuk
Departamento Energía Solar
Comisión Nacional de Energía Atómica
(CNEA)
Instituto de Nanociencia y
Nanotecnología
CNEA-Consejo Nacional de
Investigaciones Científicas y Técnicas
Buenos Aires, Argentina
nadiakondratiuk@cnea.gov.ar

Mónica Martínez Bogado
Departamento Energía Solar
Comisión Nacional de Energía Atómica (CNEA)
Instituto de Nanociencia y Nanotecnología
CNEA-Consejo Nacional de Investigaciones Científicas y Técnicas
Buenos Aires, Argentina
monicamartinez@cnea.gov.ar

Mariana Tamasi
Departamento Energía Solar
Comisión Nacional de Energía Atómica (CNEA)
Instituto de Nanociencia y Nanotecnología
CNEA-Consejo Nacional de Investigaciones Científicas y Técnicas
Buenos Aires, Argentina
marianatamasi@cnea.gov.ar

Resumen— Los sensores solares de posición son dispositivos fotovoltaicos que se utilizan para determinar la posición del Sol, tanto en sistemas terrestres como espaciales. En Argentina, el Departamento Energía Solar de la Comisión Nacional de Energía Atómica cuenta con amplia experiencia en el desarrollo de sensores gruesos de posición de silicio para aplicaciones satelitales, los cuales tienen una precisión de 5°. Estos sensores han acumulado una herencia espacial de más de 20 años. La problemática tratada en este trabajo consiste en la elaboración de un sensor capaz de determinar la posición del Sol con una precisión de 1°, utilizando la tecnología disponible en el país. Con este objetivo, se estudiaron diversos diseños y se describen los pasos seguidos en la elaboración del diseño seleccionado; haciendo énfasis en los desafíos encontrados durante el proceso. Los sensores diseñados tienen en común que emplean detectores formados por un arreglo de fotodiodos de silicio cristalino, además de una ventana que limita y direcciona la luz que llega al detector. En este trabajo se presentan los primeros resultados obtenidos con el proceso de fabricación de los sensores.

Keywords—sun position sensor, silicon, FSS.

I. INTRODUCCIÓN

El Departamento Energía Solar (DES) de la Comisión Nacional de Energía Atómica (CNEA) cuenta con experiencia en el desarrollo de sensores fotovoltaicos para medir la radiación global a nivel terrestre, así como en el desarrollo de sensores gruesos de posición (CSS sus siglas en inglés, *Coarse Sun Sensor*) utilizados en distintos satélites [1,2]. Los CSS elaborados en el DES tienen una herencia de más de 20 años y 2.500.000 horas de vuelo hasta agosto 2024. Estos sensores alcanzan una precisión de 5°.

Los sensores solares de posición son dispositivos fotovoltaicos que se utilizan para detectar la posición del Sol en un determinado marco de referencia. Estos sensores se pueden utilizar en aplicaciones terrestres tales como en seguidores solares para la medición de la radiación solar directa, la orientación de paneles solares con seguimiento solar, sistemas fotovoltaicos o térmicos con concentración o para la protección de instrumentos sensibles a la radiación solar, entre otras aplicaciones. El uso espacial de estos dispositivos implica la integración de los sensores al sistema de control de actitud de satélites como sensores gruesos o finos.

El diseño del dispositivo determina si la medición se puede realizar en uno o dos ejes, el campo de visión del sensor, la sensibilidad y la linealidad de la respuesta. En la bibliografía se encuentran distintas alternativas tecnológicas en cuanto a la estructura y configuración de estos sensores. Por ejemplo, en [3] y en [4], presentan un resumen de diferentes tecnologías empleadas en sistemas fotovoltaicos terrestres con seguimiento solar, donde en algunos casos se emplea una trayectoria predeterminada y en otros casos se controla la orientación de los paneles solares utilizando como referencia la medición de sensores solares de posición. Por otro lado, en [5], se presenta un resumen del estado de la técnica de los sensores solares de posición para aplicaciones terrestres y espaciales, donde se describen diferentes tecnologías, materiales y principios de operación.

La problemática tratada en este trabajo consiste en la elaboración de un sensor capaz de determinar la posición del Sol con una precisión de 1°, utilizando la tecnología disponible en el país.

II. DISEÑO DEL SENSOR DE POSICIÓN SOLAR

Los sensores que se proponen elaborar consisten en un detector formado por un arreglo de fotodiodos y una ventana, separada del detector y alineada con este, que cumple la función de limitar y direccionar la luz que llega al detector, como se muestra en la Fig. 1. Con estos sensores se puede determinar la posición de Sol en un eje con un detector de dos cuadrantes (Fig. 1) o en dos ejes si se utiliza un detector de cuatro cuadrantes. La posición del Sol se obtiene al comparar el área iluminada en cada fotodiodo.

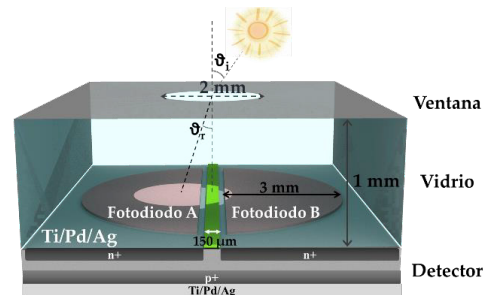


Fig. 1. Diseño del sensor de posición para medición en un eje.

El detector consiste en un arreglo de dos o cuatro fotodiodos integrados en un sustrato de silicio, acotados en un cuadrado de 12 mm de lado. Cada fotodiodo es una juntura n^+pp^+ . La ventana consiste en una apertura en una capa delgada de metal, que se deposita sobre un sustrato de vidrio que cumple la función de separador entre el detector y la ventana. La geometría de la ventana y los fotodiodos se definen con procesos de fotolitografía. Para la selección de la geometría y tamaño de la ventana, así como del arreglo de fotodiodos, se realizó un trabajo de comparación que se puede encontrar en [6].

Las dimensiones de las estructuras a elaborar se detallan en la Fig.1. El ancho de los contactos se diseñó de 100 μm tomando en cuenta la experiencia adquirida en la elaboración de los dedos metálicos de los CSS. La separación entre fotodiodos se diseñó de 150 μm , tomando en cuenta el valor de la longitud de difusión reportada por otros investigadores del grupo [7]. El área activa de cada fotodiodo se diseñó como porciones de un círculo de 3 mm de radio y la ventana se diseñó de 1 mm de radio.

III. ELABORACIÓN DEL SENSOR

A. Infraestructura y equipamiento disponible

Las capacidades tecnológicas existentes en el país permiten la fabricación de dispositivos para aplicaciones específicas. Para la elaboración de los sensores el DES cuenta con un área limpia Clase 10.000. Para los procesos de oxidación, difusión y recocido de contactos se cuenta con un horno de alta temperatura marca THERMCO (Fig. 2). Para los depósitos de metales mediante evaporación por efecto Joule, se cuenta con una evaporadora marca Leybold-Heraeus modelo Univex 300. Los procesos de fotolitografía se realizan con un equipo EVG-620 en la sala limpia del Departamento de Micro y Nano Tecnología (DMN) de CNEA, que permite la alineación de la máscara y posterior iluminación de la fotorresina. Para cortar los sustratos, el DES cuenta con una sierra de corte con alineación manual del fabricante MTI-Corporation, que tiene la ventaja que se puede utilizar para sustratos gruesos. Por otro lado, el DMN cuenta con una sierra semiautomática DISCO DAD3240 con alineación óptica, para cortar obleas de Si.



Fig. 2. Horno de alta temperatura para procesos de oxidación, difusión y recocido de contactos.

B. Procesos de fabricación

Los pasos propuestos para la elaboración del detector del dispositivo se resumen en la Fig. 3. El paso más importante es la elaboración de las juntas localizadas, las cuales se obtienen mediante la difusión de dopantes de forma localizada al utilizar una máscara dura de SiO_2 . Se utilizaron sustratos de Si-c Czochralski (Cz) tipo p pulido espejo, de origen comercial, de 101,6 mm y con orientación $\langle 100 \rangle$, espesor de

600 μm y con resistividad de 1 Ωcm . Para los procesos de definición de la máscara dura de SiO_2 , de definición de contactos metálicos y para definir la geometría de la ventana, se diseñaron las máscaras de fotolitografías.



Fig. 3. Pasos para la elaboración del arreglo de fotodiodos del detector.

Para la elaboración de la ventana se propusieron los pasos que se describen en la Fig. 4. A diferencia del detector, el proceso de fabricación comienza con un pre-corte del sustrato. Hay que tener un especial cuidado en la limpieza del vidrio para favorecer la adhesión del metal. Se utilizaron como sustrato de vidrio láminas portaobjetos de vidrio sódico-cálcico de 76 x 26 mm^2 y 1 mm (tol. $\pm 0,05$ mm) de espesor.

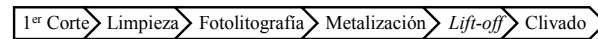


Fig. 4. Pasos para la elaboración de la ventana.

Los procesos de fotolitografía con alineación de máscaras y corte de los sensores de Si se utilizaron las instalaciones mencionadas del DMN, el resto de los procesos se realizaron en las instalaciones del DES.

IV. RESULTADOS

A. Elaboración del detector de dos y cuatro cuadrantes

En el proceso de elaboración, la limpieza de las obleas y el acondicionamiento de la superficie deben realizarse antes de cada paso importante del proceso. La limpieza inicial es un proceso secuencial y se realizó siguiendo los pasos descritos en la Fig. 5.

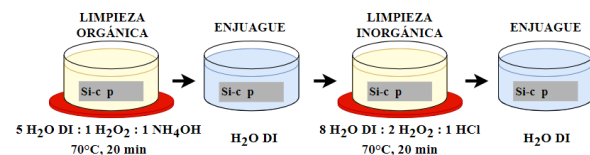


Fig. 5. Pasos de la limpieza inicial del sustrato de Si.

Para la obtención de las zonas tipo n de forma localizada en la cara frontal del sustrato de Si, se elaboró una máscara dura de SiO_2 para el proceso de difusión. El crecimiento del SiO_2 se realizó en ambiente de oxígeno de alta pureza (99,999%). Se realizaron crecimientos de 270 y 400 nm de espesor, medido mediante elipsometría.

Para definir la máscara dura de SiO_2 se realizó una fotolitografía en dos pasos para obtener 15 μm de espesor de fotorresina positiva AZ-9260. Luego, en el caso del crecimiento de 270 nm, se removió el óxido expuesto mediante un ataque químico húmedo en solución BHF de HF con NH_4F . El resultado del ataque químico, antes de remover la fotorresina, se muestra en la Fig. 6a. Para remover el SiO_2 del crecimiento de 400 nm, el ataque químico húmedo no fue efectivo y fue necesario realizar un ataque químico seco, haciendo uso del RIE (*Reactive Ion Etching*). Por esto se descartó el espesor de 400 nm de SiO_2 para los futuros procesos de elaboración del detector.

La formación de las juntas n^+pp^+ ocurre de forma simultánea en un mismo proceso en el horno de difusión. Por un lado, la formación de la juntura n^+p se realizó mediante difusión de fósforo a partir de una fuente líquida de POCl_3 , siguiendo la receta estándar de difusión del laboratorio [8].

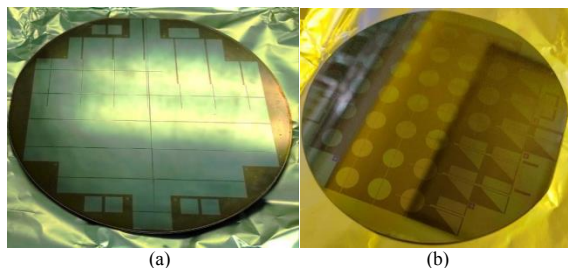


Fig. 6. a) Primer paso de fotolitografía y ataque químico húmedo de SiO₂, b) segundo paso de fotolitografía, definición del área de contactos.

Por otro lado, la juntura pp⁺ en la parte posterior de la oblea, se elabora mediante la difusión de aluminio a partir de una capa de aproximadamente 1 μm de espesor de Al de alta pureza (99,998%), previamente evaporada. Como control del proceso, posterior a la difusión, se midió la resistencia de capa de la oblea.

Luego de elaborar las juntas localizadas, se pasó a depositar los contactos metálicos. Estos deben ser óhmicos, tener baja resistencia de contacto con el sustrato y tener baja resistencia serie. Antes de proceder con la metalización, hay que tener en cuenta los requisitos del dispositivo a elaborar. El contacto posterior es común a todos los dispositivos y cubre completamente la cara posterior p⁺. Para el contacto de la cara frontal, hay que considerar que el área activa o fotosensible de los fotodiodos debe quedar expuesta. Además, cuando se elabora un arreglo de fotodiodos los contactos frontales deben estar perfectamente alineados con su respectiva área activa, es decir, con los pasos previos de la fabricación. El área donde van los contactos metálicos frontales se definió mediante fotolitografía con fotorresina positiva AZ-9260 de 7 μm, Fig. 6b.

Luego de la fotolitografía y previo al depósito de los metales, se realizó un ataque con BHF a la muestra para remover la capa de óxido de silicio dopado con fósforo que se crea durante el proceso de difusión y garantizar un buen contacto óhmico.

Los contactos metálicos están formados por una multicapa de titanio, paladio y plata, depositados en ese orden. Cada capa se deposita mediante evaporación térmica en cámara de vacío, sin romper el vacío entre los depósitos. Para remover la fotorresina se realiza un proceso de *lift-off*, donde se disuelve la fotorresina en acetona y se remueve el metal depositado encima de la fotorresina, Fig. 7. Una vez finalizado el *lift-off* la muestra se limpia primero con isopropanol y luego con H₂O DI.

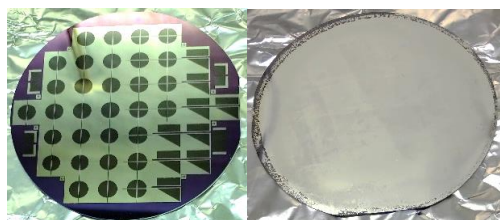


Fig. 7. Contactos metálicos frontal y posterior después del *lift-off*.

Como último paso de la elaboración de los contactos, se realizó un recocido a 400°C durante 20 min en la misma boca del horno donde se realiza la oxidación, en un ambiente de 4% de H₂ y 96 % de N₂ (*forming gas*). En este paso se realiza el sinterizado de los metales para obtener un buen contacto

óhmico entre el metal y el semiconductor, además actúa como pasivante de la superficie. Finalmente, la oblea se corta y se separan los detectores, como se muestran en la Fig. 8.

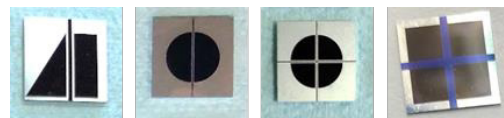
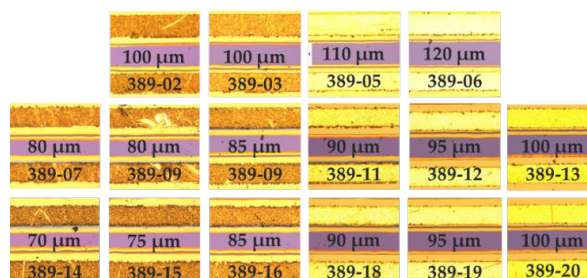
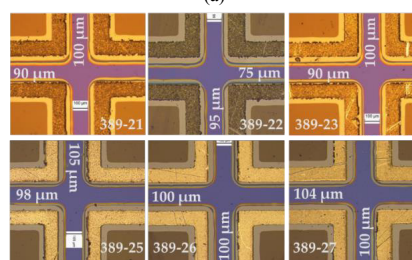


Fig. 8. Detectores de diferentes diseños cortados.

En la Fig. 9 se muestran las mediciones realizadas en el microscopio óptico del ancho de la barrera de SiO₂ en los detectores de dos y cuatro cuadrantes respectivamente. Se observa que, partiendo de una máscara con una separación de 150 μm de ancho, con el proceso de fotolitografía y ataque húmedo del óxido no se obtiene un ancho mucho menor al deseado. Además, se observa que, en los detectores de cuatro cuadrantes, no se obtiene el mismo ancho en ambos ejes. Esto se puede deber a un sobre revelado de las muestras o simplemente a que el proceso de ataque químico húmedo es un proceso isotrópico.



(a)



(b)

Fig. 9. Ancho de la barrera de óxido, después de terminado el detector de a) dos cuadrantes, b) cuatro cuadrantes.

B. Ventana

Para la elaboración de la ventana se siguieron los pasos mencionados en la Fig. 3. Inicialmente, se realizó un marcado o pre-corte de 0,5 mm de profundidad de la oblea de vidrio (Fig. 10a). Realizar el corte como primer paso cumple varios propósitos: asegurar una correcta alineación del corte con la metalización ya que la sierra no tiene alineación óptica, evitar la manipulación de la muestra una vez metalizada y, por último, crear un escalón en el borde de la ventana que sirve para la alineación con el detector y de encastramiento en el soporte del sensor.

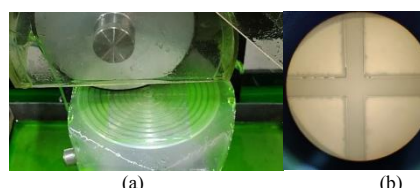


Fig. 10. a) Pre-corte del vidrio y b) alineación de la fotolitografía.

Luego, se hizo una limpieza orgánica e inorgánica (Fig. 5) para mejorar la adherencia del metal. Una vez limpia la muestra, se realizó una fotolitografía para definir la posición de la abertura de la ventana, esta fotolitografía se hizo sobre la cara del vidrio sin cortes y se alineó la máscara con las líneas de corte realizadas en la otra cara (Fig. 10b). Luego se pasa a la metalización en la evaporadora. Se hicieron metalizaciones con Al y con Ti/Pd/Ag. Se optó utilizar la misma multicapa que en los contactos por dos razones, primeramente, porque mostró mejor adherencia al vidrio que el Al y, por otro lado, se puede hacer la metalización de la ventana en el mismo paso de evaporación de los contactos metálicos. Se hicieron ventanas con aperturas cuadradas y circulares.

Posteriormente, se realizó el proceso de *lift-off* para remover el metal y la fotorresina que protege la apertura de la ventana (Fig. 11). Las ventanas se cortan de 12 x 12 mm² quebrando el vidrio por las zonas pre-cortadas.

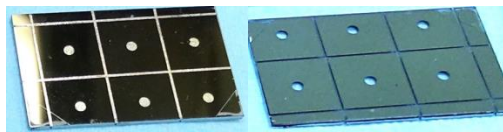


Fig. 11. Ventana metalizada, antes y después del *lift-off*.

C. Integración en el soporte

El primer prototipo de sensor solar de posición con el diseño propuesto requiere de una base o soporte para ensamblar el conjunto detector-ventana. El soporte se diseñó para garantizar la alineación entre ellos. En la Fig. 12 se presenta el prototipo elaborado. El soporte es una base plástica torneada para las dimensiones del detector y el vidrio, cuenta con una tapa que encastra en la base y que se ajusta con tornillos, de esta forma se asegura una buena alineación, un buen contacto y que solo llegue al detector la luz que pasa por la ventana. Este soporte sirve para las futuras caracterizaciones de los dispositivos elaborados.

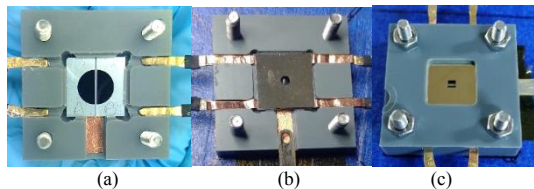


Fig. 12. Soporte diseñado para alinear la ventana con el detector, a) detector en el soporte, b) ventana colocada sobre el detector con contactos de cobre, c) detector y ventana integrados en el soporte.

V. CONCLUSIONES

Se elaboraron las diferentes componentes de los sensores diseñados. Se pusieron a punto las técnicas de fabricación para elaborar los arreglos de fotodiodos, en particular la elaboración de la máscara de SiO₂. De las mediciones realizadas se concluyó que es necesario hacer máscaras con una mayor separación entre fotodiodos para asegurar obtener

el valor propuesto en el diseño, se propone que el ancho de la barrera en la máscara sea de 180 μm, con el objetivo de obtener una separación entre fotodiodos que sea mayor que la longitud de difusión de los portadores minoritarios, y así asegurar una buena aislación eléctrica entre fotodiodos.

Para la elaboración de la ventana, se propone hacer pruebas con otros metales en próximos trabajos, en particular cromo, dado que es un metal que resiste más la manipulación sin rayarse.

Además, se diseñó y fabricó un soporte para ensamblar los componentes del sensor. El soporte elaborado facilitará la caracterización eléctrica de los dispositivos. El diseño propuesto permite un ensamble simple y rápido de los sensores.

El trabajo que continua en este tema es realizar la caracterización eléctrica de los sensores elaborado. Las mediciones preliminares muestran que los detectores que tienen una separación mayor a 100 μm presentan una buena respuesta fotovoltaica, y que el soporte elaborado es de especial ayuda para realizar una caracterización confiable del dispositivo.

AGRADECIMIENTOS

Los autores agradecen la ayuda recibida por Andrés Di Donato y José María Olima para poner a punto las diferentes técnicas utilizadas.

REFERENCIAS

- [1] C. G. Bolzi, M. G. Martínez Bogado y M. J. Tamasi, "Reseña del desarrollo de sensores solares en CNEA para misiones satelitales", *Energías Renovables y Medio Ambiente*, 31, 2684-0073 (2013).
- [2] M. M. Bogado, M. Tamasi, C. Bolzi y D. Raggio, "Desarrollo de sensores solares en argentina, aplicaciones terrestres y espaciales", *Revista Brasileira de Energia Solar*, 6(1) (2015).
- [3] H. Mousazadeh, A. Keyhani, A. Javadi, H. Mobli, K. Abrinia y A. Sharifi, "A review of principle and sun-tracking methods for maximizing solar systems output". *Renewable and Sustainable Energy Reviews*, 13(8), 1800–1818 (2009). doi:10.1016/j.rser.2009.01.022
- [4] A. Awasthi, A. K. Shukla, M. Manohar S.R., Ch. Dondariya, K.N. Shukla, D. Porwal, G. Richhariya. "Review on sun tracking technology in solar PV system. *Energy Reports*", 6, 392-405 (2020). doi: https://doi.org/10.1016/j.egy.2020.02.004.
- [5] L. Salgado-Conrado. "A review on sun position sensors used in solar applications. *Renewable and Sustainable Energy Reviews*", 82(3), 2128-2146 (2018). doi: https://doi.org/10.1016/j.rser.2017.08.040
- [6] M. Díaz Salazar, N. Kondratiuk, A. Moreno, M. Martínez Bogado, S. Pavoni Oliver, M. Tamasi; "Design and simulation of sun position sensors for space applications: A comparative study". *Rev. Sci. Instrum.* 95 (7), 075104, (2024). https://doi.org/10.1063/5.0199540
- [7] J.C. Plá, M. Tamasi, C.G. Bolzi, G.L. Venier, J.C. Durán, "Short circuit current vs cell thickness in solar cells under rear illumination: a direct evaluation of the diffusion length", *Solid-State Electronics*, 44(4), 719-724 (2000).
- [8] M. Tamasi, "Celdas Solares para Uso Espacial: Optimización de Procesos y Caracterización". Tesis para optar al título de Doctor en Ciencia y Tecnología - Mención Física (2003)

Construcción de un dispositivo de medición de resistencia eléctrica transepitelial-endotelial (TEER) aplicable a la investigación de cultivos celulares

José Iván González Jorge
Departamento de Ciencias Químicas
IQUIFIB-CONICET
Facultad de Farmacia y Bioquímica
Universidad de Buenos Aires
CABA, Argentina
jigonalez930209@gmail.com

Santiago Sobral
IQUIFIB-CONICET
Facultad de Farmacia y Bioquímica
Universidad de Buenos Aires
CABA, Argentina
ssobral.teq@gmail.com

María Celina Bonetto
IQUIFIB-CONICET
Facultad de Farmacia y Bioquímica
Universidad de Buenos Aires
CABA, Argentina
celinatt@yahoo.com.ar

Ana Laura Rinaldi
Departamento de Ciencias Químicas
Facultad de Farmacia y Bioquímica
Universidad de Buenos Aires
CABA, Argentina
alrinaldi@ffyb.uba.ar

Santiago Cosci
Departamento de Ciencias Químicas
Facultad de Farmacia y Bioquímica
Universidad de Buenos Aires
CABA, Argentina
santiago.cosci@gmail.com

Romina Carballo
Departamento de Ciencias Químicas
IQUIFIB-CONICET
Facultad de Farmacia y Bioquímica
Universidad de Buenos Aires
CABA, Argentina
rocar@ffyb.uba.ar

Resumen—Las células endoteliales y epiteliales, en organismos multicelulares, forman barreras semipermeables cuya integridad es crucial estudiar para comprender procesos como el transporte de moléculas, difusión de fármacos, respuesta a infecciones y desarrollo de tejidos, entre otros. La técnica de resistencia eléctrica transepitelial-endotelial (TEER) permite evaluar cuantitativamente la confluencia celular y la permeabilidad de estos modelos *in vitro* mediante mediciones no invasivas. En este trabajo se presenta LPD-TEER, un dispositivo desarrollado con un cabezal de cuatro electrodos y un módulo electrónico que aplica una pequeña corriente alterna para medir la resistencia de la monocapa celular crecida sobre una membrana semipermeable. Se describen los materiales, calibración, metodología empleados y la compatibilidad con múltiples vías de comunicación para la transferencia de datos. LPD-TEER demostró ser una herramienta portable y de alta resolución para monitorear *in situ* la cinética del crecimiento celular, estableciendo que las células epiteliales intestinales CACO-2 alcanzan la confluencia óptima a los 11 días. Esta técnica simple, pero poderosa, permite estudiar la fisiología e interacciones moleculares en modelos de barreras celulares.

Palabras claves—TEER, cultivos celulares, espectroscopia de impedancia electroquímica

I. INTRODUCCIÓN

En organismos multicelulares, las células endoteliales y epiteliales constituyen interfaces de permeabilidad selectiva y los modelos *in vitro* construidos a partir de ellas permiten la investigación de los parámetros que controlan la integridad de las mismas y los procesos de transporte y el pasaje de moléculas. Por otra parte, la evaluación de la confluencia celular (constitución de la monocapa de células) y el posterior análisis de la funcionalidad de estos modelos de cultivo celulares son aplicables a la investigación en diferentes campos que involucran el transporte molecular y de fármacos, la evaluación de esa permeabilidad y la difusión en células endoteliales de los vasos sanguíneos o capilares adyacentes, el desarrollo y ensayo de vacunas, los procesos de injuria celular, las alteraciones frente a infecciones virales en las células epiteliales del pulmón y/o intestino, la ingeniería de tejidos y estudio de los defectos morfológicos de los mismos, entre

otros [1]. Si bien se han establecido algunas metodologías y protocolos que permiten definir la confluencia celular y el estudio de la integridad de estas barreras, estos procedimientos en su mayoría emplean moléculas fluorescentes o radioactivas (que pueden interferir en los procesos estudiados) o involucran técnicas de microscopía donde la observación visual es por aproximación y sujetas a la apreciación del operador. Como alternativa, surgen técnicas no invasivas, basadas en la medición de la resistencia eléctrica transepitelial-endotelial (TEER) de células crecidas sobre una membrana porosa. TEER es una técnica cuantitativa, una herramienta experimental útil y objetiva, para definir y caracterizar un tejido funcional *in vitro*, evaluar la confluencia celular y evidenciar los procesos de permeabilidad e integridad de dichas membranas celulares, a partir de una medición analítica altamente sensible. Las mediciones de espectroscopia de impedancia electroquímica (EIS) en todo el rango de frecuencias (100 KHz a 0,1 Hz) permiten modelar con resistencias y capacitores en paralelo las capas de células epiteliales o endoteliales que nos brindan un circuito eléctrico equivalente, y por ende estudiar el flujo de iones a través de las vías paracelulares y transcelulares y recuperar parámetros que caracterizan las propiedades de esa membrana [2]. TEER, en particular, resulta ser una aplicación simplificada de las mediciones de (EIS) ya que se mide la resistencia eléctrica (en ohms) a una frecuencia previamente optimizada, generalmente, a bajas frecuencias [3].

En el mercado existe equipamiento para llevar adelante estas mediciones de resistencia eléctrica transepitelial-endotelial. En general, estos instrumentos consisten de un cabezal con electrodos que tiene dos partes, que se insertan por arriba y por debajo de los transwells® donde crecen las células endoteliales/epiteliales. Cuando las células alcanzan la confluencia, se produce un cambio significativo en los valores de resistencia en comparación con el valor basal (a tiempo cero). En los últimos años, un gran número de trabajos incluyen la medición de TEER como uno de los métodos más comunes para el estudio, por ejemplo, de la infección de virus H1N1 en modelos epiteliales *in vitro* de pulmón, en la comprensión de los detalles de la infección pulmonar a nivel

celular en diseños tridimensionales y la acción de fármacos, entre otros [4, 5].

En este trabajo presentamos LPD-TEER, un instrumento diseñado y constituido por un cabezal con un sistema de cuatro electrodos que se sumergen en la cámara donde crecen las células y un módulo electrónico de control, adquisición, procesamiento y múltiples vías de comunicación para el monitoreo de los procesos que ocurren sobre sistemas biológicos. LPD-TEER fue optimizado y empleado para evaluar la confluencia celular en un cultivo de células de epitelio intestinal.

II. EXPERIMENTAL

A. Materiales, equipamiento y metodología

Se utilizaron placas comerciales de 16 pocillos con sus respectivos transwells® con membranas de poros de 0,4 μm . Para la preparación de las soluciones se utilizó agua desionizada. Se emplearon soluciones patrones de KCl de distinta concentración para la calibración del equipo (LPD-TEER) en el rango de valores de resistencia de 50 a 50000 ohms \times cm^2 . Posteriormente se procedió al uso de LPD-TEER para la evaluación de la confluencia celular de cultivos de células epiteliales intestinales CACO-2 crecidas en medio EMEM (EBSS) con agregado de glutamina, aminoácidos no esenciales y suero fetal bovino en atmósfera de CO_2 (5%) y a 37 °C.

LPD-TEER es un dispositivo sensor diseñado y fabricado en nuestro laboratorio y consta de un cabezal con un sistema de cuatro electrodos de Ag/AgCl (de 2 mm de ancho \times 3 mm de largo), lavables, esterilizables y reutilizables, y un módulo electrónico de control y adquisición (con alta resolución para la adquisición, gran capacidad de procesamiento, diversas interfaces de comunicación y conectividad). Los electrodos son fabricados con una tecnología de circuitos impresos combinada con impresión serigráfica de tinta de plata. El cabezal de electrodos se incorpora en un soporte con agarraderas que permite su posicionamiento adecuado (vertical a 90°) en la celda de adquisición. Las mediciones se realizan mediante la aplicación de una señal de corriente alterna (AC, del orden de los μA) a través de los electrodos colocados a ambos lados de la monocapa celular crecida sobre una membrana semipermeable. A una determinada frecuencia (previamente optimizada por única vez mediante experimentos de EIS), se mide la corriente y el voltaje que circulan a través de la capa de células. Mediante la ley de Ohm, se determina la resistencia de este sistema y se normaliza la medida por un factor de corrección que tiene en cuenta el área total, el tamaño y la densidad de poros (especificado por el fabricante de las membranas).

III. RESULTADOS Y DISCUSIÓN

LPD-TEER es un dispositivo desarrollado específicamente para los sistemas transwells®, respetando la geometría de los pocillos de cultivo y que permite el posicionamiento del cabezal del electrodo (tipo palillo) de manera de reducir al mínimo la perturbación de las células y su proceso de crecimiento. La Fig. 1 muestra el diseño de una celda clásica para la medición de TEER. Como puede observarse, la membrana semipermeable donde se fijan y crecen las células define dos compartimentos de modo que cada par de electrodos del cabezal entra en contacto con el medio de cultivo de cada uno de esos lados (apical y basal).

La medición de TEER consiste en la obtención del valor de resistencia eléctrica, la cual se calcula mediante la ley de Ohm como el cociente entre voltaje y corriente. Si bien esta resistencia puede ser determinada a partir de las corrientes que resulten de la aplicación de un voltaje DC a los electrodos, este procedimiento no es conveniente debido al daño que puede producir esta modalidad tanto sobre las células como sobre los electrodos (reacciones de óxido-reducción no esperadas que alteran, por ejemplo, el funcionamiento biológico) [2]. Por ello, en el diseño de LPD-TEER una señal de corriente alterna (AC) de unos pocos microamperes es aplicada al sistema, a una frecuencia determinada (baja frecuencia, previamente determinada por experimentos de EIS), permitiendo la medición de valores de resistencia en el rango de 50 a 50000 Ω con una resolución de 0,1 Ω . La metodología incluye la medida de la resistencia de la membrana semipermeable sola (sin células) denominada resistencia basal (R_{basal}) y de la resistencia a través de la capa de células crecidas sobre dicha membrana (R_{total}). A continuación se describe el procedimiento completo para llevar adelante la medición con LPD-TEER:

- 1-Sembrado de células en los pocillos previamente acondicionados, dejando pocillos sin células para la medición de los blancos.
- 2-Incubación de las células de interés de acuerdo al protocolo específico para su crecimiento.
- 3-Desinfección/ descontaminación de los electrodos según especificaciones.
- 4-Estabilización del sistema (electrodos/muestra) a temperatura controlada.
- 5-Medición de la resistencia de la celda en los pocillos cultivados (R_{total} (Ω)).
- 6-Medición de la resistencia de la celda en los pocillos blancos (R_{basal} (Ω)).
- 7-Cálculo de la resistencia de la monocapa celular (R_{celular} (Ω)= R_{total} (Ω)- R_{basal} (Ω)) y normalización por el factor de corrección de área especificado por el fabricante de las membranas (valor de TEER resultante ($\Omega \times \text{cm}^2$) = R_{celular} (Ω) \times M área (cm^2)).
- 8-Repetición de los pasos 3 a 7 en distintos estadios de crecimiento a fin de evaluar la cinética del proceso y la confluencia celular, o los cambios según la exposición a estímulos luego de alcanzada la monocapa de células.

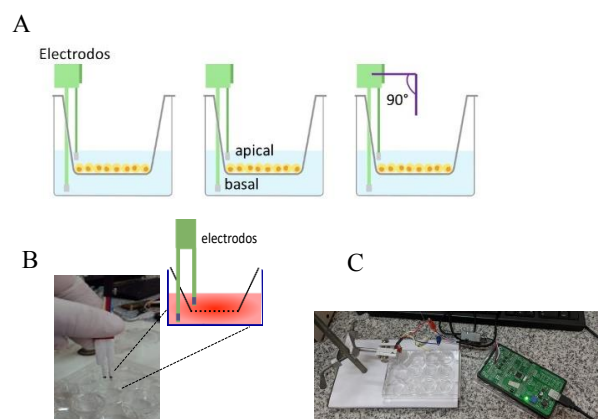


Fig. 1. (A) Esquema del diseño de una celda clásica para la medición de TEER. (B) Fotografía del cabezal de electrodos del LPD-TEER en una placa transwells®. (C) Fotografía del prototipo α del dispositivo LPD-TEER.

LPD-TEER permite el registro de la conductancia iónica de la vía paracelular en la monocapa epitelial, el flujo de agua y el tamaño de los poros de las uniones estrechas (debido a la medición a bajas frecuencias), tal como se representa en la Fig. 2 y en el siguiente link (<https://youtu.be/2T5w8HZdMW8?si=e4G4NU9GDYOTkv5Y>).

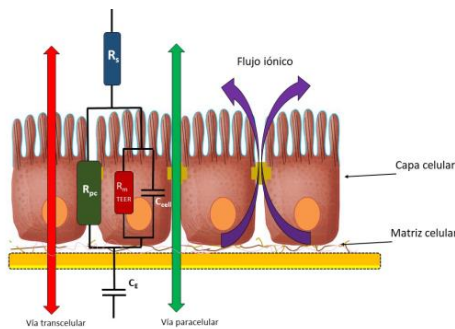


Fig. 2. Esquema de la monocapa de epitelio intestinal incluyendo el diagrama del circuito eléctrico equivalente.

Para poder llevar a cabo estas mediciones, el dispositivo requiere una calibración frente a soluciones patrones de KCl de distinta conductividad, en el rango de valores de resistencia de 50 a 50000 $\Omega \times \text{cm}^2$. En la Fig. 3 se muestra la curva de calibración correspondiente, obtenida para mediciones por triplicado.

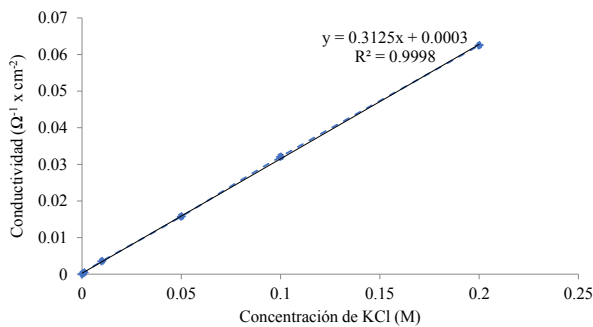


Fig. 3. Curva de calibración para LPD-TEER frente a soluciones patrones de KCl en el rango de 10^{-5} M a 10^{-1} M, empleando membranas de 0,4 μm en los transwells®. (n=3)

El dispositivo LPD-TEER es un instrumento de fabricación nacional que presenta un módulo de detección de alta resolución, alta capacidad de procesamiento y múltiples vías de comunicación para facilitar la interconectividad a diferentes sistemas. De esta manera, LPD-TEER permite la recolección *in situ* o remota de la información (Fig. 4). Es decir, se trata de un equipamiento portátil, portátil que proporciona una interfaz para la transferencia de datos por vía directa (a través de una conexión USB) o inalámbrica (WIFI, bluetooth) para el monitoreo continuo y autónomo (almacenamiento de valores). Esto último, favorece significativamente el trabajo en el flujo laminar, reduciendo la probabilidad de contaminaciones o perturbaciones a los sistemas biológicos.

Finalmente, LPD-TEER fue empleado para evaluar el seguimiento de la confluencia celular de cultivos de células CACO-2. Se obtuvieron valores de TEER de 156, 298, 357, 463 y 95 $\Omega \times \text{cm}^2$ para 3, 6, 9, 11 y 18 días de incubación, respectivamente, con un inóculo inicial de 300 mil células. De esta manera, se estableció que el tiempo óptimo para la constitución de la monocapa de CACO-2 se alcanza a los 11 días de incubación. Esta determinación es crucial para definir monocapas polarizadas de células del epitelio intestinal que permiten estudiar su funcionalidad, por ejemplo, en la regulación del ATP extracelular o frente a nutrientes o fármacos.

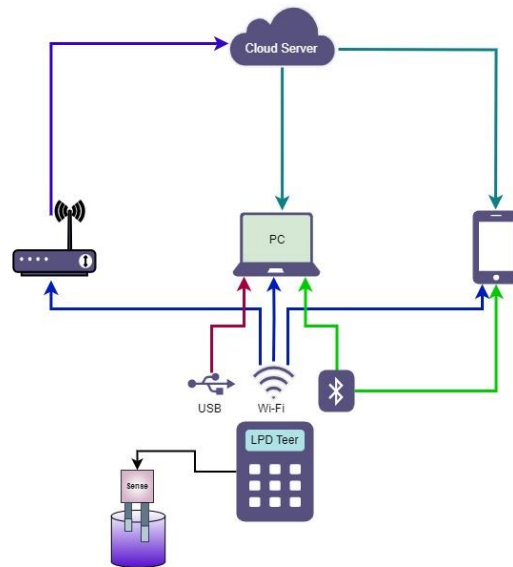


Fig. 4. Esquema de las distintas interfaces de comunicación desde el dispositivo sensor LPD-TEER.

IV. CONCLUSIONES


En este trabajo hemos diseñado, fabricado y evaluado de manera completa un nuevo dispositivo sensor para la medición de la resistencia eléctrica transepitelial-endotelial, LPD-TEER, que permite el estudio de cultivos celulares y la potencialidad de la investigación de estos modelos *in vitro*. La simplicidad de los experimentos basados en la medición de TEER y la capacidad de correlacionar estos resultados con otros experimentos de transporte (que involucren espectroscopia de impedancia electroquímica) hacen que el uso de esta técnica sea una herramienta analítica útil para comprender la fisiología de células endoteliales y/o epiteliales, y su interacción con las moléculas blanco en el estudio de patologías y fármacos de diseño.

AGRADECIMIENTOS

Los autores agradecen los financiamientos otorgados por UBA (UBACyT2023 Mod I 20020220200052BA) y ANPCyT (PICT 2021 GRF T1 00269). J. I. G. J. agradece a CONICET por la beca doctoral.

REFERENCIAS

- [1] C.M. Sakolish, M.B. Esch, J. J. Hickman, M. L. Shuler, G.J. Mahler, "Modeling Barrier Tissues in vitro: methods, achievements and challenges", *EBioMedicine*, vol. 5, pp. 30-39, 2016.

- 
- [2] K. Benson, S. Cramer, H-J. Galla, “Impedance-based cell monitoring: barrier properties and beyond”, *Fluids and Barriers of the CNS*, vol. 10:5, pp. 1-11, 2013
- [3] D. H. Elbrecht, C. J. Long, J. J. Hickman, “Transepithelial/endothelial Electrical Resistance (TEER) theory and applications for microfluidic body-on-a-chip devices”, *J Rare Dis Res Treat.*, vol. 1(3), pp. 46-52, 2016.
- [4] C. Liu, X. Wu, X. Bing, W. Qi, F. Zhu, N. Guo, C. Li, X. Gao, X. Cao, M. Zhao, M. Xia, “H1N1 influenza virus infection through NRF2-KEAP1-GCLC pathway induces ferroptosis in nasal mucosal epithelial cells”, *Free Rad. Bio. Med.*, vol. 204, pp. 226-242, 2023.
- [5] Y. Xu, N. Shrestha, V. Preat, A. Beloqui, “An overview of in vitro, ex vivo and in vivo models for studying the transport of drugs across intestinal barriers”, *Adv. Drug Delivery Rev.*, vol. 175, pp. 113795, 2021

Desarrollo de sensores solares para uso espacial

Analia Moreno
Departamento Energía Solar
Comisión Nacional de Energía Atómica
(CNEA)
Buenos Aires, Argentina
Instituto de Nanociencia y
Nanotecnología
CNEA-Consejo Nacional de
Investigaciones Científicas y Técnicas
analiaveronicamoreno@cnea.gob.ar

Martha Díaz Salazar
Departamento Energía Solar
Comisión Nacional de Energía Atómica
(CNEA)
Buenos Aires, Argentina
Instituto de Nanociencia y
Nanotecnología
CNEA-Consejo Nacional de
Investigaciones Científicas y Técnicas
marthadiazsalazar@cnea.gob.ar

Nadia Kondratiuk
Departamento Energía Solar
Comisión Nacional de Energía Atómica
(CNEA)
Buenos Aires, Argentina
Instituto de Nanociencia y
Nanotecnología
CNEA-Consejo Nacional de
Investigaciones Científicas y Técnicas
nadiakondratiuk@cnea.gob.ar

Mónica Martínez Bogado
Departamento Energía Solar
Comisión Nacional de Energía Atómica
(CNEA)
Buenos Aires, Argentina
Instituto de Nanociencia y
Nanotecnología
CNEA-Consejo Nacional de
Investigaciones Científicas y Técnicas
monicamartinez@cnea.gob.ar

Claudio Bolzi
Departamento Energía Solar
Comisión Nacional de Energía Atómica
(CNEA)
Buenos Aires, Argentina
claudiobolzi@cnea.gob.ar

Mariana Tamasi
Departamento Energía Solar
Comisión Nacional de Energía Atómica
(CNEA)
Buenos Aires, Argentina
Instituto de Nanociencia y
Nanotecnología
CNEA-Consejo Nacional de
Investigaciones Científicas y Técnicas
marianatamasi@cnea.gob.ar

Resumen—Los sensores solares gruesos, CSS, son instrumentos para medir la posición del Sol y forman parte del control de actitud de un satélite. En este trabajo se presentan las diferentes etapas del proceso de elaboración, integración y ensayo de los CSS fabricados por el Departamento Energía Solar de la Comisión Nacional de Energía Atómica de Argentina. La experiencia adquirida y las capacidades existentes permiten la producción de sensores para aplicaciones específicas. Los CSS elaborados cumplen con las normas de calidad de la industria espacial nacional e internacional.

Palabras claves—sensores solares gruesos, CSS, ambiente espacial, satélites

I. INTRODUCCIÓN

El Departamento de Energía Solar (DES) de la Comisión Nacional de Energía Atómica (CNEA) ha desarrollado radiómetros fotovoltáicos para uso terrestre y espacial desde finales de la década del 90 [1]. La motivación siempre ha sido contar en el país con dispositivos de bajo costo y eventualmente comercializar en forma directa, como el caso de los radiómetros y sensores de uso espacial, o dominar la tecnología para una potencial transferencia al sector productivo [2].

Los sensores fotovoltaicos, en general, pueden utilizarse en cualquier situación donde la excitación de entrada sea radiación luminosa, en el intervalo de longitudes de onda donde éstos son sensibles, entregando a la salida una señal eléctrica. Para orientar un satélite o los paneles solares en el caso de satélites geoestacionarios al Sol, se utilizan sensores primarios o sensores solares gruesos (*Coarse Sun Sensor*, CSS) en general apareados o dispuestos en un arreglo de sensores. La señal de salida de los sensores previamente calibrada permite el control de actitud del satélite para su orientación respecto al Sol. El subsistema de control de actitud es una parte importante del sistema de navegación de un satélite. Por un lado, debe tener cierta precisión y, por otra parte, debe ser un sistema muy robusto y confiable para asegurar el éxito de la misión.

En la actualidad, el DES elabora sensores solares gruesos de posición, los cuales se diseñan a la medida de los requerimientos de cada misión espacial. Estos sensores cuentan con una herencia de más de 20 años y 2.300.000 horas de vuelo a febrero de 2024.

En el año 2011 se lanzó el satélite SAC-D que utilizó paneles solares integrados y ensayados por CNEA, además, esta misión llevaba doce CSS elaborados en el DES. En base a los requisitos de tamaño y de corriente de cortocircuito se diseñaron y fabricaron dispositivos de 12 mm de lado, con área activa circular de 48 mm² y dedos metálicos de 100 µm de ancho, dispuestos en forma radial, como se muestra en la Fig. 1. Esta misión fue el producto de una cooperación entre la Comisión Nacional de Actividades Espaciales (CONAE) y la *National Aeronautics and Space Administration* (NASA). Contó además con revisiones internacionales tanto de la CONAE como de representantes del Centro Goddard y del *Jet Propulsion Laboratory* (JPL) de la NASA. [3] [4] [5]

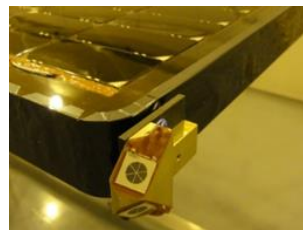


Fig. 1. Sensor de posición integrado al panel de vuelo del SAC-D.

Esta tecnología también se empleó para la elaboración de los CSS de los satélites SAOCOM 1A y SAOCOM 1B (Fig. 2), los cuales fueron diseñados a medida de los requisitos de cada misión. Los satélites SAOCOM 1A y SAOCOM 1B se lanzaron en octubre de 2018 desde la Base Aérea de Vandenberg (EE. UU.), y en agosto de 2020 desde Cabo Cañaveral en la Florida (EE. UU.), respectivamente. [6]

Otros proyectos de la industria aeroespacial donde se han empleado los CSS elaborados en el DES son el Proyecto cohete - sonda VS-30, a cargo de la CONAE y la Agencia Espacial Brasileira (AEB) que fue lanzado en 2007 desde Natal (Brasil), el satélite brasileño de observación de la Tierra Amazonia-1 [7], que se lanzó en febrero de 2021 y el pequeño satélite argentino Cube Bug-2. Se diseñaron, elaboraron e integraron los CSS para el satélite argentino SABIA-Mar que será lanzado en el año 2025 [8].

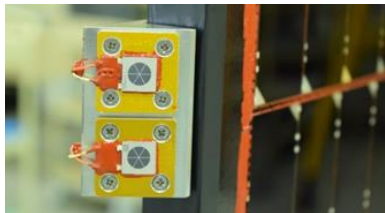


Fig. 2. Sensores solares gruesos montados en el panel solar del SAOCOM 1A.

A principios de 2020 el DES comenzó con un proyecto para proveer a la empresa INVAP de 23 sensores solares gruesos de posición. Los mismos formarán parte del sistema de control de actitud que se comercializó a una empresa europea, OHB-Italia S.p.A., para la misión NAOS (*National Advanced Optical System*). Cabe destacar que estos sensores serían la primera exportación que realizó la Argentina de componentes espaciales al mercado europeo.

El objetivo de este trabajo es presentar y describir el diseño, la elaboración, la integración y los ensayos de calificación y caracterización a los que son sometidos los sensores solares de posición desarrollados en los laboratorios del DES perteneciente a CNEA.

II. SENSORES SOLARES GRUESOS

En estos sensores la posición del Sol se obtiene de la relación entre la corriente fotogenerada y el ángulo de incidencia de la fuente de luz. Los CSS realizan una medición indirecta de la posición del Sol a partir de la ley del coseno o respuesta angular (Fig. 3), que relaciona la corriente de cortocircuito (I_{CC}) de los sensores con el ángulo de incidencia de la radiación (θ), según: $I(\theta) = I(0^\circ) * \cos(\theta)$. Con este principio de medición se puede obtener información de actitud en un eje.

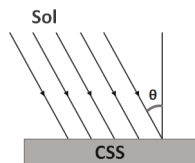


Fig. 3. Esquema del funcionamiento de un sensor solar grueso.

En el siguiente diagrama (Fig. 4) se observan los pasos involucrados en un proyecto de sensores espaciales.

I. DISEÑO Y ELABORACIÓN DEL SENSOR

La grilla frontal y el área activa de los sensores fabricados en CNEA se diseñan en función de la corriente requerida en cada misión. En general, el área activa del sensor es circular, lo que le da simetría en la respuesta respecto al ángulo azimutal.

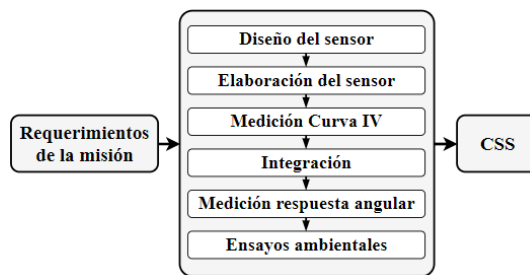


Fig. 4. Pasos involucrados en el desarrollo de sensores solares satelitales.

Los sensores gruesos se elaboran a partir de obleas de Si monocristalino de origen comercial tipo Czochralski, dopadas con boro y con una resistividad de aproximadamente $1 \Omega\text{cm}$. Su estructura n+pp+ se logra a partir de una codifusión de fósforo y aluminio [9] en un horno de difusión a 950°C , obteniéndose una resistencia de capa en la cara frontal de aproximadamente $50\text{-}70 \Omega/\text{cuad}$. Los contactos metálicos frontales (tipo grilla) y posterior completo están formados por una multicapa de Ti-Pd-Ag. Los contactos frontales se elaboran con técnicas de fotolitografía para definir el área activa (Fig. 5).

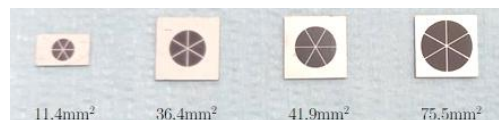


Fig. 5. Sensores con diferentes tamaños de área activa.

II. CARACTERIZACIONES ELÉCTRICAS

Las caracterizaciones eléctricas de los sensores para uso satelital son curva corriente tensión (I-V) y respuesta angular. La curva I-V nos permite conocer los parámetros eléctricos más importantes de un sensor fotovoltaico, como la I_{CC} y la tensión de circuito abierto V_{OC} , y a partir de la respuesta angular podemos relacionar la I_{CC} con el coseno del ángulo de incidencia del Sol.

A. Curva característica corriente – tensión (I-V)

Para la medición de la curva característica corriente – tensión (I-V) de celdas solares y sensores de radiación en condiciones controladas se dispone de un simulador solar de estado estacionario de alta fidelidad “Close-match” TS-Space con espectro AM0 e irradiancia equivalente a 1367 W/m^2 normalizadas y una carga electrónica.

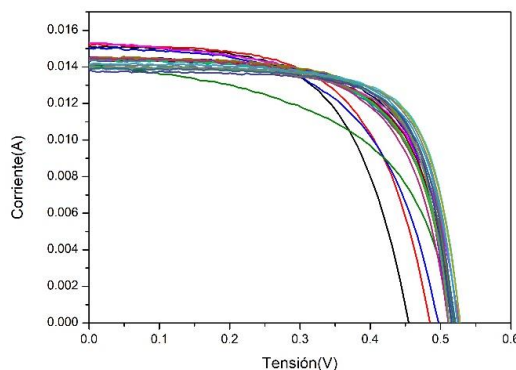


Fig. 6. Curvas I-V de un lote de sensores de una misma difusión.

Para el control de la temperatura del dispositivo a medir, se diseñó y construyó una base que utiliza el efecto Peltier, controlada electrónicamente y que trabaja en el intervalo de temperaturas cercanas a la normalizada (28 ± 1) °C. De la curva I-V (Fig. 6) se extraen los datos eléctricos de los sensores, en particular la I_{CC} , además se pueden obtener la tensión a circuito abierto (V_{ca}), el factor de forma (FF) y el punto de máxima potencia (P_{max}).

B. Respuesta angular

La respuesta angular se establece como la variación de la I_{CC} en función del ángulo de incidencia. Se muestra a modo de ejemplo la caracterización de un sensor para ángulos entre 0° y 90° en ambos sentidos para una temperatura fija. En la Fig. 7 se muestra la variación de la I_{CC} con el ángulo para una irradiancia de 1367 W/m² a una temperatura de 28 °C. Se caracteriza además la simetría del sensor realizando mediciones al variar el ángulo azimutal para cada posición del ángulo de inclinación. Esto, a su vez, proporciona una estimación del error de la respuesta para cada uno de los ángulos de inclinación.

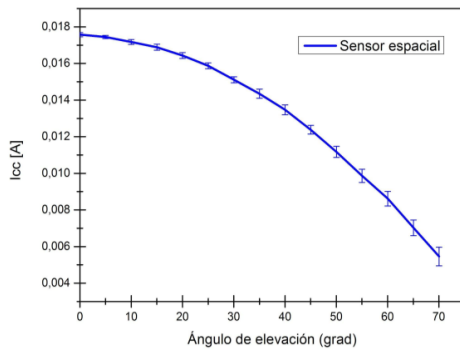


Fig. 7. Respuesta angular de un sensor espacial y la desviación debido a la simetría.

El campo de visión de los CSS elaborados en el DES es de 180° y se logra definir la posición del Sol con una resolución de 5°. [10]

III. INTEGRACIÓN DE LOS SENSORES

El proceso de fabricación del conjunto (CSS montado en la base-soporte) consta de las siguientes etapas:

- Soldadura de los interconectores frontal y posterior de Kovar® plateado de 30 µm de espesor
- Pegado del vidrio de protección de 100 µm de espesor
- Medición de la curva I-V del conjunto sensor con interconectores y vidrio
- Inspección visual del conjunto
- Pegado de los colectores de Kovar® y sensores a la base de aluminio
- Soldadura de los cables e interconectores a los colectores
- Pegado de los cables a la base o soporte
- Cobertura de la soldadura
- Ensayo de tracción de los cables
- Inspección final: medición eléctrica e inspección visual

IV. ENSAYOS AMBIENTALES

El momento más crítico durante la puesta en órbita de un satélite es el lanzamiento, debido a que el mismo se ve

expuesto a altas aceleraciones inducidas por las vibraciones del vehículo lanzador, ondas acústicas, entre otras. Una vez en órbita se ve expuesto a variaciones de temperatura de gran amplitud debido a los eclipses propios del movimiento orbital, radiación cósmica, viento solar, etc. Todo esto lleva a que se deben realizar ensayos ambientales según el requerimiento de cada misión. Se hacen ensayos de calificación sobre modelos de ingeniería y ensayos de aceptación para verificar errores de manufactura, asegurando el correcto funcionamiento de los sistemas durante la vida útil del satélite

A. Ensayos mecánicos

Los impactos son cargas de alta intensidad y corta duración (por ejemplo, alta aceleración pico y contenido de alta frecuencia). Estos pueden ser provocados por eventos de separación y despliegue, y pueden causar daños en los componentes del satélite.

Las pruebas de impacto consisten en la aplicación de un pulso de impacto o una vibración del espectro de respuesta al impacto en la interfaz mecánica del objeto de prueba. Estas pruebas garantizan que el sensor resistirá los impactos presentes en el entorno de lanzamiento. Los sensores pasaron exitosamente el ensayo donde alcanzaron más de 2000 g a una frecuencia de 10000 Hz.

Los ensayos de vibración son una parte fundamental para la calificación de los instrumentos electrónicos, ya que permite simular las condiciones a las que están sometidos estos equipos durante su vida en servicio. Los CSS fueron sometidos a una frecuencia de 2 kHz y una densidad espectral de aceleración de 0,03244 g²/Hz. Esta calificación fue realizada en todas las misiones donde se han utilizado los CSS desarrollados, superando el ensayo con éxito en todos los casos.

Posterior a cada calificación y para corroborar el correcto funcionamiento eléctrico de los sensores se realizan mediciones de curvas IV e inspecciones visuales.

B. Ensayos térmicos

Para simular el efecto de envejecimiento y fatiga mecánica debido a los cambios de temperatura durante el tiempo de vida en órbita, debido, por ejemplo, a la entrada y salida de eclipse, se realiza un ensayo de ciclado térmico ultrarrápido de 500 ciclos entre -100 °C y 100 °C en un equipo diseñado y construido en el DES (Fig. 8a).

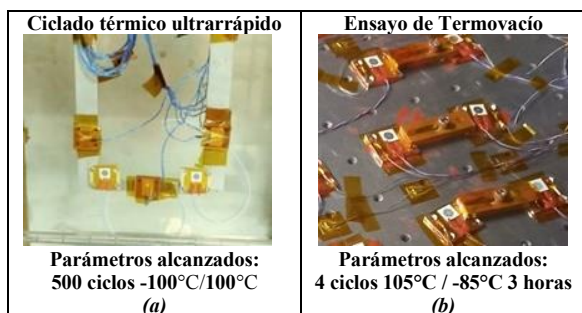


Fig. 8. (a) Montaje de sensores de ingeniería en la cámara caliente. (b) Sensores de vuelo montados en la cámara de termovaciación.

El mismo consta de dos cámaras, entre las que se mueve alternativamente el dispositivo, la superior es la cámara caliente y la inferior correspondiente a la cámara fría. Además, para garantizar que no se presenten defectos de fabricación los

sensores se someten a un ensayo de ciclado térmico en vacío (Fig. 8b).

C. Daño por radiación

Los componentes utilizados en el espacio están sometidos al bombardeo de partículas cargadas de diversas energías. El cual introduce en la estructura de los sensores deteriorando, en consecuencia, sus propiedades electrónicas. Los ensayos de daño por radiación realizados en Tierra, bajo condiciones controladas y normalizadas, permiten estudiar la resistencia de los dispositivos fotovoltaicos al ambiente espacial y predecir el comportamiento de los sensores al final de su vida útil. [11]

Aprovechando las facilidades y disposición del acelerador Tandem en CNEA [12], se realizaron diversas experiencias de irradiación con protones de distintas energías y con electrones. Tanto las experiencias como las simulaciones permiten predecir en función de la órbita de cada misión el comportamiento del sensor al final de la vida útil. Para este estudio se realiza la medición de curva IV, vida media de portadores minoritarios de la base y respuesta espectral, antes y después de la irradiación, para obtener el coeficiente de daño en cada caso. Se realizaron ensayos correspondientes a órbitas LEO para distintas misiones. Para reproducir en el laboratorio con protones de 10 MeV el daño en el espacio, se realizaron simulaciones con el programa Spenvs para obtener la fluencia equivalente. Los sensores fueron irradiados con el método JPL [13] [14]. Con este método se obtuvo una fluencia equivalente de $1,8 \times 10^{11}$ p/cm² [15].

Los sensores se caracterizan mediante la medición de la curva IV y la respuesta espectral (RE), antes y después de la irradiación. En la Tabla I se presentan los resultados obtenidos y el daño calculado para cada muestra irradiada. Los resultados obtenidos son consistentes con una degradación de la estructura cristalina, esperada para una misión con las características simuladas.

TABLA I. DAÑO CALCULADO DE LA DEGRADACIÓN DE LA I_{cc}.

Sensor	I _{cc} IV [mA]		Daño [%]	I _{cc} RE [mA]		Daño [%]
	antes	después		antes	después	
1	18,10	16,80	7,18	18,50	16,10	12,97
2	15,60	13,80	11,54	15,40	13,50	12,34
3	15,60	13,80	11,54	15,20	13,60	10,53

V. CONCLUSIONES

Las caracterizaciones realizadas en el DES demuestran que, con la curva I-V, los lotes de sensores elaborados presentan parámetros y comportamientos similares y mediante la respuesta angular se puede afirmar que estos sensores tienen una respuesta que reproduce la ley del coseno. Además, poseen un campo visual de casi 180° lo cual es una ventaja frente a los 60 o 70° que ofrecen otros sensores comerciales.

Algunos de los ensayos mecánicos presentados, como el ensayo de impacto, se realizaron para certificar los CSS para su exportación al mercado europeo. Este fue llevado a cabo en España, pudiendo de aquí en más ofrecerlos con esta calificación.

Actualmente se está desarrollando una línea de sensores solares finos para ampliar los dispositivos de vuelo ofrecidos por el DES. Estos sensores ofrecen una mayor resolución en la medición de la posición del Sol.

El desarrollo tecnológico de sensores produce un impacto relevante en la industria espacial argentina. La fabricación de componentes y subsistemas en el país y la posibilidad de adaptación a las distintas misiones o requerimientos espaciales permite el reemplazo de componentes comerciales de muy alto costo con sensores nacionales que cumplen con las normas de calidad de la industria espacial nacional e internacional.

REFERENCIAS

- [1] C. G. Bolzi, J. C. Durán, O. Dursi, G. Renzini y H. Grossi Gallegos, "Construcción y ensayo de piranómetros fotovoltaicos de bajo costo desarrollados en la C.N.E.A.," Avances en Energías Renovables y Medio Ambiente (AVERMA), vol. 3, 1999.
- [2] C. Bolzi, M. Tamasi, M. M. Bogado y J. Plá, "Radiómetros fotovoltaicos de bajo costo desarrollados en la CNEA: prototipo comercial," Avances en Energías Renovables y Medio Ambiente, vol. 6, 2002.
- [3] C. G. Bolzi, M. G. Martínez Bogado y M. J. L. Tamasi, "Reseña del desarrollo de sensores solares en CNEA para misiones satelitales," Energías Renovables y Medio Ambiente, vol. 31, pp. 29-36, 06 2013.
- [4] M. M. Bogado, M. Tamasi, C. Bolzi y D. Raggio, "Desarrollo de sensores solares en argentina, aplicaciones terrestres y espaciales," Revista Brasileira de Energia Solar, vol. 6, n° 1, 2017.
- [5] M. Alurralde, M. Barrera, C. Bolzi, C. Bruno, P. Cabot, E. Carella, J. D. Santo, J. Durán, D. F. Slezak, J. F. Vázquez, A. Filevich, C. Franciulli, J. García, E. Godfrin, L. González, V. Goldbeck, A. Iglesias y M. M. Bogado, "Development of solar arrays for Argentine satellite missions," Aerospace Science and Technology, vol. 26, n° 1, pp. 38-52, 2013.
- [6] C. G. Bolzi, P. Cabot, E. Carella, J. D. Santo, J. C. Durán, J. F. Vázquez, E. M. Godfrin, V. Goldbeck, L. González, M. G. M. Bogado, A. Moglioni, S. Muñoz, S. L. Nigro, J. M. Olima, J. L. Pérez, J. Plá, D. Raggio, C. Rinaldi y O. Romanelli, "Paneles solares de la misión satelital SAOCOM 1A: integración y ensayos," Energías Renovables y Medio Ambiente, vol. 40, pp. 1-8, 2017.
- [7] INPE, "http://www.inpe.br/amazonia1/en/about_satellite/," [En línea].
- [8] CONAE, "https://www.argentina.gob.ar/ciencia/conae/misiones-espaciales/sabia-mar," [En línea]. Available: https://www.argentina.gob.ar/ciencia/conae/misiones-espaciales/sabia-mar.
- [9] P. A. Basore, "Defining terms for crystalline silicon solar cells," Progress in photovoltaics: research and applications, vol. 2, pp. 177-179, 1994.
- [10] M. Diaz Salazar, N. Y. Kondratiuk, A. Moreno, M. G. Martínez Bogado, M. J. L. Tamasi y J. Di Santo, "Caracterización angular automatizada de sensores solares fotovoltaicos," AVERMA, 02 2018.
- [11] J. Barth, C. Dyer y E. Stassinopoulos, "Space, atmospheric, and terrestrial radiation environments," IEEE Transactions on Nuclear Science, vol. 50, n° 3, pp. 466-482, 2003.
- [12] M. Alurralde, C. Bolzi, J. D. Santo, J. F. Vázquez, J. García, L. González, M. L. Ibarra, M. G. Martínez Bogado, S. Muñoz, J. M. Olima, J. I. Pérez, D. Raggio, O. Romanelli, C. Rinaldi, H. Socolovsky y Tama, "Technological Facilities for Development, Fabrication, Integration and Testing of Solar Arrays for Space Applications," de Proceedings of the 31st Annual AIAA/USU Conference on Small Satellites, Utah, EEUU, 2017.
- [13] H. Tada, J. Carter Jr, B. Anspaugh y R. Downing, "Solar cell radiation handbook," 1982.
- [14] M. Alurralde, M. Tamasi, C. Bruno, M. M. Bogado, J. P. b, J. F. Vázquez, J. Durán, J. Schuff, A. Burlon, P. Stoliar y A. Kreiner, "Experimental and theoretical radiation damage studies on crystalline silicon solar cells," Solar Energy Materials and Solar Cells, vol. 82, n° 4, pp. 531-542, 2004.
- [15] M. J. L. Tamasi, M. G. Martínez Bogado, S. E. Rodríguez, I. S. Prario, H. P. Socolovsky, J. C. Plá, M. A. Alurralde, C. Nigri y A. Filevich, "Diseño, fabricación, caracterización y ensayos de sensores fotovoltaicos para la misión satelital Aquarius-SAC-D," Avances en Energías Renovables y Medio Ambiente, vol. 11, pp. 1-8, 2007.

Desarrollo de sensores solares para aplicaciones terrestres

Nadia Kondratiuk
 Departamento Energía Solar
 Comisión Nacional de Energía Atómica
 (CNEA)
 Buenos Aires, Argentina
 Instituto de Nanociencia y
 Nanotecnología
 CNEA-Consejo Nacional de
 Investigaciones Científicas y Técnicas
nadiakondratiuk@cnea.gob.ar
 ORCID: 0009-0004-5720-9873

Analia Moreno
 Departamento Energía Solar
 Comisión Nacional de Energía Atómica
 (CNEA)
 Buenos Aires, Argentina
 Instituto de Nanociencia y
 Nanotecnología
 CNEA-Consejo Nacional de
 Investigaciones Científicas y Técnicas
analiveronicamoreno@cnea.gob.ar
 ORCID: 0000-0002-4455-4668

Martha Díaz Salazar
 Departamento Energía Solar
 Comisión Nacional de Energía Atómica
 (CNEA)
 Buenos Aires, Argentina
 Instituto de Nanociencia y
 Nanotecnología
 CNEA-Consejo Nacional de
 Investigaciones Científicas y Técnicas
marthadiazsalazar@cnea.gob.ar
 ORCID: 0000-0002-2092-0010

Mónica Martínez Bogado
 Departamento Energía Solar
 Comisión Nacional de Energía
 Atómica
 (CNEA)
 Buenos Aires, Argentina
 Instituto de Nanociencia y
 Nanotecnología
 CNEA-Consejo Nacional de
 Investigaciones Científicas y
 Técnicas
monicamartinez@cnea.gob.ar
 ORCID: 0000-0002-1878-9535

Claudio Bolzi
 Departamento Energía Solar
 Comisión Nacional de Energía
 Atómica
 (CNEA)
 Buenos Aires, Argentina
claudiobolzi@cnea.gob.ar
 ORCID: 0009-0001-9896-1699

José Olima
 Departamento Energía Solar
 Comisión Nacional de Energía
 Atómica
 (CNEA)
 Buenos Aires, Argentina
joseolima@cnea.gob.ar

Mariana Tamasi
 Departamento Energía Solar
 Comisión Nacional de Energía
 Atómica
 (CNEA)
 Buenos Aires, Argentina
 Instituto de Nanociencia y
 Nanotecnología
 CNEA-Consejo Nacional de
 Investigaciones Científicas y
 Técnicas
marianatamasi@cnea.gob.ar
 ORCID: 0000-0001-8294-2023

Resumen — El Departamento de Energía Solar (DES) de la Comisión Nacional de Energía Atómica (CNEA) desarrolla sensores fotovoltaicos terrestres para distintas aplicaciones, desde radiómetros para medición de radiación global hasta sensores de posición satelital. Actualmente se desarrollan radiómetros para aplicaciones específicas considerando diferentes partes del espectro solar, como la medición del índice de vegetación de diferencia normalizada (NDVI, por sus siglas en inglés) y la radiación ultravioleta.

Palabras claves—radiómetros fotovoltaicos, NDVI, radiación ultravioleta

I. INTRODUCCIÓN

El Departamento de Energía Solar (DES) de la Comisión Nacional de Energía Atómica (CNEA) ha desarrollado radiómetros fotovoltaicos para uso terrestre y espacial desde finales de la década del 90 [1]. Los sensores fotovoltaicos, en general, pueden utilizarse en cualquier situación donde la excitación de entrada sea radiación luminosa, en el intervalo de longitudes de onda donde éstos son sensibles, entregando a la salida una señal eléctrica. La fabricación de estos sensores y su adecuación mediante distintos encapsulados, la modificación de su respuesta espectral y/o su acoplamiento a un sistema de adquisición de datos, pueden generar distintos instrumentos: sensores de radiación solar global, de radiación solar fotosintéticamente activa (PAR, por sus siglas en inglés), de radiación ultravioleta (UV), para medición del índice de vegetación de diferencia normalizada (NDVI, por sus siglas en inglés) y sumergibles.

La medición de la energía proveniente del Sol se considera necesaria, entre otras cosas, para:

- estudiar el impacto que los cambios en los niveles de radiación, debido a las variaciones periódicas o anómalas, tienen sobre las condiciones climáticas (variaciones en la nubosidad, en la cantidad de partículas en suspensión en la atmósfera y en el agua que se puede precipitar, se verían inmediatamente reflejadas en la radiación medida),
- determinar la influencia que la radiación solar a nivel de superficie tiene en el rendimiento de cosechas,
- estudiar el balance energético o el crecimiento de un cultivo particular,
- evaluar la evapotranspiración potencial del suelo y determinar así su estado hídrico (agua disponible y necesidad de riego),
- planificar el secado de productos vegetales con mayor eficiencia, y
- diseñar adecuadamente y monitorear sistemas fotovoltaicos.
- alertar de manera temprana sobre los efectos negativos que una prolongada exposición a la radiación ultravioleta puede implicar sobre la salud humana.

Los primeros radiómetros se realizaron utilizando celdas fotovoltaicas de silicio monocristalino desarrolladas y fabricadas en el DES de 25 mm de lado [1], desde entonces se ha ido modificando su diseño y adecuándolos a las necesidades de los usuarios. Es así como se adaptaron los sensores de radiación global a necesidades específicas tales como la medición de la radiación PAR, la radiación UV y se están realizando las adecuaciones para tener un primer

prototipo de radiómetro para medir el índice de vegetación NDVI.

II. RADIÓMETROS PARA LA MEDICIÓN DE RADIACIÓN GLOBAL

Los sensores para aplicaciones terrestres desarrollados, denominados radiómetros o solarímetros, constan de una base de aluminio, sobre la cual se monta el elemento sensor protegido por una cubierta de vidrio difusor sellado en su periferia. La cubierta de vidrio tiene dos finalidades, por un lado, proteger al sensor fotovoltaico de las condiciones ambientales y por el otro, mejorar la respuesta angular debido al esmerilado superficial del mismo.

El elemento sensor es una celda fotovoltaica de silicio monocristalino diseñada y fabricada por el DES [2], en particular estos sensores tienen un área activa aproximadamente de $0,13 \text{ cm}^2$. La salida eléctrica de los dispositivos es una salida de tensión del orden de los milivolts y dentro del intervalo de error, lineal con la radiación solar. En la Fig. 1 se muestra el instrumento terminado.

Como ensayo en condiciones reales de utilización algunos de estos radiómetros han sido distribuidos a distintos grupos de investigación de Argentina desde hace varios años. Algunos de los ensayos de los radiómetros están siendo realizados en condiciones reales de operación en ambientes adversos (alta radiación UV, gran amplitud térmica, etc.), con es el caso de la región de la Puna en el Norte Argentino. Además, se ha instalado un radiómetro en el laboratorio del *International Center of Earth Science (ICES)* situado en la cadena montañosa del volcán Peteroa [3]. Dos de estos instrumentos de radiación global fueron instalados en la Base Marambio en la Antártida Argentina. Uno de ellos está acoplado con un sistema fotovoltaico del proyecto IRESUD (proyecto cuya finalidad es introducir en el país tecnologías asociadas con la interconexión a la red eléctrica) y otro en posición horizontal. Estos radiómetros se encuentran acoplados al sistema fotovoltaico instalado allí por dicho proyecto y mide la radiación solar para poder evaluar el recurso y el instrumento en condiciones extremas. Estos radiómetros son calibrados por el Grupo de Estudios de la Radiación Solar (GERSolar) de la Universidad Nacional de Lujan (UNLu).



Fig. 1. Radiómetro global desarrollado en el DES.

III. RADIÓMETROS PAR

Para estudiar el balance energético o el crecimiento de un cultivo particular, si bien puede disponerse en general del dato de radiación global (medida o estimada), no es frecuente contar con valores de radiación fotosintéticamente activa (PAR), la que puede ser definida como la fracción del espectro solar comprendida entre 400 y 700 nm. Se desarrollaron radiómetros para la medición de la radiación PAR. Para esto, se trabajó paralelamente en el uso de filtros comerciales y el

desarrollo de procesos para la fabricación de multicapas dieléctricas delgadas tanto sobre el sensor como en las cubiertas para limitar la respuesta espectral.

Como primera aproximación se calculó la respuesta espectral que tendría un radiómetro PAR utilizando un filtro comercial, como se muestra en la Fig. 2. La misma se obtuvo a partir de la respuesta espectral medida de un sensor de silicio y la transmitancia del filtro. Los primeros prototipos desarrollados con filtro comercial calibraron en el Grupo de Estudios de la Radiación Solar (GERSolar) de la Universidad Nacional de Luján y están siendo utilizados por organismo nacionales públicos y privados. Estos radiómetros son constructivamente similares a los de radiación global al que se adiciona filtro óptico que recorta su respuesta espectral.

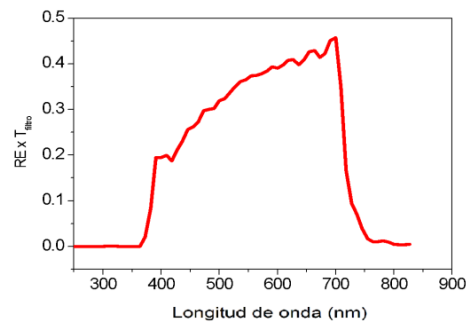


Fig. 2. Respuesta espectral de un radiómetro PAR a partir de un filtro comercial.

IV. RADIÓMETROS SUMERGIBLES

Se diseñó y fabricó un sensor solar fotovoltaico de silicio monocristalino y el soporte para un radiómetro fotovoltaico sumergible apto para uso en distintos medios acuáticos [4]. El desarrollo de este instrumento tiene aplicaciones en distintas áreas, por ejemplo, para la apicultura y la producción de algas. El diseño se planteó de acuerdo con la señal del sensor debido a su atenuación al ser sumergido, así como la adaptación de las dimensiones. Los resultados mostraron un buen comportamiento del instrumento sometido a presiones equivalentes a distintas profundidades y cumplió con las especificaciones planteadas originalmente. Por último, se realizaron calibraciones antes y después de los ensayos.

El radiómetro se construyó de manera que tenga simetría cilíndrica y consta de un cuerpo o base y una tapa vidriada, esta última protegida por una brida que se une al cuerpo por medio de tornillos. El interior fue diseñado de manera que permita la integración del sensor y su conexión de manera estanca. A partir de un análisis de distintos materiales posibles, se decidió utilizar polipropileno como material tanto para la base como para la brida, como se muestra en la Fig. 3. La elección del polipropileno fue por sus cualidades inertes tanto en agua dulce como salada, la tolerancia a ambientes ligeramente ácidos o básicos, su facilidad para el maquinado entre otras propiedades mecánicas. La medición de la corriente de cortocircuito del sensor (parámetro lineal con la radiación solar) se realiza midiendo la caída de potencial sobre una resistencia conocida. Para el caso de los radiómetros terrestres desarrollados en el DES la resistencia está integrada dentro del cuerpo del radiómetro. Para el radiómetro sumergible se decidió colocar la resistencia en la caja de conexionado del adquisidor de datos para tener una mayor libertad en caso de necesitar variar el valor de esta.



Fig. 3. Imágenes del radiómetro sumergible en proceso de armado (superior) y terminado (inferior).

V. RADIÓMETROS ULTRAVIOLETAS

La aplicación de los sensores de radiación ultravioleta es muy amplia: desde usos en grupos de investigación de diferentes disciplinas como la biología, agronomía, etc., hasta mediciones en zonas de alto nivel de radiación UV donde se puede estudiar el impacto de los cambios en los niveles de radiación debido a variaciones periódicas o anómalas. En el transcurso de su vida, las personas en sus distintas actividades propias se exponen a la radiación del Sol por diversos motivos. El 80 % de los efectos indeseables que origina la exposición solar se debe al espectro ultravioleta B (UVB), comprendido entre los 290 nm y 320 nm de longitud de onda. Poder conocer la dosis de exposición es fundamental ya que existe una relación directa entre su magnitud y el desarrollo de neoplasias, fotoenvejecimiento, mutaciones, cataratas e inmunosupresión. De esta manera se puede alertar de manera temprana sobre los posibles efectos negativos para la salud en las poblaciones de distintos emplazamientos.

Para que un radiómetro de silicio funcione como un sensor de radiación ultravioleta, es necesario la utilización de un filtro óptico que recorte la porción del espectro que no se desea medir. En una primera etapa del desarrollo de los sensores, se realizaron simulaciones numéricas para obtener la transmisión de filtros de películas delgadas de capas metal-dieléctricas con el fin de optimizar el diseño, para poder medir en bandas estrechas específicas del espectro UV. Estos filtros se utilizan desde la década del 60 y en los últimos años se ha estudiado en detalle para su aplicación en el rango ultravioleta [5, 6].

Se pudo observar que los diseños de multicapas de Al_2O_3 permitirían la obtención de un filtro que permite medir el espectro UVB, ya que se puede lograr que la longitud de onda central sea la adecuada, variando el espesor del material dieléctrico (Fig. 4).

Para la optimización del dispositivo es necesario aumentar la respuesta espectral en la región ultravioleta de la celda de silicio. En particular el objetivo es modificar el proceso de difusión de dopantes que determinan la juntura np de la celda solar. Se realizaron diferentes procesos de difusión de fósforo

sobre sustratos de silicio tipo p variando distintos parámetros como tiempos y caudal de gases en varias etapas del proceso.

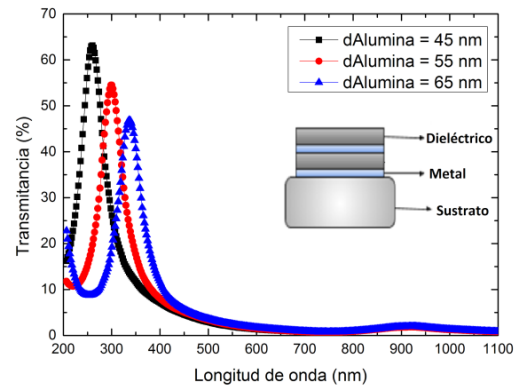


Fig. 4. Transmitancia de los filtros UV diseñados para un espesor de las películas de aluminio de 10 nm.

Estas variaciones se realizaron con el objetivo de obtener muestras con menor profundidad de juntura y menor concentración de dopante tipo n, siendo estas características fundamentales para una mayor respuesta espectral en el espectro ultravioleta. El diseño del primer prototipo del radiómetro ultravioleta elaborado en el DES se muestra en el Fig. 5.

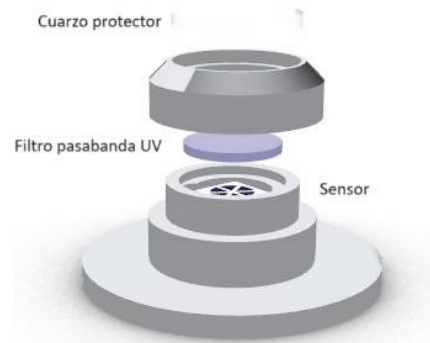


Fig. 5. Diseño del primer prototipo de radiómetro ultravioleta elaborado en el DES.

VI. SENSOR DE MEDICIÓN DEL ÍNDICE DE VEGETACIÓN DE DIFERENCIA NORMALIZADA (NDVI)

De los índices de vegetación conocidos, el NDVI es de los más importantes y usados. Utiliza las bandas del rojo y el infrarrojo cercano y nos permite calcular la salud de una planta en un estado fenológico concreto. La respuesta espectral que tiene la vegetación sana muestra un claro contraste entre el espectro visible, especialmente la banda roja, y el infrarrojo cercano. Mientras que en el visible los pigmentos de la hoja absorben la mayor parte de la energía que reciben, en el infrarrojo, las paredes de las células de las hojas, que se encuentran llenas de agua, reflejan la mayor cantidad de energía. En contraste, cuando la vegetación sufre algún tipo de estrés, ya sea por presencia de plagas o por sequía, la cantidad de agua disminuye en las paredes celulares por lo que la reflectividad disminuye el infrarrojo y aumenta paralelamente en el rojo al tener menor absorción clorofílica. Esta diferencia en la respuesta espectral permite separar con relativa facilidad la vegetación sana de otras cubiertas.

Las longitudes de onda involucradas se encuentran en el intervalo de respuesta de los sensores de silicio. Para desarrollar el primer prototipo se llevó a cabo el diseño y la construcción de una base para montar los sensores y los filtros comerciales que recortan el espectro en las longitudes de onda de interés. Esta base tiene una disposición de dos sensores que miden hacia arriba y dos hacia abajo (Fig. 6), en ambos pares de sensores uno de los sensores mide en el visible, 630 nm y el otro en el infrarrojo cercano, 800 nm.

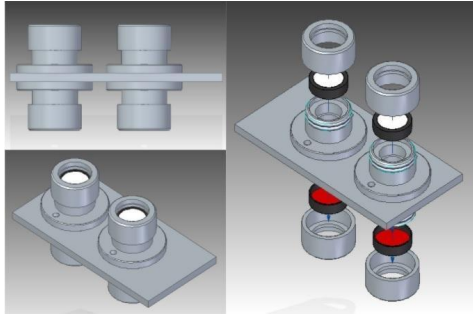


Fig. 6. Esquema de montaje de sensores y filtros para medir NDVI.

VII. CONCLUSIONES

Desde finales de la década del '90 se viene trabajando en el desarrollo de radiómetros, como de la interacción y la posibilidad de adaptación de los instrumentos a las necesidades específicas de los usuarios. Se construyeron instrumentos confiables de bajo costo y disponibles tanto para el área comercial, agrícola, meteorológica, entre otras, además de la sustitución de componentes de fabricación nacional en la industria espacial.

Se inició con el desarrollo de radiómetros terrestres con aplicaciones específicas y se adecuaron a las necesidades de distintos usuarios. Se diseñaron los dispositivos y sus componentes para que cumplan con los requisitos de medición. Se continúa con la elaboración y optimización de los dispositivos con el fin de obtener los primeros prototipos.

En particular se contempló el desarrollo de radiómetros para la medición de radiación correspondiente a distintas regiones del espectro electromagnético (UV, UVB, PAR). Las ventajas de desarrollar estos dispositivos residen principalmente en la posibilidad de proporcionar a empresas, instituciones universitarias y de ciencia y tecnología una herramienta fiable, con una disponibilidad más inmediata y a un costo menor en comparación con los instrumentos comerciales importados.

REFERENCIAS

- [1] C. G. Bolzi, J. C. Durán, O. Dursi, G. Renzini y H. Grossi Gallegos, "Construcción y ensayo de piranómetros fotovoltaicos de bajo costo desarrollados en la C.N.E.A.", *Avances en Energías Renovables y Medio Ambiente (AVERMA)*, vol. 3, 1999.
- [2] C. G. Bolzi, L. M. Merino, M. J. L. Tamasi, J. C. Plá, J. C. Durán, C. J. Bruno, ... y L. B. Quintero, "Elaboración y caracterización de celdas y paneles solares de silicio cristalino para su ensayo en el satélite SAC-A", *Avances en Energías Renovables y Medio Ambiente*, vol. 1, 1997.
- [3] C. Guzmán, C. Hucailuk, M. Tamasi, M. M. Bogado, y D. Torres, "Anomalías encontradas en los parámetros registrados en la estación de medición de la terma del Volcán Peteroa", *Actas de ICES IX*, pp. 186-194, 2013.
- [4] C. G. Bolzi, M. J. L. Tamasi, M. G. Martínez Bogado y J. C. Plá, "Radiómetros fotovoltaicos de bajo costo desarrollados en la C.N.E.A.: prototipo comercial", *Avances en Energías Renovables y Medio Ambiente*, vol. 6, 2002.
- [5] Z. Jakšić, M. Maksimović, y M. Sarajlić, "Silver-silica transparent metal structures as bandpass filters for the ultraviolet range", *Journal of Optics A: Pure and Applied Optics*, vol. 7, no. 1, pp. 51, 2004.
- [6] J. Mu, P. T. Lin, L. Zhang, J. Michel, L. C. Kimerling, F. Jaworski, y A. Agarwal, "Design and fabrication of a high transmissivity metal-dielectric ultraviolet band-pass filter", *Applied Physics Letters*, vol. 102, no. 21, pp. 213105, 2013.

Diseño de un medidor de flujo "drop and play" para el monitoreo de canales de irrigación

Hesner Coto
División de Posgrado e Investigación
TecNM/IT la Laguna
Torreón, Coah. México
hesnercf@lalaguna.tecnm.mx

Alexia Trejo
TecNM/IT la Laguna
Torreón, Coah. México
aletrejo97327@gmail.com

Axel David Neave
TecNM/IT la Laguna
Torreón, Coah. México
axl.david.neave@gmail.com

Karla Guevara
Departamento de Ingeniería Química
TecNM/IT la Laguna
Torreón, Coah. México
vguevaraa@lalaguna.tecnm.mx

Emmanuel Gómez
División de Posgrado e Investigación
TecNM/IT La Laguna
Torreón, Coah, México
egomezram@gmail.com

Francisco Valdés
División de Posgrado e Investigación
TecNM/IT La Laguna
Torreón, Coah. México
fvaldesp@lalaguna.edu.mx

Abstract— La agricultura en México se sustenta en la irrigación de más de 6.5 millones de hectáreas, con una eficiencia global promedio inferior al 40% y utilizando alrededor del 80% del volumen de agua disponible. En el Distrito de Riego 017, conformado por 17 módulos en Coahuila y Durango, el agua se distribuye desde dos presas a través de una red de más de 6000 kilómetros. Estudios en este distrito han revelado importantes pérdidas de agua por conducción, baja eficiencia de riego y deficiencias en la medición de los volúmenes entregados.

En este contexto, se presenta el diseño de un medidor de flujo, orientado a la medición de gasto o caudal en canales de riego, sin necesidad de obra civil o preparación para su uso. El medidor se ancla mediante una cuerda en una de las riberas del canal, se configura el área transversal del mismo y se lanza al agua. El medidor se alinea de manera automáticamente, paralelo a la corriente y en las posiciones idóneas para realizar las mediciones de velocidad del fluido y posteriormente calcular el caudal. Las mediciones son transferidas vía inalámbrica a la nube para su almacenamiento y posterior análisis.

Keywords—Drop and play, medidor de flujo, canales de irrigación

I. INTRODUCCIÓN

La agricultura en México depende de la irrigación de más de 6.5 millones de hectáreas, utilizando para ello alrededor del 80% del volumen total del agua disponible, con una eficiencia global promedio inferior al 40%. En el caso particular del Distrito de Riego 017 (DR017), conformado por 17 módulos: 9 en el estado de Coahuila y 8 en Durango, el agua proviene de dos presas de almacenamiento, cuatro presas derivadoras, diversos tanques de almacenamiento y 3 200 pozos [1]. Para su distribución se utiliza una red de más de 6 000 kilómetros entre tramos de río, canales principales, secundarios, de riego y drenes [2].

En el caso particular de los módulos del DR017 dentro de la Comarca Lagunera, se riega una superficie promedio anual de 87 240 hectáreas de cultivo, que demandan un volumen de 1 345 millones de metros cúbicos (Mm³), principalmente para garantizar el alimento de más de 600 000 cabezas de ganado lechero de alta productividad. Estudios realizados a finales de la década del 90 mencionan importantes pérdidas de agua en 225km del río Razas, 2 432km de canales principales y secundarios, y más de 4 330km de regaderas sin revestimiento. Por otra parte, el aprovechamiento subterráneo ha originado déficits anuales de más de 585 Mm³, lo que manifiesta una evidente sobreexplotación de los mantos acuíferos de la región [3]. En las parcelas, la eficiencia promedio de riego por gravedad es baja, debido

principalmente a pérdidas de agua por escurrimiento e infiltración originadas por el sobre riego, al aplicar volúmenes superiores a los requeridos por los cultivos [4].

Ya sea por conducción, aprovechamiento subterráneo o riego parcelario por gravedad, la medición de los volúmenes de agua distribuidos y utilizados es insuficiente, alarmando que un recurso tan importante para el desarrollo humano no sea administrado adecuadamente, al punto, de que estudios plantean el desconocimiento de la cantidad de agua entregada como una problemática fundamental de la mayoría de los Distritos de Riego [3, 5, 6]. En el contexto antes descrito, contar con un medidor de flujo continuo, económico y versátil (variedad de canales, localizaciones y condiciones de medición) cobra una relevancia incalculable, teniendo en cuenta la importancia actual de los recursos hídricos.

La medición de caudales líquidos es un tema ampliamente tratado en ramas afines a la instrumentación (electrónica, mecánica). Sin embargo, en casos de grandes caudales y redes de distribución tan amplias como las existentes en los Distritos de Riego, la situación es diferente. El equipamiento es caro y requiere costosas infraestructuras para su instalación. Además, la mayoría de los métodos de medición que se utilizan deben ser realizados por una o más personas [7], por lo que el muestreo no es continuo y las variaciones propias de los flujos naturales por gravedad introducen errores extremadamente grandes [6].

Entre las opciones documentadas para la medición del gasto en los canales de irrigación se encuentran: método del flotador, método de rastreo por tinte, tablilla graduada para medir la carga hidráulica por velocidad, vertederos, estimación de gastos utilizando tubos de sifón, ruedas hidráulicas, medidores ultrasónicos y molinete hidrométricos. Todos ellos necesitan, de una manera u otra, de la supervisión de operadores, de la preparación de los lugares de medición o la instalación de obra civil para su correcto funcionamiento, o ambas. De todas las mencionadas, los vertederos y el molinete hidrométricos son las más utilizadas en la región.

II. METODOLOGÍA

El principio de medición seleccionado para la implementación del medidor de flujo se basa en el molinete hidrométrico, por lo que para la validación del mismo se decidió utilizar dos métodos. En el primero método se realizan mediciones ciegas (sin conocer el valor real del caudal) utilizando el medidor de flujo "drop and play" en un segmento de canal recto con varias secciones transversales diferentes y sin extracciones. En estas mediciones no se cuenta con un patrón de comparación directa, pero por las condiciones del

canal las mediciones en cada sección transversal deben arrojar caudales o gastos iguales. En el segundo método se utilizarán los resultados obtenidos por un molinete hidrométrico como patrón de calibración.

Al utilizar un molinete hidrométrico tradicional para la medición del aforo en un canal de irrigación, es necesario seleccionar un tramo recto y uniforme del canal, evitando cambios bruscos en su geometría que puedan afectar la precisión y exactitud de las mediciones. Se prepara el molinete, asegurándose de que esté en buen estado y calibrado, y se posiciona en el agua de acuerdo con la metodología seleccionada (las mediciones más utilizadas se realizan a 0.6 de la profundidad, o promediando las profundidades a 0.2 y 0.8 de la profundidad de cada sección). Iniciando el cronómetro posterior a seleccionar el escandallo según la corriente, se permite que el molinete se sumerja completamente en el agua, registrando la velocidad durante al menos un minuto para obtener lecturas estables. Se repite este proceso varias veces en el mismo punto para garantizar la consistencia de los datos. Luego, moviendo el molinete a lo largo de diversas secciones transversales del canal, se obtiene un perfil de velocidad completo (típicamente se mide en dos o tres secciones). Es fundamental realizar mediciones en diferentes puntos para capturar la variabilidad del flujo en el canal. Con las velocidades registradas, se procede al cálculo del caudal por sección, multiplicando la velocidad promedio por el área transversal del flujo en cada una de las secciones definidas. El gasto final se obtiene como la sumatoria de todas las secciones o a través de tabuladores.

En la Figura 1 se puede apreciar el comportamiento o perfil de velocidades en la sección transversal de un canal, razón principal por lo que las mediciones se deben realizar en varios puntos del mismo. El medidor “drop and play” es capaz de posicionarse de manera automática en varios puntos del canal para realizar las mediciones.

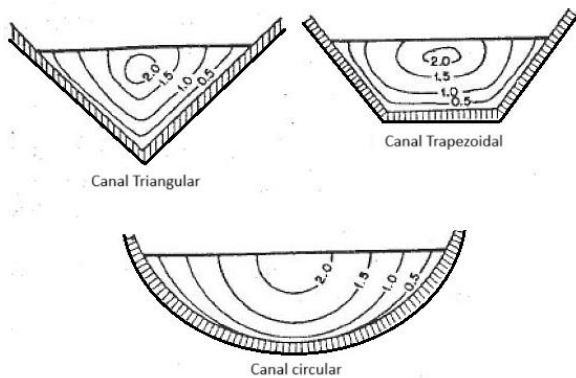


Fig. 1. Distribución de velocidades del flujo en la sección transversal de varios canales de irrigación [7].

Para la impresión de los prototipos se utilizó una impresora Bambu Carbón X1, con filamento PETG. Mientras que para la impermeabilización de los modelos se utilizó resina foto curable UV.

III. RESULTADOS

Después de varias iteraciones y modificaciones, se obtuvo un dispositivo orientado a la medición del gasto en canales de irrigación, que después de anclado en una de las orillas del canal haciendo uso de una cuerda o tensor, puede ser arrojado

al mismo (*drop and play*) y comenzar a funcionar. Una vez en el agua el dispositivo se orientará automáticamente a partir del control del timón de cola, manteniendo la tensión del tensor y la posición deseada durante el tiempo necesario. Se realizan múltiples mediciones de velocidad del flujo en varias posiciones transversales, para posteriormente calcular el gasto total fluyendo por el canal.



Fig. 2 Medidor de flujo basado en carenado RG65 y molinete hidrométrico tradicional.

Para la medición del caudal en canales de irrigación, sin necesidad de obra civil o intervención de operadores (medición automática), se propone un dispositivo compuesto principalmente por una boya tipo embarcación, con carena tipo velero RG65 (ver Figura 2), con un casco más estrecho y plano en comparación con otros veleros. La proa (parte delantera) es afilada y la popa (parte trasera) más ancha. Cuenta con una quilla de perfil delgado y un bulbo. La quilla (Q) es la aleta vertical que se extiende hacia abajo desde el casco, mientras que el bulbo (Em) contiene peso adicional en la parte inferior de la quilla para mejorar la estabilidad y el equilibrio del dispositivo de medición.

El timón de cola (Tc) se encuentra controlado por un servomotor alojado dentro del casco, y es el encargado de modificar el perfil de la boya con respecto a la corriente del canal, generando una relación de fuerzas que junto con las del tensor, permite mover el dispositivo por el canal, siguiendo un segmento de circunferencia de radio igual a Tconf (ver Figura 3). El tensor de longitud Tconf se encuentra conectado al dispositivo a través de un codificador rotativo de dos ejes o giroscopio, el que permite medir el ángulo que forma el dispositivo respecto a la vertical y la horizontal (Am1 y Am2). Tanto el servomotor, como el codificador rotativo de dos ejes, son atendidos por un circuito electrónico basado en microcontrolador alojado dentro del casco (Unidad de control, UC).

Los ángulos Am1 y Am2, medidos del codificador rotativo de dos ejes, junto a los elementos de configuración precargados en la UC previo a realizar las mediciones (datos del canal a medir), permitirán el cálculo geométrico de la posición del dispositivo en la superficie de la corriente del

canal. Dicha posición podrá ser controlada por la UC a partir del accionamiento del timón de cola (T_c), para realizar las mediciones en los lugares necesarios de manera automática.

Para realizar las mediciones, basado en el principio del molinete hidrométrico, el bulbo cumple la doble función de lastre y molinete, brindando estabilidad al instrumento y funcionando como elemento de medición o transductor. El bulbo se encuentra normalmente en la posición mostrada, longitudinalmente orientado con la quilla. Dentro del bulbo se encuentra, además del lastre (pesos a base de plomo), un generador de imanes permanentes. En el momento que el dispositivo se encuentre en la posición deseada de medición, la UC realizará las mediciones.

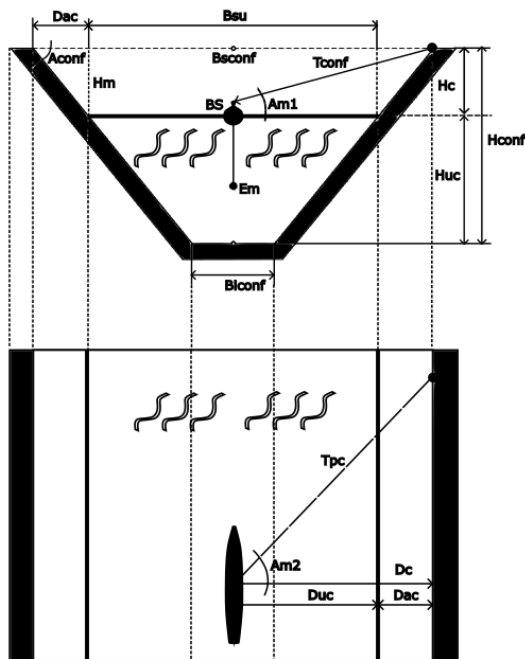


Fig. 3 Ejemplo de geometría de canal y disposición de ángulos para el cálculo de la posición del medidor de flujo.

La UC se encargará de utilizar el accionamiento del generador de imanes permanentes por la corriente de agua del canal según las necesidades del sistema, como elemento de medición o como generador. Para realizar las mediciones garantizará una alta impedancia conectada al generador, el que girará libremente produciendo una tensión proporcional a la velocidad del flujo. Cuando se utilice como generador, la energía producida será almacenada en baterías instaladas dentro del casco, que permitirán la operación ininterrumpida del dispositivo.

Conectada a la UC, también dentro del casco, se encuentra un dispositivo de comunicación multiprotocolo (GSM y Wifi). El que permite la configuración inalámbrica del dispositivo, así como la extracción de los datos medidos y recopilados por el dispositivo. En la Figura 4 se puede apreciar una de las pruebas de concepto realizadas, donde el control de posición del medidor de flujo en el canal se realizó de manera manual utilizando circuitos de radiocontrol comerciales.



Fig. 4. Pruebas del prototipo en canales de irrigación.

IV. CONCLUSIONES

Después de realizadas las pruebas de concepto se comprobó la validez del diseño, logrando un posicionamiento adecuado y estable del medidor de flujo en varias posiciones del canal. Se comprobó también la impermeabilización del casco y la suficiencia del timón de cola para la navegación.

El uso de un giroscopio con magnetómetro permitió la medición adecuada de los ángulos necesarios para determinar la posición de la embarcación en el canal, a partir del anclaje de la misma a la parte superior del mismo. Como trabajo futuro se propone la aplicación de algoritmos de control que accionando el timón de cola permitan la colocación automática del medidor en varias posiciones del canal. Así como el método para la obtención de la velocidad promedio del flujo, ya que las mediciones se pueden realizar en varias posiciones del canal, pero siempre a la misma profundidad.

AGRADECIMIENTOS

Los autores agradecen el soporte financiero del Tecnológico Nacional de México y del Consejo Nacional de Humanidades, Ciencias y Tecnologías para la realización del proyecto cuyos resultados se exponen.

REFERENCIAS

- [1] Ramos-Cruz, C. M., Estrada-Ávalos, J., Delgado-Ramírez, G., Miguel-Valle, E., & Alemán, D. D. (2018). Estimación de la eficiencia de riego superficial parcelario en un módulo del distrito 017 Región Lagunera. *Revista Chapingo Serie Zonas Áridas*, 17(2), 21-30.
- [2] CONAGUA, 2013. Asesoría y transferencia de tecnología al plan de riegos de los módulos del Distrito de riego 017 región lagunera en el estado de Coahuila. Informe final 2012.
- [3] Hernández, M. F., & Alhers, R. (1999). *Naturaleza y extensión del mercado del agua en el DR 017 de la Comarca Lagunera*, México. Instituto Internacional del Manejo del Agua.
- [4] García Domínguez, M. Y., Sánchez Cohen, I., García Herrera, G., Moreno Díaz, L., Trejo Calzada, R., & Hernández Martínez, M. A. (2010). Evaluación de la eficiencia de riego en el Módulo IV del Distrito de Riego 017 Comarca Lagunera, México. *Revista Chapingo Serie Zonas Áridas*, 9(2), 99-106.
- [5] Saénz, E. M., Vélez, E. P., García, A. E., & Hernández, A. L. S. (2002). Problemas operativos en el manejo del agua en distritos de riego. *Terra latinoamericana*, 20(2), 217-225.
- [6] Arrellano Monterosas, J. L. (2020). *La gestión de los Distritos de Riego de México: problemática y retos*, México. Segundo seminario temático. CONAGUA. Organismo de Cuenta Frontera Sur.
- [7] Martín, E. C., & Muñoz, C. (2017). *Cómo Medir el Flujo de Agua en los Canales de Riego a Cielo Abierto y en las Tuberías de Compuertas*.

Desarrollo de un microdosímetro de estado sólido para uso en protonterapia

D. G. Mercado^(1,2), **J. I. Drovandi**^{*(1,2)}, **L. Cervantes Schamun**^(1,2), **N. Kondratiuk**^(1,3), **N. Boggio**^(1,2), **M. J. Deiana**^(1,2), **M. Martinez Bogado**^(1,3), **G. Santa Cruz**⁽⁴⁾, **G. M. Berlín**^(1,2)

(1) Instituto de Nanociencia y Nanotecnología (CNEA - CONICET), CAC, Av. Gral. Paz 1499 (B1650KNA) San Martín, Buenos Aires, Argentina

(2) Depto. de Micro y Nanotecnología, GDTyPE, CAC, Comisión Nacional de Energía Atómica, Av. Gral. Paz 1499 (B1650KNA) San Martín, Buenos Aires, Argentina.

(3) Depto. de Energía Solar, GIyA, CAC, Comisión Nacional de Energía Atómica, Av. Gral. Paz 1499 (B1650KNA) San Martín, Buenos Aires, Argentina.

(4) Gerencia de Área Aplicaciones Nucleares a la Salud (GAANS), Sede Central, CNEA, Av. del Libertador 8250, Buenos Aires, Argentina

*Correo Electrónico (autor de contacto): juandrovandi@cnea.gob.ar

Abstract—En el presente trabajo, se describen los avances realizados en el diseño y fabricación de la primera generación de microdosímetros de estado sólido orientados a su utilización en protonterapia. Dichos dispositivos están siendo desarrollados a través de procesos de microfabricación en las instalaciones del CAC-CNEA y se podrán complementar a las facilidades de las que dispondrá el futuro Centro Argentino de Protonterapia tanto para ensayos experimentales como clínicos.

Keywords—Microdosimetría, dosímetros, microfabricación, protonterapia, implantación iónica.

I. INTRODUCCIÓN

Un microdosímetro es un dispositivo que permite medir dosis de radiación depositada a una escala micrométrica. En los últimos años se empezó a utilizar tecnología basada en semiconductores para diseñar dosímetros que puedan operarse con precisión micrométrica. Algunas de las ventajas que poseen con respecto a los TEPC (*Tissue equivalent proportional counter*, el estándar actual para microdosimetría) son: su reducido tamaño, no requieren de un caudal gaseoso, poseen un voltaje de funcionamiento muy bajo y una resolución espacial sumamente alta (de hasta 10 μm , un diámetro celular promedio). Además, cuentan con una gran cantidad de unidades sensibles que pueden ser distribuidas en el espacio de manera que su respuesta sea equivalente a la de un conjunto de células siendo esto de gran importancia para aplicaciones físico-médicas en tratamientos de radioterapia e investigación [1-3].

El proceso de fabricación del microdosímetro está compuesto por un flujo de proceso preliminar de 43 etapas, 31 de las cuales consisten en procesos de microfabricación y las restantes de caracterización. Estos procesos abarcan desde el dopaje del semiconductor, que permite delimitar los volúmenes sensibles, hasta el encapsulado del dispositivo final. En una primera instancia se utilizará silicio como semiconductor, con dopaje tipo N de fósforo y tipo P de boro.

El diseño consiste en un arreglo de diodos PIN (p-intrínseco-n) conectados entre sí y distribuidos geoméricamente sobre un sustrato de silicio (ver Fig. 1), junto con un *guard ring* (GR).

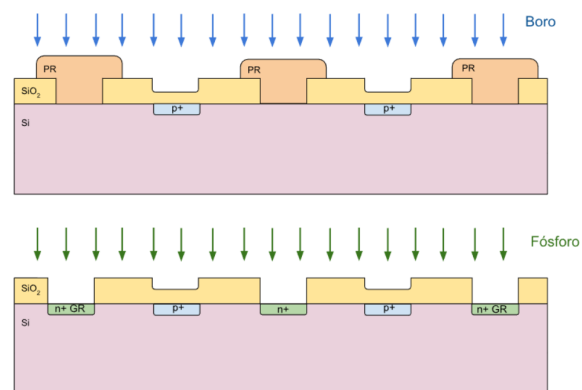


Fig. 1: Corte transversal del dispositivo. Se observan las máscaras de SiO_2 y de fotorresina (PR, por *photoresist*) se destacan las zonas de dopaje tipo p (boro, en azul) y tipo n (fósforo, en verde) y el orden de los elementos a implantar.

Para que el dispositivo funcione de manera óptima una de las etapas más importantes en la microfabricación es poder controlar de manera precisa no sólo la concentración de los dopantes que forman los diodos sino también su geometría y localización [4]. El presente trabajo describe el desarrollo y microfabricación de una máscara de implantación de SiO_2 y fotorresina sobre un sustrato de silicio de alta resistividad, con el propósito de definir las zonas de la implantación.

La implantación iónica de boro y fósforo se llevará a cabo en el Campus Tecnológico e Nuclear, del Instituto Superior Técnico en Lisboa, Portugal, en donde se previamente se realizarán pruebas de implantación a distintas energías y distintos ángulos de inclinación en obleas de silicio $\langle 100 \rangle$. Los resultados de la implantación serán caracterizados mediante SIMS (espectrometría de masa de iones secundarios) y ECV (medida de capacitancia-voltaje electroquímico).

II. MATERIALES Y MÉTODOS

A. Simulaciones

Para el desarrollo de los dispositivos se optó por el dopaje mediante la técnica de implantación iónica de átomos de boro (región p) y fósforo (región n) sobre silicio, ya que permite lograr perfiles con alta precisión y repetibilidad con respecto a la técnica de difusión de dopantes.

Para llevar a cabo la implantación de ambos iones (boro y fósforo) en regiones separadas de forma sencilla, se diseñó una máscara constituida por distintos espesores de SiO₂ térmico y fotorresina. Ciertos espesores de SiO₂ frenan los iones en determinadas zonas, permitiendo su paso en las regiones a dopar. El rango o profundidad de los iones de boro y fósforo, con la misma energía y en un mismo material, difiere debido a sus masas atómicas, siendo que el boro tiene mayor penetración por ser más “liviano” que el fósforo. Estas características de los iones permiten diseñar máscaras con distintos espesores en diferentes regiones, con el fin de implantar de forma selectiva para lograr regiones dopadas p y n.

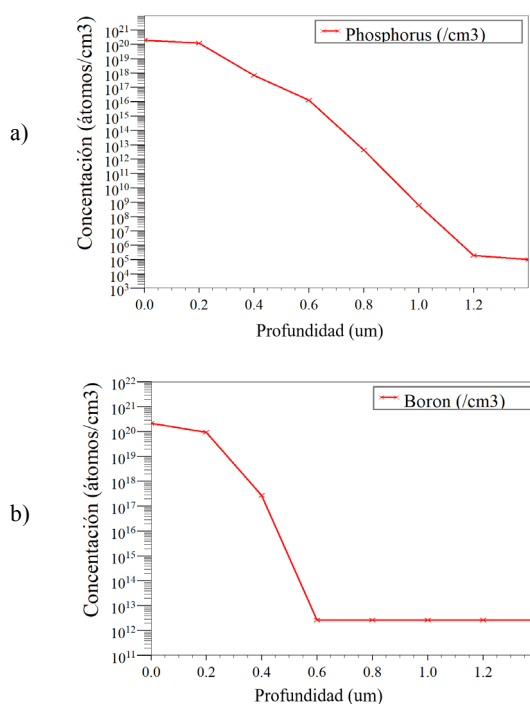


Fig. 2: a) Perfil de concentración en profundidad de iones de fósforo con energías de 35 keV. b) Perfil de concentración en profundidad de iones de boro con energías de 55 keV.

Empleando técnicas computacionales de simulación de procesos y dispositivos se evaluaron implantaciones iónicas y recocidos térmicos con diversidad de energías y fluencias sobre distintos espesores de SiO₂, hasta lograr regiones con concentraciones de 1×10^{20} at/cm³ [5]. Dejando espesores de 150 nm de SiO₂ en las regiones de implantación de boro, se lograron las concentraciones planteadas empleando fluencias de 5×10^{15} , y energías de 35 keV para el fósforo y 55 keV para el boro (ver Fig. 2 a) y b))

B. Microfabricación

i. Oxidación térmica

Para poder microfabricar la máscara de implantación se oxidaron térmicamente obleas de silicio <100> de alta resistividad (~3000 Ω.cm), logrando espesores de 415 nm de SiO₂.

ii. Máscaras para fotolitografía

Se diseñaron y fabricaron dos fotomáscaras con los patrones de los microdosímetros (Fig.3), en donde una de las máscaras se utiliza para transferir el patrón de la región donde se implantará fósforo, mientras que la segunda máscara se usa para la región donde se implantará boro. Para el desarrollo de las mismas se empleó el equipo Heidelberg DWL66.

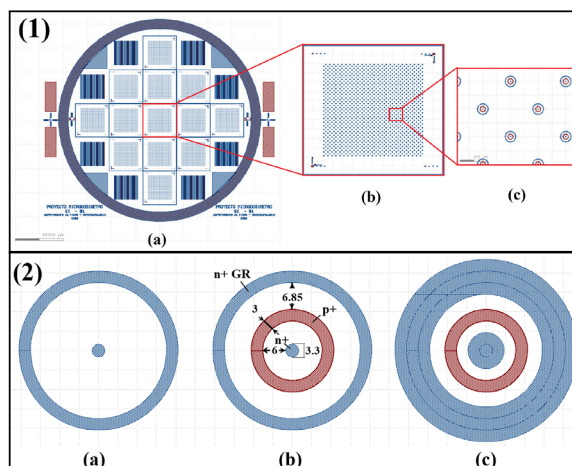


Fig. 3: 1) vista superior de la distribución de los microdosímetros en la superficie de la oblea; 2) detalle de las zonas tipo p y tipo n en un dispositivo individual.

iii. Fotolitografía y etching

Partiendo de una oblea con 415 nm de SiO₂, se procedió a elaborar la máscara para realizar la implantación iónica. En la Fig. 4 se presenta el flujo de procesos para la microfabricación de la máscara.

Se realizaron tres fotolitografías con el alineador de máscaras EVG610, para las cuales se emplearon la fotorresina positiva AZ1518 y la fotorresina negativa AZ2070. Para lograr buenos resultados se evaluaron distintas estrategias, como fueron la remoción de bordes (EBR del inglés *Edge Bead Removal*), distintos espesores de fotorresina, y pruebas para lograr el ensanchamiento del patrón a transferir en la última etapa [6].

Otro paso de vital importancia en el proceso es el ataque controlado de SiO₂, con el fin de alcanzar espesores planteados con precisión. Para esto se evaluaron tres métodos distintos como son el ataque químico por vía húmeda con buffer de ácido fluorhídrico (BHF), ataque seco de *Reactive Ion Etching* (RIE) mediante argon milling (anisotrópico) o mediante C₄F₈ (isotrópico). Estos últimos utilizando el Oxford PLASMALAB80.

El proceso de microfabricación se podría resumir en tres etapas:

1. Etapa #1: Primera fotolitografía con posterior ataque y remoción de 415 nm de SiO₂.
2. Etapa #2: segunda fotolitografía con alineación, y un posterior ataque y remoción de 150 nm de SiO₂.

- Etapa #3: tercer fotolitografía utilizando la primera fotomáscara para que la resina AZ2070 actúe de barrera de implantación.

Posteriormente a cada una de las litografías se llevaron a cabo inspecciones visuales mediante microscopía óptica, y tras realizar ataques de RIE se fueron caracterizando los espesores resultantes de óxido mediante elipsometría espectroscópica con el equipo Horiba Auto SE.

Etapa	Paso	Descripción
1		Fotolitografía empleando la resina AZ1518 de 1,8 μm . Se utiliza la máscara #1.
		Ataque seco (RIE) de 400 nm de SiO_2 con C_4F_8 hasta alcanzar el silicio. Remoción de resina utilizando plasma de O_2 .
2		Fotolitografía alineando con la máscara #2, empleando la resina AZ1518 de 1,8 μm .
		Ataque seco (RIE) con C_4F_8 de 250 nm de SiO_2 , hasta alcanzar un espesor de 150 nm. Remoción de resina utilizando plasma de O_2 .
3		Fotolitografía alineando con la máscara #1, empleando la resina negativa AZ2070 de 7 μm .

Fig. 4: Flujo de procesos para la fabricación de máscaras de SiO_2 y fotorresina.

III. RESULTADOS

Las diferentes pruebas de ataque realizadas en muestras con SiO_2 revelaron tasas de ataque de aproximadamente 5 nm/min para el ataque anisotrópico (*Ar-milling*), y de aproximadamente 16 nm/min para el ataque isotrópico (C_4F_8). Posteriormente, tal como se presenta en la Fig. 5 se caracterizaron los perfiles mediante SEM/FIB FEI Quanta para analizar su isotropía. Basándonos en dichos resultados, se optó por utilizar la receta con C_4F_8 ya que posee una tasa de ataque mayor y más controlable que la de *Ar-milling*. Además, no se observaron diferencias significativas en la anisotropía del proceso, posiblemente debido a los espesores de ataque en el orden de los nanómetros.

En la primera etapa del proceso se llevó a cabo la fotolitografía con una máscara cuyo patrón incluye las regiones donde se implantará fósforo, compuestas por el círculo central y el anillo exterior. Se aplicó la fotorresina positiva AZ1518 con un espesor de 1,8 μm , logrado mediante el procedimiento de “spin coating” a 4000 rpm.

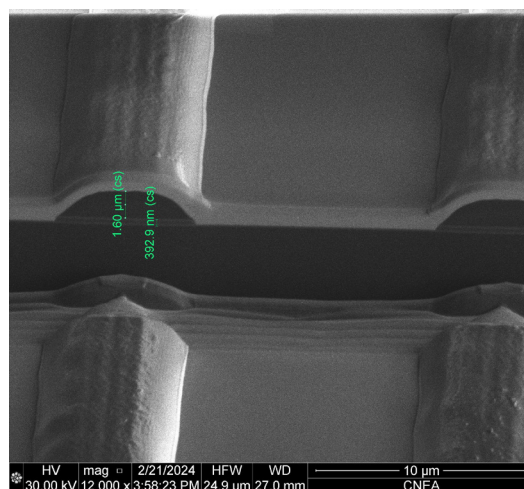


Fig. 5: Perfil de SiO_2 atacado por C_4F_8 .

De esta forma la oblea con SiO_2 quedó completamente cubierta con fotorresina, salvo en las regiones que se planeaban atacar. A continuación, se realizó un ataque seco de RIE utilizando una receta isotrópica con C_4F_8 y O_2 que permite atacar el SiO_2 de forma controlada. La misma utiliza una potencia 100 W de RF, 27 sccm de C_4F_8 y 3 sccm de O_2 , todo el proceso a 5°C. Al establecerse que la tasa media de ataque del equipo para este procedimiento es de 16 nm/min, se ejecutó el mismo durante 35 min con el objetivo de bajar los 415 nm. Posteriormente, con el elipsómetro se midió un espesor final de 4,23 nm de SiO_2 , el valor estándar para SiO_2 nativo.

Para la segunda etapa del proceso se comenzó por la segunda fotolitografía, la cual requirió alinear figuras colocadas en la fotomáscara con las marcas transferidas a la oblea durante la primera etapa. Nuevamente, se utilizó la resina positiva AZ1518 con un espesor de 1,8 μm . Para mejorar el contacto entre oblea y fotomáscara, mejorando la alineación y resolución, se removieron los bordes de resina en la oblea por EBR. Tras el paso de spin coating de la resina, se vertió el solvente AZEBR con un dispositivo creado ad-hoc sobre los bordes de la oblea, mientras la misma giraba a 2500 rpm. Tras la fotolitografía, se observó, mediante microscopía óptica, que las zonas previamente atacadas se encontraban cubiertas con resina, mientras que la región central de los dispositivos, donde se planea implantar boro, quedaron descubiertas.

Mediante la misma técnica de RIE que en la etapa anterior, se realizó un ataque de 250 nm de SiO_2 , hasta alcanzar un espesor final de 150 nm. Para lograr esto, se empleó la misma receta isotrópica con C_4F_8 y O_2 , llevando a cabo el ataque en cuatro etapas para tener un control más preciso sobre la tasa de ataque; ya que la misma no es uniforme en procesos que abarcan varios minutos. Inicialmente, considerando una tasa de ataque de 16 nm/min, se planteó eliminar 125 nm de SiO_2 . Tras el tiempo de ataque calculado se caracterizó un espesor de 309,33 nm, valor con el cual se calculó la nueva tasa de ataque. Este procedimiento se repitió dos veces más, donde se midieron espesores de 232,69 nm y 204,09 nm, respectivamente. Por

último, el ataque final resultó en un espesor final de 154,14 nm de SiO₂ en las regiones de interés. Tras el paso de RIE, se eliminó la fotorresina mediante un plasma de O₂.

Para completar el flujo de proceso, se debían cubrir con fotorresina las áreas atacadas inicialmente (n+ y n+ GR, ver Fig.3-(2)-b). Para ello, se utilizó nuevamente la primera fotomáscara, pero esta vez con la fotorresina negativa AZ2070 con un espesor de 7 µm. La elección de una resina negativa permitió la transferencia del patrón inverso al de la primera etapa, proporcionando una protección adecuada a estas regiones. Por otro lado, se buscaba ensanchar los patrones de la máscara de forma tal que se asegure la cobertura de dichas zonas. Se evaluaron distintas opciones, como alejar la máscara del sustrato y aumentar la dosis en la exposición. Tras varias pruebas, se optó por emplear el equipo de fotolitografía en modo “*vacuum contact*”, con un incremento en la dosis de exposición del triple respecto de la utilizada generalmente. En la Fig. 6 (c) se presenta el resultado final, para el cual se lograron diámetros finales de 7,23 µm con una altura de 6,98 µm.

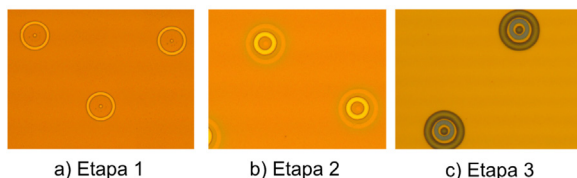


Fig. 6: Resultados de las distintas etapas implicadas en la microfabricación de la máscara de implantación.

La oblea completa con las máscaras de implantación se presenta en la Fig. 7:

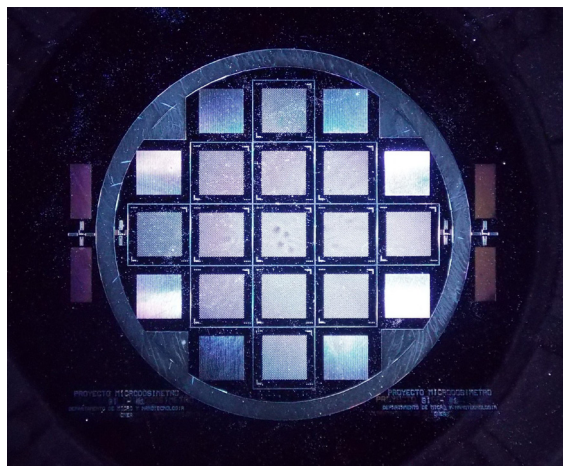


Fig. 7: Fotografía de la oblea finalizada, con la máscara de SiO₂ y fotorresina.

IV. TRABAJO FUTURO

La oblea microfabricada será enviada al Campus Tecnológico e Nuclear, del Instituto Superior Técnico en Lisboa, para ser implantada con las energías y fluencias determinadas en las simulaciones. Una vez implantada, se removerá el SiO₂ utilizado como máscara y se realizará un proceso de recocido térmico típicamente aplicado tras las implantaciones iónicas. Este paso es necesario para reparar

los defectos provocados sobre la red cristalina del silicio y para inducir a la activación eléctrica de las impurezas introducidas. Tras dicha etapa, restaría microfabricar las pistas y contactos eléctricos para caracterizar eléctricamente los dispositivos.

V. CONCLUSIONES

En el presente trabajo se describió el proceso de microfabricación de una máscara de SiO₂ y fotorresina para hacer dopaje por implantación iónica de boro y fósforo sobre un sustrato de silicio, utilizado para el desarrollo de microdosímetros de estado sólido. Una vez determinados los espesores necesarios para lograr los perfiles de concentración en profundidad de cada dopante, mediante procesos de fotolitografía se definió la geometría del dispositivo y con posterior ataque isotrópico por RIE con C₄F₈ se alcanzaron los espesores requeridos. Se obtuvieron espesores de 154,14 nm de SiO₂ en las regiones donde se plantea implantar boro, y se removieron los 415 nm de SiO₂ en las regiones donde se plantea implantar fósforo. Esta última región se cubrió con 7 µm de fotorresina, con el fin de frenar los iones de boro durante su implantación. Para garantizar una cobertura completa, se ensanchó deliberadamente el patrón de la máscara, aumentando la dosis durante la exposición en la fotolitografía.

VI. AGRADECIMIENTOS

Queremos agradecer especialmente al Mg. Diego Pérez por haber realizado un excelente trabajo con el SEM/FIB que permitió lograr un mejor entendimiento de los procesos involucrados. Así mismo dar las gracias al Ing. Claudio Ferrari por la fabricación de las fotomáscaras y al Téc. Gabriel Bosch por la asistencia técnica en fotolitografía. Debemos destacar el asesoramiento de parte de la Dra. Katharina Lorenz y del Dr. Marco Peres sobre los procesos de implantación iónica y a la Ing. Mariel Valeriano y la Dra. Sara Gonzalez por poner a disposición todo su conocimiento y experiencia en microdosimetría. Por último, es importante mencionar que los avances en este proyecto no hubieran sido posibles sin los aportes del Ing. Andrés Di Donato, Jefe de la División de Dispositivos Microelectromecánicos quien nos brinda su invaluable conocimiento en microelectrónica y del Ing. Juan José Bonaparte, Jefe del Departamento de Micro y Nanotecnología por compartir toda su experiencia y conocimiento en procesos de microfabricación.

REFERENCIAS

- [1] A.B. Rosenfeld. Novel detectors for silicon based microdosimetry, their concepts and applications .Nucl. Instr .Methods Phys Res Sect A: Acc Spectromet, Detect Assoc Equip , 2016.
- [2] N. S. Lai, W. H. Lim, A. L. Ziebell, M. I. Reinhard, A. B. Rosenfeld, A. S. Dzurak, Development and Fabrication of Cylindrical Silicon-on-Insulator Microdosimeter Arrays , IEEE Transactions on Nuclear Science 56, 1637 , 2009
- [3] C. Fleta, S. Esteban, M. Baselga, D. Quirion, G. Pellegrini, C. Guardiola, M. A. Cortés-Giraldo, J. G. López, M. C. J. Ramos, F.Gómez, M. Lozano. 3D cylindrical silicon microdosimeters: Fabrication, Simulation and Charge Collection Study. Journal of Instrumentation, 10, 2015.
- [4] M.Nastasi,J.W.Mayer , Ion Implantation and Synthesis of Materials, Springer,2006
- [5] <http://www.srim.org/SREM.htm>
- [6] M.Madou , Fundamentals Of Microfabrication and nanotechnology , Vol III, 3er. Ed. , CRC Press , 2011

Microfabricated heaters for thin films TCR characterization

Tomás Molina
Departamento de Micro y Nano
Fabricación
Instituto Nacional de Tecnología
Industrial (INTI)
Buenos Aires, Argentina
tmolina@inti.gov.ar

María Belén Kramar
Departamento de Micro y Nano
Fabricación
Instituto Nacional de Tecnología
Industrial (INTI)
Buenos Aires, Argentina
mkramar@inti.gov.ar

Laura Malatto
Departamento de Micro y Nano
Fabricación
Instituto Nacional de Tecnología
Industrial (INTI)
Buenos Aires, Argentina
lmalatto@inti.gov.ar

Eliana Gabriela Mangano
Departamento de Micro y Nano
Fabricación
Instituto Nacional de Tecnología
Industrial (INTI)
Buenos Aires, Argentina
emangano@inti.gov.ar

Alex Lozano
Dirección Técnica de Micro y Nano
Tecnologías
Instituto Nacional de Tecnología
Industrial (INTI)
Buenos Aires, Argentina
alozano@inti.gov.ar

Abstract—In this paper two designs of heaters for thin films TCR characterization are presented. During this process, its thermoelectric behaviour was simulated using Ansys Mechanical. Additionally, they were microfabricated on two different substrates and subsequently characterized. From the simulation, the temperature distribution on the sample was obtained. Moreover, from the experimental characterization, temperature outputs were measured as a function of the power supplied. The influence of the substrate material on its performance was also studied.

Keywords—heater, NiCr, TCR, thin film, microfabrication, simulation and coupled thermal-electric.

I. INTRODUCTION

The study of materials is fundamental in the micro-electromechanical systems (MEMS) design and application. Because of that, how the conditions of deposition and post-deposition treatment influence the crystallinity and electrical properties of thin films are of technological importance [1-4]. More specifically, the resistivity and its variation with temperature and time are properties of interest to determine the suitability of a material for a particular application. Furthermore, being capable of determining the dependence of these electrical properties with certain process variables could help to improve the microfabrication.

This paper reports on the design, simulation, microfabrication, and experimental characterization of nichrome (NiCr) heaters on alumina and glass substrates. These heaters were specifically designed to integrate a universal probe (Jandel, from Bridge Technology) for 4-point resistivity measurements expanding its capabilities for thermal characterizations. The idea is to study the resistivity variation with the temperature of thin films and then calculate its temperature coefficient of resistance (TCR). For this reason, the heaters must be able to heat the samples to reach at least a temperature difference of 30°C from room temperature. One challenge was to restrict the thickness of the heating system to fit into the available space given by the needles travel. Another one was reducing the thermal loss to the probe chuck to make the system more efficient.

II. DESIGN

The device must heat thin film samples during its resistivity tests. To be incorporated into the universal probe, the total thickness of the system must not exceed 3 mm. It includes a thin film heating resistance and its substrate, the sample to be characterized and an insulator. With the lumped model of Fig.1, the electrical power P_{total} was obtained:

$$P_{total} = \varepsilon^{-1} h_{conv} A_{surf} \Delta T_{req} \quad (1)$$

$$\varepsilon = \left[1 + \left(\frac{e_s}{\lambda_s} + \frac{1}{h_{conv}} \right) \left(\frac{e_b}{\lambda_b} + \frac{e_i}{\lambda_i} \right)^{-1} \right]^{-1} \quad (2)$$

$$P_{total} = \frac{V^2}{R_h}, \quad (3)$$

where ε is the power efficiency, h_{conv} is the convection heat transfer coefficient, A_{surf} is the area exposed to convection, ΔT_{req} is the temperature difference required, V is the applied voltage, R_h is the electrical resistance of the heater, λ_x and e_x are the thermal conductivity and the thickness of an x material respectively (see Fig.1)

NiCr was chosen as the heating resistor material because of its convenient properties for the application. It has high electrical resistivity (1–1,5 $\Omega\mu\text{m}$), high thermal conductivity (19 $\text{Wm}^{-1} \text{K}^{-1}$), low temperature coefficient of resistance

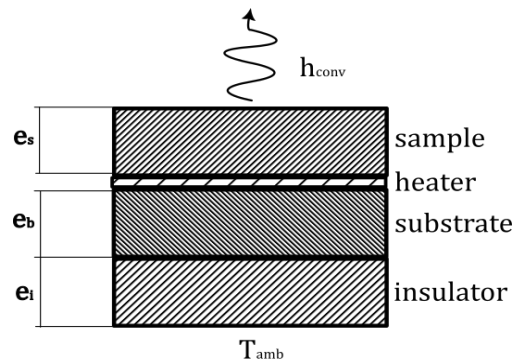


Fig.1. Diagram of the lumped model for the device design.

(TCR), high-temperature stability and high oxidation resistance [5]. Two types of substrates were used, 75x50x1 mm³ glass slides and 50 mm diameter alumina (96% Al₂O₃) discs with a thickness of 0,6 mm. A 0,5 mm air gap was used as the insulator. Given the properties of the materials and the temperature difference required, the resistance was calculated considering the power source limitations. Two geometries were proposed to meet the resistances required with a film thickness of 200 nm, referred as HJ200 and HJ2400 (Fig.2).

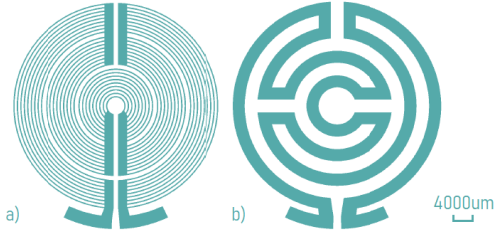


Fig.2. Masks designs for heaters referred as a) HJ-200 and b) HJ-2400 with 200 µm and 2400 µm trace width respectively.

III. SIMULATION

To determine the performance of the designs proposed, a stationary coupled thermal-electric model of the heaters was developed and solved using Ansys[®] Mechanical thermo-electric solver.

The domain considered includes the NiCr heater, the substrate (glass or alumina), an insulator layer (air) and a sample (a standard glass slide). The material properties used, thermal conductivity and electric resistance, are summarized in Table I.

At the base of the system, under the insulator, a uniform temperature condition is set to 22 °C. At the top faces of the domain, a convection condition is applied. The heat transfer coefficient was estimated using the natural convection correlation [6] with air, the exposed surface area and a temperature difference of 50 °C resulting in $h = 8,2 \text{ W}/(\text{m}^2\text{K})$. For the electrical boundary condition, an input voltage difference is set between the ends of the heater.

The model was meshed with a 500 µm and 200 µm side size on the plane of the heaters, for the HJ2400 and HJ200 designs respectively. In the normal direction, the sizes of cells are 500 µm (Fig.3).

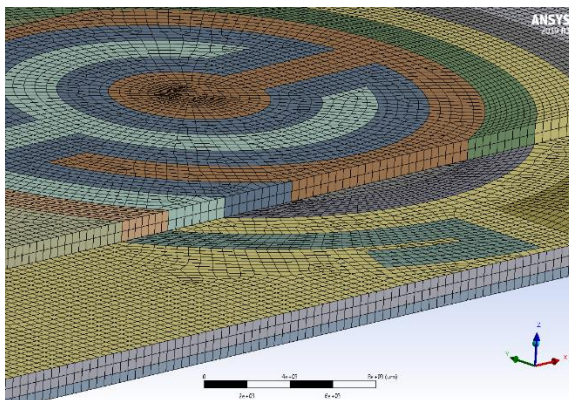


Fig. 3. Mesh for the numerical mode for the heaters simulation.

The numerical model was solved for different input voltages, ranging from 30 V to 70 V. Temperature, Joule heat and current density were extracted to determine the temperature distribution and the resistance of the heaters.

TABLE I. MATERIAL PROPERTIES SET ON SIMULATIONS

Material	Properties	
	Thermal Conductivity [$\text{Wm}^{-1}\text{K}^{-1}$]	Electric resistivity [$\Omega\mu\text{m}$]
Nichrome	19	1,07
Glass	1,3	10^{20}
Alumina	30	10^{20}
Air	0,026	10^{20}

IV. MICROFABRICATION

The heaters were fabricated at INTI's cleanroom using thin-film microfabrication technology.

The process started with the cleaning of the substrates in piranha solution (98 wt % H₂SO₄ and 30 wt % H₂O₂, volume ratio of 2:1 for 10 minutes, at room temperature) to remove organic contamination.

Then, a conventional photolithography process was performed with a TI35E (Microchemicals) photoresist in image reversal mode to create the patterns shown in Fig.2. The substrates were spin-coated, exposed with a flexible film photomask and soft baked (at 90 °C for 20 minutes). Next, the flood exposure step (an exposure without mask) and the development were carried out.

The NiCr alloy (Ni-Cr 80/20 wt %) thin film was deposited through DC magnetron sputtering. A Boc Edwards Auto 500 physical vapour deposition system was used with the following conditions: $5,07 \cdot 10^{-3}$ mbar of working pressure, 20 sccm of Ar, 200 W of DC power and 30 minutes of deposition time. The final step was a lift-off process.

V. CHARACTERIZATION

After the fabrication, the heaters were tested in the setup presented in Fig.4. The temperature was registered at the centre of the upper side of a glass slide. This was acquired with a Tek Now SM-300 precision thermometer and a type K thermocouple. The substrates were placed on a rubber sheet with a ring shape to generate vacuum under the substrates to thermally isolate them from the chuck.

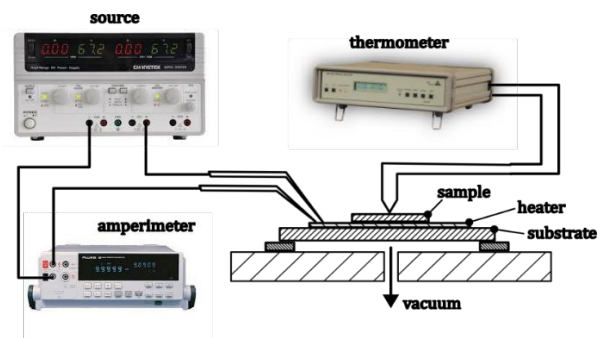


Fig. 4. Diagram of the experimental characterization.

The power was supplied by an SPD-3606 DC power source ranging from 30 V to 70 V. Additionally, the circulating current was registered for each voltage value with a Fluke 45 multimeter. All measurements were made after 20 minutes to allow the system to reach a thermal steady state.

From the characterization and simulations, the resistance of the different designs in relation to voltage and current was obtained, see Table II. It should be noted that for the simulation there is no distinction between substrate as the model is not able to consider that interaction. Considering that, there is a difference between simulation and experimental results. The relative difference between the resistance of the heaters measured and simulated was between 4-16 % and 29-31 % for glass and alumina substrates respectively. This discrepancy could be caused by the thin film thickness variations and/or the roughness of the substrate.

TABLE II. ELECTRICAL RESISTANCES OF THE HEATERS

Material	Resistance [kΩ]		Simulation
	Glass	Alumina	
HJ2400	1,11	1,50	1,16
HJ200	0,85	1,33	1,01

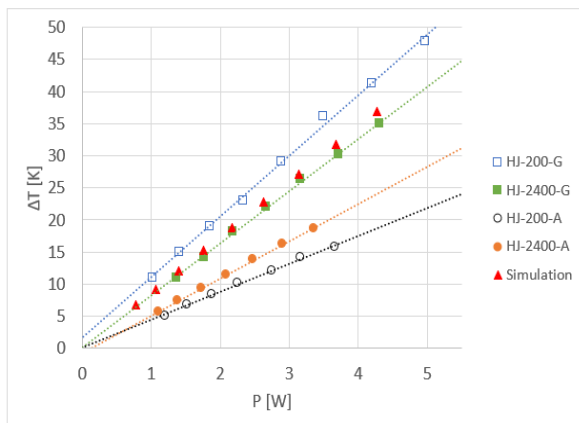


Fig.5. Curves showing the difference of temperature as a function of power and voltage supplied for both designs and substrates (A is for alumina and G is for glass substrates).

Another relevant result is the relationship between input power and temperature difference obtained on the sample with respect to ambient temperature. Fig.5 shows the results from the experimental characterization and the simulations. Simulations do not vary greatly between designs, so they are represented as a unique set of points. The designs with alumina as the substrate show less temperature response as a function of input power.

The temperature distribution of the different designs was estimated by numerical simulations. The Fig.6 shows how the longitudinal and horizontal section of the profile changes with input power. To characterize the uniformity, the relative temperature profile θ was calculated as

$$\theta = \frac{T(x, y) - T_{amb}}{T(0, 0) - T_{amb}} \quad (4)$$

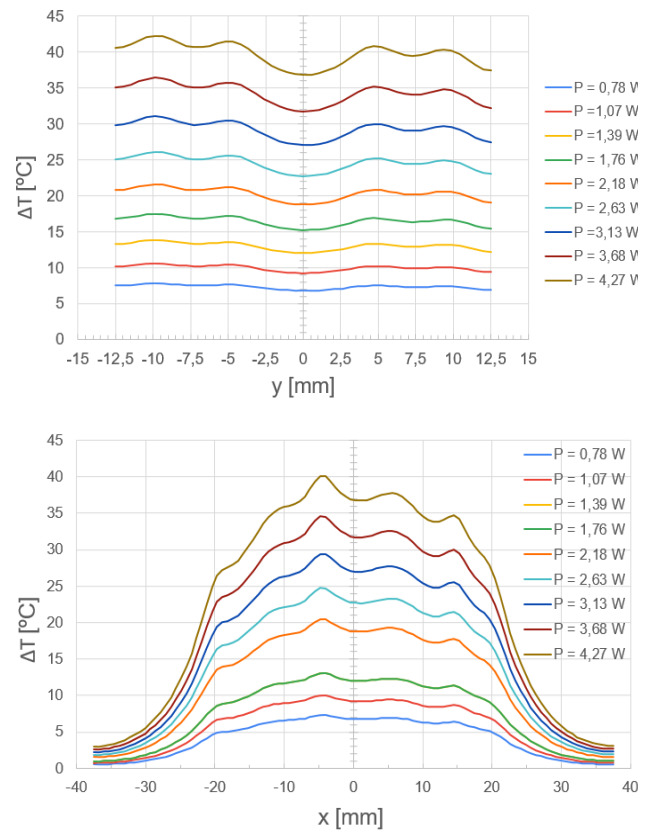


Fig.6. Temperature profiles simulated for HJ-2400 on glass substrate across $x=0$ and $y=0$.

In Fig.7, the relative thermal profiles of the four devices are compared. For glass, at 25 mm from the center, the θ value is 0,4. In contrast, on alumina, this parameter is 0,85. For maximum power input, this means a 24 °C and 6 °C temperature difference for glass and alumina respectively. The more uniform temperature profiles of the alumina substrates are explained by its higher thermal conductivity. The two-dimensional distributions for all cases are presented on Fig.8.

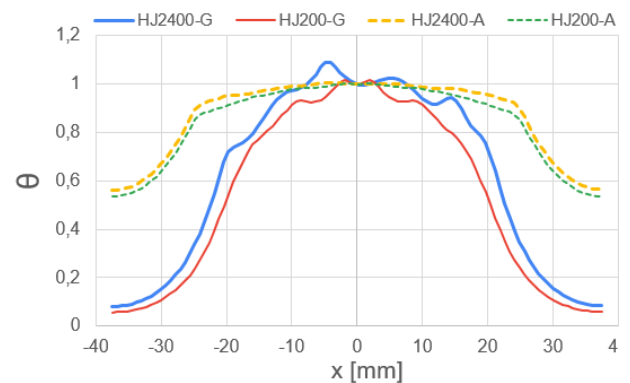


Fig.7. Comparison of relative temperature (θ) simulated profiles at $y=0$ for the different designs and substrates

Additionally, a thermographic camera FLIR T 400 was used to evaluate the thermal distribution on a sample on top of the heater (Fig.9). It is important to note that the color scale seen in the images is different between materials because of its different thermal emissivity.

VI. CONCLUSIONS

In this work, two different heaters were designed, simulated, microfabricated and characterized successfully for TCR evaluation of thin films.

Experimental and simulations results showed a discrepancy in the resistance obtained with different substrates. This indicates that the model requires an experimental value of resistivity to adjust to the measurements. This property can vary with the material of the substrate, deposition and post-processing conditions (e.g., annealing).

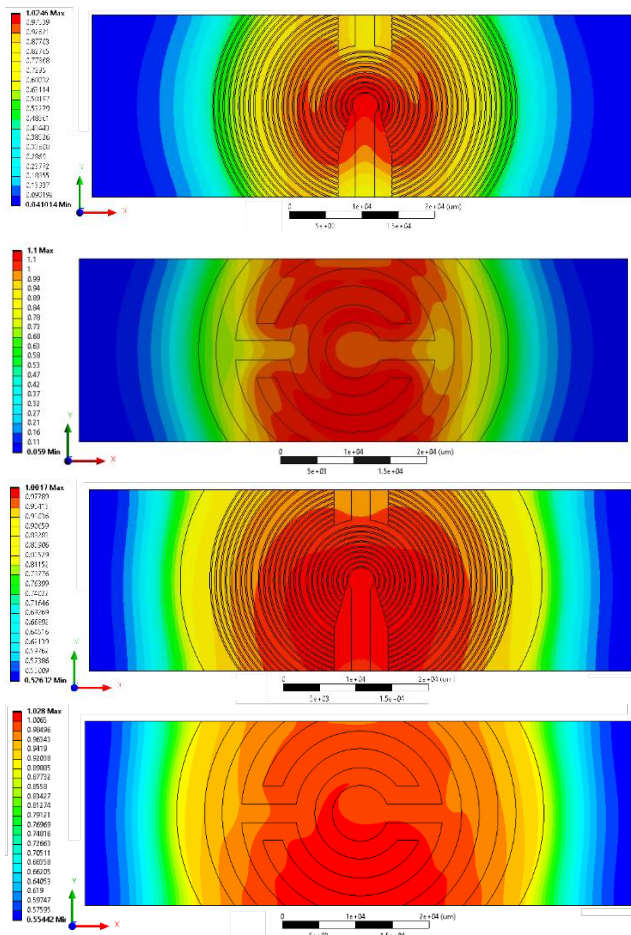


Fig.8. Relative temperature level maps (from the top to the bottom): HJ-200-G, HJ-2400-G, HJ-200-A and HJ-2400-A.

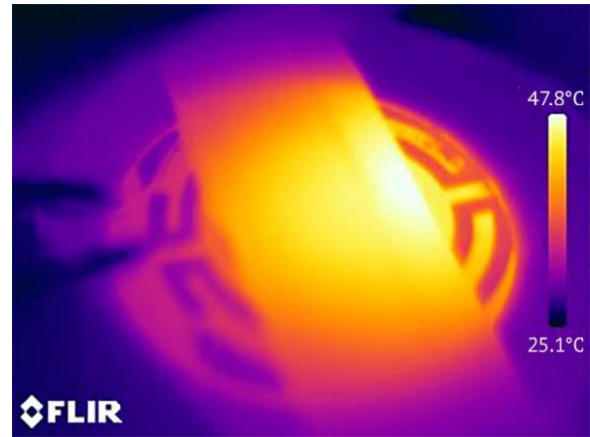


Fig.9. Thermographic image of the HJ-2400-A heater with a sample (a glass slide) on top of it.

In addition, it was observed that the temperature profiles are more uniform in the devices with the alumina substrates due to its higher thermal conductivity, resulting in a 24 °C

temperature difference compared to a 6 °C. On the other hand, the characterization showed major heat loss in the designs with the same substrates. This indicates a trade-off between temperature uniformity and power efficiency. This could be addressed by adding a highly thermal conductive layer over the heater.

Nevertheless, all the designs reached the temperature difference required so the devices can be used for the intended application.

ACKNOWLEDGMENT

The authors thank to the *Dpto. Desempeño de materiales* and *Dpto. Integración de Sistemas Micro y Nano Electrónicos* of INTI.

REFERENCES

- [1] Das, S., Akhtar, J. Comparative Study on Temperature Coefficient of Resistance (TCR) of the E-beam and Sputter Deposited Nichrome Thin Film for Precise Temperature Control of Microheater for MEMS Gas Sensor. In: Jain, V., Verma, A. (eds) Physics of Semiconductor Devices. Environmental Science and Engineering. Springer, Cham. 2014
- [2] Ting-Ting Wu et al., "Electrical properties of micro-heaters using sputtered NiCr thin film," The 8th Annual IEEE International Conference on Nano/Micro Engineered and Molecular Systems, Suzhou, 2013, pp. 466-469.
- [3] Lifei Lai, Xianzhu Fu, Rong Sun, Ruxu Du, Comparison of microstructure and electrical properties of NiCr alloy thin film deposited on different substrates, Surface and Coatings Technology, Volume 235, 2013, pp 552-560.
- [4] Imam H. Kazi, P.M. Wild, T.N. Moore, M. Sayer, The electromechanical behavior of nichrome (80/20 wt.%) film, Thin Solid Films, Volume 433, Issues 1–2, 2003, pp 337-343
- [5] Jeroish, Z.E., Bhuvaneshwari, K.S., Samsuri, F. et al. Microheater: material, design, fabrication, temperature control, and applications—a role in COVID-19. Biomed Microdevices 24, 3 2022.
- [6] Jack Philip Holman. Heat Transfer. McGraw-Hill Companies, 2002, pp. 342–344.



6 |

Nuevos materiales y nanomateriales para sensores

New materials and nanomaterials
for sensors

Novos materiais e nanomateriais
para sensores

Unveiling the link between morphology and humidity sensitivity in rare-earth-doped ceria nanostructures

Pedro P. Ortega
Center for the
Development of Functional
Materials (CDMF)
Federal University of São
Carlos (UFSCar)
São Carlos, Brazil
pedro.ortega@hotmail.com.br

Michele Astolfi
Department of Physics and
Earth Sciences
University of Ferrara
(UNIFE)
Ferrara, Italy
stlmhl@unife.it

Celso M. Aldao
Institute of Scientific and
Technological Research in
Electronics (ICYTE)
University of Mar del Plata
(UNMdP)
Mar del Plata, Argentina
cmaldao@fi.mdp.edu.ar

Sandro Gherardi
Department of Physics and
Earth Sciences
University of Ferrara
(UNIFE)
Ferrara, Italy
ghrsdr@unife.it

Giulia Zonta
Department of Physics and
Earth Sciences
University of Ferrara
(UNIFE)
Ferrara, Italy
zntgli@unife.it

Miguel A. Ponce
Physics and Engineering
Research Center –
CIFICEN (UNCPBA-
CICPBA-CONICET)
Tandil, Argentina
mponce.sensors@gmail.com

Elena Spagnoli
Department of Physics and
Earth Sciences
University of Ferrara
(UNIFE)
Ferrara, Italy
elena.spagnoli@unife.it

Nicolò Landini
Department of Physics and
Earth Sciences
University of Ferrara
(UNIFE)
Ferrara, Italy
lndncl@unife.it

Alexandre Z. Simões
School of Engineering and
Sciences
São Paulo State University
(UNESP)
Guaratinguetá, Brazil
alezipo@yahoo.com

Barbara Fabbri
Department of Physics and
Earth Sciences
University of Ferrara
(UNIFE)
Ferrara, Italy
fbbbb@unife.it

Cesare Malagù
Department of Physics and
Earth Sciences
University of Ferrara
(UNIFE)
Ferrara, Italy
malagu@fe.infn.it

Elson Longo
Center for the
Development of Functional
Materials (CDMF)
Federal University of São
Carlos (UFSCar)
São Carlos, Brazil
elson.liec@gmail.com

Abstract— In this work, we used the screen-printing technique to prepare thick films based on Eu-doped ceria nanostructures with controlled morphologies synthesized via the microwave-assisted hydrothermal method. The samples were characterized via XRD, Raman, UV-Vis, FE-SEM, and TEM techniques. The humidity sensing characteristics of the samples were analyzed considering different relative humidity percentages. Eu-doped ceria nanorods displayed the best performance towards humidity sensing, with a response about 150% higher than the Eu-doped nanopolyhedra and sphere-like nanoparticles. We concluded that tailoring the surface characteristics of the nanostructures via morphological control is essential for improving the performance of chemoresistive-based gas sensing devices.

Keywords— Ceria, nanostructures, morphology, gas sensors, humidity.

I. INTRODUCTION

Accurate humidity measurement is of utmost importance in multiple fields due to its impact on physical and chemical reactions [1–3]. For gas sensing devices, humidity is a particularly omnipresent interferent that significantly influences their detection and selectivity. Therefore, developing sensing materials able to measure the humidity levels in the environment precisely and efficiently is essential.

Ceria is a promising sensing material due to its intrinsic non-stoichiometry (CeO_{2-x}), cycling between Ce^{3+} and Ce^{4+} oxidation states, and surface reactivity [4]. For

chemoresistive-based gas sensing materials, several approaches can be used to improve the sensing properties, such as semiconductor choice, the use of dopant agents, size and morphological control of particles, and heterostructures, among others [5]. In recent years, doping ceria with lower oxidation state cations has been used to enhance its non-stoichiometry by creating oxygen vacancies, leading to improved reactivity and sensing properties [6]. The morphological control of nanostructures has also gathered considerable attention due to the potential increase of surface reactivity, which can improve their sensitivity [7].

In this work, we have synthesized nanostructures of Eu-doped ceria (8 wt% Eu) with different morphologies (irregular/sphere-like nanoparticles, nanorods, nanocubes, and nanopolyhedra) via the microwave-assisted hydrothermal (MAH) method. These nanostructures were then used to prepare thick films via the screen-printing technique. The humidity sensing properties of these films were assessed by using different relative humidity percentages (RH%), and the results were discussed based on the morphological differences between the samples.

II. METHODOLOGY

A. Synthesis and characterization of the nanostructures

The Eu-doped ceria nanostructures were synthesized via the MAH method. In a typical procedure, the metal precursors (cerium nitrate hexahydrate, $\text{Ce}(\text{NO}_3)_3 \cdot 6\text{H}_2\text{O}$, and europium (III) oxide, Eu_2O_3) are dissolved in deionized water in the appropriate proportions considering 8 wt% Eu-

This study was financed by the São Paulo State Research Foundation (FAPESP), process numbers 2018/26550-0, 2021/10780-0, and 2013/07296-2.

doping [8]. Next, a mineralizer agent (sodium hydroxide, NaOH) is added to precipitate the metal hydroxides ($\text{Ce}(\text{OH})_4$ and $\text{Eu}(\text{OH})_3$). After agitation and homogenization, the resultant solution is transferred to a Teflon autoclave and placed inside a microwave oven operating at 2.45 GHz and 800 W. The system cooled down to room temperature naturally. After the synthesis is performed at a determined temperature and time, the samples are centrifuged and washed several times. Finally, a light-yellow powder is obtained. Table I summarizes the synthesis parameters used to obtain each nanostructure. The synthesis time for all samples was 8 minutes.

TABLE I. SYNTHESIS PARAMETERS USED TO PREPARE EU-DOPED CERIA NANOSTRUCTURES WITH CONTROLLED MORPHOLOGIES

Sample	Morphology	Mineralizer	Temperature (°C)
Undoped ceria	Irregular Sphere-like	pH 10	100
Eu-doped	Irregular Sphere-like	pH 10	100
Eu-doped	Nanopolyhedra	0.06 M	180
Eu-doped	Nanocubes	6 M	200
Eu-doped	Nanorods	6 M	140

The structural and morphological properties of the samples were analyzed by multiple techniques. X-ray diffraction (XRD) was performed in a Rigaku DMax/2500PC with $\text{CuK}\alpha 1$ radiation in the 20-90° range. Raman spectroscopy was carried out in a Horiba LabRAM iHR 550 with 541 nm argon laser. UV-Vis diffuse reflectance spectra was collected in a Perkin Elmer Lambda 1050 and the Kubelka-Munk function was used to estimate the bandgap energy. HRTEM was carried out in a Phillips TEM-FEI CM 120 to investigate the morphology and exposed planes of the nanostructures.

B. Preparation and characterization of the sensing films

Thick films were prepared from the as-synthesized nanostructures using the screen-printing technique. First, the samples were mixed with organic vehicles (ethyl cellulose and α -terpineol) to obtain a paste. The paste was then homogenized and deposited onto alumina substrates (equipped with golden electrodes on the top and platinum heaters on the back) in Aurel Automation C920 instrument. The films were heat treated at 120°C for 2 h, 250°C for 12 h, and 500°C for 4 h to eliminate the organic materials. Finally, the substrates were bonded with gold wires in TO39 supports and connected inside a sealed gas chamber to perform the humidity sensing measurements.

The films were characterized via FE-SEM using a Zeiss FEG-VP Supra 35 microscope. The sensing measurements were carried out in a hermetically sealed gas chamber at the same time for all samples. The operating temperature was based on previous results in the literature and set at 380°C [8]. The RH% inside the chamber was controlled via mass-flow meters, using dry synthetic air as the carrier. The total gas flow rate through the chamber was 500 sccm. Different RH% were used and the sensing response (S) of the films were calculated using (1):

$$S = (G_{\text{gas}} - G_{\text{air}})/G_{\text{air}} \quad (1)$$

where G_{air} and G_{gas} are the conductance of the films in dry synthetic air and humid air atmospheres, respectively.

III. RESULTS AND DISCUSSION

A. Characterization of the nanostructures

The XRD analysis of the nanostructures confirmed the formation of the cubic fluorite-type phase of CeO_2 (Fig. 1). No reflections associated with secondary phases were identified. Sharper reflections were observed for the Eu-doped ceria nanocubes, indicating higher crystallinity for this sample.

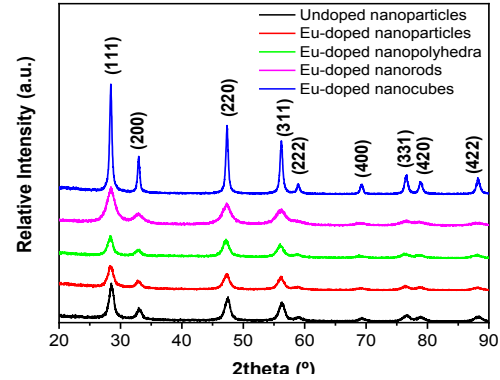


FIGURE 1. XRD PATTERN OF THE NANOSTRUCTURED UNDOPED AND EU-DOPED CERIA SAMPLES

Raman spectroscopy (Fig. 2) confirmed the formation of the CeO_2 phase for all samples, which is consistent with the XRD analysis. The nanocubes, with the sharpest peak and position closest to pure ceria ($\sim 465 \text{ cm}^{-1}$), exhibited the highest crystallinity and least structural disorder. Conversely, nanorods and nanopolyhedra showed broader peaks (indicating larger Ce-O clusters and lower symmetry) and a slight shift (redshift) of the main peak, potentially due to oxygen vacancies or dopant effects. The additional peak around 600 cm^{-1} suggests the presence of oxygen vacancies in the samples.

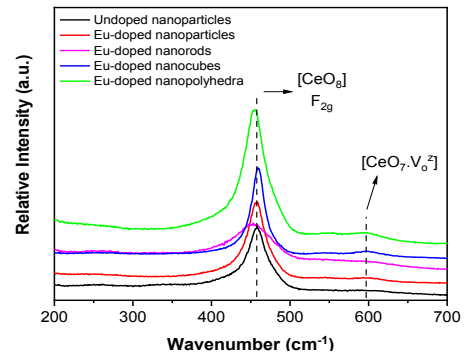


FIGURE 2. RAMAN SPECTRA OF THE NANOSTRUCTURED UNDOPED AND EU-DOPED CERIA SAMPLES

Fig. 3 shows the HRTEM micrographs of the samples. The synthesis conditions shown in Table I resulted in different morphologies: irregular/sphere-like undoped and Eu-doped nanoparticles (Fig. 3a and 3b, respectively), and Eu-doped nanopolyhedra (Fig. 3c), nanorods (Fig. 3d), and nanocubes (Fig. 3e). The average size distribution of the samples and exposed facets of the samples are summarized

in Table II. The morphologies obtained in this study can arise from two main processes: oriented attachment (OA) and Ostwald ripening (OR), both dependent on the synthesis conditions [7,9,10]. Lower temperature and mineralizer concentration favored sphere-like growth, while higher temperatures promoted oriented attachment (nanorods) or a combination of both mechanisms (nanocubes). Low mineralizer concentration led to nanopolyhedra via Ostwald ripening processes.

TABLE II. AVERAGE PARTICLE SIZE AND EXPOSED FACETS OF THE UNDOPED AND EU-DOPED CERIA NANOSTRUCTURES

Sample	Morphology	Size (nm)	Exposed facets
Undoped ceria	Irregular Sphere-like	5.4 ± 0.1	(111), (200)
Eu-doped ceria	Irregular Sphere-like	6.3 ± 0.7	(111), (200)
Eu-doped ceria	Nanopolyhedra	5.1 ± 0.1	(111), (220), (200), (311)
Eu-doped ceria	Nanocubes	10.6 ± 0.5	(200)
Eu-doped ceria	Nanorods	50.7 ± 1.1 (length) 7.4 ± 0.1 (width)	(200)

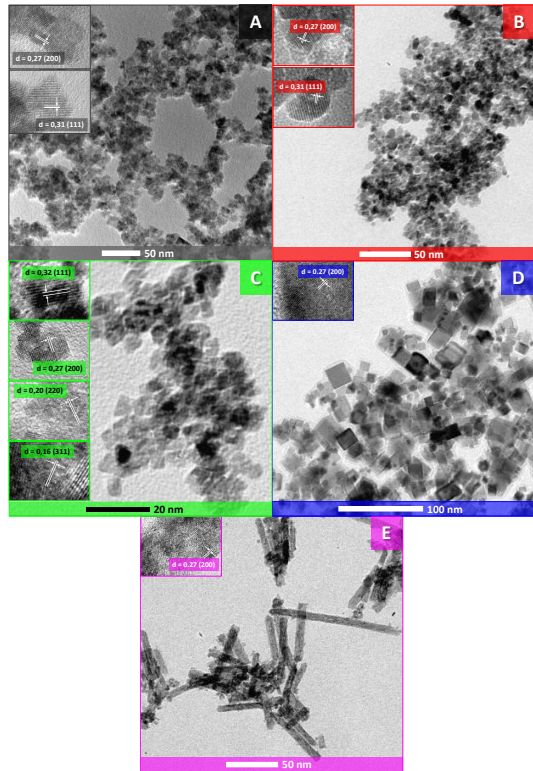


FIGURE 3. HRTEM IMAGES OF THE UNDOPED AND EU-DOPED CERIA NANOSTRUCTURES: (A) UNDOPED NANOPARTICLES, (B) EU-DOPED NANOPARTICLES, (C) EU-DOPED NANOPOLYHEDRA, (D) EU-DOPED NANOCUBES, AND (E) EU-DOPED NANORODS.

The bandgap energies (E_{gap}) and specific surface areas (SSA) of the samples are shown in Table III. The estimated E_{gap} values matched the literature, with slightly decreased energies for the Eu-doped samples due to structural defects. The specific surface area (SSA) decreased after Eu-doping for most samples (Table III), probably due to changes in surface chemistry and agglomeration. The Eu-doped nanorods displayed the highest SSA, which might be

associated with their high aspect ratio and lower agglomeration.

TABLE III. ESTIMATED BANDGAP ENERGIES AND SPECIFIC SURFACE AREAS OF THE SAMPLES

Sample	Morphology	E_{gap} (eV)	SSA (m^2/g)
Undoped ceria	Irregular Sphere-like	2.72 ± 0.01	109.04 ± 0.27
Eu-doped ceria	Irregular Sphere-like	2.71 ± 0.02	73.18 ± 0.60
Eu-doped ceria	Nanopolyhedra	2.65 ± 0.01	33.92 ± 0.05
Eu-doped ceria	Nanocubes	2.59 ± 0.05	49.24 ± 0.27
Eu-doped ceria	Nanorods	2.49 ± 0.08	171.84 ± 0.35

B. Characterization of the films

FE-SEM images (Fig. 4) shows the films made from the as-synthesized nanostructures were uniform and porous. Such porosity is crucial for gas sensing applications. Notably, the original morphologies of the nanostructures were mostly retained after deposition and thermal treatment, especially for the nanorods and nanocubes.

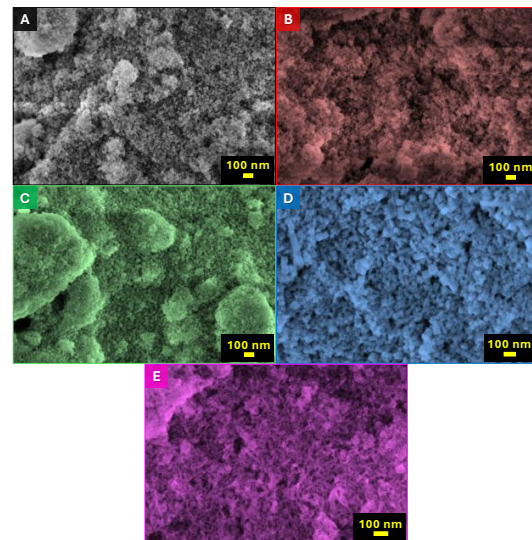


FIGURE 4. FE-SEM IMAGES OF THE FILMS PREPARED FROM THE UNDOPED AND EU-DOPED CERIA NANOSTRUCTURES: (A) UNDOPED NANOPARTICLES, (B) EU-DOPED NANOPARTICLES, (C) EU-DOPED NANOPOLYHEDRA, (D) EU-DOPED NANOCUBES, AND (E) EU-DOPED NANORODS.

Fig. 5 shows the sensing behavior of the films towards different relative humidity percentages. Water molecules act as a reducing agent; then, for n-type semiconductors such as CeO_2 , the conductivity should increase upon exposure to humidity, as observed in Fig. 5. The Eu-doped ceria nanorods had the best performance, displaying responses 60% and 150% higher than those of the undoped irregular/sphere-like nanoparticles and Eu-doped ceria nanopolyhedra, respectively. The contributing factors to these results might be the lower bandgap values, high specific surface area, and exposed facets associated with the nanorods. Moreover, previous studies [11] indicate that water molecules are more stable and display better dissociation on the (200) facets of CeO_2 , in agreement with previous discussion of this work.

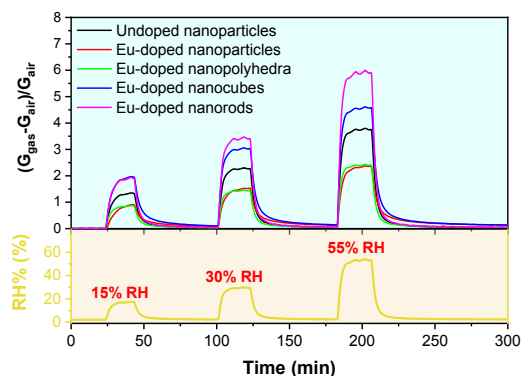


FIGURE 5. HUMIDITY SENSITIVITY OF FILMS PREPARED FROM THE UNDOPED AND EU-DOPED CERIA NANOSTRUCTURES

Two mechanisms have been proposed to explain the electrical conduction variation in semiconductors during the interaction with water molecules: protonic and ionic/electronic conduction. Protonic conduction corresponds to the movement of H^+ ions through physisorbed water layers on the surface of the semiconductor (also known as Grotthuss mechanism [12,13]). In our case, this mechanism should be reduced or absent since the formation of physisorbed water layers are impaired at the operating temperature of this study. Therefore, electronic conduction should be dominant. Humidity increases the conductivity by transferring electrons from adsorbed water molecules to the semiconductor (non-dissociative or dissociative adsorption [14]) and by replacing surface adsorbed oxygen species for water molecules. In both processes, water molecules act as an electron donor, increasing the conductivity. For ceria-based compounds, surface reactivity increases in the following order: (111) < (220) < (311) < (200) [15]. Therefore, Eu-doped ceria nanorods exhibited the highest surface area, defect concentration, and (200) facet exposure, likely promoting faster water dissociation and enhanced conductivity, leading to their superior humidity response. The interplay of these factors requires further study, but it highlights the potential of tailoring dopants and morphologies to optimize gas-sensing properties in ceria-based materials for future devices.

IV. CONCLUSIONS

In this study, we investigated the effect of morphology on the humidity sensing properties of ceria nanostructures. We synthesized undoped and Eu-doped ceria with various morphologies (irregular/sphere-like, polyhedron, cube, and rod) using the microwave-assisted hydrothermal method. These nanostructures were then used to create thick films via the screen-printing technique. The Eu-doped nanorods showed the best humidity sensing performance, with a significantly higher response compared to other morphologies. This superior performance was attributed to their high surface area, structural defects, and dominant exposure of water-reactive facets. Our findings highlight

the importance of morphology control in designing ceria-based materials for high-performance gas sensor devices.

ACKNOWLEDGMENT

We gratefully acknowledge the São Paulo State Research Foundation (FAPESP) for their financial support to this work, which was made possible through process numbers 2018/26550-0, 2021/10780-0, and 2013/07296-2 (CEPID/CDMF).

REFERENCES

- [1] C. Birleanu et al., "Relative humidity influence on adhesion effect in MEMS flexible structures", *Microsyst. Technol.*, vol. 28, pp. 1–11, 2022.
- [2] E. Poonia et al., "Aero-gel based CeO_2 nanoparticles: synthesis, structural properties and detailed humidity sensing response", *J. Mater. Chem. C.*, vol. 7, pp. 5477–5487, 2019.
- [3] N.S.M. Azmi, D. Mohamed, M.Y.M. Tadz, "Effects of various relative humidity conditions on copper corrosion behavior in bentonite", *Mater. Today Proc.*, vol. 48, pp. 801–806, 2022.
- [4] P.P. Ortega et al., "Tuning structural, optical, and gas sensing properties of ceria-based materials by rare-earth doping", *J. Alloys Compd.*, vol. 888, pp. 161517, 2021.
- [5] Z. Dong et al., "3D flower-like Ni doped CeO_2 based gas sensor for H_2S detection and its sensitive mechanism", *Sens. Act. B Chem.*, vol. 357, pp. 131227, 2022.
- [6] W.Y. Hernández, O.H. Laguna, M.A. Centeno, J.A. Odriozola, "Structural and catalytic properties of lanthanide (La, Eu, Gd) doped ceria", *J. Solid State Chem.*, vol. 184, pp. 3014–3020, 2011.
- [7] R.C. Oliveira et al., "Influence of Synthesis Time on the Morphology and Properties of CeO_2 Nanoparticles: An Experimental–Theoretical Study", *Cryst. Growth Des.*, vol. 20, pp. 5031–5042, 2020.
- [8] P.P. Ortega, R.A.C. Amoresi, M.D. Teodoro, E. Longo, M.A. Ponce, A.Z. Simões, "Relationship among morphology, photoluminescence emission, and photocatalytic activity of Eu-doped ceria nanostructures: A surface-type effect", *Ceram. Int.*, vol. 49, pp. 21411–21421, 2023.
- [9] M. Lin, Z.Y. Fu, H.R. Tan, J.P.Y. Tan, S.C. Ng, E. Teo, "Hydrothermal synthesis of CeO_2 nanocrystals: Ostwald ripening or oriented attachment?", *Cryst. Growth Des.*, vol. 12, pp. 3296–3303, 2012.
- [10] C.S. Riccardi, R.C. Lima, M.L. dos Santos, P.R. Bueno, J.A. Varela, E. Longo, "Preparation of CeO_2 by a simple microwave–hydrothermal method", *Solid State Ionics*, vol. 180, pp. 288–291, 2009.
- [11] D.R. Mullins, "The surface chemistry of cerium oxide", *Surf. Sci. Rep.*, vol. 70, pp. 42–85, 2015.
- [12] Y. Xing, L.X. Zhang, H. Xu, Y.Y. Yin, M.X. Chong, L.J. Bie, "Defect-rich ultrathin Sn_2O_3 nanosheets with dominant polar (100) facets for efficient gas and humidity sensor applications", *Sens. Act. B Chem.*, vol. 349, pp. 130816, 2021.
- [13] B. Fabbri et al., "Crystalline microporous organosilicates with reversed functionalities of organic and inorganic components for room-temperature gas sensing", *ACS Appl. Mater. Interfaces.*, vol. 9, pp. 24812–24820, 2017.
- [14] E. Spagnoli, M. Valt, A. Gaiardo, B. Fabbri, V. Guidi, "Insights into the Sensing Mechanism of a Metal-Oxide Solid Solution via Operando Diffuse Reflectance Infrared Fourier Transform Spectroscopy", *Nanomaterials*, vol. 13, pp. 2708, 2023.
- [15] R.A.C. Amoresi et al., " CeO_2 Nanoparticle Morphologies and Their Corresponding Crystalline Planes for the Photocatalytic Degradation of Organic Pollutants", *ACS Appl. Nano Mater.*, vol. 2, pp. 6513–6526, 2019.

Exploration of wavelength-selective photodiodes for Si-based integrated electrophotonic sensors

1st Alfredo González-Fernández

Electronics Department

National Institute of Astrophysics, Optics and Electronics (INAOE)

Puebla, Mexico

ORCID: 0000-0002-9944-7923

2nd Joaquín Hernández-Betanzos

Chemical Transducers Group

IMB-CNM (CSIC)

Barcelona, Spain

ORCID: 0000-0001-9235-1024

Abstract—This work proposes a method to obtain photodiodes with different responsivity peaks in monolithically integrated electrophotonic systems using SRO light emitters in order to advance towards integrated spectroscopy for sensing applications. Fabrication simulations of photodiodes obtained using different parameters were performed to investigate the feasibility of varying photodiode responsivity while maintaining the thermal treatments necessary for the production of nanostructured silicon light emitters.

The results identified viable fabrication conditions for producing three distinct photodiodes on both p-type and n-type silicon wafers without altering the thermal annealing process. However, considerations of cost and time associated with the complete fabrication process revealed that the increased economic expenditure may be prohibitively high for most applications. These findings suggest that while selective detection of specific wavelengths emitted by SRO-based emitters can theoretically be achieved by fabricating different photodiodes on a single wafer, the associated costs may offset the benefits, potentially undermining the advantages of full silicon integration. Consequently, further research into alternative photodetector types and wavelength demultiplexing strategies remains relevant.

Keywords—Integrated electrophotonics, Photonic LOC, Novel sensor fabrication strategies, wavelength selective photodetectors

I. INTRODUCTION

Spectroscopy, particularly in the visible range, is one of the most widely used techniques for characterization in chemical and biological research [1]–[3]. Historically, the instruments required for accurate light spectrum characterization have been bulky, delicate, and difficult to operate. However, in the past decade, significant strides have been made in compacting these systems. Despite these advancements, most rely on the miniaturization and coupling of individual discrete components. This approach means that setups for specific applications often still depend on external optical elements or moving parts, limiting complex integration and portability. Consequently, incorporating spectroscopy into a Laboratory On a Chip (LOC) approach remains challenging.

Monolithically integrating a light source, a mechanism for guiding the radiation to interact with an analyte, and a method for detecting and analyzing the light post-interaction

could pave the way for a spectrometer-based LOC. Moreover, achieving this integration using standard Complementary Metal Oxide Silicon (CMOS) fabrication techniques and materials would offer numerous potential advantages, including extreme miniaturization, cost reduction, and the capability to perform information processing and transmission on a single chip.

In previous work, we reported the development of Si-based wide-spectrum Light Emitting Capacitors (LECs) based on nanostructured Silicon Rich Silicon Dioxide (SRO), fabricated using standard CMOS technologies. These LECs have been integrated with a self-aligned waveguide (WG) and a photodiode, forming a photonic-electronic transduction system known as the Emitter-Waveguide-Detector (EWD) system [4]. Additionally, the concept of detecting changes in the refractive index of materials for biological sensing has also been demonstrated [5].

However, extending this concept to fully integrated spectrometry necessitates developing a method for analyzing specific wavelengths of interest emitted by the relatively broad-ranging LECs (typically from 400 nm to 900 nm). This task is particularly challenging due to the monolithic nature of the proposed architectures, which precludes the use of external gratings or prisms for wavelength separation and detection—the traditional approach in spectroscopy.

Several strategies could potentially address this challenge. One approach involves tuning the emission characteristics of the active material in the LEC through fabrication processes. Another option is the integration of structures such as Bragg gratings or the use of sophisticated photonic elements for Wavelength Division Multiplexing (WDM). Unfortunately, the first approach has proven non-viable due to insignificant spectral changes. The latter two approaches present other currently insurmountable challenges, as the fabrication of small structures required for visible light exceeds the capabilities of current photolithographic technology [4].

Given the novelty of integrated visible-light emitters and photodetectors, optimizing the design of the latter for specific wavelengths presents an underexplored yet promising approach to solving the issue of wavelength separation. This approach leverages CMOS compatibility, enabling the placement of multiple photodetectors on the same chip, each potentially

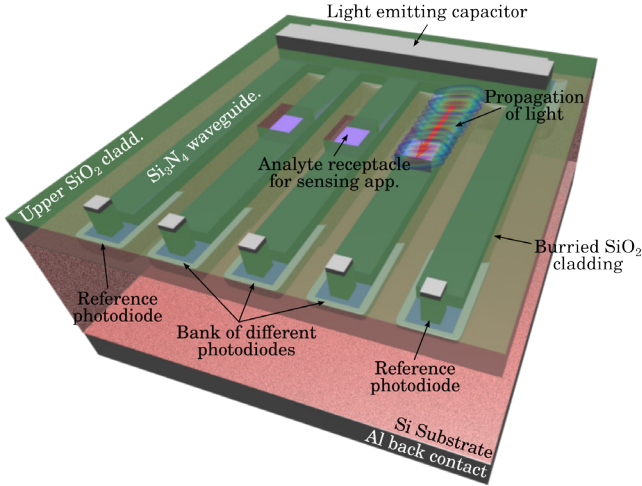


Fig. 1. Rendered design of an integrated spectrometer, utilizing a set of five EWDs. Two EWDs serve as reference arms, while the remaining three contain a cavity in the top cladding for analyte placement. The central photodiodes are designed to exhibit different responsivity curves to analyze distinct sections of the spectrum emitted by the integrated LECs.

tuned to detect specific spectral regions.

As mentioned earlier, integrated pn-junction photodetectors using this technology have been demonstrated. However, when implementing Si-based emitters like those reported in [4], the wafers are subjected to relatively high thermal treatments (ranging from 900 °C to 1100 °C for up to 240 min, depending on the LEC design). These thermal treatments can severely affect the configuration of pn-based photodetectors, which are highly sensitive to thermal changes. Consequently, a carefully designed process is required to optimize the responsivity of photodetectors for specific wavelength ranges. When integrating different photodiodes within a single process, the doping dose remains the primary design variable (apart from geometrical considerations) since the thermal processes necessary for SRO fabrication exceed those typically used for photodiode formation and will dominate dopant diffusion.

In this work, we explore the possibility of designing different photodiodes for EWD structures by controlling the implantation dose, taking into account the thermal treatments required for fabricating Si₃N₄/SRO self-aligned Emitter-WG configurations.

II. SIMULATION OF THE DEVICES

A. Design Considerations

Figure 1 illustrates the concept of implementing a sensor chip using a set of EWDs, as described in [4], coupled with a bank of photodiodes capable of detecting different bands of the spectrum of light transmitted through waveguides and emitted by integrated LECs.

To achieve photodiodes with different responsivities on a single substrate, two primary parameters must be controlled: the depletion region width (w_j) and its depth. The primary contribution to photocurrent (I_{ph}) arises from electron-hole

pairs (e-h) photogenerated within this region, as those outside are likely to recombine due to the absence of an electric field to separate the carriers. Only a fraction of e-h pairs generated within the diffusion length of the electrons will contribute to I_{ph} .

In this scenario, the photodetectors can be modeled as forming an abrupt junction, where the depletion region effectively starts at the junction depth (x_j). The depletion region within the higher doping zone is expected to be negligible, marking the penetration depth of the shortest wavelength detectable. While x_j cannot be significantly altered by electrical bias, w_j can be, resulting in modifications to the portion of the spectrum contributing to I_{ph} . A larger reverse bias applied to the photodiode increases the portion of the spectrum contributing to I_{ph} .

The objective, then, is to establish fabrication conditions for pn junctions that yield different values of x_j on a single substrate by adjusting only implantation doses and energies. This approach is necessary because the overall thermal budget of the process is dominated by the requirements for fabricating the LECs.

B. Fabrication

The EWD systems can be fabricated on both p-type and n-type Si substrates, with both possibilities explored to determine the optimal results. Based on the previously reported photodiodes in [4] and the operational limits of the ion-implantation equipment available at the fabrication facilities (Cleanroom at the IMB-CNM), Silvaco-Athena software was employed to simulate the fabrication process under various ion implantation conditions for n-type and p-type Si wafers with resistivities of 12 Ω · cm and 40 Ω · cm, respectively.

A thermal treatment at 1100 °C for 240 min was simulated in all cases, as this is required for the annealing of the SRO emitters. Other less significant thermal processes were also simulated, but the dominance of the former was clearly confirmed. Systematic variations in implantation energy from 30 keV to 150 keV of Boron (for n-type Si) and Phosphorus (for p-type Si) were applied, with ion doses ranging from $1 \times 10^{15} \text{ cm}^{-2}$ to $1 \times 10^{17} \text{ cm}^{-2}$. The fabrication of an anode and cathode Al contact on the top and bottom (or bottom and top) of the structures was also simulated. Figure 2 shows a cross-sectional simulation result for an n-type wafer using Athena.

C. Electro-Optical Response

The electrical behavior of the various structures was analyzed using Silvaco-Atlas by monitoring the current-voltage (I - V) characteristics at the anode-cathode terminals under the simulation of a light beam perpendicular to the surface, with a total optical power of 80 nW. This power level is an estimate of the optical power reaching the photodetectors in EWD systems similar to those reported in [4].

Calculations of I under a reverse bias of $V = -20 \text{ V}$ for different incident wavelengths λ were performed to obtain the responsivity curve for each combination of implantation dose

TABLE I
SIMULATION RESULTS USING SILVACO-ATHENA FOR BORON IMPLANTATION INTO N-TYPE WAFERS.

Label	n-type substrate resistivity ($\Omega \times \text{cm}$)	Dose (cm^{-2})	Energy (keV)	Junction Depth (μm)
N1	12	1×10^{17}	100	6.31321
N2	12	1×10^{16}	150	4.50121
N3	12	5×10^{15}	50	3.88351

TABLE II
SIMULATION RESULTS USING SILVACO-ATHENA FOR PHOSPHOROUS IMPLANTATION INTO P-TYPE WAFERS.

Label	p-type substrate resistivity ($\Omega \times \text{cm}$)	Dose (cm^{-2})	Energy (keV)	Junction Depth (μm)
P1	40	1×10^{17}	150	5.55789
P2	40	5×10^{16}	50	4.47839
P3	40	5×10^{16}	30	3.71106

and energy. Responsivity is defined as the relation of I_{ph} to λ . The results were compared to identify the three sets of parameters for each substrate type that exhibited the greatest separation between responsivity peaks.

III. RESULTS AND DISCUSSION

After analyzing all the curves, the conditions that showed the largest differences between responsivities are presented in Table I for n-type substrates and in Table II for p-type substrates.

Figures 3 and 4 show the behavior of the photodiodes obtained under these parameters when reverse biased at 20 V.

A clear shift in the responsivity peak can be observed in both substrate types. The wavelength detection range spans from 500 nm to beyond 1000 nm, which represents a significant improvement over previously reported photodiodes in EWD systems that detected wavelengths between 630 nm and

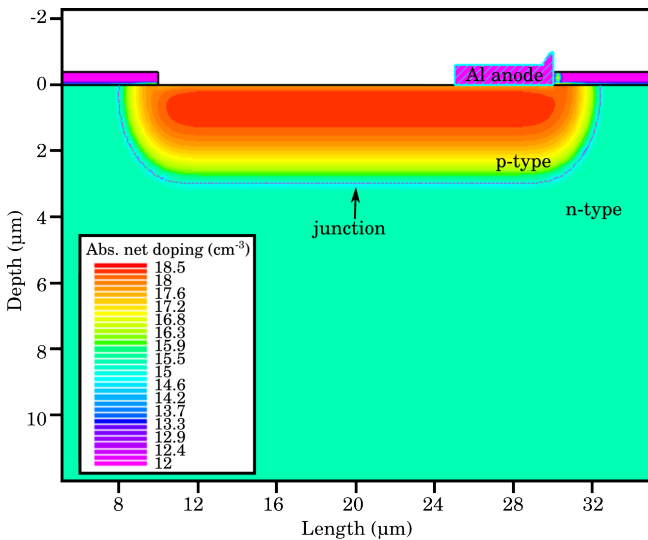


Fig. 2. Cross-sectional view of a simulated pn junction in an n-type wafer.

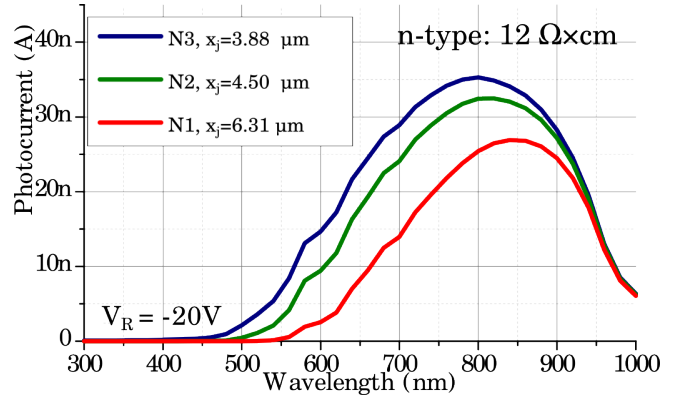


Fig. 3. Responsivity curves for simulated photodiodes fabricated using the conditions shown in Table I.

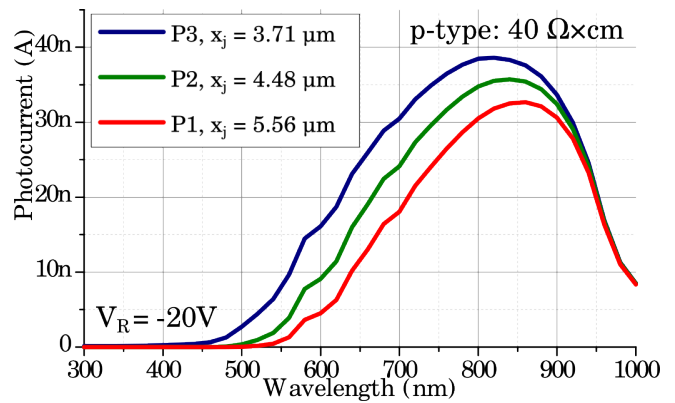


Fig. 4. Responsivity curves for simulated photodiodes fabricated using the conditions shown in Table II.

760 nm at a larger reverse bias of 35 V, covering less than 23% of the spectra emitted by the LECs [4]. In contrast, the new designs, N3 and P3, cover over 70% of the spectrum at a lower reverse bias of 20 V.

However, the shifts are smaller than 50 nm in all cases, with significant overlap in the detected spectra. The area under each curve in Figures 3 and 4 represents the expected photocurrent produced by the photodiode for constant optical power corresponding to each λ . Comparing the areas between N1, N2, and N3, as well as P1, P2, and P3, reveals that the differences in expected photocurrents for the same incident light are less than 10 nA in all cases. This would require highly complex instrumentation to distinguish between the three sections of the spectrum, which, although more feasible with a monolithic CMOS approach compared to external instrumentation, is still far from ideal.

Finally, when considering the fabrication costs, the relatively high implantation doses and the time required to fabricate three different photodiodes with these characteristics lead to increased expenses, potentially outweighing the advantages of using CMOS procedures. This suggests that the approach is only viable for very specific applications.

IV. CONCLUSION

An improved photodetector design was presented, achieving a 48% increase in light detection from the LEC compared to previous reports. Shifts in peak detection wavelength were also theoretically achieved by varying doses and energies without requiring any other modifications to the fabrication flow. However, the shifts were below 50 nm, resulting in photodetection changes of less than 10 nA in all cases, while fabrication costs significantly increased with the inclusion of multiple photodetectors. This indicates that further investigation into different approaches for integrating wavelength-selective photodetectors is necessary, as the presented method may not be cost-effective except for highly specific, demanding applications.

ACKNOWLEDGMENT

The authors acknowledge support from CONAHCYT and funding from the European Union's Horizon 2020 research and innovation programme under the Marie Skłodowska-Curie grant agreement No. 801342 (Tecniospring INDUSTRY), as

well as the Government of Catalonia's Agency for Business Competitiveness (ACCIÓ).

REFERENCES

- [1] Chen, J., Chen, W., Zhang, G., Lin, H., & Chen, S.-C. (2017). "High-resolution compact spectrometer based on a custom-printed varied-line-spacing concave blazed grating". *Optics Express*, 25(11), 12446. <https://doi.org/10.1364/OE.25.012446>
- [2] Tran, M. H., & Fei, B. (2023). "Compact and ultracompact spectral imagers: technology and applications in biomedical imaging". *Journal of Biomedical Optics*, 28(04). <https://doi.org/10.1117/1.JBO.28.4.040901>
- [3] Wang, R., Ansari, M. A., Ahmed, H., Li, Y., Cai, W., Liu, Y., Li, S., Liu, J., Li, L., & Chen, X. (2023). "Compact multi-foci metalens spectrometer". *Light: Science & Applications*, 12(1), 103. <https://doi.org/10.1038/s41377-023-01148-9>
- [4] González-Fernández, A. A., Aceves-Mijares, M., Pérez-Díaz, O., Hernández-Betanzos, J., & Domínguez, C. (2021). "Embedded silicon nanoparticles as enabler of a novel cmos-compatible fully integrated silicon photonics platform". *Crystals*, 11(6), 630. <https://doi.org/10.3390/cryst11060630>
- [5] Pérez-Díaz, O., Estrada-Wiese, D., Aceves-Mijares, M., & González-Fernández, A. A. (2023). "Functionalization of a Fully Integrated Electrophotonic Silicon Circuit for Biotin Sensing". *Biosensors*, 13(3), 399. <https://doi.org/10.3390/bios13030399>

Síntesis no hidrolítica de ZnO como precursor para el dopaje con metales de transición en la fabricación de sensores

David Leopoldo Brusilovsky
 Instituto de Materiales de Misiones
 CONICET-UNaM
 Posadas, Misiones, Argentina
dbrusilovsky@fceqvn.unam.edu.ar

Abstract

La síntesis de las nanopartículas de óxido de zinc (ZnO) se basó en la técnica del sol-gel no hidrolítico utilizando diferentes precursores químicos, específicamente nitrato y acetato de zinc disueltos en alcohol bencílico. La estructura cristalina se determinó mediante difracción de rayos X (XRD), la morfología y el tamaño de las partículas se analizaron con un microscopio electrónico de barrido (SEM).

Keywords—nanopartículas, zinc, sol-gel

I. INTRODUCCIÓN

El óxido de zinc es principalmente un compuesto inorgánico que se encuentra en forma de polvo, de color blanco e insoluble en agua. Se encuentra en forma de mineral zincita dentro de la corteza terrestre. En forma de polvo, se utiliza principalmente en lubricantes, pinturas, caucho, ungüentos, baterías, vidrio, cosméticos y papel. El óxido de zinc es un material semiconductor binario II-VI que posee propiedades piroeléctricas y piezoeléctricas. En el rango nano, tiene una brecha de banda de 3.37 eV, una gran energía de enlace excitónica (60 meV) y una movilidad de Hall del orden de $200 \text{ cm}^2\text{V}^{-1}\text{s}^{-1}$ a temperatura ambiente [1-8]. La síntesis de nanopartículas de ZnO siguen siendo un área de investigación de sumo interés, incluso después de que numerosos investigadores de todo el mundo hayan realizado un amplio trabajo al respecto. Es un material versátil para el dopaje de diferentes metales de transición, entre otros óxidos metálicos. Con una amplia variedad de estructuras morfológicas, alta movilidad electrónica y defectos portadores de tipo n, es adecuado para una serie de aplicaciones, como dispositivos de memoria, espintrónica, dispositivos optoelectrónicos, células solares y sensores [9-14].

La técnica de sol-gel no hidrolítica ha alcanzado un sólido reconocimiento como una metodología poderosa para la síntesis de materiales basados en óxidos. Destacándose los xerogeles de óxidos mixtos con una composición y mesoporosidad cuidadosamente controladas, junto con nanopartículas de óxidos altamente cristalinas con un control preciso sobre su tamaño y forma. Además, se logran obtener superestructuras y películas mediante diversos métodos de deposición [17]. Existe una amplia variedad de sensores basados en ZnO, teniendo en cuenta su alta movilidad electrónica, amplia

brecha de banda, biocompatibilidad, bajo costo, excelente sensibilidad, tiempo de respuesta y recuperación favorables, y simplicidad en la fabricación. Los sensores basados en ZnO están ganando mucho interés ante otros sensores basados en semiconductores de óxidos metálicos.

II. MATERIALES Y MÉTODOS

A. Materiales

Los precursores de zinc, acetato y nitrato, fueron proporcionados por Carlo Erba, los solventes, alcohol bencílico, tetrahydrofurano y etanol por Biopack. Todos los reactivos usados fueron de grado de pureza analítica.

B. Métodos

Se prepararon soluciones de las sales precursoras a una concentración de 50 mM en alcohol bencílico. Procediendo a calentarlas a 180°C con reflujo durante un período de 14 días. Las suspensiones resultantes se centrifugaron, y el precipitado se lavó con tetrahydrofurano y etanol en secuencia. El material obtenido se secó a 60°C durante 24 horas en una estufa y se sometió a un tratamiento térmico en un horno de mufla a 350°C y 600°C durante 2 horas cada uno.

C. Caracterización de las nanopartículas

La estructura cristalina se determinó mediante difracción de rayos X (XRD), el patrón de difracción de rayos X (XRD) se obtuvo aplicando la técnica de Bragg-Brentano, utilizando un difractor RIGAKU SmartLab SE, operando a 40 kV y 50 mA, utilizando radiación Cu K α ($k = 0.15406 \text{ nm}$), escaneando 2θ en un rango de 10–80°, velocidad de escaneo de $10^\circ \text{ min}^{-1}$ y un paso de 0.02° . El análisis de las fases cristalinas se realizó comparando los difractogramas con la base de datos COD (Crystallography Open Database). La morfología y el tamaño de las partículas se analizaron con un microscopio electrónico de barrido (SEM), el aparato utilizado fue un microscopio electrónico de barrido SEM-FEI-Quanta200 y se emplearon dos detectores: de electrones secundarios y de rayos X.

III. RESULTADOS Y DISCUSIÓN

Se obtuvieron los espectros de difracción de rayos X (XRD) de las nanopartículas de óxido de zinc sintetizadas. Los principales picos encontrados, tanto para los precursores nitratos y los acetatos, corresponden a

reflexiones de Bragg con valores de estructuras de fase hexagonal de ZnO, (tarjeta estándar 2300112) y esto confirma la presencia de nanopartículas de óxido de zinc. El tamaño promedio de las cristalitas calculado a partir de la fórmula de Scherrer fue de 19,4 nm para precursor nitrato y 32,2 nm para precursor acetato. El patrón XRD observado indica la ausencia de otras impurezas. Esto confirma además que las partículas de ZnO obtenidas presentan regiones cristalinas nanométricas dentro de las partículas obtenidas (Fig. 1 y Fig. 2)

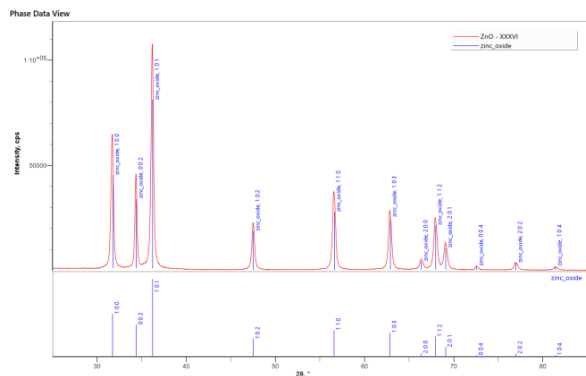


Fig. 1. Difractogramas de las nanopartículas de óxido de zinc en base a precursor acetato.

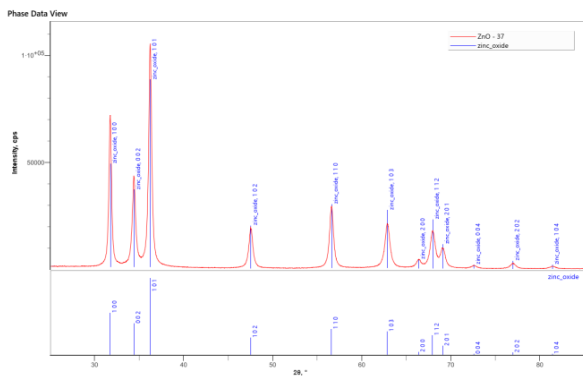


Fig. 2. Difractogramas de las nanopartículas de óxido de zinc en base a precursor nitrato.

Se obtuvieron imágenes de barrido tanto para los precursores de sales de nitrato y de acetato. Las partículas obtenidas a partir del precursor de acetato se presentaron desagregadas y con un tamaño nanométrico de aproximadamente 30-50 nm. Las partículas obtenidas a partir del precursor de nitrato mostraron una morfología esférica con un diámetro aproximado de 500 nm, compuestas por agregados de nanopartículas de aproximadamente 30 nm cada una. (Fig. 3 y Fig. 4)

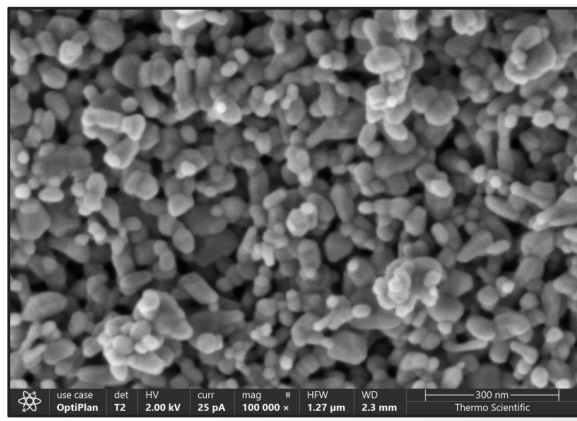


Fig. 3. Micrografías SEM de las nanopartículas de ZnO en base a precursor acetato.

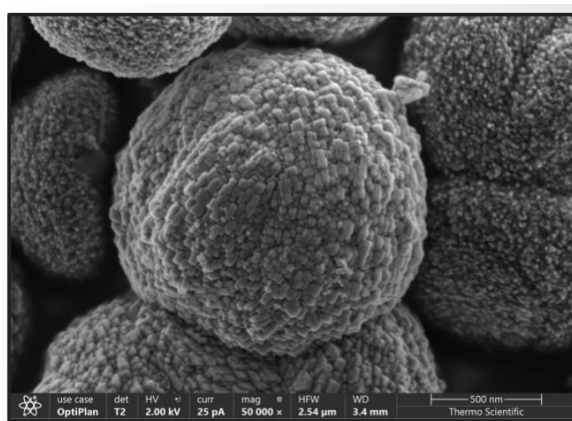


Fig. 4. Micrografías SEM de las nanopartículas de ZnO en base a precursor nitrato.

IV. CONCLUSIONES

Este estudio ilustra la síntesis exitosa de nanopartículas de óxido de zinc, ZnO, a través de una ruta sol-gel no hidrolítica a bajas temperaturas. La reacción entre acetato de zinc y el alcohol bencilico conduce a formas de partículas cristalinas desagregadas de tamaño nanométrico. La reacción entre nitrato de zinc y el alcohol bencilico conduce a formas de partículas cristalinas de tamaño nanométrico aglomeradas. Optimizando los tratamientos térmicos se podrían obtener partículas dispersas. El proceso es simple, permite escalar en cantidades de gramos, y conduce a materiales nanométricos altamente cristalinos. El proceso de dopaje con metales de transición como plata, cobre, cobalto, etc. para la obtención de nanomateriales con propiedades sensoriales podrá efectuarse eficientemente y de forma controlada en relación a la composición estequiométrica de las propiedades deseadas [18-20].

V. REFERENCIAS

- [1] Fu, Y. S.; Ji, S. H.; Chen, X.; Ma, X. C.; Wu, R.; Wang, C. C.; Duan, W. H.; Qiu, X. H.; Sun, B.; Zhang, P.; Jia, J. F.; Xue, Q. K. "Manipulating the Kondo Resonance through Quantum Size Effects". *Phys. Rev. Lett.* 2007, 99, 256601.
- [2] Daniel, M. C.; Astru, D. *Gold Nanoparticles: Assembly, Supramolecular Chemistry, Quantum-Size-Related Properties, and*

- Applications toward Biology”, Catalysis, and Nanotechnology. *Chem. Rev.* 2004, 104, 293–346.
- [3] S. Jacobs and C. P. Bean, “Fine particles, thin films and exchange anisotropy,” in *Magnetism*, vol. III, G. T. Rado and H. Suhl, Eds. New York: Academic, 1963, pp. 271–350.
- [4] Satoh, N.; Nakashima, T.; Kamikura, K.; Yamamoto, K. “Quantum size effect in TiO₂ nanoparticles prepared by finely controlled metal assembly on dendrimer templates”. *Nat. Nanotechnol.* 2008, 3, 106–111.
- [5] Wang, B. X.; Zhou, L. P.; Peng, X. F. “Surface and size effects on the specific heat capacity of nanoparticles”. *Int. J. Thermophys.* 2006, 27 (1), 139–151Y.
- [6] Yorozu, M. Hirano, K. Oka, and Y. Tagawa, “Electron spectroscopy studies on magneto-optical media and plastic substrate interface,” *IEEE Trans. J. Magn. Japan*, vol. 2, pp. 740–741, August 1987 [Digests 9th Annual Conf. Magnetism Japan, p. 301, 1982].
- [7] Zhang, T.; Dong, W.; Keeter-Brewer, M.; Konar, S.; Njabon, R. N.; Tian, Z. R. “Site-Specific Nucleation and Growth Kinetics in Hierarchical Nanosyntheses of Branched ZnO Crystallites”. *J. Am. Chem. Soc.* 2006, 128, 10960–10968.
- [8] Wang, Z.; Gong, J.; Su, Y.; Jiang, Y.; Yang, S. “Six-Fold-Symmetrical Hierarchical ZnO Nanostructure Arrays: Synthesis, Characterization, and Field Emission Properties”. *Cryst. Growth Des.* 2010, 10 (6), 2455–2459.
- [9] Bagnall, D. M.; Chen, Y. F.; Zhu, Z.; Yao, T.; Koyama, S.; Shen, M. Y.; Goto, T. “Optically pumped lasing of ZnO at room temperature”. *Appl. Phys. Lett.* 1997, 70, 2230–2232.
- [10] Chu, S.; Olmedo, M.; Yang, Z.; Kong, J.; Liu, J. “Electrically pumped ultraviolet ZnO diode lasers”. *Si. Appl. Phys. Lett.* 2008, 93, 181106
- [11] Liu, L.; Tan, X.; Teng, D.; Wu, M.; Wang, G. “Simultaneously enhancing the angular-color uniformity, luminous efficiency, and reliability of white light-emitting diodes by ZnO@SiO₂ modified silicones”. *IEEE Trans. Compon., Packag., Manuf. Technol.* 2015, 5 (5), 599–605.
- [12] Choi, M. J.; Kim, M. H.; Choi, D. K. “A transparent diode with high rectifying ratio using amorphous indium-gallium-zinc oxide/SiN_x coupled junction”. *Appl. Phys. Lett.* 2015, 107, 053501.
- [13] Park, S. E.; Shrout, T. R. “Ultrahigh strain and piezoelectric behavior in relaxor based ferroelectric single crystals”. *J. Appl. Phys.* 1997, 82, 1804.
- [14] Roundy, S.; Wright, P. K. “A piezoelectric vibration based generator for wireless electronics”. *Smart Mater. Struct.* 2004, 13, 1131–1142.
- [15] Vioux, A., Hubert Mutin, P. (2016). Nonhydrolytic Sol-Gel Technology. In: Klein, L., Aparicio, M., Jitianu, A. (eds) *Handbook of Sol-Gel Science and Technology*. Springer, Cham. https://doi.org/10.1007/978-3-319-19454-7_28-1.
- [16] Sucheai, M.; Christoulakis, S.; Moschovis, K.; Katsarakis, N.; Kiriakidis, G. “ZnO transparent thin films for gas sensor applications”. *Thin Solid Films* 2006, 515, 551–554.
- [17] Ahn, M. S.; Ahmad, R.; Bhat, K. S.; Yoo, J. Y.; Mahmoudi, T.; Hahn, Y. B. “Fabrication of a solution-gated transistor based on valinomycin modified iron oxide nanoparticles decorated zinc oxide nanorods for potassium detection”. *J. Colloid Interface Sci.* 2018, 518, 277–283.
- [18] Kumar, R.; Al-Dossary, O.; Kumar, G.; Umar, A. “Zinc Oxide Nanostructures for NO₂ Gas-Sensor Applications: A Review”. *Nano-Micro Lett.* 2015, 7 (2), 97–120.
- [19] Chandra, L.; Dwivedi, R.; Mishra, V. N. “Highly sensitive NO₂ sensor using brush coated ZnO nanoparticles”. *Mater. Res. Express* 2017, 4 (10), 105030
- Chen, H. I.; Chi, C. Y.; Chen, W. C.; Liu, I. P.; Chang, C. H.; Chou, T. C.; Liu, W. C. “Ammonia Sensing Characteristic of a Pt Nanoparticle/Aluminum-Doped Zinc Oxide Sensor”. *Sens. Actuators, B* 2018, 267, 145–154.

Desarrollo de una película sensora de alta sensibilidad para gas H₂S usando SnO₂ nanoestructurado

Mariana P. Poiasina
DEMAPE
UNIDEF (CITEDEF-CONICET)
Villa Martelli, Bs.As. Argentina
mpoiasina@citedef.gov.ar

Marcelo D. Cabezas
DEMAPE
UNIDEF (CITEDEF-CONICET)
Villa Martelli, Bs.As. Argentina
mcabezas@citedef.gov.ar

Cristian L. Arrieta
DEA-Microelectrónica
CITEDEF-MINDEF
Villa Martelli, Bs.As. Argentina
carrieta@citedef.gov.ar

Norberto G. Boggio
Dpto. de Micro y Nanotecnología
INN (CAC-CONICET)
San Martín, Bs.As. Argentina
norbertoboggio@cnea.gov.ar

Claudio A. Gillari
DEA-Microelectrónica
CITEDEF-MINDEF
Villa Martelli, Bs.As. Argentina
cgillari@citedef.gov.ar

Claudia D. Bojorge
DEMAPE
UNIDEF (CITEDEF-CONICET)
Villa Martelli, Bs.As. Argentina
cbojorge@citedef.gov.ar

Resumen—En este trabajo se presentan los resultados de la realización y la caracterización de una película sensora, estudiada con el fin de desarrollar un sensor altamente sensible para la detección de gas sulfhídrico (H₂S). Para ello, se sintetizó dióxido de estaño (SnO₂) nanocristalino dopado con óxido de cobre (CuO) al 5% en peso, conformando una película delgada multicapas.

Palabras claves—sensor de gas, H₂S, película delgada, multicapas, SnO₂:CuO, nanomateriales.

I. INTRODUCCIÓN

El SnO₂ es un semiconductor cerámico con la capacidad de cambiar su resistividad eléctrica en respuesta a la exposición a ciertos gases tóxicos y/o explosivos. Esta característica lo convierte en un material de gran utilidad en aplicaciones de sensado de gases y monitoreo ambiental. El mecanismo de sensado se basa en reacciones de óxido-reducción entre el material sensible y el gas detectado, generando un cambio en la resistividad eléctrica proporcional a la concentración del gas objetivo.

El H₂S es un gas altamente tóxico que se produce naturalmente por la descomposición de la materia orgánica. En diversas industrias, como la petrolera, del pescado, producción de biogás y tratamiento de aguas residuales, existe el riesgo de exposición a concentraciones peligrosas de este gas. Por ende, los dispositivos de monitoreo y control son esenciales para garantizar la seguridad laboral, con límites de exposición recomendados de (10-15) ppm en aire [1-3].

Para mejorar la sensibilidad del material sensor y reducir su temperatura óptima de operación (T_o) es conveniente aumentar el área superficial del material, con lo que se consigue un mayor contacto entre el gas analito y el material sensible y, en consecuencia, un mayor número de reacciones de óxido-reducción en la superficie. En este sentido, el uso de materiales nanocristalinos en forma de película delgada es ventajoso [4].

Para aumentar la selectividad del SnO₂, es necesario dopar el material agregando poca cantidad de otros

elementos, ya sean átomos de metales u óxidos metálicos [5]. En particular, el CuO en una concentración del 5 % en peso presenta una alta sensibilidad para la detección de H₂S (g) [6].

En este trabajo se presentan los resultados de la síntesis y la caracterización de una película delgada multicapas de SnO₂ nanocristalino dopado con CuO, para el sensado de bajas concentraciones de H₂S (g) en aire.

II. PARTE EXPERIMENTAL

Se sintetizó SnO₂ nanocristalino dopado con CuO, en forma de película delgada multicapas, utilizando los métodos de *sol-gel* y *dip-coating*.

Se preparó una solución precursora 0.5 M de SnCl₂·2H₂O en etanol absoluto, 1% de ác. láctico y 5% en peso de CuCl₂·2H₂O, en baño termostático entre (80-100) °C por 3-4 hs, en agitación constante.

Se utilizaron sustratos de silicio (Si) con una capa aislante de óxido de silicio. Los mismos fueron lavados siguiendo una secuencia de tres pasos: primero se enjuagaron en agua destilada para eliminar restos de polvo y partículas generadas durante el corte, luego fueron sumergidos en una solución de ácido sulfúrico (H₂SO₄) y peróxido de hidrógeno (H₂O₂) (3:1) con el fin de eliminar restos orgánicos de la superficie y, por último, se volvieron a enjuagar con agua destilada y se secaron en estufa el tiempo necesario.

Para la realización del depósito por *dip-coating* el sustrato fue sumergido en la solución precursora a una velocidad constante de 12 cm/min, a temperatura ambiente. Se utilizó un equipo construido en el laboratorio. Luego de cada depósito, las muestras fueron sometidas a un tratamiento térmico necesario para la descomposición del material precursor y la cristalización del SnO₂. Este tratamiento consistió en un calentamiento lento, a una velocidad de 1°C/min hasta alcanzar los 400°C, manteniendo esta temperatura durante 120 min y luego enfriando a la misma velocidad.

El procedimiento de depósito y el tratamiento térmico se repite sucesivamente para formar el sistema multicapas. Se realizaron películas con un total de 3 capas superpuestas.

El material obtenido fue caracterizado estructural y eléctricamente. Para la caracterización por Difracción de Rayos X (DRX) se utilizó un difractómetro Malvern Panalytical Empyrean perteneciente al Laboratorio de Cristalografía Aplicada de la UNSAM. Esta técnica permitió verificar la formación de SnO₂ cristalino, determinar la fase y tamaño promedio de cristalita del material obtenido.

Mediante Microscopía Electrónica de Barrido (FESEM) se observó la morfología de la superficie y el perfil del sistema multicapas. Para esto se utilizó un equipo Karl Zeiss FESEM DSM 982 Gemini del Centro de Microscopía Avanzada de la Facultad de Ciencias Exactas y Naturales (FCEyN) de la UBA.

Mediante Espectrometría de Energía Dispersiva (EDS) (INTI-Mecánica) se analizó la composición química de las muestras.

Finalmente, la película sensora fue caracterizada eléctricamente para determinar T_o y el rango de sensibilidad. El sistema de medición está formado por una fuente de corriente de precisión, un electrómetro de alta impedancia, electroválvulas de conmutación de gases para realizar las mediciones alternando la circulación de aire puro y aire con una mezcla de gas y por reguladores máscicos de caudal para cambiar la concentración de H₂S (g) en aire. A través de dos contactos de Ag realizados sobre la película, se le hace circular una corriente eléctrica y se mide la diferencia de potencial entre los contactos usando el electrómetro de alta impedancia. Se midieron los valores de resistencia realizando ciclos alternados de aire puro y aire con gas, a una temperatura determinada de operación. Con los valores de resistencia medidos se calcularon la sensibilidad S y la sensibilidad relativa S_r según las ecuaciones (1) y (2), respectivamente:

$$S = R_{air} / R_{air+gas} \quad (1)$$

$$S_r = (R_{air} - R_{air+gas}) / R_{air} \quad (2)$$

siendo R_{air} y $R_{air+gas}$ los valores de las resistencias en aire y en aire más gas. Las mediciones fueron repetidas a diferentes temperaturas para determinar T_o .

III. RESULTADOS

El difractograma DRX de la película obtenida, verifica la formación de SnO₂ cristalino con estructura rutilo tetragonal y un tamaño promedio de cristalita de 9 nm (Fig. 1).

Las Figs. 2a-b muestran micrografías FESEM de la superficie a diferentes magnificaciones, donde se puede ver un film homogéneo con un tamaño de grano del orden de los 10 nm. En la Fig. 2c se observa el perfil del sistema multicapas con el que se pudo determinar que el espesor aproximado es de 230 nm. El análisis químico cualitativo realizado por EDS (Fig. 3) revela la presencia de los

elementos químicos correspondientes a la película: SnO₂ y CuO y al sustrato: Si.

En las Figs. 4a y 4b se muestran los valores obtenidos de sensibilidad y sensibilidad relativa, respectivamente, en función de la temperatura de operación para 10ppm de H₂S en aire. Se puede ver que la máxima sensibilidad se alcanza entre los 140 y 150 °C (T_o). La Fig. 5 muestra la respuesta de la película sensora a 140 °C, alternando ciclos de aire y 10ppm de H₂S en aire. Estos resultados demostraron una sensibilidad satisfactoria de estas películas para la detección de H₂S (g) cumpliendo con los límites de concentración esperados (10 - 15) ppm.

IV. CONCLUSIONES

Los estudios realizados en el presente trabajo indicaron que el SnO₂ nanocristalino dopado con CuO (5% en peso) es un material sensible, adecuado para la detección de bajas concentraciones de gas H₂S, entre (10 – 15) ppm en aire. La temperatura óptima de trabajo del material obtenido está en rango de 140-150 °C.

Este trabajo sienta las bases para el futuro desarrollo de un dispositivo para la detección de gas H₂S, con potenciales aplicaciones en diversas industrias.

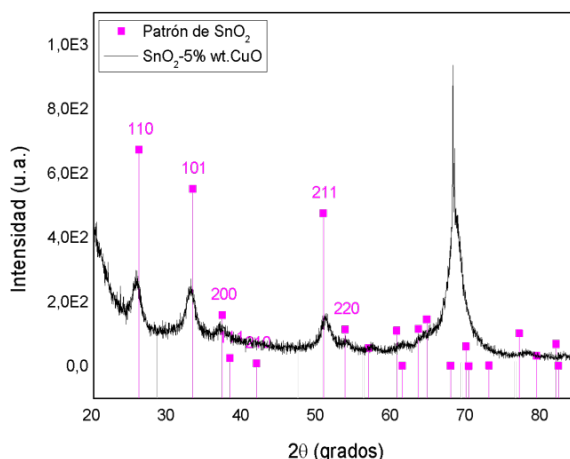
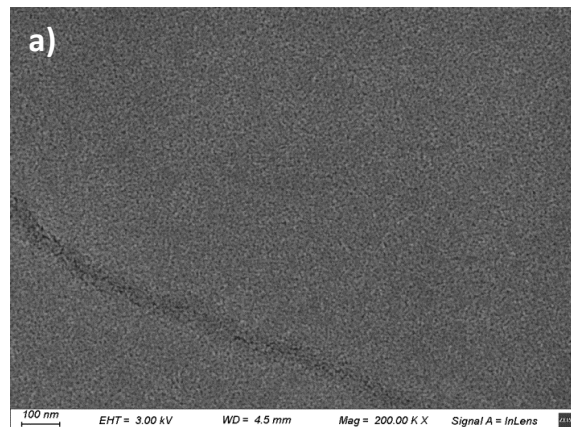


Fig. 1: Difractograma del SnO₂:CuO donde se identifica la fase de rutilo tetragonal.



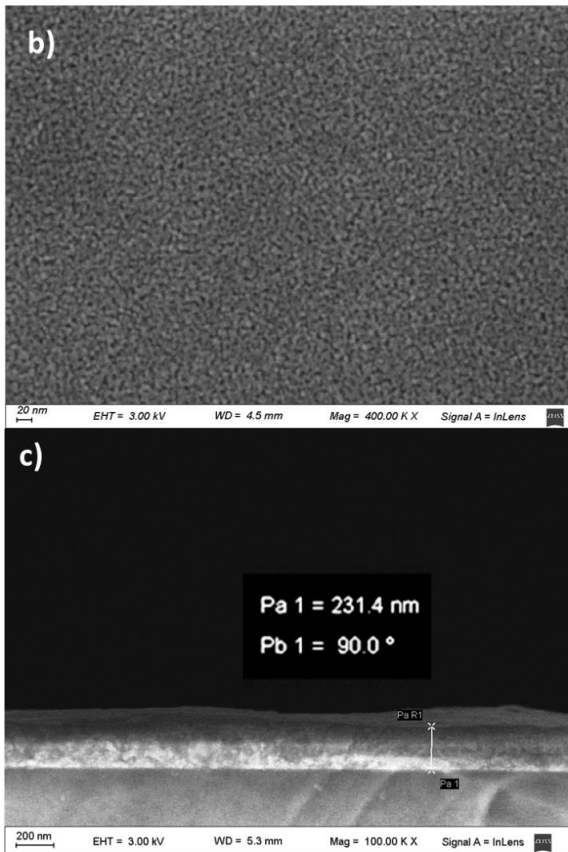


Fig. 2: Micrografía FESEM de la superficie de la película de SnO₂:CuO: a) con magnificación 200.00 KX, b) con magnificación 400.00 KX. c) Micrografía del perfil y determinación del espesor.

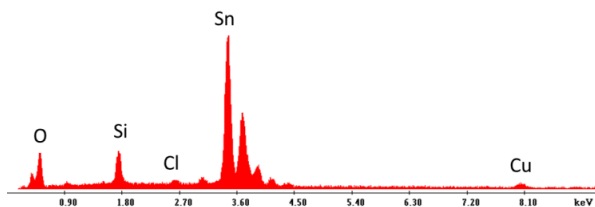


Fig.3: Espectro EDS de la película.

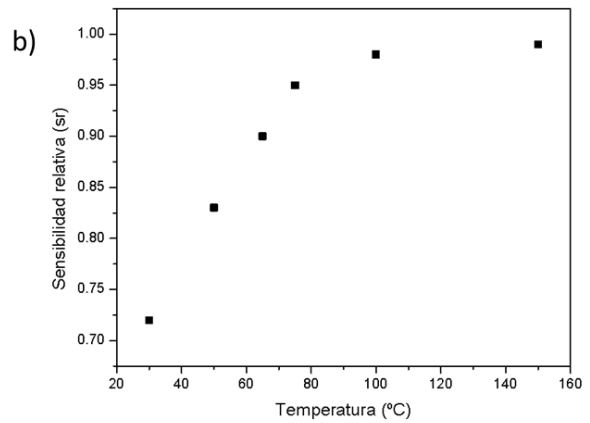
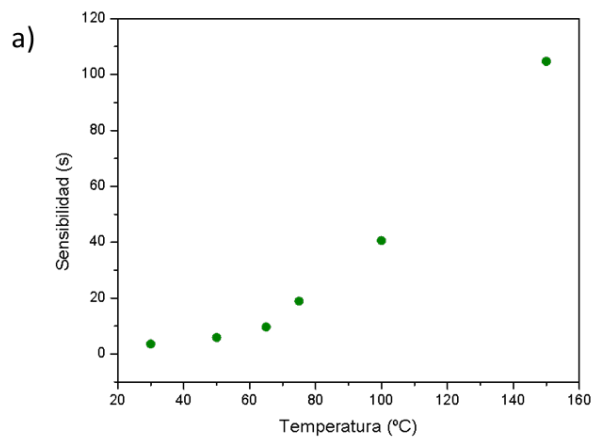


Fig. 4: a) Sensibilidad (S) en función de la temperatura para 10 ppm de H₂S (g) en aire. b) Sensibilidad relativa (Sr) en función de la temperatura para 10 ppm de H₂S (g) en aire.

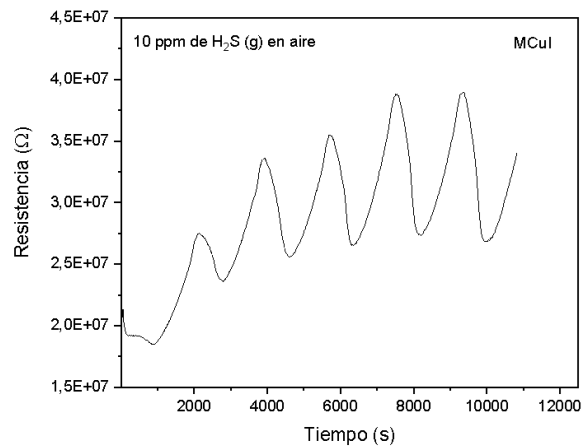


Fig. 5: Cambios en la resistencia eléctrica del sensor expuesto a ciclos de aire/ aire+gas, para 10 ppm de H₂S en aire, a una temperatura de operación de 140 °C.

AGRADECIMIENTOS

Los autores agradecen al Dr. Diego Lamas y equipo del Laboratorio de Cristalografía Aplicada de la Universidad Nacional de San Martín (UNSAM), por la colaboración en la caracterización con la técnica DRX. Este trabajo fue financiado por CONICET (PUE 2018-018).

REFERENCIAS

- [1] <https://www.osha.gov/hydrogen-sulfide>
- [2] <https://www.cdc.gov/spanish/niosh/npg-sp/npgd0337-sp.html>
- [3] Corresponde a la legislación de Argentina: <http://www.argentina.gob.ar/normativa/nacional/resoluci%C3%B3n-295-2003-90396/texto>
- [4] S. Hooker, Nanotechnology Advantages Applied to Gas Sensor Development. The Nanoparticles 2002 Conference Proceedings, 2002.
- [5] J. Tamaki, T. Maekawa, N. Miura, N. Yamazoe, "CuO-SnO₂ element for highly sensitive and selective detection of H₂S", Sensors and Actuators B 9, 197-203, 1992.
- [6] A. Ayes, A. Alyafei, R. Anjum, R. Mohamed, M. Buharb, B. Salah, M. El Muraikhi, "Production of sensitive gas sensors using CuO/SnO₂ nanoparticles", Applied Physics A, 125:550, 2019.

Análisis de epitaxias de $\text{Hg}_{1-x}\text{Cd}_x\text{Te}$ obtenidas por VPE

Javier L. M. Núñez García
 DEMAPE
 UNIDEF-CITEDEF-MINDEF
 Villa Martelli, Bs. As., Argentina
 Centro de Tecnologías Químicas (CTQ)
 UTN FRBA
 Almagro, CABA, Argentina
 jnunez@citedef.gob.ar

Raúl L. D'Elía
 DEMAPE
 UNIDEF-CITEDEF-MINDEF
 Villa Martelli, Bs. As., Argentina
 UTN FRBA
 Almagro, CABA, Argentina
 rdelia@citedef.gob.ar

Diego G. Franco
 LAHN
 CNEA-CAB
 Bariloche, Argentina
 diego.franco@cab.cnea.gov.ar

Ulises E. Gilabert
 SEGEMAR, INTI
 San Martín, Bs. As., Argentina
 Centro de Tecnologías Químicas (CTQ)
 UTN FRBA
 San Martín, Bs. As., Argentina
 ulisesgilabert@yahoo.com.ar

Resumen—Este artículo se basa en el estudio de epitaxias de HgCdTe obtenidas por el método Vapour Phase Epitaxy mediante el uso de diferentes técnicas de caracterización.

Palabras clave: HgCdTe , SEM, EDS, Mediciones Hall, IR.

I. INTRODUCCIÓN

Las epitaxias de $\text{Hg}_{1-x}\text{Cd}_x\text{Te}$ (MCT) son materiales semiconductores de gran importancia tecnológica debido a su capacidad para detectar la radiación infrarroja (IR). Esta tecnología tiene una amplia gama de aplicaciones en diversos campos, como por ejemplo en cámaras IR para detectar pérdidas de fluidos en destilerías, seguimientos y guiados de misiles, etc. Existe una gran variedad de métodos para la obtención del MCT, desde sencillos como *Vapour Phase Epitaxy* (VPE) que se utiliza a escala laboratorio debido a sus menores costos y más sencillez, hasta más complejos y de costos elevados como *Molecular Beam Epitaxy* (MBE) que se utiliza a escala industrial.

En el método VPE se utiliza una ampolla de cuarzo en cuyo interior se realiza vacío (entre 10^{-4} y 10^{-5} torr) [1]. Se coloca dentro de la misma el material fuente, una oblea de HgTe policristalino, y el sustrato monocristalino (CdTe , CdZnTe), separados entre sí por una distancia pequeña, y en el fondo de la cápsula una gota de Hg . Los elementos que formarán la película se convierten en fase vapor, y se transportan hacia el sustrato que se encuentra a una temperatura más baja generando la formación de la epitaxia en la superficie. Dando lugar además a un proceso de interdifusión entre el Cd proveniente del sustrato, y del Hg proveniente del material fuente que se deposita sobre el sustrato. Las películas que se obtienen por este método VPE presentan un gradiente de composición perpendicular a la superficie plana externa. Las ventajas de utilizar este método son que es simple, económico y permite obtener epitaxias de buena calidad, por eso es un método muy utilizado en laboratorios de investigación. Sin embargo, el control y seguimiento de los parámetros de interés en esta metodología, si no se los realiza con extremo cuidado, pueden generar diferentes problemas en la calidad de los crecimientos.

Las epitaxias de MCT crecidas en nuestro laboratorio se obtuvieron mediante la técnica VPE sobre sustratos de CdTe y CdZnTe . Estos sustratos con pulidos mecánico químicos, de caras paralelas, permiten el crecimiento de la epitaxia de MCT que copia la misma estructura cristalina del sustrato subyacente. En este trabajo la muestra 1 fue crecida sobre un sustrato de CdZnTe de $1\text{cm} \times 1\text{cm}$, mientras que las muestras 2 y 3 sobre sustratos de CdTe de $1\text{cm} \times 2\text{cm}$. Las epitaxias fueron caracterizadas por Microscopía Óptica (MO), Microscopía Electrónica de Barrido (SEM), Espectroscopía Dispersiva de Rayos X (EDS/EDX) y mediciones Hall. Cabe aclarar que las muestras seleccionadas corresponden a muestras que presentaron defectos asociados a las condiciones experimentales. Para ello se realizaron diferentes estudios para detectar los problemas que los generaron durante el crecimiento, con el fin de obtener muestras monocristalinas.

II. PARTE EXPERIMENTAL

A. Microscopía Óptica

Por medio de esta técnica se verificó el estado de la superficie de las diferentes muestras (Fig. 1). Se observó y analizó la superficie de cada muestra. Para la observación de la muestra 1 por MO fue necesario realizar un pulido previo. Debido a la fragilidad de la muestra se procedió a pulirla utilizando un trípode de pulido especial destinado a la fabricación de láminas delgadas para TEM. En la figura (1a) se observan las rayas de pulido artesanal/manual. La figura (1b), muestra 3, no presenta, a este nivel de aumento, ninguna imperfección en su superficie, lo que sugiere que se trata de una muestra monocristalina.

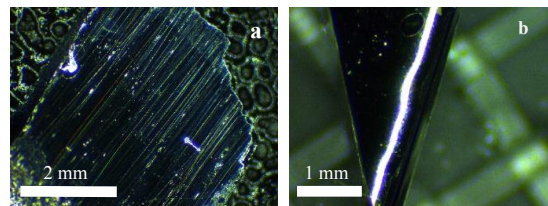


Fig. 1. Imágenes MO de epitaxias de MCT. a) Muestra 1 donde se aprecian las rayas de pulido; b) Muestra 3 sin defectos superficiales aparentes.

B. Microscopía Electrónica de Barrido (SEM)

Por medio del uso de un haz de electrones enfocados para obtener imágenes de la superficie de la muestra con mayor resolución y profundidad de campo que la MO, se observó la superficie con alta y baja resolución mediante SEM. Se utilizó un SEM Karl Zeiss NTS-Supra 40 perteneciente a la facultad de ciencias exactas de la UBA y otro modelo SEM FEI Inspect S50 de la Comisión Nacional de Energía Atómica Centro Atómico Bariloche. Se buscó por este medio identificar las imperfecciones superficiales observables por este método. En el caso de la muestra 1 (Fig. 2) se evaluó la uniformidad del pulido y la presencia de posibles imperfecciones generadas por el pulido. En la muestra 2 (Fig. 3) se detectó la presencia de diferentes granos (Fig. 3 a y 3 b), y en uno en particular se encontraron formaciones triangulares como pozos (Fig. 3 c). Para la muestra 3 la superficie se ve uniforme (muestra monocristalina).

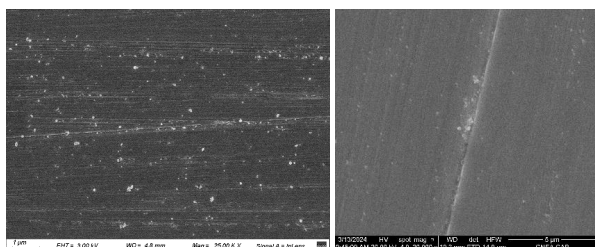


Fig.2. Superficie pulida Muestra 1

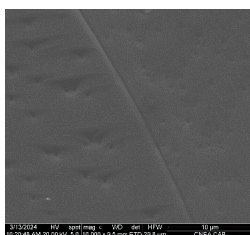
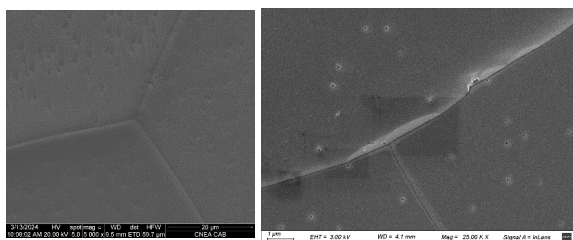


Fig. 3. Muestra 2. a), b), c) Se observa la presencia de diferentes granos.



Fig. 4. Muestra 3 (monocristalina)

C. Espectroscopía Dispersiva de Rayos X (EDS/EDX)

Como complemento a las micrografías obtenidas mediante SEM, se realizó EDS de las muestras en CNEA-CAB, con el fin de determinar la composición del material depositado sobre los sustratos. Se excitan los átomos de la muestra con una fuente de rayos X, provocando que emitan rayos con una energía específica propia de cada elemento, lo que permite identificarlos.

Este tipo de análisis además de determinar los elementos presentes en la epitaxia, permite calcular sus fracciones molares y detectar si hay alguna impureza o problemas de estequiometría.

Para ello se realizaron mediciones en varios puntos de cada muestra, con las cuales se construyó un gráfico y una tabla por cada punto medido similares a la Figura 5 y la Tabla I. A partir de estos valores se realiza el cálculo de la composición de cada punto y luego se calcula el promedio entre todos los puntos de cada muestra para determinar su composición (Tabla II: Composición de cada muestra).

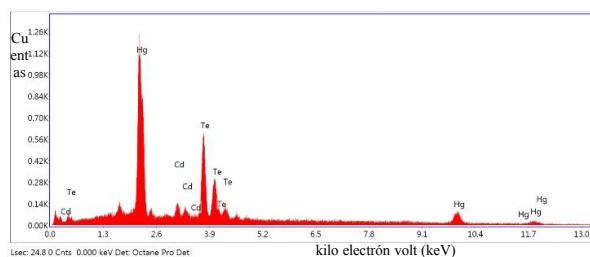


Fig. 5. Diagrama EDS de una zona de la Muestra 3

Tabla I: Resultados cuantitativos de EDS para el punto

Element	Weight %	Atomic %	Net Int.	Error %	Kratio	Z	R	A	F
CdL	5.3	7.2	69.9	20.1	0.043	1.089	0.940	0.721	1.049
TeL	46.8	56.2	463.7	7.1	0.399	1.032	0.958	0.800	1.030
HgL	47.9	36.5	104.5	15.8	0.510	0.935	1.021	0.998	1.141

correspondiente a la Figura 5.

Tabla II: Composición de cada muestra

	Material	Muestra 1	Muestra 2	Muestra 3
Zona 1	Cd	0,15	0,07	0,08
	Te	0,57	0,57	0,55
	Hg	0,28	0,35	0,37
Zona 2	Cd	0,1	0,08	0,07
	Te	0,56	0,58	0,55
	Hg	0,34	0,35	0,38
Promedio	Cd	0,13	0,07	0,07
	Te	0,57	0,58	0,55
	Hg	0,31	0,35	0,38

D. Mediciones Hall

El efecto Hall se genera por la interacción entre corrientes eléctricas y campos magnéticos que atraviesan la muestra. Este fenómeno permite caracterizar las propiedades eléctricas de los semiconductores obtenidos, determinando el tipo (n o p), la resistividad (ρ), la movilidad (μ) y la densidad de los portadores de carga, tanto para las muestras como para los sustratos [2, 3].

Número de portadores (n o p):

$$n = \frac{B \times \left(\frac{V_r}{120}\right) \times 10^{-6}}{e \times d \times \Delta V} \quad \text{con } I = \frac{V_r}{120}$$

Donde:

- “B” es el módulo del campo magnético en Tesla (T).
- “e” es la carga del electrón: $e = 1,602 \times 10^{-19}$ Coulomb (C).
- “d” es el espesor de la muestra en μm
- “I” intensidad de corriente eléctrica en Ampere (A).
- “ V_r ” voltaje en Volts (V).
- “ ΔV ” Promedio del Voltaje Hall en Volts.

Resistividad (ρ):

$$\rho = \frac{\pi}{\ln 2} \times d \times \frac{(R1 + R2)}{2} \times \frac{1}{10^4}$$

Donde:

- “R1” y “R2” se obtienen por la técnica de Van der Pauw.

Movilidad (μ)

$$\mu = \frac{1}{e \times \rho \times n}$$

La evaluación de la resistividad es de vital importancia en la industria de la fabricación de semiconductores y dispositivos electrónicos. Es un aspecto fundamental para garantizar la calidad y la uniformidad de los materiales empleados. El rango de resistividad es crucial para garantizar un funcionamiento correcto de los dispositivos [4].

Utilizando un equipo fabricado íntegramente en nuestro laboratorio [5], se llevaron a cabo mediciones Hall en las muestras de MCT. La Tabla III presenta los resultados obtenidos para las capas epitaxiales y los sustratos utilizados:

Tabla III: Mediciones Hall

Muestra		T (K)	Nº de portadores (n o p) [$1/\text{cm}^3$]	Resistividad (ρ) [$\Omega \text{ cm}$]	Movilidad (μ) [$\text{cm}^2/\text{V} \cdot \text{s}$]
Tipo	Material				
Sustrato	CdZnTe	297	$4,277 \times 10^{13}$	554,077	263,419
Epitaxia n° 1	HgCdTe	297	$1,054 \times 10^{17}$	0,043	1369,958
Epitaxia n° 1	HgCdTe	77 (Nitrógeno)	$1,447 \times 10^{17}$	0,039	1094,364
Sustrato	CdTe	297	$1,024 \times 10^{13}$	845,914	720,665
Epitaxia n° 2	HgCdTe	297	$1,199 \times 10^{17}$	0,047	1110,190
Epitaxia n° 2	HgCdTe	297	$1,708 \times 10^{17}$	0,047	1215,218
Epitaxia n° 2	HgCdTe	77 (Nitrógeno)	$1,070 \times 10^{17}$	0,042	1075,615
Epitaxia n° 3	HgCdTe	297	$6,140 \times 10^{16}$	0,042	2393,457
Epitaxia n° 3	HgCdTe	297	$4,651 \times 10^{16}$	0,042	3159,682
Epitaxia n° 3	HgCdTe	77 (Nitrógeno)	$1,345 \times 10^{17}$	0,039	1205,497

III. RESULTADOS

A partir de los diferentes análisis que se realizaron a cada una de las muestras, tanto por las técnicas de EDS como las mediciones Hall, se determina que se ha depositado/crecido el material sensible sobre el sustrato. Los resultados del análisis cualitativo muestran que las epitaxias de MCT poseen gran cantidad de Hg y poca de Cd ($x \approx 0,2$).

Se observan pequeñas variaciones en la cantidad de Cd, lo cual puede deberse a un problema en la variación del perfil de temperatura dado que según datos bibliográficos una leve desviación del mismo, genera modificaciones en la composición del material [6]. En nuestras condiciones de crecimiento se busco que el material a crecer se ubique en una zona donde la temperatura supere los 600°C , pero que exista un *plateau* en el que se mantenga constante con la mínima variación.

En una muestra se generó un sobredeposito de HgTe (material fuente) como se puede ver en la Figura 6. Esto podría deberse a que durante el proceso de crecimiento se cortó la energía eléctrica lo que generó que el horno continúe calentándose debido a la inercia térmica generando que el material fuente se vaporice en gran proporción. Al enfriarse el sistema ese material se solidificó en la superficie del material crecido. Es importante destacar además que la adaptación de la técnica de preparación de láminas delgadas para TEM, permitió pulir las muestras sin perder el material depositado

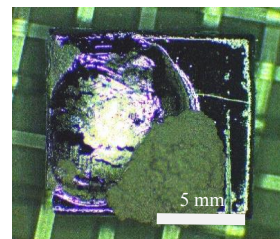


Fig. 6. Muestra crecida con sobredeposito de HgTe

Las muestras crecidas sobre los sustratos de CdTe, a diferencia de las crecidas sobre CdZnTe, presentan en su composición una menor cantidad de Cd. Lo que demuestra la mayor afinidad de la epitaxia con el CdZnTe [7].

Es importante aclarar que el tamaño de la superficie de los sustratos de CdTe es mayor, y también su espesor.

IV. CONCLUSIONES

Los resultados obtenidos son muy importantes no solo porque demuestran la presencia de una capa de MCT sobre los sustratos, sino también porque permitieron identificar problemas en las condiciones de crecimiento. Además, se concluye que el método de obtención de láminas delgadas para TEM por medio del uso de trípode de pulido se puede utilizar para el pulido de estos materiales sin generar imperfecciones a nivel superficial.

Se comprobó, mediante las mediciones Hall y EDS, que en todos los crecimientos se logró obtener epitaxias de MCT, tanto para sustratos de CdZnTe, como para sustratos de CdTe. Si bien varía levemente la cantidad de Cd y Hg entre las muestras de diferentes sustratos, en todas se mantiene la cantidad de Te. Esta leve variación, inherente a que el Hg posee mayor coeficiente de difusión en el CdTe que en el CdZnTe, por esta razón es que el Hg está en mayor proporción que el Cd en las muestras de CdTe. No obstante, esta diferencia no representa un inconveniente para las propiedades finales del material.

Los resultados experimentales muestran que se debe tener un mejor control en la variación del perfil de temperaturas en el horno durante el crecimiento, especialmente en la zona de ubicación de la muestra, y en extremo cerrado del horno. Para ello se realizará, en futuros experimentos, el seguimiento durante todo el tiempo de crecimiento de la variación de temperatura mediante la utilización de una computadora con software adecuado para realizar el control a distancia. Esto permitirá detectar en caso que suceda un cambio brusco de temperatura en la zona de crecimiento.

La elección de la técnica de crecimiento de las epitaxias para la obtención de MCT depende de la escala de producción y los recursos disponibles. Mientras que las técnicas industriales ofrecen mayor complejidad y costos elevados, la VPE se presenta como una alternativa más accesible para aplicaciones a escala de laboratorio.

En relación a la muestra 1 para su utilización en un dispositivo, se deberá eliminar completamente las rayas del

pulido mecánico mediante un pulido químico. Podemos concluir que el pulido mecánico por medio de la técnica de trípode fue realizado en condiciones adecuadas dado que se logró evitar la pérdida de la capa de MCT y no se generaron defectos superficiales detectables con MO o SEM.

Como la muestra 2 presenta diferentes granos en su superficie, no resulta un material apto para su utilización en dispositivos de detección IR.

La muestra 3 no se encontraron imperfecciones en las caracterizaciones realizadas, ni tampoco se observaron diferentes granos. El material *asgrown* constituye una epitaxia útil para dispositivos.

AGRADECIMIENTOS

Los autores de este trabajo agradecemos a la UTN FRBA y la UNIDEF (CITEDEF-MINDEF) por los subsidios otorgados para la realización de estos trabajos. A Paula Troyón operadora del SEM de la Comisión Nacional de Energía Atómica quien realizó un excelente trabajo analizando las muestras por SEM y EDS. A todos los autores de este trabajo y a Horacio Cánepa por su colaboración.

REFERENCIAS

- [1] G. Cohen-Solal, Y. Marfaing, F. Bailly, "Croissance épitaxiale de composés semiconducteurs par évaporation-diffusion en régime isotherme", in Rev. Physics Applied, vol. 1, 1966, p.11.
- [2] M. H. Aguirre, "Estudio de los defectos en $Hg_{1-x}Cd_xTe$ pre y post-Implantado en el Proceso de Creación de la Juntura N/P", Tesis Doctoral de la Universidad de Buenos Aires, Facultad de Ciencias Exactas y Naturales, Departamento de Física, 2001.
- [3] R. W. Miles, "Properties of Narrow Gap Cadmium-based Compounds", in Emis Datareviews Series, No. 10, P. Capper, Edr. London: Inspec Publication, 1994, pp.221-225.
- [4] A. G. Korotaev, I. I. Izhnin, K. D. Mynbaev, A. V. Voitsekhovskii, S. N. Nesmelov, S. M. Dzyadukh, et al, "Hall-effect studies of modification of $HgCdTe$ Surface properties with ion implantation and thermal annealing" in Surface & Coatings Technology, vol. 393, Elsevier, 2020, 125721.
- [5] E. Heredia, "Construyendo un equipo para mediciones de efecto Hall", Tesis de Licenciatura; FCEN-UBA, Departamento de Física, 1988.
- [6] K. Adamiec, M. Grudzien, Z. Nowak, J. Pawluczyk, J. Piotrowski, J. Antoszewski, J. Dell, Ch. Musca, L. Faraone, "Isothermal Vapour phase Epitaxy as a versatile technology for infrared photodetectors", in Proceedings of SPIE, vol. 2999, 1997, p 34.
- [7] U. E. Gilbert, "Estudio de las propiedades superficiales e interfaciales de películas monocristalinas de $Hg_{1-x}Cd_xTe$ crecidas en fase vapor sobre distintos sustratos", Tesis Doctoral de la Universidad de Buenos Aires, Facultad de Ciencias Exactas y Naturales, Departamento de Química Inorgánica, Análítica y Química Física, 2007.

Enhancing bacterial detection with bactericidal nanostructured titania electrodes

Betania Garcia
Advanced Biosensors Laboratory,
Nanosystems Institute.
Universidad Nacional de San Martin.
San Martin, Buenos Aires, Argentina
bgarciamendez@unsam.edu.ar

Bo Su
Biomaterials Engineering Group,
Dental School.
University of Bristol.
Bristol, England, United Kingdom
b.su@bristol.ac.uk

Diego Pallarola
Advanced Biosensors Laboratory,
Nanosystems Institute.
Universidad Nacional de San Martin.
San Martin, Buenos Aires, Argentina
d.pallarola@unsam.edu.ar

Abstract—In the coming years, an increase in joint replacement surgeries is anticipated, with a 10% failure rate prompting surface modifications for bactericidal action and improved implant integration. Despite significant advancements in implant technology, individuals with compromised immune systems remain susceptible to pathogens, increasing the risk of biofilm formation and potential revision surgeries.

To address these challenges, current research efforts are focused on nanostructured surfaces, particularly those utilizing titanium. However, electrochemical bacterial biosensing faces limitations due to titanium oxide's high capacitance. This study proposes the fabrication of bactericidal titania electrodes to enhance the sensitivity of microbial detection. By incorporating antimicrobial properties into the electrode design, this approach aims to improve bacterial detection efficiency, contributing to the advancement of implant bioengineering.

Keywords—electrochemistry, biosensing, ITO, titanium oxide, bacteria, nanostructure, implant.

I. INTRODUCTION

Projections indicate a substantial increase in joint replacement surgeries in the coming years. Given a 10% failure rate within the first two decades, we propose surface modifications to implants to provide bactericidal properties and ensure better implant integration within the patient [1].

There have been considerable advancements in implant development over time. This evolution began with the use of biocompatible materials and the introduction of aseptic and sterilization procedures. The focus has now shifted towards designing lighter materials or materials with specific properties that promote integration [2].

Current failures are largely due to the weakening of the patient's immune system in the presence of an implant, making them more susceptible to pathogens. In cases where biofilm formation is observed, antibiotic treatments may not be sufficient, potentially leading to a second surgery [1].

In this context, the implementation of preventive measures is crucial. This has led to ongoing efforts to fabricate nanostructured surfaces using biocompatible materials for implant applications. Numerous studies have shown that nanostructures, such as nanowires, nanopikes, and nanopillars, can prevent bacterial infection due to their mechanical impact on bacterial cell walls [3-4].

Nevertheless, to gain a deeper understanding of bacterial interactions, real-time monitoring is essential, which can be

This work has received funding from the European Union's Horizon 2020 Research and Innovation Programme under the Marie Skłodowska-Curie grant agreement No 872869. Bio-TUNE project.

achieved using electrochemical techniques [5-6]. Titanium, a biocompatible material, is used in this study. Both pure titanium and some of its alloys are used in implant fabrication, and several methodologies can be applied to produce nanostructured titanium oxide [3-4].

In this specific case, a fingerprint nanopattern, which is composed of a block copolymer, serves as a template. This template facilitates the growth of titanium oxide through an anodizing process [7-8]. However, the use of these titanium surfaces in electrochemical bacterial biosensing is limited due to the high capacitance of anodic titanium oxide, which makes it difficult to obtain a well-defined signal of the expected response. As a proposed strategy, a layer of titanium is deposited onto indium tin oxide (ITO), a material known for its excellent conductive properties for these applications [9].

II. SYNTHESIS AND CHARACTERIZATION OF NANOSTRUCTURED ELECTRODES

A. Preparation of samples

The samples used are glass substrates measuring 10x20 mm or 10x10 mm, each coated with a 150 nm layer of ITO. They underwent a meticulous cleaning process, which involved successive steps of acetone, isopropanol, and a solution of hydrogen peroxide and ammonia. Following this thorough cleaning, each sample was rinsed repeatedly with deionized water and dried prior to the deposition of a 100 nm thick titanium layer using sputtering.

B. Formation of the fingerprint pattern

On top of the titanium layer of the samples obtained in the previous step, a thin film of polystyrene-b-poly-2-vinylpyridine (PS-b-P2VP) block copolymer is deposited using spin coating (Fig. 1.). Initially, this film exhibits a micellar structure, and upon applying an annealing treatment with solvent vapor, its structure changes, forming a fingerprint-like pattern (Fig. 2.A.). Titanium oxide grows, mimicking the pattern of the copolymer block, through an anodizing process in oxalic acid, where the film-coated surface serves as the anode and a platinum sheet as the cathode, applying 10 V at 20 °C. Upon completion, the film is removed, carefully dried, and subjected to oxygen plasma etching at maximum intensity for 30 minutes for removing the organic material (Fig. 2.B.). The nanotopographies of

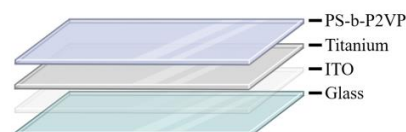


Fig. 1. Scheme of the samples prepared for the nanostructured electrodes.

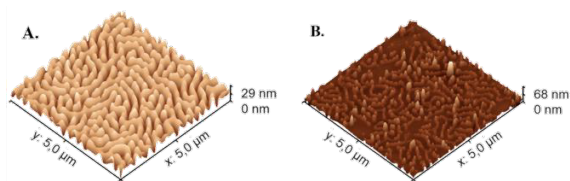


Fig. 2. 3D AFM measurements: A. Block copolymer film with fingerprint nanostructure and, B. Anodic titanium oxide fingerprint nanostructures after plasma etching.

these samples were characterized using atomic force microscopy (AFM).

C. Nanotopographical effect

For bacterial assays, two types of bacteria, *E. coli* and *S. aureus*, are employed. A solution is prepared from a starter culture with an Optical Density at 600 nm (OD_{600}) of 0.2, equivalent to a concentration of 10^7 CFU/mL. From this solution, a dilution is made to achieve a concentration of 10^8 CFU/mL. Sterile surfaces are incubated with the bacteria and examined using epifluorescence microscopy. The LIVE/DEAD kit is utilized, enabling the labelling of live bacteria in green and bacteria with compromised cell walls (dead) in red. The quantification of bacteria is determined using the ImageJ software, and it is compared with the control (surface without nanostructures).

D. Real-time electrobiosensing

Bacterial experiments are conducted inside an incubator at 37 °C over several hours. The electrochemical cell is connected to a potentiostat for impedance and voltammetry measurements. The fabricated sample is used as the working electrode, with an Ag/AgCl electrode (saturated KCl) as the reference, and a coiled platinum wire as the counter electrode. Tris-HCl buffer is used as the electrolyte solution with ferrocenemethanol (redox probe) for detection. These measurements are repeated periodically to monitor real-time interactions. The small voltage amplitude applied (± 10 mV) ensures the system is not destroyed or modified.

Variations in charge transfer resistance from Nyquist plots often provide information about the type of processes occurring on the surface, along with the Bode diagram. At high alternating current frequencies, more current passes directly through the cell membranes, allowing for the measurement of cell coverage and growth rate. Conversely, at low frequencies, the current mainly flows between cells, enabling the evaluation of barrier function and the quantity of adhered cells.

III. PRELIMINARY FINDINGS AND FUTURE PERSPECTIVES

The nanostructured electrodes engineered in this research not only present a multitude of potential applications within the domain of medical implants, but they also represent a significant breakthrough in the field of bacterial biofilm control. These electrodes are fabricated with a specific focus on limiting the development of bacterial biofilms, a common and critical issue in medical implantology.

In addition to their ability to curtail bacterial proliferation, these nanostructured materials are imbued with analytical capabilities that allow for the real-time monitoring of bacterial activity on implant surfaces. This unique feature facilitates the early detection of infections and enables immediate medical intervention, thereby significantly enhancing clinical outcomes and reducing patient-associated risks.

These findings underscore the instrumental role of such nanostructured materials in augmenting the biocompatibility of medical implants and mitigating associated infections. This marks a noteworthy progression in the field of implantable medicine and the protection of global health.

ACKNOWLEDGMENT

This work has received funding from the European Union's Horizon 2020 Research and Innovation Programme under the Marie Skłodowska-Curie grant agreement No 872869, Bio-TUNE project. We would like to express our gratitude to the School of Bio and Nanotechnology at the Universidad Nacional de San Martín and the Dental School at the University of Bristol for their support in facilitating the development of this project. BG acknowledges the support of CONICET for providing a doctoral scholarship.

REFERENCES

- [1] K. Su, L. Tan, X. Liu, Z. Cui, Y. Zheng, B. Li, Y. Han, Z. Li, S. Zhu, Y. Liang, X. Feng, X. Wang, and S. Wu, "Rapid photo-sonotherapy for clinical treatment of bacterial infected bone implants by creating oxygen deficiency using sulfur doping," *American Chemical Society Nano* 2020, 14, 2077–2089, January 2020.
- [2] S. Todros, M. Todesco and A. Bagnò, "Biomaterials and their biomedical applications: from replacement to regeneration," *Processes* 2021, 9, 1949, October 2021.
- [3] M. I. Ishak, R. Cuatrecasas-Delint, X. Liu, W. Xu, P. M. Tsimbouri, A. H. Nobbs, M. J. Dalby and B. Su, "Nanotextured titanium inhibits bacterial activity and supports cell growth on 2D and 3D substrate: A co-culture study," *Biomaterials Advances* 2024, 158, 213766, January 2024.
- [4] C. Zhou, R. Koshani, B. O'Brien, J. Ronholm, X. Cao and Y. Wang, "Bio-inspired mechano-bactericidal nanostructures: a promising strategy for eliminating surface foodborne bacteria," *Current Opinion in Food Science* 2021, 39:110–119, January 2021.
- [5] A. Khoshroo1, M. Mavaei, M. Rostami, B. Valinezhad-Saghezi and A. Fattahi, "Recent advances in electrochemical strategies for bacteria detection," *BioImpacts* 2022, 12(6), 567-588, October 2022.
- [6] V. Guglielmini, E. Fuhry, T. J. Neubert, M. Kuhl, D. Pallarola, and K. Balasubramanian, "Real-time monitoring of cell adhesion onto a soft substrate by a graphene impedance biosensor" *American Chemical Society Sensors* 2024, 9, 1, 101–109, December 2023.
- [7] R. Fontelo, D. Soares da Costa, R.L. Reis, R. Nova-Carballal and I. Pashkuleva, "Bactericidal nanopatterns generated by block copolymer self-assembly," *Acta Biomaterialia* 2020, 112, 174-181, August 2020.
- [8] T. Sjöström, L. E. McNamara, L. Yang, M. J. Dalby, and B. Su, "Novel anodization technique using a block copolymer template for nanopatterning of titanium implant surfaces," *American Chemical Society Applied Materials & Interfaces* 2012, 4, 11, 6354–6361, November 2012.
- [9] D. Pallarola, A. Bochen, V. Guglielmini, T. A. Oswald, H. Kessler, and J. P. Spatz, "Highly ordered gold nanopatterned indium tin oxide electrodes for simultaneous optical and electrochemical probing cell interactions," *American Chemical Society Analytical Chemistry* 2017, 89, 18, 10054–10062, August 2017.

Metal nitride nanofilms applied in a microfluidic, impedimetric e-tongue for soil analyses

Carla Daniela Boeira
Gleb Wataghin Institute of Physics
Campinas State University
Campinas, Brazil
boeira@unicamp.br

Leonardo Mathias Leidens
Gleb Wataghin Institute of Physics
Campinas State University
Campinas, Brazil
leidens@unicamp.br

Maria Helena Gonçalves
Gleb Wataghin Institute of Physics
Campinas State University
Campinas, Brazil
maria.hg@ifi.unicamp.br

Fernando Alvarez
Gleb Wataghin Institute of Physics
Campinas State University
Campinas, Brazil
fernandoplasmaliits@gmail.com

Antonio Riul Jr.
Gleb Wataghin Institute of Physics
Campinas State University
Campinas, Brazil
riul@unicamp.br

Abstract—Efficient agricultural tools are crucial for precise agriculture, aiming to maximize productivity and resource efficiency while minimizing costs and environmental impacts. This involves the development of enhanced tools to efficiently map soil nutrients for precise agricultural input application. Smart sensors, including electronic tongues, streamline in-situ macronutrient detection, field sample collection, and remote monitoring, providing rapid and reliable qualitative and quantitative assessment of liquid samples. This study aims to coat the sensor units with advanced materials composed of metallic nitrides deposited through the Dynamic Glancing Angle Deposition (DGLAD) technique. This technique enables control over film thickness, porosity, and roughness, allowing for the direct use of these materials in sensor units to capture specific chemical species at the electrode interface, thereby facilitating the detection of these nutrients in soils.

Keywords—*e-tongue, DGLAD, nitrides, precision agriculture*

I. INTRODUCTION ()

The growing global demand for food, without a proportional increase in production area, emphasizes the necessity for a more effective utilization of agricultural and natural resources. This highlights the importance of creating improved tools for precision farming that allow for the efficient use of fertilizers and herbicides, thereby reducing costs and environmental impacts [1,2]. Accurate application of agricultural inputs demands effective mapping of macronutrients; however, the current expenses and time required for traditional physicochemical analyses lead to inadequate sample density for proper mapping [3]. Exploring the development of intelligent sensors for on-site macronutrient detection, simplified field sample collection, and automated remote monitoring, the utilization of electronic tongues simplifies monitoring and produces results with fast and dependable qualitative and quantitative evaluation of samples in liquid media [4]. Commercial sensors utilize interdigitated gold electrodes (IDEs), which require protective adaptations for use in harsh environments such as soils, without compromising their efficiency. To enhance the electrical and mechanical properties of these sensor units, coatings of metallic nitrides can be applied using the Dynamic Glancing Angle Deposition (DGLAD technique) [5]. This technique enables precise control over the growth of nanostructured thin films of metallic nitrides, such as TiN, CrN, and BN (titanium nitride, chromium nitride, and boron nitride respectively) [6,7]. These films exhibit distinct

physicochemical characteristics, including mechanical resistance to corrosion and suitability for biological applications. In addition to thickness control, manipulating the porosity and roughness of the metallic nitride films allows for their direct use on IDEs, resulting in more robust sensor units in harsh environments. The combination of these materials is also advantageous for exploring the cross-sensitivity of sensor units, essential for creating a fingerprint of the analyzed samples and facilitating subsequent recognition of soil macronutrients.

II. MATERIALS AND METHODS

A. Thin films deposition

The thin film deposition equipment used for sample preparation is a Multipurpose Thin Films machine equipped with an RF sputtering system, Model RF300, operating at 13.6 MHz with a maximum power of 300W, and a target approximately 5.1 cm in diameter. It also includes a modified sample holder allowing for angle variation during deposition. To prepare the samples, the chamber is evacuated to a pressure of $\sim 1.7 \times 10^{-4}$ Pa using a system of mechanical and turbomolecular pumps (Edwards, Next 400 Model). During film deposition, a constant flow of Ar:N₂ gas mixture fed by a mass flow controller (MKS, Series 600) maintains a working pressure of approximately 1 Pa through a downstream pressure control system. The RF power is set at 150 W for Titanium (Ti) and Chromium (Cr) targets and 75W for the boron nitride (BN) target. The films are deposited onto interdigitated electrodes (IDEs) printed on a printed circuit board (PCB) at room temperature (30°C). The distance between the targets and the PCB was maintained at 6 cm. The sample undergoes an oscillatory movement, shifting once from the target front to an angle of $\pm 85^\circ$. By automatically controlling the substrate support movement, atoms land on the substrate at different angles during the deposition process to achieve the desired nanostructure formation. In this study, three out of four IDEs were coated with nitride films (TiN, CrN, and BN). Deposition times were chosen based on the sputtering rate of each film to obtain films with the same thickness, while one IDE was left uncoated for comparison.

B. Solution analyses to Microfluidic e-Tongue Impedance Measurements

The printed circuit board was placed in a microchannel molded in PDMS, with dimensions of 500 micrometers in width and height, and 4 cm in length, covering the four

collinear detection units. Inlet and outlet ports were created using a biopsy punch. Subsequently, it was reversibly sealed through mechanical pressure using an acrylic plate and stainless steel screws on the PCB. Impedance measurements were conducted at frequency range of 1–10⁶ Hz using a Solartron 1260A impedance/gain-phase analyzer. Utilizing computer software developed by the M.L. Braunger, et al [1], the sensing units were automatically directed to the testing equipment during the experiment. All sensing units are housed within the same microchannel, where five independent measurements of each analyte were automatically executed. The operator's role was limited to manipulating the e-tongue setup for analyte changes and channel cleaning. Between each analyte sample, the device underwent a rinse with 5 mL of deionized water to prevent cross-contamination. Three solutions were employed as analytes in the system: ultrapure water, a 1 mmol solution of KCl, and a 1 mmol solution of NaCl. These solutions were utilized to assess the films' performance for salts that constitute soil macronutrients.

C. Data analyses

The open-source software Orange is employed for data analysis and visualization. The impedance data acquired from the electronic tongue undergo analysis and visualization within Orange using Principal Component Analysis (PCA), a statistical method facilitating the detection of patterns and structures within the original dataset. This process unveils relationships between variables and offers valuable insights for sample differentiation. In the context of electronic tongue data, the PCA score plot commonly reveals clusters grouping similar samples. Additionally, the software enables the utilization of the k-means algorithm to identify these clusters, with their efficacy assessed through the silhouette coefficient (SC).

III. RESULTS AND DISCUSSION

The utilized electronic tongue effectively distinguishes the solutions ultra-pure water, KCl, and NaCl solutions. The SC is calculated based on the number of principal components (PCs) used in PCA to reconstruct the original data. As observed in Figure 1a), an SC of 0.717 is noted for the uncoated electrode (bare); in Figure 1b), an SC of 0.834 is observed to electrode with CrN coated; in Figure 1c), an SC of 0.746 is observed to electrode with BN coated; and finally, for Figure 1d), an SC of 0.773 is observed to electrode with TiN coated. All SC values indicate a robust cluster structure and excellent discrimination between different analytes, suggesting successful differentiation among them. It is also verified that there are no signs of cross-contamination, indicating that tests demonstrate successful discrimination between NaCl and KCl at equimolar concentrations for the different IDEs studied.

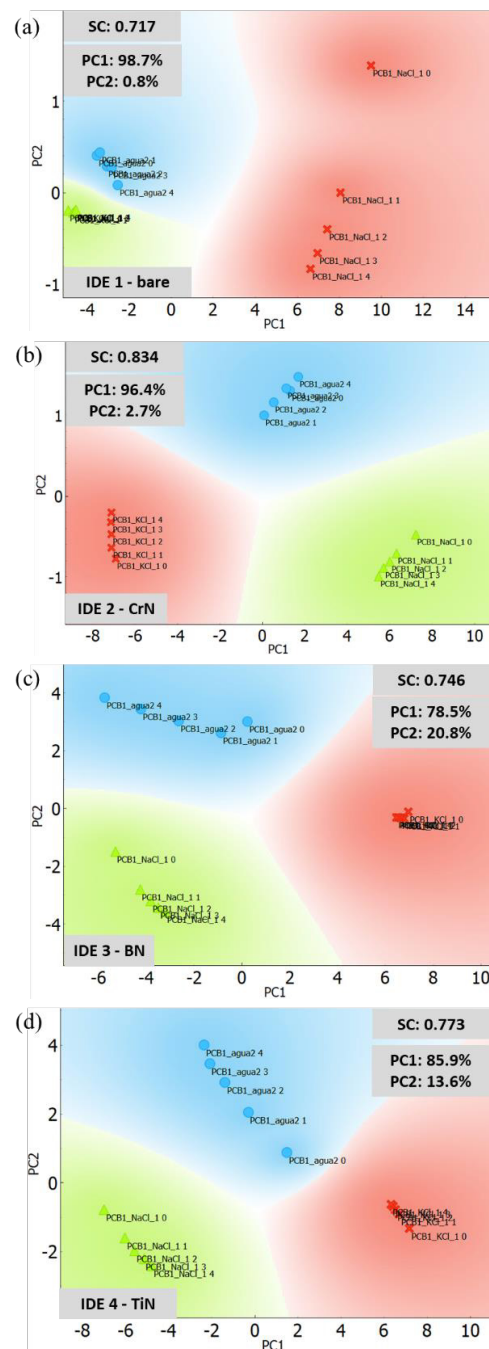


Figure 1. PCA score plots of the electronic tongue utilized here for the three different analytes for IDEs a) bare; and coated b)CrN; c)BN; d)TiN across the entire frequency range analyzed.

IV. CONCLUSION

The chosen nitrides exhibit distinct responses to the test solutions, showing successful discrimination between NaCl and KCl at equimolar concentrations for the different films deposited on the interdigitated electrodes. This advancement aims to simplify the detection of macronutrients in soil, potentially enhancing the device's selectivity for broader applications.

ACKNOWLEDGMENT

This work was supported partially by the Fundação de Amparo à Pesquisa do Estado de São Paulo (FAPESP) Projects #2023/07552-0 and #2022/08216-1, the Instituto Nacional de Engenharia de Superfícies (INES) and Instituto Nacional de Eletrônica Orgânica (INEO), CNPq and CAPES.

REFERENCES

- [1] M.L. Braunger, et al., "Microfluidic electronic tongue applied to soil analysis", *Chemosensors*. vol 5, pp 1–10, 2017. <https://doi.org/10.3390/chemosensors5020014>.
- [2] H.J. Kim, K.A. Sudduth, J.W. Hummel, "Soil macronutrient sensing for precision agriculture", *J. Environ. Monit.* vol. 11 1810–1824. 2009 <https://doi.org/10.1039/b906634a>.
- [3] R.A. Viscarra Rossel, et al. "Soil Sensing: An Effective Approach for Soil Measurements in Space and Time", Elsevier Inc., 2011. <https://doi.org/10.1016/B978-0-12-386473-4.00005-1.G>.
- [4] F.M. Shimizu, M.L. Braunger, A. Riul, "Electronic Tongues", IOP Publishing, Bristol, UK, 2021. <https://doi.org/10.1088/978-0-7503-3687-1>.
- [5] Taschuk, M. T., et al., "Handbook of Deposition Technologies for Films and Coatings". Science, Applications and Technology. vol 13 pp. 621-678, 2010. <https://doi.org/10.1016/B978-0-8155-2031-3.00013-2>
- [6] M.J.M. Jimenez, et al. "Effect of the period of the substrate oscillation in the dynamic glancing angle deposition technique: A columnar periodic nanostructure formation", *Surf. Coatings Technol.* vol. 383, pp. 125237, 2020. <https://doi.org/10.1016/j.surfcoat.2019.125237>.
- [7] V.G. Antunes, C.A. Figueroa, F. Alvarez, "A comprehensive study of the TiN/Si interface by X-ray photoelectron spectroscopy", *Appl. Surf. Sci.* vol 448, pp 502–509. 2018. <https://doi.org/10.1016/j.apsusc.2018.04.005>.

High-entropy nitride coatings applied as sensing units in an impedimetric e-tongue

Leonardo M. Leidens
“Gleb Wataghin” Institute of Physics
Campinas State University
Campinas, Brazil
leidens@unicamp.br

Carla D. Boeira
“Gleb Wataghin” Institute of Physics
Campinas State University
Campinas, Brazil
boeira@unicamp.br

Maria Helena Gonçalves
“Gleb Wataghin” Institute of Physics
Campinas State University
Campinas, Brazil
maria.hg@ifi.unicamp.br

Fernando Alvarez
“Gleb Wataghin” Institute of Physics
Campinas State University
Campinas, Brazil
fernandoplasmaliits@gmail.com

Antônio Riul Jr.
“Gleb Wataghin” Institute of Physics
Campinas State University
Campinas, Brazil
riul@unicamp.br

Abstract — The continuous evolution of sensing technologies has been vital in addressing complex challenges across various sectors, from quality assessment to medical diagnostics. Electronic tongues (e-tongues) are inspired by the human sense of taste and are a possible key tool in the rapid and sensitive detection of analytes based on their chemical signatures. Although a potential strategy, the system's reliability still presents some issues, such as contamination and low durability under harsh conditions. One of the possible solutions is the integration of advanced coatings on the surface of the sensor array. High-entropy nitride thin films, obtained by a modified physical vapor deposition technique, are preliminary suggested as candidates. More than protecting, these materials may add new functionalities and enhance the sensing capabilities based on the precise control of properties during deposition.

Keywords — E-Tongues, High-Entropy, Nitrides, Thin films

I. INTRODUCTION

Magnetron sputtering is known as a precise method within the physical vapor deposition (PVD) set of techniques, allowing for the controlled deposition of thin films with nanoscale precision. This technique enables the uniform coating of a myriad of substrates with materials of varying compositions. The versatility of magnetron sputtering makes it a relevant tool in fabricating functional coatings tailored for specific applications, from both scientific and technological points of view.

Among the materials already widely deposited by PVD is the whole class of metallic nitrides, such as chromium (CrN) and titanium nitrides (TiN). These films are used as protective coatings on demanding applications and a series of other possibilities. Once the system was well-explored, modifications were proposed to further explore the technique. Recently, a paper has shown that a modified CrN hard coating is obtained by including appropriated computer-controlled motion of the substrate relative to the sputtering target during deposition, i.e., by Dynamic Glancing Angle Deposition (DGLAD) [1,2]. Some other works [3,4] obtained peculiar nanostructures depending on the periods of oscillation of the substrate during deposition. These results have shown a promising modulation of the films' microstructural and mechanical properties such as a columnar multi-layered structure, residual stress, Young's modulus, crystallite size, hardness, and texture. Therefore, properties such as porosity and roughness could be controlled and permit the application on sensing devices with specific and selective pores.

More than this, the expertise of precisely controlling such films permitted the expansion of the frontiers, by producing other advanced materials, such as high entropy alloys (HEA) and their nitride form, high entropy nitrides (HEN).

High-entropy metallic alloys and high-entropy nitride thin films represent distinct classes of materials with unique characteristics and applications [5]. High-entropy metallic alloys, often referred to as high-entropy alloys (HEAs), are composed of multiple metallic elements in near-equimolar ratios, resulting in a random solid solution structure. These alloys exhibit exceptional mechanical properties, such as high hardness, tensile strength, and ductility, making them suitable for applications in structural materials, aerospace components, and high-temperature environments. In contrast, high-entropy nitride thin films consist of nitride-forming elements in equimolar proportions, offering enhanced hardness, wear resistance, and corrosion resistance. These thin films find applications as protective coatings, wear-resistant surfaces, and in advanced sensing technologies due to their tailored properties and compatibility with electronic devices.

The distinction lies in their elemental composition and the resulting properties, with high-entropy metallic alloys excelling in bulk mechanical properties and high-entropy nitride thin films excelling in surface properties and functional coatings [6]. The fundamental premise behind high-entropy thin films is to create materials with a multitude of elements, each contributing to the material's overall properties in a balanced manner. This approach offers several advantages. For example, the combination of multiple elements in equimolar ratios can lead to improved hardness, tensile strength, and ductility compared to conventional materials. Moreover, high-entropy thin films allow for the fine-tuning of electrical, optical, magnetic, and thermal properties by adjusting the composition and structure. Finally, regarding sensing and other applications, it is important to note that these materials can impart excellent corrosion resistance, oxidation resistance, and thermal stability to these films.

As cited, high-entropy nitride thin films represent a class of materials with remarkable mechanical strength, thermal stability, and chemical resistance. These films exhibit a synergistic combination of properties that surpass traditional coatings. When synthesized through magnetron sputtering, high-entropy nitride thin films offer enhanced durability and performance, making them ideal candidates for protective layers in electronic tongue sensor arrays [7].

The integration of magnetron sputtering, and high-entropy nitride thin films form suggests a new era in advanced sensing solutions. Electronic tongues equipped with these innovative

coatings may exhibit unparalleled sensitivity and reliability, making them important tools for environmental monitoring, food quality assessment, medical diagnostics, and beyond. The ability to tailor material properties and structures further enhances the adaptability of these sensors, ensuring their effectiveness across diverse applications.

Electronic tongues, inspired by the human sense of taste [7,8], support the rapid and sensitive detection of analytes based on their chemical signatures. By using high-entropy nitride thin films as functional coatings on sensor arrays produced via magnetron sputtering, electronic tongues gain unprecedented capabilities.

The key advantages of this integration include heightened sensitivity to analytes, enhanced selectivity against interferences, and prolonged durability under demanding conditions.

II. MATERIALS AND METHODS

Three different films were grown onto a PCB (printed circuit board) using the DGLAD technique [1,2]. In this set of experiments, two angular positions and two contents of nitrogen were explored. Figure 1 (a) and (b), respectively, schematically show the deposition system and expected deposition on the sensor.

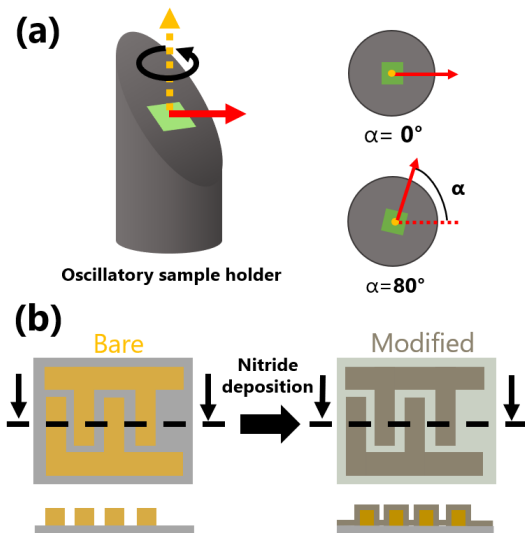


Figure 1. In (a) the schematic of the sample holder is presented, and two deposition angles are illustrated. The nitride deposition on the sensor is schematically shown in (b).

The substrate was introduced in the deposition chamber and it was pumped to a pressure of $\sim 6 \cdot 10^{-5}$ Pa using a system of mechanical and turbomolecular pumps (Edwards, Model nExt 400). The deposition chamber is equipped with a sputtering source (Model RF300, 13.6 MHz, 300 W maximum power, ~ 5.1 cm diameter target) and a moveable sample holder. The sputtering target was the multi-metallic target used to produce high-entropy thin films, as reported elsewhere [5,6], composed of Ti, Ta, V, Zr, and Nb. The target-to-substrate distance was approximately 6 cm. The high-entropy nitride (HEN) film depositions were performed in a chamber pressure of ~ 1 Pa (downstream throttle-controlled) discharge (using an RF system and a nominal power of 150 W) of a gaseous mixture of Ar (99.999%) and N_2 (99.999%)

independently fed through mass flow meters controllers (MKS, 600 Series). The three films were deposited onto interdigitated electrodes (IDEs) printed on a printed circuit board (PCB) at room temperature (30°C). The thickness of the films is maintained at ~ 100 nm. Currently, all the coatings are being subjected to physical and chemical characterization. At the same time, the potential use of the e-tongue is being explored with different solutions.

III. RESULTS AND DISCUSSION

Firstly, it is possible to note in Figure 2 (a) that the IDEs on which the films were deposited are different from the bare (used as a control). The micrographs shown in the same figure highlight the differences among the IDEs and the configuration being maintained even after deposition. Since the films are nanometric, it is possible to note the difference in the color. Indirectly, such a change also indicates the difference in the material.

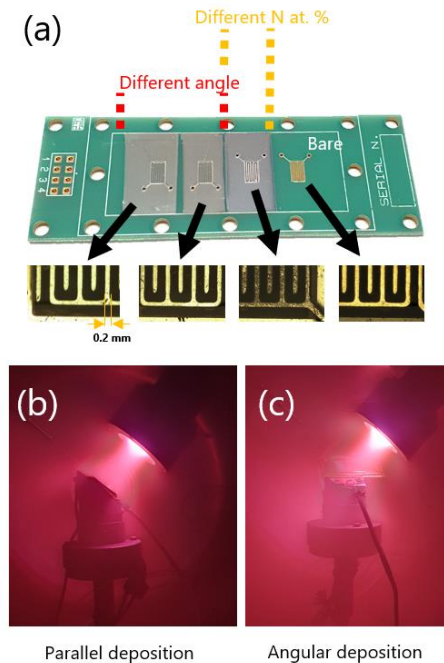


Figure 2. The PCB used for the deposition is presented in (a), with the macro- and micrographs of the bare and the modified IDEs. In (b) and (c), respectively, the depositions using the parallel and angular positions are shown.

Preliminary experiments show that the XRD pattern of the films changes when the deposition parameters are evaluated (not shown). Moreover, it was observed that the electric properties of the HEN thin films are different, making them suitable for exploration in the sensing tests (e-tongues).

IV. CONCLUSION

In conclusion, the collaborative efforts in harnessing magnetron sputtering and high-entropy nitride thin films form are propelling sensing technologies to unprecedented heights. The fusion of precision deposition techniques, advanced materials engineering, and functional coatings has

paved the way for next-generation electronic tongues capable of meeting the evolving demands of modern-day sensing challenges. As the research and development continue to unfold, we anticipate that the possibility of tuning the properties of HEN films at the same time of protecting the sensing units may enhanced the application of e-tongues on scenarios that are not possible to this day.

ACKNOWLEDGMENT

This work was supported partially by the Fundação de Amparo à Pesquisa do Estado de São Paulo (FAPESP) Projects #2023/07552-0 and #2022/08216-1, the Instituto Nacional de Engenharia de Superfícies (INES) and Instituto Nacional de Eletrônica Orgânica (INEO), CNPq and CAPES.

REFERENCES

- [1] M.J.M. Jimenez, V. Antunes, S. Cucatti, A. Riul, L.F. Zagonel, C.A. Figueroa, D. Wisnivesky, F. Alvarez, Physical and micro-nanostructure properties of chromium nitride coating deposited by RF sputtering using dynamic glancing angle deposition, *Surf. Coatings Technol.* 372 (2019) 268–277
- [2] M.J.M. Jimenez, V.G. Antunes, L.F. Zagonel, C.A. Figueroa, D. Wisnivesky, F. Alvarez, Effect of the period of the substrate oscillation in the dynamic glancing angle deposition technique: A columnar periodic nanostructure formation, *Surf. Coatings Technol.* 383 (2020) 125237.
- [3] M.O. Jensen, M.J. Brett, Porosity engineering in glancing angle deposition thin films, *Appl. Phys. A Mater. Sci. Process.* 80 (2005) 763–768.
- [4] D.X. Ye, T. Karabacak, R.C. Picu, G.C. Wang, T.M. Lu, Uniform Si nanostructures grown by oblique angle deposition with substrate swing rotation, *Nanotechnology.* 16 (2005) 1717–1723.
- [5] F. Cemin, L. Luis Artico, V. Piroli, J. Andrés Yunes, C. Alejandro Figueroa, F. Alvarez, Superior in vitro biocompatibility in NbTaTiVZr(O) high-entropy metallic glass coatings for biomedical applications, *Appl. Surf. Sci.* 596 (2022)
- [6] F. Cemin, S.R.S. de Mello, C.A. Figueroa, F. Alvarez, Influence of substrate bias and temperature on the crystallization of metallic NbTaTiVZr high-entropy alloy thin films, *Surf. Coatings Technol.* 421 (2021).
- [7] F.M. Shimizu, M.L. Braunger, A. Riul, “Electronic Tongues”, IOP Publishing, Bristol, UK, 2021.
- [8] M.L. Braunger, et al., “Microfluidic electronic tongue applied to soil analysis”, *Chemosensors.* vol 5, pp 1–10, 2017.

Effect of mineralizing agent on the performance of ceria-based nanomaterials towards gas sensors.

Miguel A. Ponce
Physics and Engineering Research
Center – CIFICEN (UNCPBA-
CICPBA-CONICET)
Tandil, Argentina
mponce.sensors@gmail.com

Celso M. Aldao
Institute of Scientific and
Technological Research in Electronics
(ICYTE), National Research Council
(CONICET), Mar del Plata, Argentina
cmaldao@fi.mdp.edu.ar

Carlos Macchi
CIFICEN (UNCPBA-CICPBA-
CONICET) and Instituto de Física de
Materiales Tandil (UNCPBA), Pinto
399, B7000GHG, Tandil, Argentina
cemacchi@gmail.com

Pedro Ortega
Center for Research and Development
of Functional Materials, Federal
University of São Carlos (UFSCar),
São Carlos, Brazil
pedro.ortega@hotmail.com

Alexandre Simoes Zirpoli
School of Engineering and Sciences,
São Paulo eState University (UNESP),
Guaratinguetá, Brazil
alezipo@yahoo.com

Leandro Silva Rosa Rocha
Materials Engineering Department,
Federal University of São Carlos
(UFSCar), São Carlos, Brazil
leandro.rocha@ufscar.br

Francisco Moura
Advanced Materials Interdisciplinary
Laboratory (LIMAv), Federal
University of Itajubá – Campus Itabira,
Itabira, Minas Gerais, Brazil
franciscomoura@unifei.edu.br

Abstract—In this work, thick films based on CeO₂ nanostructures were electrically tested upon CO atmosphere exposure. The samples were prepared with distinct chemical potential, using KOH (2 and 4 M) and NaOH (2 and 4 M) solutions. The nanostructures were synthesized using the microwave-assisted hydrothermal method and characterized via XRD, Raman, UV-Vis, specific surface area, and FEG-SEM techniques. The mineralizing agent and its associated chemical potential, used in the synthesis of CeO₂ nanostructures via MAH method, significantly changed the performance of the material towards CO-sensing.

INTRODUCTION

Semiconductor metal oxides stand out due to their unique physicochemical properties and its inherent properties such as high specific surface area in porous materials and tunable band gap energy, all of which can be modified to enhance the detection of hazardous and/ or explosive gases [1-2]. Despite having been extensively researched, there is still much room for improving the performance of metal oxides nanomaterials. In this regard, rare-earth oxides have proved to be an important class of multifunctional materials.

Cerium oxide (Ceria, CeO₂), as a well-known functional rare earth material, has been widely applied in fields such as catalysts, optics and gas sensors [3-4]. Its unique physicochemical properties rely on the availability of the outermost *4f* shell [5]. Considering the catalytic oxidation volatile organic compounds (VOCs), ceria stands out due to its redox property. Additionally, CeO₂ shows excellent thermal stability and oxygen storage capacity, which may be ascribed to its oxygen rich structure. The microstructure being closely related to the catalytic activity, CeO₂ shows excellent shape-selectivity especially to crystal plane defects [6-9]. Ceria is an n-type semiconductor with a direct band gap of 3.2 eV, has been considered the emerging material for gas sensing due to its quick response to the target gas [10]. Despite its advantages towards the sensing of a wide range of hazardous gases and extensive research, CeO₂ still lack key aspects to enable its practical application as gas sensors, *e.g.*, poor selectivity and low response. On the other hand, Rocha *et al.* [11], Ortega *et al.* [12], and Oliveira

et al. [13] focused on the synthesis and characterization of ceria nanoparticles doped with rare-earth elements (La, Eu, and Pr, respectively), showing how different doping concentrations affected their sensing response. Considering the application of CeO₂ nanostructures for CO gas sensing, it becomes important to understand the influence of MAH method parameters (*i.e.*, time and mineralizing agent) on the vacancies' formation, morphology and crystal plane defects of CeO₂ particle morphology. In this context, this work provides a comprehensive analysis of the structural and optical properties of CeO₂ nanostructures synthesized via MAH method, employing KOH (2 and 4 M) and NaOH (2 and 4 M) as mineralizing agents. Thus, we provide insights into the chemical potential associated to the type of mineralizing agent and how it affects defects dynamics within the materials' structure and, its utmost influence in the CO-sensing response with neutral, reducing and oxidant atmospheres.

EXPERIMENTAL SECTION

Ceria nanostructures (CeO₂) were synthesized via MAH. First, cerium nitrate (Ce(NO₃)₃·6H₂O, Sigma-Aldrich-purity 99.9%) was dissolved in 40mL of distilled water under constant magnetic stirring at room temperature for homogenization. In this mixtures, NaOH (2 and 4 M) and KOH (2 and 4 M) solutions were added drop-wise until pH 10 to obtain the samples named NaOH 2M, NaOH 4M, KOH 2M, and KOH 4M, respectively. Both mineralizer agents employed (NaOH and KOH) were acquired from Synth (99.9 % purity). At this stage, a light-yellow slurry solution, derived from Ce hydroxides precipitation, was observed. The solution color turned purple after agitation for 1 hour. This solution was then transferred into a sealed Teflon container and placed inside a microwave oven (2.45 GHz, 800 W) as previous published by our group [11]. Structural, optical and microstructural characterization of the nanostructures were investigated according to the data previously published in the literature [13]. The band-gap energy was determined from the UV-Vis data. Tauc plots via the Kubelka-Munk function allows assigning the y-axis corresponding to the transformed Kubelka-Munk function ($[F(R_{\infty})/hv]^{1/2}$) and the x-axis to

the photon energy. The band-gap energy corresponds to the interception point between the extrapolation of the linear fit of the curves and the x-axis. Thick films, Figure 1, were prepared from the nanostructures synthesized via MAH and electrically measured [13]. First, various heating and cooling cycles with a rate of 5°C/min in vacuum were performed before the resistance values were measured, in order to remove moisture from the surface. Then, air (atmospheric pressure) and carbon monoxide (100 mmHg and 200mmHg) atmospheres were introduced and the changes in resistance were observed over time, with an applied excitation current of 1 mA, using the two-wire technique with a DC-type measurement. An Agilent 3440 A multimeter was used for the electrical resistance measurements. Figure 1 illustrates the schematic film deposition.

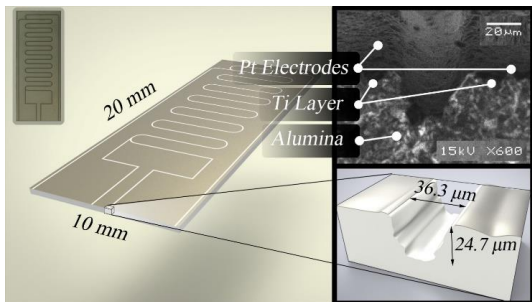


Figure 1. Thick films shape.

STRUCTURAL CHARACTERIZATION

Figure 2 (a-b) shows the XRD diffraction patterns obtained for all samples - KOH 2M, KOH 4M, NaOH 2M, and NaOH 4M.

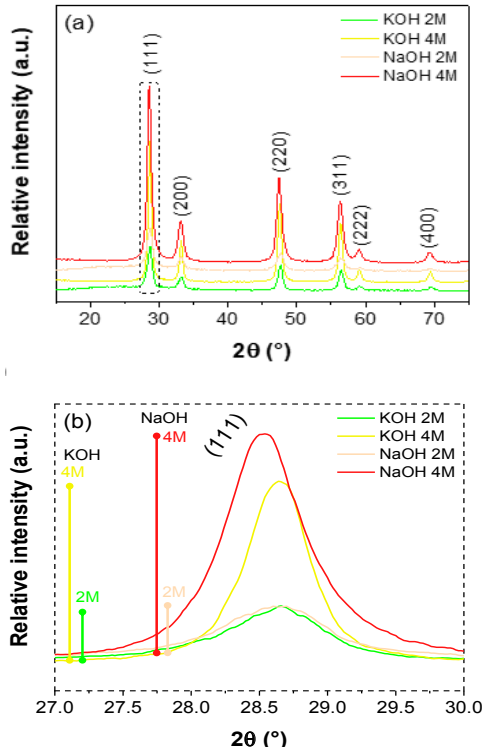


Figure 2. DRX diffraction patterns

All peaks were well indexed to the pure fluorite-like cubic structure of CeO₂ (ICSD #24887), without any secondary phase peaks. As a consensus, two mechanisms can explain the CeO₂ particle growth in hydrothermal conditions: oriented attachment (OA) and Ostwald ripening (OR) [14–16], with the OA occurring because of effective collisions among nuclei with the same crystallographic orientation followed by the OR process, also known as dissolution-recrystallization, which causes an increase in the crystallinity of CeO₂ nanoparticles. Given the low solubility of ceria particles in water, the OR process plays an important role in hydrothermal reactions, forming crystals with defined morphologies via the dissolution of smaller nuclei [17]. According to the XRD results the peaks in the pattern become more intense and defined, as the chemical potential of NaOH and KOH increases.

OPTICAL RESPONSE

Figure 3 (a-d) shows Tauc plots for all samples, while the respective band gap values can be found in Table 1. It is known that vacancies cause disorder in the crystalline lattice of ceria by exciting electrons in the forbidden region of the band-gap. As a consequence, the semiconductor has its band-gap reduced, thus resulting in increased intrinsic conductivity. As reported, the pristine ceria has a band-gap value of 6eV stemming from electronic transitions between O 2p–Ce 5d levels. However, the presence of structural defects can reduce this value due to an intermediate transition to empty Ce 4f levels, as observed in reduced ceria samples.

ELECTRICAL CHARACTERIZATION OF SENSORS

Figure 4 (a-d) shows the electrical response, resistance vs. time, recorded under different atmospheres (air, CO and vacuum). These measurements were carried out in order to verify the response (in terms of resistivity) of the CeO₂ sensor film obtained using different chemical potentials and mineralizing agents. The results indicate a significant drop in the response time (t_{resp}) of the films

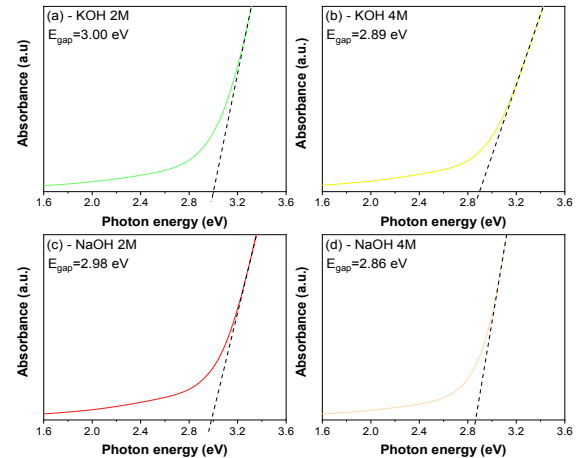
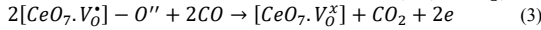
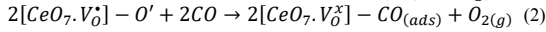
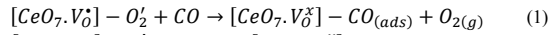


Figure 3. Tauc plots.

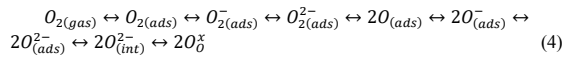
Samples	FWHM (cm ⁻¹)	I _d /I _{F2g}	E _g
KOH 2M	16.62	0.102	3.00
KOH 4M	18.96	0.042	2.89
NaOH 2M	28.60	-	2.98
NaOH 4M	18.64	-	2.81

Table 1.

when KOH was used as a mineralizing agent. The recovery time of all films was in the order of tenths of a second. Sensing of CO molecules occurs following a well described mechanism, where oxygen (O_2) is adsorbed and ionized on the surface of the film, turning into O^- and O^{2-} ions through electron capture. The increase in conductance with increasing CO concentration is correlated with its reducing behavior, causing it to release electrons in the conduction band. Its action on the CeO_2 surface can be represented by Equations 1–3:



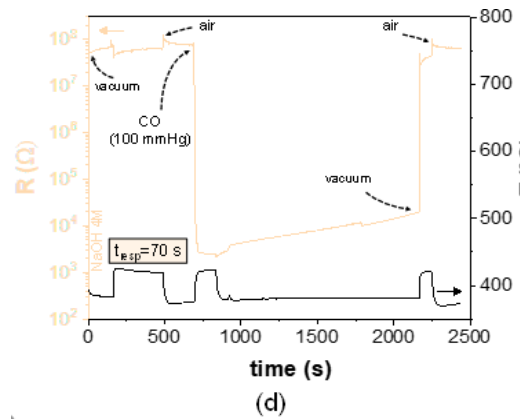
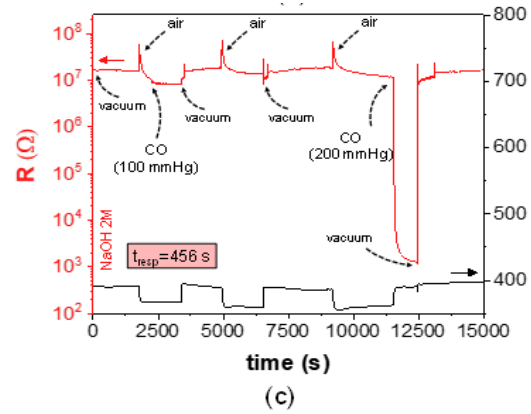
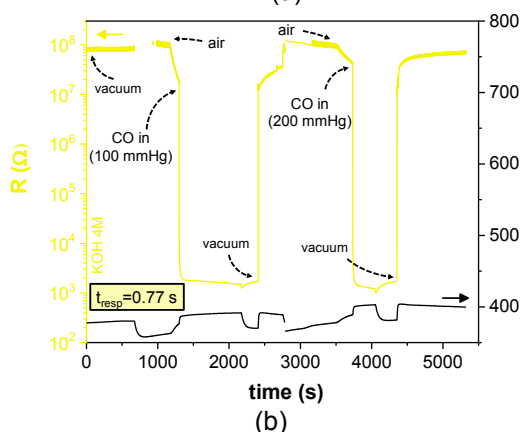
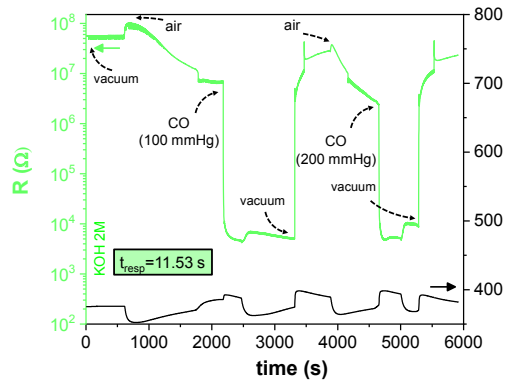
Above $200^\circ C$, the adsorbed oxygen can in-diffuse, annihilate vacancies, and therefore reduce the number of charge carriers, as shown by Equation 4. Inversely, if the oxygen undergoes an out-diffusion, vacancies can be formed, as follows:



Interstitial oxygen can migrate to the surface, generating oxygen vacancies (V_O^i) if the sample is treated with a reducing agent such as CO, according to Equation 5:



Therefore, after treatment at $400^\circ C$ in carbon monoxide atmosphere, an increase in the amount of oxygen vacancies is expected. At this point, it is worth mentioning that the samples were stored in ambient conditions and that, before the measurements, three heating cycles up to $400^\circ C$ were performed at a heating rate of $5^\circ C/min$ to assure the elimination of adsorbed oxygen species and humidity.



CONCLUSIONS

The CeO_2 thick films synthesized with KOH showed a superior sensing behavior towards CO detection due to an increase in the long-/short-range disorder within the CeO_2 structure, decreasing the E_{gap} value, facilitating light absorption and increasing the surface area. The sensing response towards CO was investigated under different operating temperatures, CO concentrations, and synthetic air. As expected for chemoresistive gas sensors, increasing the operating temperature and CO concentration improved the response to CO. The response time of sample KOH 4 M ($t_{resp}=0.77$ s) significantly improved compared to the samples synthesized with NaOH ($t_{resp}=456$ and 70 s from NaOH 2 M and NaOH 4 M, respectively). Ultimately, the results showed in this study prove that the mineralizing agent, and its associated chemical potential, used in the synthesis of CeO_2 nanostructures via MAH method significantly change the performance of the material towards CO-sensing. The use of KOH 4 M as mineralizing agent yielded the best response. These results provide promising developments for gas sensing applications.

ACKNOWLEDGMENT

The authors would like to thank the following Brazilian agencies for their financial support: The National Council for Scientific and Technological Development (CNPq) and the São Paulo Research Foundation (FAPESP) (grants Nos. 13/07296-2 (CEPID), 2018/20590-0 (PD) and 2020/02352-5 (BEPE)). We also acknowledge the funding from the Agencia Nacional de Promoción Científica y Tecnológica, Argentina (PICT 2015-1832) and the Consejo Nacional de Investigaciones Científicas y Técnicas, Argentina (PUE 22920200100016CO-IFIMAR).

REFERENCES

- [1] Hoskins JA. Carbon Monoxide: The Unnoticed Poison of the 21 st Century. *Indoor and Built Environment* 1999;8:154–5. <https://doi.org/10.1177/1420326X9900800305>.
- [2] Liu F, Lin X, Zhang M. Global, Regional, and National Burden of Accidental Carbon Monoxide Poisoning, 1990–2019: A Systematic Analysis for the Global Burden of Disease Study 2019. 2020. <https://doi.org/10.21203/rs.3.rs-129365/v1>.
- [3] Mattiuzzi C, Lippi G. Worldwide epidemiology of carbon monoxide poisoning. *Hum Exp Toxicol* 2020;39:387–92. <https://doi.org/10.1177/0960327119891214>.
- [4] Rocha LSR, Aparecido Ciola Amoresi R, Duarte TM, Marana NL, Sambrano JR, Aldao CM, et al. Experimental and theoretical interpretation of the order/disorder clusters in CeO₂:La. *Applied Surface Science* 2020;510:145216. <https://doi.org/10.1016/j.apsusc.2019.145216>.
- [5] Michael da Silva Procópio A, Silva Rosa Rocha L, Mariela Desimone P, Giulietti G, Manuel Aldao C, Longo E, et al. Effect of thermal treatment on the 4f-hopping conductivity of CeO₂ exposed to CO(g) atmosphere. *Materials Science and Engineering: B* 2023;292:116403. <https://doi.org/10.1016/j.mseb.2023.116403>.
- [6] Yan D, Mo S, Sun Y, Ren Q, Feng Z, Chen P, et al. Morphology-activity correlation of electrospun CeO₂ for toluene catalytic combustion. *Chemosphere* 2020;247:125860. <https://doi.org/10.1016/j.chemosphere.2020.125860>.
- [7] Cao T, You R, Li Z, Zhang X, Li D, Chen S, et al. Morphology-dependent CeO₂ catalysis in acetylene semihydrogenation reaction. *Applied Surface Science* 2020;501:144120. <https://doi.org/10.1016/j.apsusc.2019.144120>.
- [8] Deus RC, Cilense M, Foschini CR, Ramirez MA, Longo E, Simões AZ. Influence of mineralizer agents on the growth of crystalline CeO₂nanospheres by the microwave-hydrothermal method. *Journal of Alloys and Compounds* 2013;550:245–51. <https://doi.org/10.1016/j.jallcom.2012.10.001>.
- [9] Deus RC, Foschini CR, Spitova B, Moura F, Longo E, Simões AZ. Effect of soaking time on the photoluminescence properties of cerium oxide nanoparticles. *Ceramics International* 2014;40:1–9. <https://doi.org/10.1016/j.ceramint.2013.06.043>
- [10] Sayle TXT, Parker SC, Catlow CRA. The role of oxygen vacancies on ceria surfaces in the oxidation of carbon monoxide. *Surface Science* 1994;316:329–36. [https://doi.org/10.1016/0039-6028\(94\)91225-4](https://doi.org/10.1016/0039-6028(94)91225-4).
- [11] Rocha LSR, Cilense M, Ponce MA, Aldao CM, Oliveira LL, Longo E, et al. Novel gas sensor with dual response under CO(g) exposure: Optical and electrical stimuli. *Physica B: Condensed Matter* 2018;536:280–8. <https://doi.org/10.1016/j.physb.2017.10.083>.
- [12] Ortega PP, Rocha LSR, Cortés JA, Ramirez MA, Buono C, Ponce MA, et al. Towards carbon monoxide sensors based on europium doped cerium dioxide. *Applied Surface Science* 2019;464:692–9. <https://doi.org/10.1016/j.apsusc.2018.09.142>.
- [13] Cristina de Oliveira R, Cabral L, Cabral AC, Almeida PB, Tibaldi N, Sambrano JR, et al. Charge transfer in Pr-Doped cerium oxide: Experimental and theoretical investigations. *Materials Chemistry and Physics*, 2020;249:122967. <https://doi.org/10.1016/j.matchemphys.2020.122967>.
- [14] Lin M, Fu ZY, Tan HR, Tan JPY, Ng SC, Teo E. Hydrothermal Synthesis of CeO₂ Nanocrystals: Ostwald Ripening or Oriented Attachment? *Crystal Growth & Design* 2012;12:3296–303. <https://doi.org/10.1021/cg300421x>.
- [15] Wu N-C, Shi E-W, Zheng Y-Q, Li W-J. Effect of pH of Medium on Hydrothermal Synthesis of Nanocrystalline Cerium(IV) Oxide Powders. *Journal of the American Ceramic Society* 2002;85:2462–8. <https://doi.org/10.1111/j.1151-2916.2002.tb00481.x>.
- [16] Yuan Q, Duan H-H, Li L-L, Sun L-D, Zhang Y-W, Yan C-H. Controlled synthesis and assembly of ceria-based nanomaterials. *Journal of Colloid and Interface Science* 2009;335:151–67. <https://doi.org/10.1016/j.jcis.2009.04.007>.
- [17] de Oliveira RC, Amoresi RAC, Marana NL, Zaghete MA, Ponce M, Chiquito AJ, et al. Influence of Synthesis Time on the Morphology and Properties of CeO₂ Nanoparticles: An Experimental–Theoretical Study. *Crystal Growth & Design* 2020;20:5031–42. <https://doi.org/10.1021/acs.cgd.0c00165>.

Synthesis, structural and electrical characterization of ZnO:In₂O₃ heterostructures

Samantha Custódio Silva Lemos
Physical and Analytical Chemistry
Department
Universitat Jaume I
Castellón de la Plana, Spain
custodio@uji.es

Miguel A. Ponce
Physics and Engineering Research
enter (CIFICEN-CONICET)UNCPBA
Tandil, Argentina
mponce.sensors@gmail.com

Matias E. Mazzei
Institute of Materials Science and
Technology (INTEMA-CONICET)
University of Mar del Plata
Mar del Plata, Argentina
matias.mazzei.96@gmail.com

Celso M. Aldao
Institute of Scientific and Technological
Research in Electronics (ICYTE)
University of Mar del Plata
Mar del Plata, Argentina
cmaldao@fi.mdp.edu.ar

Daniel Coelho do Amaral
Advanced Materials Interdisciplinary
Laboratory (LIMAv)
Federal University of Itajubá, Campus
Itabira, Itabira, Minas Gerais, Brazil
(daniel.strides@gmail.com)

Paula M. Desimone
Institute of Materials Science and
Technology (INTEMA-CONICET)
University of Mar del Plata
Mar del Plata, Argentina
desimone.mariela@gmail.com

Elson Longo
Center of Research and Development of
Functional Materials (CDMF), Federal
University of São Carlos (UFSCar),
São Carlos, SP, Brazil
elson.liec@gmail.com

Marcelo Assis
Biomaterials and Bioengineering Lab
Translational Research Centre San
Alberto Magno, Catholic University of
Valencia San Vicente Mártir (UCV)
Valencia, Spain
marcelostassis@gmail.com

Abstract— In this work, we investigated films based on In₂O₃ and ZnO heterostructures and the influence of their relative composition on CO detection. Powders were synthesized by the microwave-assisted hydrothermal method. XRD and Raman spectroscopy confirmed the formation of wurtzite ZnO, a body-centered In₂O₃ structure and In₂O₃:ZnO heterostructures. The 25%Zn/75%In sample has better performance towards CO detection because its higher concentration of carriers and oxygen vacancies.

Keywords—heterostructures, zinc oxide, indium oxide, carbon monoxide detection.

I. INTRODUCTION

Problems associated with pollution and environmental safety require real-time monitoring of the medium conditions, given the flammable, explosive or toxic nature of released gases. Therefore, gas detection devices provide an essential service in verifying the conditions of industrial and domestic environments, playing an important role in reducing adverse effects, to humans and environment, resulting from exposure to certain gases [1-3].

In the field of materials science, metal oxide semiconductors attract great interest due to their high stability and the possibility of withstanding a wide range of changes to make them suitable for a specific application. In this context, the rich chemistry of metallic oxide semiconductors constitutes a remarkable aspect, mainly attributed to the presence of structural and electronic defects, as well as variable structural deficiencies of oxygen, which can modify several aspects, such as structure, size, properties and morphology, affecting the surface and defining its own characteristics. In this context, the development of gas sensors based on semiconductor metal oxides has shown enormous potential in the detection of gases such as hydrogen, acetone and carbon monoxide [4-6]. The value of the sensor response is due to the change in conductivity of the sensitive metal oxide layer, so the gas detection properties of a metal oxide system are modulated by factors such as particle size, morphology, crystalline and electronic structure.

The controllable design and precise modulation of the functional properties of materials has always been the goal of materials researchers. The present work deals with the

preparation of high active material surfaces, based on In₂O₃ and ZnO heterostructures prepared by the microwave assisted hydrothermal method, adjusting synthetic parameters on the obtaining of different phases crystallization and in the manipulation of the morphologies, and consequently, unveiling characteristics of the exposed surfaces. The sensing performance evaluation will include study on phenomena related to the morphology, structural and electronic arrangement of the material, exploring the synergic effect of the oxides in the formation of high selectivity sensors.

II. EXPERIMENTAL SECTION

A. Synthesis procedure

The samples were obtained by dissolving 0.004 moles of the cation in 50 ml of distilled water. Under constant stirring, 30 drops of HNO₃ were added to this solution. The precursor for indium used was In(CH₃CO₂)₃ and for zinc, it was Zn(CH₃CO₂)₃·2H₂O. The pH of the solutions was adjusted to 12.0 using an aqueous solution of KOH (3M). To obtain samples with different In/Zn ratios, the proportional variation of the mole quantity of the cations was carried out. The prepared solutions were transferred to an autoclave and sealed to undergo the microwave heating process. The solutions were heated to 160 °C for 32 minutes, with a heating rate of 10 °C/min. The precipitated powder was washed several times with distilled water and ethanol. The samples namely Zn, SJ1, SJ2, SJ3, SJ4, SJ5, and In corresponds to pure ZnO, 87.5% Zn/12.5% In, 75% Zn/25% In, 50% Zn/50% In, 25% Zn/75% In, 12.5% Zn/87.5% In, and pure In₂O₃.

B. Characterizations

The structural properties of the samples were thoroughly examined using a variety of advanced techniques. X-Ray Diffraction (XRD) analysis was employed to characterize the crystalline phase, utilizing a D/Max-2500PC instrument. Raman spectroscopy, with an iHR550 spectrometer equipped with a charge-coupled device detector, and an Argon-ion laser operating at 633 nm (with a power output of 200mW), provided further insights. Morphological assessments were conducted using a SEM Supra 35-VP microscope at 5 kV.

For the electrical characterization, a paste composed of 1,2-propanediol as the organic binder and the powder of the sample, was meticulously prepared and deposited onto a silicon wafer acting as a substrate. For the creation of an interdigitated structure, a 200 nm thick platinum layer was sputter-deposited onto the substrate, as detailed elsewhere [7]. Following paste deposition, and to enhance adhesion and facilitate binder evaporation, the samples were subjected to a 24-hour drying process at 100°C in ambient air. Subsequently, the samples underwent a heating step at 200°C for 1 hour in an air atmosphere, with a heating rate of 1°C/min, aimed at completely evaporating the binder. Subsequent to these preparations, the electrical measurements were conducted. The investigation of this material electrical behavior in the presence of carbon monoxide gas provides valuable insights into its response mechanisms. The measurements took place within a controlled chamber, ensuring precise regulation of temperature, pressure, and gas composition. The electrical resistance was quantified using an Keithley 2110 digital multimeter. Initially, two heating and cooling cycles were carried out in the presence of air (1 atm), vacuum (10^{-4} atm), and CO (0.13 atm) to assess the films performance at specific temperatures within these distinct atmospheres. By tracking changes in conductivity, it was feasible to ascertain the material response under different atmospheres.

III. RESULTS AND DISCUSSION

The XRD technique provides information about long-range order in the structure. From the analysis of Fig. 1, peaks indexed to the wurtzite-type structure of zinc oxide (JCPDS 36-1451, space group P63mc) and peaks corresponding to the cubic body-centered In_2O_3 structure (JCPDS 06-0416, space group $\text{Ia}\bar{3}$) are observed. In sample SJ5 (12.5% Zn/87.5% In), in addition to the peaks of the bcc- In_2O_3 structure, a peak at $2\theta = 32.63^\circ$ corresponding to the (110) plane of the rhombohedral phase rh- In_2O_3 is observed, according to PDF no. 72-0683 (JCPDS, [1969]), indicating the formation of a mixture of bcc and rh- In_2O_3 phases. The Raman spectra of the samples display characteristic bands of the vibration modes of In_2O_3 and ZnO (Fig. 2). The band around 437 cm^{-1} corresponding to ZnO wurtzite structure is related to the E_2 (high) mode. The peaks at 101, 334 and 581 cm^{-1} are ascribed to E_{2L} , $3E_{2H}-E_{2L}$ and $E_1(\text{LO})$ phonon modes, respectively. The main signals related to the bcc- In_2O_3 were observed at 131 cm^{-1} (A_{1g}), which is related to In-O (vibration of InO_6 structure units), at 308 cm^{-1} , attributed to the bending vibration of the InO_6 octahedron (superposition of the F_{2g} and A_g modes), and at 497 and 633 cm^{-1} are also assigned to the stretching vibrations of the InO_6 octahedrons. The Raman spectrum of SJ5 presents a strong band at 162 cm^{-1} , attributed to the A_g symmetry of rh- In_2O_3 , indicating the coexistence of cubic and rhombohedral phases of In_2O_3 , which is in agreement with the X-ray diffraction characterization. The FEG-SEM analysis of the powders is depicted in Fig. 3, revealing distinct morphologies for each sample. In the pure ZnO sample (Zn), a homogeneous distribution of particles with a size of 40 nm is observed. As we progress to sample SJ1, a heterogeneous medium emerges, characterized by the initial

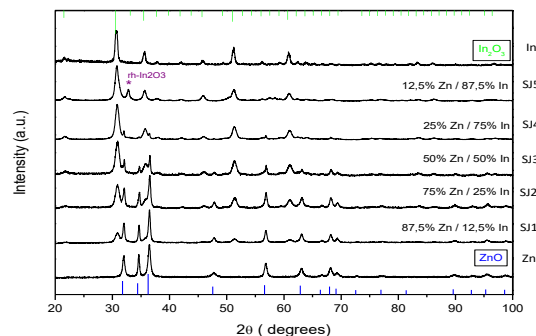


Fig. 1. XRD patterns of the samples.

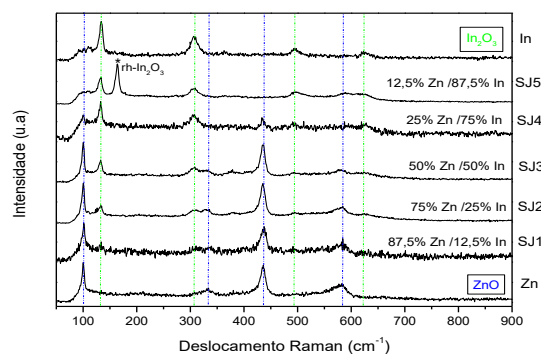


Fig. 2. Raman spectra at room temperature of the samples.

formation of elongated structures. With an increase in In content, a well-defined cylindrical morphology is observed. Further elevating the In content leads to the formation of faceted cylindrical structures. Notably, in sample SJ4, where the proportion of Zn decreases relative to In (25% Zn/75% In), a significant reduction in particle size occurs. Conversely, as the In content increases to 87.5%, particle size enlarges, accompanied by the formation of cubes. Lastly, the sample composed of pure In_2O_3 (In) exhibits the formation of smaller cubes compared to those observed in SJ5.

To observe the dependence of conductivity (G) with temperature (T), the variation of conductance versus the inverse of temperature is shown in Fig. 4. This plot is also known as an Arrhenius plot ($G = A \cdot \exp(-E_a/kT)$, where A is the prefactor, E_a is the effective activation energy, and k is the Boltzmann constant).

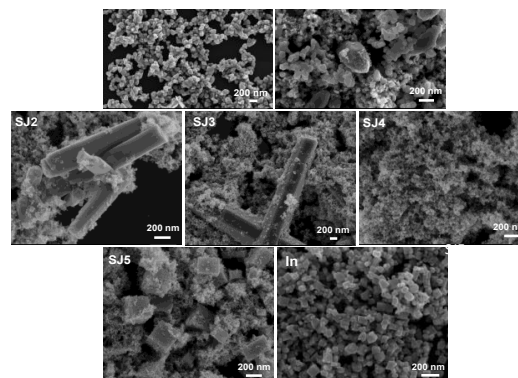


Fig. 3. FEG-SEM images of the samples

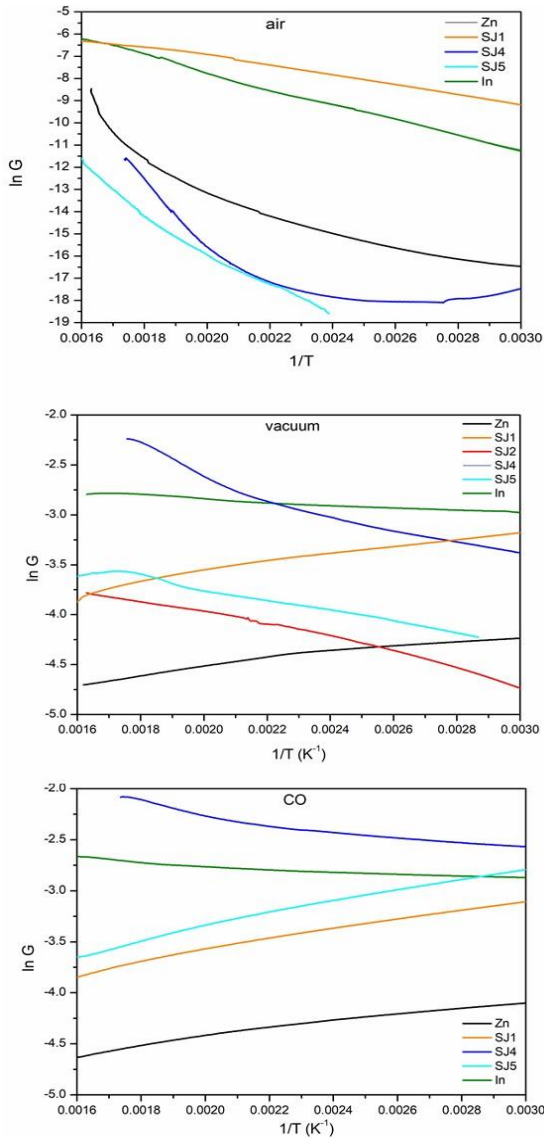


Fig. 4. Arrhenius plot of the samples films in air, vacuum, and CO atmospheres.

The effective activation energy was estimated from the slope of the cooling down process from 350 °C to 30 °C in air. The activation energies and the prefactors for each film are presented in Table 1. Fig. 4 shows that the conductance increases following the sequence: air, vacuum, and carbon monoxide, for each sample. The increase in the conductance could be characterized by a rise in electron concentration which implies the diffusion of oxygen out of the grains. This behavior implies the creation of oxygen vacancies. The conductance of SJ4 sample is higher than other samples, which could be explain because of the rise of the prefactor value (Table 1), which is related to the density of carriers.

IV. CONCLUSIONS

In summary, high active material surfaces, based on In_2O_3 and ZnO heterostructures were prepared by the microwave assisted hydrothermal method at low temperature. XRD

analysis of the different nanostructures confirmed the formation of the wurtzite structure of zinc oxide, cubic

TABLE I. Values of the Ea and A calculated for the samples.

Sample	Ea (eV)	A
ZnO	0.42	0.00406
SJ1	0.64	5.388
SJ4	0.79	8.68
SJ5	0.74	4.87
In	0.30	0.49009

body-centered In_2O_3 structure and mixtures of bcc and rh- In_2O_3 phases. Raman analysis is in agreement with the X-ray diffraction characterization. The FEG-SEM analysis of the powders showed distinct morphologies for each sample. Sample SJ4 showed a better response toward CO than the other samples. This result could be related to a higher density of carriers.

ACKNOWLEDGMENT

The authors acknowledge the University of Mar del Plata and National Research Council (CONICET). This work was supported by the ANPCyT (Agencia Nacional de Promoción Científica y Tecnológica, Argentina) and CONICET (grants PICT-2021-I-INVI-0652 and PIBAA0661). Also, this work was funded in part by Fundação de Amparo à Pesquisa do Estado de São Paulo – FAPESP (FAPESP CEPID-finance code 2013/07296-2), Financiadora de Estudos e Projetos – FINEP, Conselho Nacional de Desenvolvimento Científico e Tecnológico – CNPq, and Coordenação de Aperfeiçoamento de Pessoal de Nível Superior – CAPES (finance code 001). M.A. acknowledges the “Juan de la Cierva” fellowship with code JDC2022-049934-I.

REFERENCES

- [1] I. Boehme, U. Weimar, N. Barsan, “Unraveling the Surface Chemistry of CO Sensing with In_2O_3 Based Gas Sensors”, *Sensors and Actuators B: Chemical*, vol. 326, p. 129004, January 2021.
- [2] K. Hu et al, “Ternary heterojunctions synthesis and sensing mechanism of Pd/ZnO– SnO_2 hollow nanofibers with enhanced H_2 gas sensing properties”, *Journal of Alloys and Compounds*, v. 850, p. 156663, 2021.
- [3] P.P. Ortega, L.S.R. Rocha, J.A. Cortés, M.A. Ramirez, C. Buono, M.A. Ponce, A.Z. Sinoes, “Towards carbon monoxide sensors based on europium doped cerium dioxide”, *Applied Surface Science*, v. 464, p. 692–699, 2019.
- [4] G.N. Gerasimov, V.F. Gromov, M.I. Ikim, O.J. Illegbusi, S.A. Ozerin, L.I. Trakhtenberg, “Structure and gas-sensing properties of SnO_2 - In_2O_3 nanocomposites synthesized by impregnation method”, *Sensors and Actuators B: Chemical*, v. 320, October 2020.
- [5] L.S.R. Rocha, R.A.C. Amoresi, H. Moreno, M.A. Ramirez, M.A. Ponce, C.R. Foschini, E. Longo and A.Z. Simoes, “Novel Approaches of Nanoceria with Magnetic, Photoluminescent, and Gas-Sensing Properties”, *ACS Omega*, v. 5, n. 25, p. 14879–14889, June 2020.
- [6] B. Yang, Z. Zhang, C. Tian, W. Yuan, Z. Hua, S. Fan, Y. Wu, X. Tian, “Selective detection of methane by HZSM-5 zeolite/Pd- SnO_2 gas sensors”, *Sensors and Actuators B: Chemical*, vol. 321, p. 128567, October 2020.
- [7] C. Macchi, M.A. Ponce, P.M. Desimone, C.M. Aldao, A. Somoza, “Vacancy-like defects in nanocrystalline SnO_2 : influence of the annealing treatment under different atmospheres”, *Philos. Mag. Part A: Mater. Sci.* 98 (8), p. 673–692, 2017.



7 |

Sensores en electrónica impresa

Printed electronic sensors

Sensores em eletrônica impressa

Dispositivos electrónicos impresos mediante tecnología Inkjet basados en nanopartículas de plata

Fabián De Vita

Laboratorio Nanofab

Fundación Argentina de Nanotecnología Fundación Argentina de Nanotecnología Fundación Argentina de Nanotecnología

Buenos Aires, Argentina

fdevita@fan.org.ar

Martín Lucero

Laboratorio Nanofab

Buenos Aires, Argentina

mlucero@fan.org.ar

Brian Daniel Horowicz

Laboratorio Nanofab

Buenos Aires, Argentina

bhorowicz@fan.org.ar

Abstract—En este trabajo se generaron distintos dispositivos electrónicos utilizando tintas conductoras de nanopartículas de plata depositadas sobre distintos sustratos empleando tecnología inkjet. Se investigaron distintos parámetros de fabricación como pulso de eyección, cantidad de boquillas, viscosidad de tinta y condiciones de post tratamiento. Para la impresión de los distintos electrodos se empleó una impresora semi industrial con tecnología inkjet, con capacidad de realizar post tratamiento de sinterizado. Con los dispositivos impresos desarrollados, se ensamblaron sensores de presión y temperatura, los cuales fueron testeados dentro del laboratorio.

Index Terms—Nanopartículas de plata, electrónica impresa, tintas conductoras, sensores

I. INTRODUCCIÓN

En la última década aumentó considerablemente el número de publicaciones que hacen referencia a la utilización de distintos tipos de tintas funcionales basadas en nanomateriales, en la producción de distintos dispositivos impresos flexibles, que tienen como aplicación final su uso en distintos wearables, dispositivos IOT, textiles inteligentes y cuidado de la salud.

La formulación de tintas conductoras es una tarea compleja en la cual debemos considerar distintos parámetros, entre ellos, viscosidad, tensión superficial, el sustrato en el que se depositarán y la flexibilidad final del material. Además, la formulación tiene que mantenerse estable en el tiempo, para evitar la obstrucción de los cabezales del sistema de impresión. Por lo tanto, la tarea de formulación de tintas es uno de los procesos fundamentales, y se utilizan elementos como material conductor, estabilizantes, solventes, entre otros. Sin embargo, los componentes de las tintas funcionales deben seleccionarse cuidadosamente, para que las pistas fabricadas tengan la conductividad deseada luego del sinterizado.

Para depositar las tintas funcionales existen diversas técnicas: flexografía, screen printing inkjet printing, entre otros. La tecnología de inkjet consiste en un sistema de cabezales que permiten la eyección de tintas con un control preciso. De esta manera permite la producción de pistas con una resolución micrométrica, ajustando parámetros como el número de boquillas, pulsos y frecuencias empleadas. Este proceso cuenta con la ventaja de obtener valores bajos en términos de costos y tiempos de producción.

En la Fundación Argentina de Nanotecnología (FAN), dentro de su laboratorio nanofab, existe una planta piloto de

electrónica impresa, en la cual distintas compañías de toda la argentina desarrollan numerosos dispositivos electrónicos impresos gracias al equipamiento Ceradrop Ceraprinter con el que se cuenta. Desde su instalación, se desarrollan diariamente desde sensores de presión, CO_2 y baterías de litio ultra delgadas.

En este trabajo se presentarán distintos casos de aplicación a partir de la producción de tintas funcionales de plata y el posterior desarrollo de dispositivos flexibles aplicados a la industria. [1] [2] [3] [4]

II. EXPERIMENTAL

A. Preparación de tintas conductoras

La tinta se preparó utilizando nitrato de plata ($AgNO_3$) que es la fuente de iones plata, un agente estabilizante y un reductor.

En un primer paso se sintetizaron las nanopartículas de plata, mediante reducción química. Una fracción de nitrato de plata se disolvió en agua bidestilada, y se calentó a $90^\circ C$, luego se añadieron distintas proporciones del agente reductor (borohidruro de sodio, monoetanolamina) bajo agitación magnética a 400 rpm durante 20 min. Siguiendo se añadió el agente estabilizante (polivinilpirrolidona, ácido poliacrílico) gota a gota, bajo agitación magnética a 400 rpm.

Las partículas obtenidas fueron lavadas a través de ciclos de coagulación y lavado. Para ello a las partículas recién obtenidas se les añadió una fracción de acetona, y mediante centrifugación se descartó el sobrenadante. Al sedimento se lo resuspendió en etanol absoluto. El ciclo se repitió cinco veces para eliminar el exceso de estabilizante. [1] [2] [3] [4]

B. Caracterización de tintas conductoras

Las tintas obtenidas fueron caracterizadas mediante microscopía de fuerza atómica (AFM) Nanosurf Flex AFM. Espectrometría UV-Visible DLAB modelo UV1000. Determinación de viscosidad Viscosímetro rotacional MYR V2L

C. Diseño de sensores a fabricar

El diseño de sensores se generaron en curvas/vectores, utilizando un software de código libre de diseño, implementado para el cálculo, simulación y desarrollo de circuitos electrónicos. El mismo permite exportar el diseño para ajustar

la dimensión en el área de impresión, en extensión dxf. Para la fabricación de los dispositivos se tuvo en cuenta su geometría y la resolución de cada uno de los componentes evitando los posibles problemas al momento de imprimir los distintos patrones. Los archivos obtenidos se importan en el software slicer propio de la marca del equipo inkjet, se ajustan los parámetros necesarios y se carga en el software de impresión final.

D. Aplicación de tintas

Para verificar el proceso de impresión por inyección de tinta y evaluar el desempeño de cada formulación, las tintas se utilizaron para la impresión mediante el equipo Ceradrop Ceraprinter x-series, empleando cartuchos piezoeléctricos de 2.4 pL. Los parámetros seleccionados en la impresora inkjet Ceradrop Ceraprinter fueron los representados en la tabla 1.

Antes de las pruebas de impresión, las tintas fueron previamente filtradas con un filtro de jeringa de Nylon 0,20 μm para evitar la obstrucción de las boquillas por la formación de agregados de partículas. Después de la filtración, las tintas se sonicaron durante 10 minutos para eliminar las burbujas. Se emplearon distintos tipos de sustratos base, entre ellos papel fotográfico brillante, Kapton, y vidrio.

A las impresiones realizadas se les realizó un post proceso térmico, empleando el horno infrarrojo del equipo y luego por medio de una manta calefactora a 150°C durante 2hs.

TABLE I: Parámetros del proceso inkjet. [1] [3]

Parámetro de impresión	Valor asignado
Distancia entre gotas	10 μm
Diámetro de gotas	30 μm
Frecuencia de impresión	1500 Hz
Número de boquillas empleadas	8
Número de capas impresas por sensor	3

III. RESULTADOS

A. Preparación y caracterización de tintas conductoras

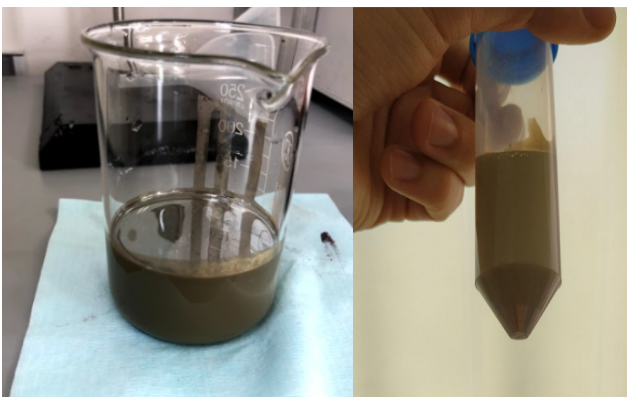


Fig. 1: Tintas sintetizadas en el laboratorio.

En la Fig. 3 se muestran imágenes obtenidas de microscopia AFM realizadas en modo tapping, donde se puede observar que las partículas obtenidas presentan una morfología esférica.

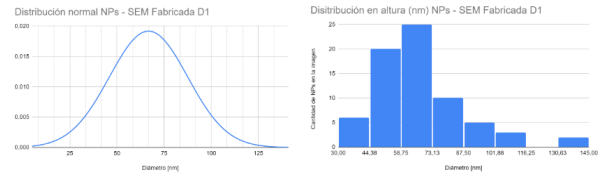


Fig. 2: Distribución de tamaños nanopartículas sintetizadas.

A su vez se muestra un gráfico Fig. 2 que demuestra la distribución de tamaño de las nanopartículas obtenidas, siendo el tamaño medio de aproximadamente 66,73 nm y un desvío estándar de 20,77 nm. Esta morfología es acorde al proceso de impresión inkjet que se quiere llevar a cabo, ya que el tamaño de las partículas sintetizadas disminuyen la posibilidad de obturar las boquillas del cabezal del equipo.

La formulación de la tinta tiene que ser tal que los patrones impresos sean conductores luego del post tratamiento de curado a cierta temperatura, y además tengan una viscosidad y tensión superficial adecuada para su correcta eyección.

Para el proceso de impresión inkjet es fundamental conocer los valores de viscosidad de las tintas a utilizar. Este valor debe estar entre 8 y 12 cPs, para que la tinta pueda ser eyectada sin grandes dificultades.

Por un lado, si la viscosidad del fluido es demasiado alta (> 30 cPs a temperatura ambiente), es fácil de ajustar. Se puede utilizar un cabezal con calefacción de manera que la viscosidad disminuya con la temperatura. Otro método es disminuir la concentración del contenido sólido dentro de la tinta.

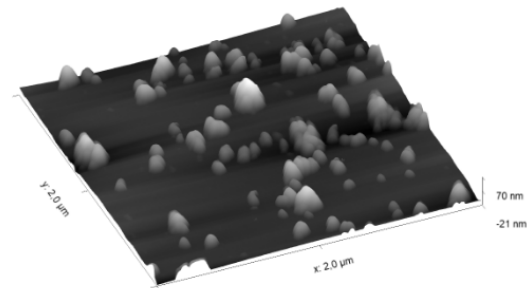


Fig. 3: Tintas sintetizadas en el laboratorio.

Por otro lado, si la viscosidad de la tinta es demasiado baja, puede modificarse la tinta agregando humectantes miscibles con agua, de baja volatilidad, como etilenglicol o glicerol.

En el laboratorio se realizaron mediciones de viscosidad empleando un viscosímetro rotacional MYR V2L.

Se analizaron tintas de plata con contenido sólido de entre 8% y 40%. Las tintas con mayor contenido sólido presentaron una viscosidad promedio de 37 cPs, con lo cual fue necesario aumentar la temperatura del cabezal para poder eyectarlas sin complicaciones.

El rango de viscosidades medidas para tintas de contenido sólido de entre 8% y 40% van de 10 a 37 cPs respectivamente, con lo cual son compatibles para su uso en tecnología inkjet.

B. Aplicación de tintas

Todas las tintas formuladas en el laboratorio presentaron una correcta eyección en todo el rango de pulsos estudiado (Fig. 4).

Los pulsos se variaron desde 15 a 45V y la frecuencia de eyección entre 500 a 1500Hz.

Empleando estos parámetros, fue posible realizar el prototipo de distintos sensores.

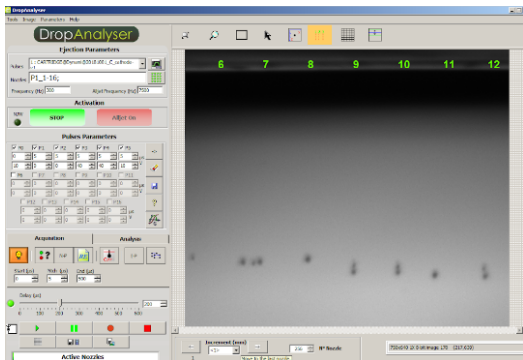


Fig. 4: Imagen software empleado para control de eyección de gotas.

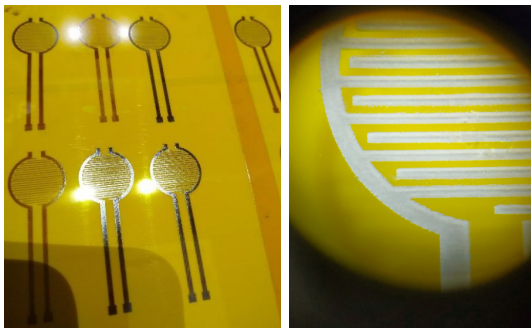


Fig. 5: Sensores de presión FSR impresos empleando kapton como sustrato.

Dentro de los sensores fabricados mediante electrónica impresa en la Fundación Argentina de Nanotecnología se encuentran los sensores de presión o FSR (Fig. 5). Este desarrollo fue llevado a cabo junto con la startup Ebers Biomed. El acceso a este tipo de tecnología inkjet permitió que la empresa pudiera llevar a cabo las primeras etapas de desarrollo de la geometría y distribución de sus sensores (Fig. 6).

Por otro lado se imprimieron sensores de temperatura sobre papel fotográfico como sustrato (Fig. 7). Esta matriz fue desarrollada en aproximadamente 15 minutos de impresión. Lo que brinda una ventaja en cuanto a tiempos de producción



Fig. 6: Aplicación de los sensores de presión flexibles para la producción de plantillas inteligentes para prevenir amputaciones.

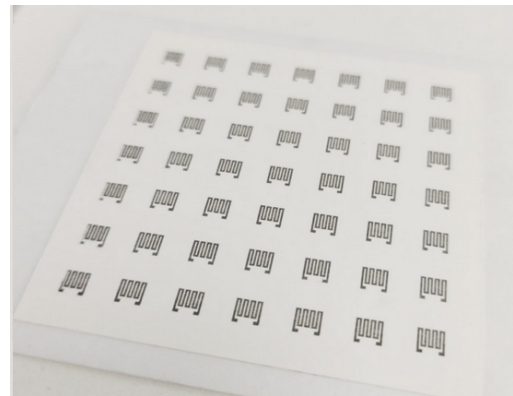


Fig. 7: Matriz de sensores de temperatura impresos sobre papel fotográfico.

y baja cantidad de materia prima necesaria para el prototipado de sensores.

Actualmente la FAN se encuentra trabajando junto con una empresa del rubro Agro, en el desarrollo de sensores de temperatura y CO_2 para su aplicación en cultivos, empleando electrónica impresa.

REFERENCES

- [1] Aroche A.F. Schuck A. et al. Fernandes, I.J. Silver nanoparticle conductive inks: synthesis, characterization, and fabrication of inkjet-printed flexible electrodes. 2020.
- [2] Ming-Hsiu Tsai Jung-Tang Wu, Steve Lien-Chung Hsu and Weng-Sing Hwang. Inkjet printing of low-temperature cured silver patterns by using agno3/1-dimethylamino-2-propanol inks on polymer substrates. *The Journal of Physical Chemistry C*, 2011.
- [3] H.W. Lee Q.J. Liew. Inkjet-printed flexible temperature sensor based on silver nanoparticles. 2020.
- [4] Q. Huang Q. Xu W. Shen, X. Zhang and W. Song. Preparation of solid silver nanoparticles for inkjet printed flexible electronics with high conductivity. 2014.

Sensor resistivo flexible desarrollado con tecnologías de electrónica impresa

Fabrizio Pascual
Horacio Berardi
Ingeniería Electrónica
Universidad Nacional de San
Martín (UNSAM)
Buenos Aires, Argentina
fberardi@estudiantes.unsam.edu.
ar

Damian Ricalde
Dto. Prototipado
Microelectrónico y Electrónica
Impresa
Instituto Nacional de Tecnología
Industrial
Buenos Aires, Argentina
dricalde@inti.gov.ar

Julián Marinoni
Dto. Prototipado
Microelectrónico y Electrónica
Impresa
Instituto Nacional de Tecnología
Industrial
Buenos Aires, Argentina
marinoni@inti.gov.ar

Mariano Roberti
Dto. Prototipado
Microelectrónico y Electrónica
Impresa
Instituto Nacional de Tecnología
Industrial
Buenos Aires, Argentina
froberty@inti.gov.ar

Theo Rodríguez Campos
Dto. Prototipado
Microelectrónico y Electrónica
Impresa
Instituto Nacional de Tecnología
Industrial
Buenos Aires, Argentina
trodriguez@inti.gov.ar

Alex Lozano
DT. de Micro y Nanotecnologías
Instituto Nacional de Tecnología
Industrial
Buenos Aires, Argentina
alozano@inti.gov.ar

Mijal Mass
Dto. Prototipado
Microelectrónico y Electrónica
Impresa
Instituto Nacional de Tecnología
Industrial
Buenos Aires, Argentina
*mmass@inti.gov.ar

Liliana Fraigi
Escuela de Ciencia y Tecnología
UNSAM
Dto de Electrónica
Universidad Nacional
Tecnológica – UTN-FRBA
Buenos Aires, Argentina
lili@frba.utn.edu.ar

Resumen — Los sensores resistivos flexibles tienen una amplia gama de aplicaciones, desde la monitorización de movimientos articulares del cuerpo humano hasta la medición de parámetros mecánicos industriales. En este trabajo se describe el análisis, diseño, fabricación y caracterización de un sensor resistivo, de bajo costo, impreso por un proceso de serigrafía sobre un sustrato flexible. El diseño propuesto permite variar el valor de la resistencia final modificando sólo una máscara de las tres que involucra su proceso de fabricación. Se obtuvo un sensor flexible de precisión, con una dispersión menor al 0,3%, que permite detectar al menos, cuatro radios de curvatura diferentes (125, 90, 65 y 50mm) además del valor de reposo (R_0) y capaz de realizar más de mil flexiones garantizando su desempeño. Estos sensores se desarrollaron en la planta piloto de Electrónica Impresa del Instituto Nacional de Tecnología Industrial (INTI).

Palabras clave— electrónica impresa, sensor flexible, sensor resistivo, impresión funcional, fabricación aditiva.

I. INTRODUCCION

El constante avance de la tecnología y la creciente automatización en el sector industrial presentan oportunidades y desafíos en el ámbito del desarrollo de dispositivos electrónicos flexibles. En particular, los sensores flexibles, han adquirido un papel protagónico en diversas aplicaciones gracias a sus atributos de flexibilidad, elasticidad y estabilidad. Su alcance es esencial tanto en la detección de movimiento humano [1,2], en la monitorización y diagnósticos clínicos [3,4], en la creación de piel electrónica adaptable (*e-skin*) [5], como en la implementación de pantallas táctiles flexibles [6], y hasta en la integración en robots industriales [7].

Dentro de la categoría de sensores flexibles, se destacan los sensores resistivos, por su capacidad de medir cambios en la resistencia eléctrica en respuesta a deformaciones mecánicas. Esta propiedad los hace ideales para aplicaciones que requieren una alta sensibilidad y precisión, convirtiéndolos en componentes esenciales en sistemas de monitoreo y control [8]. Así mismo, la Electrónica Impresa (EI) se presenta como una tecnología emergente que puede

suplir las necesidades de estos sensores resistivos flexibles, siendo livianos, adaptables, de bajo costo de fabricación y accesibles.

En el presente trabajo se realizó el análisis, diseño, fabricación y caracterización de sensores resistivos impresos flexibles (SRIF) para ser utilizados en la medición de movimientos articulares, mediante guantes de rehabilitación, brazos robóticos o exoesqueletos y dispositivos de interacción/interfaces dirigidos por gestos humanos.

II. EXPERIMENTAL

A. Diseño

Con el objetivo de evaluar el cambio de la resistencia de los SRIF en función de la deformación, se diseñó un sensor que cuenta con 14 resistores en serie de 5mm x 5mm, (L_c x W) conectados mediante conductores de 1mm (L_{Ag}) x 5mm (W), dando como resultado un sensor con una zona activa de 84mm de largo y 91mm en total, considerando los pads de contacto, según la “Fig. 1”. Esta configuración permite ajustar el valor de la resistencia total, sólo modificando el largo L_{Ag} de la capa conductora “Metal 2”. Es decir, el valor de la resistencia final es inversamente proporcional a L_{Ag} .

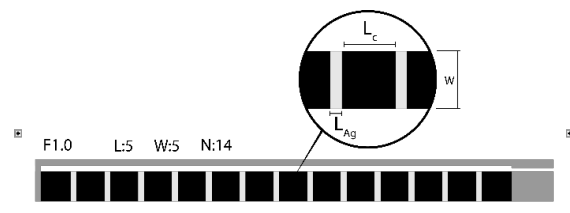


Fig. 1. Diseño del sensor resistivo flexible impreso con el detalle de las dimensiones de L_{Ag} , L_c y W .

En la “Fig. 2” se observan las 3 capas que configuran al sensor. La “Fig. 2a” muestra el diseño de la máscara de la primera capa conductora (Metal 1); la “Fig. 2b” la capa

resistiva y la “Fig. 2c” la última capa conductora (Metal 2) que se imprime sobre la capa resistiva. Mediante esta secuencia de fabricación, se puede obtener una familia de SRIF con el mismo largo y diferentes valores de la resistencia final modificando sólo el L_{Ag} .

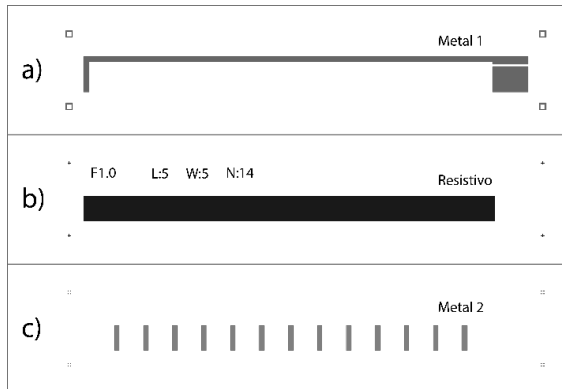


Fig. 2. Diseño de las máscaras del sensor resistivo flexible impreso: (a) Metal 1; (b) Resistiva; (c) Metal 2.

Las diferentes capas de los sensores fueron generadas mediante un programa de diseño CAD (Inkscape). Las máscaras se fabricaron, en una empresa gráfica nacional, sobre una filmina con una resolución de 3600 dpi.

B. Materiales y proceso de impresión

Se seleccionó la impresión serigráfica como proceso de fabricación de los SRIF. Se utilizó una impresora serigráfica semiautomática (EKRA modelo Microtronic II) ajustando los parámetros de impresión (presión, velocidad, *snap off*, material de espátulas) para lograr la fidelidad dimensional del diseño y espesor característico del proceso.

Para la fabricación de los sensores se utilizó una tinta conductora de plata (Ag) (SCAG-003, Mateprincs) y una tinta resistiva de carbón (C) (C2030519P4, Gwent). Teniendo en cuenta las especificaciones de sus hojas de datos, se seleccionaron las mallas con la cantidad de hilos por pulgada (*mesh*) adecuadas para cada tinta. La transferencia de los diseños a dichas mallas se realizó mediante un proceso fotolitográfico sobre una película fotosensible de 50 μ m (Ulano®).

Las impresiones se realizaron sobre sustratos de tereftalato de polietileno (PET) de 100 μ m de espesor. El curado de las tintas se realizó en un horno de secado Thermal TH400DH y, para no alterar las condiciones de los sustratos, se variaron las condiciones de curado especificadas por los fabricantes, prolongando los tiempos y reduciendo la temperatura (TABLA I).

TABLA I - TIEMPOS Y TEMPERATURAS DE CURADO PARA LAS TINTAS UTILIZADAS EN LA FABRICACIÓN DE LOS SENSORES

Tinta	Curado
Conductora (Plata) (Mateprincs-SCAG-003)	60' @ 80°C
Resistiva (Carbón) (Gwent-C2030519P4)	30' @ 60°C

Por último, los SRIF se laminaron con el adhesivo bifaz 467MP de 3M, a través de un probador flexográfico QD™ Flexo, con una fuerza de 1,26 kgf/cm² sobre un PET (Mylar® cristal, Decom) de 250 μ m de espesor para darle mayor rigidez y estabilidad al sensor. Finalmente, el largo total del dispositivo SRIF fabricado es de 110mm.

III. CARACTERIZACIÓN

Una vez fabricados los sensores se llevó a cabo la caracterización dimensional y eléctrica.

A. Caracterización dimensional

Se midieron y compararon las dimensiones en los ejes X e Y de los diseños de las máscaras, de su transferencia a las mallas y de las impresiones, mediante la cámara fiducial de la impresora inkjet Dimatix modelo DMP-2850, con resolución micrométrica. En lo que respecta a la caracterización de los espesores, se utilizó un perfilómetro por interferometría (Zeiss modelo 5104802).

B. Caracterización eléctrica

Se utilizó un SMU (Unidad de Fuente y Medida) Keithley 2602B, en conexión a 2 hilos debido a que el valor de la resistencia de los sensores es superior a 1K Ω .

La caracterización eléctrica por deformación mecánica es fundamental para comprender cómo responden estos sensores ante fuerzas de deformación controladas.

Para la caracterización mecánica dinámica, se desarrolló un sistema automatizado con un motor paso a paso (Nema 17) y mordazas de caras planas paralelas. Mediante éste se llevaron a cabo ensayos cíclicos de los SRIF, permitiendo un control preciso (6,78 μ m por paso) y repetible de las condiciones de ensayo. Además, se logró evitar de esta manera la manipulación de las muestras en cada conexión y desconexión “Fig. 3”.

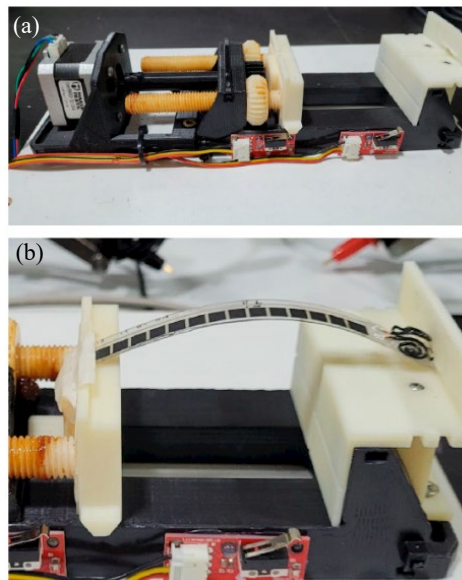


Fig. 3. Sistema de caracterización automatizado. (a) Banco de ensayo mecánico. (b) Caracterización dinámica de un sensor resistivo impreso flexible fabricado por serigrafía con tintas de Ag y C.

Considerando este sistema de caracterización dinámico, se toma como parámetro de comparación, el radio de curvatura que tendrá el sensor al flexionarse. Este parámetro, se relaciona matemáticamente con el ángulo que forma el sensor flexionado a través de la longitud de un arco de circunferencia (“Fig 4”) y se puede calcular según (1).

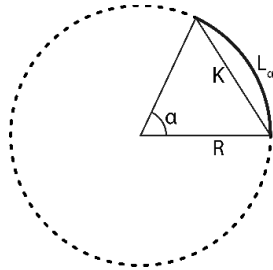


Fig. 4. Diagrama de la cuerda de una circunferencia. Siendo R el radio de curvatura, La el largo del arco, α el ángulo y K el largo de la cuerda que une los puntos de esta circunferencia sin cruzar por el centro.

$$\alpha = \frac{L\alpha}{R} \quad (1)$$

Por otra parte, como el sistema de caracterización genera un movimiento axial, relacionamos por trigonometría nuestra variable de control, K, siguiendo (2).

$$K = 2 \cdot R \cdot \sin \frac{\alpha}{2} \quad (2)$$

Dicho esto, y según caracterizaciones preliminares en las que observamos que no se obtenían diferencias apreciables entre los valores de las resistencias medidas con radios de curvatura mayores a 150mm, se decide comenzar a trabajar con radios a partir de 125mm.

Finalmente, se establecieron cuatro radios de curvatura de: 125 (R125), 90 (R90), 65 (R65) y 50mm (R50), además del valor de reposo (R_{∞}) y se llevaron a cabo las mediciones como se muestra en la “Fig. 5”. Cabe mencionar que, entre una medición y otra, el sensor permanece en reposo durante 5 segundos, mientras que entre cada ciclo, el tiempo de reposo fue de 90 segundos.

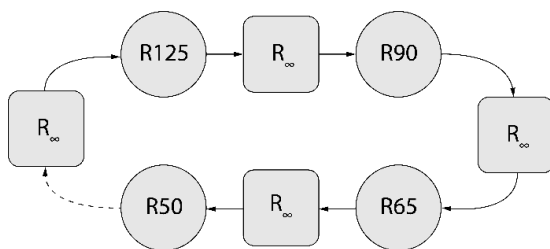


Fig. 5. Diagrama de un ciclo completo de mediciones. Se repitieron 300 ciclos por cada SRIF.

Se ensayaron 3 SRIF con el mismo diseño y proceso de fabricación, repitiendo cada ciclo un total de 300 veces con el objetivo de obtener la desviación de los valores de resistencia para cada uno de los puntos de medición.

Por último, se estudió la estabilidad de la resistencia de los sensores sin deformación en función de las variaciones de temperatura. Las muestras, fueron expuestas a diferentes

temperaturas desde 25°C hasta 65°C con incrementos de 5°C, dejando estabilizar los valores en cada medición.

IV. RESULTADOS

De las caracterizaciones dimensionales y eléctricas se obtuvieron los siguientes resultados.

A. Caracterización dimensional

Se pudo observar que las dimensiones en los ejes X e Y de los sensores se redujeron aproximadamente 30µm. Este valor representa menos del 1%, considerándose despreciable para el funcionamiento de estos dispositivos. A su vez, dicho valor se encuentra dentro de los márgenes de error de la tecnología empleada.

Los resultados de las mediciones de espesor se muestran en la TABLA II:

TABLA II - ESPESORES DE LAS TINTAS EN LOS SENSORES IMPRESOS.

Tinta	Espesores promedio [µm]
Conductora (Plata) (Mateprincs-SCAG-003)	29
Resistiva (Carbón) (Gwent-C2030519P4)	27

B. Caracterización eléctrica

En la “Fig. 6” se muestran los valores promedio, máximo y mínimo de las variaciones de resistencia de los sensores en función de los radios de curvatura establecidos.

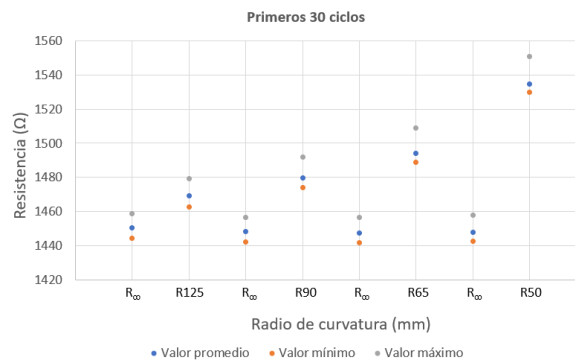


Fig. 6. Valores de resistencias en los primeros 30 ciclos.

Durante los primeros 30 ciclos se observan los valores promedio de resistencia para cada radio de curvatura (marca azul), los cuales permiten distinguir una variación en la resistencia de los SRIF. Sin embargo, debido a la alta dispersión de las mediciones, los valores máximos (marca gris) obtenidos son muy próximos a los valores mínimos (marca naranja) del radio de curvatura inmediato superior. Esta alta dispersión impide diferenciar con claridad en qué nivel de deformación se encuentra el sensor.

Luego de realizar 300 ciclos por cada sensor, se observó una disminución significativa en la dispersión de las mediciones para cada radio de curvatura, obteniéndose como resultado cinco puntos bien diferenciados, como se puede observar en la “Fig. 7”.

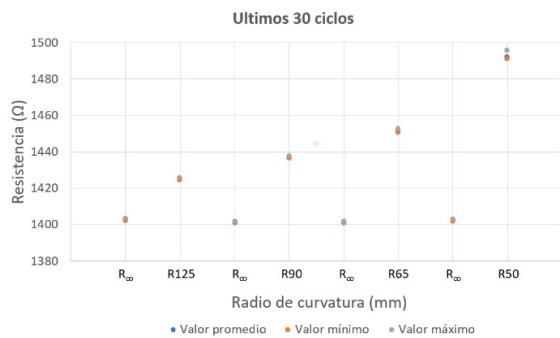


Fig. 7. Valores de resistencias en los últimos 30 ciclos.

Comparando los resultados de las primeras mediciones realizadas con estas últimas (“Fig. 6” y “Fig. 7”), se puede observar que los valores de las resistencias y sus dispersiones tienden a disminuir, alcanzando valores de dispersión en el rango de 0,28% a 0,06%.

En cuanto a la caracterización térmica, los valores de resistencia no se vieron afectados de manera significativa con el aumento de la temperatura.

V. CONCLUSIONES

Como resultado de este trabajo se pueden obtener las siguientes conclusiones:

- Se logró desarrollar una serie de sensores resistivos impresos flexibles (SRIFs), mediante un proceso serigráfico, de bajo costo y factible para su producción local y regional.
- Se logró un diseño que permite variar fácilmente el valor de la resistencia final, modificando sólo una máscara en el proceso de fabricación del dispositivo.
- Se fabricó y caracterizó un conjunto de sensores resistivos impresos flexibles, capaces de discriminar variaciones de resistencia de manera precisa, para radios de curvatura de 125mm, 90mm, 65mm y 50mm y en su posición de reposo (R_{∞}).
- Se observó que los sensores fabricados en este trabajo mejoraban su precisión al aumentar la cantidad de ciclos de

flexión, alcanzando una dispersión menor al 0,3% al llegar a los 300 ciclos.

- Los sensores fabricados fueron sometidos a más de mil flexiones sin alterar su correcto funcionamiento, lo cual evidencia un alto ciclo de vida.

- De los resultados obtenidos en las caracterizaciones térmicas se desprende que, la resistencia de los sensores no sufre cambios significativos con la variación de la temperatura en el rango ensayado de 25°C a 65°C.

RECONOCIMIENTOS

Los autores agradecen la colaboración de los alumnos de la Cátedra de Tecnología Electrónica, curso 2023, de la Carrera de Ingeniería Electrónica de la UTN-FRBA.

REFERENCIAS

- [1] Cheng-Yi Huang et al. “Flexible Pressure Sensor with an Excellent Linear Response in a Broad Detection Range for Human Motion Monitoring”; ACS Applied Materials & Interfaces; Enero 2023.
- [2] Lingyan Duana, Dagmar D'hooge y Ludwig Cardon; “Recent progress on flexible and stretchable piezoresistive strain sensors: From design to application”; Progress in Materials Science; Octubre 2023.
- [3] Junchen Yan, Anping Chen y Shuyun Liu; “Flexible sensing platform based on polymer materials for health and exercise monitoring”; Alexandria Engineering Journal ; Septiembre 2023.
- [4] Nan Wen et al. “Emerging flexible sensors based on nanomaterials: recent status and applications”; Journal of Materials Chemistry A; Noviembre 2020.
- [5] Pu Nie, et al. “High-Performance Piezoresistive Electronic Skin with Bionic Hierarchical Microstructure and Microcracks”; ACS Applied Materials & Interfaces; Abril 2017.
- [6] C. Ouyang, D. Liu, K. He y J. Kang; “Recent Advances in Touch Sensors for Flexible Displays”; IEEE Open Journal of Nanotechnology, vol. 4, pp. 36-46; Noviembre 2022.
- [7] Jiyong Min, Jisung Pack, Heon Park y Youngsu Cha; “Classification of Floor Materials Using Piezoelectric Actuator–Sensor Pair and Deep Learning for Mobile Robots”; IEEE Access. PP.1-1.10.1109/ACCESS.2024.3367435; Enero (2024).
- [8] Ziyi Feng, Ziyang Liu, Tianying Shao y Yifei Zhang ; “Application of nanomaterials in flexible sensors”; Proceedings of the 2023 International Conference on Functional Materials and Civil Engineering ; 2023

Optimización de formulación de tintas y diseño de electrodos para impresión *inkjet* de sensores de pH

Emanuel Bilbao
 Depto. de Nanomateriales Funcionales
 Instituto Nacional de Tecnología
 Industrial
 San Martín, Argentina
 ebilbao@inti.gob.ar

Anahí Medrano
 Depto. de Nanomateriales Funcionales
 Instituto Nacional de Tecnología
 Industrial
 San Martín, Argentina
 amedrano@inti.gob.ar

Sunil Kapadia
 Dept. of Digital Printing and Imaging
 Technology
 Technische Universität Chemnitz
 Chemnitz, Alemania
 sunil.kapadia@mb.tu-chemnitz.de

Reinhard R. Baumann
 Dept. Printed Functionalities
 Fraunhofer ENAS
 Chemnitz, Alemania
 ORCID: 0000-0002-2920-6243

Gabriel Ybarra
 Depto. de Nanomateriales Funcionales
 Instituto Nacional de Tecnología
 Industrial
 San Martín, Argentina
 gybarra@inti.gob.ar

Leandro N. Monsalve
 Depto. De Nanomateriales Funcionales
 Instituto Nacional de Tecnología
 Industrial
 San Martín, Argentina
 monsalve@inti.gob.ar

Resumen—En este trabajo se aborda la optimización de tintas funcionales de polianilina y nanotubos de carbono para impresión por inyección de tinta (*inkjet*). El objetivo es lograr películas conductoras que puedan reproducir diseños en una sola pasada. Se estudió el efecto del agregado de diferentes aditivos para mejorar la eyección de las gotas, secado y uniformidad de película. Las tintas optimizadas se utilizaron para imprimir un sensor de pH electroquímico con una sensibilidad semejante a la de un sensor comercial (60 mV/dec).

Palabras clave—sensor de pH, tinta, nanotubos de carbono, polianilina, *inkjet*

I. INTRODUCCIÓN

La formulación de tintas conductoras es un factor clave para lograr que un dispositivo electrónico impreso ingrese al mercado. Muchas tintas comerciales o experimentales tienen un buen comportamiento en cuanto a la imprimibilidad y funcionalidad, pero no logran tener un buen desempeño respecto a la estabilidad del proceso de impresión, o a la necesidad de imprimir múltiples capas para lograr películas de conductividad adecuada. Si bien se pueden imprimir muchos dispositivos completamente funcionales utilizando la impresión *inkjet*, el proceso completo de impresión resulta tedioso, requiriendo realizar múltiples pasadas y una gran cantidad de dispositivos defectuosos. Por otro lado, en las tintas pueden encontrarse solventes peligrosos o contaminantes, lo cual presenta riesgos a la salud humana o al ambiente de trabajo en el caso de que la impresión se lleve a cabo en una escala de producción industrial.

Los sensores de pH son extremadamente útiles en diferentes aplicaciones, tales como salud, alimentos, y monitoreo ambiental. El desarrollo de sensores impresos de bajo costo a gran escala, por lo tanto, es muy valioso. Los sensores de mayor uso en la industria son potenciométricos, en los cuales se mide la diferencia de potencial entre el electrodo de trabajo, cuyo potencial varía con el pH del medio, y otro de referencia, que se mantiene a potencial constante. Previamente, estuvimos trabajando en la fabricación de electrodos de trabajo sensibles al pH, utilizando como base electrodos de carbón serigrafados desarrollados como plata forma para la detección de enfermedades infecciosas [1], y desarrollando una tinta de polianilina (PANI) imprimible

por *inkjet* para conferirle a estos electrodos capacidad de respuesta al pH [2].

El desempeño funcional de los electrodos de carbón serigrafados con PANI impresa por *inkjet* resultó muy satisfactorio, con una sensibilidad superior a la de los electrodos de pH comerciales (62 mV/dec) y selectividad al pH frente a otros cationes. Por otro lado, en relación al proceso de impresión, la fabricación de dicho electrodo requirió la impresión de cinco capas de tinta de PANI, y la tinta presentó estabilidad por hasta 5 h.

Basándonos en estos hechos previos, en este trabajo nos enfocamos en la optimización de la fabricación de un sensor de pH potenciométrico basado en PANI, que incluya tintas electrodos de trabajo como de referencia, utilizando únicamente impresión *inkjet*, con el objetivo de reducir el tiempo de impresión y alcanzar condiciones de fabricación escalables y con buen rendimiento.

Para lograr imprimir un sensor completamente por *inkjet* de forma escalable y con buen rendimiento, es necesario abordar varios aspectos. Por un lado, se debe contar con tintas que permitan la impresión de capas funcionales en una sola pasada y de forma reproducible. Por otro lado, se debe adecuar el diseño de los electrodos a las propiedades de las películas impresas para lograr la funcionalidad deseada. En este trabajo, se optimizaron las propiedades de una tinta de PANI y otra de nanotubos de carbono (NTC) desarrolladas en nuestro laboratorio, mientras que se utilizaron formulaciones ya optimizadas para la impresión del área activa del electrodo de referencia [3] y tintas comerciales de plata y SU8 para la impresión de los contactos y el encapsulado de la zona perimetral a los electrodos respectivamente.

II. MATERIALES Y MÉTODOS

A. Generalidades

La anilina (de Anedra, Argentina) fue destilada dos veces antes de su uso. Los siguientes reactivos fueron de grado ACS y se utilizaron sin purificar. De Anedra, se adquirieron: HCl al 37% m/m, persulfato de potasio (KPS) y polivinilpirrolidona K30 (PVP). De Biopack (Argentina) se adquirieron: persulfato de amonio (APS), dodecil sulfato de sodio (SDS) y glicerol. De Merck, se obtuvieron: soluciones de referencia pH 4.01, 7 y 10 (20 °C), y dimetacrilato de etilenglicol (EGDMA). De Fluka, acrilato de etilo (EA). De

E. B. agradece al INTI, al MinCyT, al BMBF, a la Universidad del Oeste y a CONICET por la beca de finalización de doctorado para llevar a cabo parte de este trabajo.

Sigma Aldrich, metacrilato de metilo (MMA), ácido metacrílico (MAA) y polivinilbutiral (PVB). Los NTC marca NC7000 fueron adquiridos de Nanocyl (Bélgica). De Utdots, se adquirió la tinta de plata UTDAgIJ. De Kayaku Advanced Materials, se adquirió la tinta XP PriElex SU8 (SU8). De Clorox (Argentina) se compró la vandina comercial Ayudín® (NaClO 55 g L⁻¹). Se utilizó Dowanol® PM provisto por Bassegraf-INK (Argentina). El aglutinante acrílico Joncryl 617 fue proporcionado por Crilen (Argentina, producido bajo licencia de BASF). Se utilizaron películas de polietilenoftalato (PEN) de 125 µm de espesor como sustrato para la impresión.

B. Formulación de tintas de PANI

En primer lugar, se sintetizaron nanofibras de PANI de acuerdo al método descrito por Kaner [4]. Resumidamente, se preparan dos soluciones: por un lado, una solución de 100 mL que contiene 0,5 M de anilina y 1 M de HCl; por el otro, una solución de 100 mL que contiene 0,125 M de APS y 1 M de HCl. Luego, se mezclan ambas soluciones agitando brevemente, y se deja descansar por 24 h. Luego se enjuaga 2 veces centrifugando y reemplazando el sobrenadante por agua desionizada. Para determinar la concentración de la suspensión resultante, se toma una alícuota de volumen y se seca a 105 °C hasta llegar a peso constante.

Además, se sintetizó una resina acrílica (denominada R3) con una concentración de polímero de 30% m/m, con la siguiente composición másica de monómeros: 69% de EA, 28% de MMA, 2,9% MAA y 0,1% EGDMA como entrecruzante, KPS como iniciador y SDS como estabilizador. Los detalles de la síntesis se discuten en una publicación previa [5].

A partir de estos materiales, se formularon tintas conteniendo 0,5% de nanofibras de PANI, 0,5% de R3, 1% SDS, y cantidades variables de glicerol, PVP y Dowanol PM.

C. Formulación de tintas de NTC

De forma similar a las tintas de PANI, se formularon diferentes tintas de NTC a partir de NTC, PVP, SDS, Dowanol PM, Joncryl 617 y glicerol.

D. Formulación de otras tintas

Para imprimir el electrodo de referencia, además se formularon dos tintas: una oxidante (ClOx), que contiene 2,8 g/L de NaClO y 3,25 g/L de NaCl; y una de PVB, que contiene 4% de PVB, 36% de metanol, 30% de xileno, 15% de alcohol de diacetona y 15% de butanol.

E. Caracterización de tintas

Las tintas se caracterizaron por su viscosidad y tensión superficial. La tensión superficial se midió por el método de Du Noüy utilizando un tensiómetro de fuerza Sigma 700, de Biolin Scientific. La viscosidad se midió con un viscosímetro rotatorio Myr VR 3000 Series. También se imprimieron estructuras de prueba por *inkjet*, y se midió la resistividad utilizando un multímetro Keithley 2000.

F. Impresión por *inkjet*

El sensor se imprimió sobre un sustrato de PEN utilizando una impresora de materiales Dimatix DMP 2850, de Fujifilm. El diseño se muestra en la Fig. 1, y en la Tabla I se indica el orden de impresión de las capas, la resolución utilizada, el número de pasadas y el posprocesamiento de cada una.

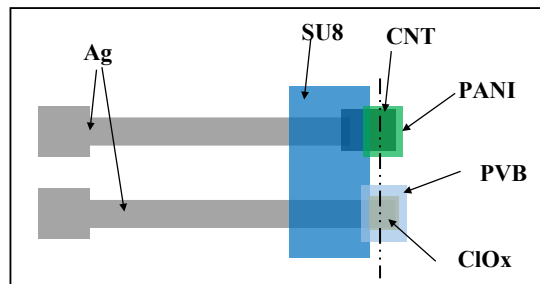


Fig. 1. Diseño de sensor de pH.

TABLA I. COMPOSICIÓN Y PROPIEDADES DE LAS TINTAS DE PANI. TODAS LAS TINTAS TIENEN 0,5% PANI, 0,5% RESINA R3 Y 1% SDS.

Orden	Capa	Resolución (dpi)	Nº de pasadas	Posprocesamiento
1º	Ag	1693	1	Horno 150 °C por 1 h
2º	CNT	2540	1	Horno 120 °C por 20 min
3º	SU8	2540	1	Horno 150 °C por 1 h
4º	ClOx	1693	2	Secado natural en aire
5º	PVB	2540	4	Secado natural en aire
6º	PANI	2540	1	Horno 120 °C por 20 min

III. RESULTADOS Y DISCUSIÓN

A. Diseño del dispositivo

Para diseñar el sensor de pH, se consideró una zona sensible, expuesta a la solución a medir, un contacto eléctrico, y una zona protegida, que pone en contacto a ambas partes protegiéndolas del ambiente.

Con respecto al electrodo de trabajo, se sabe que, al recubrir con PANI un electrodo de carbón, se obtiene una sensibilidad al pH similar a la de un electrodo de pH comercial. A partir de experimentos preliminares, se determinó que la interacción de la muestra con el contacto de plata reduce la sensibilidad, por lo cual se recubrió el contacto entre la pista de Ag y el electrodo de NTC.

El electrodo de referencia consiste en una pista de plata, sobre la cual se imprimió la solución ClOx, a fin de generar una superficie de AgCl con un exceso de NaCl. Para estabilizar la concentración superficial se recubrió con una película de PVB.

B. Optimización de la tinta de PANI

Los componentes comunes a todas las tintas fueron estudiados en un trabajo previo [2], donde se estableció el rol de estabilizante del SDS para las nanofibras de PANI, permitiendo el agregado de otros aditivos sin comprometer la estabilidad de la suspensión; y se sintetizó e incorporó la resina R3 para mejorar la resistencia al desgaste manteniendo la flexibilidad. En este trabajo, para optimizar la tinta, se formularon diferentes tintas de PANI con diferentes proporciones de glicerol, PVP y Dowanol PM. Se denominaron "Txx", donde "xx" representa el porcentaje de glicerol en la tinta. Por otro lado, se formularon tintas con el agregado de 0,5% de PVP y 3% de Dowanol PM, en cuyo caso se agregó el sufijo "+" al nombre de la tinta.

En la Tabla I se resume la formulación de las tintas de PANI y sus propiedades. Si bien se observó que las propiedades no cambiaron de forma significativa, se observó un aumento de la viscosidad con al incrementar la concentración de glicerol, y un aumento de la tensión superficial con el agregado de Dowanol PM y PVP.

Para caracterizar las películas se imprimieron pistas (Fig. 2) de 5 mm de largo (L) y 150 μm de ancho, y se calculó la resistencia superficial (ρ_s) a través de la Ec. 1, utilizando la resistencia medida entre los extremos (R), el ancho de la pista medido por análisis de imágenes (W).

$$\rho_s = (RW) / L \quad (1)$$

En la Fig. 2 se observa que la tinta que no tiene glicerol (T0+) hay una acumulación de sólidos en el borde de la pista, y una resistividad mucho mayor que las demás tintas. Esto puede explicarse por una falta de homogeneidad en la distribución de partículas de PANI, que no logran una buena percolación en la película. Por otro lado, la tinta que no tiene PVP ni Dowanol PM (T15) presenta gotas satélites, y no forman una pista con un borde suave. Esto puede deberse a una tensión superficial más baja y menor viscosidad, que permite el movimiento de la tinta fresca sobre el sustrato. Dado que la capa de PANI debe cubrir un área con una relación de aspecto aproximadamente cuadrada, el exceso de tinta puede distribuirse de forma homogénea y no representa un inconveniente para la impresión.

TABLA II. COMPOSICIÓN Y PROPIEDADES DE LAS TINTAS DE PANI. TODAS LAS TINTAS TIENEN 0,5% PANI, 0,5% RESINA R3 Y 1% SDS.

Tinta	Aditivos			Propiedades	
	Glicerol	PVP	Dowanol PM	Viscosidad (mPa s)	Tensión superficial (mN/m)
T0	0%	-	-	1,1	35,4
T15	15%	-	-	1,6	35,8
T0+	0%	0,5%	3,0%	1,5	37,2
T15+	15%	0,5%	3,0%	2,0	37,3

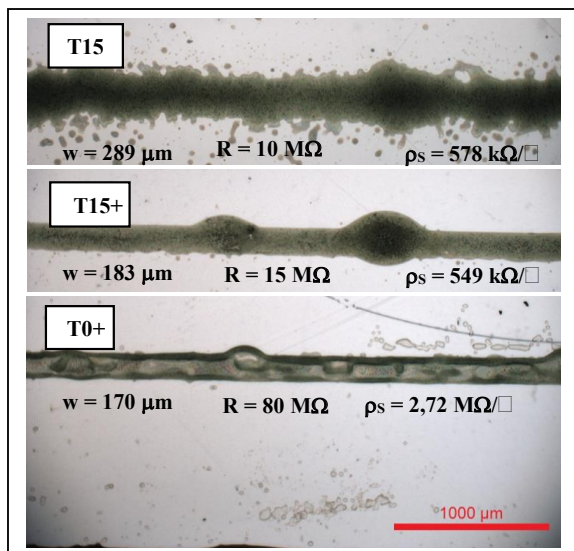


Fig. 2. Pistas de tintas de PANI, con sus respectivos anchos de pista, resistencias y resistividades superficiales calculadas

Con respecto a la tinta T0, la interacción entre la tinta y el sustrato no permitió la formación de una pista continua. Teniendo en cuenta estos resultados, se seleccionó la tinta T15+ para imprimir la capa de PANI.

C. Optimización de la tinta de NTC

Para la optimización de la tinta de NTC se tomó como base una formulación de NTC para flexografía desarrollada en nuestro laboratorio [6], y se modificaron las concentraciones para ajustar las propiedades de acuerdo con las especificaciones recomendadas para la impresión *inkjet* [7]. De manera análoga a lo realizado con la tinta de PANI, se hicieron distintas formulaciones con NTC con diferentes cantidades de aditivos. En la Tabla II se muestran las formulaciones, su denominación y su caracterización. Se observa un incremento en la viscosidad a medida que aumenta la concentración de glicerol en la formulación, y también se observa que la tensión superficial no presenta cambios significativos.

Luego, se imprimieron pistas de prueba con el mismo diseño ($L=5 \text{ mm}$, $w=150 \mu\text{m}$) para medir la resistividad superficial (Fig. 3). Con la tinta NTC-IJ2 se logró la mayor exactitud del ancho de pista, pero la mayor resistividad; mientras que con la tinta NTC-IJ4 se logró la menor resistividad superficial, con un ancho de pista casi del doble del que fue diseñado. La tinta NTC-IJ3 presentó un comportamiento intermedio, que satisface tanto el criterio de reproducibilidad de diseño como el de conductividad. Por lo tanto, se eligió la tinta NTC-IJ3 para imprimir la capa de NTC en el sensor de pH.

TABLA III. COMPOSICIÓN Y PROPIEDADES DE LAS TINTAS DE NTC. TODAS LAS TINTAS TIENEN 0.4% DE NTC, 0,2% DE PVP, 0,8% DE SDS Y 1.6% DE RESINA JONCRYL 617

Tinta	Aditivos			Propiedades	
	Glicerol	SDS	Dowanol PM	Viscosidad (mPa s)	Tensión superficial (mN/m)
NTC-IJ1	0%	0,83%	2,50%	1,7	37,1
NTC-IJ2	8,3%	0,83%	2,50%	2,1	36,9
NTC-IJ3	16,7%	0,83%	2,50%	2,6	36,4
NTC-IJ4	25%	0,75%	2,25%	3,2	37,2

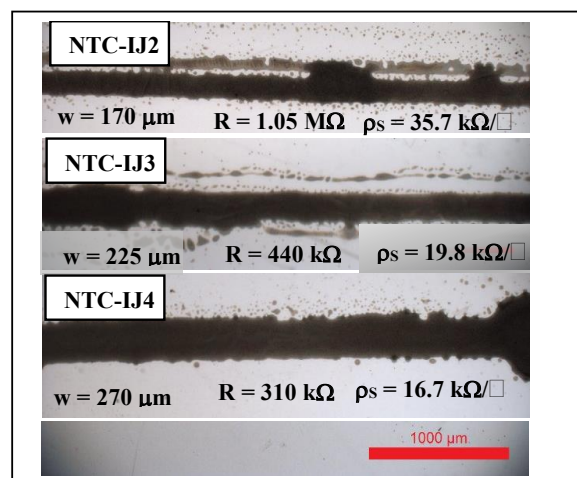


Fig. 3. Pistas de tintas de NTC, con sus respectivos anchos de pista, resistencias y resistividades superficiales calculadas

D. Impresión del electrodo de trabajo

Una vez seleccionadas las tintas de PANI y NTC, se avanzó en la impresión del sensor. Con las tintas T15+ y NTC-IJ3, se imprimió el electrodo de trabajo de un sensor de pH completamente por *inkjet*. Se imprimió una hoja A4, en la cual se hicieron entrar 156 sensores. En la Fig. 4 se muestra la parte activa de un sensor de pH terminado.

Tanto con la tinta de PANI como con la de NTC, se realizaron impresiones por 5 h sin observar obturación de boquillas en los cabezales de impresión, con lo cual se puede concluir que las tintas tienen un desempeño robusto y que pueden ser utilizadas para imprimir en una escala de producción mayor.

El posprocesamiento para las tintas de PANI y NTC en horno fue un paso necesario, ya que si se dejaba secar se requirió un proceso de secado de 30 min a 130 °C luego de cada capa de tinta, ya que la presencia de glicerol no permite que la tinta se seque por evaporación en condiciones ambientales. En la Fig. 4 se observa que la película de carbón mantuvo la geometría rectangular a pesar de haberse impreso una parte sobre plata y otra parte sobre PEN. También se observa que la película de PANI tiene una distribución homogénea y recubre de forma completa el electrodo de NTC.

Finalmente, se midió la respuesta potenciométrica del sensor en función del tiempo (Fig. 5).

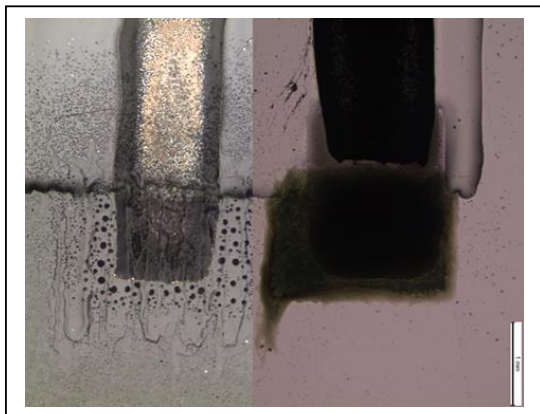


Fig. 4. Sensor de pH impreso por *inkjet*. La longitud de barra de escala equivale a 1 mm.

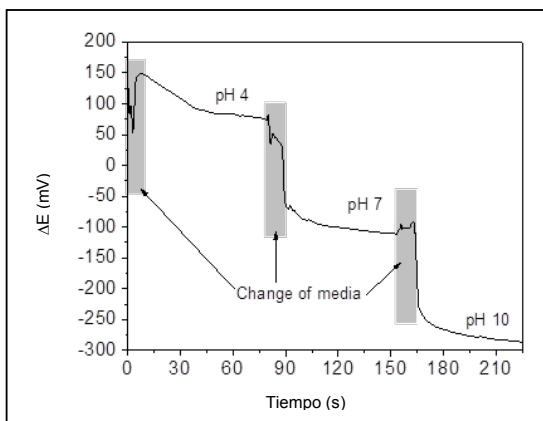


Fig. 5. Respuesta del sensor en función del tiempo al colocarse en soluciones buffer de pH 4, 7 y 10.

El potencial se estabilizó dentro de los primeros 30 s luego de sumergir el sensor en cada buffer, de manera semejante a lo que ocurre con los pHmetros comerciales. Por otro lado, a partir de los potenciales estabilizados en función del pH, se calculó una sensibilidad de 60,2 mV/dec con un $R^2=0,9998$. Esta sensibilidad también es comparable con los medidores de pH comerciales. Tanto el tiempo de respuesta como la sensibilidad son semejantes a los de los pHmetros comerciales, por lo cual el desempeño del sensor es satisfactorio para la medición de estas soluciones.

La fabricación del electrodo de referencia se fabricó de acuerdo al método definido por Moya y col. [3], y ya fue discutido en su trabajo. Como perspectiva de trabajo futuro, se podría trabajar en una optimización de la formulación de PVB para poder imprimirse en una sola capa, y también en la formulación de la solución ClOx. También se podría evaluar la respuesta del sensor en muestras con matrices complejas.

IV. CONCLUSIONES

Se formularon y optimizaron tintas de PANI y NTC para imprimir sensores de pH por *inkjet*. Estas tintas se lograron imprimir en una sola pasada con una resolución de 2540 dpi, y pudieron reproducir los patrones establecidos por diseño. Para obtener una película consolidada, fue necesario aplicar un postratamiento en horno a 120 °C por 20 min. También se imprimió un electrodo de referencia de acuerdo con el método de Moya y col., y el sensor exhibió un tiempo de respuesta inferior a 30 s y una sensibilidad de 60,2 mV/dec. Estos resultados son promisorios para aplicar estos sensores en aplicaciones que requieran pequeños volúmenes, ya que por su geometría plana podrían obtener una medida con una gota que conecte los dos electrodos, o aplicarse sobre una superficie húmeda.

REFERENCES

- [1] M. E. Cortina, L. J. Melli, M. Roberti, M. Mass, G. Longinotti, S. Tropea, P. Lloret, D. A. R. Serantes, F. Salomón, M. Lloret, A. J. Caillava, S. Restuccia, et al., "Electrochemical magnetic microbeads-based biosensor for point-of-care serodiagnosis of infectious diseases" *Biosens. Bioelectron.*, vol 80, pp. 24-33, 2019.
- [2] E. Bilbao, S. Kapadia, V. Riechert, J. Amalvy, F. N. Molinari, M. M. Escobar, R. R. Baumann, L. N. Monsalve, "Functional aqueous-based polyaniline inkjet inks for fully printed high-performance pH-sensitive electrodes", *Sensors Actuators B Chem.*, vol 346, 2021.
- [3] A. Moya, R. Pol, A. Martínez-Cuadrado, R. Villa, G. Gabriel, M. Baeza, "Stable full-inkjet-printed solid-state Ag/AgCl reference electrode", *Anal. Chem.*, vol. 91, pp. 15539-15546, 2019.
- [4] D. Li, R. B. Kaner, "Shape and aggregation control of nanoparticles: not shaken, not stirred", *J. Am. Chem. Soc.*, vol. 128, pp. 968-975, 2006.
- [5] J. I. Amalvy, "Semicontinuous emulsion polymerization of methyl methacrylate, ethyl acrylate, and methacrylic acid", *J. Appl. Polym. Sci.*, vol. 59, pp. 339-344, 1996.
- [6] O. Garate, L. Veiga, A. V. Medrano, G. Longinotti, G. Ybarra, L. N. Monsalve, "Waterborne carbon nanotube ink for the preparation of electrodes with applications in electrocatalysis and enzymatic biosensing", *Mater. Res. Bull.*, vol. 106, pp. 137-143, 2018.
- [7] Fujifilm, "Materials printer jetttable fluid formulation guidelines". https://asset.fujifilm.com/www/mk/files/2020-03/f87cf334c234bd7fe1a7f682a9b75cb3/Dimatix_Materials_Printer_Jetttable_Fluid_Formulation_Guidelines_05-13.pdf (accedido el 17/4/2024)

Calefactor flexible para fluidos intravenosos obtenidos por procesos de electrónica impresa

Joaquín Bonilla
Universidad Nacional de San
Martín (UNSAM)
Buenos Aires, Argentina
jmarcillabonanno@estudiantes.unsam.edu.ar

Damian Ricalde
Dto Prototipado Microelectrónico
y Electrónica Impresa
Instituto Nacional de Tecnología
Industrial
Buenos Aires, Argentina
dricalde@inti.gov.ar

Mariano Roberti
Dto Prototipado Microelectrónico
y Electrónica Impresa
Instituto Nacional de Tecnología
Industrial
Buenos Aires, Argentina
froberty@inti.gov.ar

Julián Marinoni
Dto Prototipado Microelectrónico
y Electrónica Impresa
Instituto Nacional de Tecnología
Industrial
Buenos Aires, Argentina
marinoni@inti.gov.ar

Alex Lozano
DT. de Micro y Nanotecnologías
Instituto Nacional de Tecnología
Industrial
Buenos Aires, Argentina
alozano@inti.gov.ar

Mijal Mass
Dto Prototipado
Microelectrónico y Electrónica
Impresa
Instituto Nacional de Tecnología
Industrial
Buenos Aires, Argentina
*mmass@inti.gov.ar

Liliana Fraigi
Escuela de Ciencia y Tecnología
UNSAM
Dto de Electrónica
Universidad Nacional Tecnológica –
UTN-FRBA
Buenos Aires, Argentina
lili@frba.utn.edu.ar

Resumen — En el presente trabajo se detalla el diseño, fabricación y caracterización de dos modelos de calefactores flexibles para fluidos intravenosos para un rango de 20°C a 33°C, utilizando impresión serigráfica sobre sustratos PET. Para su desarrollo se tuvieron en cuenta la selección de los materiales, la geometría de los calefactores en función de la distribución de calor, la velocidad de calentamiento, la variación con la temperatura, la tensión de alimentación, entre otros aspectos fundamentales. Se obtuvo un calefactor de tipo fractal con una capa de tinta Ag de 22Ω@20°C y otro de tipo interdigital con una capa de tinta de carbón/grafito con electrodos de Ag de 10.7Ω@20°C; TCR de 1200ppm/°C y de 1100ppm/°C; y velocidades de calentamiento cuasi-lineales de 0.16°C/min y 0.34°C/min entre 10°C a 70°C, respectivamente.

Palabras clave—*electrónica impresa, calefactores flexibles, impresión serigráfica, fluidos intravenosos*

I. INTRODUCCION

Los fluidos intravenosos (FIV) son soluciones líquidas administradas directamente en el torrente sanguíneo mediante vía intravenosa, siendo una de las intervenciones más utilizadas en medicina. El objetivo de dicha administración es la de mantener o restablecer el estado de equilibrio del medio interno, homeostasis, garantizando el correcto funcionamiento de los sistemas del cuerpo. Dichos fluidos cumplen varios propósitos en la atención médica, tales como conservar el volumen extracelular, mantener la hidratación y el equilibrio tanto de electrolitos como de nutrientes del organismo.

La temperatura de los FIV es un aspecto crítico en la administración de tratamientos médicos, ya que tiene un impacto significativo en la salud del paciente. La temperatura óptima para la transfusión de los mismos suele estar en el rango de 20°C a 25°C (68 a 77°F); sin embargo, existen evidencias de un efecto favorable con 33°C [1]. Mantener esta temperatura es fundamental por varias razones: evitar la hipotermia o hipertermia inducida por fluidos, mejorar la absorción y la tolerancia del paciente, reducir el estrés fisiológico, entre otros [2,3]. Su

temperatura no debe superar los 37°C ya que puede aumentar el riesgo de contaminación bacteriana, por lo que se deben seguir las medidas de asepsia adecuadas.

La monitorización constante de la temperatura y atención a las prácticas seguras de administración de FIV son fundamentales para evitar riesgos y garantizar la seguridad del paciente durante la infusión intravenosa.

En este trabajo presentamos el desarrollo de dos modelos de calefactores flexibles mediante el proceso de impresión serigráfica: 1) arreglo de curva fractal de Moore de orden 4, impreso con una sola capa de tinta de Ag; 2) de electrodos interdigitados con tinta de Ag, mediante una configuración del tipo paralelo que se genera entre los electrodos sobre una resistencia impresa con tinta de carbón/grafito.

La motivación de este desarrollo radica en la necesidad de encontrar una solución innovadora, económica y efectiva para el calentamiento de FIV. En la actualidad, las alternativas tradicionales enfrentan una serie de desafíos tecnológicos y/o económicos que dificultan su adopción generalizada.

II. EXPERIMENTAL

A. Diseño de los calefactores

Los diseños de los calefactores propuestos se enfocan en lograr una distribución de temperatura lo más uniforme posible y estable, sobre un área específica de 10cm x 10cm, el cual coincide con el de las etiquetas gráficas que contienen la información de las bolsas de transfusión comerciales. La velocidad de calentamiento es otra característica que se consideró en el diseño.

En cuanto a los materiales, se eligió PET como sustrato, el cual posee una flexibilidad adecuada para nuestra aplicación, soporta las temperaturas requeridas, hay disponibilidad en el mercado local y su costo no es elevado. En el caso de las tintas, se utilizaron:

- Tinta resistiva de carbón/grafito, Gwent C2030519P4.
- Tinta conductora de Ag, Mateprincs SCAG-003.

Con el fin de preservar la integridad de los fluidos, se propuso obtener un valor intermedio de temperatura de 28°C, en un lapso menor a 30 minutos. Para ello, debemos determinar la potencia requerida en función del volumen y el tipo de líquido que se va a calentar, obedeciendo a (1):

$$P = C_{\text{líquido}} \cdot \frac{\Delta T_{\text{líquido}}}{\Delta t} \quad (1)$$

siendo $C_{\text{líquido}}$ la capacidad térmica del líquido, la cual se calcula conociendo la masa y el calor específico del mismo. Para llevar a cabo las pruebas de concepto, se utilizó 400ml de agua corriente. Calculando $C_{\text{líquido}}$ y reemplazando los valores en (1), se llega a:

$$P = 1674,4 \text{ J/}^\circ\text{C} \cdot \frac{(28-20)^\circ\text{C}}{30.60 \text{ seg}} = 7,44 \text{ W} \quad (2)$$

Utilizando una tensión de alimentación nominal de 12V, se calcula el valor de la resistencia mediante (3):

$$R = \frac{V_{\text{nom}}^2}{P} = \frac{(12\text{V})^2}{7,44 \text{ W}} = 19,35 \Omega \quad (3)$$

Con este valor de R y a partir de (4):

$$R = \rho_{\square} \cdot \frac{L}{W} \quad (4)$$

Calculamos la relación de aspecto ($N = \frac{L}{W}$) para ambos diseños, conociendo las resistividades de las tintas: de carbón/grafito ($\rho = 45 \Omega/\square$), y de Ag ($\rho = 45 \text{ m}\Omega/\square$):

$$N_{\text{carbón/grafito}} = 0,43 \quad (5)$$

$$N_{\text{Ag}} = 430 \quad (6)$$

A partir del estudio publicado por Charan et al. [4], que se centra en el diseño de calefactores con forma de meandro, donde se exploran diversas curvas fractales como posibles geometrías, se elige para el presente trabajo la curva fractal de Moore de orden 4. Esta curva logra una distribución de temperatura más uniforme, cumple con la especificación de N_{Ag} y genera una L_{Ag} más reducida en comparación con los diseños convencionales, lo que conlleva a un ahorro de tintas. Se pueden generar a través de su representación alfabética mediante un sistema de Lindenmayer, comúnmente conocido como sistema L [4].

El layout del patrón de los calefactores se realizó mediante la utilización del software “Inkscape”, el cual incluye una herramienta de generación de representaciones gráficas de sistemas de Lindenmayer y un conjunto de parámetros para generar una estructura como la que se muestra en la “Fig. 1”.

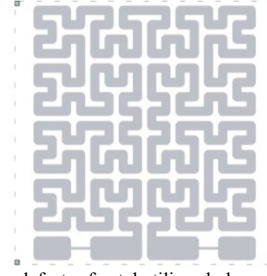


Fig. 1. Diseño del calefactor fractal utilizando las curvas de Moore de orden 4.

Para el segundo diseño se partió del trabajo de Park et al. [5], que propone un diseño de resistencias paralelas para disminuir la resistencia total “Fig. 2”.

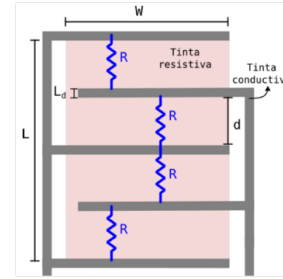


Fig. 2. Esquema del calefactor interdigital de carbón/grafito

En este diseño se plantean N pistas conductoras de ancho L_d separadas por una distancia d. Si se imprime por encima de todas las pistas conductoras un rectángulo de tinta resistiva de ancho W y largo L, entonces la resistencia entre dos pistas consecutivas sigue la forma de (7), mientras que la resistencia total resulta del paralelo de $(N - 1)$ resistencias según (8). De esta forma se logra un bajo valor de resistencia sin aumentar la complejidad del diseño ni de los costos.

$$R = \rho_{\square} \cdot \frac{d}{W} \quad (7)$$

$$R_{\text{Total}} = \rho_{\square} \cdot \frac{d}{W} \cdot \frac{1}{(N-1)} \quad (8)$$

Con los parámetros geométricos de diseño que se listan en la TABLA I, se calcula la resistencia total aplicando (8):

$$R_{\text{Total}} = 45 \frac{\Omega}{\square} \cdot \frac{22,5 \text{ mm}}{90 \text{ mm}} \cdot \frac{1}{(5-1)} = 2,81 \Omega$$

TABLA I: Valores dimensionales del diseño

L [mm]	W [mm]	A [mm ²]	d [mm]	L _d [mm]	N
91	91	8100	22	1	5

B. Fabricación de los calefactores

Luego de fabricar las máscaras de los respectivos calefactores sobre una filmína con una resolución de impresión de 3600 dpi, se procedió a la preparación de las mallas, seleccionando la cantidad de hilos por pulgadas (*mesh*) según las especificaciones de cada tinta. La transferencia de los diseños a dichas mallas se realizó mediante un proceso fotolitográfico sobre una película fotosensible de 50µm (Ulano®).

Para la impresión se utilizó una impresora serigráfica semiautomática (EKRA modelo Microtronic II) controlando los parámetros de presión y velocidad de espátula, y la distancia entre la malla y el sustrato (*snap off*). Finalmente, para el proceso de curado de las tintas, se utilizó una estufa de secado Thermal TH400DH.

III. CARACTERIZACIÓN Y RESULTADOS

Las caracterizaciones eléctricas, tanto debidas a deformaciones mecánicas como a cambios de temperatura, se realizaron con la unidad de fuente y medida (SMU) Keithley 2602B [6]. El estudio de las deformaciones es necesario ya que, al llenarse las bolsas de transfusión, estas aumentan su volumen, lo que provoca que los calefactores flexibles adheridos a ellas “copien” su forma, se flexionen y puedan, por lo tanto, cambiar su valor de resistencia original. Específicamente, nos concentramos en investigar cómo cambia la resistencia de los dispositivos sometidos a esas deformaciones. Para ello se analizaron dos muestras de películas flexibles impresas utilizando estructuras de soporte fabricadas por impresión 3D, con diferentes radios de curvatura “Fig. 3”: 200mm; 175mm; 150mm; 125mm; 100mm; 50mm y 25mm. Por cada muestra, se realizaron 5 repeticiones alternadas con la posición inicial sin deformación. Queda pendiente aumentar la cantidad de ciclos entre flexión y relajación de al menos 1000 repeticiones con el fin de determinar el orden de influencia de la flexión.

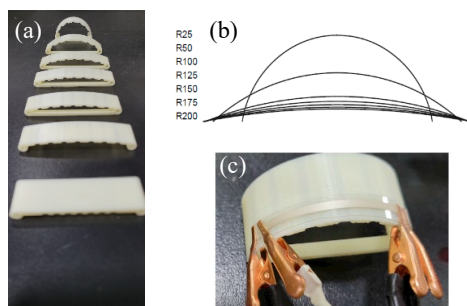


Fig. 3. (a) Estructuras de soporte para ensayos de deformación; (b) Esquema de las diferencias entre los siete radios de curvatura estipulados; (c) Medición de una muestra deformada en la estructura de radio de 25mm.

Las muestras estudiadas soportaron adecuadamente los esfuerzos mecánicos aplicados en todos los radios de curvatura. Ambas muestras impresas han manifestado una variación en su resistencia eléctrica menor al 3%.

Para la caracterización térmica de los dispositivos, se utilizó un banco compuesto por una cámara infrarroja termográfica FLIR One PRO, que permite analizar la distribución térmica en toda el área de los calefactores, como así también medir temperatura en diferentes puntos de la muestra. Esta cámara se conecta al puerto USB tipo C de un celular que se utiliza mediante la aplicación FLIR One o Thermal Camera+.

La “Fig. 4” muestra las imágenes capturadas con la cámara infrarroja para los dos diseños de calefactores. Ambos se encuentran de manera extendida sin deformaciones de los sustratos. La imagen termográfica del calefactor fractal “Fig. 4a” presenta una distribución de temperatura con un alto grado de uniformidad en toda su

área, observable a través de las diversas tonalidades de color. También se indican tres valores de temperatura ubicados en distintas zonas del dispositivo. En el caso de la imagen termográfica del calefactor interdigital “Fig. 4b”, se observa que la distribución de temperatura no es uniforme. Dichas variaciones se hacen más evidentes en las pistas conductoras de Ag, en especial en las cercanías de los pads de alimentación. Ambos calefactores se plantearon para cubrir un área de 10x10cm debido a las condiciones de contorno tales como potencia y resistividad de las tintas utilizadas.

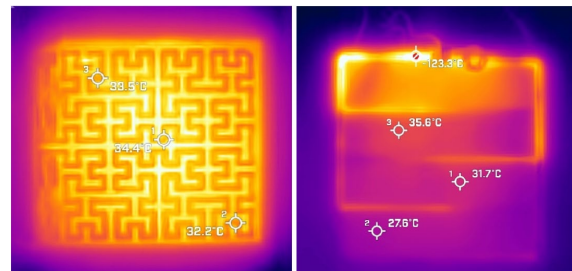


Fig. 4. Imágenes infrarrojas; (a) Calefactor Fractal de 10x10cm y (b) Calefactor Interdigital de 10x10cm.

Para estudiar la repetibilidad de la variación de la temperatura a lo largo del tiempo y el tiempo de respuesta de los respectivos calefactores se realizaron tres mediciones para dos dispositivos de cada modelo de calefactor. Dichas mediciones se realizaron con un termistor PTC modelo KTY81 de NXP, colocado en el interior de la bolsa y un circuito electrónico de control. Los ensayos para los calefactores flexibles fractales se llevaron a cabo desde una temperatura inicial aproximada de 10°C hasta alcanzar los 33°C calefaccionando las bolsas de transfusión conteniendo 400ml de agua. Se obtuvo una respuesta cuasi-lineal ($R^2 \approx 0,98$) que se puede aproximar a una velocidad de calentamiento de 0.16°C/min (25 minutos por cada 4°C). Como se observa en la “Fig. 5”, las dos muestras (“Fractal1” y “Fractal2”) presentan pendientes similares.

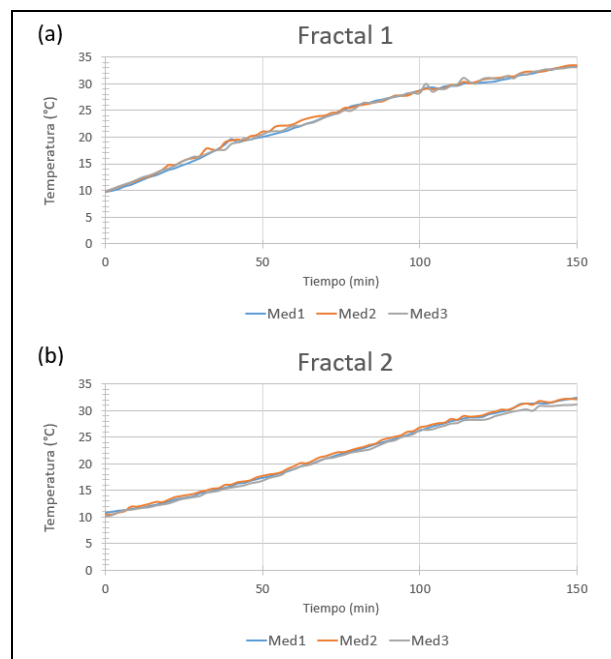


Fig. 5. Variación de la temperatura en función del tiempo de los calefactores (a) Fractal1; (b) Fractal2.

De manera análoga, se repite el procedimiento con los dispositivos interdigitales, donde las tres mediciones realizadas para cada muestra presentaron similitud entre sus curvas “Fig. 6”. Sin embargo, en este caso, mostraron una velocidad de calentamiento aproximada de $0.34^{\circ}\text{C}/\text{min}$ (casi 12 minutos por cada 4°C), lo que corresponde a más del doble de la velocidad de calentamiento obtenida para los calefactores fractales.

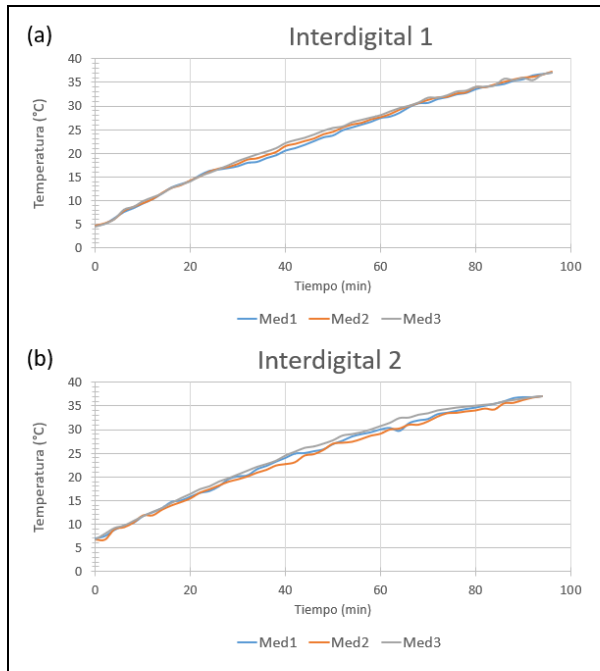


Fig. 6. Variación de la temperatura en función del tiempo de los calefactores (a) Interdigital1; (b) Interdigital2

Asimismo, se estudió el comportamiento de los calefactores por cambios de temperatura externos en un rango más amplio, desde 20°C a 70°C , obteniéndose un $\text{TCR}_{\text{Fractal}} = 1200\text{ppm}/^{\circ}\text{C}$, y $\text{TCR}_{\text{Interdigital}} = 1100\text{ppm}/^{\circ}\text{C}$.

Finalmente, con el objetivo de evaluar los procesos de impresión se realizaron las medidas dimensionales en ambos modelos. Para las mediciones X e Y de las impresiones se utilizó la cámara fiducial de una impresora inkjet Dimatix modelo DMP-2850, la que permite medir con resolución micrométrica. En lo que respecta a la caracterización del espesor, se utilizó un perfilómetro por interferometría (Zeiss modelo 5104802). En ambos calefactores las variaciones en X e Y no superan el 1%. En cuanto a los espesores, el valor promedio de la tinta de Ag del calefactor fractal fue de $24.33\mu\text{m}$ y para el interdigitado, el de la tinta de carbón/grafito fue de $23.68\mu\text{m}$.

IV. CONCLUSIONES

Como resultado de este trabajo se pueden obtener las siguientes conclusiones:

- Se ha logrado desarrollar una serie de calefactores flexibles para su aplicación en el calentamiento de fluidos intravenosos, mediante el proceso de impresión serigráfica como una opción innovadora de producción local/regional y de costos accesibles.

- Se diseñaron dos modelos de calefactores, uno del tipo fractal que corresponde a la curva de Moore de orden 4, impreso con una sola capa de tinta de Ag ($22\Omega @ 20^{\circ}\text{C}$); el otro de electrodos interdigitados de tinta de Ag que reduce la resistencia total mediante una configuración del tipo paralelo, con tinta de carbón/grafito ($10.7\Omega @ 20^{\circ}\text{C}$).

- Ambos modelos de calefactores han alcanzado las temperaturas necesarias de 20°C a 33°C de máxima, para la aplicación propuesta.

- Ambos diseños han arrojado buenos resultados en las caracterizaciones eléctricas del valor de la resistencia frente a las deformaciones mecánicas (menor al 3%), como así también en las variaciones de la resistencia frente a cambios de temperatura (TCR), siendo de $1200\text{ppm}/^{\circ}\text{C}$ para el calefactor fractal y de $1100\text{ppm}/^{\circ}\text{C}$ para el calefactor interdigital.

- El calefactor fractal presentó una mejor distribución de temperatura en el total de la superficie del sustrato, en comparación con el calefactor interdigital. El desbalance térmico producido en este último puede originarse debido a la distribución asimétrica de corriente eléctrica en el dispositivo, producto de la ubicación de los pads de contacto. Se estima que con un rediseño de las pistas conductoras es posible mejorar la uniformidad de temperatura en el dispositivo.

- De los TCR obtenidos en ambos calefactores se desprende la posibilidad de utilizarlos simultáneamente con una doble funcionalidad: como calefactores y sensores de temperatura.

RECONOCIMIENTOS

Los autores agradecen la colaboración de los alumnos de la Cátedra de Tecnología Electrónica, curso 2023, de la Carrera de Ingeniería Electrónica de la UTN-FRBA.

REFERENCIAS

- [1] R. Ferrer Roca. Management of temperature control in post-cardiac arrest care: an expert report. <https://www.sciencedirect.com/science/article/pii/S0210569120302138>; 2021
- [2] L. Lázaro Paradinas. Conocimiento enfermero sobre hipotermia inducida tras parada cardiorrespiratoria: revisión bibliográfica. <https://www.elsevier.es/es-revista-enfermeria-intensiva-142-articulo-conocimiento-enfermero-sobre-hipotermia-inducida-S1130239911000915>; 2011.
- [3] Daniel Simancas Racines. Evidencias científicas sobre las estrategias utilizadas para la prevención de reacciones adversas asociadas a la transfusión de concentrados de glóbulos rojos. <https://www.semanticscholar.org/paper/Evidencias-cient%C3%ADficas-sobre-las-estrategias-para-a-Racines/0a1e4c454a8ae94820765a396e3892a679b4a6d8>; 2019.
- [4] K. K. S. Charan, et al. “Design of Heating Coils Based on Space-Filling Fractal Curves for Highly Uniform Temperature Distribution,” MRS Advances, vol. 5, pp. 1007-1015; <https://doi.org/10.3390/polym14020249>; 2020.
- [5] Park, H. K., Kim, S. M., Lee, J. S., Park, J.-H., Hong, Y.-K., Hong, C. H., & Kim, K. K. Flexible plane heater: Graphite and carbon nanotube hybrid nanocomposite. Synthetic Metals, 203, pp. 127-134; <https://doi.org/10.1016/j.synthmet.2015.02.015>; 2015.
- [6] Keithley Live, Programming a 2600B SMU. https://www.youtube.com/watch?v=TtmqD0SPDbM&t=2224s&ab_channel=Tektronix



8 |

Acondicionamiento de señales e instrumentación

Signal conditioning and instrumentation

Condicionamento de sinais e instrumentação

Sensores inteligentes y redes inalámbricas

Smart sensors and wireless networks

Sensores inteligentes e redes sem fio

Utilización de sensor de humedad y temperatura digital para la estimación del contenido de humedad de equilibrio de la madera

Emiliano Jose Arduini

*Departamento de Industria de la Madera y el Mueble
Instituto Nacional de Tecnología Industrial (INTI)
Buenos Aires, Argentina
earduini@inti.gov.ar*

Damian Alejandro Gherscovic

*Departamento de Industria de la Madera y el Mueble
Instituto Nacional de Tecnología Industrial (INTI)
Buenos Aires, Argentina
dgherscovic@inti.gov.ar*

Resumen—La madera ha sido un material fundamental a lo largo de la historia humana. Con propiedades únicas como excelente aislante térmico, eléctrico y acústico, así como una alta relación resistencia-peso y baja densidad, la madera es una materia prima versátil para diversos productos. Sin embargo, enfrenta limitaciones debido a su susceptibilidad al biodeterioro y a la inestabilidad dimensional causada por su naturaleza higroscópica, lo que conlleva a hinchazón y contracción con cambios de humedad. Para abordar estos desafíos, es crucial comprender el contenido de humedad de equilibrio higroscópico de la madera. En este estudio se desarrolló un dispositivo de monitoreo en tiempo real utilizando sensores digitales de temperatura y humedad para medir el contenido de humedad de equilibrio de la madera. Los resultados demostraron una fuerte relación entre la humedad relativa, la temperatura y el contenido de humedad de equilibrio estimado. La funcionalidad del dispositivo se validó mediante comparaciones gráficas y monitoreo de datos en tiempo real, mostrando su potencial en aplicaciones industriales de la madera y la investigación científica.

Palabras claves: *madera, humedad relativa, humedad de equilibrio higroscópico, contenido de humedad de equilibrio.*

I. INTRODUCCIÓN

La madera ha acompañado a la humanidad a lo largo de su historia. Nuestra relación con este material se remonta a más de dos millones de años atrás, cuando los primeros humanos utilizaron ramas para sus actividades vitales.

Entre sus características, la madera posee una serie de propiedades que la convierten en una materia prima de excelente calidad para la fabricación de ciertos productos. Destacándose las siguientes:

- Es un excelente aislante térmico, eléctrico y acústico cuando está seca.
- Tiene una gran relación peso-resistencia.
- Tiene un bajo peso en relación a su volumen.

En contraste con las propiedades anteriormente mencionadas, son pocos los factores limitantes de su uso. Siendo los más determinantes, la predisposición al biodeterioro y la inestabilidad dimensional. Esto se debe a que es un material higroscópico, que se hincha cuando absorbe agua y se contrae cuando la pierde.

Durante la remoción del agua, la madera puede sufrir cambios no deseados en su forma. Si estos defectos no pueden ser controlados, es posible que la madera no sea un material apropiado para los usos que podría destinarse, ya que la aparición de defectos como grietas, rajaduras y deformaciones, limita considerablemente sus aplicaciones.

Es por ello que el contenido óptimo de humedad de la madera depende del uso que se le vaya a dar, como por ejemplo si la madera se destina a la fabricación de un instrumento musical o de un durmiente de ferrocarril.

La madera es un material higroscópico que sigue las leyes que rigen para los cuerpos porosos. Cuando una pieza de madera permanece suficiente tiempo en un ambiente con condiciones constantes de temperatura y humedad relativa, se establece un equilibrio entre la presión parcial de vapor de agua en el aire y la que existe dentro de la madera. Una vez alcanzado este equilibrio, la humedad de la madera deja de variar y se dice que ha alcanzado su contenido de humedad de equilibrio higroscópico (HEH). Este contenido de humedad permanecerá constante mientras las características del aire que rodea la madera no cambian [1, 2, 3, 4].

La madera, especialmente cuando se utiliza en exteriores, está sujeta a cambios rápidos en las condiciones ambientales. Debido a esto, excepto para espesores muy delgados, generalmente no puede alcanzar su HEH antes de que cambien nuevamente la temperatura y la humedad relativa del entorno. Por lo tanto, el contenido de humedad de la madera cambia menos de lo esperado según las condiciones meteorológicas y, en general, con cierto retraso con respecto a estas condiciones. Este fenómeno se conoce como inercia higroscópica [5].

El conocimiento del HEH de la madera es crucial para diversas aplicaciones prácticas, especialmente en usos exteriores. Es fundamental seleccionar la madera más adecuada para cada ambiente específico con el fin de evitar cambios dimensionales y deformaciones no deseadas [6; 7; 8; 9].

Los valores de HEH de la madera se han determinado experimentalmente en función de las características del aire que la rodea. A presión atmosférica constante se puede hacer variar los parámetros humedad relativa y temperatura del aire y a partir de allí establecer los valores de HEH de la madera correspondientes a cada condición dada.

Por lo tanto, el HEH de la madera puede determinarse teóricamente mediante gráficos y ecuaciones que, utilizando valores constantes de temperatura y humedad relativa del entorno, proporcionan un valor específico del HEH de la madera [10, 11, 3; 12; 13; 14]. Simpson [15] evaluó varios modelos de predicción del HEH de la madera y concluyó que el enfoque basado en la teoría de sorción de Hailwood y Horrobin ofrece la mejor representación del contenido de humedad de equilibrio en relación con la temperatura y la humedad relativa, independientemente de la especie de madera.

Un método clásico para medir el HEH es mediante la medición de la resistencia eléctrica de una pequeña muestra de madera o placa de celulosa colocada entre dos electrodos [16]. Sin embargo, este método de medición presenta desventajas como la sensibilidad a la calidad de la placa y el requerimiento frecuente de mantenimiento y limpieza.

El objetivo de este trabajo fue desarrollar un dispositivo que permita la medición en tiempo real y el registro del contenido de humedad de equilibrio higroscópico de la madera, utilizando sensores digitales de temperatura y humedad relativa ambiente e integrando tecnologías de almacenamiento en la nube y fabricación aditiva.

II. METODOLOGÍA

Para la estimación del valor de HEH de la madera se utilizaron datos compilados por el USDA (United States Department of Agriculture Forest Service), que proporcionan información sobre la sorción y desorción promedio de varias especies de madera en función de la humedad relativa y la temperatura [17]. Utilizando estos datos como variables de entrada y aplicando técnicas de análisis de regresión lineal múltiple, se desarrolló en R Studio un modelo que permite predecir el valor del HEH de la madera en función de la humedad relativa y la temperatura del ambiente.

Para el desarrollo del dispositivo, se utilizó el sensor STH31 de Sensirion, que ofrece una alta precisión en la medición de humedad relativa y temperatura ambiente. Este sensor tiene un rango de medición que va desde 0% hasta 100% de humedad relativa, con una precisión de $\pm 2\%$. Además, puede medir temperaturas en un rango que va desde -40°C hasta 125°C [18]. La comunicación con el microcontrolador se realiza a través de una interfaz I2C, lo que permite una integración sencilla y eficiente del sensor en el sistema.

Como plataforma principal para el dispositivo se utilizó el microcontrolador ESP32, debido a sus capacidades de bajo consumo de energía, su procesador de doble núcleo y su integración de WiFi y Bluetooth. Estas características hacen que el ESP32 sea ideal para aplicaciones IoT (Internet of Things) y de sistemas embebidos. Además, su compatibilidad con múltiples interfaces de comunicación, incluyendo I2C, facilita la conexión con el sensor STH31 y otros dispositivos periféricos.

Para la visualización de los datos, se empleó una pantalla TFT (Thin Film Transistor) de 1,77" que ofrece una matriz de puntos a color adecuada para mostrar información de manera clara y legible.

A su vez, se realizó la integración del ESP32 con la plataforma ThingSpeak para facilitar el almacenamiento y la visualización de datos en la nube. ThingSpeak es una plataforma de IoT que permite recopilar, analizar y visualizar datos de dispositivos conectados a internet en tiempo real.

El gabinete del dispositivo fue fabricado utilizando tecnología de fabricación aditiva (impresión 3D). Esta metodología permitió diseñar y crear el gabinete de manera rápida y precisa, con la capacidad de personalizar la forma y

la estructura del dispositivo según las necesidades específicas.

III. RESULTADOS

Los resultados del análisis de regresión lineal múltiple realizado en R Studio, indican una relación significativa entre la variable de respuesta (HEH) y las variables predictoras humedad relativa y temperatura. El modelo tiene la siguiente fórmula:

$$\text{HEH} = 1,704 + 0,204 \times \text{HR} - 0,065 \times T$$

siendo:

HEH el contenido de humedad de equilibrio higroscópico, en %;

HR la humedad relativa del aire, en %;

T la temperatura del aire, $^{\circ}\text{C}$.

El R cuadrado ajustado ($R^2 = 0,9242$) indica que aproximadamente el 92,42% de la variabilidad en HEH puede ser explicada por las variables humedad relativa y temperatura en este modelo. Esto sugiere que el modelo es altamente predictivo para la variable de respuesta. El F estadístico ($F = 7289$) también es muy alto con un valor p extremadamente pequeño ($p < 2,2 \times 10^{-16}$), lo que respalda la significancia global del modelo.

En la Fig. 1 podemos observar la comparación entre el valor de HEH obtenido de las tablas con datos compilados por el USDA y el valor de HEH estimado por el modelo de regresión lineal múltiple. Los puntos azules representan la relación entre estos dos valores, para diferentes observaciones. La línea roja punteada representa la línea de referencia donde la HEH de tabla es igual a la HEH estimada.

En la Fig. 2 podemos observar la relación entre la HEH estimada y las dos variables predictoras del modelo (humedad relativa y temperatura). Cada punto en el gráfico representa una observación de temperatura y humedad relativa, y está coloreado según el valor estimado de HEH. En naranja se representan los valores más bajos de HEH estimada y en azul los valores más altos de HEH estimada.

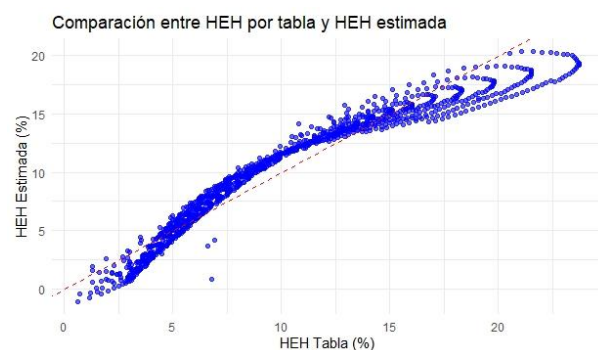


Figura 1. Comparación entre el valor de HEH obtenido de las tablas del USDA y el valor de HEH estimado por el modelo.

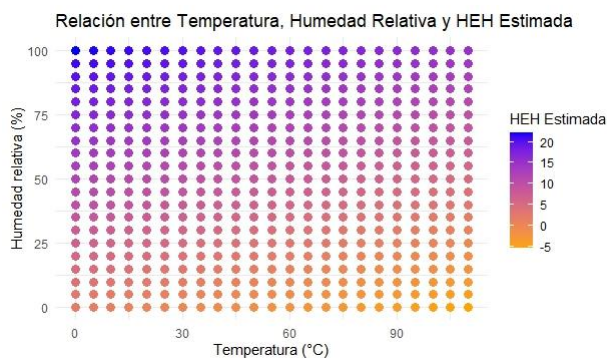


Figura 2. Relación entre la HEH estimada, humedad relativa y temperatura

En la Fig. 3 se muestra el dispositivo terminado y funcionando, objetivo del presente trabajo. En el mismo se observa la medición de temperatura y humedad Relativa junto con la respectiva estimación de la HEH.

En la Fig. 4 se presenta una captura de la plataforma de IoT ThingSpeak en donde se almacenan los datos de las mediciones en tiempo real. El dispositivo desarrollado envía los datos en tiempo real a dicha plataforma, y estos se encuentran disponibles desde cualquier lugar con conexión a internet.



Figura 3. Dispositivo de medición de HEH de la madera.



Figura 4. Plataforma ThingSpeak donde se almacenan los datos de las mediciones.

IV. CONCLUSIONES

El modelo de regresión lineal múltiple muestra que tanto la humedad relativa como la temperatura tienen efectos significativos sobre la variable de respuesta (HEH), con un alto nivel de ajuste del modelo a los datos observados. El modelo presentado en este trabajo no se encuentra reportado anteriormente en la literatura científica.

La combinación del sensor SHT31 y el microcontrolador ESP32 proporciona las capacidades necesarias para desarrollar un dispositivo capaz de calcular y mostrar el valor del contenido de humedad de equilibrio higroscópico de la madera utilizando un modelo lineal múltiple.

A su vez, la integración con ThingSpeak proporciona una solución integral para la gestión de datos en proyectos IoT, permitiendo aprovechar las capacidades de la nube para almacenar, visualizar y analizar datos de manera eficiente y escalable.

La medición del HEH de la madera realizada en este estudio se considera general, ya que utiliza datos que abarcan varias especies de madera. Sin embargo, para aplicaciones más específicas o para especies particulares de madera, será necesario realizar estudios específicos adicionales. Estos estudios específicos permitirán ajustar los modelos y las mediciones según las características únicas de cada especie de madera.

Este dispositivo tiene aplicaciones potenciales en la industria maderera, la investigación científica y otras áreas donde se requiere monitoreo preciso del contenido de humedad de equilibrio higroscópico de la madera. La metodología utilizada asegura la precisión y estabilidad de las mediciones, con el objetivo de contribuir al avance en el campo de la sensorización ambiental y la monitorización de materiales.

AGRADECIMIENTOS

Agradecemos a nuestro director de centro Edgardo Adrián Fontana por brindarnos el apoyo y tiempo para realizar este desarrollo.

BIBLIOGRAFÍA

- [1] J. Siau, *Transport processes in wood*, Springer-Verlag. Berlin Heidelberg, New York, USA, 1984, pp. 245.
- [2] C. Skaar, *Wood-water relations*, Springer-Verlag. Berlin Heidelberg, New York, USA, 1988, pp. 283.
- [3] W. T. Simpson, *Equilibrium moisture content of wood in outdoor locations in the United States and Worldwide*, Res. Note. FPL-RN-268, USDA, Forest Products Laboratory, Madison, USA., 1998.
- [4] E. Baraúna y V. de Oliveira, *Umidade de equilíbrio da madeira de angelim vermelho (Dinizia excelsa Ducke), guariúba (Clarisia racemosa Ruiz&Pav.) e tauari vermelho (Carinianamicrantha Ducke) em diferentes condições de temperatura e umidade relativa*, *Acta Amazónica* 39 (1):91-96, 2009.
- [5] H. Alvarez y J. Fernández-Golfín, *Humedad de la madera en la construcción: valores recomendados y riesgo de cambio dimensional, en España*, Centro de investigación forestal, CIFORINIA, AITIM 182: 65-71, 1996.
- [6] E. Bluhm, R. Rosende, W. G. Kauman, *Determinación de la humedad de equilibrio de la madera en todas las zonas climáticas de Chile*, *Actas de la reunión sobre productos forestales*, Instituto Forestal, Informe Técnico 21: 136-143, Santiago, Chile, 1965.
- [7] E. C. Peck, *Moisture content of wood in use*. Forest Products Laboratory, Madison, USDA, 1965, pp. 10.
- [8] R. Rosende, *Contenido de humedad de equilibrio de algunas maderas chilenas*, *Actas de la reunión sobre investigación en productos forestales*, Instituto Forestal, Informe Técnico 36:135-144, Santiago, Chile, 1969.
- [9] N. Vergara y V. González, *Humedad de equilibrio para Eucalyptus globulus en distintas zonas climático-habitacionales de Chile*, *Actas Simposio Los eucaliptos en el desarrollo forestal de Chile*, Instituto Forestal, Pucón-Chile, 1993, pp. 585-599.
- [10] W. T. Simpson, *Equilibrium moisture content prediction for wood*, *Forest Products Journal* 21 (5): 48-49, 1971.
- [11] W. T. Simpson, *Predicting equilibrium moisture content of wood by mathematical models*, *Wood and Fiber* 5 (1): 41-49, 1973.
- [12] A. P. M. Galvão, *Estimativas da umidade de equilíbrio da madeira em diferentes cidades do Brasil*, IPEF 11: 53-65, 1975.
- [13] S. Avramidis, *Evaluation of "three-variable" models for the prediction of equilibrium moisture content in wood*, *Wood Science and Technology*, 23:251-258, 1989.
- [14] Z. Chen, E. Mougél, P. Perré, R. Youngs, *Equilibrium moisture content of Norway spruce at low temperature*, *Wood and Fiber Science* 41(3):325-328, 2009.
- [15] W. T. Simson, *Predicting Equilibrium Moisture Content of Wood by Mathematical Models*, Forest Products Laboratory, Forest Service, USDA, 1973.
- [16] W. T. Simpson, *Dry Kiln Operator's Manual*, Forest Products Society, 1997.
- [17] J. Acuerdo de Cartagena, *Manual del Grupo Andino para el secado de maderas*, Lima, Perú, 1989, pp. 226-231.
- [18] *Datasheet SHT3x-DIS. Sensirion. Version 6. 2019*
- [19] N. P. Peña, *Predicción del contenido de humedad de equilibrio de la madera en función del peso específico de la pared celular y variables ambientales*, *Madera Ciencia y Tecnología* 13 (3):253-266, 2011.
- [20] J. A. Montoya Arango, *Determinación de las curvas isotermas de sorción y el PSF-Punto de saturación de las fibras de la especie Bambu phyllotachys pubescens Mazel*, *Scientia et Technica* año XIII, Universidad Tecnológica de Pereira, 2017.
- [21] F. Kollmann, *Tecnología de la madera y sus aplicaciones*, Tomo 1, 1959.
- [22] *Curso de secado de maderas*, INTI Madera y Muebles. Buenos Aires, Argentina, 2004.
- [23] A. Calderón, *Secado de la Madera*, Cuadernos de Dasonomia, Serie Didáctica No 13, Facultad de Ciencia Agrarias, Universidad Nacional de Cuyo.

Mobility of AGVs supported with Visible Light Communication

Paula Louro
ISEL-IPL
CTS-UNINOVA-LASI
Lisbon, Portugal
paula.louro@isiel.pt

Manuel A. Vieira
CTS-UNINOVA-LASI
Lisbon, Portugal
mvieira@deetc.isiel.ipl.pt

Gonçalo Galvão
ISEL-IPL
Lisbon, Portugal
a45903@alunos.isiel.pt

Manuela Vieira
ISEL-IPL
CTS-UNINOVA-LASI
DEE/ECT-UNL
Lisbon, Portugal
mv@isiel.pt

Abstract — This paper explores Autonomous Guided Vehicles (AGV) mobility in dense industrial environments, utilizing Visible Light Communication (VLC) technology for data transmission between infrastructures and vehicles, establishing X2X links. Tetrachromatic white Light Emitting Diodes (LEDs) and dedicated pinpin photodiodes facilitate simultaneous lighting and data transmission, while VLC-based indoor positioning enables guidance services with tailored coding schemes for each link. Analyzing AGV flow regulation within warehouse lanes similar to urban traffic flow, a urban mobility simulator generates movement data. A reinforcement learning scheme, integrating agent-based modeling with VLC queuing/request/response behaviors, efficiently schedules routes, ensuring optimal travel and avoiding congestion. Proof-of-concept is demonstrated through evaluations of travel time and traffic flows.

Keywords— Visible light communication, positioning system, guidance system, mobility, autonomous guided vehicle

I. INTRODUCTION

Autonomous Guided Vehicles (AGVs) are driverless carts widely utilized in industrial and distribution settings for material movement [1]. AGVs streamline operations across various industries, enhancing inventory management, production flexibility, and staff efficiency. They facilitate data-driven analytics, predictive maintenance, and reliability improvement. Originally used in manufacturing, AGVs now serve diverse industrial applications including warehouse logistics and container terminal operations [2]. Some AGVs feature robotic arms or serve as collaborative robots (cobots), extending their functionality to tasks like picking and assembly. AGVs are prominent in automotive, logistics, e-commerce, food, pharmaceuticals, and more [3]. Leveraging sensor technologies such as LiDAR and cameras, along with simultaneous localization and mapping algorithms, AGVs navigate autonomously through industrial environments [4].

VLC technology [5, 6] enhances AGV collaboration in dense industrial environments by providing accurate indoor positioning and mapping. LED light sources are modulated to encode data, offering advantages like high-speed transmission, immunity to electromagnetic interference, and enhanced security. The dense deployment of VLC transmitters makes it ideal for indoor localization and navigation [7, 8].

This paper discusses the integrated movement of AGVs performing tasks in indoor environments. AGV fleet management treats their movements similar to vehicular traffic, controlled by intelligent agents based on congestion conditions [9, 10]. Vehicular communication relies on visible links, facilitating Lamp-to-Vehicle (L2V), Vehicle-to-Vehicle (V2V), Vehicle-to-Infrastructure (V2I), and Infrastructure-to-Vehicle (I2V) channels [11].

The proposed system is modelled using the SUMO urban mobility simulator [12], with a Reinforcement Learning (RL) algorithm effectively scheduling AGV routes [13, 14]. Simulation experiments validate the method's efficiency in travel and congestion avoidance [15].

The indoor localization system combines optical wireless communication, computer algorithms, smart sensors, and an optical sources network, constituting a collaborative cyber-physical system approach.

II. ARCHITECTURE OF THE VLC SYSTEM

The communication network uses four different VLC Channels ensuring communication Lamp-to-Vehicle (L2V), Vehicle-to-Vehicle (V2V), Vehicle-to-Infrastructure (V2I) and Infrastructure-to-Vehicle (I2V), as illustrated in Figure 1.

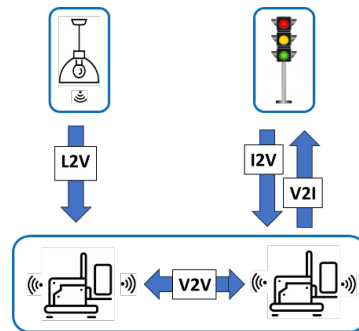


Fig. 1. Communication channels established using visible signals.

A. VLC transmitter and receiver

The VLC system utilizes tetra-chromatic white LEDs, with each LED containing independently controllable red,

green, and blue emitters. This configuration enables the creation of distinct data transmission channels by controlling each emitter separately. A single L2V transmitter comprises four LEDs arranged in a square formation, with only one emitter from each LED utilized for transmission. In V2V and V2I communication, only a single LED emitter is used. These tetra-chromatic LEDs emit distinct wavelengths in the red (620 nm), green (530 nm), blue (470 nm), and violet (405 nm) bands. These LEDs meet illumination standards, making them suitable for lighting and communication. Their effective channel separation and wide coverage area make them ideal for communication applications.

The VLC receiver features pinpin photodiodes with a-SiC:H/a-Si:H heterostructures, optimized for modulated wavelengths from RGB LEDs in the visible range. Its sensitivity is influenced by external optical bias, favoring short wavelengths under back violet background illumination and longer wavelengths under front illumination. The device acts as both a short-pass filter for back illumination and a long-pass filter for front illumination, with tuning options for short, medium, and long spectral regions. Front illumination enhances the red spectrum, while back illumination boosts the blue signal.

B. Indoor positioning and guidance based services

Indoor positioning with VLC uses L2V communication, where LEDs in ceiling lamps are arranged in a square configuration, defining unit navigation cells. Each cell is divided into footprints, assigned to different optical excitations. Figure 2 depicts the L2V transmitter configuration, unit navigation cell, and corresponding footprints. Footprint regions (#1, #2, ..., #9) correspond to optical excitations shown in Figure 2. Matrix notation identifies each emitter in the VLC transmitter network, transmitting data to determine navigation cell positions.

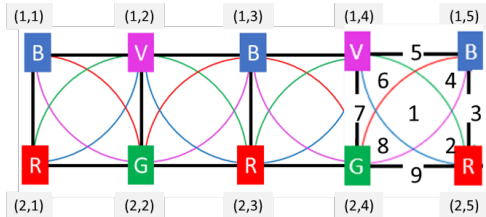


Fig. 2. Square configuration of VLC transmitters of the L2V link showing the unit navigation cell and footprints inside the unit navigation cell.

Each L2V VLC transmitter uniquely identifies its position within the indoor space, defining navigation cells. Within each cell, resolution is enhanced by measuring optical patterns, resulting in 9 distinct regions. Vehicle guidance along lanes and directional changes are facilitated by transmitting respective directions via the I2V link.

C. VLC protocols

Data transmission requires a specific modulation scheme. We use On-Off Keying (OOK), valued for its simplicity in VLC systems. In OOK modulation, the presence of a signal is represented by one level (usually the "on" state), while the absence of a signal is represented by another level (usually the "off" state). In other words, the carrier signal is switched on and off to represent digital data.

The communication protocol, outlined in Table I, controls information exchange, including synchronization, identification, and payload sections within each transmitted frame. The frame structure is systematic and standardized, with variations based on the type of communication (1-4: 1-L2V, 2-V2V, 3-V2I, 4-I2V). Each frame is 64 bits long, featuring specific blocks at the beginning and end to support synchronization of successive data frames.

TABLE I. CODIFICATION PROTOCOLS.

L2V	SYNC	1	x	y	END	h	m	s	Payload				EOF		
V2V	SYNC	2	x	y	Lane (0-7)	#AVG	END	h	m	s	x'	y'	#N	Payload	EOF
V2I	SYNC	3	x	y	TL (0-15)	#AVG	END	h	m	s	x'	y'	#N	Payload	EOF
I2V	SYNC	4	x	y	TL (0-15)	ID-AVG	END	h	m	s	x'	y'	#N	phase/Payload	EOF

The data frame consists of modular blocks, each comprising 4 bits, except for SYNC and timeline-related blocks (h-hour, m-minute, s-second), which use 5 bits each. Each VLC link's coding begins and ends with SoH and EOF blocks ([10101] and [0000], respectively), ensuring synchronization. The transmitter's position is coded as x and y in matrix notation, while timeline details are coded as {END, h, m, s} ([111] for END). Other codes include Lane, TL, #AVG, x' and y', ID-AVG, and #N, facilitating effective encoding and decoding of AGV movement information. This protocol guarantees synchronization and data integrity in VLC communication.

At the receiver, the photodetector generates a multiplexed signal based on input optical signals. With the VLC transmitter's 4 independent emitters, the output signals can combine one to four optical excitations, yielding 16 photocurrent levels. Bit decoding corresponds to assigning each photocurrent level to the respective optical excitation, achieved through previous system calibration to adjust photocurrent levels.

III. RESULTS AND DISCUSSION

A. AGV Traffic Scenario

Inside the warehouse, AGVs navigate corridors to pick up goods from predefined aisles. AGV flow is determined by assigned routes and stop times for aisle operations. AGVs adhere to right-hand traffic rules, using right lanes for forward and right turns, and left lanes exclusively for left turns. Tasks begin at the charging station, with AGVs following their routes until reaching the packaging station. AGVs can start operations from the packaging station while charging, upon receiving new collection instructions. The simulated scenario, depicted in Figure 4, comprises multi-intersections with two 4-way intersections having 2 lanes per arm.

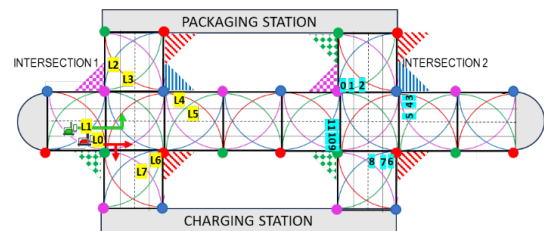


Fig. 3. Lanes and aisles inside the warehouse.

Central traffic light systems, managed by Central Managers (CMs), control traffic flow. Four traffic flows along cardinal points are considered, with binary choices

(turn left/straight or turn right) in road request and response segments. In intersection 1, even lanes (L0, L2, L4, L6) enable right turns or forward movements, while odd lanes allow left turns. Unit navigation cells defined by optical transmitters in the L2V channel are depicted along corridors, along with respective footprints. Each intersection has three traffic lights for possible movements (forward, turn left/right) in the convergent lane, totalling 12 traffic lights per intersection (TL0, TL1, ..., TL11). Intersection 2 displays corresponding traffic lights, regulating flows from north to south (TL0, TL1, TL2), east to west (TL3, TL4, TL5), south to north (TL6, TL7, TL8), and west to east (TL9, TL10, TL11). Traffic lights are ordered by turns, with lower orders for right turns (TL0, TL3, TL6, TL9), higher for left turns (TL2, TL5, TL8, TL11), and intermediate for forward movements (TL1, TL4, TL7, TL10).

B. VLC signals

Using the described spatial layout, optical communication was simulated with multiple AGVs moving eastward along lane L0, as depicted in Figure 4. The foremost AGV in the lane, located at position $R_{3,10}$ (x and y in matrix notation), communicates with the intersection agent via V2I communication. It transmits a request for forward movement at the intersection and communicates the number and positions of trailing AGVs (AVG1, AVG2, and AVG3), occupying positions $R_{3,8}$, $R_{3,6}$, and $R_{3,4}$ simultaneously.

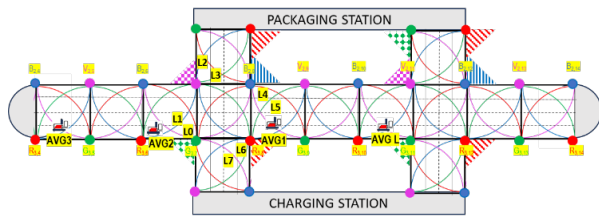


Fig. 4. Simulation scenario.

Using the communication protocol defined in Table I, the VLC system was configured to establish data transmission from each link. The optical signals measured at the receivers of links V2I and V2V are displayed in Figure 5.

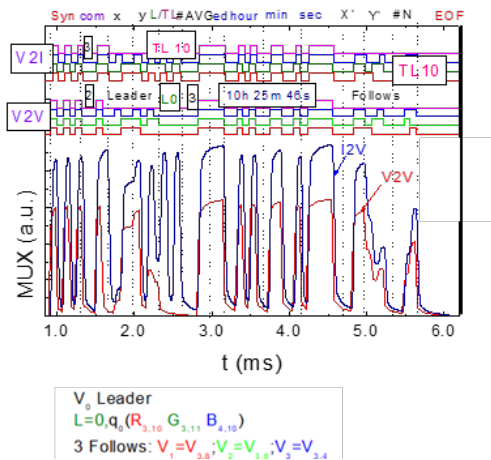


Fig. 5. Experimental data acquired by the receiver of the V2V and V2I VLC links.

The transmitted optical signals from each transmitter are represented on the top of the figure. In the I2V link, the leading AGV transmits a bit sequence following the protocol in Table I. The receiver detects different signal levels, each corresponding to a specific input combination. Decoding these levels using appropriate calibration signals allows recovery of the input optical signals. The frame begins with synchronization bits, followed by communication type (3 for V2I), position ($R_{3,10}$, $G_{3,11}$, $B_{4,10}$), intersection movement request (TL = 10 for forward movement), communication time (10:25:46), number of AGVs behind in the lane (3), and their coordinates: (3,8) for AVG1, (3,6) for AVG2, and (3,4) for AVG3, transmitted by red, green, and blue transmitters. In the V2V link, the leading AGV transmits synchronization bits, communication type (2 for V2V), position ($R_{3,10}$, $G_{3,11}$, $B_{4,10}$), movement lane (L = 0 for forward or right turn), communication time (10:25:46), number of AGVs behind in the same lane (3), and their coordinates: (3,8) for AVG1, (3,6) for AVG2, and (3,4) for AVG3.

In Figure 6 is displayed the optical signals acquired by the receiver of the I2V VLC link at the second intersection. The transmitted optical signals from each transmitter are represented on the top of the figure.

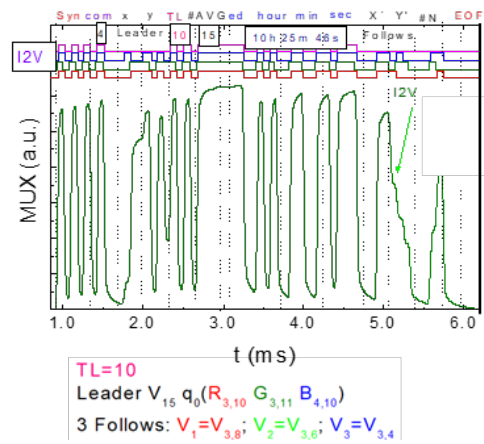


Fig. 6. Experimental data acquired by the receiver of the I2V VLC link located at intersection #2.

In this communication, the block after the synchronization bits, define an I2V communication (ID=4), followed by the identification of the corresponding traffic light (TL=10), the identification of the leading AGV (15 in this case), the communication time and the number of leading AGV's followers (3), and respective coordinates: (3,8), (3,6) and (3,4). This is in accordance with the information transmitted by the AVG L

C. Dynamic Traffic Model

AGV flow dynamics were assessed using SUMO, an open-source traffic simulation package for large networks. The simulation configured the scenario previously described and evaluated average speed and halting over a fixed period (one hour). Figure 7 compares average speeds and halting trends over time for low and high traffic AGV scenarios, assuming flows of 1800 and 2300 AGVs per hour, respectively.

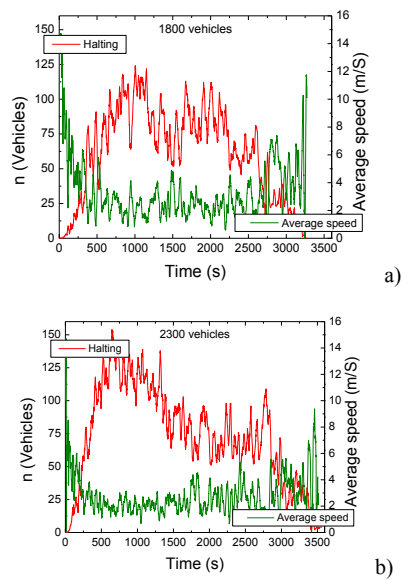


Fig. 7. Comparison of average speed and halting in both scenarios, a) 1800 AGV/hour. b) 2300 AGV/hour.

Figure 7 data shows an initial spike in speed at the start of halting simulations, gradually decreasing as the simulation progresses. This acceleration is due to fewer AGVs at intersections, allowing faster movement.

However, as more AGVs enter the system, average speed notably drops until the end of the simulation. As AGVs empty out, remaining ones have more space, leading to increased speed due to reduced congestion. Higher waiting AGV volumes correspond to decreased speed, while lower volumes result in increased speed, aligning with traffic dynamics expectations.

IV. CONCLUSIONS

The proposed application monitors and manages AGV movement in an optimized warehouse for material collection and transport. VLC links facilitate AGV flow, reducing congestion and waiting times. Various coding protocols were defined for VLC links, with experimental data obtained for V2V, V2I, and I2V links. Using the SUMO simulator, the same scenario was analyzed as urban traffic flow, considering low and high flows to simulate average speed and halting trends over a period. Results can predict traffic actions, prevent congestion, and reduce travel time, enhancing collection and transportation efficiency.

ACKNOWLEDGMENT

This work was sponsored by FCT – Fundação para a Ciência e a Tecnologia, within the Research Unit CTS – Center of Technology and systems, reference UID/EEA/00066/2020 and IPL/IDI&CA2024_INUTRAM_ISEL.

REFERENCES

- [1] Faiza Gul, Syed Sahal Nazli Alhady, Wan Rahiman, "A review of controller approach for autonomous guided vehicle system", *Indonesian Journal of Electrical Engineering and Computer Science*, Vol. 20, No. 1, October 2020, pp. 552-562 DOI: 10.11591/ijeecs.v20.i1.pp552-562.
- [2] Roodbergen, K. J., Vis, I. F. (2009). "A survey of literature on automated storage and retrieval systems." *European Journal of Operational Research*, 194(2), 343-362.
- [3] Hsiao, P. C., & Chang, S. L. (2019). "The application of Automated Guided Vehicles (AGVs) in different manufacturing systems: A literature review." *Procedia CIRP*, 81, 570-575.
- [4] P. Louro, M. Vieira, M. A. Vieira, "Geolocalization and navigation by visible light communication to address automated logistics control," *Opt. Eng.* 61(1), 016104 (2022), doi: 10.1117/1.OE.61.1.016104.
- [5] Căilean, A.M.; Dimian, M. "Current Challenges for Visible Light Communications Usage in Vehicle Applications: A Survey". *IEEE Communications Surveys & Tutorials* 2017, 19, 4, pp. 2681-2703. doi: 10.1109/COMST.2017.2706940 364.
- [6] Chowdhury, M. Z.; Hossan, M. T.; Islam, A.; Jang, Y. M. "A Comparative Survey of Optical Wireless Technologies: Architectures and Applications". *IEEE Access* 2018, 6, 9819-9840, doi: 10.1109/ACCESS.2018.2792419
- [7] O'Brien, D. et al. "Indoor Visible Light Communications: challenges and prospects," *Proc. SPIE* 7091, 709106, pp. 60-68 (2008).
- [8] Parth. H., Pathak, X., Pengfei, H. and Prasant, M., "Visible Light Communication, Networking and Sensing: Potential and Challenges," September 2015, *IEEE Communications Surveys & Tutorials* 17(4): Fourthquarter 2015, pp. 2047 – 2077 (2015).
- [9] Caputo, S., et al. "Measurement-based VLC channel characterization for I2V communications in a real urban scenario," *Veh. Commun.*, vol. 28, Apr. 2021, Art. no. 100305.
- [10] Vieira, M. A., Vieira, M., Vieira, P. and Louro, P., "Optical signal processing for a smart vehicle lighting system using a-SiCH technology," *Proc. SPIE* 10231, *Optical Sensors 2017*, 102311L (2017).
- [11] P. Louro, M. Vieira, M. A. Vieira, "Bidirectional visible light communication," *Opt. Eng.* 59(12), 127109 (2020), doi: 10.1117/1.OE.59.12.127109.
- [12] Keskin, M.F.; Sezer, A.D.; Gezici, S. Localization via Visible Light Systems. *Proceedings of the IEEE* 2018, 597 106, 1063–1088. doi:10.1109/JPROC.2018.2823500
- [13] Junping Zhang, Fei-Yue Wang, Kunfeng Wang, Wei-Hua Lin, Xin Xu, and Cheng Chen. "Data-driven intelligent transportation systems: A survey". *IEEE Transactions on Intelligent Transportation Systems*, 12(4):1624–1639, 2011.
- [14] Liang, X., Du, X., Wang, G., and Han, Z., "A Deep Reinforcement Learning Network for Traffic Light Cycle Control," in *IEEE Transactions on Vehicular Technology*, vol. 68, no. 2, pp. 1243-1253, Feb. 2019, doi: 10.1109/TVT.2018.2890726.
- [15] Vieira, M.A.; Galvão, G.; Vieira, M.; Louro, P.; Vestias, M.; Vieira, P. "Enhancing Urban Intersection Efficiency: Visible Light Communication and Learning-Based Control for Traffic Signal Optimization and Vehicle Management". *Symmetry* 2024, 16, 240. <https://doi.org/10.3390/sym16020240>.

Non-Invasive Moisture Sensing and Classification Using Ultra-Wideband Signals

Raymundo Albert

Departamento de Inteligencia Artificial
Instituto Nacional de
Tecnología Industrial
Buenos Aires, Argentina
ralbert@inti.gob.ar

Edgardo Marchi

Departamento de Inteligencia Artificial
Instituto Nacional de
Tecnología Industrial
Buenos Aires, Argentina
emarchi@inti.gob.ar

Cecilia Galarza

Centro de Simulación Computacional
Consejo Nacional de Investigaciones
Científicas y Técnicas
Buenos Aires, Argentina
cgalarza@csc.conicet.gov.ar

Abstract—This paper presents a novel method for sensing and classifying water content in dielectric materials. Moisture levels are obtained by non-invasive methods using digitally processed electromagnetic signals. Those signals are the scattering produced within the measured material when illuminated with an Ultra-Wideband pulse. The pulse generation, signal detection, and discretization hardware was built on a custom design developed at INTI. The collected information is processed through a non-linear pipeline to finally perform classification according to the water content of the target. We show that the precision of the proposed sensing architecture is comparable with standard methods that may be invasive. As a non-invasive method, this new sensor has great potential for applications such as farming and construction industries, among others.

Index Terms—Non-Invasive Sensing, Classification, DSP, Ultra-Wideband

I. INTRODUCTION

A scattering phenomenon occurs when an electromagnetic wave strikes a small object and deviates its direction of propagation. The received echoes contain unique features that can be used to identify the target. A challenging application is the determination of moisture content on wet samples. Previous works have shown promising results by measuring moisture content in bulk materials using UWB (Ultra WideBand) signals [1], [2]. Moreover, impulsive UWB systems together with machine learning methods have gained increasing attention as a means of solving different classification problems. In [3], [4], the non-destructive characterization, based on the target scattered field, was analyzed.

In this work, we build on these results and present a novel sensing method to estimate moisture content using the reflection of UWB signals. We address the sensing problem in non-controlled measurement environments, where disturbance and interference are inevitably present. We have worked towards this end on all the stages of the sensing platform comprising both the hardware and the digital processing pipeline.

When a radar illuminates a static target, a suitable approximation to the transient behavior of the scattered field is represented as the sum of complex exponentials [5], which in this context are commonly referred to as *natural frequencies* or *modes*. It was observed that such natural frequencies only depend on the size, shape, and electrical properties of the

scattering object, and are independent of the relative position between the radar and the target. In this paper, we propose a moisture classification strategy using the natural frequencies of the wet samples. Specifically, we associate natural frequencies with a percentage of water content and devise a non-linear classification scheme using statistical learning principles.

The paper is organized as follows. Section II introduces the hardware platform used as the sensor. In section III a detailed description of the measurement setup is provided. Section IV presents the proposed algorithm and data pipeline. Finally, section V shows the obtained results and concludes this work.

II. UWB SENSING PLATFORM

An Impulse-Radio (IR) UWB sensing platform was developed to transmit the UWB electromagnetic pulse and receive the scattered echoes of the Target Under Test (TUT). The platform has a System-on-Chip (SoC) for pulse generation and signal preprocessing. The digital subsystem is preceded by an analog front-end (AFE), and a pair of UWB Vivaldi antennas for transmitting and receiving the electromagnetic signals.

The FPGA area of the SoC is responsible for signal preprocessing, and noise reduction through ensemble averaging. On the other hand, the Processing System within the SoC coordinates subsystems and handles the real-time data transfer with the PC through a Gbit Ethernet link. A custom computer application was developed to plot the acquired signal in real time and record the data in Python's `numpy` format.

Fig. 1 shows a simplified scheme for the hardware sensing platform. In this work, the platform is specified by the parameters listed in Table I. The interested reader can find more information about the platform development process in [6].

III. MEASUREMENT SETUP

To build a reference dataset for algorithm development and testing, we worked with six identical plastic containers labeled from 1 to 6. These containers were filled with $6kg$ of dry sand and used as TUTs. The objective is to identify water content within the container regardless of its relative position from the antennas. The experimental setup is shown in Fig. 2.

Each TUT was measured in 8 different angles ranging from 0° to 180° with a step of 45° , and 2 distances from the

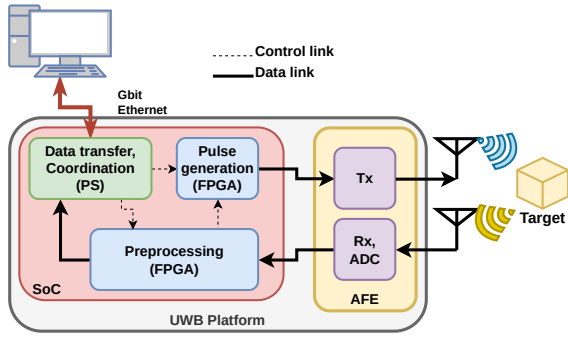


Fig. 1: UWB Platform scheme

TABLE I: Configured platform parameters

Parameter	Value
Pulse Width (PW)	$1.8ns$
Pulse Bandwidth @ $-20dB$ (PBW)	$847,5MHz$
Center frequency (F_c)	$3,785GHz$
Sampling frequency (F_s)	$5,04GSps$
Frame averaging (FA)	16
Frames per second (FPS)	$7,85MHz/FA = 490,625kHz$
RF Channels	2 (Quadrature modulation I,Q)
Bits per sample	12, 12 (I, Q)
Frame length	640 Samples

Tx/Rx antennas (70cm and 80cm respectively) according to the procedure shown in Algorithm 1. TUT number 5 was set aside as a control sample. This container was only measured when no water was added, to keep a dry reference TUT.

Measurements were made in two different environments: a Semi-Anechoic Chamber (SAC) and a standard indoor environment. Both setups are shown in Fig. 3. Table II summarizes the tests made in each location by identifying the tested container (TUT number) and the water content added to it.

Finally Fig. 4 shows the absolute magnitude of some captured signals for different TUTs. It can be seen that received

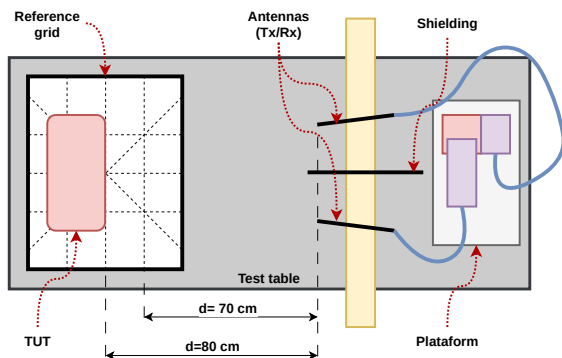


Fig. 2: Test setup diagram.

Algorithm 1 Measurement procedure

- 1: For TUT 6 in SAC and each TUT in $\{1, 2, 3, 4\}$ in the laboratory.
- 2: A Dry TUT is placed over the grid at angle = 0° and $d = 80 cm$.
- 3: An approximately 1min signal is recorded.
- 4: The TUT is rotated 45° .
- 5: **if** TUT is at angle = 215° and $d = 80 cm$ **then**
- 6: TUT is moved to $d = 70 cm$ and 0° then go to 3.
- 7: **else if** TUT position is angle = 215° and $d = 70 cm$ **then**
- 8: 100ml of water is added to the TUT and the mix is homogenized.
- 9: **if** The mix is saturated **then**
- 10: End TUT measurement and go to 17.
- 11: **else**
- 12: Go to 3
- 13: **end if**
- 14: **else**
- 15: Go to 3
- 16: **end if**
- 17: **if** There are TUTs pending to be measured. **then**
- 18: Go to 2 for the next TUT.
- 19: **else**
- 20: End measurement.
- 21: **end if**

TABLE II: TUTs measurements

Location	TUT number	Water content (Δ)
SAC	1, 2, 3, 4, 5, 6	0
	6	0 to 1300ml
Lab	5	0
	1, 2, 3, 4	0 to 1300ml

signals contain information about the water content of the target embedded in the information on its radar cross-section. This fact poses a challenge since we only need to extract the features for moisture characterization.

IV. PROCESSING AND CLASSIFICATION PIPELINE

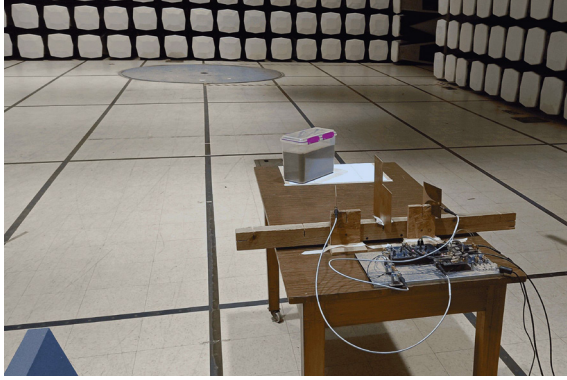
Consider L frames taken from one signal of the form

$$y_k^{(\ell)} = x_k^{(\ell)} + w_k^{(\ell)} = \sum_{i=1}^r c_i^{(\ell)} z_i^k + w_k^{(\ell)}, \quad k = 1, 2, \dots; \quad (1)$$

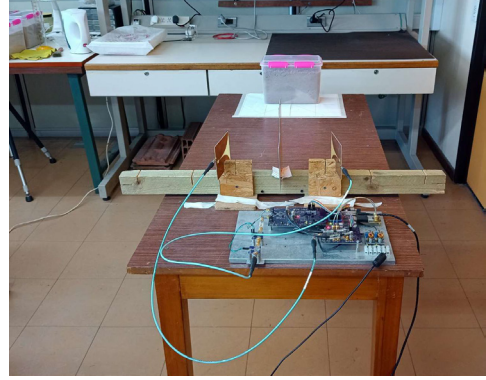
$$\ell = 1, 2, \dots, L,$$

where $w_k^{(\ell)}$ represent some noise associated with the measurement. Each signal corresponds to a class defined by varying water content in the TUTs. Hence, the classification problem is to design an algorithm that categorizes new observations into these classes based on a finite set of labeled noisy observations. Time-domain signals exhibit robust spikes due to specular reflections and antenna coupling. Environmental data (commonly referred to as *clutter*) is another problematic disturbance with a heavy impact on classification accuracy.

To minimize the effect of clutter and antenna coupling, an estimated background signal is subtracted from the received



(a) SAC



(b) Laboratory

Fig. 3: Test setup in both environments.

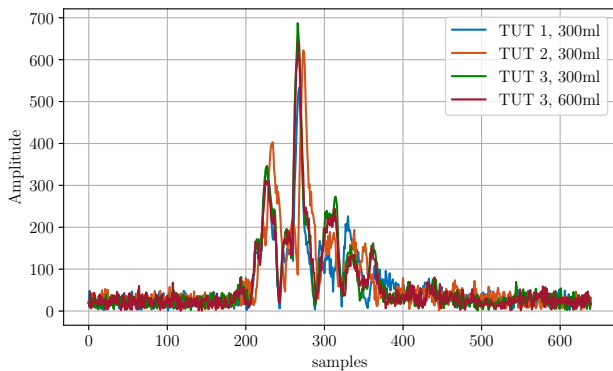
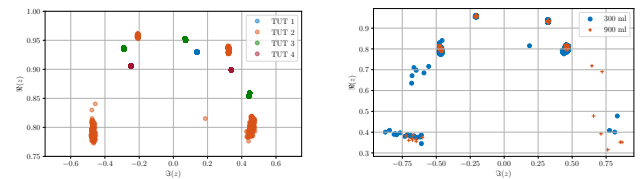


Fig. 4: Measured signal for different TUTs with 300ml of water content, and both 300 and 600ml for TUT 3.

signal. This is done by applying a Least Square Estimator to measurements obtained when transmitting the pulse with no target present.

The spectral estimation process or natural modes estimation is then the next stage of the processing chain. As the total number of modes is unknown, we first estimate the order of the system. Noisy signals of the same class produce a cluster of natural modes typically with different sizes for each mode with some potential overlapping, thereby complicating the classification task.

With these L signals a tensor is built, $\mathcal{Y} \in \mathbb{C}^{n \times n \times L}$, where the frontal slices are $n \times n$ Hankel matrices built from the signals sample $y_k^{(\ell)}$ and $n \geq r$. To estimate the natural modes a tensor rank decomposition is performed [7], followed by a spectra estimation [3]. However, the number of modes, r , has to be estimated as an input parameter to the respective algorithm. To estimate r the method introduced in [8] was used. In Fig. 5 an example of estimated natural modes is shown. In Fig. 5a the natural modes for different TUTs and the same water content do not coincide in location; in Fig. 5b the natural modes for TUT 4 and different water content are



(a) Natural modes when TUTs have 300ml content water.

(b) Natural modes of TUT 4 for different water content.

Fig. 5: Natural modes for different TUTs and water content

very close to each other, this illustrates the complexity of the classification task.

In [9] the Radon Cumulative Distribution Transform (Radon-CDT) was proposed to turn not-linearly separable classes of n -dimensional densities into linearly separable ones. Therefore to take advantage of this property, a probability density function of the position of the natural modes in the z -plane needs to be estimated and then the Radon-CDT of this image is calculated. The idea of the Radon-CDT is to first slice the 2-dimensional density into a set of one-dimensional distributions and then apply CDT to the one-dimensional distributions.

In line with [9], given Radon-CDT does not prescribe an optimal classifier, a Linear Discriminant Analysis (LDA) [10] is then utilized to diminish dimensionality and extract features from Radon-CDT image, thus reducing computational complexity during classification. Subsequently, the classifier is trained on these features to accurately recognize and classify them, enabling prediction of the class for a new input signal.

V. EXPERIMENTAL RESULTS

We constructed a dataset as explained before. Measurements obtained in the laboratory at 0° and 180° with the TUTs positioned at 80cm and 70cm were considered. The water contents are grouped into 3 classes as in table III.

The dataset of natural modes is utilized for comparing two distinct classification strategies: one uses the pre-processing

TABLE III: Classes for water content

Class No.	Δ (ml)
1	$0 \leq \Delta \leq 400$
2	$500 \leq \Delta \leq 800$
3	$900 \leq \Delta \leq 1300$

TABLE IV: Test accuracy using Linear SVM and the Radon-CDT for natural modes dataset.

	Testing Accuracy
Linear SVM	0.36
Radon-CDT	0.937

scheme outlined before, and for the other one we have trained a Support Vector Machine (SVM) with linear kernel directly on the natural modes. In the first case, to generate the Radon-CDT images, we used a Gaussian kernel with a bandwidth of 0.05 for density estimation. The classifiers were trained using TUTs 1,2 and 3. TUT 4 was left to test the classifiers. We used a 10-fold cross-validation scheme on each training strategy. The test accuracy results in Table IV, reveal that utilizing an LDA classifier with the Radon-CDT images yields superior accuracy. An illustration is presented in Fig. 6, where LDA is applied to all 3 classes and their corresponding Radon-CDT transform domain of TUT 4 to show the linear separability property. Also, the figure depicts the separation lines obtained by training the linear discriminant.

We use the probe HydraProbe© [11] to compare our technique with a different procedure to measure moisture content. The probe inserted into the soil returns the average water content inside the surrounding cylinder 3cm in diameter. HydraProbe© is regularly used to measure soil moisture by performing an invasive procedure. The reported uncertainty introduced by the commercial probe [11] ranges from 60ml/l to 20ml/l, dependent on the soil texture.

In the case of the technique proposed in this paper, the uncertainty is related to Δ , the spread of each class introduced in Table III. The total volume of each plastic container is 6.084l, then the uncertainty for classes 1 and 3 is

$$\delta = \frac{400ml}{6.084l} = 66ml/l.$$

Similarly, class 2 has an uncertainty of $\frac{300ml}{6.084l} = 49ml/l$. The overall uncertainty associated with UWB measurements remains comparable to the uncertainty of the HydraProbe© for a single measurement per plastic container. The uncertainty of the probe can be improved with additional measurements; however, this necessitates further invasive measurements.

VI. CONCLUSION

A complete UWB sensing platform for moisture sensing and classification was presented. Incorporating a non-linear processing module, such as the Radon-CDT, resulted in an effective strategy to render problems linearly separable in the transformed space. Moreover, Machine Learning methods trained with such input can obtain excellent classification

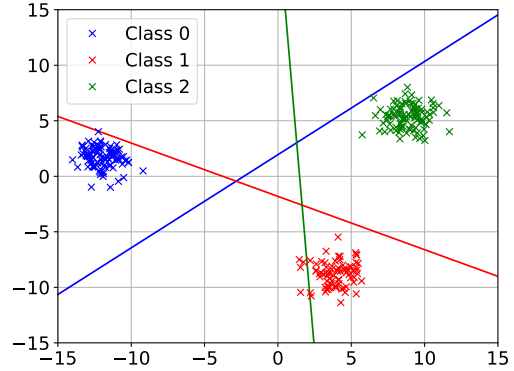


Fig. 6: LDA projections for test data and separation lines.

performance. Further investigation is required to define classification classes with smaller moisture spread. However, this work proves that the proposed hardware and the processing pipeline have great potential to implement non-invasive moisture sensors.

REFERENCES

- [1] O. Schimmer, A. Gulck, F. Daschner, J. Piotrowski, and R. Knochel, "Noncontacting determination of moisture content in bulk materials using sub-nanosecond uwb pulses," *IEEE Trans. on Microw. Theory Techn.*, vol. 53, no. 6, pp. 2107–2113, 2005.
- [2] H. Mextorf, F. Daschner, M. Kent, and R. Knöchel, "Non-contacting moisture sensing using a dedicated uwb time domain instrument," in *2012 The 7th Ger. Microw. Conf.*, 2012, pp. 1–4.
- [3] M. Bouza, A. Altieri, and C. G. Galarza, "Robust target classification using uwb sensing*," *IEEE Access*, vol. 11, pp. 44 267–44 277, 2023.
- [4] A. Uthayakumar, M. P. Mohan, E. H. Khoo, J. Jimeno, M. Y. Siyal, and M. F. Karim, "Machine learning models for enhanced estimation of soil moisture using wideband radar sensor," *Sensors*, vol. 22, no. 15, 2022.
- [5] C. E. Baum, "On the singularity expansion method for the solution of electromagnetic interaction problems," 1971.
- [6] M. Cervetto, E. Marchi, and C. G. Galarza, "A Fully Configurable SoC-Based IR-UWB Platform for Data Acquisition and Algorithm Testing," *IEEE Embed. Syst. Lett.*, vol. 13, no. 2, pp. 53–56, Jun. 2021.
- [7] T. G. Kolda and B. W. Bader, "Tensor decompositions and applications," *SIAM Review*, vol. 51, no. 3, pp. 455–500, 2009.
- [8] J. Papy, L. De Lathauwer, and S. Van Huffel, "A shift invariance-based order-selection technique for exponential data modelling," *IEEE Signal Process. Lett.*, vol. 14, no. 7, pp. 473–476, 2007.
- [9] S. Kolouri, S. R. Park, and G. K. Rohde, "The radon cumulative distribution transform and its application to image classification," *IEEE Trans. Image Process.*, vol. 25, no. 2, pp. 920–934, 2016.
- [10] C. M. Bishop, "Pattern recognition and machine learning (information science and statistics)," 2007.
- [11] Stevens, "Hydraprobe." [Online]. Available: <https://stevenswater.com/products/hydraprobe/>

Sistema de Enfriamiento para Hipotermia Cerebral Selectiva

Dr. Mauricio Mercado¹
email: maury.mercado@icloud.com

Dr. Federico Salles²
email: federico.salle@gmail.com

Dra. Corina Puppo¹
email: coripuppo@gmail.com

Dr. Leandro Moraes¹
email: moraesoronoz@gmail.com

Dr. Alberto Biestro¹
email: mapibies@vera.com.uy

Ing. Bernardo Yelicich¹
email: byelicich@hc.edu.uy

Dra. Matilde Lisarrague²
email: matildelissarrague@gmail.com

MSc. Ing. Hector Gomez¹
email: hector.gomez@ieee.org

¹ Unidad Académica de Medicina Intensiva Laboratorio de Neuromonitoreo Centro de Tratamiento Intensivo del Hospital de Clínicas, Cátedra de Medicina Intensiva, Hospital de Clínicas, Facultad de Medicina Universidad de la República (UdelaR) Montevideo, Uruguay

² Unidad Académica de Neurocirugía Hospital de Clínicas, Facultad de Medicina Universidad de la República (UdelaR) Montevideo, Uruguay

Resumen— Las lesiones cerebrales traumáticas (TCE) continúan siendo una causa de muerte significativa, requiriendo atención urgente y tratamiento integral en la Unidad de Cuidados Intensivos (UCI) para mejorar los resultados del paciente y minimizar las secuelas a largo plazo. Recientemente, la craniectomía descompresiva (CD) y la hipotermia han ganado atención como métodos terapéuticos potenciales. Sin embargo, la hipotermia sistémica puede llevar a efectos secundarios no deseados. Por lo tanto, se ha propuesto un sistema de enfriamiento craneal-cerebral selectivo para controlar la hipertensión intracraneal (HIC) sin inducir hipotermia sistémica.

Palabras clave— hipotermia selectiva, trauma de cráneo, temperatura, enfriamiento cerebral.

I. INTRODUCCIÓN

Las lesiones cerebrales traumáticas siguen siendo la principal causa de muerte y discapacidad en adultos jóvenes en los países desarrollados¹. El traumatismo craneoencefálico grave (TCE), que es definido como una lesión cerebral con una puntuación en la Escala de Coma de Glasgow (SCG) inferior a 9, representa una entidad clínico-patológica de alta complejidad, que requiere el ingreso a la unidad de cuidados Intensivos (UCI), considerada como una emergencia neuroquirúrgica por su alta morbimortalidad y la alta prevalencia de discapacidad².

El tratamiento del TCE grave requiere una evaluación inicial exhaustiva, una toma de decisiones rápida y precisa, y un plan de manejo eficiente y seguro. Es fundamental para el personal médico abordar adecuadamente la situación en el momento óptimo, lo que constituye un desafío importante para el equipo tratante (neurocirujanos, neurólogos, intensivistas, enfermeras especializadas, etc.). La intervención urgente y el tratamiento integrado apoyado con los estudios de imagen y la neurocirugía son cruciales para mejorar el pronóstico del paciente, con el objetivo de minimizar las secuelas a largo plazo³. El enfoque del tratamiento de la Hipertensión Intracraneal (HIC) a nivel internacional ha estado influenciado por las directrices de manejo establecidas por la Brain Trauma Foundation (BTF)⁴

y más recientemente por el consenso de Seattle⁹. La craniectomía descompresiva (CD) es señalada en estas guías como una de las medidas más robustas para el control de la HIC refractaria a las medidas de primer y segundo nivel. La CD consiste en un procedimiento quirúrgico que implica la extracción de una porción significativa del cráneo con el fin de aumentar el espacio intracraneal y aliviar la presión intracraneal². A pesar de ello, la revisión sistemática de los estudios sobre CD como medida terapéutica de control de la HIC en el TCE muestra su ineficacia en reducir la HIC y evitar la muerte al tiempo que es mucho menos efectivo en reducir la discapacidad resultante^{10,11}.

Otro recurso planteado en casos de HIC refractaria es la hipotermia sistémica (HTSis) leve a moderada (35 a 32°C). La HTSis leve a moderada ha demostrado tener un efecto robusto en la reducción de la hipertensión intracraneal (HIC). Sin embargo, su uso en pacientes es problemático pues por sus efectos sistémicos nocivos pueden contrarrestar sus beneficios neurológicos a tal punto que los pacientes tratados tienen igual o peor resultado que en pacientes control^{5,12}. Por esta razón surge la idea de aplicar hipotermia selectiva (HTSel) a nivel intracraneano evitando los efectos sistémicos de la HTSis al tiempo que se alcanzaría un efecto sinérgico con la CD tanto en el control de la HIC como en la neuroprotección⁵. En esa línea es que la ventana ósea creada por la craniectomía descompresiva podría ser utilizada como un “pasadizo” para la inducción y mantenimiento de la hipotermia en el encéfalo⁶. De este modo, se plantea la aplicación local de la hipotermia para controlar la HIC después de la craniectomía descompresiva, sin generar hipotermia sistémica, mediante el desarrollo de un sistema de enfriamiento que genera hipotermia selectiva. En esta primera etapa del estudio describimos el desarrollo del dispositivo y su funcionamiento básico en el laboratorio.

II. DESARROLLO

En el proyecto de bioingeniería que estamos llevando a cabo en el Hospital de Clínicas de la UdelaR (*Proyecto Mosquito*) se propone la construcción de un sistema de enfriamiento craneal-cerebral selectivo para el tratamiento de

estos pacientes que consiste en aplicar frío mediante un casco en cuyo interior circula líquido refrigerante a baja temperatura.

Las temperaturas en todo el sistema se controlan en un módulo de control y la temperatura cerebral del paciente se controlará mediante un monitor de temperatura de uso médico y su señal continua será adquirida por el sistema CONTINE¹³.

A. Materiales y Métodos

En la figura se puede apreciar el sistema en su conjunto.

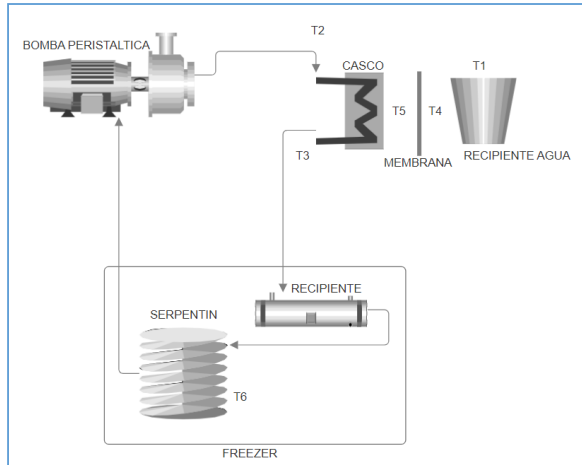


Figura 1. Esquema general del sistema

El sistema consiste en un freezer Marca Aplicool modelo X30 de 60W de potencia eléctrica, que alberga en su interior un serpentín de cobre de 3 metros de largo 9mm de diámetro, una bomba peristáltica YOKOGAWA SERTec 8RH2-DM25W480 acoplada a un motor YOKOGAWA SC-H8A25KW326 de 25W y 100V, el recipiente es un recipiente de líquido de frenos automovilístico de 1 litro útil.

Dentro del freezer se utilizó una solución de Glicerol en agua bidestilada al 50% de proporción en volumen para que permanezca en estado líquido a -16°C y dentro del circuito se utilizó alcohol etílico al 70%.

El sistema de control consta de un microcontrolador Arduino UNO que toma las medidas de 6 sondas de temperatura DS18B20 encapsuladas en acero inoxidable. Se trata de sondas de temperatura muy precisas impermeables con un rango de trabajo de -55 a 125°C , teniendo $\pm 0.5^{\circ}\text{C}$ de precisión de -10 a 85°C . las sondas tienen integrada la electrónica que nos provee una interfaz digital y un protocolo de comunicación 1-WIRE lo que hace muy sencilla la implementación.

Los puntos de medida están indicados en la Figura 1 y se eligieron de tal manera que se pueda estimar la potencia de enfriamiento del sistema.

El casco que se está utilizando proviene del casco de un sistema de enfriamiento de cuero cabelludo para pacientes con tratamiento de quimioterapia marca Dignimed modelo Digni-cap que utiliza unos conectores auto bloqueantes marca COLDER.

Las tuberías son de silicona y algunas de ellas están aisladas térmicamente.

En esta etapa del desarrollo se están haciendo pruebas in vitro, utilizando como fantoma un recipiente de acero inoxidable con agua en su interior, entre el casco y la superficie del recipiente se colocó silicona platino curada que tiene una conductividad térmica aproximada de entre $0,15$ y $0,30 \text{ W}/(\text{m}^{\circ}\text{K})$, que es del orden de la conductividad térmica del cuero cabelludo, (si bien no se encontró bibliografía sobre la conductividad térmica del cuero cabelludo, se hizo una suposición de que es similar a la conductividad térmica de la piel⁷, se utilizó un espesor de 5mm en un valor aproximado al espesor del cuero cabelludo⁸).

El funcionamiento es de tipo ON/OFF, con un ciclo de histéresis de 2 grados y el control se hace actualmente con un módulo de temperatura exterior MH1210W que actúa sobre la bomba, Se está trabajando para que el control se realice directamente en el módulo de control.

Como control de temperatura tenemos tres umbrales que se deben respetar:

- T superficie de la piel $> 3^{\circ}\text{C}$
- T cerebral central $< 34^{\circ}\text{C}$
- T sistémica $> 35.5^{\circ}\text{C}$

En los experimentos que se realizaron actualmente se controla el sistema utilizando solamente el umbral a) tomando como temperatura de la superficie T5 de la gráfica.

Para poder integrar las condiciones b) y c) se deben integrar al sistema las temperaturas de los monitores del paciente, para eso se utilizará el sistema de adquisición y monitoreo CONTINE, desarrollado en el CTI del Hospital de Clínicas, UdeLaR.

B. Resultados

En esta etapa estamos midiendo la potencia de enfriamiento neta del sistema completo.

En el recipiente con 3.5 litros de agua a temperatura ambiente de 23°C se enciende el sistema.

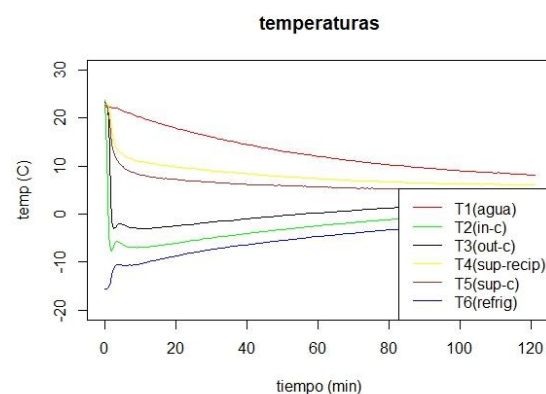


Figura 2. Determinación de temperaturas

Esperado el lapso en que la temperatura del recipiente se estabiliza, se calcula la potencia aproximada mediante la fórmula:

$$P = \frac{m \cdot c \cdot \Delta T}{t}$$

donde:

m = 3500g es la masa del agua

c = 4.184 J / (g K) es el calor específico del agua delta T es el delta de temperatura (el delta es lo mismo que °K)

t = 7273.251 es el tiempo en segundos

resultando P = 28.6W

C. Conclusiones

La potencia de enfriamiento neta lograda con el sistema es bastante auspiciosa teniendo en cuenta todas las pérdidas que se generan en los tubos, en la propia bomba que genera calor, y en la transferencia mediante el casco que dista de ser ideal.

Suponiendo que la superficie de la cabeza es aproximadamente del 7% de la del cuerpo humano y un consumo de 2000kCal diario dividido en un período de 16h despierto, llegamos a que en la cabeza se disipan aproximadamente del orden de los 10W, por lo que las primeras pruebas realizadas son auspiciosas.

La próxima etapa es la realización de un fantoma mas aproximado a la realidad, utilizaremos un cráneo craniectomizado, cuero cabelludo fabricado con silicona, dura madre real en formaldehído, y como símil del parénquima cerebral utilizaremos hidrogel de colágeno, ya que tiene unas propiedades térmicas similares a las del cerebro.

III. BIBLIOGRAFÍA

- [1]. Corrigan, J.D., Selassie, A.W. and Orman, J.A. The epidemiology of traumatic brain injury. *J Head Trauma Rehabil*, 2010 25, 72-80.
- [2]. Tagliaferri, F., Compagnone, C., Korsic, M. et al. A systematic review of brain injury epidemiology in Europe. *Acta Neurochir* 2006 148, 255–268
- [3]. Karagianni MD, Tasiou A, Brotis AG, Tzerefos C, Lambrianou X, Alkiviadis T, Kalogeras A, Spiliotopoulos T, Arvaniti C, Papageorgakopoulou M, Gatos C, Fountas KN. Critical Assessment of the Guidelines-Based Management of Severe Traumatic Brain Injury with the Appraisal of Guidelines for Research and Evaluation II. *World Neurosurg*. 2023 Aug;176:179-188.
- [4]. Carney, Nancy PhD; Totten, Annette M. PhD; O'Reilly, Cindy BS; Ullman, Jamie S. MD; Hawryluk, Gregory W.J. MD, PhD; Bell, Michael J. MD; Bratton, Susan L. MD; Chesnut, Randall MD; Harris, Odette A. MD, MPH; Kissoon, Niranjan MD; Rubiano, Andres M. MD; Shutter, Lori MD; Tasker, Robert C. MBBS, MD; Vavilala, Monica S. MD; Wilberger, Jack MD; Wright, David W. MD; Ghajar, Jamshid MD, PhD. Guidelines for the Management of Severe Traumatic Brain Injury, Fourth Edition. *Neurosurgery* 80(1):p 6-15, January 2017.
- [5]. Muengtaweepongsa S, Srivilaithon W. Targeted temperature management in neurological intensive care unit. *World J Methodol*. 2017 Jun 26;7(2):55-67
- [6]. Szczygielski J, Muller A, Mautes AE, Sippl C, Glameanu C, Schwerdtfeger K, et al. Selective Brain Hypothermia Mitigates Brain Damage and Improves Neurological Outcome after Post-Traumatic Decompressive Craniectomy in Mice. *J Neurotrauma* 2016 Oct 31;34(8):1623-35.
- [7]. Holman, J. P. (1945). Heat transfer in living tissue. II. Experimental measurements. *Journal of Applied Physics*, 16(9), 669-676. DOI: <https://doi.org/10.1063/1.1707393>
- [8]. Liu, Y., & Wang, X. (2006). Study on the thickness of human scalp by ultrasonography. *Skin Research and Technology*, 12(4), 262-266. DOI: <https://doi.org/10.1111/j.1600-0846.2006.00140.x>
- [9]. Hawryluk GWJ, Aguilera S, Buki A, Bulger E, Citerio G, Cooper DJ, Arrastia RD, Diring M, Figaji A, Gao G, Geocadin R, Ghajar J, Harris O, Hoffer A, Hutchinson P, Joseph M, Kitagawa R, Manley G, Mayer S, Menon DK, Meyfroidt G, Michael DB, Oddo M, Okonkwo D, Patel M, Robertson C, Rosenfeld JV, Rubiano AM, Sahuquillo J, Servadei F, Shutter L, Stein D, Stocchetti N, Taccone FS, Timmons S, Tsai E, Ullman JS, Vespa P, Videtta W, Wright DW, Zammit C, Chesnut RM. A management algorithm for patients with intracranial pressure monitoring: the Seattle International Severe Traumatic Brain Injury Consensus Conference (SIBICC). *Intensive Care Med*. 2019 Dec;45(12):1783-1794. doi: 10.1007/s00134-019-05805-9
- [10]. Sahuquillo J, Dennis JA. Decompressive craniectomy for the treatment of high intracranial pressure in closed traumatic brain injury. *Cochrane Database Syst Rev*. 2019 Dec 31;12(12):CD003983. doi: 10.1002/14651858.CD003983.pub3
- [11]. Kolas AG, Adams H, Timofeev IS, Corteen EA, Hossain I, Czosnyka M, Timothy J, Anderson I, Bulters DO, Belli A, Eynon CA, Wadley J, Mendelow AD, Mitchell PM, Wilson MH, Critchley G, Sahuquillo J, Unterberg A, Posti JP, Servadei F, Teasdale GM, Pickard JD, Menon DK, Murray GD, Kirkpatrick PJ, Hutchinson PJ; RESCUEicp Trial Collaborators. Evaluation of Outcomes Among Patients With Traumatic Intracranial Hypertension Treated With Decompressive Craniectomy vs Standard Medical Care at 24 Months: A Secondary Analysis of the RESCUEicp Randomized Clinical Trial. *JAMA Neurol*. 2022 Jul 1;79(7):664-671. doi: 10.1001/jamaneurol.2022.107
- [12]. Thakur K, Kaur H, Dhandapani M, Xavier T, Srinivasan G, Gopichandran L, Dhandapani S. Systematic review exploring the effect of therapeutic hypothermia on patients with intracranial hypertension. *Surg Neurol Int*. 2022 Jun 3;13:237. doi: 10.25259/SNI_194_2022.
- [13]. Gomez H, Camacho J, Yelicich B, Moraes L, Biestro A, Puppo C. Development of a multimodal monitoring platform for medical research. *Annu Int Conf IEEE Eng Med Biol Soc*. 2010;2010:2358-61. doi: 10.1109/IEMBS.2010.5627936. PMID: 21097226.

DetECCIÓN DE POZOS EN PLACAS DE ENSAYOS MEDIANTE REDES NEURONALES Y TRANSFERENCIA DE CONOCIMIENTO

Emmanuel Rosa Delgado, Michael Rivera¹ Lazú, José O. Sotero Esteva*

Departamento de Matemáticas, Universidad de Puerto Rico en Humacao, Humacao, Puerto Rico

{emmanuel.rosa2, michael.rivera, jose.sotero}@upr.edu

*ORCID 0000-0001-9508-3766

Resumen—El uso de aparatos móviles para el análisis colorimétrico de ensayos químicos en contextos fuera de laboratorios es un área de continua gestión. En este contexto las plataformas en las que se ejecutan estos ensayos suelen estar hechos de materiales noveles, de bajo costo y ambientalmente amigables. Esto introduce dificultades adicionales ya que estos materiales pueden mostrar deformaciones y ser usados bajo iluminaciones de tipo variado. Este trabajo aborda la detección de pozos en placas de ensayos de 96 pozos hechas de materiales de que sujetos deformaciones. El método utilizado aprovecha la detección parcial usando transformadas de Hough y la aplicación de redes neuronales. El uso de transferencia de conocimiento hace posible que el conjunto de entrenamiento necesario sea pequeño y la intervención humana en su etiquetado sea mínima. Se muestra además un método para la evaluación sistemática de la efectividad de la técnica aplicada.

Index Terms—Análisis colorimétrico, transformada de Hough, redes neuronales

I. INTRODUCCIÓN

La literatura menciona con frecuencia creciente el uso de teléfonos móviles junto con plataformas innovadoras para realizar análisis fuera del entorno de laboratorio [1]–[3]. Ejemplos de ello son las aplicaciones móviles que facilitan los análisis preliminares de pruebas químicas en placas de 96 pozos, eliminando la necesidad de utilizar equipos costosos y voluminosos fuera del laboratorio. Un caso documentado es la aplicación *Spotxel® Microplate Reader* [4]. Esta y otras aplicaciones similares presentan en la pantalla del aparato una plantilla visual de la placa que el usuario debe alinear con la placa que se va a analizar. Este mecanismo asume que la placa a analizar es rígida, estándar y requiere destreza por parte del usuario.

En este estudio, implementamos técnicas que pueden permitir que aplicaciones de este tipo operen sin estos requisitos. Estas se basan en el uso de métodos de procesamiento de imágenes que han demostrado ser efectivos para este tipo de problema, con el objetivo de generar conjuntos de entrenamiento para una red neuronal con mínima intervención humana. Durante el entrenamiento se aprovecha, a su vez, la técnica de transferencia de conocimiento desde una red que ha sido entrenada para otros fines, lo que permite que su entrenamiento converja con un esfuerzo computacional relativamente bajo.

Este trabajo ha sido financiado por el programa PENN-UPR Partnerships for Education and Research in Materials bajo el auspicio de la Fundación Nacional de Ciencias de los EE.UU. (NSF-DMR-2122102).

I-A. Trasfondo

Dado que estas aplicaciones están diseñadas para operar mayormente fuera de un entorno de laboratorio formal, es preferible que las plataformas en las que se realizan estos ensayos estén fabricadas con materiales innovadores, de bajo costo y respetuosos con el medio ambiente, como las placas de ensayo de 96 pozos hechas de acetato de celulosa [5]. Estos materiales presentan nuevos retos para efectuar colorimetría efectiva, entre otras razones, por ser materiales inherentemente flexibles y deformables.

En la última década y media hemos sido testigos de una explosión de aplicaciones de inteligencia artificial, muchas de ellas basadas en redes neuronales. Cuando se aplican redes neuronales para analizar problemas científicos, los investigadores se encuentran inicialmente con dos desafíos fundamentales: diseñar una red que se ajuste a la aplicación y generar un conjunto de entrenamiento de alta calidad y amplio, con miles o incluso decenas de miles de ejemplos etiquetados manualmente. Además, se requiere equipo informático sofisticado y costoso para llevar a cabo el entrenamiento. Sin embargo, recientemente se han presentado ejemplos del uso de la transferencia de conocimiento, la adaptación de las redes neuronales y la transferencia de la información almacenada de una red a otra, que mitigan estos obstáculos.

En un trabajo anterior presentamos un método de detección de pozos en placas de 96 pozos con deformaciones basado en el método de Hough [6]. En una de sus formulaciones, el método de Hough sirve para detectar círculos en imágenes que han sido preprocesadas para detectar bordes de figuras. Efectos naturales en la imagen imposibilitan la detección precisa de bordes. El método de Hough provee para ajustar la tolerancia a estos defectos. Pero un sólo conjunto de parámetros no produce las clasificaciones esperadas en todas las imágenes. En el caso de la detección de pozos de placas de ensayo la ausencia de círculos, repeticiones, o detección de círculos espurios son problemas comunes. En nuestro trabajo previo comenzamos la detección de los pozos con parámetros elegidos de manera deliberada para subestimar significativamente la detección de círculos. Luego se itera el procedimiento incrementando la sensibilidad del método hasta que se obtiene al menos una fila de 12 pozos y una columna de 8 pozos detectados. Los pozos restantes se obtienen usando interpolación.

El mérito de el presente estudio radica en la demostración

de un método que genera un conjunto de entrenamiento para una red neuronal que identifica pozos en placas de ensayo con mínima intervención humana, basándose en técnicas estándar de procesamiento de imágenes. Además, se utiliza la transferencia de conocimiento para alcanzar altos niveles de precisión en la red neuronal con un conjunto de entrenamiento pequeño, y se emplea un método de medición de la precisión de los resultados altamente automatizado y confiable. Esta estrategia puede ser aplicada a otros problemas similares con ajustes mínimos.

II. MÉTODOS, SOFTWARE Y EQUIPO

II-A. Insumo

El insumo del sistema consiste de imágenes en formato RGB de placas de ensayos de 96 pozos estándar de colores blanco o negro bajo las fuentes de iluminación solar indirecta, flash, y lámparas LED y fluorescente. Imágenes adicionales iluminadas con luz ultravioleta son tomadas con placas blancas solamente. Dado que en fases posteriores de este proyecto será el desarrollo de aplicaciones para teléfonos móviles las fotos fueron tomadas con ese tipo de aparatos. Cada imagen termina representada como un arreglo de tres dimensiones $I(i, j, c)$ en el cual cada entrada está asociada a un pixel donde i, j son números enteros que representan la fila y la columna del pixel y $c = 0, 1, 2$ corresponden a las intensidades de rojo, verde y azul R, G, B enteros entre 0 y 255 .

II-B. Datos para Entrenamiento

El conjunto de datos para el entrenamiento consiste de pares de imágenes I_n con su respectivo etiquetado. El etiquetado que describe las aperturas de los pozos de la placa consiste de una imagen en tonos de grises representada como una matriz de dos dimensiones $P_n(i, j)$ que almacena p_n valores distintos, uno por cada pozo, según se ilustra en la Figura 1.

II-B1. Imágenes para el conjunto de datos: El objetivo es que el conjunto de datos para el entrenamiento tenga imágenes de placas recortadas y deformadas como muestra la foto izquierda de la Figura 1. Inicialmente se selecciona una imagen representativa de cada una de las variantes descritas en la sección II-A para un total de nueve fotos. Antes de ser incluidas en el conjunto de entrenamiento las imágenes crudas son pasadas por un filtro gaussiano multidimensional [7] para la ecualización de brillantez que reduce el ruido y facilita la detección de los bordes de la placa que son localizados con un filtro tipo Sobel [8]. Con estos bordes detectados la imagen original sin filtros es recortada para remover trasfondo innecesario quedando sólo las placas. en este punto se ejecuta una transformación de perspectiva para corregir la deformación trapezoidal.

Este conjunto inicial de imágenes es aumentado mediante un proceso de deformación controlada en distintos grados. Para lograr este efecto se definió un mapa en el que la i -ésima fila es proyectada a una parábola usando la transformación

$$(i, j) \rightarrow (i, -\frac{k}{h^2}((x-h))^2 + k) \quad (1)$$

donde (h, k) son las coordenadas del vértice de la parábola, $h = M/2$, y $k = 0, 20, 40, 60, \dots, 200$ representa la cantidad de pixeles por encima de la horizontal del vértice. Se seleccionó la forma de una parábola por su similitud al efecto producido por apretar por los bordes una lámina flexible. Pero el método es adaptable a cualquier transformación definible con funciones de uso común.

En este punto el conjunto inicial de nueve imágenes se ha expandido a 99 imágenes.

II-B2. Etiquetado de las imágenes: Las imágenes pre-procesadas son sometidas al proceso de detección de círculos usando la transformada de Hough variando el parámetro umbral de acumulación incrementando paulatinamente la sensibilidad del método hasta que se consigue una detectar una porción de los 96 pozos. Se hace notar que en la mayoría de los casos esto no identifica la totalidad de los pozos. En este punto se producen las imágenes objetivo, el conjunto P_n descrito arriba, en escala de grises con negro representando trasfondo sin pozos y áreas con distintos grados de gris para cada pozo detectado como se muestra en la Figura 1.

II-C. Red Neuronal

La red neuronal se construye basada en las redes neuronales de tipos Faster-RCNN [9] y Mark-RCNN [10] provistas por las funciones FastRCNNPredictor y MaskRCNNPredictor del paquete TorchVision [11]. Esta red viene pre-entrenada con el conjunto de entrenamiento COCO-v1 [12] para la detección de diversos objetos. El uso de las redes con pesos pre-establecidos consigue una transferencia de conocimiento a nuestra red. Esta red es sometida a entrenamiento adicional con el conjunto de entrenamiento descrito en la sección anterior. Los nuevos pesos de la red son almacenados para uso posterior.

El conjunto de datos para entrenamiento es dividido en un subconjunto de entrenamiento de 50 imágenes etiquetadas y el de prueba de 49 imágenes etiquetadas. El método de optimización utilizado fue el descenso de gradiente estocástico con momentum con tasa de aprendizaje inicial de 0.005 decreciendo por 10 % cada tres pasos.

Mediciones de la pérdida en los conjuntos de entrenamiento y de prueba acopiados durante el entrenamiento muestran que pasadas las dos épocas las pérdidas de validación se hacen mayores que las de entrenamiento dando muestras de sobre-

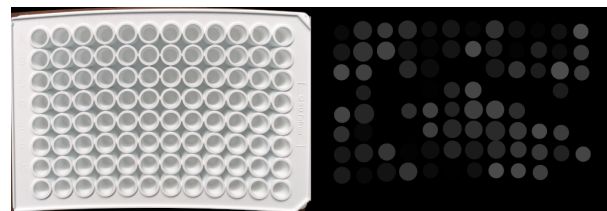


Figura 1. Ejemplo de un par de imágenes insumo-objetivo en el conjunto de entrenamiento de la red neuronal. (izquierda) imagen de la placa deformada $k=60$ pixeles en el centro. (derecha) imagen-objetivo mostrando el subconjunto de los pozos detectados por el método de Hough.

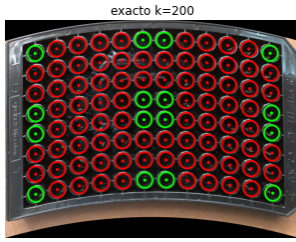


Figura 2. Placa de ensayos con deformación máxima marcada con centros considerados exactos. Los centros de pozos de color verde son los determinados visualmente en la placa sin deformar. Los rojos son resultado de la interpolación.

entrenamiento de la red, razón por la cual se seleccionó detener el entrenamiento cumplidas las dos épocas.

II-D. Localizaciones “Exactas” de pozos para la Evaluación

Una corroboración visual de los resultados podría considerarse como una validación de la precisión del modelo. Sin embargo, la función de pérdida usada para el entrenamiento del modelo mide la diferencia entre la predicción del modelo en el conjunto de prueba y el etiquetado que se hizo automáticamente con una técnica de procesamiento de imágenes.

Para corroborar cuantitativamente que, en efecto, el método de etiquetado automatizada produce resultados robustos que producen un modelo con resultados precisos definimos un método que mide la distancia entre la localización de los centros de pozos predichos por el modelo y la de los centros exactos determinados como sigue. Esto permite también comparar la precisión de este modelo con la de otros métodos de detección de pozos.

La localización exacta de los centros de los pozos se hace mediante una detección visual de los pozos localizados en las esquinas y centros de las placas sin deformar luego de haber sido procesadas según descrito en la Sección II-A (Figura 2). Con estas coordenadas se calculan las coordenadas de los centros de los demás pozos con una interpolación simple.

Luego las coordenadas de los centros de los pozos en las imágenes deformadas de manera controlada se calculan aplicando la transformación usada para la deformación (Ecuación 1) a las coordenadas de los centros detectadas en las placas sin deformar.

II-E. Implementación

La programación fue escrita en lenguaje *Python* versión 3.12.3. Para la lectura y escritura de imágenes, conversión de colores, y filtrado se utilizó *Skimage* (v 0.22.0) [8], *Numpy* (v 1.25.2) [13] para cálculos numéricos con arreglos, *Scipy* (v 1.13.0) [7] para el filtro gaussiano, *OpenCV* (v 4.9.0) [14] para las transformaciones de perspectivas y *Matplotlib* (v 3.8.4) [15] para la producción de gráficas. Las redes neuronales fueron implantadas usando *PyTorch* (v 2.1.2.post100) [16] y *TorchVision* (v 0.16.1+b88453f). Para el entrenamiento de la red se utilizó un servidor equipado con CPUs con 64 hilos de procesamiento y tres GPUs marca NVIDIA modelo

Tesla V100 con 16GB de memoria y 640 procesadores de Tensores cada uno. Las otras partes del proceso se ejecutaron en computadoras personales con CondaForge [17].

III. RESULTADOS

III-A. Medición de Error

Para cuantificar la precisión del presente método de detección de pozos definimos los conjuntos de medidas de errores como

$$E(k) = \{d(c_{i,j}^k, w_{i,j}^k) \mid i = 1, \dots, 8, j = 1, \dots, 12\}$$

donde k es el parámetro de deformación, $c_{i,j}^k$ es el centro exacto del pozo en la fila i , columna j en la placa deformada k pixeles, $d(c_{i,j}^k, w_{i,j}^k)$ es la distancia entre $c_{i,j}^k$ y el centro detectado $w_{i,j}^k$. Las coordenadas exactas de los centros de los pozos $c_{i,j}^0$ de las placas sin deformar ($k = 0$) fueron obtenidas identificando visualmente los centros de 16 pozos localizados en los bordes y el centro de la placa y generando el resto por interpolación. Para computar los centros $c_{i,j}^k$ para placas deformadas ($k > 0$) se aplicó la fórmula (1) a los centros $c_{i,j}^0$ de la placa sin deformar.

Placas de ambos colores negras y blancas mostraron niveles de error muy similares. La gráfica de violín (figura 3) muestra una variabilidad relativamente pequeña para ambos colores con muy pocos casos por encima de los 10 pixeles. No hay crecimiento del error al aumentar el grado de deformación. El error promedio para las placas negras fue de 4.48 pixeles mientras que para las blancas fue de 4.97 pixeles. Para todas las placas que tienen dimensiones que superan los 2000 por 3000 pixeles, estos errores son menores que un 0.14 % de la diagonal de la placa. La tabla I muestra los errores relativos pormenorizados por color y fuente de luz. La comparación con los resultados del trabajo previo que corrobora una disminución del error de los centros de los pozos encontrados por la red neuronal comparado con la combinación Hough-interpolación.

Al examinar los errores promedio por pozo (figura 4) no se observa un patrón con respecto a la localización de los promedios de error menores o mayores. En particular, no hay diferencias apreciables entre la precisión en los bordes de las placas en comparación con los centros.

La figura 5 muestra el resultado al someter una foto de una placa representativa de un contexto común en el que un usuario tomaría la foto. La placa está colocada sobre

Tabla I
PORMENORIZACIÓN DE ERRORES
COMO PORCIENTO DE LA DIAGONAL
DE LA FOTO RECORTADA

Fuente de iluminación	Hough+interpolación		Red Neuronal	
	negra	blanca	negra	blanca
Sol indirecto	0.46 %	0.47 %	0.11 %	0.16 %
Fluorescente	0.36 %	0.54 %	0.12 %	0.12 %
Lámpara LED	0.68 %	0.24 %	0.12 %	0.09 %
Flash	0.48 %	0.38 %	0.15 %	0.14 %
Ultravioleta	(n/a)	0.33 %	(n/a)	0.18 %

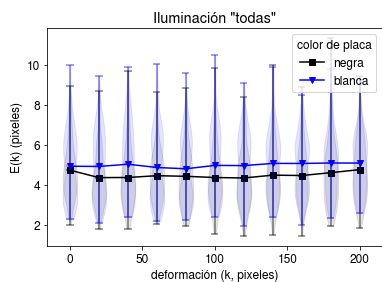


Figura 3. Errores promedio según el nivel de deformación de localización (k) y las distribuciones de errores alrededor de estos.

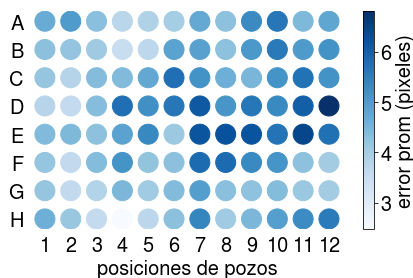


Figura 4. Error promedio por cada posición de pozo en la placa.

una mesa de madera y la sombra de quien toma la foto se proyecta parcialmente sobre ella. La foto no fue sujeta a ningún tipo de pre-procesamiento. Se observa que la red detectó razonablemente todos los pozos.

IV. DISCUSIÓN

La captación precisa para el análisis colorimétrico de placas de ensayo de 96 pozos empieza por la localización precisa de los pozos. Los resultados obtenidos aquí mejoran los obtenidos anteriormente por la combinación de la transformada de Hough e interpolación que a su vez mejoraba significativamente el resultado del uso de la transformada de Hough únicamente. De hecho, los errores medidos aquí son tan pequeños que que podrían ser atribuibles tanto a la red neuronal como a error humano en la localización visual de los centros “exactos”.

Además, el método utilizado aquí muestra el potencial de ser aplicable a otros tipos de medios para el análisis colorimétrico como por ejemplo en aparatos fluidicos. Por último, se ha demostrado que la combinación de la generación automática de conjuntos de entrenamiento combinado con la transferencia de conocimiento de redes neuronales previamente entrenadas para tareas afines elimina la necesidad de construir manualmente conjuntos de entrenamiento extensos.

RECONOCIMIENTOS

Los autores reconocen la ayuda los grupos de la Dra. Vibha Bansal y el Dr. Ezio Fasoli de los Departamentos de Química de la Universidad de Puerto Rico en Cayey y Humacao respectivamente.

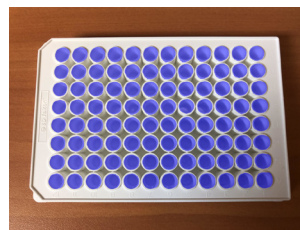


Figura 5. Pozos encontrados por la red neuronal (áreas azules) en una foto de una placa sin pre-procesar.

REFERENCIAS

- [1] G. M. Fernandes, W. R. Silva, D. N. Barreto, R. S. Lamarca, P. C. F. L. Gomes, J. F. da S Petruc, and A. D. Batista, “Novel approaches for colorimetric measurements in analytical chemistry—a review,” *Analytica Chimica Acta*, vol. 1135, pp. 187–203, 2020.
- [2] L. F. Capitán-Vallvey, N. Lopez-Ruiz, A. Martinez-Olmos, M. M. Erenas, and A. J. Palma, “Recent developments in computer vision-based analytical chemistry: A tutorial review,” *Analytica Chimica Acta*, vol. 899, pp. 23–56, 2015.
- [3] S. Banik, S. K. Melanthota, Arbaaz, J. M. Vaz, V. M. Kadambalithaya, I. Hussain, S. Dutta, and N. Mazumder, “Recent trends in smartphone-based detection for biomedical applications: a review,” *Analytical and Bioanalytical Chemistry*, vol. 413, pp. 2389–2406, 2021.
- [4] N. Qin, Z. Liu, L. Zhao, M. Bao, X. Mei, and D. Li, “Promising instrument-free detections of various analytes using smartphones with spotxel® reader,” *Analytical Sciences*, vol. 39, no. 2, pp. 139–148, 2023.
- [5] G. B. Gomez-Dopazo, R. J. A. Nieves, R. L. A. Rivera, S. M. C. Morera, D. R. Nazario, I. Ramos, I. J. Dmochowski, D. Lee, and V. Bansal, “Cellulose acetate microwell plates for high-throughput colorimetric assays,” *RSC advances*, vol. 14, no. 22, pp. 15319–15327, 2024.
- [6] E. Rosa Delgado and J. O. Sotero Esteva, “Detection of wells in images of deformed 96-wells plates,” *MRS Advances*, pp. 1–6, 2024.
- [7] P. Virtanen, R. Gommers, T. E. Oliphant, M. Haberland, T. Reddy, D. Cournapeau, E. Burovski, P. Peterson, W. Weckesser, J. Bright, et al., “Scipy 1.0: fundamental algorithms for scientific computing in python,” *Nature methods*, vol. 17, no. 3, pp. 261–272, 2020.
- [8] S. Van der Walt, J. L. Schönberger, J. Nunez-Iglesias, F. Boulogne, J. D. Warner, N. Yager, E. Goullart, and T. Yu, “scikit-image: image processing in python,” *PeerJ*, vol. 2, p. e453, 2014.
- [9] R. Girshick, “Fast r-cnn,” in *Proceedings of the IEEE international conference on computer vision*, pp. 1440–1448, 2015.
- [10] K. He, G. Gkioxari, P. Dollár, and R. Girshick, “Mask r-cnn,” in *Proceedings of the IEEE international conference on computer vision*, pp. 2961–2969, 2017.
- [11] T. Maintainers et al., “Torchvision: Pytorch’s computer vision library, november 2016,” 2023.
- [12] T.-Y. Lin, M. Maire, S. Belongie, J. Hays, P. Perona, D. Ramanan, P. Dollár, and C. L. Zitnick, “Microsoft coco: Common objects in context,” in *Computer Vision—ECCV 2014: 13th European Conference, Zurich, Switzerland, September 6–12, 2014, Proceedings, Part V 13*, pp. 740–755, Springer, 2014.
- [13] C. R. Harris, K. J. Millman, S. J. Van Der Walt, R. Gommers, P. Virtanen, D. Cournapeau, E. Wieser, J. Taylor, S. Berg, N. J. Smith, et al., “Array programming with numpy,” *Nature*, vol. 585, no. 7825, pp. 357–362, 2020.
- [14] G. Bradski, “The opencv library. dr dobb’s j softw tools,” *The OpenCV Library. Dr Dobb’s J Softw Tools*, 2000.
- [15] J. D. Hunter, “Matplotlib: A 2d graphics environment,” *Computing in science & engineering*, vol. 9, no. 03, pp. 90–95, 2007.
- [16] A. Paszke, S. Gross, S. Chintala, G. Chanan, E. Yang, Z. DeVito, Z. Lin, A. Desmaison, L. Antiga, and A. Lerer, “Automatic differentiation in pytorch,” 2017.
- [17] C.-F. Community, “The conda-forge project: Community-based software distribution built on the conda package format and ecosystem,” *Zenodo*, 2015.

Tecnología IoT para Sensores Inteligentes y Redes Inalámbricas: Un Enfoque en la Evolución hacia un Nodo de Monitoreo Ambiental

Ing. Matías Caccia

Grupo de Investigación en Ruido Ambiental (GIRA),
Departamento de Ciencia y Tecnología, Universidad Nacional de
Tres de Febrero (UNTREF), Sáenz Peña, Argentina.
Comisión de Investigaciones Científicas de la Provincia de
Buenos Aires (CICPBA), La Plata, Argentina.
Buenos Aires, Argentina
mcaccia@untref.edu.ar

Dr. Esteban Lombera

Grupo de Investigación en Ruido Ambiental (GIRA),
Departamento de Ciencia y Tecnología, Universidad Nacional de
Tres de Febrero (UNTREF), Sáenz Peña, Argentina.
Buenos Aires, Argentina
elombera@untref.edu.ar

Resumen—Este trabajo presenta la evolución de un módulo de medición de ruido urbano hacia un nodo sensor de datos ambientales avanzado y versátil, enmarcado en el paradigma del Internet de las Cosas (IoT) y las Redes de Sensores Inalámbricas (WSNs). El objetivo es desarrollar un dispositivo compacto y eficiente capaz de recopilar diversos indicadores ambientales y transmitirlos de forma inalámbrica a una plataforma en la nube para su análisis. El diseño del nuevo nodo sensor se centra en la eficiencia energética, bajo costo, escalabilidad y el uso de software y hardware libres. Incorpora una variedad de sensores, incluyendo micrófonos MEMS para medir ruido urbano, sensores de temperatura, presión atmosférica y puertos que permiten agregar sensores adicionales a través del protocolo I2C. La conectividad inalámbrica a través de WiFi y el protocolo MQTT aseguran una transmisión eficiente de datos a una base de datos en la nube. La alimentación eléctrica se realiza mediante baterías, con la opción de carga mediante energías renovables. El componente principal del nodo es el chip ESP32, que procesa las señales de los sensores y las transmite a la nube. Además, se incorporan características de mantenimiento eficiente, como actualizaciones inalámbricas de firmware (sistema Over The Air) y LEDs indicadores para diagnóstico de problemas. Este trabajo demuestra que la combinación de tecnologías de IoT, sensores de bajo costo y redes inalámbricas permiten avanzar hacia una monitorización ambiental más precisa, accesible y escalable, con aplicaciones potenciales en la creación de redes de sensores ambientales urbanos y mejorar el diagnóstico de contaminación en estos entornos.

Keywords—IoT, Red de Sensores, Sonómetro, ESP32, Contaminación Ambiental

I. INTRODUCCIÓN

La proliferación de la contaminación ambiental en entornos urbanos ha emergido como una preocupación primordial en la intersección de la calidad de vida y el desarrollo sostenible. Esta polución puede ser física (sonora o lumínica) o química (óxidos de carbono, partículas con diámetro reducido, entre otros). Con el continuo crecimiento de la población, especialmente en áreas urbanas, surge la necesidad de abordar los efectos adversos del ruido ambiental y otros contaminantes en la salud humana y el medio ambiente [1]. Según las proyecciones de las Naciones Unidas, se estima que para el año 2050, el 68% de la población mundial residirá en zonas urbanas, lo que resalta la importancia crítica de encontrar soluciones efectivas para mitigar la contaminación en todas sus formas [2].

Argentina, como uno de los países más urbanizados del mundo, se enfrenta a desafíos significativos en la gestión de

la calidad ambiental en sus ciudades, donde el impacto del ruido generado por el tráfico vehicular y otras fuentes antropogénicas, así como los efectos de contaminantes químicos como los óxidos de nitrógeno (NO_x), las partículas en suspensión (PM), entre otros, son preocupaciones crecientes para la salud pública y el medio ambiente. En respuesta a estos desafíos, se han desarrollado diversas iniciativas y proyectos para monitorear y gestionar la contaminación en entornos urbanos empleando tecnologías y paradigmas con mayor facilidad de aplicación y costos en descenso.

En las secciones siguientes se detalla la evolución de un nodo de medición de ruido urbano hacia un sistema de monitoreo ambiental más completo, que expande su capacidad de medición de contaminantes, incluyendo a los del tipo químico. El enfoque principal de este desarrollo se centra en proporcionar una solución que sea escalable, rentable y altamente precisa para la recolección de datos ambientales en tiempo real. Se discutirá el diseño de este nodo de monitoreo ambiental y se propondrán posibles líneas de investigación para mejorar aún más la eficacia y la utilidad de este enfoque innovador para la evaluación de la calidad ambiental en entornos urbanos a través de redes inalámbricas.

II. ESTADO DEL ARTE Y ANTECEDENTES

Gracias a múltiples revisiones de la literatura relacionada a sistemas de monitoreo de ruido urbano y sensores ambientales, se ha observado un panorama de constante evolución. Existen trabajos de investigación que fueron presentados con un alto nivel de innovación en la comprensión y gestión de la contaminación en entornos urbanos empleando el paradigma del Internet de las Cosas. Iniciativas como SONYC en Nueva York y LIFE MONZA en Italia han proporcionado distintas perspectivas sobre la implementación de redes de sensores de bajo costo para monitorear y analizar la contaminación acústica en áreas urbanas densamente pobladas [3][4]. Estos proyectos demuestran la viabilidad y eficacia de emplear tecnologías asequibles y de consumo masivo para recolectar datos continuos de ruido.

Simultáneamente, los avances en tecnologías de sensores y redes de sensores inalámbricos (WSNs) han impulsado la capacidad de los sistemas de monitoreo ambiental para obtener datos precisos y en tiempo real. La miniaturización y reducción de costos en los sensores del tipo Sistemas Micro Electro Mecánicos (MEMS), han posibilitado la

integración en dispositivos compactos y económicos, facilitando la implementación de redes de sensores distribuidas en entornos urbanos. Además, el desarrollo de algoritmos avanzados de procesamiento de señales y la mejora en la eficiencia de las redes inalámbricas han ampliado la capacidad de comunicación y la cobertura de las WSNs, lo que permite una recolección de datos más eficiente y un monitoreo más preciso de las condiciones ambientales [5].

Los avances tecnológicos han mejorado los sistemas de monitoreo ambiental y ofrecen nuevas oportunidades para investigar e innovar en la gestión de la calidad del medio ambiente en áreas urbanas. La combinación de tecnologías de sensores avanzados con comunicaciones inalámbricas ofrece un potencial significativo para comprender y abordar los desafíos ambientales urbanos de manera más efectiva. En este contexto, el proyecto presentado en este documento aprovecha estos avances al implementar un sistema de monitoreo ambiental escalable, económico y altamente preciso para contribuir a la gestión sostenible del aire y el ruido en entornos urbanos.

III. DISEÑO Y DESARROLLO DEL NODO SENSOR

El punto de partida de este proyecto es un nodo sensor de datos ambientales previamente desarrollado, el cual se diseñó inicialmente para medir el ruido urbano [6]. Este nodo ha sido objeto de evolución y mejora para convertirse en un sistema capaz de medir una gama más amplia de contaminantes ambientales. A continuación, se detalla el diseño y desarrollo de este nodo sensor de datos ambientales, destacando sus componentes principales y su funcionalidad. En cada parte, se incluyen las actualizaciones para el nuevo módulo.

A. Hardware del módulo principal

El nodo sensor original poseía una computadora de placa simple marca Raspberry Pi modelo 3B+, elegida por sus dimensiones compactas, capacidad de conexión inalámbrica y potencia de cálculo. El transductor utilizado es un micrófono MEMS de bajo costo, modelo INMP441, conectado empleando el protocolo I2S para transferencia de datos. En la Figura 1 se muestra el módulo original y su carcasa para protección del exterior.

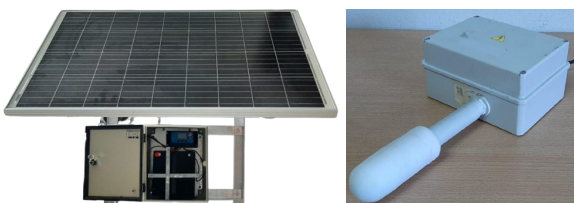


Fig. 1. Nodo central para mediciones de ruido urbano (derecha) y el sistema de autonomía eléctrica (izquierda).

El nuevo módulo emplea un microprocesador de la familia ESP32, el cual cuenta con puerto de conexión para la comunicación con el micrófono utilizado originalmente, puertos SPI para la transferencia de datos a una tarjeta microSD y terminales para la transferencia de información por protocolo I2C. Este último permite la comunicación con el sensor BMP180 (medidor de presión atmosférica y temperatura ambiente), entre otros. Se incorporó además un conversor analógico a digital ADS-1115 para poder ampliar el módulo y poder hacer lecturas de sensores analógicos (por ejemplo los de familia MQ para medir contaminantes

químicos). En las Figuras 2 y 3 se muestran renderizaciones de la placa principal diseñada para el nuevo nodo.

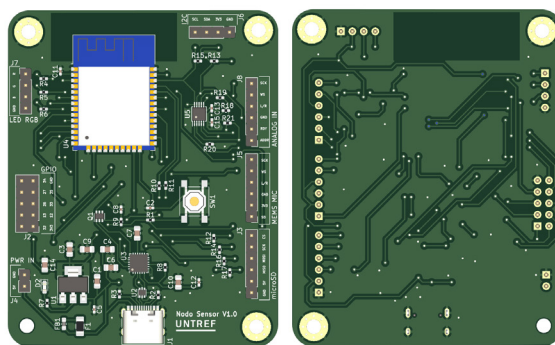


Fig. 2. Vistas frontal y trasera de la placa electrónica para el nodo de procesamiento central.

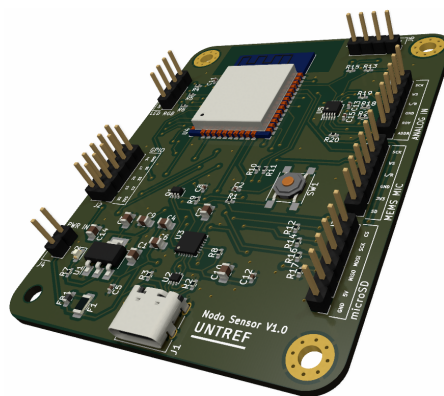


Fig. 3. Vista 3D del nodo central con los componentes posicionados.

B. Software del módulo principal

Los códigos empleados para la recolección de información y procesamiento de las señales acústicas del módulo original fueron desarrollados empleando Python. Se utilizaron diversas librerías para poder tomar los datos del micrófono (*sounddevice*), aplicar filtros de ponderación temporal y frecuencial (*SciPy*), procesar la información en paralelo para evitar la pérdida de datos (*Threading*) y otras que permitieron comunicación directa con la base de datos en la nube y facilitar el almacenamiento de los registros. Además, se implementaron diversas alternativas para controlar contingencias y garantizar la autonomía y funcionamiento constante.

El principal cambio y desafío en el nuevo sistema radica en la migración del lenguaje de programación interpretado de alto nivel hacia uno compilado optimizado para sistemas embebidos (C/C++), lo que habilitó la utilización de un sistema operativo de tiempo real (*FreeRTOS*). Esta transición implicó transformar las etapas de recolección de datos, procesamiento de señales, controles de contingencia y almacenamiento de datos a aplicaciones ejecutadas con una lógica y tiempos específicos. La arquitectura del nuevo sistema se basa en la utilización de tareas concurrentes asegurando un procesamiento eficiente de los datos de audio y lecturas de sensores ambientales. Se han diseñado tareas dedicadas a la lectura de sensores mientras que otra tarea se encarga del procesamiento de estos datos.

Esta estrategia garantiza una gestión eficaz de los recursos del microcontrolador y facilita la expansión de las capacidades del sistema para incluir nuevas lecturas y mejorar lograr una completa caracterización de los cambios en las condiciones ambientales.

El uso de colas FreeRTOS para la comunicación entre tareas destaca como una característica clave de la implementación. Esto permite una transferencia segura y eficiente de datos entre las tareas de lectura de variables medidas y las de procesamiento, garantizando una sincronización efectiva. Además, esta estructura simplifica la incorporación de nuevos sensores al sistema, ya que solo se necesita agregar una tarea adicional para capturar los datos del nuevo sensor y enviarlos a la cola para su procesamiento. Esta flexibilidad permite adaptar fácilmente el sistema a diferentes entornos y necesidades de monitoreo ambiental sin realizar cambios extensos en el código existente.

Además, esta implementación permite la configuración y aplicación de filtros digitales de respuesta al impulso finita (FIR) escritos en lenguaje ensamblador para compensar la respuesta natural del sistema y ponderar en el dominio frecuencial las lecturas registradas. Esto permite calcular con precisión el nivel sonoro continuo equivalente con ponderación A [7].

C. Diseño del sistema de autonomía eléctrica

La sección del nodo que engloba la batería, panel solar, regulador de carga y adaptador de voltaje, ha permanecido constante desde el diseño original hasta su evolución. La capacidad de la batería se estima en función del consumo energético del módulo central, asegurando al menos 24 horas de autonomía sin recarga. Para la Raspberry Pi se asumió un consumo promedio de 500 mA por hora. El conjunto de panel solar y regulador aseguran una carga eficiente y proporcionan protección contra descargas. El uso de un microcontrolador programado en un nivel de abstracción bajo reduce el consumo energético, lo que permite disminuir el tamaño y costo de la batería y el panel solar. A pesar de esto, se utilizan los mismos componentes para poder conectar entre 5 y 10 nodos, creando así una red de sensores ambientales.

D. Diseño de la carcasa y montaje del módulo

Originalmente, se utilizaron dos cajas IP-65 para almacenar todos los componentes. La primera es una pequeña caja de PVC con la Raspberry Pi y el regulador de voltaje. Dos abrazaderas de cable de plástico garantizan que los cables de entrada para la fuente de alimentación y la salida del micrófono no presenten riesgo de entrada de agua o polvo. El micrófono está protegido con un filtro "anti pop". La segunda caja, más grande y de metal, contiene la batería y el regulador de carga. Se diseñó y ensambló un marco de aluminio para facilitar la movilidad y la instalación del sistema de autonomía eléctrica. Estos dos compartimentos están unidos con un cable UTP de categoría 5.

E. Base de datos y sitio web de visualización

Se optó por externalizar la configuración de un portal web para la presentación de los datos recopilados, con el objetivo de asegurar su accesibilidad e interpretación. La sección principal del portal exhibió niveles registrados en las

últimas 24 horas, la última medición realizada y la ubicación del módulo. Además, el diseño incluye información pertinente sobre el proyecto, el grupo de investigación y sus miembros.

La página web accede a los datos almacenados en una base de datos del servidor de Google Cloud Firestore, donde los sellos de tiempo únicos de cada entrada proporcionan la organización necesaria para presentar los resultados de manera ordenada.

La evolución del módulo hacia uno con mejores prestaciones y menor costo se ha logrado mediante la publicación de las mediciones realizadas mediante el protocolo MQTT a un broker ubicado en una instancia AWS en la nube. Este enfoque garantiza una transmisión eficiente de datos permitiendo una comunicación robusta y confiable entre el nodo sensor y la infraestructura de almacenamiento remoto.

En la nube, una aplicación generada con Python se suscribe al broker MQTT para recibir los datos transmitidos por los nodos sensores, los cuales son posteriormente almacenados en una base de datos InfluxDB. Esta arquitectura facilita la gestión y el análisis de grandes volúmenes de datos ambientales en tiempo real. Con la herramienta Grafana (o Node-Red) se proporciona una interfaz gráfica intuitiva y flexible para la visualización y el monitoreo de estos datos.

IV. CARACTERIZACIÓN DEL MICRÓFONO

Para lograr una medición precisa del ruido urbano y evaluar su impacto en la contaminación acústica, se recurre al micrófono de topología MEMS modelo INMP441. La evaluación del nivel sonoro continuo equivalente ponderado A, un indicador clave de contaminación acústica, requiere un proceso de filtrado frecuencial para poder compensar la respuesta en frecuencia natural del sistema. Esta compensación se logra mediante registros simultáneos utilizando un micrófono de medición Earthworks M50 como referencia, mientras ambos son excitados por un ruido rosa.

Posteriormente, se calcula la función de transferencia del sistema con referencia al micrófono y se suaviza la curva resultante mediante fracciones de banda de octava, normalizando a 1 kHz y luego invirtiendo respecto al eje de magnitud. El filtro objetivo resultante es aproximado empleando el método "firwin2" de la biblioteca Scipy de Python. Es necesario que exista un equilibrio entre una respuesta en frecuencia adecuada y una cantidad de coeficientes que no perjudiquen el tiempo de procesamiento mínimo. Esto se obtiene empleando un algoritmo de optimización iterativa basado en el método de descenso del gradiente estocástico (SGD). Con los coeficientes del filtro inverso ya encontrados, se emplea un algoritmo que permite adaptarlos al lenguaje ensamblador para optimizar el rendimiento del sistema sin comprometer su capacidad de procesamiento.

La Figura 4 ilustra los resultados de la magnitud y fase del filtro objetivo junto con su versión final, mostrando la magnitud invertida obtenida a partir de las mediciones y la aproximación final del filtro inverso.

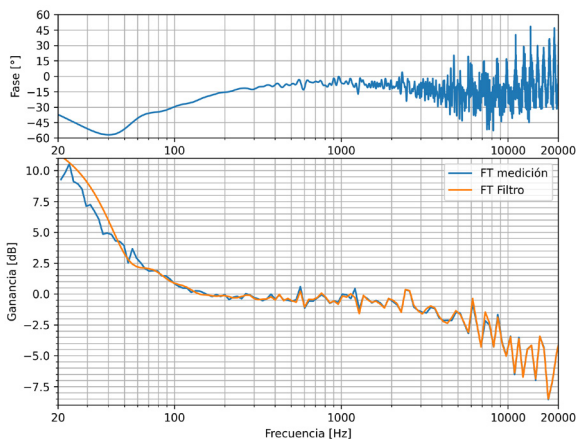


Fig. 4. Magnitud y fase de las funciones de transferencia del micrófono (azul) y del filtro generado para compensar la respuesta natural del mismo (naranja).

V. APLICACIONES POTENCIALES Y BENEFICIOS

El nodo sensor de datos ambientales ofrece una amplia gama de aplicaciones en la monitorización ambiental urbana. Desde el monitoreo de la contaminación acústica para la generación de mapas dinámicos de ruido urbano, hasta la evaluación de la calidad del aire. Además, su capacidad para integrar sensores adicionales permite una exploración más profunda de contaminantes químicos, lo que resulta fundamental para identificar áreas problemáticas y tomar medidas correctivas. Al mismo tiempo, el nodo sensor proporciona una valiosa herramienta para la investigación científica, la planificación urbana y la concientización pública sobre los problemas ambientales en entornos urbanos.

La utilización de sistemas de bajo costo y alta escalabilidad en la creación de redes de sensores ambientales ofrece numerosos beneficios. Estos sistemas permiten una mayor cobertura espacial al reducir los costos de implementación y mantenimiento, lo que facilita el despliegue de una red más densa de sensores. Además, al ser escalables, estos sistemas pueden adaptarse fácilmente a diferentes entornos y necesidades, lo que los hace ideales para aplicaciones urbanas donde se requiere una amplia cobertura y flexibilidad. Esto no solo reduce los costos asociados con la implementación de redes de sensores ambientales, sino que también democratiza el acceso a datos ambientales en entornos urbanos, lo que promueve una mayor participación pública en la protección del medio ambiente y la sostenibilidad urbana.

Además, la tecnología IoT agrega otra capa de beneficios significativos a los proyectos que buscan implementar nuevos sensores en entornos urbanos. La capacidad de conexión inalámbrica y la infraestructura IoT permiten llevar nuevos desarrollos a puntos de difícil acceso o donde las redes cableadas tradicionales no son viables. Esto significa que áreas remotas o de difícil acceso pueden ser monitoreadas, proporcionando datos para la toma de decisiones y la gestión ambiental. La flexibilidad de la tecnología IoT permite una rápida iteración y despliegue, acelerando el proceso de innovación en la monitorización ambiental urbana. Esta capacidad de adaptación y expansión facilita la implementación de soluciones personalizadas para abordar desafíos específicos en diferentes entornos urbanos, mejorando así la calidad de vida de los ciudadanos y promoviendo un desarrollo urbano sostenible.

VI. CONCLUSIONES Y TRABAJOS FUTUROS

En este documento se presentó la evolución de un nodo de monitoreo acústico a uno ambiental. Se emplearon metodologías que combinan tecnologías avanzadas de sensores y redes inalámbricas para ofrecer una solución escalable, rentable y precisa para recopilar datos ambientales en tiempo real. Al emplear herramientas como MATLAB para el análisis y diseño de filtros correctivos, y al optimizar el código en lenguaje ensamblador para maximizar el rendimiento del sistema, se establece un marco replicable y adaptado para satisfacer las necesidades de otros sensores, asegurando así la precisión de las mediciones del nodo central. Esta metodología es recomendable y será aplicada en el resto de sensores para garantizar la calidad y confiabilidad de los datos recopilados.

La combinación de sistemas de bajo costo y alta escalabilidad con la tecnología IoT ofrece una amplia gama de beneficios, desde una mayor cobertura espacial hasta una rápida iteración y despliegue de nuevos sensores. Esto permite la monitorización efectiva de áreas remotas o de difícil acceso, proporcionando datos valiosos para abordar desafíos ambientales específicos en diferentes entornos urbanos. Además, al democratizar el acceso a datos ambientales, se promueve una mayor conciencia pública sobre la importancia de la protección del medio ambiente y se fomenta una mayor participación ciudadana en la toma de decisiones relacionadas con la sostenibilidad urbana. La evolución de este nodo de monitoreo ambiental representa un paso adelante en la creación de redes de sensores ambientales eficientes y accesibles, con aplicaciones potenciales que abarcan desde la gestión de residuos hasta la mitigación del cambio climático, contribuyendo así a mejorar la calidad de vida en entornos urbanos.

REFERENCIAS

- [1] L. Goines, L. Hagler. "Noise pollution: a modern plague". *South Med J.* 2007 Mar;100(3):287-94.
- [2] United Nations. (2018). *World Urbanization Prospects: The 2018 Revision*.
- [3] C. Mydlarz, M. Sharma, Y. Lockerman, B. Steers, C. Silva, J.P. Bello. "The life of a New York city noise sensor network" in *Sensors* 19, no. 6: 1415, 2019.
- [4] C. Bartalucci, F. Borchi, M. Carfagni, R. Furfèri, L. Governi, A. Lapini, R. Bellomini, S. Luzzi, L. Nencini. "The smart noise monitoring system implemented in the frame of the Life MONZA project" in *Proceedings of the EuroNoise*, 2018.
- [5] W. Dargie, C. Poellabauer. "Fundamentals of wireless sensor networks: theory and practice", John Wiley & Sons, 2010.
- [6] M. Caccia, E. Sacerdoti, E.N. Lombera. "Acquisition Module for a Wireless Acoustic Sensor Network Suitable for Argentinian Urban Environments" in *Journal of Ecological Engineering* 23, no. 12, 2022.
- [7] M. Caccia, F.R. Vallone, G. Rodriguez Jannots, E. Sacerdoti, M. Yommi, H. San Martín. "Noisen: Un Dispositivo IoT para la Medición Precisa y Visualización de Contaminación Acústica en Ambientes Médicos Críticos," en XVIII Congreso Argentino de Acústica - AdAA 2023, Universidad Nacional de Quilmes, Diciembre 2023.

Enhancing Urban Intersection Efficiency: Leveraging Visible Light Communication for Traffic Optimization

Manuel Augusto Vieira
*Electronics Telecommunications and
Computer Dept.*
ISEL, CTS-UNINOVA and LASI
Lisbon, Portugal
mv@isel.pt

Paula Louro
*Electronics Telecommunications and
Computer Dept.*
ISEL, CTS-UNINOVA and LASI
Lisbon, Portugal
paula.louro@isel.pt

Manuela Vieira
*Electronics Telecommunications and
Computer Dept.*
ISEL, CTS-UNINOVA, LASI and NOVA
School of Science and Technology
Lisbon, Portugal
mv@isel.ipl.pt

Pedro Vieira
*Electronics Telecommunications and
Computer Dept.*
ISEL, IT
Lisbon, Portugal
mv@isel.pt

Gonçalo Galvão
*Electronics Telecommunications and
Computer Dept.*
ISEL,
Lisbon, Portugal
A45903@alunos.isel.pt

Alessandro Fantoni
*Electronics Telecommunications and
Computer Dept.*
ISEL, CTS-UNINOVA and LASI
Lisbon, Portugal
alessandro.fantoni@isel.pt

Abstract— This paper presents a method using Visible Light Communication (VLC) to improve traffic signal efficiency and manage vehicle trajectories at urban intersections. It combines VLC localization services with learning-based traffic signal control for a multi-intersection traffic system. VLC enables communication between vehicles and infrastructure, aiding in joint transmission and data collection. The system aims to reduce waiting times for pedestrians and vehicles while enhancing safety. It's flexible, adapting to various traffic movements during signal phases. Cooperative mechanisms balance traffic flow between intersections, improving road network performance. Evaluated using the SUMO urban mobility simulator, it shows reduced waiting and travel times. A agent based scheme optimizes traffic signal scheduling based on VLC behaviors. The proposed approach is decentralized and scalable, suitable for real-world traffic scenarios.

Keywords— *Intelligent Transport System (ITS), Visible Light Communication, traffic signal control, urban intersections, traffic flow optimization, pedestrian safety, SUMO simulator, cooperative communication.*

I. INTRODUCTION

The transportation landscape is rapidly evolving with the integration of smart sensors, Visible Light Communication (VLC), and artificial intelligence. VLC, using light intensity modulation from LEDs for data transmission, shows promise in revolutionizing Smart Mobility solutions and addressing societal goals such as reducing emissions and enhancing traffic safety [1]. It is widely implemented in various domains, including vehicular communication and traffic signal systems, highlighting its versatility and efficiency. However, current traffic signal optimization often overlooks pedestrian dynamics within intersections, necessitating comprehensive systems that consider both vehicular and pedestrian flows.

This paper proposes integrating VLC localization services with learning-based traffic signal control to manage pedestrian and vehicular traffic holistically [2]. Leveraging Reinforcement Learning (RL) concepts, the system optimizes

traffic flow and enhances safety by considering interactions between vehicles and pedestrians. It introduces a pedestrian mobility model tailored for outdoor scenarios, analyzing multiple pedestrian behaviors, and incorporating them into the traffic signal control scheme. Validated through a case study in Lisbon's downtown, the model integrates pedestrian preferences to optimize routing algorithms [3].

Simulation experiments validate the effectiveness of the approach, utilizing real intersection data to demonstrate improved traffic flow and reduced waiting times.

II. TRAFFIC CONTROL CHALLENGES:

A. Pedestrian Dynamics and Complexity in Multi-Intersection Environments

Traffic signal control research has traditionally prioritized vehicles, but there's now a shift towards pedestrian-friendly systems to prevent delays and accidents [4,5]. Sidewalks present challenges due to bi-directional flow, and differing speeds and movements between pedestrians and vehicles further complicate matters [6]. Our adaptive traffic control considers factors like queue lengths in neighboring intersections to balance scalability and efficiency. Our strategy is designed to address real-time traffic demands by modeling current and anticipated future traffic flows. Compared to traditional fixed coil detectors, our adaptive system in V2X environments gathers more granular data, including vehicle positions, speeds, queue lengths, and stopping times. V2V links play a crucial role in safety functionalities like pre-crash sensing, while V/P2I links provide valuable information to connected vehicles.

B. Integrating V-VLC for Innovative Traffic Solutions

With wireless tech advancements and connected vehicle (CV) [7] systems like V2V and V2I, integrating VLC localization with learning-based traffic control can manage both pedestrian and vehicular traffic in multi-intersections. It employs RL to enhance safety and reduce waiting times using

V2V, V/P2I, and I2V/P communications. This approach synchronizes signal control in real-time, considering pedestrian and vehicle factors in the state and reward design, utilizing sidewalks for crucial pedestrian location info. SUMO simulations [8] assess the V-VLC system's effectiveness, with agent-based models learning to optimize traffic flow dynamically. Dynamic diagrams and state matrices illustrate the concept, showing potential for optimal traffic control policies.

III. UNLOCKING TRAFFIC CONTROL

A. VLC background

The V-VLC system, as depicted in Fig. 1a, utilizes a mesh cellular hybrid structure with two controllers. The "mesh" controller at streetlights relays messages to vehicles, while the "mesh/cellular" hybrid controller acts as a border-router for edge computing. [9] [10] [11].

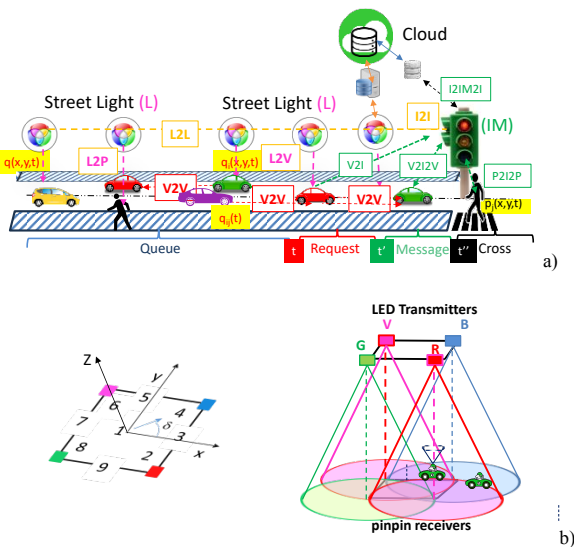


Fig. 1. a) 2D representation of the simultaneous geo-localization as a function of node density, mobility and transmission range. b) Emitter and receivers' relative positions. Illustration of the coverage map in the unit cell: footprint regions (#1-#9) and steering angle codes (2-9).

The proposed architecture enables Infrastructure-to-Cloud communication (I2IM) through embedded computing platforms for processing and sensor interfacing. It also facilitates peer-to-peer communication (V2V) among vehicles, enhancing data sharing.

The Vehicular Visible Light Communication system (V-VLC) consists of a transmitter generating modulated light and a receiver detecting light variation, both wirelessly connected. LED-produced light is modulated using ON-OFF-keying (OOK) amplitude modulation (Fig. 1b). Square unit cells in the environment feature tetra-chromatic white light (WLEDs) sources at cell corners. The V-VLC system uses coded signals transmitted by devices like streetlights, headlights, and traffic lights to communicate directly with identified vehicles and pedestrians (L/I2V/P), or indirectly between vehicles through their headlights (V2V). PIN-PIN photodetectors within mobile receivers receive and decode coded signals. This information aids in pinpointing positions within the network and provides directional guidance along cardinal points for drivers/pedestrians [10].

The system employs queue/request/response mechanisms and temporal/space relative pose concepts to manage vehicle passage through intersections. Vehicle speed is determined using transmitter IDs for tracking, while mesh nodes estimate indirect V2V relative poses in scenarios with multiple neighboring vehicles.

The integration of VLC enables direct monitoring among pedestrians, vehicles, and infrastructure, focusing on critical aspects such as queue formation and pedestrian corner density to enhance road safety. P2I2P communication enables travel time calculations, while real-time data on speed and waiting times are analyzed using transmitter tracking IDs.

B. Traffic Scenario and Phasing Diagram

The simulated scenario, as shown in Fig. 2a, features two intersections, each with two 4-way junctions, consisting of 2 lanes per arm spanning 100 meters in total length.

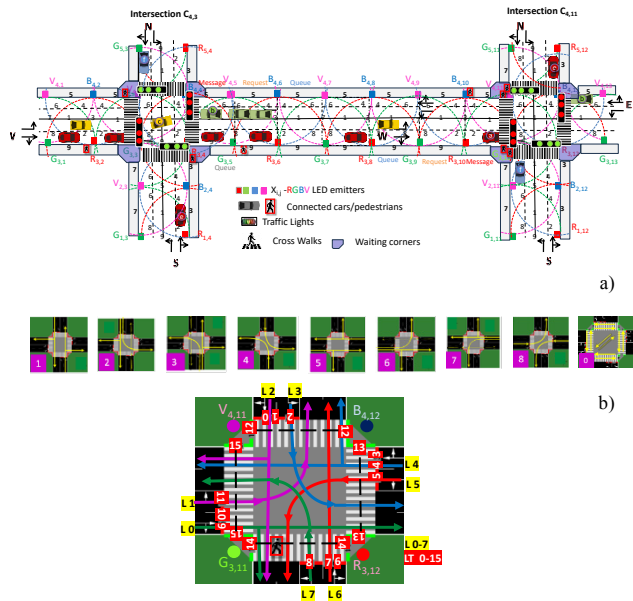


Fig. 2. Simulated scenario: Four-legged intersection (X_{ij}), the generated footprints (1-9) and the connected cars and pedestrians. b) Phasing diagram and schematic diagram of the C2 intersection with coded lanes (L/0-7) and traffic lights (TL/0-15).

Traffic flows from compass directions, with lanes indicating movement options: right lanes for right turns or going straight, and left lanes for left turns only. Central traffic light systems, regulated by Intelligent Managers (IMs), control traffic. Features like emitters (streetlamps), pedestrian lanes, waiting areas, and crosswalks are integrated. Four traffic flows along cardinal points are considered, with road request and response segments offering binary choices (turn left/straight or turn right). Assumptions include a total influx of 2300 cars per hour, primarily from east and west directions, with 25% expected to turn and 75% to continue straight. Pedestrian influx is around 11200 per hour, crossing in all directions at an average speed of 3 km/h.

Fig. 2b outlines intersection phase progressions within a structured cycle length, comprising eight vehicular phases and an exclusive pedestrian phase. Each phase is subdivided into discrete time sequences, providing a comprehensive temporal framework. [11] [12].

Each flow (illustrated by the different vehicle colors) comprises vehicles moving straight or making left turns, with specific vehicles representing top requests in the sequence.

The assumption is that specific vehicles, labeled $a_1, b_1, a_2, b_2, a_3, c_1, b_3, e_1, a_4, c_2, a_5,$ and f_1 , represent the top requests in the given sequence.

C. Communication protocol, coding, and decoding techniques

Data transmission in the VLC system follows a synchronous approach using a 64-bit data frame structure. Information is encoded using On-Off Keying (OOK) modulation, with each luminaire containing WLEDs (RGBV), enabling simultaneous transmission of four signals. A PIN-PIN demultiplexer decodes the message based on calibrated amplitudes of RGBV signals. The communication protocol includes components like Start of Frame (SoF) for synchronization, Identification Blocks encoding communication type (COM) and localization (position, time), and other ID Blocks for additional identifiers, Traffic Message containing vehicle information, and End of Frame (EoF) indicating the end of transmission. This structured protocol ensures efficient encoding and decoding of critical movement information, maintaining synchronization and data integrity in the VLC system. In Table 1 the communication protocol is depicted.

Table 1. Communication protocol

	COM	Position		ID (veic)	Time				payload			EOF
		x	y		END	Hour	Min	Sec	Car IDx	Car IDy	nr behind	
L2V	Sync	1	x y	0 bits	END	Hour	Min	Sec				EOF
V2V	Sync	2	x y	Lane (0-7) Veic. (nr)	END	Hour	Min	Sec	Car IDx	Car IDy	nr behind	EOF
V2I	Sync	3	x y	TL (0-15) Veic. (nr)	END	Hour	Min	Sec	Car IDx	Car IDy	nr behind	EOF
I2V	Sync	4	x y	TL ID (0-15) Veic.	END	Hour	Min	Sec	Car IDx	Car IDy	nr behind	EOF
P2I	Sync	5	x y	TL (0-15) Direct.	END	Hour	Min	Sec				EOF
I2P	Sync	6	x y	TL (0-15) Phase	END	Hour	Min	Sec				EOF

Decoding the information received from the photocurrent signal captured by the photodetector involves a critical step reliant on a pre-established calibration curve [12]. This curve meticulously maps each conceivable decoding level to a sequence of bits. Essentially, the calibration curve serves as a guide, facilitating the establishment of associations between photocurrent thresholds and specific bit sequences.

IV. RESULTS

A. VLC Algorithms

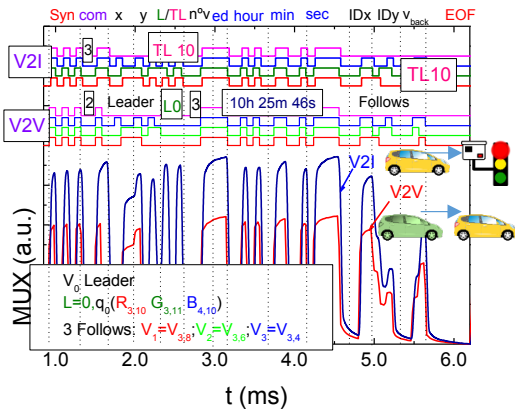


Fig. 3. MUX signal request assigned to different types of communication. On the top the decoded messages are displayed.

Fig. 3 displays the decoded optical signals (at the top of the figures) and the signals received (MUX) by the receivers in a V2V (COM 2) and V2I (COM 3) communication scenario involving a leader vehicle a_0 at position $(R_{3,10}, G_{3,11}, B_{4,10})$. This vehicle is communicating with the agent at the second intersection (C2) on lane L0 (direction E) at 10:25:46 and is followed by three other vehicles (Veic. nr) $V_1, V_2,$ and V_3 with the same direction, located at positions $(IDx, y) R_{3,8}, G_{3,6}$ and $R_{3,4}$, respectively.

Fig.4 demonstrates the MUX signal and the decoded messages sent by the traffic lights to pedestrians ($I2P_{1,2}$). This visual representation helps to understand the communication between pedestrians waiting in the corners and the corresponding traffic lights, providing insights into the signals exchanged for pedestrian crossings at both intersections (C1 and C2).

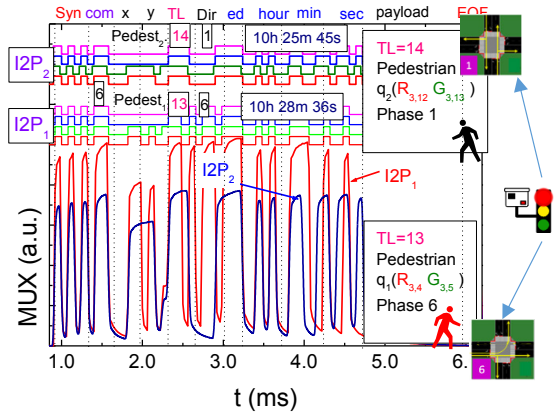


Fig. 4. Normalized MUX signal responses and the corresponding decoded messages, displayed at the top, sent by the IM to pedestrians waiting in the corners ($I2P_{1,2}$) (b) at various frame times.

Upon pedestrian q_2 receiving information from the traffic light C2, it becomes evident that the current active phase is N-S (Phase 1), signifying that the pedestrian did not arrive in time for their designated phase (Phase 0). Consequently, the pedestrian is required to wait for an estimated cycle time of 3 (cycle time) minutes before being granted the opportunity to cross. Subsequently, the pedestrian crosses the crosswalk, covering the distance to the next intersection in approximately 1 minute and 50 seconds. Upon arrival, the pedestrian waits in the designated waiting zone at position $R_{3,4}-G_{3,5}$ until the pedestrian phase becomes active once again. At 10:28:35, the pedestrian establishes communication with traffic light TL13 at the C1 (P2I). The traffic light promptly responds ($I2P_1$) at 10:28:36, providing crucial information that the currently active phase is the final one in the cycle (Phase 6). These interactions highlight the effectiveness of the pedestrian's communication with the traffic lights, enabling them to stay informed about the active phase, waiting time, and make decisions accordingly.

B. Dynamic Traffic Control: Integrating Pedestrian Consideration

Assessing the effectiveness of the proposed V-VLC system in multi-intersection utilizes the Simulation of Urban MObility (SUMO), employing agent-based simulations. SUMO tests traffic control algorithms, manages intersections, and oversees pedestrian crossings, mirroring

real-world conditions. For data analysis, SUMO collects and analyzes simulation data, including vehicle trajectories, travel times, congestion levels, and pedestrian movements.

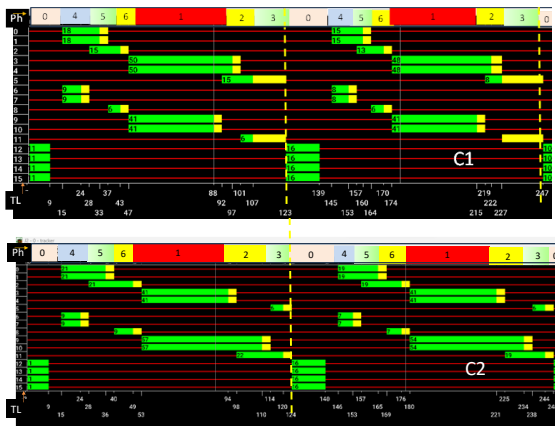


Fig. 5. State phasing diagrams for C1 and C2 intersections.

The simulation scenario, adapted to the SUMO simulator, provides insights into traffic light signals and vehicle/pedestrian movements within the terminals. In Fig. 5 a state diagram was generated for C2 intersection, incorporating both vehicles in the lanes (2300v/h) and pedestrians (11200 p/h) in the sidewalks during two cycles of 120 seconds. These diagrams offer insights into the dynamic behavior of traffic light signals and carrier/pedestrian movements within the simulated terminals. As can be observed in the diagrams it is possible to distinguish the different cycles that occur during the simulation. It always begins with a pedestrian phase (Phase 0), during which some pedestrians can cross the crosswalk, turning red for

pedestrians starting from 11 seconds. Then, phases dedicated to vehicles (Phases 1-8) take place until it concludes at 123 seconds. At this moment, the second cycle begins, with the pedestrian phase becoming active again. The same process repeats until 247 seconds, marking the end of this second cycle and the initiation of a third cycle. These diagrams align with the analysis conducted for pedestrians.

V. CONCLUSIONS

This paper sets the groundwork for advancing intelligent traffic management by highlighting the potential of VLC technology to enhance safety and efficiency at urban intersections. Our focus was on optimizing both vehicular and pedestrian traffic, addressing the previously overlooked aspect of pedestrian phases. By analyzing agents' behavior and decision-making, particularly concerning pedestrian safety, we aimed to refine the timing of pedestrian phases.

In the domain of traffic optimization, our state representation incorporates environmental information, vehicle and pedestrian distribution data from V-VLC messages, and a proposed phasing diagram guiding agent actions. We developed dynamic and intelligent control system models to securely manage traffic at two connected intersections. Through Reinforcement Learning and the SUMO simulator, we conducted a thorough analysis. With an agent at each intersection, the system optimizes traffic lights based on communication from VLC-ready vehicles, devising strategies to enhance flow and coordinate with other agents for overall traffic optimization.

ACKNOWLEDGMENT

This work was sponsored by FCT – Fundação para a Ciência e a Tecnologia, within the Research Unit CTS – Center of Technology and Systems, reference UID/EEA/00066/2020.

REFERENCES

- O'Brien, D. et al. "Indoor Visible Light Communications: challenges and prospects," Proc. SPIE 7091, 709106, pp. 60-68 (2008).
- Liang, X., Du, X., Wang, G., and Han, Z., "A Deep Reinforcement Learning Network for Traffic Light Cycle Control," in IEEE Transactions on Vehicular Technology, vol. 68, no. 2, pp. 1243-1253, Feb. 2019, doi: 10.1109/TVT.2018.2890726.
- Sousa, I., Queluz, P., Rodrigues, A., and Vieira, P. "Realistic mobility modeling of pedestrian traffic in wireless networks". In 2011 IEEE EUROCON-International Conference on Computer as a Tool, pp. 1-4. IEEE (2011).
- Ding, T.; Wang, S.; Xi, J.; Zheng, L.; Wang, Q. "Psychology-Based Research on Unsafe Behavior by Pedestrians When Crossing the Street" Adv. Mech. Eng. 2015, 7, 203867.
- Oskarski, J., Guminska, L., Miszewski, M., & Oskarska, I. (2016). "Analysis of Signalized Intersections in the Context of Pedestrian Traffic". Transportation Research Procedia, 14, 2138-2147., doi:10.1016/j.trpro.2016.05.229
- Elbaum, Y.; Novoselsky, A.; Kagan, E. A "Queueing Model for Traffic Flow Control in the Road Intersection". Mathematics 2022, 10, 3997. doi: 10.3390/math10213997
- Yousefi, S., Altman, E., El-Azouzi, R., and Fathy, M., "Analytical Model for Connectivity in Vehicular Ad Hoc Networks," IEEE Transactions on Vehicular Technology, 57, pp.3341-3356 (2008).
- Alvarez Lopez et al., "Microscopic Traffic Simulation using SUMO". In: 2019 IEEE Intelligent Transportation Systems Conference (ITSC), pp. 2575-2582. IEEE. The 21st IEEE International Conference on Intelligent Transportation Systems, 4-7. Nov. 2018, Maui, USA.
- Yousefpour, A., et al., "All one needs to know about fog computing and related edge computing paradigms: A complete survey", Journal of Systems Architecture, Volume 98, pp. 289-330 (2019).
- Vieira, M. A., Vieira, M., Louro, P., Vieira, P. "Cooperative vehicular visible light communication in smarter split intersections," Proc. SPIE 12139, Optical Sensing and Detection VII, 1213905 (17 May 2022); doi: 10.1117/12.2621069.
- Galvão, G., Vieira, M., Louro, P., Vieira, M. A., Véstias, M., and Vieira, P. "Visible Light Communication at Urban Intersections to Improve Traffic Signaling and Cooperative Trajectories," 2023 7th International Young Engineers Forum (YEF-ECE), Caparica / Lisbon, Portugal, 2023, pp. 60-65, doi: 10.1109/YEF-ECE58420.2023.10209320.
- Vieira, M.A.; Galvão, G.; Vieira, M.; Louro, P.; Vestias, M.; Vieira, P. "Enhancing Urban Intersection Efficiency: Visible Light Communication and Learning-Based Control for Traffic Signal Optimization and Vehicle Management". Symmetry 2024, 16, 240. https://doi.org/10.3390/sym16020240.

Indoor Guidance in Multi-Terminal Airports through Visible Light Communication

Manuela Vieira
Electronics Telecommunications and Computer Dept.
 ISEL, CTS-UNINOVA, LASI and NOVA School of Science and Technology
 Lisbon, Portugal
 mv@isel.ipl.pt

Manuel Augusto Vieira
Electronics Telecommunications and Computer Dept.
 ISEL, CTS-UNINOVA and LASI
 Lisbon, Portugal
 manuel.vieira@isel.pt

Gonçalo Galvão
Electronics Telecommunications and Computer Dept.
 ISEL,
 Lisbon, Portugal
 A45903@alunos.isel.pt

Paula Louro
Electronics Telecommunications and Computer Dept.
 ISEL, CTS-UNINOVA and LASI
 Lisbon, Portugal
 paula.louro@isel.pt

Pedro Vieira
Electronics Telecommunications and Computer Dept.
 ISEL, IT
 Lisbon, Portugal
 pedro.vieira@isel.pt

Alessandro Fantoni
Electronics Telecommunications and Computer Dept.
 ISEL, CTS-UNINOVA and LASI
 Lisbon, Portugal
 alessandro.fantoni@isel.pt

Abstract— This study introduces an innovative method for guiding navigation in busy airports using Visible Light Communication (VLC) technology. By utilizing existing lighting fixtures to transmit encoded messages via light signals, users can receive location-specific guidance. The system employs tetrachromatic LEDs and VLC capabilities to efficiently transmit data, supported by a mesh cellular hybrid structure that enhances flexibility without the need for traditional gateways. Integrating VLC into Edge/Fog architecture maximizes its benefits such as wireless connectivity and secure communication while leveraging existing infrastructure. This integration allows for distributed data processing, storage, and communication at the network edge, improving system performance. The study develops a detailed airport model and analyzes navigation for pedestrians and luggage/passenger carriers. Users equipped with PINPIN optical sensors interpret light signals for localization and positioning, supported by a tailored communication protocol and coding techniques for reliable transmission.

Keywords— *Visible Light Communication (V-VLC), Wayfinding, Indoor Navigation, User Behavior, Agent-Based simulator, Edge/Fog Architecture.*

I. INTRODUCTION

VLC is a data transmission technology [1, 2, 3] that can easily be employed in indoor environments since it can use the existing LED lighting infrastructure with simple modifications [4, 5, 6]. In the sequence, we propose to use modulated visible light, carried out by white low-cost LEDs. The LEDs are capable of switching to different light intensity levels at a very fast rate, imperceptible by a human eye. This functionality can be used for communication where the data is encoded in the emitting light. A mobile receiver is used to demodulate and decode the electrical signal generated at a photodetector. This means that the LEDs are twofold by providing illumination as well as communication. Multi colored LEDs based luminaires can provide further possibilities for signal modulation and detection in VLC systems [7]. The use of white polychromatic LEDs offers the possibility of Wavelength Division Multiplexing (WDM) which enhances the transmission data rate. A WDM receiver based on tandem a-SiC:H/a-Si:H PIN/PIN light-controlled

filter was used [8, 9]. Here, when different visible signals are encoded in the same optical transmission path, the device multiplexes the different optical channels, performs different filtering processes (amplification, switching, and wavelength conversion) and finally decodes the encoded signals recovering the transmitted information.

Fine-grained indoor localization technology presents various applications, particularly beneficial in complex environments like airports. By implementing VLC technology the indoor navigation can be significantly improved, offering users precise location information and enhancing their overall experience in crowded indoor environments [10, 11]. Passengers can receive precise directions to boarding gates, check-in counters, baggage claim areas, lounges, and other amenities, reducing confusion and enhancing their overall experience. Additionally, it enables real-time tracking and management of assets such as luggage carts and maintenance equipment, optimizing their deployment and utilization throughout the airport. For airport retailers, indoor localization facilitates personalized promotions, wayfinding assistance, and location-based services, leading to increased sales and customer satisfaction. Ultimately, this technology streamlines operations, improves passenger experience, and enhances safety and security measures, contributing to a more efficient and enjoyable air travel experience for all stakeholders..

II. METHODOLOGY

A. VLC background

The system model is structured around two primary modules: the transmitter and the receiver (Figure 1). The transmitter module plays a crucial role in converting sender data into byte format before transmitting it as light signals. White light tetra-chromatic sources (WLEDs) with four polychromatic LEDs are utilized, each representing a data channel. Only one LED chip is modulated at a time for data transmission, while the others control white light perception. An ON-OFF Keying (OOK) modulation scheme encodes data onto light signals, which are then received by a VLC receiver. The receiver, equipped with a MUX photodetector, filters and transforms light signals into electrical signals for decoding. Signal processing techniques are employed to reconstruct the

data signal at the data processing unit for user output. Receivers position themselves to overlap transmitter range circles for multiplexed (MUX) signal reception, acting as both positioning systems and data transmitters. Different receiver orientations within a unit square cell are considered for nuanced resolution in localization [9][12].

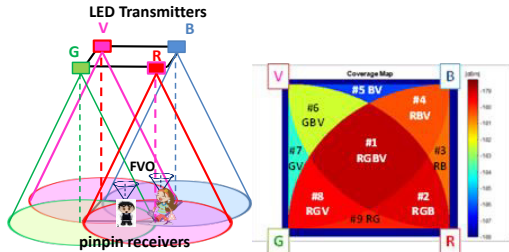


Fig. 1. Transmitters and receivers 3D relative positions, footprints and coverage map in the square topology.

B. Lighting Plan Layout, Architecture and Geolocation

In VLC tracking, geographical coordinates are used to guide users through buildings and towards specific destinations [12] [13]. This is facilitated by employing cells for positioning and a Central Manager (CM) to manage the system and generate optimal routes. A mesh cellular hybrid structure is introduced to enhance network architecture, enabling direct device-to-device communication and secure pathways. Each WLED emits a unique VLC signal, serving as an identification beacon, allowing precise user trajectory determination. The indoor route, containing spatial and temporal data, provides valuable insights into user movements. Users personalize their points of interest for wayfinding services, and average speeds are assigned based on the device type. Information is transmitted to the appropriate receivers by emitters within the infrastructure, such as Light Traffic controllers or signboards, positioned at crosswalks. In Figure 2 the edge/fog architecture and the request communications between the Devices (D2D), the Devices and the Infrastructures (D2I) or the responses from the Infrastructure to the Devices /pedestrians (I2D/P) is draft. The user positions can be represented as $q(x, y, z, t)$ by providing the horizontal positions (x, y) [12].

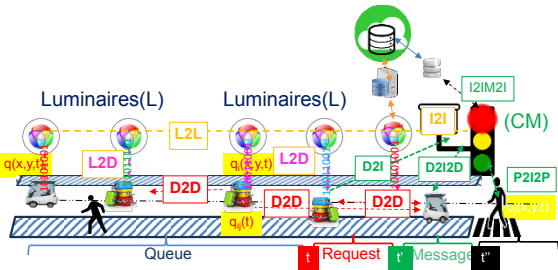


Fig. 2. One lane draft of the Edge/Frog hybrid architecture.

C. Communication protocol, coding, and decoding techniques

Data transmission in the VLC system follows a synchronous approach using a 64-bit data frame structure. Information is encoded using On-Off Keying (OOK) modulation, with each luminaire containing WLEDs (RGBV), enabling simultaneous transmission of four signals. A PIN-PIN demultiplexer decodes the message based on

calibrated amplitudes of RGBV signals. The communication protocol includes components like Start of Frame (SoF) for synchronization, Identification Blocks encoding communication type (COM) and localization (position, time), and other ID Blocks for additional identifiers, Traffic Message containing vehicle information, and End of Frame (EoF) indicating the end of transmission. This structured protocol ensures efficient encoding and decoding of critical movement information, maintaining synchronization and data integrity in the VLC system. In Table 1 the communication protocol is depicted.

Table 1. Communication protocol

	SoF	COM	Position		ID (device)		Time				payload			EoF
			x	y	0 bits	(nr)	END	Hour	Min	Sec	Device IDx	Device Dy	nr behind	
L2D	Sync	1	x	y	Lane (0-7)	Device (nr)	END	Hour	Min	Sec	Device IDx	Device Dy	nr behind	EoF
D2D	Sync	2	x	y	TL (0-15)	Device (nr)	END	Hour	Min	Sec	Device IDx	Device Dy	nr behind	EoF
D2I	Sync	3	x	y	TL (0-15)	ID Device	END	Hour	Min	Sec	Device IDx	Device Dy	nr behind	EoF
I2D	Sync	4	x	y	TL (0-15)	ID Device	END	Hour	Min	Sec	Device IDx	Device Dy	nr behind	EoF
P2I	Sync	5	x	y	TL (0-15)	N,S,E,W	END	Hour	Min	Sec				EoF
I2P	Sync	6	x	y	TL (0-15)	Phase	END	Hour	Min	Sec				EoF

Decoding the information received from the photocurrent signal captured by the photodetector involves a critical step reliant on a pre-established calibration curve [13]. This curve meticulously maps each conceivable decoding level to a sequence of bits. Essentially, the calibration curve serves as a guide, facilitating the establishment of associations between photocurrent thresholds and specific bit sequences.

III. AIRPORT MODEL

The capacity of an airport is closely tied to its gateways, boarding areas, and aircraft door layouts. Assigning these areas involves a coordinated process, tailored to specific objectives and criteria for each scenario. Objectives may include enhancing customer service by minimizing travel distances for pedestrians or passenger/luggage carriers during landing, transit, baggage claim, terminal changes, or shopping.

Airports are assessed based on factors like walking distances between terminal facilities and accessibility to ground transportation and parking. This research enhances our understanding of pedestrian behavior within terminal corridors, informing better decisions in terminal facility design. The airport model is generated using footprints of a multi-level airport collected from available sources and displayed on user receivers for orientation [14].

The simulated scenario includes two terminal intersections with four-way arms and moving lanes, along with sidewalks and areas for shopping, dining, or resting. Traffic management involves directing carriers along cardinal points using road request and response segments, exclusive passenger lanes, waiting areas, and crosswalks. Central traffic light systems controlled by a Central Manager regulate carrier flow and prevent collisions.

Pedestrians on sidewalks have the freedom to move in both directions. It's a prerequisite that destinations can be targeted by user requests to the CM within a specific request distance (D/P2I) and any floor changes notified if applicable. The indoor route throughout the airport is communicated to the user via a responding message (message distance range; I2D/P) transmitted by the traffic signals, which also function as routers or mesh/cellular nodes (refer to Figure 2).

This request/response framework provides landmark-based instructions to help carriers identify decision points

where a change of direction is necessary (action). Furthermore, it offers information to users to confirm that they are on the correct path. The Simulated scenario and environment with the optical infrastructure (X_{ij}), the generated footprints (1-9) and the connected luggage and pedestrians' flow are displayed in Fig.3a. In Fig.3b the schematic diagram of Terminal 2 with coded lanes (L/0-7) and traffic lights (TL/0-15) is draft.

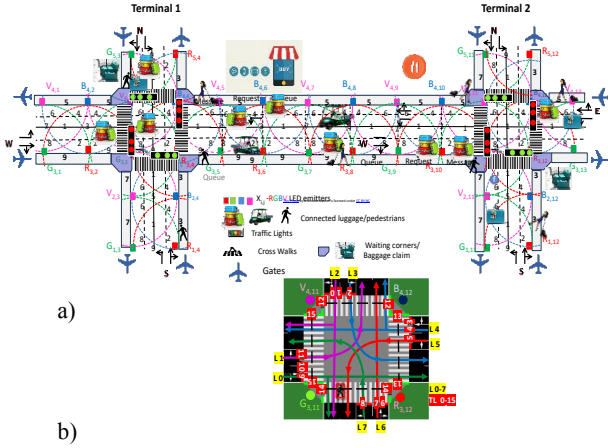


Fig. 3. a) Simulated scenario and environment with the optical infrastructure (X_{ij}), the generated footprints (1-9) and the connected luggage and pedestrians' flow. b) Schematic diagram of Terminal 2 with coded lanes (L/0-7) and traffic lights (TL/0-15)

Pedestrians on sidewalks have the freedom to move in both directions. It's a prerequisite that destinations can be targeted by user requests to the CM within a specific request distance (D/P2I) and any floor changes notified if applicable. The indoor route throughout the airport is communicated to the user via a responding message (message distance range; I2D/P) transmitted by the traffic signals, which also function as routers or mesh/cellular nodes (refer to Figure 2).

This request/response framework provides landmark-based instructions to help carriers identify decision points where a change of direction is necessary (action). Furthermore, it offers information to users to confirm that they are on the correct path.

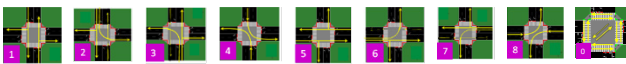


Fig. 4. Schematic of a one cycle phase diagram with eight moving walkway phases and an exclusive pedestrian phase.

Fig.4 visually outlines intersection phase progressions (actions) within a structured cycle length, comprising eight AGV carrier phases in the lanes and an exclusive pedestrian phase for the walking passengers. Each phase is subdivided into discrete time sequences, providing a comprehensive temporal framework.

IV. RESULTS

In this section the algorithms developed for guiding users through indoor spaces are described. Explanation of turn-by-turn directions, landmark highlighting, alerts, and alternate route suggestions are given. Figure 5a displays the decoded optical signals (at the top of the figures) and the signals received (MUX) by the receivers in a D2D (COM 2) and D2I

(COM 3) communication scenario involving a leader device in the moving walkway at position ($R_{3,10}, G_{3,11}, B_{4,10}$). This device is communicating with the CM at the second terminal (T2) on lane L0 (direction E) at 10:25:46 and is followed by three other devices (nr) D_1, D_2 , and D_3 with the same direction, located at positions (IDx,y) $R_{3,8}, G_{3,6}$ and $R_{3,4}$, respectively.

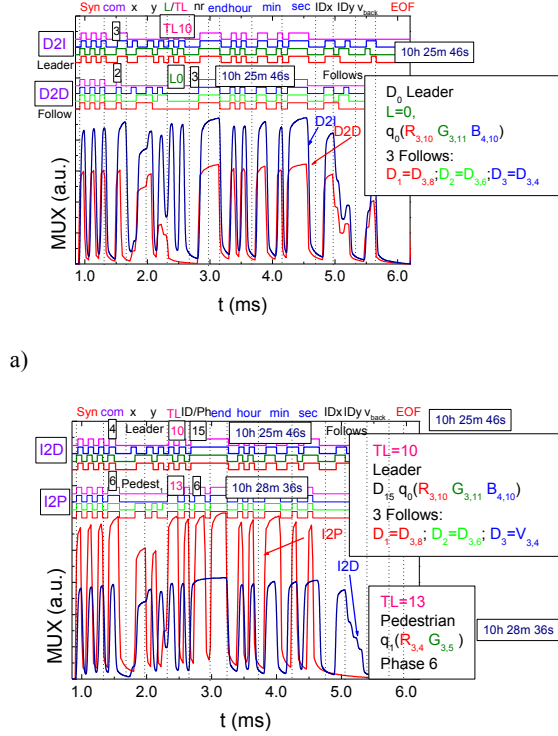


Fig. 5. MUX signal request (a) and responses (b) assigned to different types of V-VLC communication. On the top the decoded messages are displayed.

In Figure 5b, the responses (I2D and I2P) from two traffic lights (TL10 and TL13) to the crossing request from the preceding carrier $d_0 (R_{3,10}, G_{3,11}, B_{4,10})$ and a pedestrian g_1 located in the "waiting corner" of the first terminal ($R_{3,4}, G_{3,5}$) are exemplified. The timestamps "10:25:46" and "10:28:36" represent the times at which the two responses were sent respectively for the pedestrian (COM 6) and for the Passenger/luggage carrier (COM 4) and provide a reference point for when each response was generated.

Assessing the effectiveness of the proposed V-VLC system in multi-terminal airports utilizes the Simulation of Urban MObility (SUMO), employing agent-based simulations. SUMO serves as a powerful tool for optimizing traffic operations within airports, enhancing efficiency, safety, and passenger experience.

SUMO simulates vehicles, pedestrians, and entities in the airport environment, adjusting parameters like traffic density and road layouts. It tests traffic control algorithms, manages intersections, and oversees pedestrian crossings, mirroring real-world airport conditions.

For data analysis, SUMO collects and analyzes simulation data, including vehicle trajectories, travel times, congestion levels, and pedestrian movements. Visualization

capabilities aid in analysis and decision-making, while SUMO's API supports interaction with external programs for diverse traffic flow statistics. Gate assignment approaches for aircraft movement are outlined, aiming to minimize pedestrian walking distances or maximize passenger throughput. Traffic scenarios with varying cycle durations and carrier flows were considered, integrating pedestrian flows to reflect realistic scenarios.

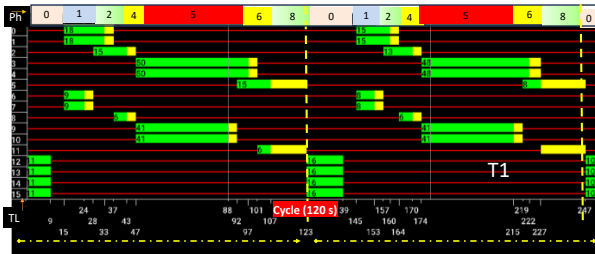


Fig. 6. State phasing diagram.

The simulation scenario, adapted to the SUMO simulator, provides insights into traffic light signals and carrier/pedestrian movements within the terminals. In Fig. 6 a state diagram was generated, incorporating both carrier in the lanes (2300d/h) and pedestrians (11200 p/h) during two cycles of 120 seconds (High traffic scenario). These diagrams offer insights into the dynamic behavior of traffic light signals and carrier/pedestrian movements within the simulated terminals. As can be observed in the diagrams, it is possible to distinguish the different cycles that occur during the simulation. It always begins with a pedestrian phase (Phase 0), during which some individuals can cross the crosswalk, turning red for pedestrians starting from 11 seconds. Then, phases dedicated to carriers (Phases 1-8) take place until it concludes at 123 seconds. At this moment, the second cycle begins, with the pedestrian phase becoming

active again. The same process repeats until 247 seconds, marking the end of this second cycle and the initiation of a third cycle. These diagrams align with the analysis conducted for pedestrians.

V. CONCLUSIONS

Utilizing VLC signals offers a promising solution for improving indoor navigation in multi-terminal airports. Integration with existing lighting infrastructure and traffic control algorithms demonstrates significant enhancements in pedestrian and carrier traffic management. By optimizing traffic flow, minimizing pedestrian walking distances, and providing real-time guidance, VLC-based systems improve accessibility and efficiency in airport environments.

The study involved generating a two-terminal airport model based on Edge/Fog architecture, establishing communication protocols, and testing VLC algorithms. These algorithms effectively transmit encoded messages, enabling localization and positioning, and reliable communication between traffic signals and user devices. Real-time guidance offers turn-by-turn directions, highlights landmarks, and suggests alternate routes, improving traffic flow management and operational efficiency.

SUMO simulations provide insights into pedestrian behavior and traffic dynamics, revealing the impact of traffic flow, road length, and cycle durations on pedestrian movement.

Future work could involve implementing Reinforcement Learning (RL) techniques with multi-agent systems in airport terminals to enhance navigation and traffic management.

ACKNOWLEDGMENT

This work was sponsored by FCT – Fundação para a Ciência e a Tecnologia, within the Research Unit CTS – Center of Technology and Systems, reference UID/EEA/00066/2020.

REFERENCES

- [1] Ozgur E., Dinc, E., Akan, O. B., "Communicate to illuminate: State-of-the-art and research challenges for visible light communications," *Physical Communication* 17 72–85, (2015).
- [2] Panta K., Armstrong, J., "Indoor localisation using white LEDs," *Electron. Lett.* 48(4), 228–230 (2012).
- [3] Komiya, T., Kobayashi, K., Watanabe, K., Ohkubo, T., and Kurihara, Y., "Study of visible light communication system using RGB LED lights," in *Proceedings of SICE Annual Conference, IEEE, 2011*, pp. 1926–1928.
- [4] Wang, Y., Wang, Y., Chi, N., Yu, J., and Shang, H. "Demonstration of 575-Mb/s downlink and 225-Mb/s uplink bi-directional SCM-WDM visible light communication using RGB LED and phosphor-based LED," *Opt. Express* 21(1), 1203–1208 (2013).
- [5] Tsonev, D., Chun, H., Rajbhandari, S., McKendry, J., Videv, S., Gu, E., Haji, M., Watson, S., Kelly, A., Faulkner, G., Dawson, M., Haas, H., and O'Brien, D. "A 3-Gb/s single-LED OFDM-based wireless VLC link using a Gallium Nitride μ LED," *IEEE Photon. Technol. Lett.* 26(7), 637–640 (2014).
- [6] O'Brien, D., Minh, H. L., Zeng, L., Faulkner, G., Lee, K., Jung, D., Oh, Y. and Won E. T., "Indoor visible light communications: challenges and prospects," *Proc. SPIE* 7091, 709106 (2008).
- [7] Monteiro E., and Hranilovic, S., "Constellation design for color-shift keying using interior point methods," in *Proc. IEEE Globecom Workshops, Dec.*, 1224–1228 (2012).
- [8] Vieira, M., Louro, P., Fernandes, M., Vieira, M. A., Fantoni A., and Costa, J., "Three Transducers Embedded into One Single SiC Photodetector: LSP Direct Image Sensor, Optical Amplifier and Demux Device" *Advances in Photodiodes InTech*, Chap.19, 403-425 (2011).
- [9] Vieira, M.A., Louro, P., Vieira, M., Fantoni, A., and Steiger-Garção, A., "Light-activated amplification in Si-C tandem devices: A capacitive active filter model" *IEEE sensor journal*, 12, NO. 6, 1755-1762 (2012).
- [10] Jovicic, A., Li, J., and Richardson, T., "Visible light communication: opportunities, challenges and the path to market," *Communications Magazine, IEEE*, vol. 51, no. 12, pp. 26–32 (2013).
- [11] S T. Komine and M. Nakagawa, "Fundamental analysis for visible-light communication system using led lights," *Consumer Electronics, IEEE Transactions on*, vol. 50, no. 1, pp. 100–107, (2004).
- [12] Vieira, M.A.; Galvão, G.; Vieira, M.; Louro, P.; Vestias, M.; Vieira, P., "Enhancing Urban Intersection Efficiency: Visible Light Communication and Learning-Based Control for Traffic Signal Optimization and Vehicle Management." *Symmetry* 2024, 16, 240. <https://doi.org/10.3390/sym16020240>.
- [13] M. Vieira, M. A. Vieira, P. Louro, A. Fantoni, P. Vieira, "Dynamic VLC navigation system in Crowded Buildings", *International Journal On Advances in Software*, v 14 n 3&4, pp. 141-150, 2021.
- [14] M. Vieira, M. A. Vieira, P. Vieira, and P. Louro "Enhancing Building Guidance: A Visible Light Communication-based Identifier (ID) System," *Sensors & Transducers journal*, Vol. 263, Issue 4, December 2023, pp. 74-81

Quantification and Characterization of Microplastics Using an App and Smartphone

Francisco Di Lullo
Laboratory of Biosensors and Bioanalysis (LABB), Department of Biological Chemistry. IQUIBICEN, University of Buenos Aires and CONICET, CABA, Argentina.
dilufan2002@gmail.com

Monica Mosquera Ortega
Laboratory of Biosensors and Bioanalysis (LABB), Department of Biological Chemistry. IQUIBICEN, University of Buenos Aires, CONICET CABA and UTN - FRGP, Argentina.
36729785700

Federico Schaumburg
INTEC (Universidad Nacional del Litoral – CONICET), Santa Fe, Argentina.
235647571

Eduardo Cortón
Laboratory of Biosensors and Bioanalysis (LABB), Department of Biological Chemistry. IQUIBICEN, University of Buenos Aires and CONICET, CABA, Argentina.
318974666

Federico Figueredo
Laboratory of Biosensors and Bioanalysis (LABB), Department of Biological Chemistry. IQUIBICEN, University of Buenos Aires and CONICET, CABA, Argentina.
272205609

Abstract — The majority of identification and quantification protocols are still based on visual counting, which is an extremely time-consuming and error-prone task due to the subjectivity of the operator. To address such a problem, there are several software analysis methods available, but they are mainly based on either the use of optical microscopy, which covers a minimal area for each sample, or need to label the particles to later identify them. The objective of the present study is to develop an economical, simple, and rapid method to detect microplastics in various environmental samples. The developed methodology aims to solve the problem of rapid microplastic detection without the need for expensive equipment or manual techniques subject to observer bias.

Keywords — software analysis, polymer, area analysis, thermo analysis, low cost.

I. INTRODUCTION

Microplastics (MPs) are considered a group of emerging contaminants. They are defined as plastic particles ranging in size from 1 μm to 5 mm. The pollution of ecosystems by MPs has been the focus of much attention, particularly in marine environments. However, MPs have also been found in the soil, in coastal waters, in animals and in humans [1].

The need for reproducible, rapid and cost-effective methods for the detection and identification of MPs in the environment is an analytical challenge. A gold standard method for detecting and quantifying MPs is still lacking. However, several approaches exist to quantify and identify MPs, including Fourier transform infrared spectroscopy, Raman spectroscopy, thermo analytical instruments, and visual methods. Spectrometers provide information on the composition and size of the polymer and can even determine the number of MPs that are present in the sample [1]. Thermo-analytical instruments, on the other hand, can be used for the identification and quantification of the mass of MPs in a sample [1]. Both of these instrumental methods are costly, time consuming, and need to be operated by highly trained technicians. In addition, these methods require that strictly

defined sample pre-treatment protocols be carried out prior to the analysis to remove the organic matter that is adsorbed on the surface of the MPs.

Visual identification of MPs is the easiest and quickest technique. The cheapest way to identify MPs is the hot needle or hot spot test. It can be performed under light microscope magnification using a flame-heated needle or soldering iron. When touched, the polymer will soften or melt, giving a positive result [2]. Fluorescence microscopy can be used to identify MPs after they have been stained with Nile Red, a hydrophobic dye that adsorbs to the surface of polymers, making it easy to identify [3]. Although widely used by researchers, Nile Red staining overestimates the number of identified MPs because the dye binds to hydrophobic organic compounds. Optical and fluorescence microscopes are used to identify and count MPs in environmental samples. However, these methods are time-consuming and often have high user variability as they depend on human intervention during sample inspection [4].

In this study a simple and practical approach for the identification and morphological characterization of MPs is given. It is a low-cost procedure that comprises a Smartphone, a heating unit and disposable glass slides. After 4 minutes the results are obtained in a semi-automatic manner surpassing the limitations given by other methods.

II. MATERIALS AND METHODS

A. Microplastics detection system

Commercial glass slides were painted with heat resistant paints available elsewhere. The samples were added to the surface of the glass slide and over a piece of aluminum plaque and placed over a conventional stirrer with a heating unit (MS-H280-Pro). Above the heating unit, a dark box containing a LED light source, and a polarizer set at 0° was aligned to illuminate the glass slide. A small hole in the dark box and above the heating unit containing the glass slide was

done to place a second polarizer at 90° with respect to the other polarizer. A Smartphone (Motorola G20) with a 50 MP digital camera was used to interrogate the sample. The Smartphone was placed outside the black box and aligned with the polarizer at 90° to observe the sample through the previously mentioned hole. The simplified scheme of the analytical set-up can be seen in Fig. 1.

B. Smartphone application

Appuente is a Smartphone application which is linked via the internet to any computer. This application allows to read a code placed closed to the glass slide to run a determined algorithm. In this case, the code used allows a photograph to be taken, which is later used to count particles along with their area, perimeter, and the longest and shortest size of each of them. In turn, the application can be opened on a computer for later extraction and analysis of the data. To perform data collection, a paper chip, containing the codes, must be generated and printed on any printer. This code consists of a barcode and 3 black squares that are used as a reference to perform the analysis.

C. Sample preparation

To carry out the experiments, polyethylene (PE) and wood cuttings were used. PE virgin pellets were obtained from a local plastic manufacturer. The materials used were independently shredded with a multiprocessor. The particles obtained were screened by sieves of 2 and 0.25 millimeters mesh, selecting the particles retained between both sieves. The particles used in all the experiments were between 0.25 and 2 mm in size.

D. Experimental considerations and data analysis

The glass slide in contact with the heat sink was placed over the heating unit. The Smartphone is aligned to read the code and the first analysis is done at room temperature to determine the initial parameters. Then the heating unit is set-up at 220 °C and the experiment start. During the warm-up interval, several photographs of the sample are taken by the

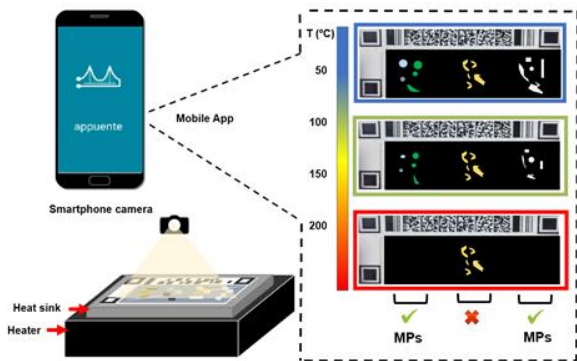


Fig. 1. Scheme diagram showing the microplastic detection system used in this study. App at 50°C, 100°C, 150°C, and 220°C. The number of particles is counted for each picture that was taken, along with their minimum and maximum size, their perimeter and area. The data obtained at each temperature is compared with the initial parameters to determine if there the particles analyzed suffer from morphological changes during the

heating ramp. The results obtained for each analysis was performed following the equation 1:

$$\Delta \text{Area} = (\text{Area}_i - \text{Area}_0) / \text{Area}_0 \quad (1)$$

Where Area_0 is the area of each particle analyzed at room temperature and Area_i is the area of each particle analyzed at a determined temperature.

III. RESULTS AND DISCUSSION

A. Smartphone application vs ImageJ

Several experiments were performed to determine the App performance to analyze particle minimum size, maximum size and area, using PE particles of different sizes at room temperature. The obtained results were compared with those obtained by using the ImageJ computer software. As can be seen in Fig. 2, area, minimum size and maximum size analyzed with the App provide high correlation with respect to ImageJ. As the higher R^2 value was obtained for area analysis, this parameter was set to be used for the following experiments.

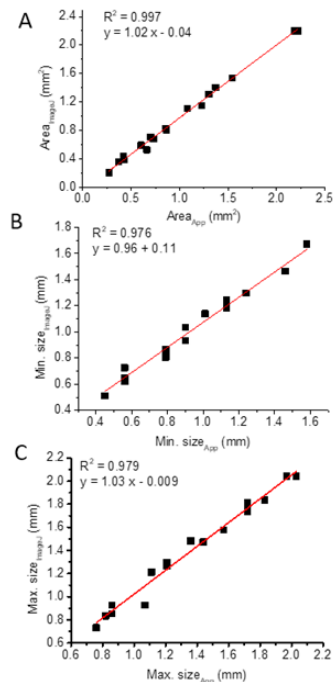


Fig. 2. Correlation plots obtained between the Smartphone App and ImageJ software for (A) Area, (B) minimum size and (C) maximum size. All experiments were performed with PE particles.

B. MPs detection

The MPs detection system was studied analyzing the surface area of PE and wood particles. As can be seen in Fig. 3, at temperatures around 50°C the PE particles do not suffer from apparent morphological changes but increasing the temperature to 150°C, some of the particles start to reduce their area. As the temperature increase to 200°C the particles-area change is evident as they are reducing in size since the glass transition temperature is reached [4]. However, some of the particles maintain their initial area. This phenomenon

could be explained as the surface contact between the particle and the glass slide is minimal, and therefore the particle could not be at the same temperature as the glass slide is. Later, as the temperature increases to 220°C another phenomenon is observed. The particles are completely melted and therefore the reflected light is minimal. That is why the App could not resolve the analysis as the particles are completely transparent. The resulting area is around zero, and the resulting value obtained is minus one. On the contrary, when wood particles were analyzed, there was no significant change in the area parameter, even at higher temperatures.

The experiments performed with PE and wood demonstrate that this approach can be used to identify PE MPs when the temperature reach the 220°C. The experiments show that all the MPs used were effectively detected without any false positive result. However, other MPs must be studied to corroborate if this analytical system could be used for MPs identification in real samples.

IV. CONCLUSION

The proposed detection system provides a simple, low cost and affordable approach for the identification of MPs. The use of a Smartphone App solves the problems related to the use of microscopes as well as the use of dyes which brings problems related to the cost and extended sample treatment time. Future experiments will be done using other polymeric materials such as polystyrene and polypropylene. Later we will perform spike tests in soil samples after performing simple extraction protocols. The detection system proposed here could replace in a near future the hot needle test or Nile Red method offering a semi-automatic approach to perform MPs analysis and detection in low resource settings.

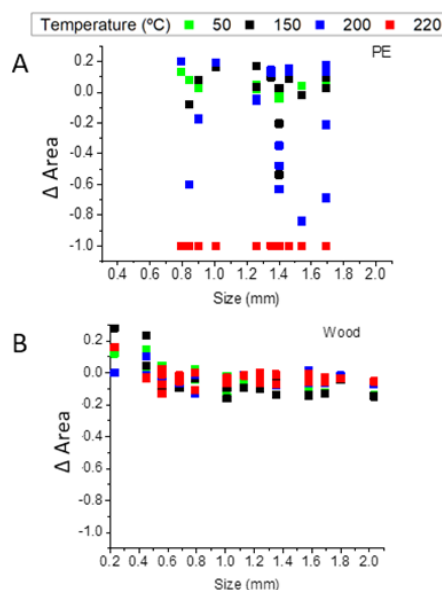


Fig.3. Experimental results showing the area variation as a function of the initial particle minimum size using (A) PE particles or (B) wood particles.

ACKNOWLEDGMENT

The authors gratefully acknowledge financial support from the National Agency of Scientific and Technological Promotion (ANPCyT) (grant BID-PICT 2020-04023) and National Council for Scientific and Technological Research (CONICET).

REFERENCES

- [1] M. E. Mosquera-Ortega, L. R. Sousa, S. Susmel, E. Cortón, F. Figueredo, "When microplastics meet electroanalysis: future analytical trends for an emerging threat," *Anal. Methods*. Vol. 15, pp 5978-5999, October 2023.
- [2] B. Beckingham, A. Apintiloaiei, C. Moore, J. Brandes, "Hot or not: systematic review and laboratory evaluation of the hot needle test for microplastic identification," *Micropl.&Nanopl.* Vol. 3, pp 1-8, April 2023.
- [3] V. C. Shruti, F. Pérez-Guevara, P. D. Roy, G. Kutralam-Muniasamy, "Analyzing microplastics with Nile Red: Emerging trends, challenges, and prospects," *J. Hazard. Mater.* Vol 423, pp 127171, September 2021.
- [4] S. Zhang, X. Yiang, H. Gertsen, P. Peters, T. Salánki, V. Geissen, "A simple method for the extraction and identification of light density microplastics from soil," *Sci. Total Environ.* Vol. 616-617, pp 1056-1065, October 2017.



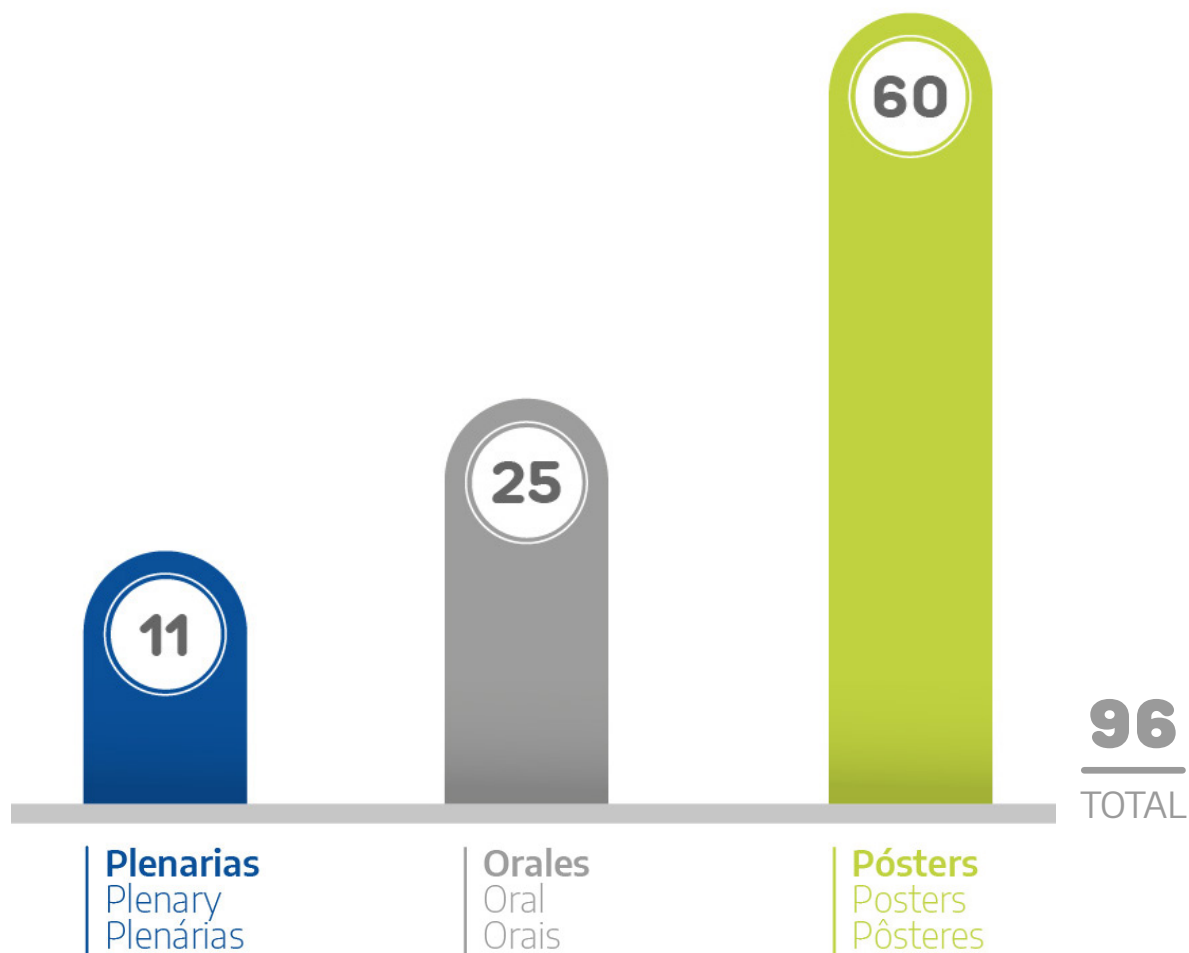
ESTADÍSTICAS 2024

2024 Statistics

Estatísticas 2024

Presentaciones

Presentations | Apresentações



Referencias

Plenarias Plenary Plenárias	11
Orales Oral Oraís	25
Pósters Posters Pôsteres	60
TOTAL	96



Referencias:

• Sensores de ondas acústicas Acoustic wave sensors Sensores de ondas acústicas	
• Microsensores y microactuadores MEMS MEMS, microsensors and microactuators Microsensores e microatuadores MEMS	10
• Sensores físicos Physical sensors Sensores físicos	
• Microsistemas analíticos integrados y lab-on-a-chip (LOC) Analytical integrated microsystems and lab-on-a-chip (LOC) Microsistemas analíticos integrados e lab-on-a-chip (LOC)	13
• Sensores microfluídicos Microfluidic sensors Sensores microfluídicos	
• Biosensores Biosensors Biossensores	11
• Sensores químicos Chemical sensors Sensores químicos	
• Sensores electroquímicos Electrochemical sensors Sensores eletroquímicos	17
• Sensores optoquímicos Optochemical sensors Sensores optoquímicos	
• Diseño y tecnología de sensores Design and technology of sensors Design e tecnologia de sensores	11
• Nuevos materiales y nanomateriales para sensores New materials and nanomaterials for sensors Novos materiais e nanomateriais para sensores	10
• Sensores en electrónica impresa Printed electronic sensors Sensores em eletrônica impressa	4
• Acondicionamiento de señales e instrumentación Signal conditioning and instrumentation Condicionamento de sinais e instrumentação	
• Sensores inteligentes y redes inalámbricas Smart sensors and wireless networks Sensores inteligentes e redes sem fio	9

País
Country | País



160
Argentina

Referencias

Argentina	160	Estados Unidos de América	5
España	48	Colombia	4
Brasil	33	Puerto Rico	3
México	12	Alemania	2
Portugal	8	Lithuania	2
Uruguay	8	Turquía	1
Italia	8	TOTAL	294



ÍNDICE DE AUTORES

Authors index

Índice de autores

ÍNDICE DE AUTORES | Authors index | índice de autores

Aceves Mijares, Mariano	p 217
Agusil, Juan Pablo	p 209, p 46
Agustinelli, Silvina	p 137, p 162
Albert, Raymundo	p 311
Alcalde Bessia, Fabricio	p 58
Alcario, Anna Martín	p 84
Aldao, Celso M.	p 279, p 253, p 283
Alonso-Chamarro, Julian	p 84, p 73, p 75, p 79, p 81, p 180, p 62
Alvarez, Fernando	p 273, p 276
Alvarez-Serna, Bryan E.	p 150
Arasa-Puig, Eva	p 180
Arduini, Emiliano José	p 303
Arjona, María Isabel	p 209, p 46
Arnal, Pablo	p 199
Arrieta, Cristian L.	p 264
Artuch, Rafael	p 81
Assis, Marcelo	p 283
Astolfi, Michele	p 253
Aviles, V. E. Manqueros	p 62
Barbosa, João Alexandre R. G.	p 133
Baró, Bárbara	p 141, p 110
Bassat, Quique	p 141, p 110
Baumann, Reinhard R.	p 294
Beleiro, Brenda Irina	p 158
Berardi, Fabrizio	p 290
Berli, Claudio L. A.	p 165
Berlin, Guido	p 244, p 97
Bernassani, Florencia	p 199, p 202
Biestro, Alberto	p 315
Bilbao, Emanuel	p 294
Boeira, Carla Daniela	p 273, p 276
Boggio, Norberto G.	p 264, p 244

Bojorge, Claudia	p 264
Bolzi, Claudio	p 233, p 237
Bonetto, María Celina	p 172, p 229, p 154
Bonilla, Joaquín	p 298
Borges, Ben-Hur Viana	p 221
Bosch, Gabriel	p 49
Bourges, Gastón	p 213
Braunger, Maria Luisa	p 86
Brusilovsky, David Leopoldo	p 261
Cabezas, Marcelo D.	p 264
Caccia, Matias	p 322
Calvo-López, Antonio	p 84, p 73, p 79, p 81, p 62
Canosa, Ana	p 69
Cantarero, Lara	p 46
Carballo, Romina	p 172, p 229, p 154
Cardillo, Maria Eugenia	p 126
Casis, Natalia	p 165
Castro, Lucas F.	p 195
Cencha, Luisa	p 165
Ceretti, Helena M.	p 130
Cerrudo, Juan Ignacio	p 43, p 36
Cervantes Schamun, Lucía	p 244
Ceto, Xavier	p 146
Chinellato Díaz, Janet	p 169
Coelho do Amara, Daniel	p 283
Coltro, Wendell K. T.	p 195
Comin, María Julieta	p 184
Cortón, Eduardo	p 100, p 195, p 199, p 202, p 334, p 205
Corzi, Damian Leonel	p 58
Cosci, Santiago	p 172, p 229, p 154
Coto Fuentes, Hesner	p 75, p 241, p 62
Couceiro, Pedro	p 75, p 62
Cowes, Diego	p 32
Cruz-Pacheco, Andrés Felipe	p 104
Cujano Ayala, Estefany	p 137
Custódio Silva Lemos, Samantha	p 283

da Mota, Achilles F.	p 221
Dabas, Paula C.	p 154
de Barros, Anerise	p 86
de Novais Schianti, Juliana	p 133, p 221, p 93
De Vita, Fabian	p 287
del Valle, Anaixis	p 106, p 141, p 110
del Valle, Manel	p 146
Delgado, Emmanuel Rosa	p 318
D'Elía, Raúl Luis	p 267
Desbas, Josaphat	p 133, p 221
Desimone, Paula Mariela	p 283
Di Donato, Andres	p 49, p 52
Di Ielsi, Pablo	p 205
Di Lullo, Francisco	p 334
Díaz Salazar, Martha	p 225, p 233, p 237
Diaz, Sebastian A	p 118
Drovandi, Juan Ignacio	p 244
Duch, Marta	p 209, p 46
Duffo, Gustavo	p 188
Elhalem, Eleonora	p 184
Eliach, Jorge	p 213
Estenoz, Diana	p 165
Estrada Wiese, Denise	p 217
Fabbri, Barbara	p 253
Fantoni, Alessandro	p 326, p 330
Farina, Silvia	p 188
Fernández Vicente, Natalia	p 73
Fernández-Escribano, Ana	p 209
Ferrari, Claudio	p 97
Ferreira dos Santos, Rômulo	p 93
Ferrer Dalmau, Jofre	p 141, p 110
Ferreyra, Nancy Fabiana	p 114
Figueredo, Federico	p 100, p 195, p 199, p 202, p 334, p 205
Fookes, Federico	p 165
Fraigi, Liliana	p 298, p 290

Franco, Diego G	p 267
Galarza, Cecilia	p 311
Galvão, Gonçalo	p 326, p 330, p 307
Gandolfi Donadío, Lucía	p 184
Garcia Mendez, Betania Sorybet	p 271
Gherardi, Sandro	p 253
Gherscovic, Damián Alejandro	p 303
Gilabert, Ulises Eduardo	p 267
Gillari, Claudio A.	p 264
Gomes, Maria Teresa	p 65
Gomez Berisso, Mariano	p 58
Gómez Ramirez, Emmanuel	p 241
Gómez Vargas, Ignacio	p 165
Gomez, Hector	p 315
Gómez, Martín	p 32
Gonçalves, Maria Helena	p 86, p 273, p 276
González Jorge, José Iván	p 172, p 229, p 154
González Rosell, Oscar	p 180
González-Fernández, Alfredo	p 257, p 217
Green, Christopher M	p 118
Guevara Amatón, Karla Victoria	p 75, p 241, p 62
Guzmán, Marcelo Nicolás	p 137, p 162
Hamer, Mariana	p 176
Hernandez Betanzos, Joaquin	p 257
Herrera, Santiago Esteban	p 184
Horcajo, Mariano Redondo	p 209
Horowicz, Brian	p 287
Izquierdo, David	p 62
Janeiro, Ana	p 176
Jotautienė, Eglė	p 213
Juárez, Agustín Nahuel	p 126
Kapadia, Sunil	p 294
Karayel, Davut	p 213
Kondratiuk, Nadia	p 225, p 233, p 237, p 244
Kramar, María Belén	p 248

Landini, Nicolò	p 253
Leidens, Leonardo Mathias	p 273, p 276
Lipovetzky, José	p 58
Lisarrague, Matilde	p 315
Lo Giudice, Agostina	p 49, p 52
Lombera, Esteban	p 322
Longo, Elson	p 253, p 283
Louro, Paula	p 326, p 330, p 307
Lozano, Alex	p 69, p 298, p 248, p 290
Lucero, Martín	p 287
Macchi, Carlos	p 279
Malagù, Cesare	p 253
Malatto, Laura	p 69, p 248
Mangano, Eliana Gabriela	p 69, p 248
Manqueros, Victor	p 75
Marchi, Edgardo	p 311
Marfa, Jennifer	p 106
Marinoni, Julián	p 298, p 290
Martí, Mercè	p 106, p 141, p 110
Martínez Bogado, Mónica	p 225, p 233, p 237, p 244
Martínez Ricci, María Luz	p 39
Mass, Mijal	p 298, p 290
Mato, German	p 58
Mattea, Facundo	p 169
Mazali, Italo O.	p 86
Mazzei, Matías E.	p 283
Medintz, Igor L	p 118
Medrano, Anahí	p 294
Mercado, Dante Guido	p 52, p 244
Mercado, Mauricio	p 315
Mercier, Pau	p 46
Mesas Gómez, Melania	p 106, p 141, p 110
Meschino, Gustavo Javier	p 137
Mieza, Ignacio	p 32
Millicovsky, Martín	p 43, p 36

Miscoria, Silvia	p 158
Molina Torres, M. Andrea	p 169
Molina, Tomás	p 69, p 248
Monroy, Andrea M.	p 130
Monsalve, Leandro	p 294
Monsalve, Yeison	p 104
Moraes, Leandro	p 315
Moreno de Oliveira, João Pedro	p 221
Moreno, Analía	p 225, p 233, p 237
Mosquera Ortega, Mónica	p 199, p 202, p 334
Moura, Francisco	p 279
Muñoz, Fernando F.	p 154
Muñoz, Gabriel	p 43, p 36
Murialdo, Silvia Elena	p 137, p 162
Nisenbaum, Melina	p 137, p 162
Núñez García, Javier Luis Mariano	p 267
Olima, José	p 237
Oliveira, Karoliny A.	p 195
Onna, Diego Ariel	p 39
Ormazábal, Aida	p 81
Orozco Holguín, Jahir	p 104, p 122
Orquiza de Carvalho, Daniel	p 133, p 221, p 93
Ortega, Pedro Paulo	p 279, p 253
Pacioni, Natalia L.	p 169
Pallarès-Rusiñol, Arnau	p 106, p 141, p 110
Pallarola, Diego	p 90, p 271
Peñalva, Albano	p 43, p 36
Pepino, Vinicius M.	p 221
Perez Cenci, Marianina	p 162
Piccoli, María Belén	p 114
Pividori Gurgo, Maria Isabel	p 106, p 141, p 110
Plaza, José Antonio	p 209, p 46
Poiasina, Mariana P.	p 264
Ponce, Maria Belen	p 130
Ponce, Miguel A.	p 279, p 253, p 283

Porras, Juan Carlos	p 106
Prado, Lara Eleonora	p 69
Puppo, Corina	p 315
Puyol Bosch, Mar	p 84, p 73, p 79, p 81
Raiger Lustman, Laura Judith	p 126
Ramírez, Gerardo	p 49
Ramirez, Silvana A.	p 130
Ramírez-Chavarría, Roberto G.	p 150
Reartes, Daiana Fernanda	p 191, p 158
Rebollo-Calderón, Beatriz	p 81
Reta, Juan	p 43, p 36
Ricalde, Damián	p 298, p 290
Rinaldi, Ana Laura	p 172, p 229, p 154
Riul Jr., Antônio	p 86, p 273, p 276
Riveral Lazú, Michael	p 318
Roberti, Mariano	p 298, p 290
Rocha, Leandro Silva Rosa	p 279
Rodrigues, V.	p 86
Rodríguez Campos, Theo	p 290
Rodríguez, Adrián	p 209, p 46
Rodriguez, Elena	p 146
Rodriguez, Marcela Cecilia	p 191, p 158
Roldán, Mònica	p 46
Roman, Augusto	p 52
Romero, Camila	p 176
Romero, Marcelo R.	p 169
Rondineau, Sebastien R. M. J.	p 93
Rosell-Ferrer, Javier	p 81
Rossi, Rosanna	p 106
Rossi, Sebastián	p 213
Rotta Ribeiro, Matheus	p 133, p 221, p 93
Rubio Scola, Ignacio	p 213
Sacco, Natalia Jimena	p 126
Saffioti, Nicolás	p 90
Salles, Federico	p 315

Sánchez, Ana	p 209
Sánchez, Ismael	p 100
Sánchez, Sergi	p 209
Santa Cruz, Gustavo	p 244
Šarauskis, Egidijus	p 213
Schaumburg, Federico	p 334
Sementa, Deborah	p 118
Serentill, Roger	p 146
Serra Padullers, Mireia	p 79
Serrano, Rachid Haddouchi	p 79
Sidlik, Walter	p 55, p 57
Silva-Neto, Habdias A.	p 195
Sobral, Santiago	p 172, p 229, p 154
Solis, Lara	p 49, p 52
Sosa, Griselda L.	p 130
Sotero Esteva, José O.	p 318
Sousa, Lucas R.	p 195, p 205
Souza, Mateus I. O.	p 221
Spagnoli, Elena	p 253
Steren, Laura B.	p 49, p 52
Stolowicz, Fabiana	p 205
Su, Bo	p 271
Suárez, Teresa	p 209
Susmel, Sabina	p 202
Tamasi, Mariana	p 225, p 233, p 237
Tohmé, Ana Laura	p 90
Tomac, Alejandra	p 162
Touloumdjian, Carolina Sofía	p 184
Ulijn, Rein V.	p 118
Urteaga, Raul	p 165
Valdés, Francisco	p 73, p 75, p 79, p 241, p 62
Vásquez Fonseca, Viviana	p 122
Vázquez, Patricia	p 209
Verissimo, Marta	p 65
Viaggio, Agustina	p 39

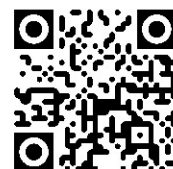
Vico, Raquel Viviana	p 114
Vieira Bueno, Renata	p 133
Vieira Neves, Daniel	p 133
Vieira, Manuel Augusto	p 326, p 330, p 307
Vieira, Manuela	p 326, p 330, p 307
Vieira, Pedro	p 326, p 330
Vlachovsky, Sandra	p 205
Vojnov, Adrián	p 205
Williams, Federico José	p 184
Ybarra, Gabriel	p 294
Yelicich, Bernardo	p 315
Zalazar, Martín	p 43, p 36
Zamora-Carreras, Héctor	p 209
Zamudio Interian, Jomahi Enrique	p 217
Zirpoli, Alexandre Simoes	p 279, p 253
Zonta, Giulia	p 253



**IBER
SENSOR** 
2024 13° CONGRESO
IBEROAMERICANO
DE SENSORES
Buenos Aires
21 al 24 octubre

IBERSENSOR es un foro de la comunidad científica de habla hispana y portuguesa, que trabaja en áreas de desarrollo de sensores de todo tipo y sus aplicaciones.

En esta edición la sede anfitriona fue el Instituto Nacional de Tecnología Industrial - INTI, Buenos Aires, Argentina.



ISBN 978-950-532-547-4



www.inti.gov.ar consultas@inti.gov.ar 0800 444 4004